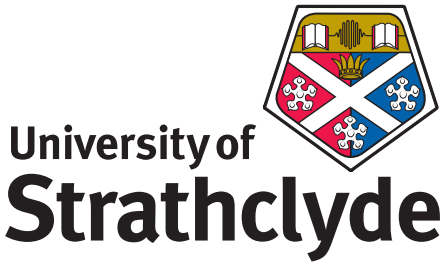

Reduced-order modelling of electrohydrodynamic flows on a circular cylinder

Rebecca Anne McKinlay

Department of Mathematics and Statistics
University of Strathclyde
Glasgow, UK
March 2024

Submitted to the University of Strathclyde for the degree of Doctor of Philosophy in the Faculty of Science.

The work presented in this thesis is the result of the author's original research which has been carried out at the University of Strathclyde between October 2019 and September 2023 under the supervision of Dr Alexander W. Wray and Professor Stephen K. Wilson. I declare that no parts of the work herein have been previously submitted for examination which has led to the award of a degree or any other qualification at the University of Strathclyde or at any other institution.

Acknowledgements

I would like to express my sincerest gratitude to my supervisors, Dr Alexander Wray and Professor Stephen Wilson, for their mentorship and guidance. Alex, thank you for your constant support, expertise, and, most importantly, your patience to explain the difficult (and simple) concepts. Stephen, thank you for your advice, knowledge, and critique which always kept this work in the right direction.

Thank you to the Carnegie Trust for the Universities of Scotland for awarding me the scholarship that has supported my research, and to the Department of Mathematics and Statistics at the University of Strathclyde for funding my visit to Indianapolis, USA to present my research at the 75^{th} Annual Meeting of the American Physical Society Division of Fluid Dynamics. I would also like to extend my thanks to Dr David Pritchard and Dr David Sibley for examining this thesis.

I must give thanks to my exceptional secondary school mathematics teacher, Mr Kevin McCann. I would not be where I am today if it weren't for your invaluable guidance and contagious enthusiasm which undoubtedly set me on the right path.

Thank you to all of my friends who have supported and uplifted me over the last four years. In particular, thank you to my best friend, Beth, for always being on my side, no matter how far apart we are. James, thank you for all the moral support. I couldn't have done any of this without you. Thank you to Erika, Florence, Kayleigh, Silvia, and Anai. Thank you Cameron, Lauren, Rachel, and Jocelyn for all the support and all the laughs. Your friendship has been indispensable.

Above all, thank you to my wonderful partner, Beth. You have helped me beyond what I could possibly attempt to express in words. This thesis would not exist without your unfaltering kindness, endless patience, love, and encouragement over the last four years. You got me through it. Thank you for everything.

Finally, this thesis is dedicated to my amazing mum and dad. Thank you for your eternal and unwavering belief in me. I am proud and grateful beyond words to have parents as kind, loving, and generous as you.

Abstract

This thesis concerns the theoretical modelling and analysis of a two-dimensional film of a perfectly conducting Newtonian liquid coating a uniformly rotating horizontal cylindrical electrode. The system is enclosed by a concentric outer electrode, with the electric potential difference between the inner and outer electrodes inducing electrostatic forces at the liquid-gas interface.

The system is investigated for both thin and thick films. A thin-film model, derived using a classical lubrication approximation, incorporates the effects of rotation, gravity, viscosity, capillarity, and electric stress, whilst a thick-film model, derived using long-wave scalings and the method of weighted residuals, also includes the additional effects of viscous dissipation and inertia.

First, as an essential precursor to the electrostatic case, the thin-film model is studied in the absence of an electric field in the case in which the inner electrode is stationary. A complete description of the late-time asymptotic behaviour of the film is derived that reveals three distinct regions of behavior, with the interplay between gravity and capillarity resulting in a capillary-ripple structure.

Next, the full thin-film model is studied. For a stationary inner electrode, under conditions of weak electrostatic effects, the qualitative behavior is unchanged from the situation in which the electric field is absent. For a rotating inner electrode, a numerical parametric study reveals four distinct behaviors: steady, periodic, transient, and outer contact (in which the film touches the outer electrode in a finite time). Linear stability and multiple-timescale analyses are performed and reveal that electrostatic effects induce instability, leading to outer contact.

Finally, the full thick-film model is investigated, revealing qualitatively similar behaviour to that in the thin-film case. The spatiotemporal distribution of the electric potential at the outer electrode is used to control the flow and, in particular, the interface is successfully controlled towards complex target shapes using optimal control.

Contents

Chapter 1

Introduction

In Sections 1.1–1.7, we give a review of the current literature and background theory regarding the subjects which form the basis of the research described in this thesis. An overview of the contents of this thesis is provided in Section 1.8, and the peer-reviewed publication and conference presentations that have arisen from the results derived in it are listed in Section 1.9.

1.1 Free-surface flows

"Free-surface flow" refers to the flow of a fluid in which one or more of the surfaces bounding the fluid are free to move, and hence whose positions are not known *a priori* and must be determined as part of the solution.

Free-surface flows have been the subject of a large number of scientific investigations [1–5] due to their central importance in a variety of contexts, as well as being of intrinsic scientific interest in their own right. For example, they are vital to our understanding of a wealth of natural geophysical and biological processes such as the flow of lava [6], avalanches [7], and mud [8], in water transport in plants [9], and the flow of liquid water on earth (for example, the flow of rivers [10], oceans [11], glacial meltwater [12, 13], tsunamis [14], and waterfalls [15]). For example, Figure 1.1 (a) shows an example of a free-surface flow, namely, an indoor waterfall. Free-surface flows are also of fundamental significance in a vast range of industrial settings such as in nanotechnology [17], chemical process engineering [18], and in a wealth of contexts in the marine, aerospace, and automotive industries. For example, liquid can move around in partially-filled cargo tanks

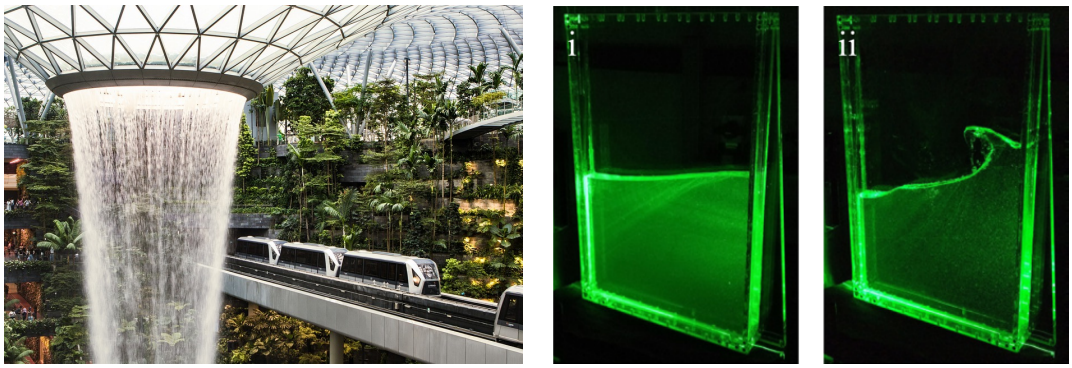

(a) (b)

Figure 1.1: (a) The tallest indoor waterfall in the world, located in Jewel Changi Airport, Singapore. Image adapted from Pixabay. Pixabay License https://pixabay.com/service/terms/#license. (b) Experimental sloshing states of water in a rectangular container shown in (i) planar and (ii) wave breaking motion. Reproduced from Bäuerlein and Avila [16], with permission from Cambridge University Press. Copyright 2021.

on ships [19] and in the fuel tanks of cars [20] and aeroplanes [21], a behaviour referred to as "sloshing". Sloshing involves complex free-surface flows which must be understood as part of successful tank design in order to ensure stable vehicle performance [22]. An experimental example of sloshing is shown in Figure 1.1 (b) [16]. Another example of industrial free-surface flow arises in the aerospace industry, in which the shape of the free surface of seas and oceans significantly affects emergency water-landing performance. Thus, precise modelling of various water conditions is vital for accurate simulations during early aircraft design stages [23, 24].

Free-surface flows are particularly complicated to understand due to the fact that, as mentioned earlier, the location of the interfaces are not known *a priori*, and hence must be determined as part of the solution to the governing equations of the particular system under investigation. In this thesis, we focus on the free-surface flow of incompressible Newtonian fluids, which are governed by the incompressible Navier–Stokes equations [25, 26], namely,

$$\nabla \cdot \mathbf{u} = 0, \tag{1.1.1}$$

$$\rho \frac{\mathrm{D}\mathbf{u}}{\mathrm{D}t} = -\nabla p + \mu \nabla^2 \mathbf{u} + \rho \mathbf{g}, \tag{1.1.2}$$

where ρ and μ are constants which denote the fluid density and dynamic viscosity, respectively, p and $\mathbf{u}$ are functions of space and time (where time is denoted by t) which denote the fluid pressure and the velocity vector field, respectively, $\mathbf{g}$ denotes acceleration due to gravity, and $\mathrm{D}/\mathrm{D}t = \partial/\partial t + \mathbf{u} \cdot \nabla$ is the material derivative. Equation (1.1.1) is referred to as the "continuity equation" and represents the conservation of mass within the fluid, whilst equation (1.1.2) is often referred to as the "momentum equation" and describes the conservation of momentum within the fluid. The Navier–Stokes equations (1.1.1) and (1.1.2) constitute a system of challenging nonlinear partial differential equations (PDEs). Due to their inherent complexity, they are widely recognised as being difficult to solve directly (indeed, proving the existence and smoothness of their solutions is one of the seven Millennium Prize Problems formulated by the Clay Mathematics Institute [27]). Performing Direct Numerical Simulations (DNS) of the Navier–Stokes equations (1.1.1) and (1.1.2) can have prohibitively high computational costs (often having wall-clock runtimes of weeks or months), whilst analytical solutions are only possible in a small number of restricted special cases. However, there are various mathematical simplifications that can be applied in order to render the Navier–Stokes equations more amenable to analysis. In this thesis, in the context of free-surface flows, we focus on the development of "reduced-order models".

1.2 Reduced-order modelling of free-surface flows

The motivation for constructing high-fidelity reduced-order models is twofold: firstly, to provide quantitatively accurate descriptions of the dynamics of fluid systems at a significantly reduced computational cost, and secondly, to facilitate the interpretation of system dynamics through analytical investigations. A widely adopted technique for the development of reduced-order models involves leveraging inherent differences in length scales within the system, whenever they exist. These differences give rise to one or more small aspect ratios, which can be used to simplify the Navier–Stokes equations by transforming them into an asymptotically-reduced structure, yielding simplified equations which can be treated as locally unidirectional. Reduced-order models complement physical experiments and DNS, allowing for detailed investigations of underlying phenomena.

This thesis focuses on studying the flow of liquids on curved surfaces, particularly cylindrical substrates. However, in order to establish the foundation for the

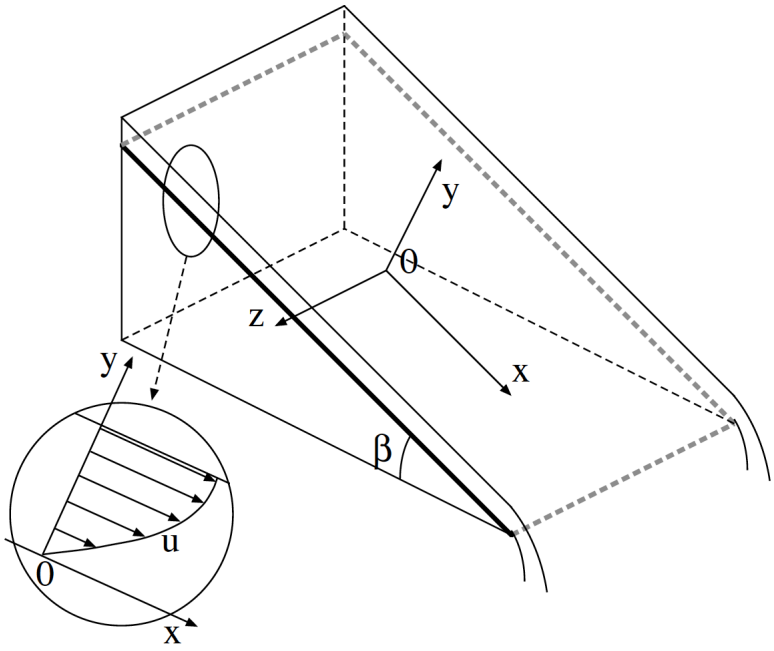

Figure 1.2: Geometry of the system considered in Section 1.2, namely, a falling film on an inclined plane, as considered by Ruyer–Quil and Manneville [29]. Reproduced from Ruyer–Quil and Manneville [29], with permission from Springer Nature. Copyright 2000.

modelling techniques used later, we first explore various methods of developing reduced-order models in a simpler context. Specifically, we discuss the relevant aspect ratio along with what is commonly referred to as the hierarchy of reduced-order models in the context of a falling film (i.e., flow driven by gravity in which liquid flows down the surface of a substrate to form a thin film) on an inclined plane in Sections 1.2.1–1.2.5 (see Kalliadasis *et al.* [28] for a comprehensive explanation of the models discussed herein). Throughout this section, we follow the notation and nondimensionalisation of Ruyer–Quil and Manneville [29]. Accordingly, the geometry considered in this section is shown in Figure 1.2 [29]. The inclined plane makes an angle β to the horizontal and x, y, and z denote the streamwise, cross-stream, and spanwise directions, respectively. Throughout this section, we restrict ourselves to the two-dimensional case in which the solution is independent of z. This simple system is a paradigm problem for more complicated free-surface flows, and has therefore been widely studied and referenced in the literature [28, 29], making it an ideal problem for introducing and discussing

reduced-order models. Moreover, the techniques discussed in this section can be extended to more complex scenarios, such as three-dimensional flow [29] and flow over non-planar geometries [30, 31].

1.2.1 Aspect ratio of flow on a planar substrate

In this section, we discuss the relevant aspect ratio of flow on a planar substrate. Note that for ease of comparison with the aspect ratios of flow on a curved substrate, which are discussed later in Section 1.4.1, throughout this section we (unconventionally) phrase our discussion in terms of nondimensional parameters, but choose not to specify the particular length scale used in the nondimensionalisation (which could be, for example, a capillary length).

In the case of two-dimensional flow on a planar substrate, there are only two length scales present within the system: a characteristic dimensionless cross-stream length scale (typically a characteristic dimensionless film thickness), which we shall denote here by H, and a characteristic dimensionless streamwise length scale (typically a characteristic dimensionless wavelength of the film), which we shall denote here by λ. In contrast to flows on curved substrates (which we discuss in Section 1.4.1), here, the characteristic radii of curvature of the substrate are infinite. Hence, the substrate has zero curvature which can therefore be ignored.

There are two situations in which a disparity in length scales within the flow typically arises, and hence there are two ways to define the aspect ratio. The first is what we shall refer to hereafter as a "thin-film approximation", in which the thickness of the film is assumed to be small (compared to unity). In other words,

$$\lambda = O(1), \qquad \delta_{\text{thin}} = H \ll 1, \tag{1.2.1}$$

where δ_{thin} denotes the thin-film aspect ratio. A schematic of the relationship between the two length scales present for flow on a planar substrate in the thin-film approximation is shown in Figure 1.3 (a). On the other hand, the second is what we shall refer to hereafter as a "long-wave approximation", in which the length of the variations in the film thickness are assumed to be large (compared to unity). In other words,

$$H = O(1), \qquad \delta_{\text{long}} = \lambda^{-1} \ll 1, \tag{1.2.2}$$

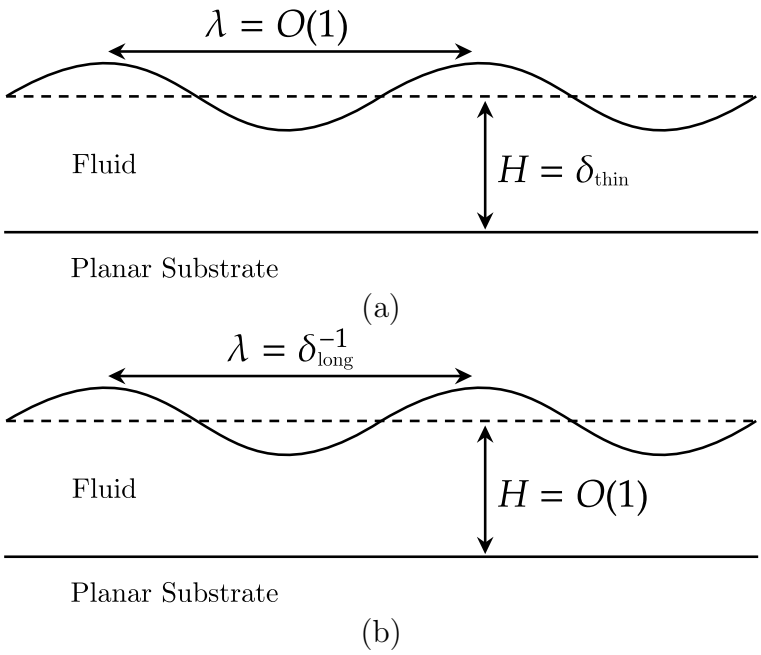

Figure 1.3: Schematic of the relationship between the two length scales H and λ present for flow on a planar substrate. (a) Thin-film approximation. (b) Long-wave approximation.

where δ_{long} denotes the long-wave aspect ratio. A schematic of the relationship between the two length scales present for flow on a planar substrate in the long-wave approximation is shown in Figure 1.3 (b). Clearly, for a planar substrate (such as that considered here) these two situations are equivalent, and so the terms "thin-film" and "long-wave" can be (and are often) used interchangeably. However, for a non-planar substrate this is no longer the case due to the introduction of additional length scales, and we need to be careful to distinguish between the two approximations. We defer further discussion of this key point until Section 1.4.1 in which we discuss the aspect ratios for flow on a cylindrical substrate.

For brevity, throughout the remainder of this section (in which we only discuss flow on a planar substrate) we exclusively use the terminology "thin-film approximation" and drop the subscripts on δ and refer to the planar aspect ratio as simply $\delta \ll 1$.

1.2.2 Gradient expansion method

We begin in this section by discussing the simplest form of reduced-order model. Applying a thin-film approximation to the Navier–Stokes equations (1.1.1) and (1.1.2) yields a system of PDEs which can be solved order-by-order via a standard perturbation expansion in powers of δ. In the literature on the hierarchy of reduced-order models, a standard perturbation expansion of this form is widely referred to as a "gradient expansion" (a historical artefact originating from early studies [29]) in order to distinguish between this classical method and the alternative perturbation methods which are described in Sections 1.2.4 and 1.2.5. Hence, for consistency with the existing literature, we shall adopt the nebulous term "gradient expansion" throughout this thesis.

The gradient expansion method leads to a single equation which describes how the dimensionless film thickness, denoted by $h = h(x,t)$, changes in space and time (where t denotes dimensionless time). Benney [32] was the first to use this method to describe a falling film on an inclined plane. Hence, the resulting model has come to be known as the "Benney equation", namely,

$$h_t + \left[\frac{1}{3}h^3 + \delta\left(\frac{2}{15}h^6 h_x - \frac{B}{3}h^3 h_x + \frac{\Gamma'}{3}h^3 h_{xxx}\right)\right]_x = 0. \tag{1.2.3}$$

The parameter $\Gamma' = \sigma\rho^{1/3}/(\mu^{4/3}(g\sin\beta)^{1/3})$ is a Kapitza number which is a dimensionless group combining certain powers of what was termed by Kapitza [33] as the "kinematic surface tension" (i.e., the constant surface tension coefficient of the free surface σ divided by the fluid density ρ), the kinematic fluid viscosity (i.e., the dynamic fluid viscosity μ divided by the fluid density), and acceleration due to gravity g. Note that, despite the fact that equation (1.2.3) is known as the Benney equation, in the original equation derived by Benney [32], the surface tension term did not actually appear in their equation because it arises at third order in δ. However, subsequent studies have demonstrated the critical importance of including surface tension effects at first order [4, 5], hence it is common to assume that the surface tension parameter is large enough such that it enters equation (1.2.3) at first order in δ. In other words, the original (unscaled) Kapitza number, denoted by Γ, has been rescaled as $\Gamma' = \delta^2\Gamma$ in deriving equation (1.2.3), where

$\Gamma' = O(1)$. The dimensionless parameter

$$B = \cot\beta \tag{1.2.4}$$

compares the cross-stream and streamwise components of the gravitational force. In particular, B quantifies the contribution of the hydrostatic pressure gradient, which vanishes for flow down a vertical wall (i.e., $B = 0$ when the wall is vertical such that $\beta = \pi/2$). Following the notation and nondimensionalisation of Ruyer–Quil and Manneville [29], the Reynolds number is defined as $Re = h_N^3/3$, where h_N is the dimensionless thickness of the uniform base state of the flow. This base state is often referred to as the "Nusselt flat film solution" and corresponds to a flow with a semi-parabolic velocity profile $u = u_N$ as obtained by Nusselt [34, 35],

$$u_N = h_N y - \frac{1}{2}y^2. \tag{1.2.5}$$

The leading-order term in the square bracket in equation (1.2.3) represents the convective effect of gravity, whilst the first-order terms represent inertial, gravitational, and capillary effects (namely, the second, third, and fourth terms in the square bracket, respectively).

The Benney equation (1.2.3) is successful in capturing the critical Reynolds number for the onset of instability (often referred to as the "instability threshold") obtained from the linearised Navier–Stokes equations (known as the Orr–Sommerfeld equations) which shows that solutions are unstable for $Re_{\text{crit}} \geq 5B/6$ [28]. However, Pumir *et al.* [36] identified that the Benney equation (1.2.3) has a significant drawback in that solutions experience spurious unphysical "blowup" close to the instability threshold, even in the presence of the regularising effects of surface tension. In particular, the film thickness h becomes infinite in a finite time, a non-physical behaviour which does not, of course, occur in experiments or in DNS of the full Navier–Stokes equations [37]. The occurrence of blowup is a direct consequence of the highly nonlinear inertial term $(h^6 h_x)_x$ contained in equation (1.2.3). Blowup occurs for moderate to large inertial effects; specifically, it occurs when the Reynolds number exceeds a limiting value which is greater than, but close to, the instability threshold Re_{crit}. The exact value of the Reynolds number at which blowup occurs depends on the Kapitza number Γ' and the inclination angle of the plane β, but typically is of order unity [28, 38]. The blowup

phenomenon persists even when higher-order terms are included in the gradient expansion, as this leads to the emergence of increasingly nonlinear terms [39, 40].

The main reason that the Benney equation (1.2.3) struggles to describe nonlinear behaviour for moderate to large Reynolds numbers is due to the fact that all flow variables are dependent on the film thickness (for example, the flux q is an explicit function of h, hence the velocity depends on h via q). In Sections 1.2.4 and 1.2.5, we show that introducing more degrees of freedom through averaging techniques allows us to describe the dynamics of the film sufficiently far from the instability threshold [29].

1.2.3 Weakly nonlinear method

Weakly nonlinear equations are, in general, more amenable to analysis than fully nonlinear equations. The weakly nonlinear model for a falling film on an inclined plane is widely known as the Kuramoto–Sivashinsky equation, which emerged as a result of Kuramoto's work on reaction-diffusion systems [41] and Sivashinsky's investigations into flame front propagation [42]. Sivashinsky and Michelson [43] applied weakly nonlinear theory to the Benney equation (1.2.3) in order to derive an evolution equation for h that is valid in the presence of inertia. They considered small interfacial perturbations about some uniform steady state $y = \bar{h}$ by setting $h = \bar{h} + \xi\check{h}$ in (1.2.3) where $\check{h} = \check{h}(x,t)$ and $\xi \ll 1$ are the shape and size of the perturbation, respectively. Additionally, they performed a Galilean transformation by rescaling the space and time variables x and t respectively as $\check{x} = x - t$ and $\check{t} = t$ in order to transform the equations into a moving frame of reference that removes the convective gravitational term but has no effect on the dynamics of the system. This yields the Kuramoto–Sivashinsky equation, namely,

$$\check{h}_{\check{t}} + \check{h}\check{h}_{\check{x}} + \check{h}_{\check{x}\check{x}} + \check{h}_{\check{x}\check{x}\check{x}\check{x}} = 0, \tag{1.2.6}$$

in which the second, third, and fourth terms represent gravitational, inertial, and capillary effects, respectively. Notably, unlike the Benney equation (1.2.3), the Kuramoto–Sivashinsky equation (1.2.6) does not exhibit blowup [29]. The Kuramoto–Sivashinsky equation (1.2.6) is applicable to a wide range of physical systems, such as interfacial flows [44, 45], and has also been widely used in control theory [46, 47] (which we discuss in Section 1.7). Previous analytical [48] and computational [43, 49, 50] studies have shown that solutions to the Kuramoto–

Sivashinsky equation (1.2.6) display a wealth of complex behaviour including periodic, quasi-periodic, and chaotic solutions. However, note that equation (1.2.6) relies on the assumption that the magnitude of the perturbation is small relative to the steady state $\bar{h}$, and, as a result, is only valid in this particular situation (this assumption could be appropriate for a system with, for example, high surface tension).

1.2.4 Integral boundary layer (IBL) method

Shkadov [51] introduced the integral boundary layer[1] (IBL) method in an attempt to address the blowup that arises in solving the Benney equation (1.2.3). Most attempts to accurately model flows with moderate Reynolds numbers revolve around relaxing the constraint that the velocity is a function of only the film thickness (i.e., relaxing the condition that $q = q(h)$). This is necessitated by the fact that in this regime, q (and potentially other parameters) evolve independently and cannot accurately be described as functions of h only [28]. Indeed, it can be seen from the Navier–Stokes equations (1.1.1) and (1.1.2) that u, for example, evolves independently. The IBL method combines the assumption of a semi-parabolic velocity profile within the film with the Kármán–Pohlhausen averaging method from aerodynamic boundary-layer theory [28, 29, 57], which was initially applied to film flows by Kapitza [33].

The first step of the IBL method is to apply a thin-film approximation to the Navier–Stokes equations (1.1.1) and (1.1.2) from which a boundary-layer equation, which we denote by $\mathcal{B}(u) = 0$, for the dimensionless streamwise velocity $u = u(x, y, t)$ is derived. Note that we do not give an account of the process of deriving a boundary-layer equation here as a comprehensive example of this process will be given in Chapter 2. The velocity u is assumed to always be of the same locally-parabolic form coinciding with the Nusselt flat film solution (1.2.5). The boundary-layer equation $\mathcal{B}(u) = 0$ is then integrated across the film thickness and evaluated subject to appropriate boundary conditions. This methodology yields a

[1]Note that the term "boundary layer" is used somewhat inaccurately here, as it does not describe a traditional high Reynolds number viscous boundary layer. Nevertheless, the equation that we derive shares structural resemblances to the Prandtl equation in boundary-layer theory [28]. Due to this parallel, the term has gained widespread acceptance in the literature [29, 31, 37, 52–56], leading us to adopt it in this thesis.

two-equation model for the film thickness h and the dimensionless volume flux,

$$q = q(x,t) = \int_0^h u \, \mathrm{d}y. \tag{1.2.7}$$

In the case of a falling film on an inclined plane, this process yields

$$\frac{5}{2}\frac{q}{h^2} - \frac{5}{6}h + \delta\left[\frac{5}{6}q_t + 2\frac{qq_x}{h} + \left(\frac{5B}{6}h - \left(\frac{q}{h}\right)^2\right)h_x - \frac{5\Gamma'}{6}h_{xxx}\right] = 0, \tag{1.2.8}$$

along with the integral form of the kinematic condition, namely,

$$h_t + q_x = 0. \tag{1.2.9}$$

Equations (1.2.8) and (1.2.9) constitute a closed system governing the evolution of the film thickness h and the flux q, and is known as "Shkadov's model" [29, 51]. As explained earlier in Section 1.2.2, to obtain equation (1.2.8), Shkadov [51] rescaled the original Kapitza number Γ as $\Gamma' = \delta^2\Gamma$, where $\Gamma' = O(1)$ and retained terms up to and including first order in δ. The first two terms in (1.2.8) correspond to streamwise gravitational acceleration and viscosity, respectively, the third, fourth, and sixth terms are inertial terms, and the fifth and final terms represent the stabilising effect of gravity and capillarity, respectively. Contrary to the Benney equation (1.2.3) in which all variables are dependent on h, the IBL method provides greater freedom to the velocity, allowing it to have its own evolution via q (which evolves independent of h). The solutions to Shkadov's model (1.2.8) and (1.2.9) remain free from blowup, and it has been shown to be successful in describing nonlinear regimes at moderate Reynolds numbers [28]. However, Shkadov's model (1.2.8) and (1.2.9) has its limitations: performing a gradient expansion on q (i.e., expanding q as $q = q_0 + \delta q_1 + \ldots$) in Shkadov's model and solving to first order in δ yields an expression for q that is inconsistent with the accurate expansion given by the Benney equation (1.2.3). In particular, the expression is identical to the terms in the square brackets in the Benney equation (1.2.3) with the exception of a coefficient of $1/9$ for the inertial term instead of the correct coefficient of $2/15$. This leads to an inaccurate estimation of the linear instability threshold, yielding $Re_{\mathrm{crit}} = B$ instead of $Re_{\mathrm{crit}} = 5B/6$ [28]. Hence, the IBL method fails to accurately predict flow behavior near the instability threshold, which therefore limits the use of Shkadov's model [28]. This issue arises from the

assumption of the semi-parabolic velocity profile because first-order corrections to the velocity profile play a crucial role in precisely predicting the instability threshold [58]. Some authors have attempted to rectify this disparity by including higher-order terms [59] or surface tension corrections [60] but were unsuccessful, with the inaccurate instability threshold being recovered in both cases. Hence, to overcome this limitation, a more precise treatment of the first-order terms is necessary [28, 61].

1.2.5 Weighted residual IBL (WRIBL) method

The limitations of the Benney equation (1.2.3) and Shkadov's model (1.2.8) and (1.2.9) were overcome by Ruyer–Quil and Manneville [29] who described a weighted residual IBL (WRIBL) approach. The WRIBL method extends the IBL method by combining a gradient expansion with a weighted residual technique which uses polynomials in y as test functions. This results in models that offer an efficient, yet highly precise, means of describing the flow dynamics.

In the WRIBL method, δ is considered to be an "ordering" parameter: specifically, it is used to assert the expected relative magnitudes of particular terms and their derivatives during the calculations rather than having an explicit value of its own, and hence is set equal to unity in the final model. This approach has been used and validated extensively by many authors including Ruyer–Quil *et al.* [29, 52, 62, 63], Kalliadasis *et al.* [28, 54], Scheid *et al.* [37], Oron and Heining [53], Thompson *et al.* [64, 65], and Wray *et al.* [31, 56]. As in the IBL method explained in Section 1.2.4, the first step of the WRIBL method is to derive a boundary-layer equation. In the case of a two-dimensional falling film on an inclined plane, to second order in δ this is given by

$$\begin{aligned}\mathcal{B}(u) = &-(u_{yy}+1)+\delta\left(u_t+uu_x+vu_y+Bh_x-\Gamma' h_{xxx}\right)\\ &-\delta^2\left[2u_{xx}+\left(u_x|_{y=h}\right)_x\right]+O(\delta^3)=0,\end{aligned} \tag{1.2.10}$$

where v can be written in terms of u as $v=-\int_0^y u_x\,\mathrm{d}y$ from the continuity equation (1.1.1) [29]. The tangential stress balance at the interface is

$$\left(u_y\right)_{y=h}=\delta^2\left[4h_xu_x-v_x\right]_{y=h}, \tag{1.2.11}$$

the no-slip and no-penetration conditions are

$$u|_{y=0} = v|_{y=0} = 0, \tag{1.2.12}$$

and the kinematic condition is

$$(h_t + uh_x - v)\,|_{y=h} = 0. \tag{1.2.13}$$

The improvement in the performance of the IBL method over the gradient expansion method rests on the treatment of the leading-order viscous term u_{yy} in equation (1.2.10). As we shall see, the WRIBL method produces models that correctly predict the linear stability threshold, do not experience blowup, and correctly describe the nonlinear dynamics for a broader range of Reynolds numbers than the Benney equation (1.2.3). It has been shown to be successful in describing the dynamics of falling films on vertical and inclined planes for intermediate Reynolds numbers [28], and has subsequently been used by many authors in various contexts [37, 52, 63, 66, 67], most relevant to the work in this thesis being the recent work by Wray *et al.* [31, 56] which will be discussed in detail in Section 1.4.4.

Ruyer–Quil and Manneville [29] formulated three WRIBL models: a two-equation system that is accurate to $O(\delta)$ (referred to as the "first-order WRIBL model"), a four-equation system that is accurate to $O(\delta^2)$ (referred to as the "full second-order WRIBL model"), and a two-equation system which is a hybrid between the two previous models in terms of complexity and accuracy (referred to as the "simplified second-order WRIBL model"). We discuss each of these in turn in Sections 1.2.5.1–1.2.5.3.

1.2.5.1 First-order model

To outline the WRIBL method, we begin by deriving a model that is accurate to first order. Following the methodology proposed by Ruyer–Quil and Manneville [29], we seek a solution for u in the form of a series expansion based on a separation of variables,

$$u(x,y,t) = a_0(x,t)f_0(y) + \delta\sum_{n=1}^{N} a_n^{(1)}(x,t)f_n^{(1)}(y) + O(\delta^2), \tag{1.2.14}$$

where the f_0 and $f_n^{(1)}$ (for $n = 1, \ldots, N$) are chosen test functions that form a complete set of basis functions in the cross-stream coordinate y for the space of sufficiently smooth functions such that $0 \leq y \leq h$ which satisfy the no-slip and no-penetration conditions (1.2.12), the tangential stress condition (1.2.11) to leading order, and the kinematic condition (1.2.13). The "(1)" superscript denotes that the terms are first order in δ. Specifically, the leading-order solution for u, which we denote by u_0, namely,

$$u_0(y) = hy - \frac{1}{2}y^2, \tag{1.2.15}$$

requires choosing $f_0(y) = u_0$, where the a_0 and $a_n^{(1)}$ (for $n = 1, \ldots, N$) are amplitudes which are to be determined. Note that when the film is uniform, the velocity distribution is semi-parabolic and every amplitude $a_n^{(1)}$ (for $n = 1, \ldots, N$) vanishes (except for a_0). Therefore, the $a_n^{(1)}$ terms account for the deviation of the velocity profile from the leading-order semi-parabolic solution (1.2.15) induced by the deformations of the interface [28]. In principle, the a_0 and $a_n^{(1)}$ (for $n = 1, \ldots, N$) can be determined by substituting the expansion (1.2.14) into the boundary-layer equation (1.2.10) and matching powers of y. However, this is, in general, an onerous process, even at first order [29, 55]. Ruyer–Quil and Manneville [29] showed that this procedure may be simplified significantly by the use of a weighted integral method. Specifically, we assume that the function space is equipped with an inner product, defined as

$$\langle \alpha_1, \alpha_2 \rangle = \int_0^h \alpha_1 \alpha_2 \, \mathrm{d}y, \tag{1.2.16}$$

for some functions $\alpha_{1,2}$. We use weight functions $w_j = w_j(x, y, t)$ (for $j = 0, \ldots, J$), which are to be determined, to define the residuals $\mathcal{R}_j = \mathcal{R}_j(x, t)$ (for $j = 0, \ldots, J$) as

$$\mathcal{R}_j = \langle w_j, \mathcal{B}(u) \rangle \quad \text{for} \quad j = 0, \ldots, J, \tag{1.2.17}$$

where u is given by (1.2.14) and $\mathcal{B}(u)$ is given by (1.2.10) (neglecting second order terms). Setting the residuals (1.2.17) to zero (i.e., setting $\mathcal{R}_j = 0$) yields a system of $J + 1$ equations for the $N + 1$ amplitudes a_0 and $a_n^{(1)}$ (for $n = 1, \ldots, N$). Hence, in general, we require $J = N$ [29].

The particular weighted residuals method is determined by the selection of the weights w_j. Common methods include the collocation method, the method of moments, and the Galerkin method, each using specific weight functions: dirac delta functions for the collocation method, polynomials in y/h for the method of

moments, and the test functions directly for the Galerkin method [28]. Increasing the number of residuals (i.e., increasing the value of J) expedites the convergence to the solution [28].

Upon truncating the boundary-layer equation (1.2.10) at first order in δ, calculation of the residuals (1.2.17) yields

$$\mathcal{R}_j = \int_0^h w_j(y) \left[-(u_{yy}+1) + \delta \left(u_t + uu_x + vu_y + Bh_x - \Gamma' h_{xxxx}\right)\right] \, \mathrm{d}y. \quad (1.2.18)$$

Whilst different weights w_j will yield different systems of equations, all will ultimately produce the same coefficients [29]. However, as we shall see, a judicious choice of the weights can make determination of the velocity substantially simpler. The key point in determining the optimum choice of weights w_j arises from the following: by (1.2.14), the $a_n^{(1)}$ terms (for $n = 1, \ldots, N$) are already first order in δ, and hence can only enter the first-order truncation of equation (1.2.18) via the leading-order viscous term u_{yy}. Hence, if this term can be written explicitly without the $a_n^{(1)}$ (for $n = 1, \ldots, N$), then they will not appear anywhere in the first-order truncation of equation (1.2.18), and hence the need to determine the $a_n^{(1)}$ and $f_n^{(1)}$ (for $n = 1, \ldots, N$) will have been completely avoided. Calculation of the weighted average of the leading-order viscous term u_{yy} yields

$$\int_0^h w_j(y) u_{yy} \, \mathrm{d}y = -\left[w_j u_y\right]_{y=0} - \left[u(w_j)_y\right]_{y=h} + \int_0^h u(w_j)_{yy} \, \mathrm{d}y, \quad (1.2.19)$$

where we have used two applications of integration by parts and applied the no-slip condition (1.2.12) and tangential stress balance (1.2.11). As mentioned earlier, in general, the number of weights that are required is equal to the number of basis functions (i.e., $J = N$) [29]. However, notably, a single weight function, w_0, suffices if we select this specific weight function in a manner that removes the dependence of the right-hand side of (1.2.19) on the $a_n^{(1)}$ (for $n = 1, \ldots, N$). In particular, we choose w_0 such that

$$w_0|_{y=0} = 0, \quad \left[(w_0)_y\right]_{y=h} = 0, \quad (w_0)_{yy} = c, \quad (1.2.20)$$

for some non-zero constant c, which is free to be chosen. The first and second conditions in (1.2.20) are chosen such that the first and second terms in (1.2.19) are zero, respectively, and the final condition is chosen such that the final term in

(1.2.19) reduces to exactly the flux (1.2.7) for $c = -1$. Solving the system (1.2.20) with the particular choice $c = -1$ yields the weight function,

$$w_0 = hy - \frac{1}{2}y^2, \tag{1.2.21}$$

which is identical to the leading-order solution f_0 (1.2.15). Indeed, as we recall, f_0 corresponds to the solution u_0 to the leading-order problem for the velocity,

$$u_0|_{y=0} = 0, \quad [(u_0)_y]_{y=h} = 0, \quad (u_0)_{yy} = -1. \tag{1.2.22}$$

Therefore, when we take into account the two instances of integration by parts used to derive (1.2.19), the likeness between the weight w_0 and the test function f_0 can be linked to the self-adjoint nature of the linear operator $L \equiv \partial_{yy}$ in the space of functions satisfying the boundary conditions (1.2.22) [28, 29, 56].

With this choice of w_0, this corresponds to the Galerkin weighted residual method, wherein, as mentioned earlier, the test functions are used as the weight functions [29, 56, 57]. The Galerkin method is the most efficient WRIBL method, leading to a minimum amount of algebra [28, 62]. Note that it is not always the case that the weight functions and test functions coincide: in some geometries, the operator of the leading-order viscous term is not self-adjoint, resulting in a disparity between the test functions and the basis functions [29].

In practice, it is more convenient to eliminate a_0 (which has no physical significance) in favour of the flux q (1.2.7) as this is a quantity which can be measured physically and, in addition, simplifies the resulting equation. Substituting the expansion for u (1.2.14) into (1.2.7) and truncating to first order yields an expression for a_0 in terms of q, namely,

$$a_0 = \frac{q - \delta \sum_{n=1}^{N} a_n \int_0^h f_n^{(1)} \, \mathrm{d}y}{\int_0^h f_0 \, \mathrm{d}y}. \tag{1.2.23}$$

Hence, evaluating the zeroth residual $\mathcal{R}_0 = \langle w_0, \mathcal{B}(u) \rangle$ and setting it equal to zero yields

$$\frac{5}{2}\frac{q}{h^2} - \frac{5}{6}h + \delta \left[q_t + \frac{17}{7}\frac{qq_x}{h} + \left(\frac{5B}{6}h - \frac{9}{7}\left(\frac{q}{h}\right)^2 \right) h_x - \frac{5\Gamma'}{6}h_{xxx} \right] = 0, \tag{1.2.24}$$

where a_0 has been eliminated in favour of q (1.2.23) [29, 52]. Equation (1.2.24)

along with the integral form of the kinematic condition (1.2.9) constitute a closed system governing the evolution of the film thickness h and the flux q, and is known as the "first-order WRIBL model". Note that this model resembles Shkadov's model (1.2.8) and (1.2.9) but with different numerical coefficients for the inertial terms. Specifically, the third, fourth, and sixth terms in equation (1.2.24) have different coefficients than the corresponding terms in equation (1.2.8). Indeed, Shkadov's model is a particular case of a simple weighted residuals modelling approach; if we instead choose $w_0 = 1$ rather than (1.2.21) then evaluation of $\mathcal{R}_0 = \langle 1, \mathcal{B}(u) \rangle$ recovers Shkadov's model (1.2.8) and (1.2.9).

The first-order WRIBL model does not exhibit blowup and, upon performing a gradient expansion on q, recovers the Benney equation (1.2.3), and hence accurately predicts the linear instability threshold. Notably, as a result of incorporating deviations from the semi-parabolic profile into the velocity field, it also captures nonlinear flow characteristics well [28, 29]. Figure 1.4 shows the results of Cimpeanu *et al.* [68] who compared results from the first-order WRIBL model (1.2.9) and (1.2.24) with those from the Kuramoto–Sivashinsky equation (1.2.6) (with slightly different coefficients due to differences in scalings), showing that the WRIBL model yields excellent agreement with DNS.

1.2.5.2 Full second-order model

Ruyer–Quil and Manneville [29] also developed a model that is accurate to second order which, in particular, incorporates the second-order viscous terms. The derivation of this extended model is cumbersome, hence here we only outline the key points and refer the reader to Ruyer–Quil and Manneville [29] or Kalliadasis *et al.* [28] for a comprehensive description.

The first key step is to determine the minimum number of polynomials that are required to provide an expression for u that is accurate to first order, which corresponds to the number of independent fields that are needed to ensure consistency at second order (for example, in Section 1.2.5.1, only one extra field, q, was necessary in addition to h to ensure consistency at first order). Ruyer–Quil and Manneville [29] showed that only two additional fields are necessary to ensure consistency at second order. We seek a solution for u in the form of a series expansion

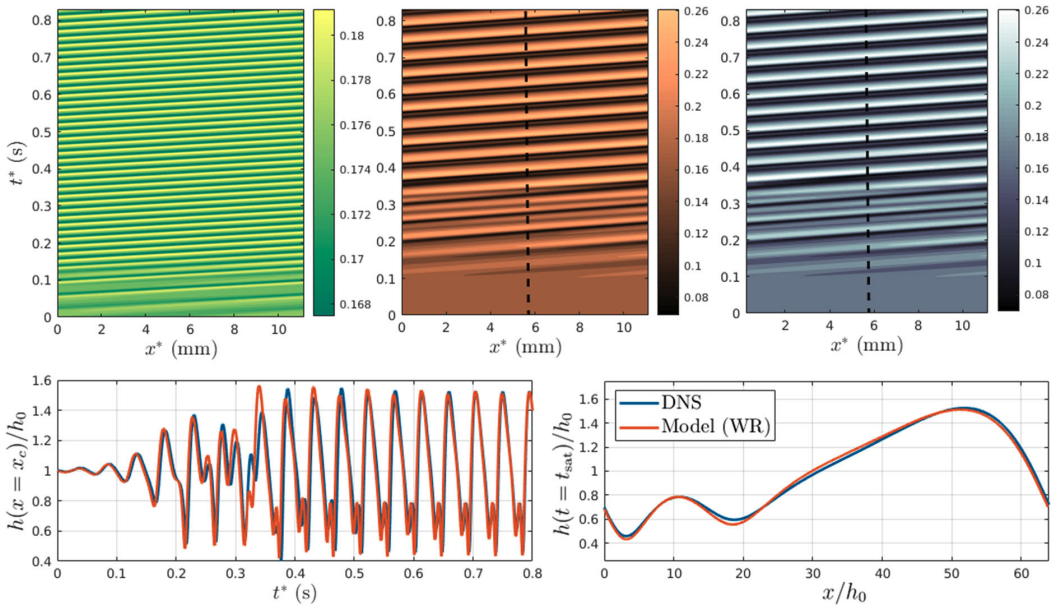

Figure 1.4: Results of calculations by Cimpeanu *et al.* [68]. The top panel shows (left-to-right) the film thickness as obtained from calculations based on the Kuramoto–Sivashinsky equation (1.2.6), the first-order WRIBL model (1.2.9) and (1.2.24), and DNS. The bottom left-hand panel shows the evolution of the film thickness and the bottom right-hand panel compares saturated interface shapes, both for the first-order WRIBL model (1.2.9) and (1.2.24) (orange) and DNS (blue). Reproduced from Cimpeanu *et al.* [68], with permission from Springer Nature. Copyright 2021.

based on a separation of variables,

$$u(x,y,t) = a_0(x,t)f_0(y) + \delta \sum_{n=1}^{N} a_n^{(1)}(x,t)f_n^{(1)}(y) + \delta^2 \sum_{m=1}^{M} a_m^{(2)}(x,t)f_m^{(2)}(y) + O(\delta^3), \tag{1.2.25}$$

where, analogous to the $f_n^{(1)}$ and $a_n^{(1)}$ in Section 1.2.5.1, the $f_m^{(2)}$ and $a_m^{(2)}$ (for $m = 1, \ldots, M$) are chosen test functions and amplitudes, respectively, which are to be determined, and the "(1)" and "(2)" superscripts denote that the terms are first and second order in δ, respectively. In a similar manner to the first-order case, an optimum choice of weight functions w_j can make evaluation of the residuals (1.2.17) significantly simpler by avoiding the requirement to compute the $f_m^{(2)}$ and $a_m^{(2)}$ (for $m = 1, \ldots, M$). To obtain an expression for u (1.2.25) that is accurate to first order, we must determine a_0 and some of the $a_n^{(1)}$ and $f_n^{(1)}$ (for $n = 1, \ldots, N$). We omit the algebraic details here and note only that Ruyer–Quil and Manneville [29] showed that at first order u involves three basis functions, which we denote here by F_0, F_1, and F_2, and hence can be written as

$$u = a_0(x,t)F_0(y) + \delta \left[a_1^{(1)} F_1(y) + a_2^{(1)} F_2(y) \right] + O(\delta^2). \tag{1.2.26}$$

where $F_0 = f_0$, F_1 is a linear combination of f_0 and $f_n^{(1)}$ for $n = 1, 2$, and F_2 is a linear combination of f_0 and $f_n^{(1)}$ for $n = 1, 2, 3, 4$. Since u given by (1.2.26) involves three basis functions, it therefore requires three weight functions w_j for $j = 0, 1, 2$. As a result, there are three residuals (1.2.17) to evaluate.

In a similar manner to in the first-order case, the key term term in the calculation of the residuals is the leading-order viscous term, u_{yy}, since the unknown amplitudes $a_m^{(1)}$ for $m = 3, \ldots, M$ can only enter into the calculation of the residuals to $O(\delta^2)$ via this term. A similar argument to the first-order case given in Section 1.2.5.1 yields $w_j = F_j$ for $j = 0, 1, 2$, coinciding, as before, with the Galerkin method. As before, a_0 can be eliminated in favour of q, and an expression for u can be obtained, namely,

$$u = \frac{3}{h}(q - s_1 - s_2) \left[\frac{y}{h} - \frac{1}{2} \left(\frac{y}{h} \right)^2 \right] + \frac{45 s_1}{h} P_1 \left(\frac{y}{h} \right) + \frac{210 s_2}{h} P_2 \left(\frac{y}{h} \right), \tag{1.2.27}$$

where $s_1 = s_1(x,t)$ and $s_2 = s_2(x,t)$ are inertial terms that account for the deviation of the velocity profile from the leading-order semi-parabolic profile (1.2.15),

and $P_1(y/h)$ and $P_2(y/h)$ are fourth-order and sixth-order polynomials, respectively [29].

Evaluation of the three residuals $\mathcal{R}_1 = 0$, $\mathcal{R}_2 = 0$, and $\mathcal{R}_3 = 0$, along with the kinematic condition (1.2.9) yields a coupled system of four partial differential equations for h, q, s_1, and s_2. The full model is cumbersome to write down, and so the reader is referred to equations (11) and (38)–(40) of Ruyer–Quil and Manneville [29]. Notably, the full second-order WRIBL model includes the effect of viscous dissipation, which was absent from the first-order WRIBL model (1.2.9) and (1.2.24) since, as previously explained, the viscous terms arise at second order in the boundary-layer equation (1.2.10) and the tangential stress balance (1.2.11). The full second-order WRIBL model does not exhibit blowup and yields excellent agreement with experiments and DNS [29]. In particular, upon performing a gradient expansion on q, s_1, and s_2, it recovers the second-order Benney equation (see equations (5.13)–(5.14c) of Kalliadasis *et al.* [28, 29, 39]).

1.2.5.3 Simplified second-order model

The complexity of the full second-order WRIBL model restricts its amenability to both analytical and numerical analysis. A simplified version, widely referred to as the "simplified second-order WRIBL model" was derived by Ruyer–Quil and Manneville [29]. The simplified model neglects second-order inertial effects by the *ad hoc* elimination of s_1 and s_2 in the velocity expansion (1.2.14), whilst still retaining second-order streamwise viscous effects. Ruyer–Quil and Manneville [62] noted that, by a linear stability analysis, it can be shown that the relaxation times of s_1 and s_2 (i.e., the characteristic times taken by s_1 and s_2 to return to a state of equilibrium) are significantly shorter than those of q (which takes longer to settle down after being disturbed), therefore partly justifying the *ad hoc* assumption that s_1 and s_2 can be neglected. Under this assumption, s_1 and s_2 may enter into the calculation at $O(\delta^2)$ via the terms

$$\int_0^h u(F_j)_{yy}\,\mathrm{d}y, \tag{1.2.28}$$

which appear in the evaluation of the residuals (1.2.17) as shown in equation (1.2.19) where, as before, $w_j = F_j$ (for $j = 0, \ldots, J$). Therefore, since $(F_0)_{yy} = (f_0)_{yy} = -1$, s_1 and s_2 do not appear in the evaluation of $\mathcal{R}_1$. Hence, only the

leading-order term $a_0 f_0$ of the velocity expansion (1.2.25) (and thus, only the leading-order basis function w_0) is required. Hence, the model involves only two fields (rather than four), namely, h and q. Therefore, evaluating the zeroth residual $\mathcal{R}_0 = \langle w_0, \mathcal{B}(u) \rangle$ yields

$$\frac{5}{2}\frac{q}{h^2} - \frac{5}{6}h + \delta\left[q_t + \frac{17}{7}\frac{qq_x}{h} + \left(\frac{5B}{6}h - \frac{9}{7}\left(\frac{q}{h}\right)^2\right)h_x - \frac{5\Gamma'}{6}h_{xxx}\right] - \delta^2\left[4\frac{q(h_x)^2}{h^2} - \frac{9}{2}\frac{q_x h_x}{h} - 6\frac{qh_{xx}}{h} + \frac{9}{2}q_{xx}\right] = 0. \tag{1.2.29}$$

The second-order terms in (1.2.29) arise from the terms $2u_{xx} + (u_x|_{y=h})_x$ in the boundary-layer equation (1.2.10) and the terms on the right-hand side of the tangental stress balance (1.2.11), and incorporate the effect of viscous dissipation that is not present in the first-order WRIBL model (1.2.24), but does not include the second-order inertial effects related to s_1 and s_2 that are present in the full second-order WRIBL model.

Equation (1.2.29) along with the kinematic condition (1.2.9) constitute a closed system governing the evolution of the film thickness h and the flux q. This model predicts the correct linear stability threshold [29], however, it does lose its second-order accuracy: specifically, it does not recover the second-order Benney equation (equations (5.13)–(5.14c) of Kalliadasis *et al.* [28]) upon performing a gradient expansion on q. Specifically, the coefficient of one of the inertial terms is 212/525 instead of the correct value 127/315 [37]. Nonetheless, the simplified second-order WRIBL model is significantly more amenable to both analytical and numerical investigations in comparison to the full second-order WRIBL model [29], and is more accurate than the first-order WRIBL model (1.2.9) and (1.2.24) [29, 62]. Hence, many studies make use of the simplified second-order WRIBL model rather than the full second-order WRIBL model [31, 37, 52, 55, 56, 69]. In this thesis, we derive a simplified second-order WRIBL model in the context of our problem.

1.3 Analysis of free-surface flows

Reduced-order models are more amenable to analytical and numerical analysis than the Navier–Stokes equations (1.1.1) and (1.1.2). In this thesis, we employ linear stability analyses, multiple-timescale analyses, and numerical methods used in solving nonlinear ordinary differential equations (ODEs) and PDEs. We briefly

outline the theory of each of these in Sections 1.3.1–1.3.3, respectively, as essential precursors to both the work in this thesis and to the discussions that follow in the remainder of this chapter.

1.3.1 Linear stability

In Chapter 4, we perform linear stability analyses which involve analysing the temporal growth rates of perturbations to "base state" solutions (i.e., steady states, such as a uniform film coating the surface of a substrate in the context of fluid flows). The perturbations can either grow, decay, or remain constant over time, indicating linear instability, stability, or neutral stability of the base state, respectively [70].

For example, consider a fluid system described by the nonlinear PDE

$$\frac{\partial \mathbf{u}}{\partial t} = \mathbf{F}(\mathbf{u}), \tag{1.3.1}$$

where $\mathbf{u} = \mathbf{u}(\mathbf{x}, t)$ denotes the solution vector, $\mathbf{x}$ denotes the spatial coordinate vector, t denotes time, and $\mathbf{F}$ denotes a general nonlinear differential operator. We consider the stability of a known steady state solution of (1.3.1) which we denote by $\mathbf{u}_0 = \mathbf{u}_0(\mathbf{x})$ (i.e., such that $\mathbf{F}(\mathbf{u}_0) = \mathbf{0}$). To investigate the linear stability of $\mathbf{u}_0$, we introduce a small perturbation $\bar{\mathbf{u}} = \bar{\mathbf{u}}(\mathbf{x}, t) \ll 1$ such that $\mathbf{u} = \mathbf{u}_0(\mathbf{x}) + \bar{\mathbf{u}}(\mathbf{x}, t)$ and substitute this into the governing equation (1.3.1) to yield

$$\frac{\partial}{\partial t}(\mathbf{u}_0 + \bar{\mathbf{u}}) = \frac{\partial \bar{\mathbf{u}}}{\partial t} = \mathbf{F}(\mathbf{u}_0 + \bar{\mathbf{u}}). \tag{1.3.2}$$

We linearise the system (1.3.2) by expanding the right-hand side of (1.3.2) as a Taylor series about $\mathbf{u}_0$ up to first-order in $\bar{\mathbf{u}}$, yielding

$$\frac{\partial \bar{\mathbf{u}}}{\partial t} = \left.\frac{\partial \mathbf{F}}{\partial \mathbf{u}}\right|_{\mathbf{u}=\mathbf{u}_0} \bar{\mathbf{u}} \equiv \mathbf{A}\bar{\mathbf{u}}, \tag{1.3.3}$$

where $\mathbf{A}$ is the "stability matrix", the spectrum of which determines the stability of the base state $\mathbf{u}_0$. To determine the eigenvalues of $\mathbf{A}$, we assume that the solution for the perturbation $\bar{\mathbf{u}}$ is of the form $\bar{\mathbf{u}} = \psi(\mathbf{x})\mathrm{e}^{-i\omega t}$ and substitute this into (1.3.3) to yield

$$(\mathbf{A} + i\omega\mathbf{I})\psi = \mathbf{0}, \tag{1.3.4}$$

where $\mathbf{I}$ is the identity matrix of same dimensions as $\mathbf{A}$, $\psi(\mathbf{x})$ are eigenvectors which represent the spatial structure of the perturbation, and $-i\omega$ denotes a complex eigenvalue of the spectrum, where ω is the angular frequency. We seek solutions of the form $\psi(\mathbf{x}) = \mathrm{e}^{inx}$, representing spatially oscillating perturbations with wavenumber n. Finally, we set $\det(\mathbf{A} + i\omega\mathbf{I}) = 0$ in order to obtain a non-trivial solution for $\psi(\mathbf{x})$, which in turn yields the "dispersion relation" which describes the relationship between ω and n. Analysing the dispersion relation allows us to understand the stability properties of the system as the real part of the eigenvalue $-i\omega$ determines the temporal growth rate of the perturbation. Specifically, if $\mathrm{Re}(-i\omega) = 0$ the perturbation remains constant, hence the steady state $\mathbf{u}_0$ is linearly neutrally stable; if $\mathrm{Re}(-i\omega) < 0$ the perturbation decays, hence $\mathbf{u}_0$ is linearly stable; and if $\mathrm{Re}(-i\omega) > 0$ the perturbation grows, hence $\mathbf{u}_0$ is linearly unstable.

1.3.2 The method of multiple scales

In Chapter 4, we perform a multiple-timescale analysis using the method of multiple scales. In this section, we provide a brief overview of this method, which finds extensive applications in, for example, applied mathematics, physics, and engineering (see, for example, Sanchez [71], Nayfeh [72], and references therein). This method is useful for analysing systems which involve multiple timescales, which arise in systems in which "slow" and "fast" processes evolve simultaneously.

A multiple-timescale analysis involves constructing a temporally uniformly-valid asymptotic description of problems whose solutions evolve on more than one (asymptotically distinct) timescale. Typically, the presence of more than one timescale is manifested by the presence of secular terms (i.e., terms which grow with time) in a naïve asymptotic solution that can be eliminated by the introduction of one of more additional timescales. For example, consider the linear damped oscillator [72]

$$u_{tt} + u = -2\epsilon u, \tag{1.3.5}$$

where $u = u(t)$ and $\epsilon \ll 1$ is a small parameter. We begin by performing a naïve expansion on (1.3.5) by assuming that $u(t)$ can be represented by an expansion of the form

$$u = u_0(t) + \epsilon u_1(t) + \epsilon^2 u_2(t) + O(\epsilon^3), \tag{1.3.6}$$

where for the expansion to be asymptotically valid we require that $\epsilon^{n+1}u_{n+1}(t)$ is

smaller than $\epsilon^n u_n(t)$ (for $n = 0, 1, 2, \ldots$). Substitution of (1.3.6) into (1.3.5) yields

$$(u_0)_{tt} + u_0 = 0, \tag{1.3.7}$$

$$(u_1)_{tt} + u_1 = -2(u_0)_t, \tag{1.3.8}$$

$$(u_2)_{tt} + u_2 = -2(u_1)_t, \tag{1.3.9}$$

at leading, first, and second order in ϵ, respectively, which have solutions

$$u_0 = a\cos(t+\phi), \tag{1.3.10}$$

$$u_1 = -at\cos(t+\phi), \tag{1.3.11}$$

$$u_2 = \frac{a}{2}\left[t^2\cos(t+\phi) + t\sin(t+\phi)\right], \tag{1.3.12}$$

respectively. Hence, the solution (1.3.6) is

$$u = a\cos(t+\phi) - \epsilon at\cos(t+\phi) + \frac{\epsilon^2 a}{2}\left[t^2\cos(t+\phi) + t\sin(t+\phi)\right] + O(\epsilon^3), \tag{1.3.13}$$

which contains secular terms at first and second order. This is due to the solutions for u_1 (1.3.11) and u_2 (1.3.12) exhibiting a resonance effect due to the forcing terms (i.e., the terms on the right-hand side of the ODEs (1.3.8) and (1.3.9)) containing terms which also arise in the complementary functions of u_1 and u_2. This resonance leads to the accumulation of energy at one or more resonant frequencies, causing the amplitude of the solution to grow without bound as time progresses, hence causing the perturbation expansion to break down. In other words, the naïve asymptotic solution becomes nonuniform. Specifically, (1.3.13) becomes nonuniform when $t = O(\epsilon^{-1})$, at which time the first order ϵu_1 term has grown to become the same size as the leading order u_0 term.

The method of multiple scales allows us to obtain uniformly-valid solutions for systems with multiple timescales, such as the one described above, by eliminating these secular terms. We introduce "slow" and "fast" timescale variables and treat these as though they were independent. Specifically, the timescales are defined as

$$T_n = \epsilon^n t \tag{1.3.14}$$

for $n = 0, \ldots, N$, where the timescale T_{n+1} is slower than T_n. In general, we assume that the solution for the unknown function $u(t;\epsilon)$ can be represented by

an asymptotic expansion of the form

$$u(t;\epsilon) = u_0(T_0, T_1, T_2, \ldots) + \epsilon u_1(T_0, T_1, T_2, \ldots) + \epsilon^2 u_2(T_0, T_1, T_2, \ldots) + O(\epsilon^3), \tag{1.3.15}$$

where the number of timescales required depends on various factors such as the desired order to which the expansion is carried out and the orders at which secular terms arise in the naïve expansion (1.3.6) (which is often a result of the physical phenomena that are incorporated into the original model). Substitution of (1.3.15) into the relevant governing equation (such as (1.3.5) in the example above) and balancing terms at each order yields a system of $N + 1$ ODEs which are solved order-by-order. In order to ensure that the solution (1.3.15) is uniform, the secular terms that arise at each order in ϵ^n (for $n = 0, \ldots, N$) are eliminated by setting their coefficients to zero and solving the resulting system of equations.

The calculations involved in applying the method of multiple scales to the example discussed above are lengthy, and so the reader is referred to Section 6.1.1 of Nayfeh [72] for details. A complete example of this method will be given in Section 4.4 in the context of our problem. The reader is also referred to Hinch and Kelmanson [73] for a sophisticated example in the context of fluid flows.

In summary, the method of multiple scales effectively captures the dynamics of both "slow" and "fast" processes, and hence accurately describes the nonuniform solution behavior, whilst avoiding the divergence caused by secular terms in the standard perturbation expansion.

1.3.3 Numerical methods

Reduced-order models are, in general, challenging to solve analytically, and it is therefore uncommon to be able to derive explicit expressions for the solution variables. Hence, a widely-used approach is to solve reduced-order models numerically in order to complement results from asymptotic analyses. For example, in the context of the planar falling-film system discussed earlier in Section 1.2, numerical solutions allow us to explore the dynamics of the system in the nonlinear regime in addition to enabling qualitative and quantitative comparisons with experimental findings. As discussed in Appendix A, we use the method of lines to solve various governing PDEs throughout this thesis and impose periodic boundary conditions on the system. The method of lines is a technique for solving PDEs by discretising

them into a system of nonlinear ODEs. In this thesis, for the reasons outlined in Appendix A, we use the centred finite-difference method for spatial discretisation in conjunction with either the backwards Euler method or the trapezoidal method for time integration. In this section, we provide a brief overview of these methods (see references [74, 75] for further details of the numerical methods discussed herein).

1.3.3.1 The finite-difference method

The finite-difference method is a numerical technique used to approximate solutions to ODEs and PDEs. Instead of obtaining the exact solution everywhere, the method obtains an approximation to the solution at a discrete set of grid points in both the spatial domain and in the time domain.

Consider a PDE of the form

$$h_t = G\left(h, h_x, h_{xx}, \ldots\right) \tag{1.3.16}$$

on a domain of length L given by $0 < x < L$, where $h = h(x,t)$ and G is a function of h and its derivatives. Equation (1.3.16) is subject to the initial condition

$$h(x,0) = h_0(x), \tag{1.3.17}$$

and periodic boundary conditions

$$\left.\frac{\partial^n h}{\partial x^n}\right|_{x=0} = \left.\frac{\partial^n h}{\partial x^n}\right|_{x=L} \tag{1.3.18}$$

for $n = 0, 1, 2, \ldots$. To solve this system, the spatial variable x is discretised as $x = x_i$ (for $i = 1, \ldots, M$) onto a uniform grid with M grid points with step size $\Delta x = L/(M-1)$. The time variable is discretised as $t = t_j$ (for $j = 0, \ldots, N$) with step size $\Delta t = t_j - t_{j-1}$ (which is not necessarily uniform). In what follows, we denote the discretised solution corresponding to h evaluated at $x = x_i$ and $t = t_j$ by $h_i^j = h(x_i, t_j)$. Hence, the periodic boundary conditions (1.3.18) are rewritten as

$$\left.\frac{\partial^n h_1^j}{\partial x^n}\right|_{x=0} = \left.\frac{\partial^n h_M^j}{\partial x^n}\right|_{x=L} \tag{1.3.19}$$

for $n = 0, 1, 2, \ldots$.

Derivatives in the PDE (1.3.16) are approximated using discrete difference approximations. As mentioned previously, in this thesis, we use centred finite-differences. For example, the first and second derivatives of h_i^j with respect to x can be approximated by using the centred difference formulae,

$$\left(h_i^j\right)_x \approx \frac{h_{i+1}^j - h_{i-1}^j}{2\Delta x} + O((\Delta x)^2), \quad \left(h_i^j\right)_{xx} \approx \frac{h_{i+1}^j - 2h_i^j + h_{i-1}^j}{(\Delta x)^2} + O((\Delta x)^2). \tag{1.3.20}$$

The centered difference method yields a second-order approximation for the derivative. This means that the error between the exact derivative and the approximation decreases quadratically with the grid spacing Δx. In comparison, one-sided difference approximations (for example, forward or backward differences) only offer first-order accuracy, leading to a larger truncation error (i.e., the error between the numerical solution and the exact solution which is introduced by neglecting higher-order terms in the Taylor series expansion).

Note that, in many physical systems, certain regions may arise in which the solution changes rapidly in time or has significant spatial variations. Hence, it is often advantageous to instead use a nonuniform spatial grid in order to focus the grid points more densely in these regions, thus providing higher resolution and accuracy where it is required without wasting computational resources where the solution changes slowly (see, for example, Sundqvist and Veronis [76], Chakraborty *et al.* [66], and Moore *et al.* [77]).

1.3.3.2 Time-stepping techniques

For time-dependent problems, a time-stepping technique is used to advance the solution from one time step to the next. Commonly used time-stepping methods include the backwards Euler method and the trapezoidal method.

The backwards Euler method is an implicit numerical method for solving ODEs and PDEs that involve a time derivative. It approximates the time derivative at the current time step t_j using the value of the solution at the next time step t_{j+1}. Specifically, this method discretises the time derivative using a backward difference approximation, namely,

$$\left(h_i^{j+1}\right)_t \approx \frac{h_i^{j+1} - h_i^j}{\Delta t}. \tag{1.3.21}$$

After applying the centred finite-difference formulae (1.3.20), substituting the

backwards difference approximation (1.3.21) into the PDE (1.3.16) and rearranging for h_i^{j+1} yields the backwards Euler method, namely,

$$h_i^{j+1} = h_i^j + \Delta t G\left(h_i^{j+1}, \ldots\right). \tag{1.3.22}$$

The backwards Euler method provides first-order accuracy and offers better stability and accuracy for stiff problems (i.e., problems in which the solutions change rapidly over certain regions) compared to explicit methods such as the forwards Euler method.

Similarly, the trapezoidal method is also an implicit time integration method. Unlike the backwards Euler method, which discretises the time derivative using a backwards difference approximation, the trapezoidal method arises from approximating the integral of (1.3.16) over the time interval $t_j \leq t \leq t_{j+1}$, i.e.,

$$\int_{t_j}^{t_{j+1}} (h_i)_t \, \mathrm{d}t = \int_{t_j}^{t_{j+1}} G\left[h_i, (h_i)_x, (h_i)_{xx}, \ldots\right] \, \mathrm{d}t, \tag{1.3.23}$$

by using the trapezoidal rule for numerical integration to yield

$$h_i^{j+1} - h_i^j = \frac{\Delta t}{2}\left[G\left(h_i^j, \ldots\right) + G\left(h_i^{j+1}, \ldots\right)\right]. \tag{1.3.24}$$

Rearranging equation (1.3.24) for h_i^{j+1} yields the trapezoidal method, namely,

$$h_i^{j+1} = h_i^j + \frac{\Delta t}{2}\left[G\left(h_i^j, \ldots\right) + G\left(h_i^{j+1}, \ldots\right)\right]. \tag{1.3.25}$$

The trapezoidal method provides second-order accuracy and offers better stability and accuracy for stiff problems compared to explicit methods.

Applying the aforementioned discrete approximations converts the time-dependent PDE (1.3.16) into a system of algebraic equations involving values of the function at different grid points. This system of equations can then be solved at each time step using various numerical techniques, such as the Newton–Raphson method (see Leveque [74] or Iserles [75] for an explanation of this well-known algorithm) in order to obtain a numerical solution.

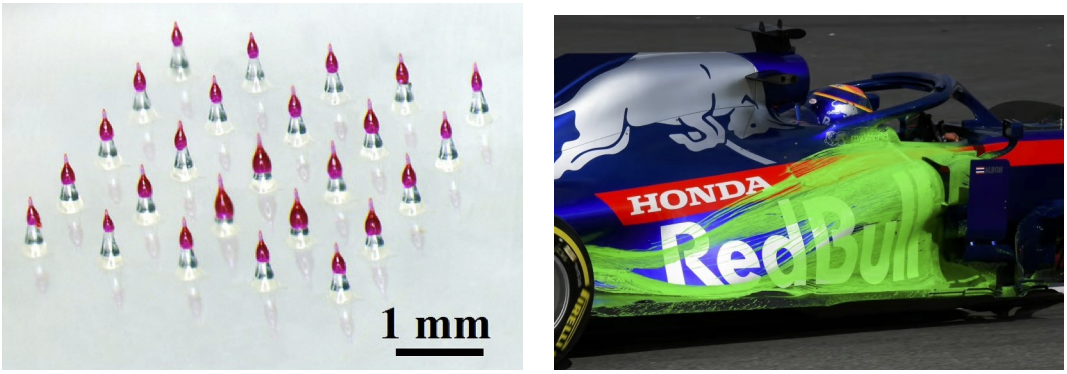

(a) (b)

Figure 1.5: (a) Coated micro-needles fabricated using a dip-coating technique. Reproduced from Liang *et al.* [82], with permission from Elsevier. Copyright 2020. (b) Flow-visualisation paint on a race car after testing. Image courtesy of Formula One Digital Media Limited [84].

1.4 Flow on curved substrates

This thesis concerns a particular category of free-surface flows wherein a fluid film coats a solid, curved substrate. The potential scope of applications for this particular type of flow is extensive [78]. For example, these flows play a significant role in biological contexts such as in coating the cornea of the human eye [79] and the lining of the lungs of land animals [80]. In addition, they are crucial to a vast range of industrial settings, such as creating edible films in the food industry for preservation against contamination and perishability [81], producing coated micro-needles for transdermal drug delivery in the pharmaceutical industry [82] (as shown in Figure 1.5 (a)), and in the painting of the bodies of automobiles [83]. For example, in the automotive and aerospace industries, engineers design vehicles with curved surfaces to achieve specific aerodynamic characteristics [85]. During vehicle development, engineers paint test models with specific coatings, enabling them to make airflow patterns visible for analysis, a technique referred to as flow visualisation. Figure 1.5 (b) shows a race car after testing with flow visualisation paint, consisting of fluorescent powder mixed with paraffin. As the paraffin evaporates, it reveals visible airflow patterns, aiding engineers in their analysis [84]. A wide variety of methods and processes are used in the application of industrial coatings, such as chemical vapor deposition (in which a solid material is deposited from a gaseous phase through a chemical reaction with the substrate),

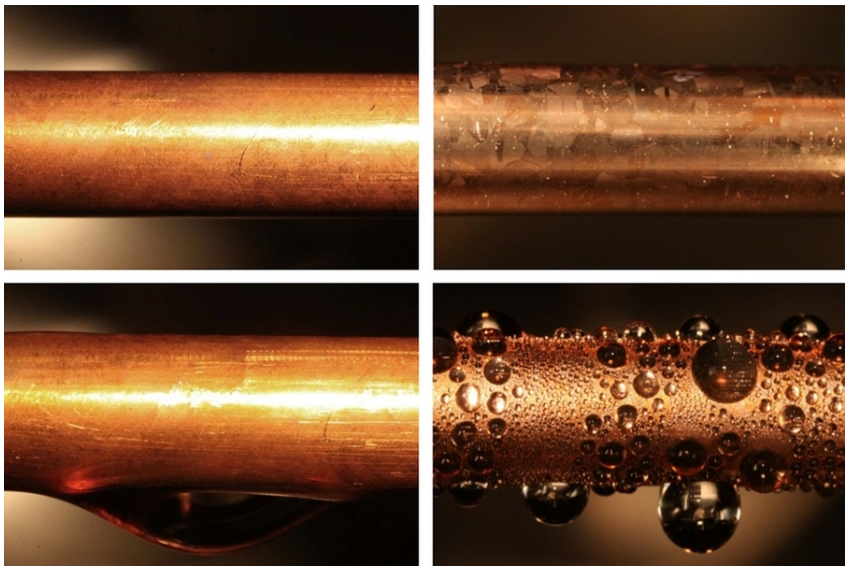

Figure 1.6: Copper condenser tubes that are uncoated (left) and coated with graphene (right). Reprinted with permission from MIT News http://news.mit.edu/ [93].

physical vapor deposition (in which a solid material is vaporised inside a vacuum chamber, which then condenses onto the substrate), and dip coating (in which an object is immersed into a pool of coating material and then withdrawn) [86].

The special case in which the substrate is cylindrical has received significant attention, both due to its relevance in various industrial contexts and as a useful paradigm for more complex scenarios. For example, it occurs in confectionery production [87], in printing methods such as flexographic printing [88], in the coating of tablets in the pharmaceutical industry [89], in the lubrication and protective coating of engine components in the automotive industry [90, 91], and in heat transfer applications, such as condensation within a heat exchanger [92]. An example of the last of these is shown in Figure 1.6, which shows an uncoated copper condenser tube (left) and a graphene-coated tube (right). At 100°C, the steam condenses to form a thin film of water that coats the surface of the uncoated tube (bottom left), whereas the coated tube exhibits desirable dropwise condensation which has a higher surface area and hence yields enhanced heat transfer rates (bottom right) [93].

Although the term "coating flow" refers to the general situation in which a liquid film coats a substrate, in this thesis, we consider only horizontal cylindrical

substrates. Hence, in order to distinguish between the scenarios in which the cylinder is rotating and in which it is stationary, throughout this thesis, we use the term "coating flow" when referring to the situation in which the cylinder is rotating, and use the term "draining flow" when referring to the situation in which it is stationary. We discuss the relevant aspect ratios for flow on a cylindrical substrate in Section 1.4.1. The existing literature surrounding coating flow and draining flow will be discussed in Sections 1.4.3 and 1.4.4, respectively. Finally, we briefly discuss flow on other curved geometries in Section 1.4.5. Throughout these sections, a is the radius of the circular cylinder (where applicable), Ω is the constant rotation rate of the cylinder (where applicable), g is acceleration due to gravity, ρ is the fluid density, μ is the fluid viscosity, σ is the constant coefficient of surface tension, and h_0 is the initial uniform film thickness (i.e., the film thickness at time $t = 0$).

1.4.1 Aspect ratios of flow on a curved substrate

In this section, we discuss the relevant aspect ratios of flow on a curved substrate. Note that, as in Section 1.2.1, throughout this section we phrase our discussion in terms of nondimensional parameters, but choose not to specify the particular length scale used in the nondimensionalisation (which could again be, for example, a capillary length).

As discussed earlier in Section 1.2.1, in the case of a planar substrate, there are only two length scales present within the system, namely, a characteristic dimensionless cross-stream length scale H (which, as before, is typically a characteristic dimensionless film thickness), and a characteristic dimensionless streamwise length scale λ (which, as before, is typically a characteristic dimensionless wavelength of the film). However, in the case of flow on a curved substrate, the two characteristic radii of curvature of the substrate are not necessarily infinite, and hence there are two additional length scales present within the system. Therefore, although for a planar substrate the thin-film and long-wave situations are equivalent (and so the terms "thin-film" and "long-wave" can be used interchangeably), for a non-planar substrate this is no longer the case and we must be careful to distinguish between the two approximations [31, 56].

In this section, we outline the difference between the thin-film and long-wave approximations on curved substrates. In particular, in what follows, we discuss

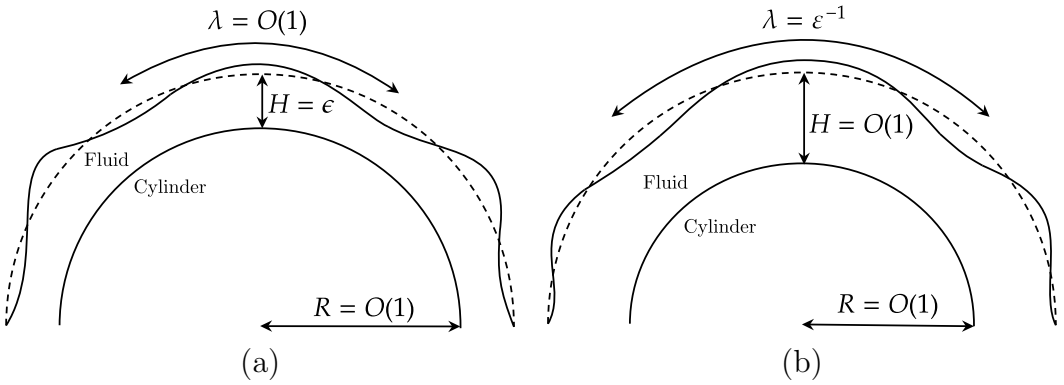

Figure 1.7: Schematic of the relationship between the three length scales H, λ, and R present for flow on a cylinder. (a) Thin-film approximation. (b) Long-wave approximation.

two-dimensional flow on a cylindrical substrate, in which case one of the characteristic radii of curvature is the dimensionless radius of the cylinder, which we denote here by R. The other is infinite and therefore can be ignored (similarly to the radius of curvature in the planar case). The discrepancy between the two approximations is a key point, and is central to our ability to accurately model the flow of "thick" films, which are defined as films for which the dimensionless characteristic film thickness is of the same order as the dimensionless characteristic radius of curvature of the substrate. Note that the principles discussed in this section can also be applied to curved substrates that have two finite radii of curvature, such as a sphere or an ellipsoid.

1.4.1.1 Thin-film approximation

As before, in the case of flow on a curved substrate, the thin-film approximation assumes that the thickness of the film is small (compared to unity). In other words,

$$R = O(1), \quad \lambda = O(1), \quad \epsilon = H \ll 1, \tag{1.4.1}$$

where ϵ denotes the thin-film aspect ratio on a curved substrate. A schematic of the relationship between the three length scales present for flow on a cylinder in the thin-film approximation is shown in Figure 1.7 (a).

1.4.1.2 Long-wave approximation

The assumption $H \ll 1$ used in the thin-film approximation (1.4.1) is quite restrictive for all but the thinnest of films. Indeed, it is often the case that reduced-order models are derived based on the thin-film approximation, but are utilised to describe a flow in which the thickness of the film can become larger than the thin-film approximation is designed to handle (for example, localised thickening may occur in films that are initially uniformly thin). For example, in the context of coating flow, the results of Peterson *et al.* [94] showed increasing error for models derived using a thin-film approximation for increasing values of the film thickness (specifically, they analysed the model derived by Pukhnachev [95], which will be discussed in Section 1.4.4). In addition, Wray *et al.* [56] showed that for coating flow in the absence of inertia and in the limit of zero gravity, the linear growth rates of the flow described by their thin-film model display poor agreement with DNS of the Stokes equations for moderately thick films, finding that the agreement becomes significantly worse as the film thickness increases. This result is shown in Figure 1.8, which shows the linear growth rate (denoted in their notation by s) as a function of the unperturbed film radius (denoted in their notation by $\bar{h}$) for the azimuthal wavenumbers (a) $n = 2$, (b) $n = 4$, and (c) $n = 6$. In particular, Figure 1.8 shows that, in general, their thin-film model (solid black) displays strong disagreement with DNS of the Stokes equations (solid red) for all but the smallest values of $\bar{h}$. As a consequence, the majority of studies that consider thick films have relied on numerical computations of the velocity profiles, height evolution, and pressure [96].

Wray *et al.* [56] revealed that it is possible to relax the restriction that the film thickness is small by instead using a long-wave approximation. In the case of a curved substrate, the long-wave approximation differs from the thin-film approximation (1.4.1) owing to the presence of the extra length scale R. In the long-wave approximation, variations in the film thickness are assumed to be large (compared to unity). In other words,

$$R = O(1), \qquad H = O(1), \qquad \varepsilon = \lambda^{-1} \ll 1, \tag{1.4.2}$$

where ε denotes the long-wave aspect ratio on a curved substrate. A schematic of the relationship between the three length scales present for flow on a cylinder in the long-wave approximation is shown in Figure 1.7 (b). Note that the long-wave

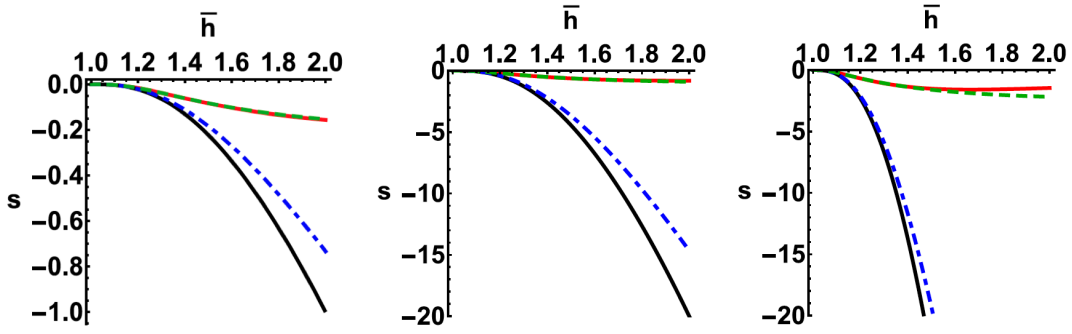

(a) (b) (c)

Figure 1.8: Plots by Wray *et al.* [56] of the linear growth rate s as a function of the unperturbed film radius $\bar{h}$ for the problem of thick-film coating flow (in the absence of inertia and in the limit of zero gravity) calculated from their second-order thick-film WRIBL model (dashed green), thick-film gradient expansion model (dot-dashed blue), thin-film model (solid black), and DNS of the Stokes equations (solid red) for the azimuthal wavenumbers (a) $n = 2$, (b) $n = 4$, and (c) $n = 6$. Reprinted from Wray *et al.* [56] with permission. Copyright 2017 Society for Industrial and Applied Mathematics. All rights reserved.

approximation assumes that $R = O(1)$ and $H = O(1)$, thus relaxing the assumption that the film thickness must be small and hence permitting the development of models which are valid for both thin films and thick films.

1.4.2 Long-wave methodology for thick films

Based on the long-wave approximation (1.4.2), Wray *et al.* [56] formulated what we shall refer to hereafter as the "long-wave methodology" for modelling thick films on curved substrates. In essence, the long-wave methodology is the introduction of appropriate scalings on the relevant parameters in the unscaled governing equations. Variations in the streamwise direction are assumed to be small (whilst those in the radial direction are not), for which we introduce the scaling

$$\partial_\theta \mapsto \varepsilon \partial_\theta. \tag{1.4.3}$$

Here, ε is an ordering parameter which, as discussed earlier in Section 1.2.5, asserts the expected relative magnitudes of particular terms and their derivatives during the calculations and is hence set equal to unity in the final model [28, 29, 37, 53].

In systems involving thick films, bulges may develop which have high interfacial curvature relative to the characteristic radius of curvature R. Hence, in order to accurately model these bulges, a common approach is to use the full form of the interfacial curvature rather than neglecting dependencies on higher-order terms [97]. Although these higher-order terms are typically neglected in a consistent asymptotic expansion, they have been shown in the literature to aid agreement with experiments and DNS [31, 56, 98, 99].

As explained by Wray *et al.* [31, 56], variations in the azimuthal direction are assumed to be small rather than rescaling θ itself owing to the fact that θ has a fixed domain length of 2π and therefore cannot be assumed to be "long". Consequently, the long-wave methodology explained herein does not constitute a formal asymptotic approach when applied to a circular cylinder. Indeed, whilst in systems with an explicit small aspect ratio (such as in the planar case discussed earlier in Section 1.2.5) the WRIBL method is asymptotically consistent (hence accurately recovering the Benney equation up to second order upon a suitable gradient expansion), in other systems this may not always be valid [31, 56]. We therefore treat ε as an ordering parameter, with the method being essentially data driven: the orders at which the respective velocity fields are retained are based on experience, the output of numerical experiments, and *post hoc* validation.

Reduced-order models derived using the long-wave methodology described herein have been shown to yield good agreement with DNS, even outside their range of formal validity (specifically, in the short-wave regime). As shown in Figure 1.8, Wray *et al.* [56] found that their reduced-order models derived using a long-wave approximation yield significantly better agreement with DNS than those derived using a thin-film approximation for both thin and thick films. Specifically, their thin-film model (solid black) performs poorly and their thick-film gradient expansion model yields some improvement in accuracy (dotted blue). However, their second-order thick-film WRIBL model (dashed green) yields excellent agreement with DNS, even when the film is as thick as the cylinder radius (i.e., for $\bar{h} = 2$). In addition, although the $n = 6$ mode (shown in Figure 1.8 (c)) is outside the range of formal validity of the long-wave approximation (since the wavelengths are not "long"), their second-order thick-film WRIBL model still yields good agreement with DNS. We defer further discussion of the results of Wray *et al.* [56] until Section 1.4.4.

1.4.3 Draining flow

Draining flow has been investigated extensively by various authors, dating back to the pioneering work of Nusselt [34, 35] who considered steady draining flow of a thin film fed by a prescribed flux of liquid delivered at the top of the cylinder. They showed that the thickness of the film varies as $|\cos\theta|^{-1/3}$, where θ is the azimuthal angle measured anticlockwise around the cylinder from the horizontal. This result indicates that the film displays left-to-right symmetry as well as top-to-bottom symmetry, and that the film extends infinitely at top and bottom of the cylinder, corresponding to $\theta = \pi/2$ and $\theta = -\pi/2$ respectively. Whilst this behaviour violates the thin-film approximation, it can be understood as the film cascading onto the top of the cylinder and subsequently falling off at the bottom of the cylinder. This analysis was later generalised to steady flow on a uniformly rotating cylinder by Duffy and Wilson [100], which we discuss in Section 1.4.4.

Unsteady draining flow has also been investigated by a variety of authors. For example, Reisfeld and Bankoff [101] theoretically investigated unsteady draining flow of a thin film, developing a model which incorporates viscosity, gravity, capillarity, thermocapillarity, and intermolecular (van der Waals) forces, and studied both isothermal and non-isothermal situations. In particular, when the film is isothermal and van der Waals forces are negligible, they found that steady solutions only exist when the Bond number (defined by Reisfeld and Bankoff [101] as $Bo = \rho g a^3/(h_{\text{avg}}\sigma)$, where h_{avg} is the average dimensional film thickness), which is a measure of the strength of the effect of gravity compared to surface tension, is zero. They showed that the film thins on the upper part of the cylinder and that the interface develops a pendant-drop-like shape on the lower part of the cylinder, as shown in Figure 1.9 (a) which shows snapshots of the isothermal interface profile for $Bo = 10^2$ from dimensionless time (denoted in their notation by τ) $\tau = 0$ to $\tau = 4$. They also showed that two symmetric regions of local thinning of the film occur, and that these regions move upwards and eventually coalesce into a single region at the top of the cylinder as gravity is reduced, as shown in Figure 1.9 (b), which shows interface shapes at time $\tau = 4$ for various values of Bo.

Evans *et al.* [102] theoretically investigated the unsteady flow of a thin film on the outer surface of a rotating horizontal cylinder, developing a three-dimensional model which incorporates viscosity, gravity, capillarity, and centrifugation. In the special case of a two-dimensional flow on a stationary cylinder, they showed

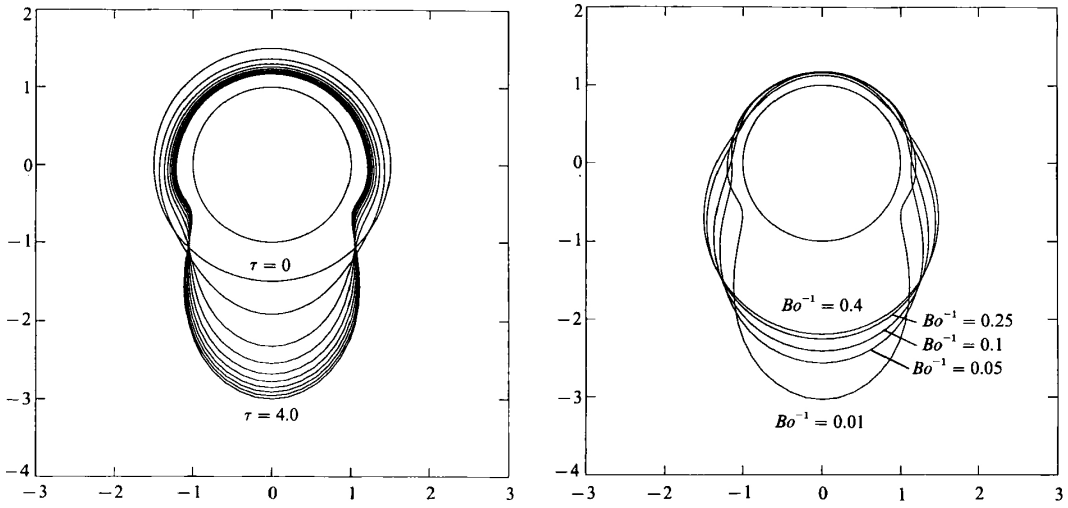

Figure 1.9: Numerical solutions of the isothermal model of Reisfeld and Bankoff [101]. Snapshots of the interface with (a) $Bo = 10^2$ for various values of τ, and (b) $\tau = 4$ for various values of Bo. Reproduced from Reisfeld and Bankoff [101], with permission from Cambridge University Press. Copyright 1992.

numerically that, in agreement with Reisfeld and Bankoff [101], a pendant drop forms on the lower part of the cylinder. In particular, Evans *et al.* [102] showed that this pendant drop approaches a steady state at late times, and obtained numerical solutions for its steady-state shape. The steady-state interface shapes are shown for various values of the dimensionless rotation rate (defined by Evans *et al.* [102] as $W = \Omega(a/g)^{1/2}$) in Figure 1.10 (a). Specifically, Figure 1.10 (a) shows steady-state interface shapes for $W = 0, 0.002$, and 0.004, in which the solid black line corresponds to the stationary case $W = 0$. They also showed that the film thickness $h = h(\theta, t)$ (where t denotes dimensionless time) at the top of the cylinder (located at $\theta = 0$ in their geometric setup) decreases monotonically, but does not reach zero in a finite time. This is shown in Figure 1.10 (b), which shows the evolution of the film thickness at the top of the cylinder for various values of W.

Subsequently, Takagi and Huppert [103] theoretically and experimentally investigated the instantaneous release of a constant volume of liquid at the top of a stationary cylinder and a stationary sphere. The unsteady flow of the thin film with an advancing front that forms is studied. In particular, in both geometries,

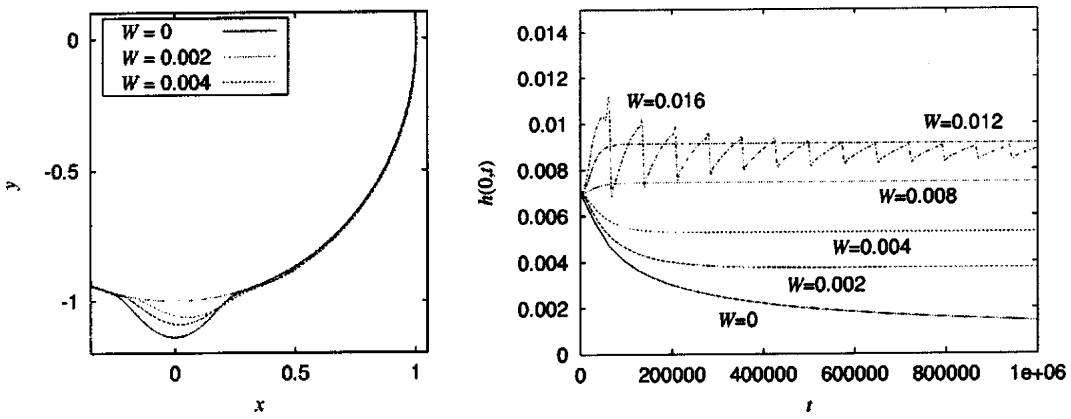

(a) (b)

Figure 1.10: Numerical solutions of the model of Evans *et al.* [102]. (a) Steady state interface shapes for dimensionless rotation rates $W = 0, 0.002$, and 0.004. (b) Evolution of the film thickness h evaluated at the top of the cylinder $\theta = 0$ for various values of W. Reprinted from Evans *et al.* [102], with the permission of AIP Publishing. Copyright 2004.

they developed models which incorporate viscosity, gravity, and capillarity, and derived asymptotic solutions for the film thickness near the top of the substrate at late times. They found that at late times the front advances as $t^{1/2}$ for the cylinder and as $t^{1/4}$ for the sphere, and that in both cases the film near the top of the substrate thins as $t^{-1/2}$. They carried out their experimental investigations for the cylindrical and spherical cases by pouring various liquids onto a perspex cylinder (the setup of which is shown in Figure 1.11) and a vinyl beach ball, respectively. Figure 1.11 (a) shows the flow on the cylinder soon after release at dimensional time $T = 0.7$ s (note that this is a "late" time within this parameter regime), at which time the bulk flow is approximately two-dimensional. They observed good agreement between their theory and the experimental results near the top of the substrate. However, they found that as the liquid front progressed it would eventually form rivulets. Subsequently, upon reaching the lower part of the cylinder, the rivulets would fall from the surface. This behaviour is shown in Figure 1.11 (b), which shows the flow at dimensional time $T = 2.7$ s, at which time rivulets have formed and continue to extend until they drip from the underside of the cylinder.

Cachile *et al.* [104] theoretically and experimentally investigated unsteady draining flow of a thin film and developed a model that incorporates viscosity, gravity, and capillarity. They observed good agreement between theoretical and

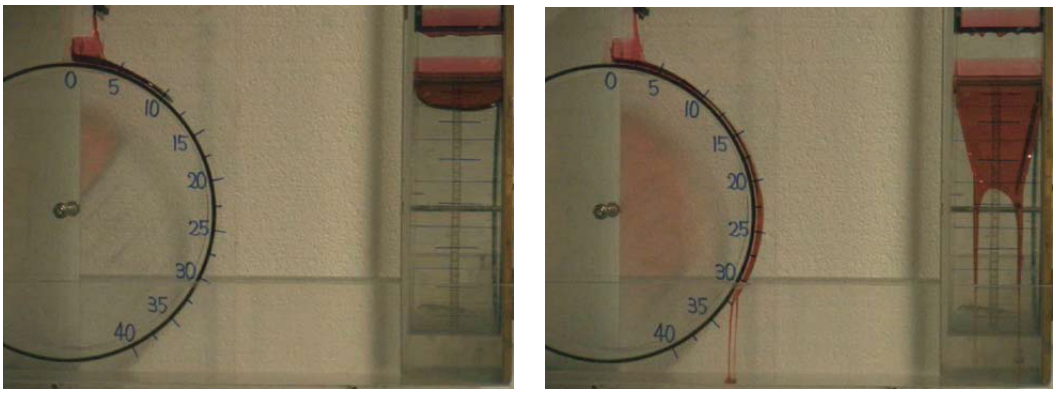

(a) (b)

Figure 1.11: Snapshots of an experiment conducted by Takagi and Huppert [103] by releasing pure glycerine on a cylinder. Results are shown at dimensional times (a) $T = 0.7$ s and (b) $T = 2.7$ s. The numbers on the cylinder indicate the perimeter in centimetres from the top of the cylinder. Reproduced from Takagi and Huppert [103], with permission from Cambridge University Press. Copyright 2010.

experimental results, the latter of which involved completely covering a steel cylinder with silicon oil. Specifically, they found that on the upper part of the cylinder there is a region in which the film thins monotonically in time as the liquid drains towards the lower part of the cylinder. They also found that a Rayleigh–Taylor-like instability occurs on the lower part of the cylinder, and determined the wavelength of the fastest-growing linear mode.

It is important to note that none of the aforementioned studies attempted to obtain a complete description of the late-time behaviour of the film, but rather, each focused on specific regions of the flow (such as, for example, the film thickness near the top of the cylinder or the pendant drop which forms on the lower part of the cylinder). None of these studies determined how the solutions in the different regions connect together to give the complete description. A recent study which did attempt to do this, albeit for flow on a sphere rather than a cylinder, is that by Qin *et al.* [105]. However, we defer discussion of this important work until Section 1.4.5 in which we consider flows on non-cylindrical geometries.

1.4.4 Coating flow

Following the publication of the influential papers by Moffatt [106] and Pukhnachev[2] [95], coating flow (and the closely related problem of "rimming flow", which describes the corresponding flow on the inside of a cylinder [109]) has gained recognition as a paradigm problem in the examination of free-surface flows. Consequently, the system has garnered significant theoretical and experimental interest. Indeed, the literature surrounding this well-studied problem is vast. Hence, in this section, we focus on what we consider to be the key works with regards to the problem studied in this thesis. For a comprehensive overview of the study of coating flows, the reader is referred to the review articles by Ruschak [110] and Weinstein and Ruschak [111], and to the work by Peterson *et al.* [94].

Most theoretical investigations into coating flow are conducted in the limit in which the liquid film is thin so that a thin-film approximation can be used (as described in Section 1.4.1). Early investigations into coating flow were primarily motivated by the aim of determining the maximum supportable weight of liquid on the cylinder, often referred to as the "Moffatt–Pukhnachev problem". Moffatt [106] theoretically and experimentally investigated steady coating flow and developed a thin-film model that incorporates the effects of rotation, viscosity, and gravity (and notably neglects capillarity), namely,

$$h_t + \left(h - \frac{1}{3} h^3 \cos\theta \right)_\theta = 0, \tag{1.4.4}$$

where θ is measured anticlockwise from the horizontal at the right-hand side of the cylinder. The first term inside the bracket in (1.4.4) represents the effect of rotation, and the second term represents gravitational effects. The model (1.4.4) admits a steady solution governed by the equation

$$h - \frac{1}{3} h^3 \cos\theta = Q, \tag{1.4.5}$$

where Q is the constant dimensionless azimuthal volume flux per unit length. Moffatt [106] sought steady solutions for the film thickness h which coat the entire surface of the cylinder, known as "full-film solutions". They derived a condition for the existence of a steady solution, finding that, for a given rotation rate, the

[2]Note that this author's name has been transliterated from Russian and is sometimes also spelled as "Pukhnachov" [107, 108].

condition can be expressed in terms of a maximum load and, for a given load, in terms of a minimum rotation rate. In particular, Moffatt [106] showed that the steady equation (1.4.5) admits such solutions only if Q remains within the range $0 < Q \leq Q_{\text{crit}}$, where $Q_{\text{crit}} = 2/3$ is referred to as the "critical" value of the flux. The solution for h corresponding to $Q = Q_{\text{crit}}$ is denoted by h_{crit} and is referred to as the critical solution. The dimensionless maximum load that can be supported on the cylinder occurs for $Q = Q_{\text{crit}}$, and is given by $M_{\text{crit}} \approx 4.4427$[3] which is referred to as the critical mass. For $0 < Q \leq Q_{\text{crit}}$, Duffy and Wilson [100] showed that the full-film solution of (1.4.5) can be given explicitly as

$$h = \begin{cases} \dfrac{2}{\sqrt{|\cos\theta|}} \sinh\left(\dfrac{1}{3}\sinh^{-1} B\right), & \text{for } \cos\theta < 0, \\ \dfrac{2}{\sqrt{\cos\theta}} \cos\left(\dfrac{2\pi}{3} - \dfrac{1}{3}\cos^{-1} B\right), & \text{for } \cos\theta > 0, \\ Q, & \text{for } \cos\theta = 0, \end{cases} \tag{1.4.6}$$

where

$$B = -\frac{3Q}{2}\text{sgn}(\cos\theta)\sqrt{|\cos\theta|}. \tag{1.4.7}$$

The full-film solution (1.4.6) is shown in Figure 1.12 (a) for several values of Q in the range $0 < Q \leq Q_{\text{crit}}$. In particular, Figure 1.12 (a) shows that the full-film solution (1.4.6) displays top-to-bottom symmetry and exhibits a maximum at $\theta = 0$, where gravity and rotation act in opposition to each other, and a minimum at $\theta = \pi$, where gravity and rotation act in harmony. Full-film solutions are smooth for $0 < Q < Q_{\text{crit}}$ (often referred to as "subcritical" values of Q), whereas the solution forms a corner at $\theta = 0$ for $Q = Q_{\text{crit}}$. Figure 1.12 (b) shows polar plots of the full-film solution (1.4.6) for two subcritical values of Q and for $Q = Q_{\text{crit}}$, in which the corner structure at $\theta = 0$ can be obviously discerned. In practice, the corner will not be sharp but will be rounded off by higher-order and/or otherwise neglected physical effects. In particular, in practice one would expect smoothing of this feature due to the effect of capillarity [95, 96]. Finally, Moffatt [106] also conducted experiments which showed the existence of a steady state for a certain range of parameters. By lowering a rotating perspex cylinder into a trough filled with golden syrup, they found that, as the rotation speed was increased, the film changed from being approximately uniform at the initial instant to displaying

[3]Note that this numerical value was originally erroneously given by Moffatt [106] as $M_{\text{crit}} \approx 4.428$.

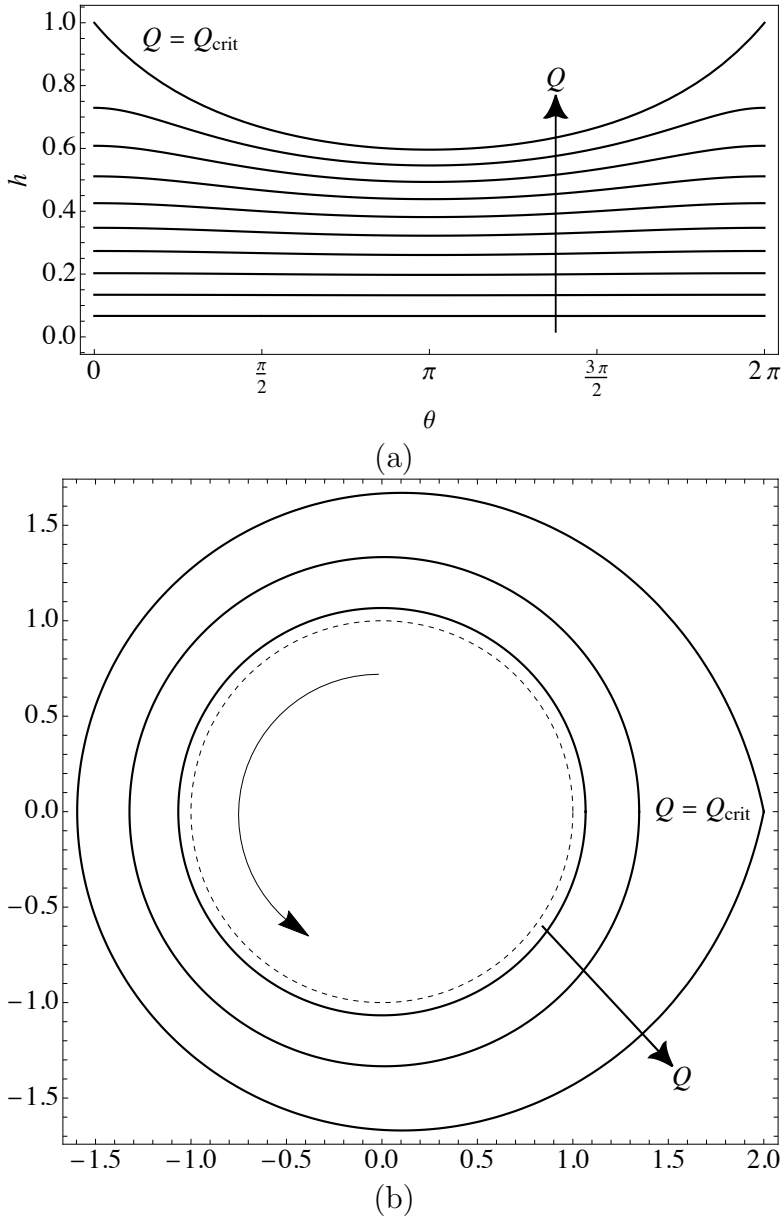

Figure 1.12: The full-film solution (1.4.7) for (a) $Q = n/15$ for $n = 1, 2, \ldots, 10$, shown as a Cartesian plot and (b) $Q = 1/15, 1/3$, and Q_{crit}, shown as a polar plot. The dotted circle in (b) shows the location of the cylinder and the arrows show the direction of increasing Q (straight arrow) and the direction of rotation (curved arrow). Note that the film thickness in (b) has been exaggerated for illustrative purposes.

periodic fluid rings. At higher speeds, an asymmetrical fluid lobe formed which rotated slightly slower than the cylinder.

The approach to the critical solution $h_{\rm crit}$ of Moffatt [106] as $Q \to Q_{\rm crit}$ was later investigated theoretically by Tougher *et al.* [112]. They performed a matching procedure between an inner solution (which is valid near $\theta = 0$) and an outer solution (which is valid away from $\theta = 0$) to derive what we shall refer to as the "composite" critical solution, which we denote here by $h_{\rm comp}$, namely,

$$h_{\rm comp} = h_{\rm crit} + \xi \left(\frac{\sqrt{6}}{2|\theta|} - \frac{1}{1 - h_{\rm crit}^2 \cos\theta} \right) + \frac{|\theta|}{6} - \sqrt{\xi + \frac{\theta^2}{6}} \quad \text{as} \quad \xi \to 0^+, \tag{1.4.8}$$

which is valid near $Q = Q_{\rm crit}$, where $\xi = Q_{\rm crit} - Q \ll 1$ (which we note is not the same small parameter as the thin-film aspect ratio ϵ). Using (1.4.8), they obtained a corresponding expansion for the critical weight $W_{\rm crit}$, namely,

$$W_{\rm crit} \simeq 4.44272 + \xi(-4.99001 + 1.22474 \ln \xi) + o(\xi) \quad \text{as} \quad \xi \to 0^+. \tag{1.4.9}$$

The validity of the critical condition for coating (and rimming) flow given by Moffatt [106] was investigated experimentally by Preziosi and Joseph [113] who considered the flow of various oils on different rotating rods using a very similar experimental apparatus to that used by Moffatt [106]. They concluded that, provided the maximum thickness of the liquid coating the outside or the inside of the cylinder is not too large compared to the radius of the cylinder, and that the Reynolds number is sufficiently small, the critical criterion from Moffatt's [106] analysis is mostly accurate.

Pukhnachev [95] proved the existence and uniqueness of steady full-film coating flow solutions of the Navier–Stokes equations, and subsequently derived a model similar to that of Moffatt [106] which includes the additional effect of capillarity, namely,

$$h_t + \left[h - \frac{1}{3} G h^3 \cos\theta + \frac{1}{3} C h^3 (h_{\theta\theta\theta} + h_\theta) \right]_\theta = 0, \tag{1.4.10}$$

where $G = \epsilon^2 \rho g a / (\Omega \mu)$ is a dimensionless gravity parameter, $C = \epsilon^3 \sigma / (\Omega \mu a)$ is an inverse capillary number, and $\epsilon \ll 1$ is the small thin-film aspect ratio as defined in Section 1.4.1. Note that when capillarity is neglected in (1.4.10) (i.e., for $C = 0$), the model of Moffatt [106] (i.e., equation (1.4.4)) is recovered up to differences in scalings. Note that, although Moffatt [106] and Pukhnachev [95] focused primarily

on coating flow, the results arising from their leading-order equations also apply to rimming flow. Specifically, if we take the (nondimensional) free surface to be located at $r = R + h(\theta)$ for coating flow, then for the corresponding rimming flow problem we take $r = R - h(\theta)$. Consequently, within the confines of the thin-film approximation, the two problems are mathematically equivalent at leading order [114]. However, it is crucial to point out that this equivalence does not persist at higher orders (see, for example, Lopes *et al.* [115]).

There have been many extensions to the Moffatt–Pukhnachev problem. As discussed, in addition to rotation, Moffatt [106] considered only leading-order gravitational and viscous effects, neglecting those of capillarity, the hydrostatic pressure gradient, and inertia, whilst Pukhnachev [95] was the first to incorporate capillarity as a a leading-order effect. The treatment of these effects in subsequent work varies. Capillarity is either neglected [116], treated again as a leading-order effect [73, 101, 107, 108, 117–119], or as a first-order effect [102, 120–122]. The hydrostatic pressure gradient is included in various higher-order models [116, 119–124], whilst, although commonly neglected, there are certain studies which explore the impact of inertial effects [121, 124]. In addition, a few authors have relaxed the strict requirement that the film of liquid be thin [56, 96]. Let us now discuss some of these extensions.

The seminal work of Hansen and Kelmanson [96] investigated steady coating flow under the influence of gravity, viscosity, and capillarity without imposing any restrictions on the thickness of the film. They compared their numerical findings with the thin-film results presented by Moffatt [106] and found that, regardless of the thickness of the film, the minima and maxima of the free surface are always located at $\theta = \pi$ and $\theta = 0$, respectively, in agreement with the result of Moffatt [106]. Moreover, they found that the critical mass consistently aligned closely with the predictions made by Moffatt [106]. However, notably, they found that the critical mass was also consistently slightly higher than Moffatt [106] predicted. As expected, they found that, with capillarity included, the corner at $\theta = 0$ in the critical solution h_{crit} that is shown in Figure 1.12 does not appear. As alluded to in Section 1.4.3, a combination of the draining flow problem considered by Nusselt [34, 35] and the coating flow problem considered by Moffatt [106] was investigated by Duffy and Wilson [100], who considered steady two-dimensional flow of a thin layer of liquid falling onto and off from the outer surface of a rotating cylinder. Using lubrication theory, they showed that four other solution branches exist in addition

to those in equation (1.4.6) which are unbounded at the top and bottom of the cylinder (i.e., at $\theta = \pm\pi/2$) referred to as "curtain" solutions. They also identified partial-film (i.e., in which parts of the cylinder surface are left uncovered) curtain solutions, which occur for $Q = 0$, and the occurrence of jump solutions, which involve a shock transitioning from a full-film solution branch to a curtain solution branch. Kelmanson [118] derived a thin-film model which incorporates rotation, viscosity, and gravity (also notably neglecting capillarity). However, contrary to Moffatt [106], they retained the first order rotation term, $h^2/2$. They found that the retention of this term results in a correction to the result for the maximum supportable load calculated by Moffatt [106] which aligns better with the numerical results of Hansen and Kelmanson [96]. However, subsequently, Wilson *et al.* [125] theoretically investigated further the maximum supportable load problem posed by Moffatt [106], finding that the agreement with Hansen and Kelmanson [96] instead deteriorates upon consistently retaining all first-order terms. By including terms up to $O(\epsilon^4)$, they revealed a marginally higher true critical mass than the prediction of Moffatt [106], achieving improved agreement with Hansen and Kelmanson [96], and found that the corner in the full-film leading-order critical solution h_{crit} is smoothed by higher-order effects, even in the absence of capillarity, and confirmed this numerically.

More recently, the focus of coating flow analyses has moved away from the challenge of determining the maximum supportable load towards exploring the existence, stability, and behaviour of solutions for the many variations of the coating flow system. For example, as discussed in Section 1.4.3, in the special case of a two-dimensional cylinder Evans *et al.* [102] theoretically investigated unsteady coating flow, deriving a model that incorporates rotation, viscosity, gravity, capillarity, and centrifugation, namely,

$$(1+\underbrace{\epsilon h}_{(a)})h_t + \left[U_\Omega\left(h+\underbrace{\frac{\epsilon}{2}h^2}_{(b)}\right) - \cos\theta\left(\frac{1}{3}h^3+\underbrace{\frac{\epsilon}{2}h^4}_{(c)}\right) + \frac{\epsilon}{3Bo}h^3\left(h_\theta + h_{\theta\theta\theta}\right) - \frac{\epsilon}{3}h^3h_\theta\left(W^2-\sin\theta\right)\right]_\theta = 0, \tag{1.4.11}$$

where $Bo = \rho g a^2/\sigma$ is a Bond number, $W = \Omega(a/g)^{1/2}$ is a dimensionless rotation rate (as defined earlier) and $U_\Omega = V_\Omega/(\epsilon^2 V)$ is a dimensionless ratio of the cylinder velocity $V_\Omega = \Omega a$ to the characteristic velocity $V = \rho g h_0^2/\mu$. Evans *et al.* [102] nu-

merically solved their model (1.4.11) using a finite-difference method (see Section 1.3.3.1). In order to simplify their numerical calculations, they neglected three first-order terms in their model, labelled as (a), (b), and (c) in equation (1.4.11), which arise due to the curvature of the cylinder surface. Upon solving the model (1.4.11) with these terms neglected, they showed a diverse array of behaviors which emerged depending on the rotation rate W. They performed a parametric study in which they varied the rotation rate W, the results of which are shown in Figure 1.10 (a) which, as discussed previously, shows the film thickness h at the top of the cylinder (which, as we recall from Section 1.4.3, is located at $\theta = 0$ in their geometric setup) over time for several values of W. They found that a bulge forms on the lower part of the cylinder, the location of which increases upwards on the right-hand side of the cylinder as W is increased, as shown in Figure 1.10 (b). Upon reaching the critical rotation speed, they observed that the solution reaches a steady state in which the bulge is held on the right-hand side of the cylinder and the interface displays top-to-bottom symmetry. When the rotation speed exceeds this critical value, the bulge begins to rotate around the cylinder.

More recently, Lopes *et al.* [115] theoretically investigated the dynamics of both coating and rimming flow under the influence of gravity, viscosity, and capillarity by developing three distinct models. The first is the most commonly used model which is the "standard lubrication model" (SLM), which assumes that the Bond number is order unity (the model derived by Pukhnachev [95], for example, is an SLM). The second is the "extended lubrication model" (ELM) which, unlike the SLM, assumes that the Bond number is small (the model derived by Evans *et al.* [102], for example, is an ELM). The final model is the "variational lubrication model" (VLM) which was derived by Lopes *et al.* [115] using a variational approach (see, for example, Xu *et al.* [126]). Unlike the classical SLM and ELM, the VLM retains the full form of the curvature rather than neglecting higher-order terms. They performed DNS of the full Stokes flow equations and compared their findings with the results of the three aforementioned models. Lopes *et al.* [115] found that the VLM yielded improved agreement compared to the SLM and ELM models and successfully captured scenarios in which, for particular parameter regimes, multiple solutions were possible (with some parameter sets displaying up to two solutions). These instances of multiple solutions were not predicted by the SLM and ELM models, which they ascribed to the neglect of higher-order curvature terms.

The linear stability (see Section 1.3.1) of coating (and rimming) flow in the presence of additional physical effects, such as capillarity, inertia, and the hydrostatic pressure gradient, has been the subject of studies by many authors, including Hosoi and Mehadevan [120], O'Brien [127, 128], Benilov and O'Brien [121], and Benilov and Lapin [122]. For leading-order rimming flow (and consequently, for leading-order coating flow), O'Brien [127] established that subcritical two-dimensional full-film solutions exhibit neutral linear stability. They inferred that a conclusive investigation of the stability of rimming flow solutions necessitates the incorporation of higher-order terms within the thin-film approximation. In a companion paper, O'Brien [128] built upon this study by considering the stability of subcritical rimming flow solutions under the influence of gravity, viscosity, and capillarity. They retained higher-order terms in the thin-film approximation and found that the linear stability of the steady state solutions depends on various parameter values. Specifically, they noted that increasing the rotation rate of the cylinder or increasing the strength of capillarity could act as stabilising influences, whereas the absence of both resulted in instability. Benilov and O'Brien [121] investigated the influence of weak inertia, a weak hydrostatic pressure gradient, and weak capillarity on the linear stability of normal modes in thin-film rimming flow by including them as higher-order terms in the lubrication model. Specifically, their model is

$$h_t + \left\{ h - \frac{1}{3}h^3\cos\theta + \alpha\left[\frac{2}{15}h^6 h_\theta(\cos\theta)^2 - \frac{8}{315}h^7\sin\theta\cos\theta - \frac{2}{15}h^5\sin\theta\right] + \frac{\beta}{3}h^3(h_\theta + h_{\theta\theta\theta}) + \frac{\varrho}{3}h^3 h_\theta\sin\theta \right\}_\theta = 0, \tag{1.4.12}$$

where $\alpha = \Omega^2 a/g$, $\beta = \sigma\varrho/(\rho g a^2)$, and $\varrho = [\rho\Omega/(\mu g a)]^{1/2}$. The first two terms in the curved brackets in (1.4.12) represent rotation and leading-order gravitational effects, whilst the terms with coefficients of α, β, and ϱ represent inertia, capillarity, and the hydrostatic pressure gradient, respectively. Benilov and O'Brien [121] considered perturbations to a nonuniform base state and found that the disturbances are neutrally stable at leading order, in agreement with the result of O'Brien [127]. At first order, they found that inertia is a destabilising influence, capillarity has a weak but noticeable stabilising effect, and the hydrostatic pressure gradient has no discernible impact on the stability. They found that the destabilising effect of inertia can be offset by increasing the viscosity of the liquid until

the timescale of the growth becomes sufficiently large so as to effectively stabilise the solution. We defer giving explicit details of their lengthy calculations until Section 4.1.2 in which we revisit their calculation in the context of our problem. For now, we note that they sought series solutions for h and ω (where ω is the angular frequency as defined in Section 1.3.1) in powers of $\alpha \ll 1$, $\beta \ll 1$, and $\varrho \ll 1$, from which they obtained their growth rate, denoted by $\mathrm{Im}(\omega)$, to be

$$\mathrm{Im}(\omega) = \alpha \mathrm{Im}(\omega_\alpha) + \beta \mathrm{Im}(\omega_\beta) + O(\varrho^2, \alpha^2, \beta^2, \varrho\alpha, \varrho\beta, \alpha\beta), \tag{1.4.13}$$

where $\mathrm{Im}(\omega_\alpha)$, and $\mathrm{Im}(\omega_\beta)$ are

$$\mathrm{Im}(\omega_\alpha) = \omega_0^2 \left(\int_0^{2\pi} \frac{\mathrm{d}\theta}{C_0} \right)^{-1} \int_0^{2\pi} \frac{D_1}{C_0^3} \, \mathrm{d}\theta, \tag{1.4.14}$$

$$\mathrm{Im}(\omega_\beta) = \omega_0^2 \left(\int_0^{2\pi} \frac{\mathrm{d}\theta}{C_0} \right)^{-1} \int_0^{2\pi} \left\{ \frac{B_1}{C_0^3} \left(1 - \frac{1}{C_0^2} \left[\omega_0^2 + 4C_0 \left(C_0\right)_{\theta\theta} - 11 \left(C_0\right)_\theta^2 \right] \right) \right\} \mathrm{d}\theta, \tag{1.4.15}$$

respectively, where C_0, B_1, D_1, and ω_0 are given by

$$C_0 = 1 - (h^{(0)})^2 \cos\theta, \tag{1.4.16}$$

$$B_1 = -2h^{(0)}h^{(1)} \cos\theta + h_0^2 (h_\theta^{(0)} + h_{\theta\theta\theta}^{(0)}), \tag{1.4.17}$$

$$D_1 = \frac{2}{15} (h^{(0)})^6 (\cos\theta)^2, \tag{1.4.18}$$

$$\omega_0 = 2\pi n \left(\int_0^{2\pi} \frac{\mathrm{d}\theta}{C_0} \right)^{-1}, \tag{1.4.19}$$

where $h^{(0)} = h^{(0)}(\theta)$ and $h^{(1)} = h^{(1)}(\theta)$ are the leading-order and first-order solutions for h (see equations (15)–(17) of Benilov and O'Brien [121] for details) and n is the integer wavenumber of the perturbations. Figure 1.13 shows the growth rate $\mathrm{Im}(\omega)$ of the first mode $n = 1$ plotted over the range $0 \leq q \leq q_{\mathrm{crit}}$ (where the flux is denoted by q in their notation) for $\beta = 0.1$ calculated from the numerical solution of the governing equation (1.4.12) (solid) and the asymptotic solution (1.4.13) (dashed) for the special case in which inertia and the hydrostatic pressure gradient are negligible (i.e., $\alpha = \varrho = 0$). In particular, Figure 1.13 shows that $\mathrm{Im}(\omega) < 0$ for all q, hence indicating that capillarity has a stabilising influence. In the general case (i.e., the case in which α, β, and ϱ are all non-zero), Benilov and

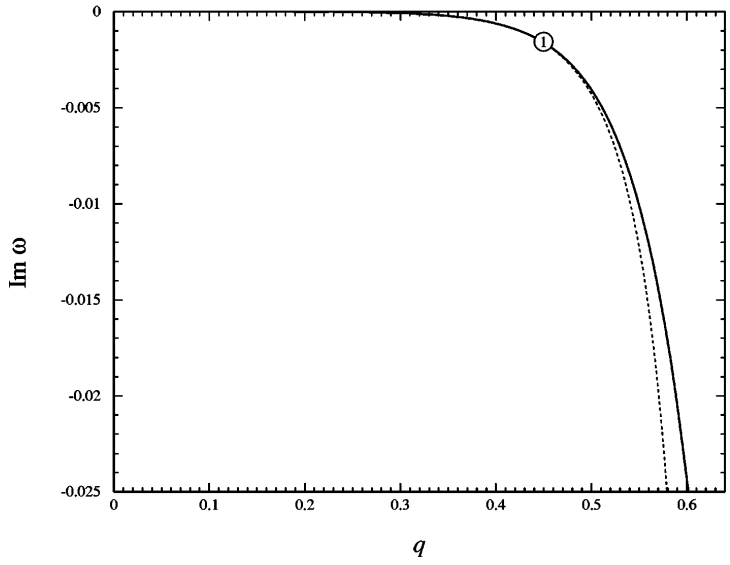

Figure 1.13: The growth rate calculated by Benilov and O'Brien [121] in the case in which $\alpha = \varrho = 0$ plotted as a function of q for $n = 1$ and $\beta = 0.1$ calculated from the governing equation (1.4.12) (solid) and the asymptotic solution $\mathrm{Im}(\omega)$ (1.4.13) (dashed) to $O(\beta)$. Reprinted from Benilov and O'Brien [121], with the permission of AIP Publishing. Copyright 2005.

O'Brien [121] calculated the growth rate of the first mode in the limit of small q, which they found to be

$$\mathrm{Im}(\omega) \approx \frac{1}{15}\alpha q^6 - 3\beta q^7 \tag{1.4.20}$$

for $q \ll 1$. Hence, in the limit of small q, instability exists if and only if

$$q \leq \frac{\alpha}{45\beta}. \tag{1.4.21}$$

Figure 1.14 shows regions of stability and instability in the $(\alpha/\beta, \langle\bar{h}\rangle)$ plane, where $\langle\bar{h}\rangle$ is the average dimensionless film thickness. In particular, Figure 1.14 shows that, perhaps counter-intuitively, thinner films are more unstable than thicker films. We return to this point in detail in Section 4.1.2.

In the same work that was discussed earlier in this section, Evans *et al.* [102] also performed a linear stability analysis on their model in the analytically tractable limit of zero gravity. Note that their equation (1.4.11) has been nondimensionalised using the characteristic velocity $V = \rho g h_0^2/\mu$. However, this is not suitable in the context of zero gravity in which $g = 0$. Hence, to consider their governing equation

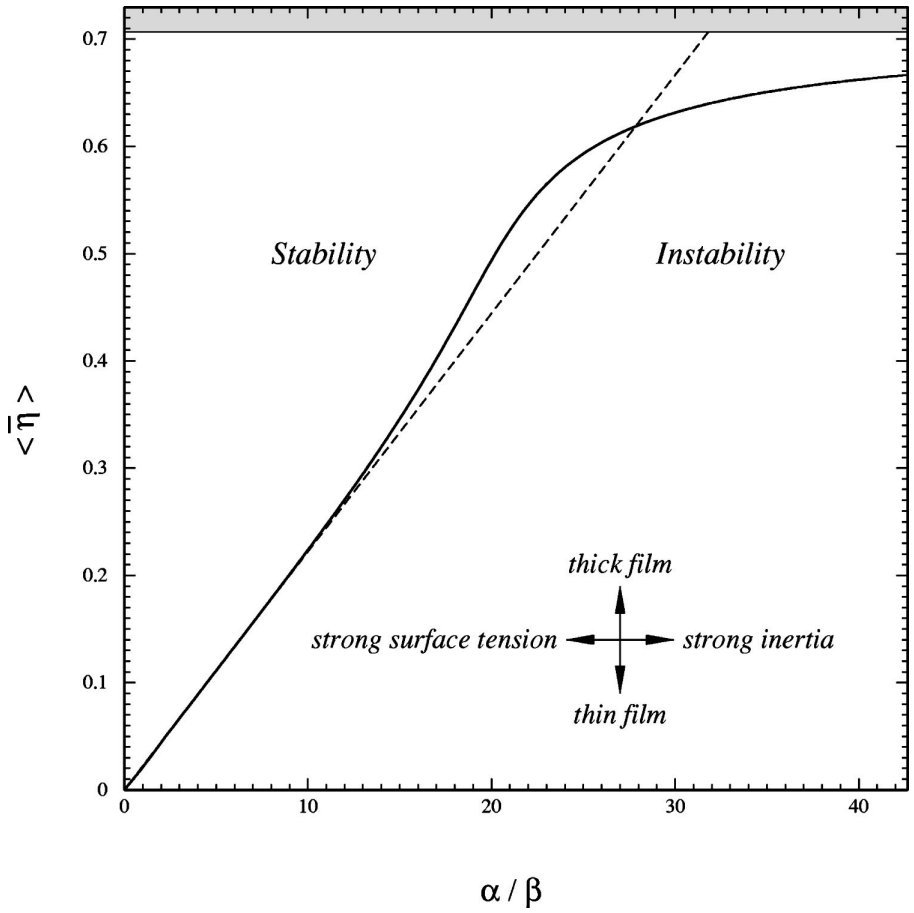

Figure 1.14: Results of the linear stability analysis of Benilov and O'Brien [121]. Regions of stability and instability in the $(\alpha/\beta, \langle\bar{\eta}\rangle)$ plane calculated from the governing equation (1.4.12) (solid) and the small-q limit (1.4.20) (dashed). The shaded region corresponds to $q > q_{\text{crit}}$. Reprinted from Benilov and O'Brien [121], with the permission of AIP Publishing. Copyright 2005.

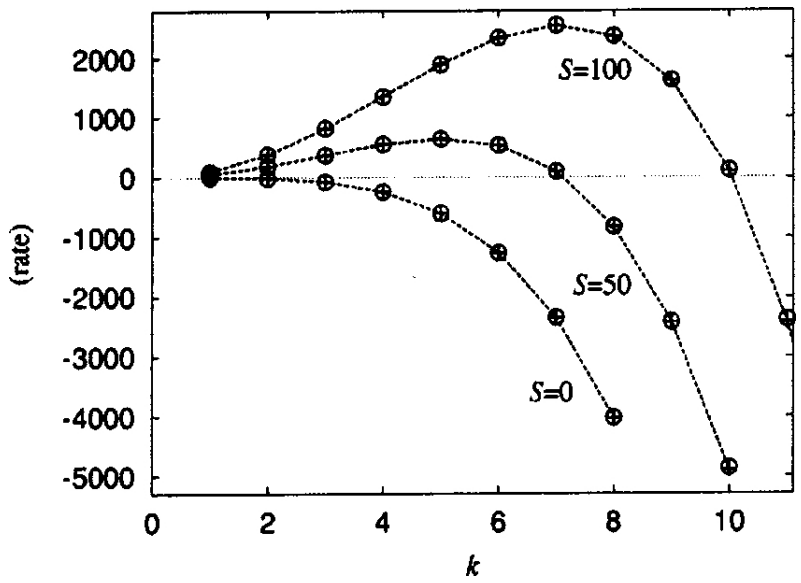

Figure 1.15: Growth rates calculated by Evans *et al.* [102] for the instability due to centrifugal acceleration for $S = 0, 50$, and 100 calculated from their analytical (1.4.23) (crosses) and numerical (circles) results. Reprinted from Evans *et al.* [102], with the permission of AIP Publishing. Copyright 2004.

(1.4.11) under zero-gravity conditions, Evans *et al.* [102] instead considered the dimensional form of (1.4.11), yielding

$$h_t + \Omega h_\theta - \frac{\sigma}{3\mu a^4}\left\{h^3\left[h_\theta + h_{\theta\theta\theta} + Sh_\theta\right]\right\}_\theta = 0, \tag{1.4.22}$$

for $g = 0$, where $S = \rho\Omega^2 a^3/\sigma$ is a Weber number, representing the ratio of centrifugation to capillarity. The linear stability analysis is tractable in this special case due to the fact that a uniform film is a solution of (1.4.22). Performing a linear stability analysis, they obtained the linear growth rate

$$\omega = -\Omega ni + \frac{\sigma h_0^3}{3\mu a^4}\left[(1+S)\,n^2 - n^4\right], \tag{1.4.23}$$

which is shown for $S = 0, 50$, and 100 in Figure 1.15, calculated from both (1.4.23) and from numerical solutions of the governing equation (1.4.22) (note that Evans *et al.* [102] denoted their wavenumber by k rather than n, however, here we choose to use n for consistency with the rest of the work presented in this thesis). They found that when the cylinder is stationary and hence there is no centrifugal acceleration

(i.e., for $S = 0$), solutions are neutrally stable for $n = 1$ and all wavenumbers $n > 1$ have negative growth rates and are therefore stable. When the cylinder is rotated, the flow becomes unstable for wavenumbers below the cutoff wavenumber, which we denote by n_c, given by

$$n_c = \lfloor \sqrt{1+S} \rfloor, \tag{1.4.24}$$

where $\lfloor \cdot \rfloor$ represents the largest integer smaller than the argument. The fastest growing wavenumber, which we denote by n_{max}, is given by

$$n_{max} = \left[\sqrt{\frac{1+S}{2}} \right], \tag{1.4.25}$$

where $[\cdot]$ represents the integer closest to the argument. For example, (1.4.25) yields $n_{max} \approx [5.0498] = 5$ and $n_{max} \approx [7.1063] = 7$ for $S = 50$ and $S = 100$, respectively. Evans *et al.* [102] found that in the presence of centrifugal effects, small perturbations grow due to centrifugation which results in the formation of bulges of liquid around the circumference the cylinder. As will be discussed in detail in Section 4.1.1 (in which we carry out a similar calculation for our problem), the value of (1.4.25) predicts the number of bulges which are expected to arise in numerical results. Indeed, Figures 1.16 (a) and (b) show interface shapes in the absence of gravity for $S = 50$ and $S = 100$, respectively, in which 5 and 7 bulges have formed by the respective times.

The complex large-time dynamics of unsteady coating flow has also been an area of interest in more recent years. Hinch and Kelmanson [73] considered a model that includes the effects of gravity, viscosity, and capillarity, which is the same as that of Puhnachev [95] (i.e., equation (1.4.10)) up to differences in scalings. In the case in which gravity and capillary effects are weak, they found that an initially uniform film evolves on four different timescales. They proposed a multiple-timescale analysis approach (see Section 1.3.2) via a two-timescale expansion of the film thickness to explain the structure of the evolution. They found that as perturbations to the free surface decay, they experience a gravity-induced phase lag relative to the cylinder due to the interactions between rotation, gravity, and capillarity. The decay of the fundamental mode is shown in Figure 1.17, which demonstrates how the interplay between gravity and capillarity influences the evolution of the film at times $t = 0$ (top row) and $t = \pi$ (bottom row). Figure

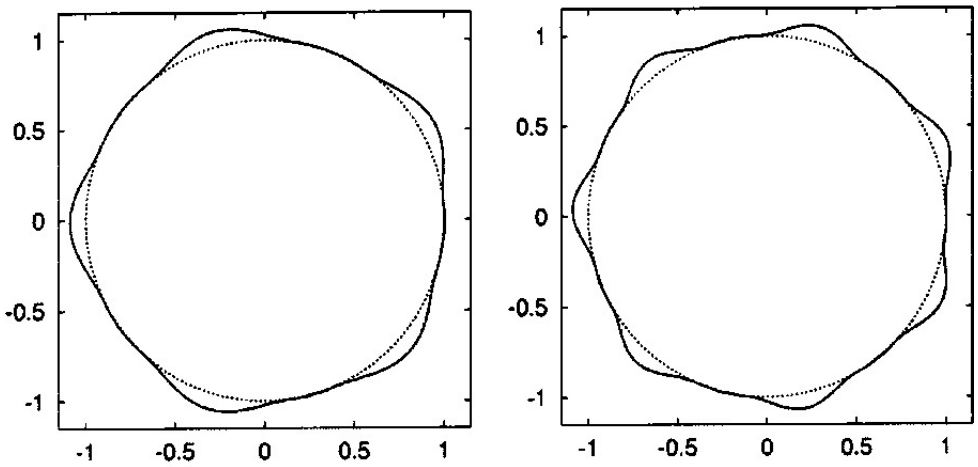

Figure 1.16: Interface shapes in the absence of gravity calculated by Evans *et al.* [102] for (a) $S = 50$ at time $t = 10^4$ with $n_{\max} = 5$ and (b) $S = 100$ at time $t = 2000$ with $n_{\max} = 7$. Reprinted from Evans *et al.* [102], with the permission of AIP Publishing. Copyright 2004.

1.17 (a) shows the influence of gravity. At time $t = 0$, the film is thinner near $\theta = 0$ and thicker near $\theta = \pi$ due to the fundamental mode disturbance caused by gravity, which slightly reduces the thickening at $\theta = 0$ and increases the thinning at $\theta = \pi$. At time $t = \pi$, the behavior is reversed: the film is thicker near $\theta = 0$ and thinner near $\theta = \pi$, as the fundamental mode disturbance induced by gravity changes sign. Figure 1.17 (b) shows the influence of capillarity. At time $t = 0$, the top and bottom of the film experience positive capillary pressure, causing a slowing down and thickening of the film in the first and third quadrants, whilst the sides experience negative pressure, leading to thinning in the second and fourth quadrants. At time $t = \pi$, this behavior is reversed. Figure 1.17 (c) shows the combined influence of gravity and capillarity. Gravity slows down the film in the first and fourth quadrants and speeds it up in the second and third, leading to a net convergence at $\theta = 0$, whilst the opposite happens at $\theta = \pi$, resulting in a net divergence. As a result, the film becomes thicker near $\theta = 0$ and thinner near $\theta = \pi$. The amplitude of the disturbance gradually decreases over time. The growth rate of the film thickness (which we denote here by ω) was found to be

$$\omega = -\frac{81\alpha}{1 + 144\alpha^2} \leq 0, \tag{1.4.26}$$

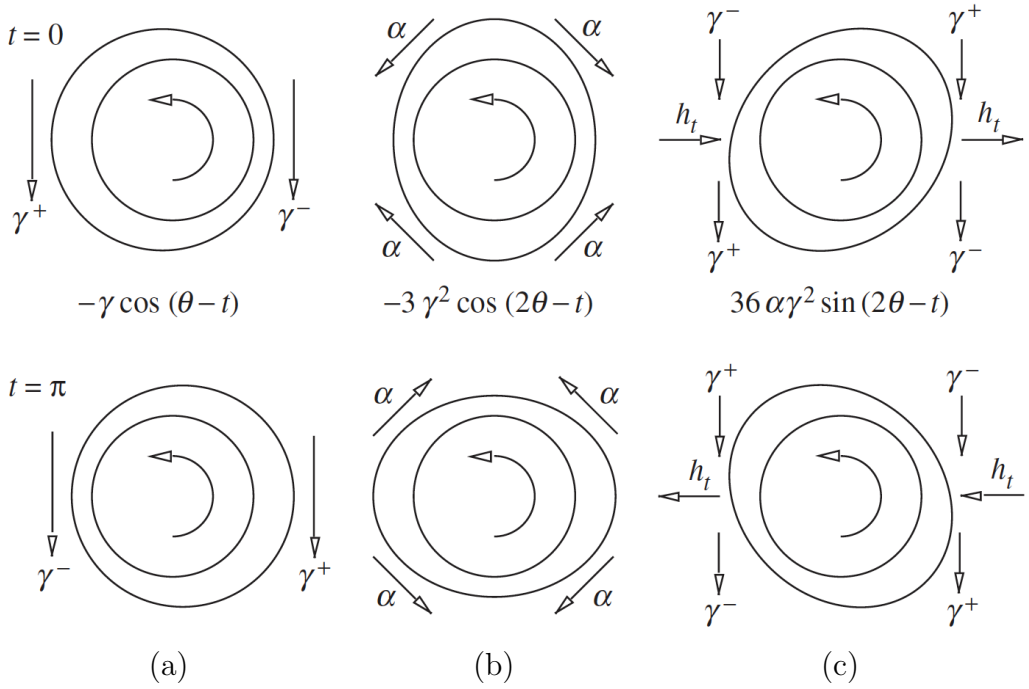

Figure 1.17: The decay of the fundamental mode. The two rows show the disturbance at time $t = 0$ and $t = \pi$, respectively. (a) Gravity acts on the fundamental mode to create the first harmonic in (b). (b) Capillary pressure gradients act to create the phase-shifted first harmonic in (c). (c) Gravity acts on the phase-shifted first harmonic to create a rate of change of amplitude of the fundamental mode. Reproduced from Hinch and Kelmanson [73], with permission from The Royal Society. Copyright 2003.

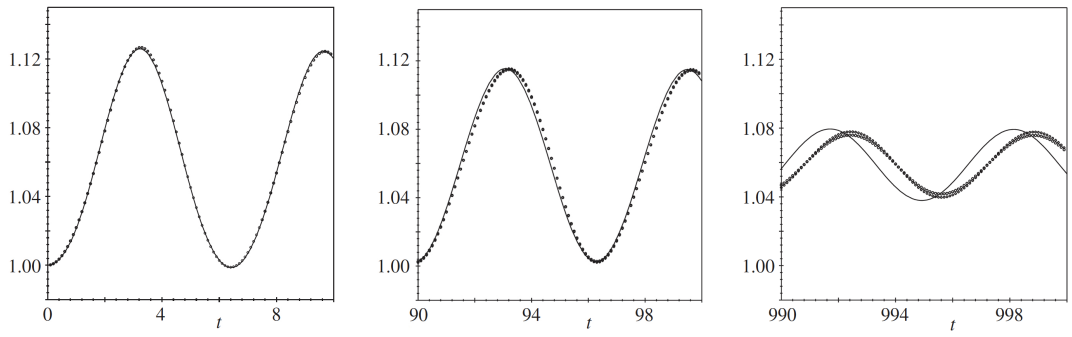

Figure 1.18: Drift of the four-term, two-timescale expansion derived by Hinch and Kelmanson [73] (solid) compared to their numerical results (circles and diamonds) for $\gamma = 0.0532$ and $\alpha = 0.0048$ at times (a) $0 \leq t \leq 10$, (b) $90 \leq t \leq 100$, and (c) $990 \leq t \leq 1000$. Reproduced from Hinch and Kelmanson [73], with permission from The Royal Society. Copyright 2003.

where $\alpha = \epsilon^3\sigma/(3\Omega\mu a)$ is an inverse capillary number. Equation (1.4.26) indicates that the solution decays unconditionally to a steady state at large times for $\alpha > 0$, and that for $\alpha = 0$ the system is neutrally stable. Specifically, the steady state is approximated by equation (5.1) of Hinch and Kelmanson [73] and is uniform to leading order in $\gamma \ll 1$ (where $\gamma = \epsilon^2\rho g a/(3\Omega\mu)$ is a dimensionless gravity parameter). The drift of the four-term, two-timescale expansion for the film-thickness is shown in Figure 1.18. Recently, Mitchell *et al.* [129, 130] generalised this result to include the effect of a steady two-dimensional irrotational airflow with circulation, and found the growth rate to be

$$\omega = -81\alpha\left(\frac{10F^4}{(1+36\alpha^2)\,(1+1296\alpha^2)} + \frac{(1+2KF)^2}{1+144\alpha^2}\right) \leq 0, \tag{1.4.27}$$

where F and K are dimensionless measures of the speed of the far-field airflow and the circulation of the airflow, respectively. Equation (1.4.27) shows that in the presence of the airflow, the solution again decays unconditionally to a steady state at large times for $\alpha > 0$ and that for $\alpha = 0$ the system is neutrally stable. We discuss the details of the lengthy calculations of Hinch and Kelmanson [73] and Mitchell *et al.* [130] in Section 4.4 in which we revisit the analysis in the context of our problem.

Kelmanson [124] extended the model given by Pukhnachev [95] to include in-

ertial effects and revisited the work of Hinch and Kelmanson [73]. They identified a two-timescale asymptotic solution for the evolution of the film thickness (which is initially uniform) in the regime of weak capillarity, in which the asymptotic solution found by Hinch and Kelmanson [73] is no longer valid. In addition, they discovered that including both capillarity and inertia causes the location of the maximum film thickness to shift away from its location at $\theta = 0$ [106] downwards towards the lower part of the cylinder. Building on the work of Kelmanson [124], Groh and Kelmanson [131–133] conducted subsequent studies investigating the large-time behavior of unsteady coating flow. Firstly, Groh and Kelmanson [131] proposed a multiple-timescale analysis approach via an m-timescale expansion of the film thickness, which yielded improved agreement with their numerically obtained solutions for the film thickness evolution when compared to the two-timescale expansion. Next, Groh and Kelmanson [132] generalised the m-timescale expansion by removing the requirement that the initial condition is a uniform film, demonstrating that the multiple-timescale asymptotic approach could yield highly accurate solutions for the film thickness not only in the cylindrical coating flow problem, but also in more general free-surface thin-film problems. Finally, Groh and Kelmanson [133] incorporated inertia into the models derived in their previous works [131, 132]. They used the multiple-timescale approaches developed therein to describe the transition from stability to instability dependent on the strength of inertia, finding that their asymptotic solution exhibited excellent agreement with their numerical results.

The coating flow (and draining flow) problem has been extended to include a variety of external physical effects. For example, non-isothermal effects have been included by various authors including Reisfeld and Bankoff [101] (as mentioned in Section 1.4.3), Duffy and Wilson [134], and Leslie *et al.* [135, 136]. Dewetting effects have been included by, for example, Thiele [137] and Lin *et al.* [138], and surfactant effects have been included by, for example, Weidner [139] and Li and Kumar [140]. As we have just mentioned, recently, Mitchell *et al.* [129, 130] extended the work of Moffatt [106] to include a nonuniform pressure distribution due to an irrotational airflow with circulation which they showed can lead to behavior which differs from that of Moffatt [106]. Specifically, they found that when the circulation of the airflow is in the same direction as the rotation of the cylinder, the maximum supportable load is consistently lower than that found by Moffatt [106]. Conversely, when the circulation is in the opposite direction to

the rotation of the cylinder, the maximum fluid mass can surpass that found by Moffatt [106]. The effect of an external magnetic field was considered by Weidner [141], who investigated theoretically how a magnetic liquid (i.e., a "ferrofluid") coating a conducting stationary cylinder responds to an induced electric current. They derived a model which incorporates the effects of rotation, gravity, viscosity, capillarity, and magnetic effects, and found that magnetic forces counteract gravity, thus slowing drainage, delaying drop formation, and potentially leading to complete cylinder circumference coverage for strong magnetic fields. Notably, the effect of a radial electric field is one which has not been considered thus far in the coating flow literature. The observation of this omission from the literature, in addition to its potential usage as a control mechanism (see Section 1.7), is the main motivation for the problem considered in this thesis, in which we consider the effect of an external electric field on coating and draining flow. We defer further discussion of electrohydrodynamic flows until Section 1.6.

In this thesis, we consider the effect of an electric field on both thin-film and thick-film coating flow. As discussed in detail in Sections 1.4.1 and 1.4.2, Wray *et al.* [56] developed a novel approach which permits the modelling of thick films on curved substrates. They outlined important differences between the thin-film and long-wave approximations for flow on curved substrates, based on which they proposed a long-wave methodology which allows the film thickness to be of the same order as the radius of curvature of the substrate, in conjunction with the WRIBL method (see Section 2.3). The long-wave methodology allows us to develop what we shall refer to hereafter as "thick-film models" (in contrast to "thin-film models", which are derived using a thin-film approximation). In the context of coating flow, Wray *et al.* [56] derived a second-order thick-film WRIBL model in the absence of inertia which includes the effects of rotation, viscosity, gravity, capillarity, and streamwise viscous dissipation, and found that it yields significantly closer agreement with the results of DNS than their thin-film model (which notably recovers that of Moffatt [106] (1.4.4) up to differences in scalings). Wray *et al.* [56] found that for moderate values of the dimensionless rotation rate (denoted in their notation by c_V), the thick-film coating flow system reaches a steady state. Figure 1.19 shows the behaviour of their thin-film model (dotted green), their second-order thick-film WRIBL model (dashed red), and DNS (solid blue) in a system with moderate values of c_V. In particular, Figure 1.19 focuses on two key parameters: the maximum value of the interface height (denoted by $h_{\max}$) and the position of

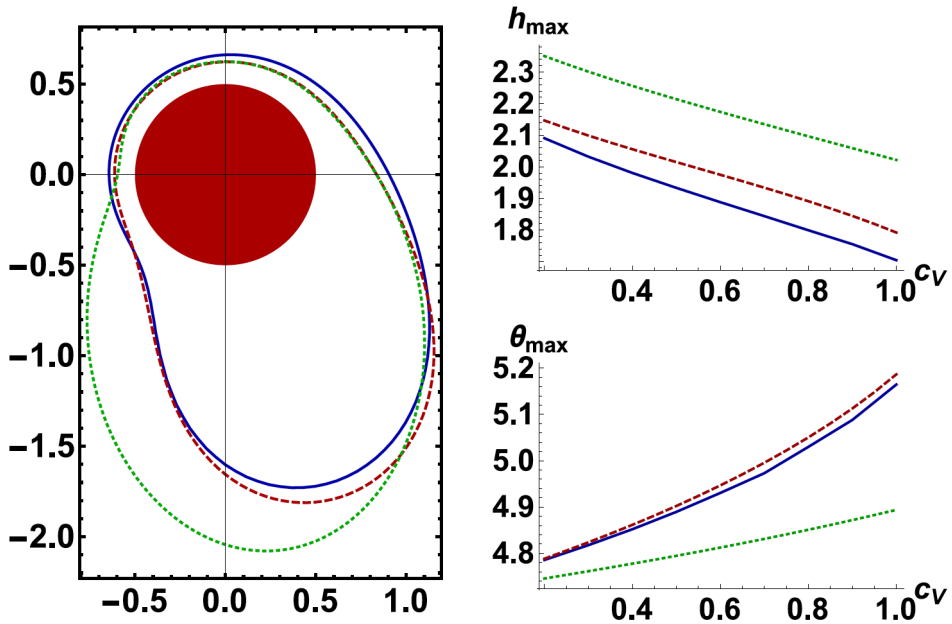

(a) (b)

Figure 1.19: (a) Steady state shapes of thick-film coating flow for $\bar{h} = 1$, $c_V = 0.8$, $\alpha = 0.5$, and $Ca = 0.2$. (b) The maximum interface height $h_{\max}$ of a steady state (top) and azimuthal position of the maximum $\theta_{\max}$ (bottom) for a range of values of the dimensionless rotation rate c_V. Lines represent DNS (solid blue), their second-order thick-film WRIBL model (dashed red), and their thin-film model (dotted green). Reprinted from Wray *et al.* [56] with permission. Copyright 2017 Society for Industrial and Applied Mathematics. All rights reserved.

this maximum (denoted by $\theta_{\max}$). Figure 1.19 (a) shows the steady-state shape calculated for $\bar{h} = 1$, $c_V = 0.8$, $\alpha = 0.5$, and $Ca = 0.2$ where, in the notation of Wray *et al.* [56], $\bar{h}$ is the dimensionless unperturbed interface location, α is the dimensionless cylinder radius, and $Ca = \mu U/\sigma$ (where U is a characteristic velocity) is a capillary number. Their thin-film model cannot accurately model the free surface of the film and does not preserve mass. On the other hand, their second-order thick-film WRIBL model agrees closely with the DNS results. Figure 1.19 (b) shows $h_{\max}$ (top) and $\theta_{\max}$ (bottom) plotted as functions of c_V. In particular, Wray *et al.* [56] found that, over the range $0.2 < c_V < 1$, their thick-film model yields a maximum error of only 5% and 0.025 radians for $h_{\max}$ and $\theta_{\max}$, respectively, whilst their thin-film model performs less well, yielding maximum errors of 18% and 0.22 radians for the respective quantities.

Recently, Wray and Cimpeanu [31] extended the work of Wray *et al.* [56] to include inertial effects. Their thick-film model is

$$\begin{aligned}
&\frac{\varepsilon}{8}(1-h^4+4h^2\ln h)\left[\frac{\kappa}{Ca}+Re(h\sin\theta)-2Re\frac{q^2}{h^2-1}\right]_\theta = q+\frac{c_V}{2}(1-h^2)\\
&-\varepsilon^2\frac{(1-h^2)^2(1+h^2)h_\theta}{2h^3}\left(\frac{q}{h^2-1}\right)_\theta+\varepsilon^2\frac{(1-h^2)(1+h^4+2h^2(\ln^2 h-1))}{4h^2}\left(\frac{q}{h^2-1}\right)_{\theta\theta}\\
&+\varepsilon\frac{Re}{16}(-1+2h^2+2h^6-h^4(3+4\ln h))\left[\left(\frac{q}{h^2-1}\right)_t+\left(\frac{q^2}{(h^2-1)^2}\right)_\theta\right],
\end{aligned} \tag{1.4.28}$$

with the kinematic condition (1.2.9), which together constitute a closed system governing the evolution of the interface height h and the flux q. Here, ε is an ordering parameter as defined in Section 1.4.1, $Re = \rho(ag)^{1/2}/\mu$ is a Reynolds number, $c_V = a\Omega(ag)^{-1/2}$ is a dimensionless rotation rate, and $Ca = \mu(ag)^{1/2}/\sigma$ is a capillary number. Note that their model is a simplified second-order WRIBL model in which second-order inertial effects have been neglected (see Section 1.2.5.3). In the absence of the inertial terms (i.e., for $Re = 0$), equation (1.4.28) recovers the model by Wray *et al.* [56] up to differences in scalings. The term $-2Re\, q^2/(h^2-1)$ in equation (1.4.28) is an important contribution: it represents centrifugation, the inclusion of which transpires to be vital for accurate modelling. They found that their model yields excellent agreement with DNS of the Navier–Stokes equations and, in addition, they investigated regimes which were previously inaccessible to thin-film models by performing a parametric study of the interfacial behaviour in

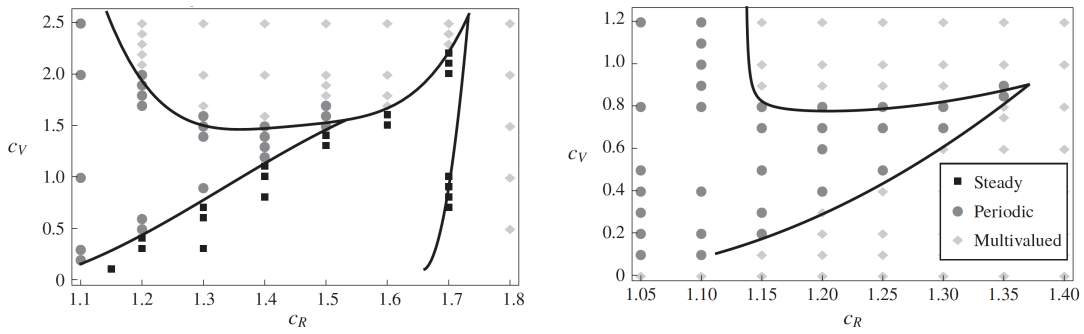

Figure 1.20: Results of the parametric study in (c_R, c_V) parameter space by Wray and Cimpeanu [31] for (a) $We = 0.59$ (capillarity is strong compared to inertia) and (b) $We = 18.8$ (capillarity is weak compared to inertia). Solid lines represent the boundaries between flow regimes as predicted by the thick-film model (1.2.9) and (1.4.28) and symbols correspond to DNS representing flow regimes which are steady (squares), periodic (circles), and multivalued (diamonds). Reproduced from Wray and Cimpeanu [31], with permission from Cambridge University Press. Copyright 2020.

(c_R, c_V) parameter space, where $c_R = h_0/a$ denotes the dimensionless initial radius of the film at time $t = 0$. Figure 1.20 shows the results of the parametric study for two different values of the Weber number $We = Re\ Ca$ (which represents the ratio of inertial to capillary effects). Figure 1.20 (a) shows that when capillarity is strong compared to inertia, steady states, periodic states, and multivalued states can arise, the last of which can include behaviours such as dripping or other forms of rupture. On the other hand, Figure 1.20 (b) shows that insufficient capillarity prevents steady states from occurring. Figure 1.20 shows that increasing the film thickness or rotation rate eventually yields multivalued states. Wray and Cimpeanu [31] explored the steady and periodic states that arise using both their thick-film model (1.2.9) and (1.4.28) and by using DNS. However, the model is insufficient to describe multivalued states due to the fact that they have parameterised by the azimuthal angle θ. Moreover, the long-wave approximation is no longer valid in this regime because the interfacial slopes are so large. Hence, these behaviours must be analysed via DNS of the Navier–Stokes equations. Some representative steady, periodic, and multivalued states are shown in Figures 1.21 (a), (b), and (c), respectively.

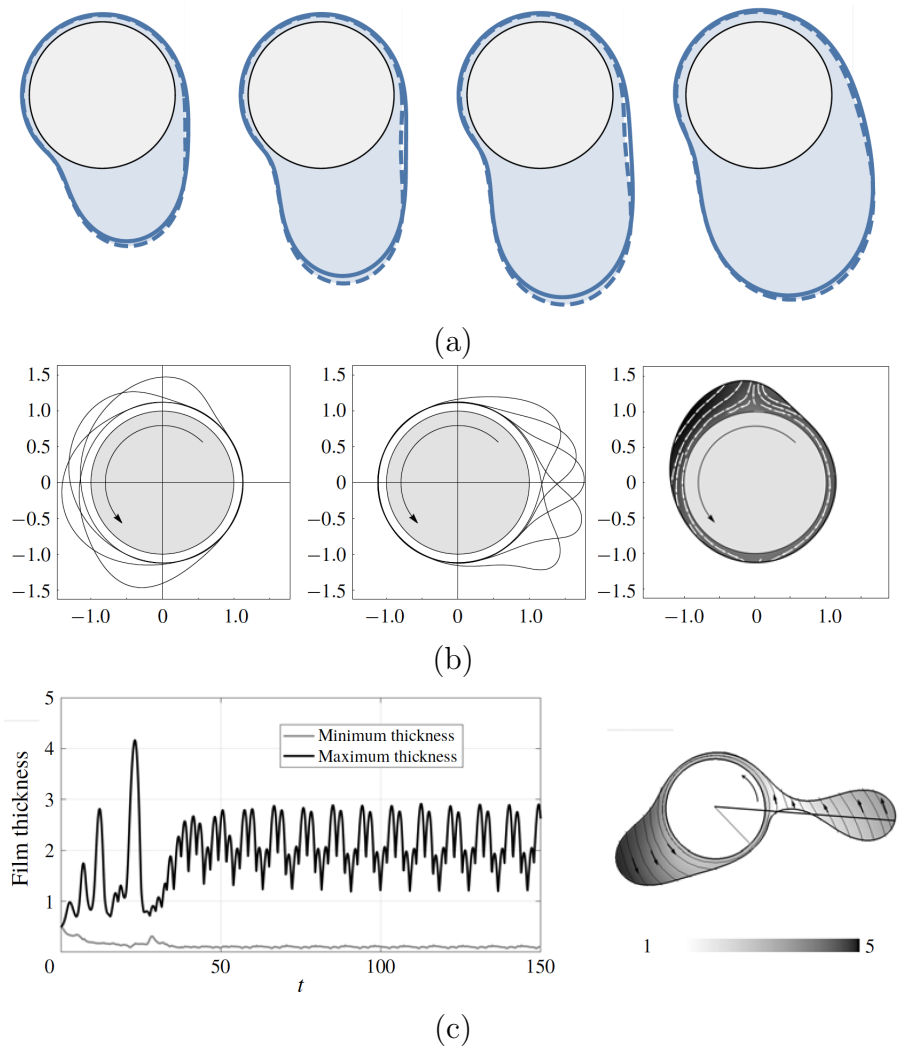

Figure 1.21: Thick-film interfaces calculated by Wray and Cimpeanu [31]. (a) Steady states: snapshots of the interface shapes for $Re = 9, 7, 5$, and 3 with $c_R = 1.3, 1.4, 1.5$, and 1.6 respectively (left-to-right). (b) Periodic states: snapshots of the interface shapes for $c_R = 1.2$ for the draining phase (left) and the inertia-capillary phase (centre), and the streamlines when the base flow $v = c_V r$ is subtracted off, showing the draining behaviour (right). (c) Multivalued states: evolution of the minimum (grey) and maximum (black) film thickness for $c_V = 1.9$ and $c_R = 1.5$ (left) and the interfacial shape and norm of the velocity field restricted to the liquid phase as extracted at the final time step (right). Representative streamlines are decorated with arrows indicating the direction of the flow, with thick lines indicating the points of minimum (grey) and maximum (black) thickness. Reproduced from Wray and Cimpeanu [31], with permission from Cambridge University Press. Copyright 2020.

Finally, note that various aspects of the coating flow problem (including the dynamics and stability thereof) have been extended to three dimensions by various authors (see, for example, Weidner *et al.* [142], Lin *et al.* [143], Evans *et al.* [102, 123], Benilov [144], and Noakes *et al.* [145]). However, for the scope of this thesis, our focus will solely be on the two-dimensional case as an important first step to understanding the dynamics of our problem.

1.4.5 Flows on other curved substrates

There have been various studies which consider flow on the surface of other substrates, such as those which are either non-cylindrical or non-circular. For example, flow on topographically patterned cylinders has been studied by authors such as Sahu and Kumar [146], Li *et al.* [147], and Parrish [148, 149], whilst flow on elliptical cylinders has been studied by Hunt [150], Li *et al.* [151], and most recently by Parrish *et al.* [149]. Flow on spherical substrates has garnered interest in recent years and has been studied by various authors such as Takagi and Huppert [103] (as discussed previously in Section 1.4.3), Lee *et al.* [152], Balestra *et al.* [153], and Kang *et al.* [154]. As mentioned in Section 1.4.3, one particular study which is important with regards to the work in this thesis in that by Qin *et al.* [105] who theoretically investigated the unsteady flow of a thin film on the outer surface of a stationary sphere using a special case of the axisymmetric model developed by Kang *et al.* [154] in which the sphere is stationary, which incorporates the effects of viscosity, gravity, and capillarity. Qin *et al.* [105] derived an asymptotic solution for the film thickness which shows that its evolution from an initially uniform film is independent of capillarity at early times. They also performed numerical simulations of the film thickness, from the results of which they inferred that four distinct "zones" of behaviour emerge at late times: a "thin-film" zone on the upper part of the sphere, a quasi-static "pendant-drop" zone on the lower part of the sphere, and two narrow inner zones that connect them, namely, a "dimple-ring" zone and a "ridge-ring" zone. Numerical solutions showing the interface evolution over dimensionless time τ for a fixed Bond number $Bo = \rho g a^2/(\sigma h_0)$ are shown in Figure 1.22. They obtained asymptotic solutions for the film thickness in each of the zones and sought to match them to those in the neighbouring zones. In particular, in the thin-film, dimple-ring, and ridge-ring zones they derived and numerically validated similarity solutions and scaling laws for the film thickness,

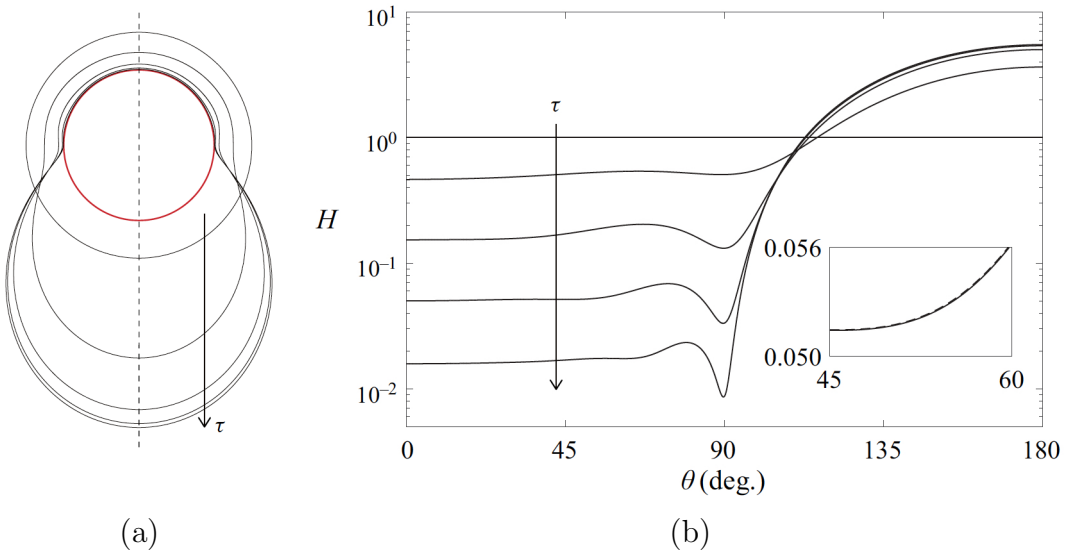

(a) (b)

Figure 1.22: Results of Qin *et al.* [105] for flow on a sphere showing the interface evolution for $Bo = 24$ at times $\tau = 0, 1, 10, 100$, and 1000. (a) Polar plot in which the film thickness has been exaggerated for illustrative purposes. (b) Semi-log plot showing the film thickness H as a function of θ. Reproduced from Qin *et al.* [105], with permission from Cambridge University Press. Copyright 2020.

whilst in the pendant-drop zone they derived and numerically validated an analytical solution for the film thickness. We defer further discussion of this key paper until Chapter 3.

1.5 Capillary-ripple structures

An important feature of some free-surface flows that is relevant to the work contained in this thesis is capillary ripples. Capillary ripples arise in regions in which a thin film transitions from a near-uniform thin film to a region with larger curvature. They are driven by capillarity and comprise of alternating minima and maxima (commonly referred to as "dimples" and "ridges", respectively) with decreasing amplitudes and widths, ultimately converging rapidly towards a uniform thin film.

Capillary ripples have been identified in a wide variety of contexts within free-surface flows [155]. The pioneering work of Wilson and Jones [156] showed that an infinite sequence of steady dimples and ridges is necessary to match a thin

liquid film of uniform thickness flowing down a vertical wall to a quiescent pool of liquid. Following this, similar structures have been found in a variety of contexts including rimming flow [119], levitated drops [157], liquid films or drops on inclined planes [114, 158, 159], elastic-plated gravity currents [160], and Leidenfrost levitation of particles [161]. For example, the study by Benilov and Benilov [159] explored the behavior of drops sliding down inclined planes. Notably, they observed the emergence of a capillary ripple in the case of larger drops. Figure 1.23 (a) shows a sketch of the asymptotic structure of what the authors termed the "large-drop solution". This solution exhibits a distinctive structure: an outer region representing the main body of the drop is connected to a thin, uniform "tail" region by means of a capillary ripple which manifests as an infinite sequence of alternating dimples and ridges. The first dimple and ridge are shown in Zones 1 and 2, respectively, whilst the ellipsis indicates the formally infinite sequence of dimples and ridges. Figure 1.23 (b) shows the results of numerical calculations by Hewitt *et al.* [160] who considered elastic-plated gravity currents, in which a viscous fluid is injected between an elastic sheet and an underlying rigid plane. Their investigation revealed a series of dimples and ridges forming as the fluid spreads. The capillary ripples present in their numerical solutions are evident in the upper inset of Figure 1.23 (b), in which the data is shown on a semi-log scale for clarity.

In Chapter 3, we show that a capillary ripple structure also arises in the context of draining flow.

1.6 Electrohydrodynamic flows

Electric fields can be utilised to produce electrohydrodynamic instabilities, thereby offering a means by which to control fluid behaviour. This has led to extensive scientific investigations [162, 163] owing to its broad range of practical applications.

For example, electrohydrodynamic flows are used in the enhancement of microfluidic mixing [164–167] and in electrohydrodynamic jet printing (also referred to as "electrospinning" or "electrospraying"). This advanced additive manufacturing technique uses electric fields to create and control jets of charged liquid droplets or fibres on the microscale and nanoscale [168–170] which enables direct printing of patterns on flexible substrates, simplifying manufacturing and expanding material choices. As a result, this technology has diverse applications such as in the manufacturing of flexible circuit boards [171], the production of hydrogels

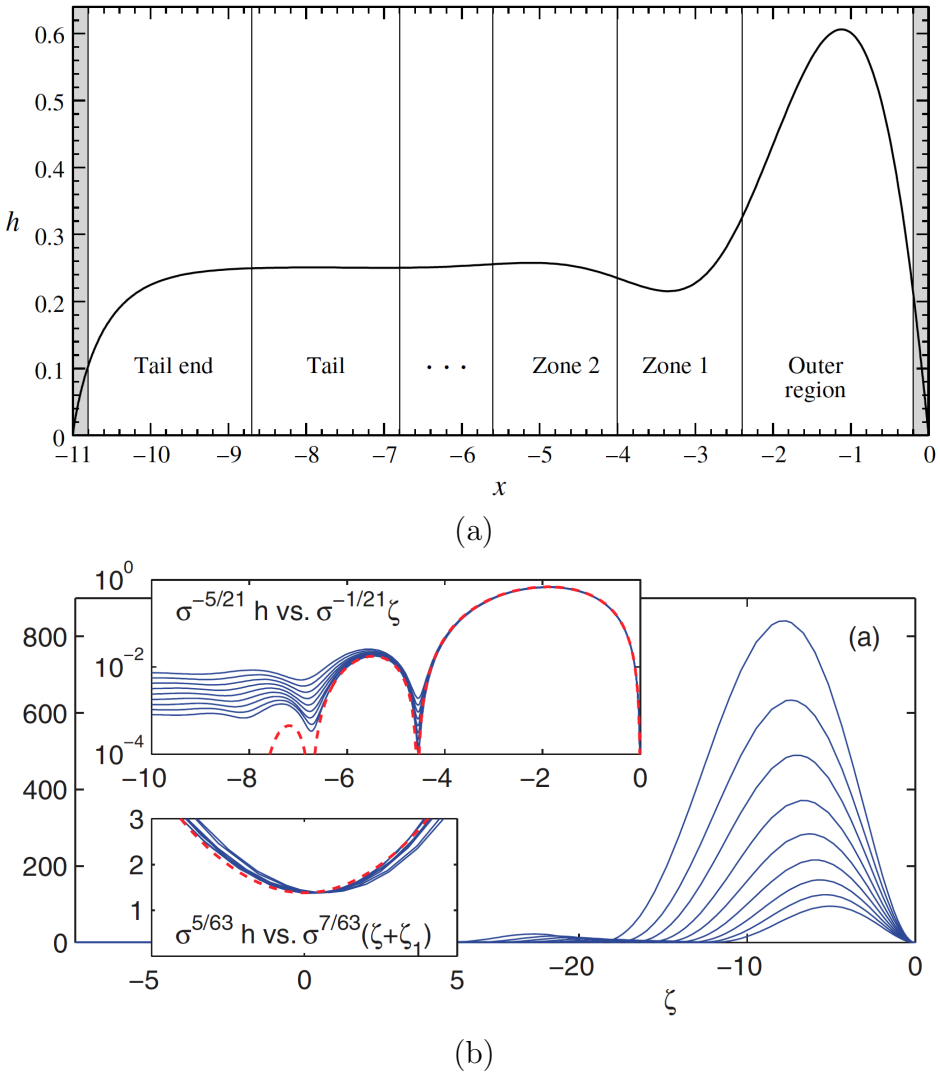

Figure 1.23: (a) A sketch of the asymptotic structure of the "large-drop solution" of Benilov and Benilov [159] in which a thick outer region (i.e., the bulk of the drop) is matched with a thin uniform region by means of a capillary ripple. Reproduced from Benilov and Benilov [159], with permission from Cambridge University Press. Copyright 2015. (b) Emergence of capillary ripples in the numerical simulations of fluid spreading within elastic-plated gravity currents, as investigated by Hewitt *et al.* [160]. The lines on the graph represent distinct pressure levels (i.e., isobars), and the upper inset presents the data on a semi-log scale, whilst the lower inset shows the region around the first dimple. The dashed red line corresponds to the authors' asymptotic predictions for the first three ridges. Reproduced from Hewitt *et al.* [160], with permission from Cambridge University Press. Copyright 2014.

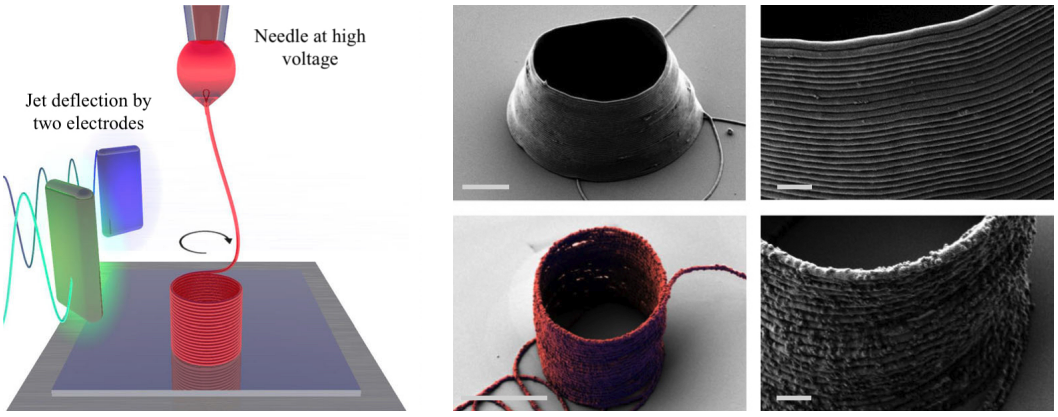

(a) (b)

Figure 1.24: (a) Schematic of the 3D printing of a cylinder. (b) Scanning Electron Microscope (SEM) micrographs at different magnifications of 3D cylindrical microstructures manufactured by electrohydrodynamic jet printing. The scale bars represent 5 μm (left) and 1 μm (right). Reproduced from Liashenko *et al.* [175], with permission from Springer Nature. Copyright 2020.

for drug delivery [172], in creating human-like robot eyes [173], and in 3D printing applications, such as in tissue engineering [174]. For example, Figure 1.24 (a) shows a schematic of a 3D printing process using an electrohydrodynamic jet to create a polymer cylinder using different inks composed of polyethylene oxide and silver nanoparticles with an applied voltage between 400 and 3000 V. The resulting printed structure is shown in Figure 1.24 (b). Typically, the electrohydrodynamic jet printing process involves the use of a needle to create a jet. However, needle-less electrospinning techniques have gained popularity due to their higher production rate [176]. Figure 1.25 (a) displays photographs of needle-less electrospinning using an applied voltage between 1000 and 2000 V using a cylinder, a disk, and a ball as fibre generators for a polymer, specifically, polyacrylonitrile (PAN), and the resulting fibres are shown in Figure 1.25 (b).

Electric fields can generate waves at the interface between two fluids, thereby leading to increased interfacial area. Hence, electrohydrodynamic flows are useful in the augmentation of heat and mass transfer rates [177–179]. Falling films are widely used in industrial processes associated with heat and mass transfer [180] (for example, in refrigeration [181], petroleum refinement [182], and desalination [183]). Darabi *et al.* [184, 185] showed experimentally that electric fields can be used to enhance evaporation in horizontal tube falling-film evaporators, in which

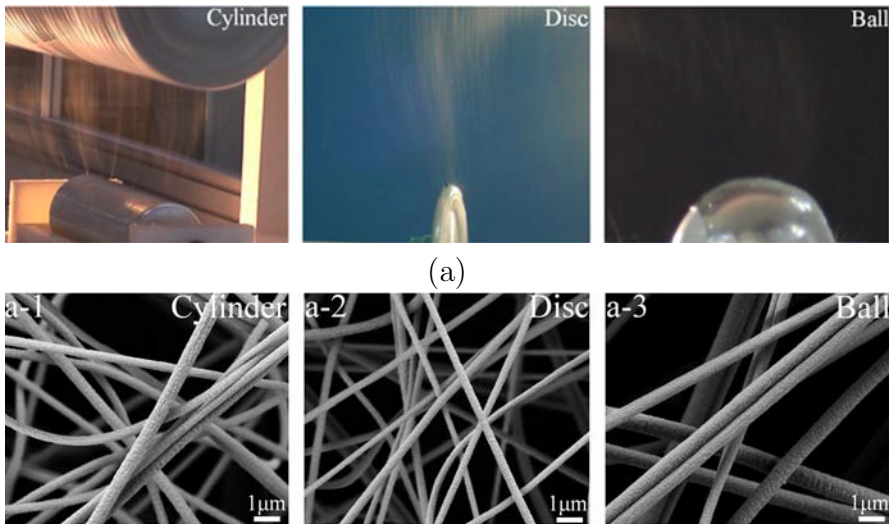

Figure 1.25: (a) Needle-less electrospinning using different fibre generators. (b) SEM images of PAN nanofibres electrospun from cylinder (radius 2 mm), disc (thickness 2 mm) and ball spinnerets, all of which have diameter 80 mm. Reproduced from Niu *et al.* [176], with permission from Informa UK Limited, trading as Taylor and Francis Group, http://www.tandfonline.com. Copyright 2012.

they succeeded in augmenting the heat transfer from the film by up to four times.

Polymer film patterning (in which microscale and nanoscale structures are introduced onto the surface of a material) has a crucial role in the creation of microprocessors used in electronic systems such as computers, smartphones, and health-trackers [186, 187], self-cleaning materials [188], and solar panels [189]. Pattern formation using electrohydrodynamic instabilities in particular has been studied extensively by many authors [190–192]. For example, destabilising vertical electric fields have been used to induce pattern formation in the context of lithographically induced self-assembly (LISA) and lithographically induced self-construction (LISC) applications [193–195]. In these methods, a uniform polymer film undergoes self-assembly, transforming into a periodic array of pillars that connect a lower substrate and upper electrode in the case of LISA, or into the shape of an upper topographically structured electrode in the case of LISC. Figures 1.26 (a) and (b) show schematic representations of the LISA and LISC setups, respectively. Figure 1.26 (a) shows the instability that arises due to the electric field (left) and the polymer columns that form and span the gap between the two electrodes (right).

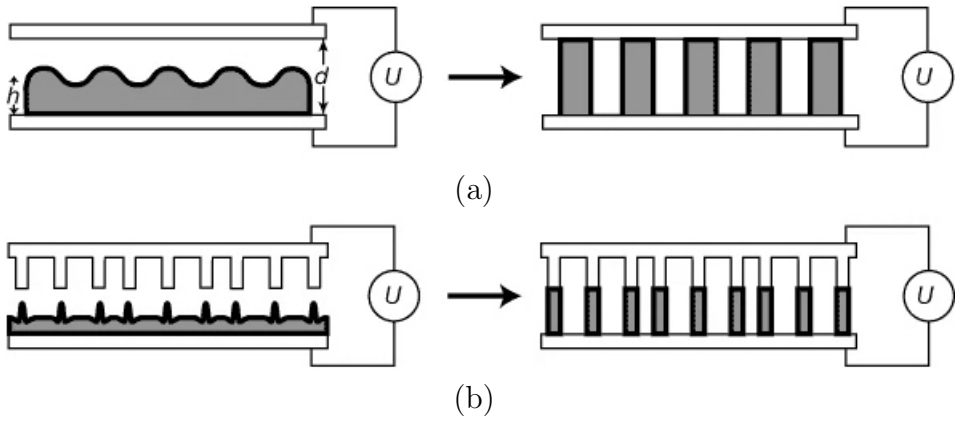

Figure 1.26: Schematic representations of a capacitor device set up for (a) LISA and (b) LISC. Reproduced from Schäffer *et al.* [194], with permission from Macmillan Magazines Ltd. Copyright 2000.

Figure 1.26 (b) shows that if the top electrode is replaced by a topographically structured electrode, the instability first occurs where the distance between the electrodes is smallest (left) which then leads to replication of the upper electrode pattern (right). Figure 1.27 (a) shows the results of some typical LISA experiments performed by Schäffer *et al.* [194] using an applied voltage of 50 V on a uniform polystyrene film, and Figure 1.27 (b) shows the result of a typical LISC experiment performed by Li *et al.* [196] in which an upper electrode patterned with lines of width 5 μm was mounted facing a polymer film, leading to a replication of the electrode topography.

This thesis concerns how the dynamics of draining flow and coating flow are affected, and can be controlled by, an external electric field. Next, in Section 1.6.1, we outline the model that we use throughout this thesis, which is known as the "Taylor–Melcher leaky-dielectric model".

1.6.1 The Taylor–Melcher leaky-dielectric model

To model the electrohydrodynamic flows in this thesis, we use the Taylor–Melcher leaky-dielectric model. This model was first outlined by Taylor [197] to explain the steady deformation of a conducting drop, and by Melcher and Taylor [198] in their subsequent review article on electrohydrodynamic flows. For comprehensive reviews on the historic and recent advancements in electrohydrodynamic flows, the reader is referred to Saville [162] and Papageorgiou [163] and the references

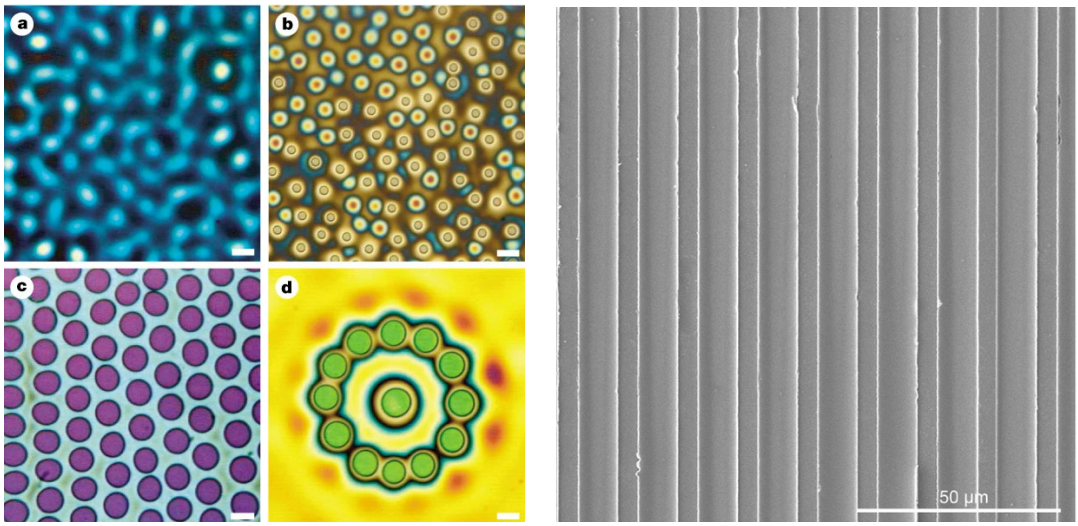

(a) (b)

Figure 1.27: (a) Optical micrographs of polymer patterns resulting from LISA experiments by Schäffer *et al.* [194]. The colours arise from the interference of light and correspond to the local thickness of the polymer structures. Reproduced from Schäffer *et al.* [194], with permission from Macmillan Magazines Ltd. Copyright 2000. (b) SEM image of polymer structures resulting from an LISC experiment performed by Li *et al.* [196]. Reproduced from Li *et al.* [196], with permission from IOP Publishing Ltd. Copyright 2011.

therein, respectively.

In the leaky-dielectric model, we assume that the characteristic timescale of electrostatic processes is large compared to that of magnetic processes, hence magnetic effects can be neglected in the absence of an external magnetic field. Hence, an electrostatic approximation of Maxwell's equations is appropriate [163] (see, for example, Feynman *et al.* [199]), namely,

$$\nabla \times \mathbf{E}_i = \mathbf{0}, \quad \nabla \cdot (\epsilon_0 \epsilon_i \mathbf{E}_i) = q^{\mathrm{e}}, \tag{1.6.1}$$

where $\mathbf{E}_i$ denotes the electric field in fluid i, $q^{\mathrm{e}} = q^{\mathrm{e}}(\mathbf{x}, t)$ is the free charge density (where $\mathbf{x}$ is the spatial coordinate vector), ϵ_i is the relative permittivity of fluid i, and $\epsilon_0 = 8.85419 \times 10^{-12}$ F m^{-1} is the permittivity of free space [200]. The first equation in (1.6.1) is Faraday's Law in the absence of magnetic effects, and states that the electric field is irrotational in the bulk of the fluid. The second equation in (1.6.1) is Gauss's Law for electricity, and states that in the bulk of the fluid the divergence of the electric field is due to local free charge density. The charge conservation equation is given by [163]

$$\frac{\partial q^{\mathrm{e}}}{\partial t} + \nabla \cdot (\sigma_i \mathbf{E}_i + q^{\mathrm{e}} \mathbf{u}_i) = 0, \tag{1.6.2}$$

where $\sigma_i \mathbf{E}_i + q^{\mathrm{e}} \mathbf{u}_i$ comes from Ohm's Law, in which σ_i is the conductivity of fluid i and $\mathbf{u}_i$ is the velocity of fluid i. The electrical bulk forces are described by the Korteweg–Helmholtz force density equation [163],

$$\mathbf{F}^{\mathrm{e}} = q^{\mathrm{e}} \mathbf{E}_i - \frac{1}{2} |\mathbf{E}_i|^2 \nabla (\epsilon_0 \epsilon_i). \tag{1.6.3}$$

The electric field exerts a force on the fluid through an additional contribution to the stress tensor, namely, the Maxwell stress tensor $\underline{\underline{\mathbf{M}}}$, defined by

$$\underline{\underline{\mathbf{M}}} = \epsilon_0 \epsilon_i \left(\mathbf{E}_i \mathbf{E}_i - \frac{1}{2} |\mathbf{E}_i|^2 \underline{\underline{\mathbf{I}}} \right). \tag{1.6.4}$$

By using (1.6.1) in (1.6.3), $\mathbf{F}^{\mathrm{e}}$ can be written in terms of the Maxwell stress tensor (1.6.4) as

$$\mathbf{F}^{\mathrm{e}} = \nabla \cdot \underline{\underline{\mathbf{M}}}. \tag{1.6.5}$$

Now, under the assumption that the permittivities ϵ_i and conductivities σ_i are

constant, equations (1.6.1) and (1.6.2) combine to yield

$$\left(\frac{\partial}{\partial t} + \mathbf{u}\cdot\nabla\right) q^{\mathrm{e}} + \frac{\sigma_i}{\epsilon_0\epsilon_i} q^{\mathrm{e}} = 0, \tag{1.6.6}$$

which has solution $q^{\mathrm{e}} = q_0^{\mathrm{e}} \mathrm{e}^{-\sigma_i/(\epsilon_0\epsilon_i)t}$ along characteristic curves (which can be interpreted as particle trajectories), where $q_0^{\mathrm{e}} = q^{\mathrm{e}}(0)$, which shows that q^{e} decays exponentially in time. As the charge relaxation time $\epsilon_0\epsilon_i/\sigma_i$ decreases, the decay becomes faster and q^{e} approaches zero more quickly. Eventually, all charge will be depleted from the bulk of the fluid, and will reside only at the interface. As a consequence, we may take

$$q^{\mathrm{e}} = 0 \tag{1.6.7}$$

in the bulk of the fluid. Combining (1.6.3), (1.6.5), and (1.6.7) yields

$$\mathbf{F}^{\mathrm{e}} = \nabla\cdot\underline{\underline{\mathbf{M}}}^{\mathrm{e}} = -\frac{1}{2}|\mathbf{E}_i|^2\nabla\epsilon_0\epsilon_i. \tag{1.6.8}$$

Therefore, under the assumption that the permittivity ϵ_i is constant, the force density and divergence of the Maxwell stress tensor are both zero in the bulk of the fluid, i.e.,

$$\mathbf{F}^{\mathrm{e}} = \nabla\cdot\underline{\underline{\mathbf{M}}}^{\mathrm{e}} = 0. \tag{1.6.9}$$

Hence, there is only charge present at the interface, meaning that coupling between hydrodynamics and electrostatics occurs only through the interfacial boundary conditions, where the role of the Maxwell stresses becomes significant. In addition, under these conditions, Gauss's Law (1.6.1) simplifies to

$$\nabla\cdot\mathbf{E}_i = 0. \tag{1.6.10}$$

It can be shown [162, 163] that the tangential components of the electric field are continuous across the interface, i.e.,

$$[\mathbf{E}\cdot\mathbf{t}_i]_2^1 = 0, \tag{1.6.11}$$

where $[\cdot]_2^1$ represents the jump in the quantity across the interface between fluids 1 and 2, and $\mathbf{t}_i$ is a tangential vector to the interface. On the other hand, there is a jump in the normal component of the electric field that is proportional to the

free charge per unit area at the interface, denoted by $Q^{\mathrm{e}} = Q^{\mathrm{e}}(t)$, i.e,

$$[\epsilon_0 \epsilon_i \mathbf{E} \cdot \mathbf{n}]_2^1 = Q^{\mathrm{e}}, \tag{1.6.12}$$

where $\mathbf{n}$ is a normal vector to the interface [163]. Finally, the charge at the interface is governed by the conservation equation for interfacial charge [163],

$$\frac{\partial Q^{\mathrm{e}}}{\partial t} + \mathbf{u} \cdot (\nabla - \mathbf{n}(\mathbf{n} \cdot \nabla)) Q^{\mathrm{e}} - Q^{\mathrm{e}} \mathbf{n} \cdot (\mathbf{n} \cdot \nabla)\mathbf{u} = [\sigma_i \mathbf{E} \cdot \mathbf{n}]_2^1 , \tag{1.6.13}$$

where the second and third terms on the left-hand side represent surface convection and surface dilation, respectively, and the term on the right-hand side represents ion conduction through the bulk of the fluid.

In this thesis, we use a special case of the leaky-dielectric model outlined above. Specifically, we consider the case in which a perfectly conducting fluid is in contact with a perfect dielectric fluid. We defer discussion of the large simplifications this makes to the model until Chapter 2. For now, the reader is referred to Case II of Papageorgiou [163].

Extensive analytical, numerical, and experimental investigations have been conducted in the field of electrohydrodynamic flows. In what follows, we discuss some electrohydrodynamic flows on planar and curved substrates in Sections 1.6.2 and 1.6.3, respectively. Note that, in the forthcoming sections, we discuss only studies that concern the effect of DC electric fields and do not discuss those which concern AC electric fields. However, the effect of AC electric fields has also been studied by various authors (see, for example, Roberts and Kumar [201] and Gambhire and Thaokar [202]).

1.6.2 Flow on planar substrates

Extensive investigations have been carried out on electrohydrodynamic flows on planar substrates. The dynamics of systems involving leaky-dielectric fluids [203], highly conductive fluids [204], and cases in which one fluid is a perfect conductor [205] have all been studied within planar geometries. In this section, we discuss only two-dimensional flows, but note that studies have also been performed in three dimensions (see, for example, Verma *et al.* [206] and Wu *et al.* [207]).

As discussed earlier, Chou *et al.* [193] discovered that thin polymer films can form pillars when subjected to a normal electric field. Since then, there have been

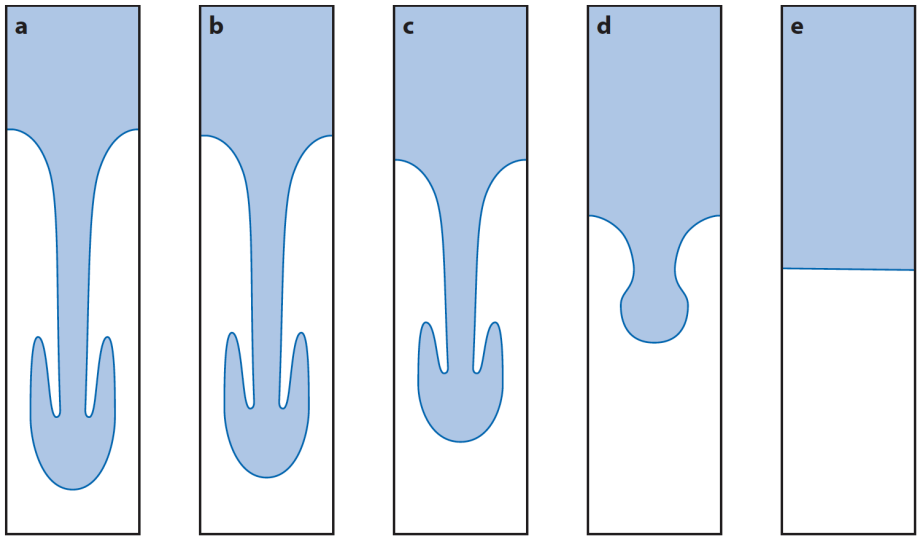

Figure 1.28: Results of DNS by Papageorgiou [163] showing stabilsation of a Rayleigh–Taylor instability using a tangential electric field. Solutions are shown at the final computational time $t = 3$. The electric field is absent in panel (a) and is increasing in strength from panels (b) to (e). Reproduced from Papageorgiou [163], with permission from Annual Reviews. Copyright 2019.

a wealth of studies concerning the stability of electrohydrodynamic flows on planar substrates. The alignment of an electric field relative to the undisturbed interface has a substantial effect on the stability; in cases in which it is destabilising, it can trigger the formation of nonuniform patterns from initially flat liquid films [193, 194], whereas in cases in which it is stabilising, it can serve as a means by which to suppress, for example, Rayleigh–Taylor or capillary instabilities [163, 208]. For example, Figure 1.28 shows DNS results of the stabilisation of a Rayleigh–Taylor instability as the strength of an applied tangential electric field is increased [163, 208].

Linear stability analyses have shown that the presence of even small amounts of conductivity significantly impacts the dynamics of electrohydrodynamic instabilities. For example, Pease and Russel [209] investigated theoretically the linear stability of the LISA process and showed that the presence of a very small amount of conductivity at the interface has a strong destabilising influence, leading to smaller wavelengths and larger growth rates than the case in which the liquid is a perfect dielectric. Similarly, Shankar and Sharma [191] considered the situation

in which both fluids are viscous leaky-dielectric polymer films, and showed that even a very small amount of conductivity can lead to unstable waves with lengths that are an order of magnitude smaller than those in perfect dielectric systems. Li *et al.* [210] showed that, in the case in which one fluid is a perfect conductor, a normal electric field is always desabilising. However, in the case in which both fluids are leaky-dielectrics, it can also be stabilising dependent on the ratios of the conductivities and permittivities of the fluids. A subsequent study by Uguz *et al.* [211] showed that leaky-dielectric systems involving a normal electric field have wider regions of parameter space that are destabilising in contrast to systems involving a tangential electric field, which often has a stabilising effect.

The exploration of electrohydrodynamic instabilities within the nonlinear regime has been facilitated by the use of numerical calculations. For example, Wu and Chou [212] investigated the LISC and LISA setup in the perfect dielectric case. In particular, they found that the frequency of the pillars that form depends on the ratio of capillarity to electrostatic effects. Later, Craster and Matar [203] investigated theoretically a similar system to Shankar and Sharma [191], consisting of two viscous leaky-dielectric films, and investigated the stability of the interface. They found that varying the system parameters (namely, the relative permittivities of the two fluids and the ratios of their conductivities, viscosities, and thicknesses) affects both the shape and frequency of the pillars that form. In particular, they found that decreasing the thickness ratio between the two films has a destabilising effect, resulting in periodic structures with decreasing wavelength. Figure 1.29 shows the steady states of the film thickness h as a function of the streamwise coordinate x for various values of the thickness ratio, denoted in the notation of Craster and Matar [203] by β. In particular, Figure 1.29 shows that reducing β produces patterns of ridges with shorter wavelengths and flat tops (top figure), whilst higher values of β result in ridges with longer wavelengths and rounded tops with larger-amplitudes (bottom figure). The ridges are separated by droplets near the bottom electrode, and fewer pillars of greater volume form as β increases. Additionally, they found that decreasing the viscosity ratio also led to the formation of pillars whose height is approximately equal to the gap between the electrodes. They also found that increasing the ratio of the dielectric constants and electric conductivities resulted in similar pillar structures forming. Ozen *et al.* [204] considered the effect of small tangential electric fields on the nonlinear dynamics and rupture of leaky-dielectric films, finding that rupture is possible but happens asymptotically

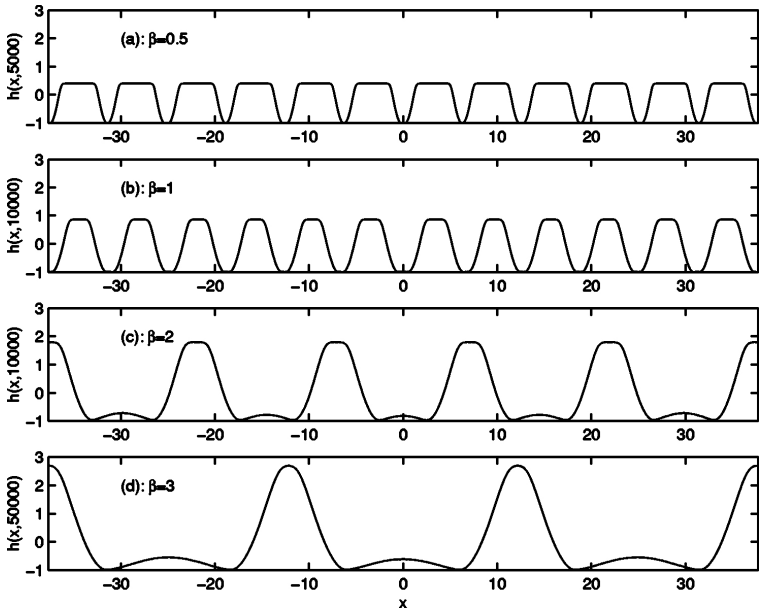

Figure 1.29: Results of numerical calculations by Craster and Matar [203] showing the effect of varying the ratio β of the thickness of the lower and upper liquid films on the steady film thickness profiles. Reprinted from Craster and Matar [203], with the permission of AIP Publishing. Copyright 2005.

at large times. Specifically, they find that the system reaches a quasi-steady state in which a number of lobes form which are connected by slowly draining trough regions whose height tends to zero asymptotically in time. Tseluiko and Papageorgiou [205] studied theoretically the nonlinear stability of a falling film on an inclined flat plane under the influence of a normal electric field in the situation in which the liquid is a perfect conductor. They used analytical and numerical techniques to find parameter ranges that support nonuniform travelling waves, time-periodic travelling waves, and complex nonlinear dynamics including chaotic interfacial oscillations. They found that a sufficiently strong electric field will drive the system to chaotic oscillations even for Reynolds numbers smaller than the critical value below which the problem in the absence of an electric field is linearly stable.

In addition to the stability properties of electrohydrodynamic flows, many authors have also investigated their behaviour and dynamics. For example, Tseluiko and Pagageorgiou [213] investigated the dynamics of the flow of a liquid film down a vertical plane under the influence of a normal electric field in the situation in

which the liquid is a perfect conductor. They performed numerical experiments which showed that the introduction of a normal electric field leads to distinct changes in the way the system decays over time. Specifically, they found that the electric field enhances instabilities, resulting in an increase in the surface area of the interface, suggesting potential applications in heat or mass transfer enhancement. Later, Wray *et al.* [55] studied the two-dimensional and three-dimensional spatiotemporal dynamics of a falling, leaky-dielectric film in the presence of an electric field. They derived WRIBL models that account for both inertia and second-order electrostatic effects which they validated against both linear theory and DNS of the Navier–Stokes equations. Recently, Keith [214] investigated theoretically a bilayer of liquid and gas contained between two electrodes using both analytical and numerical techniques. They considered three cases, namely, a perfectly conducting liquid, a highly conductive liquid and gas, and a perfect dielectric liquid and gas, from which they revealed four characteristic behaviors: "film levelling" (in which perturbations to the steady state decay), "upper contact" (in which the interface touches the upper electrode in a finite time), "film thinning" (in which local minima form where the film progressively thins), and "touchdown" (in which the interface touches the lower electrode in a finite time). They performed various parametric studies which provide insights into these diverse behaviors and the transitions between them. Figure 1.30 shows the results of one of their parametric studies performed in (L, d) parameter space (where, in the notation of Keith [214], L denotes the dimensionless domain length and d denotes the dimensionless distance between the electrodes) in the case in which the liquid is a perfect conductor. Notably, Figure 1.30 shows that upper contact occurs for small values of d (i.e., when the electrodes are close together, which in turn leads to a stronger electric field).

In addition to the study by Wray *et al.* [55], other recent studies that have used the WRIBL method to study planar flows in the presence of electrostatic effects include those by Pillai and Narayanan [215, 216] and Tomlin *et al.* [217]. In particular, Pillai and Narayanan [215, 216] derived WRIBL models governing the behaviour of perfectly conducting [215] and leaky-dielectric [216] liquid films when subjected to normal periodic electrostatic forcing. Tomlin *et al.* [217] derived a WRIBL model which they used to study the effect of a tangential electric field on perfect dielectric hanging films (i.e., systems in which liquid hangs from the underside of a planar substrate), in particular showing that electrostatic effects

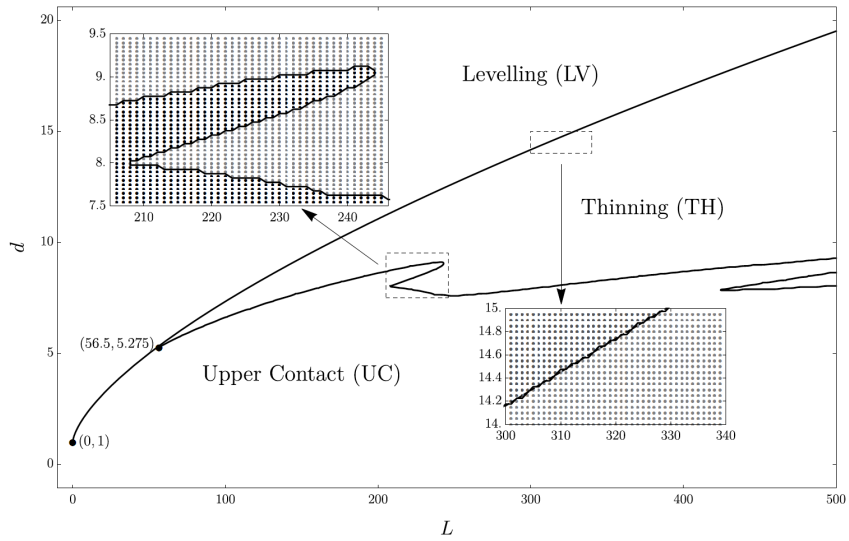

Figure 1.30: Results of the parametric study in (L, d) parameter space by Keith [214] in the case in which the liquid is a perfect conductor indicating regions in parameter space corresponding to film levelling (LV), upper contact (UC), and film thinning (TH) behaviours. Reproduced from Keith [214] with permission. Copyright 2021.

can suppress dripping. In general, the WRIBL models have been shown to exhibit strong agreement with linear stability analyses derived from the Navier–Stokes equations, accurately predicting the instability threshold, in addition to yielding good qualitative agreement with DNS calculations.

1.6.3 Flow on cylindrical substrates

There have been significantly fewer studies regarding electrohydrodynamic flows on cylindrical substrates, and none which consider azimuthal variations in the electric potential [163].

Liquid films falling on the inner or outer surface of a vertical cylinder naturally experience a Rayleigh–Plateau instability which electric fields have the potential to control or suppress [163]. For example, Wray *et al.* [218–220] investigated the effect of a radial electric field generated by a setup involving concentric cylindrical electrodes. Their investigation focused on the behavior of a thin film of liquid flowing under the influence of gravity down the outer surface of a vertical cylindrical electrode. Wray *et al.* [218] explored the linear stability and nonlinear dynamics

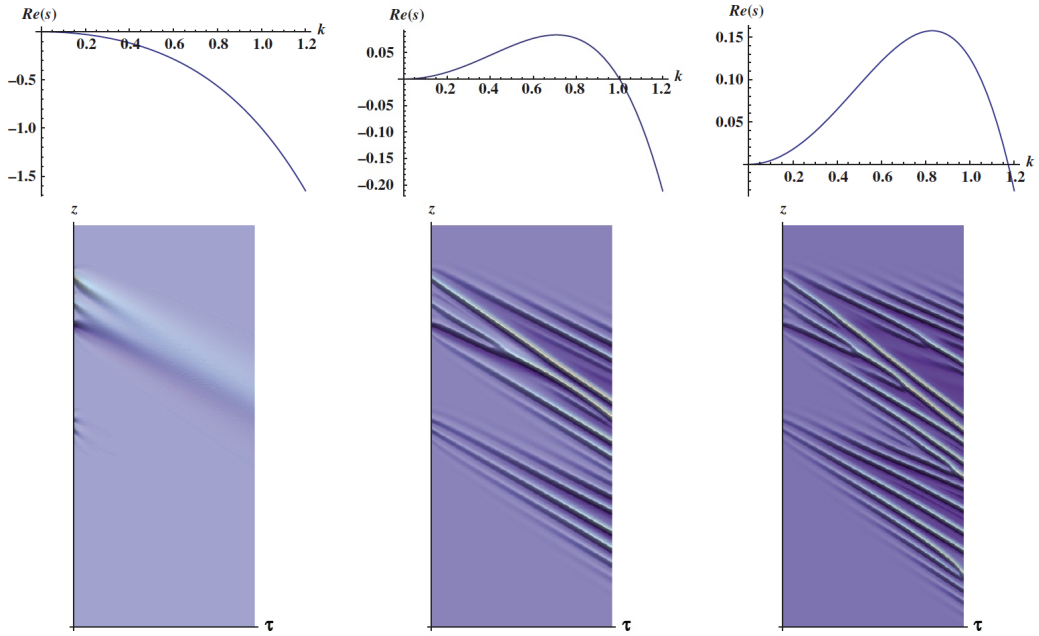

Figure 1.31: Results of calculations by Wray *et al.* [218] showing the dispersion curves (top) and respective simulations of their governing equations (bottom) for (a) stability in the presence of a stabilising electric field, (b) instability in the absence of an electric field, and (c) heightened instability in the presence of a destabilising electric field. Reproduced from Wray *et al.* [218], with permission from Oxford University Press. Copyright 2012.

of a thin leaky-dielectric film under the influence of a normal electric field. Their governing equation builds upon existing models, incorporating electrostatic effects from both normal and tangential Maxwell stresses. They showed that the electric field can either stabilise or destabilise the system, and that it is possible to use the electric field to drive the flow towards a steady state or to increase the amplitude of the nonlinear travelling waves. Figure 1.31 depicts the behavior of the system under different strengths of the tangential Maxwell stress. In Figure 1.31 (a), a stabilising electric field leads to the gradual decay of the imposed disturbance over time, indicating linear stability. On the other hand, Figures 1.31 (b) and (c) show unstable conditions in the absence of an electric field and in the presence of a destabilising electric field, respectively, resulting in the emergence of nonlinear travelling waves. These waves exhibit interesting features such as wavefront coalescence and splitting. A destabilising electric field, such as that shown in

Figure 1.31 (c), amplifies these phenomena, giving rise to higher-amplitude travelling wave structures and a broader spreading of wavefronts compared to Figure 1.31 (b). Later, Wray *et al.* [219] found that three behaviours can occur depending on the system parameters: a stable regime in which the interface is uniform, nonlinear steady-state travelling waves, and complex droplet-like behaviour that does not reach a steady state. They performed a parametric investigation to determine where in parameter space each of the behaviours occur. Finally, Wray *et al.* [220] carried out a linear stability analysis and showed that nonaxisymmetric modes become more dominant as the electric field strength is increased and that the interface either remains spatially uniform or exhibits either axisymmetric or nonaxisymmetric travelling waves dependent on both the strength of the electric field and the position of the outer electrode. In addition, they showed that the natural instability caused by the azimuthal curvature in cylindrical flows can be either enhanced or suppressed by varying the potential at the outer electrode.

It has been shown that the application of a radial electric field in a cylindrical tube with a two-fluid core-annular arrangement has a substantial impact on capillary breakup, leading to the liquid-gas interface making contact with the tube wall within a finite time [221, 222]. For example, Wang and Papageorgiou [195] investigated the (axisymmetric) situation in which two viscous fluids are contained between two concentric electrodes (i.e., the cylindrical analogue of the LISA/LISC setup). They found that electrostatic effects can lead to finite-time and infinite-time singularities in the system in which the interface touches the inner or outer electrode. In particular, they found that for leaky-dielectrics finite-time contact can occur at either electrode, whilst two-sided contact can occur for perfect dielectrics. Figure 1.32 shows the results of the parametric study by Wang and Papageorgiou [195] in (Q, R) parameter space (where, in their notation, Q denotes the ratio of the fluid permittivities and R denotes the ratio of the fluid conductivities) for a fixed electric field strength $E_b = \epsilon_2 \phi_1^2/(\sigma d) = 0.3$, where ϵ_2 is the dimensional permittivity of the outer fluid (i.e., the fluid that is initially in contact with the outer electrode), ϕ_1 is the dimensional voltage potential of the inner electrode, and d is the dimensional distance between the inner and outer electrodes. In the absence of an electric field, the interface eventually touches the nearest wall due to capillary instabilities. Under certain initial circumstances, the interface can make contact with both the inner and outer walls of the cylindrical annulus simultaneously, resulting in the formation of pillar-like rings spanning the

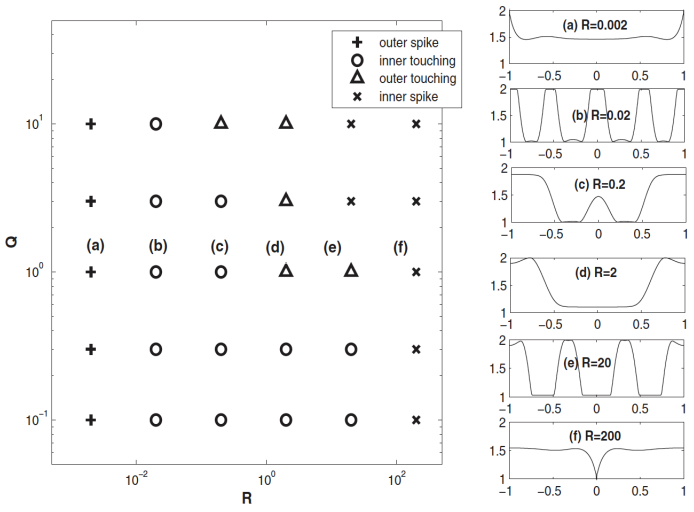

Figure 1.32: Results of the parametric study by Wang and Papageorgiou [195] in (Q, R) parameter space for $E_b = 0.3$. Symbols represent finite-time singular solutions touching the outer (+) and inner (×) tube walls and film draining solutions observed at the inner (circles) and outer (triangles) tube walls. The insets display the interface for $Q = 1$ with varying R. Reproduced from Wang and Papageorgiou [195], with permission from Cambridge University Press. Copyright 2018.

entire annular space. In the presence of an electric field, Figure 1.32 shows that for small R (i.e., when the outer layer is more conductive than the inner layer), a rapid spike finite-time singularity solution forms, touching the outer wall, whilst for large R (i.e., when the inner layer is more conductive than the outer layer), a solution touches the inner wall.

Note that the discussions throughout this section highlight a particular omission from the literature, namely, that there have been no studies on the effect of an electric field on the coating flow system (or indeed, in any horizontal cylindrical geometry). In this thesis, we endeavour to close this gap by considering coating and draining flow in the presence of an electric field.

1.7 Control of liquid films

Controlling complex systems poses a significant challenge across a wide range of fields, such as in the design of airfoils for wind turbines [223], the programming of autonomous vehicles [224, 225], stabilising the flight of atmospheric reentry

vehicles [226], and optimising financial resources in fund management [227].

The control of liquid films in particular has received significant attention by various authors [228, 229], owing to its wealth of industrial applications. Of particular relevance to the work contained in this thesis is the control of liquid films coating solid substrates. In such systems, it is often desirable to control the interface to highly corrugated shapes, for example. Indeed, this proved to be valuable in many of the examples of electrohydrodynamic flows that we discussed earlier in Section 1.6, such as in the augmentation of heat and mass transfer rates [178, 179], and in pattern formation [188, 189, 193]. On the other hand, it is often necessary to control the interface towards a flat state in order to achieve specific functional, aesthetic, or performance-related requirements, such as applying anti-reflection coatings to glass lenses [230], anti-corrosion coatings to aircraft [231], and antibacterial coatings to medical devices such as surgical instruments [232].

Control calculations of complex systems can be computationally expensive due to the intricate computations that are required which are often significantly more complex than those involved in determining the dynamics of the system. In addition, this complexity is further exacerbated by the need for a large number of computations (see Section 1.7.2). Therefore, it is often advantageous to instead perform such calculations on reduced-order models such as those discussed in Section 1.2 as they are, in general, significantly faster to compute, whilst still capturing the essential dynamics of the system.

Control mechanisms can generally be categorised as either "passive" or "active". Passive control involves using fixed elements or materials and does not rely on feedback or real-time interventions, but rather on the intrinsic properties of the materials or structures. Reduced-order models have been generalised to include effects that can be used as passive control mechanisms, such as the incorporation of surfactants [233] and the introduction of substrate topography [229]. Passive control may be effective for certain applications, but it lacks the ability to actively adapt to changing conditions. Hence, in this thesis, we focus on active control, in which real-time feedback and active interventions are used to manipulate system behavior for desired outcomes. There are two forms of active control that we will focus on: "feedback control" and "optimal control", which we discuss in Sections 1.7.1 and 1.7.2, respectively.

1.7.1 Feedback control

Feedback control is a control methodology that involves tracking the state of the system in real time in order to adjust control actions and guide the system towards a desired state. This process involves using information about the behaviour of the system in order to shape and refine the control function. The control function includes control actuators (i.e., localised sources of control or manipulation that can exert an external influence on the system dynamics) and algorithms determining how the actuators should be adjusted based on the feedback information. In the context of fluid flows, this could involve tracking features such as the interface shape or the velocity [68].

A specific kind of feedback control, often referred to as "feedback control with full state observations" (or "full-state feedback control"), assumes that the entire state of the system is observable and known and hence can provide highly accurate and effective control. However, this approach requires detailed measurements of all relevant variables across the entire system, which, in general, will not be feasible in an experimental setup. In comparison, another kind of feedback control, referred to as "proportional control" is relatively straightforward to implement and is applicable when only limited information about the system is available [68]. Often, proportional control involves pairing point actuators with "observers". Observers are systems that monitor the local behaviour of the interface and, using input data from sensors or measurement devices, generate estimates of the unmeasured states of the system. The actuator corresponding to each observer applies a force that is proportional to the difference between the observed state and the desired state.

Feedback control in the context of fluid flows has been considered by various authors in both theoretical and experimental settings [234–237]. Reduced-order models have been generalised to include effects that can be used as feedback control mechanisms, such as wall heating [67, 238] and same-fluid mass injection or extraction (often referred to as "blowing" and "suction") [64, 65, 68, 239]. In addition, some studies have used actuation mechanisms which are left unspecified [46], which we shall refer to as "abstract" actuation mechanisms.

For example, the stabilisation of the uniform film solution of the Kuramoto–Sivashinsky equation (1.2.6) (which was discussed earlier in Section 1.2.3) using feedback controls has been considered by various authors [240–242]. Gomes *et al.* [46] applied feedback control to the Kuramoto–Sivashinsky equation (1.2.6) in

the presence of electrostatic effects (caused by the application of a normal electric field) and dispersion using an abstract actuation mechanism. They controlled the film towards various states, including travelling wave solutions on long domains (where chaotic behaviour is otherwise observed) and stabilised nonuniform unstable steady states. They proved that any possible solution to the Kuramoto–Sivashinsky equation can be stabilised using a finite number of point actuated controls whose strength depends only on the difference between the observed and desired interface shapes. They found that the number of control actuators depends only on the domain length and, furthermore, that the controls are robust to uncertainty in the problem parameters, as well as to small changes in the number of controls used. An example of their results is shown in Figure 1.33, which shows feedback control of the unstable Kuramoto–Sivashinsky equation (1.2.6) towards a stabilised travelling wave solution in the absence of an electric field but in the presence of dispersive effects [46]. Recently, Tomlin and Gomes [47] investigated feedback control strategies for stabilising interface shapes governed by a multi-dimensional Kuramoto–Sivashinsky equation (i.e., a version of equation (1.2.6) adapted to include two spatial dimensions) in which the control actuators are sources of same-fluid blowing and suction at specific locations on the substrate wall. They considered both proportional control and full-state feedback control. Through proportional control, they found that by adjusting the strength, number, and arrangement of the actuators they could stabilise desired states, such as steady states or travelling wave solutions, in addition to preventing the unbounded growth of the interface which occurs when the film hangs beneath the substrate. They also showed that equally spaced actuator arrangements yielded the most favorable control performance. They compared the outcomes of proportional control with those of full-state feedback control, finding that the latter was more effective in stabilising non-trivial interface shapes.

Thompson *et al.* [64] derived models based on the Benney equation (1.2.3) and the first-order WRIBL model (1.2.9) and (1.2.24) which incorporated the effects of same-fluid blowing and suction. In a companion paper, using these models, Thompson *et al.* [65] investigated feedback control of the system by using same-fluid blowing and suction as control mechanisms and controlling based on either full or partial observations of the interface height. They found that the film behaviour can be successfully controlled, in particular, showing that this approach enables the stabilisation of various states, including a uniform film, nonuniform travelling

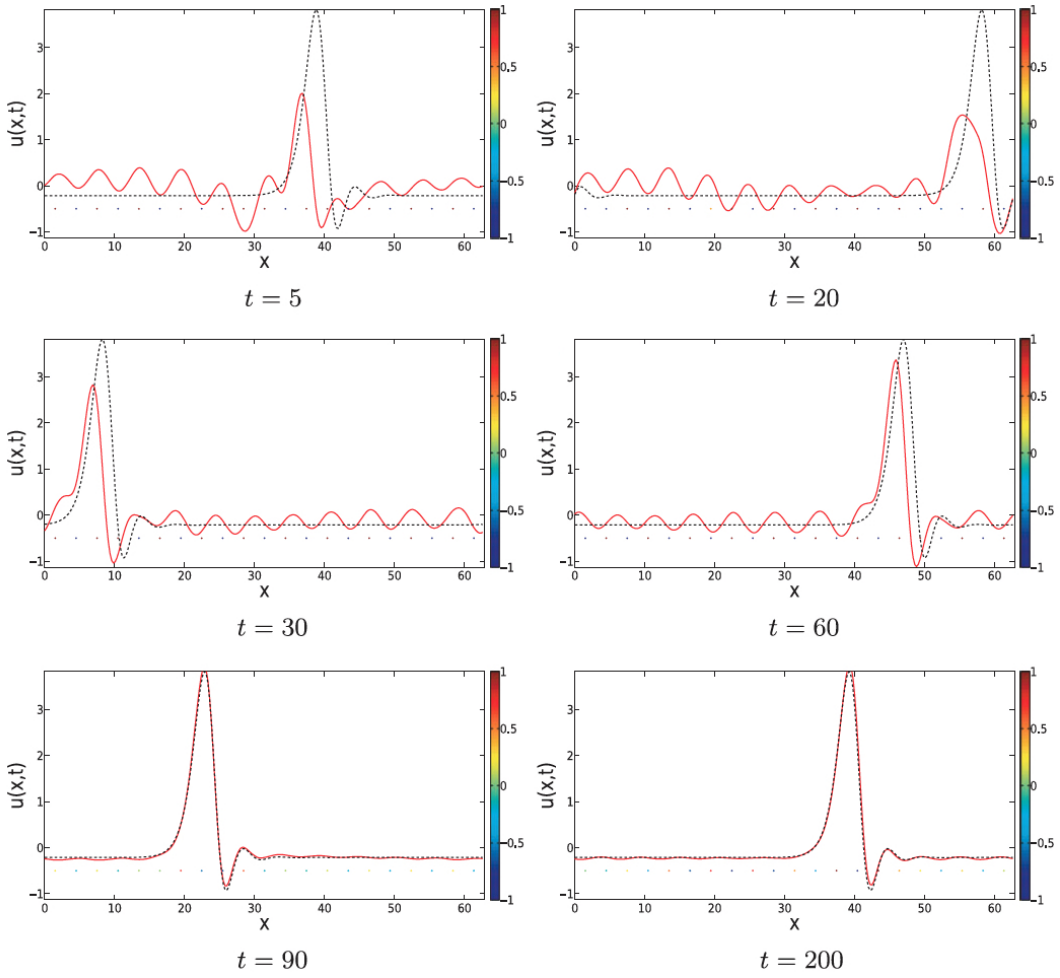

Figure 1.33: Results of control calculations by Gomes *et al.* [46] showing feedback control of the unstable Kuramoto–Sivashinsky equation (1.2.6) towards a stabilised travelling wave solution at times (left-to-right and top-to-bottom) $t = 5, 20, 30, 60, 90$, and 200. The dashed black lines represent the desired travelling wave solution and the solid red lines represent the controlled solution. Reproduced from Gomes *et al.* [46], with permission from Oxford University Press on behalf of the Institute of Mathematics and its Applications. Copyright 2017.

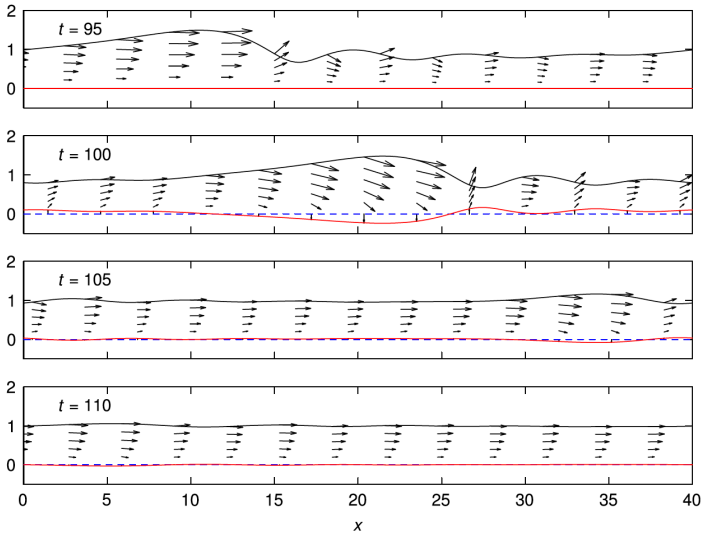

Figure 1.34: Controlled flow fields calculated from the WRIBL model of Thompson *et al.* [65] showing the interface position (solid black) the magnitude of the control (solid red), and the substrate position (dashed blue). Blowing and suction controls are applied at time $t = 100$. Reprinted from Thompson *et al.* [65], with the permission of AIP Publishing. Copyright 2016.

waves, and steady states. For example, Figure 1.34 shows the successful control (using their WRIBL model) of a travelling wave towards a uniform film using same-fluid blowing and suction, which is turned on at time $t = 100$. At this time, the magnitude of the controls is the largest. At later times, the interface is closer to a uniform state, hence smaller controls are required.

Recently, Samoilova and Nepomnyashchy [238] investigated the use of nonlinear feedback control in altering the dynamics of the oscillatory Marangoni instability within a heated thin liquid film on a planar substrate. Their control methodology involved monitoring temperature fluctuations at the interface and, in response, altering the local heat flux applied to the solid substrate. They showed that they were able to mitigate the effects of surface-tension-driven fluid motion and hence were successful in expanding the range of stability for distinct convective configurations. Moreover, they showed that the implementation of nonlinear feedback control led to the stabilisation of convective patterns, including stabilising standing waves.

In general, feedback control, although useful in terms of computational cost and success, responds primarily to the current state of the system and may not

fully consider the long-term objectives. A more comprehensive and robust (albeit more computationally expensive) alternative is offered by optimal control, which we discuss below.

1.7.2 Optimal control

Optimal control is a control methodology in which the aim is to minimise some cost functional with respect to the control. Specifically, the cost functional is the sum of the "deviation measure" (i.e., a measure of the deviation of the observed system state from the desired system state) and the cost of the control (i.e., a measure of the energy spent on the controls). The cost functional is constrained by a system of PDEs which generally constitute the governing equations of the system (for example, the relevant reduced-order model governing a fluid system along with its respective boundary conditions). In this section, we discuss some of the background theory surrounding optimal control in Sections 1.7.2.1– 1.7.2.4 before discussing some of the existing literature concerning the optimal control of fluid systems in Section 1.7.2.5.

1.7.2.1 The method of Lagrange multipliers

In general, optimisation problems are classified into two main categories: constrained problems and unconstrained problems. Unconstrained optimisation problems focus on minimising or maximising a function without any restrictions. For example, in the case of minimising some function $F = F(x,t)$ (which depends on some control variable $c = c(x,t)$) with respect to the control c, this is expressed as

$$\min_{c(x,t)} F(x,t). \tag{1.7.1}$$

On the other hand, constrained optimisation problems focus on minimising or maximising a function under specific constraints. For example, in the case of minimising F with respect to c subject to the constraints $g_i = 0$ (for $i = 1, \ldots, N$), this is expressed as

$$\min_{c(x,t)} F(x,t) \quad \text{subject to} \quad g_i(y_i(x,t)) = 0 \quad \text{for} \quad i = 1, \ldots, N, \tag{1.7.2}$$

where y_i (for $i = 1, \ldots, N$) are the solution variables of the governing equations $g_i = 0$ (for $i = 1, \ldots, N$). Solving constrained optimisation problems is substantially more difficult than solving unconstrained optimisation problems. Hence, in order to solve the optimisation problem (1.7.2), it is often desirable to recast such problems into an unconstrained formulation. In order to do this, we use the method of Lagrange multipliers. This method allows us to incorporate constraints into the cost function (i.e., the function to be minimised) by introducing the Lagrangian

$$\mathcal{L}(x, t, \lambda) = F(x, t) - \sum_{i=1}^{N} \lambda_i(x, t) g_i(y_i(x, t)), \tag{1.7.3}$$

where λ_i (for $i = 1, \ldots, N$) are Lagrange multipliers which enforce the constraints $g_i = 0$ (for $i = 1, \ldots, N$). Instead of directly minimising $F(x, t)$, we minimise the Lagrangian $\mathcal{L}(x, t, \lambda)$. Hence, the optimisation problem becomes

$$\min_{c(x,t)} \mathcal{L}(x, t, \lambda), \tag{1.7.4}$$

which is unconstrained and can therefore be solved using unconstrained optimisation methods.

In this thesis, we use what is sometimes referred to as the "adjoint method" [228] which has been successfully used by various authors in the context of the optimal control of fluid flows [229, 243, 244]. We briefly outline the adjoint method below. Specifically, our implementation of the adjoint method involves the method of steepest descent and the conjugate gradient method [245, 246] in conjunction with the golden section search method [247], which we outline in Sections 1.7.2.2–1.7.2.4. Note that a full account of the adjoint method will be given in the context of our problem in Chapter 6.

1.7.2.2 The method of steepest descent

To find the minimum of $\mathcal{L}$ (1.7.4), we use the method of steepest descent. Specifically, the method of steepest descent is an iterative optimisation technique that seeks the minimum of a function by taking steps away from some initial choice of control $c_0 = c_0(x, t)$ in the direction in which $\mathcal{L}$ (1.7.4) decreases most steeply with respect to the control c (which we shall refer to hereafter as the "descent direction") [246]. In particular, the descent direction is given by the negative of

the gradient of $\mathcal{L}$ with respect to c at each iteration, denoted by

$$g_k = -\frac{\partial \mathcal{L}_k}{\partial c_k}, \tag{1.7.5}$$

at iteration k, where we take derivatives on functional spaces to be Fréchet derivatives [243, 244] (we discuss this point later in Section 6.2.1). However, in order to compute (1.7.5) at each iteration, we must calculate the values of the solution variables y_i (for $i = 1, \ldots, N$) and the Lagrange multipliers λ_i (for $i = 1, \ldots, N$), the latter of which take the role of adjoint variables in this context. Differentiating the Lagrangian (1.7.3) with respect to the λ_i yields the governing PDEs $g_i = 0$ (for $i = 1, \ldots, N$), and differentiating the Lagrangian (1.7.3) with respect to the y_i yields equations for the λ_i, which are referred to in this context as "adjoint equations". The updated value of the control c at the next iteration $k+1$ is given by

$$c_{k+1} = c_k + \alpha_k g_k, \tag{1.7.6}$$

where c_k is the current value of c at iteration k and α_k is the current step size taken in the direction of the gradient (1.7.5) at iteration k. The step size α_k can be determined by a line search. In this thesis, we use a golden section search method to determine the optimal step size, which we discuss in Section 1.7.2.4. Finally, the updated gradient at the next iteration $k+1$,

$$g_{k+1} = -\frac{\partial \mathcal{L}_{k+1}}{\partial c_{k+1}}, \tag{1.7.7}$$

is evaluated and the process is iterated until convergence is achieved within some specified tolerance (for example, the norm of the gradient being less than some small value).

The method of steepest descent offers a high degree of simplicity with fast iterations. In general, the gradient descent method is guaranteed to converge to the global minimum if the function to be minimised is convex [246] (since convex functions have the property that all local minima are also global minima). However, if the function is non-convex (as is often the case in complex optimisation problems), although the method is still guaranteed to converge to a local minimum, this is not guaranteed to also be the global minimum.

From the discussions above, we note that active optimal control using the adjoint method involves solving the (highly nonlinear) governing PDEs and respective

adjoint equations many times. Hence, this approach is computationally expensive, but is nevertheless much more accurate than proportional control and, moreover, satisfies an optimality constraint.

1.7.2.3 The nonlinear conjugate gradient method

Conjugate gradient methods for solving nonlinear unconstrained optimisation problems modify the method of steepest descent by modifying the descent direction based on the descent direction from the previous step. In addition, after the first step, the step direction is constrained to be "conjugate" (i.e., orthogonal) to the direction most recently travelled, which leads to improved efficiency. This process is iterated, each time modifying the descent direction to make it conjugate with the previous direction. This can be expressed as follows,

$$d_k = g_k + \beta_k d_{k-1}, \tag{1.7.8}$$

where g_k is defined by (1.7.5), d_k and d_{k-1} are the current and previous values of the descent direction d at iterations k and $k-1$, respectively, and β_k is chosen to ensure that g_{k+1} and g_k become orthogonal, and can be determined by various formulae whose behaviour is difficult to anticipate, and the results are essentially based on experience. This ultimately yields different variations of the conjugate gradient method. The most commonly used (and often "default") formula is the Fletcher–Reeves formula [248],

$$\beta_k^{\mathrm{FR}} = \frac{g_{k+1}^{\mathrm{T}} g_{k+1}}{g_k^{\mathrm{T}} g_k}, \tag{1.7.9}$$

where the superscript T denotes the transpose. The choice of β_k can significantly affect the convergence behavior of the algorithm as it impacts how the method updates the search direction in each iteration. Indeed, whilst the Fletcher–Reeves formula (1.7.9) has good convergence properties, it may exhibit slower convergence for certain types of functions [249].

Widely used alternative variations of β_k include the Hestenes–Stiefel method [250], the Dai–Yuan method [251], and the Polak–Ribière method [245]. In this

thesis, we often use the Polak–Ribière method, in which β_k is given by [252]

$$\beta_k^{\mathrm{PR}} = \frac{g_{k+1}^{\mathrm{T}}(g_{k+1} - g_k)}{g_k^{\mathrm{T}} g_k}. \tag{1.7.10}$$

The Polak–Ribière formula (1.7.10) takes into account the improvement in the gradient direction in the current iteration compared to that in the previous iteration, which can lead to faster convergence and hence better computational performance for certain types of functions, especially those with varying curvature. However, it must be noted that the derivation of the Polak–Ribière formula (1.7.10) is heuristic in the sense that it is not guaranteed to be convergent in general, hence, there is no guarantee that it will work well for any particular function [245, 249]. However, it is often found to work very well in practice.

Finally, the value of the control c is updated and is given by

$$c_{k+1} = c_k + \alpha_k d_k, \tag{1.7.11}$$

where d_k is given by (1.7.8) and, as in the steepest descent method described in Section 1.7.2.2, α_k is the current step size. Finally, as before, the updated value of the gradient (1.7.7) is computed, and the iterative process described above is repeated until convergence is achieved.

1.7.2.4 The golden section search method

Once a descent direction has been determined, the optimal step size in that direction must be calculated. There are various algorithms that could be used, such as the secant method, Brent's method, or an interval bisection method. As mentioned in Section 1.7.2.2, in this thesis, we use a golden section search method to determine the optimal step size α_k.

The golden section search method is an optimisation algorithm introduced by Kiefer [247] that is designed to find an extremum (i.e., a minimum or maximum point) of some function $f(x)$ within a given interval, $[a, b]$. The method is as follows: let $f(x)$ be a function to be minimised within the interval $[a, b]$, as shown in Figure 1.35. The first step of the first iteration is to calculate two points within the interval $[a, b]$, denoted by a_1 and b_1, defined by [253]

$$a_1 = ca + (1 - c)b, \quad b_1 = (1 - c)a + cb, \tag{1.7.12}$$

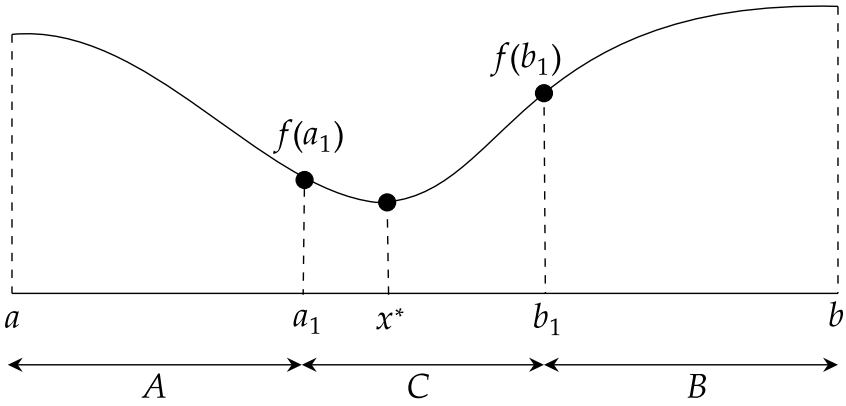

Figure 1.35: A schematic of the first step in the golden section search method in finding a local minimum x^*.

where $c = (-1 + \sqrt{5})/2$, such that they divide the interval into three sub-intervals $[a, a_1]$, $[a_1, b_1]$, and $[b_1, b]$, where the lengths of each sub-interval, denoted A, C, and B, respectively, satisfy

$$A = B, \tag{1.7.13}$$

$$\frac{C + B}{A} = \varphi, \tag{1.7.14}$$

where $\varphi = 1/c$ is the golden ratio, $\varphi \approx 1.618$. Maintaining this ratio means that the method converges quickly because it ensures that the ratio between the remaining and discarded intervals is the same in each iteration. Using another ratio would not guarantee this balance, potentially leading to slower convergence. In particular, the convergence rate of the golden section search algorithm is φ^N, where N is the number of iterations, and it was shown by Shao *et al.* [254] that for $N = 15$ the search interval will be decreased to less than 0.1% of its original length. The second step is to evaluate the function at these points (i.e., to evaluate $f(a_1)$ and $f(b_1)$) from which we can determine if a minimum or a maximum lies between these points and hence update the search. In this case, $f(a_1) < f(b_1)$, therefore the minimum must lie to the left-hand side of b_1, i.e., in the interval $[a, b_1]$ (note that if $f(b_1) < f(a_1)$, the minimum would lie to the right-hand side of a_1, i.e., in the interval $[a_1, b]$).

Assuming without loss of generality that we are in the case in which $f(a_1) < f(b_1)$, on the second iteration, the first step is again to calculate two new points a_2 and b_2 in the new interval $[a, b_1]$ to form a new search interval. We know that

a_1 lies in the interval, so we choose $b_2 = a_1$ and calculate $a_2 = ca + (1 - c)b_1$. The second step is to evaluate the function at these points. If, for example, we find that $f(a_2) > f(b_2)$, then the minimum must lie to the right-hand side of a_2, i.e., in the interval $[a_2, b_1]$. Note that since b_2 is equal to a_1, we have already computed the value of $f(b_2)$ during the previous step. This observation is crucial as it contributes to the computational efficiency of this method, further highlighting why it is favorable for use in complex problems. The interval is updated iteratively in this manner until the interval is smaller than some specified tolerance in which case the algorithm has converged.

1.7.2.5 Existing studies

The use of optimal control in the context of fluid flows has been investigated by a number of authors in various contexts [228, 229], including the identification of optimal heating strategies to actively suppress evaporative instabilities [255] and the identification of the optimal substrate shape to control the interface of a thin liquid film [256]. For example, in the same work that was discussed earlier in Section 1.7.1, Gomes *et al.* [46] also applied optimal control to the Kuramoto–Sivashinsky equation (1.2.6) in the presence of dispersion and electrostatic effects. They developed a cost functional to be minimised in order to optimise the placement of the control actuators with the aim of stabilising nonuniform unstable steady states. They proved the existence of optimal distributed controls and presented computational algorithms to find these controls. In addition, they conducted numerical simulations in order to validate the effectiveness of their optimal control approach and showed that the control is robust with respect to changes or uncertainty in the equation parameters (i.e., the viscosity coefficient, the dispersion coefficient, and the electric field strength), in the sense that the optimal controls do not change much as the parameters are varied. Later, Tomlin *et al.* [257] considered a similar situation, this time in three dimensions in the absence of dispersion and electrostatic effects, whilst incorporating the effects of same-fluid blowing and suction for use as control mechanisms. In particular, they considered a more general control approach in which actuation is not restricted to a finite set of points but is spatially distributed across the substrate. They investigated optimal control strategies and, through numerical simulations and analyses, found that that the controls are effective in suppressing instabilities and chaos, demonstrating potential applications

for stabilising fluid flows and preventing undesirable phenomena such as dripping.

One of the key papers with regards to the work in this thesis is that by Boujo and Sellier [243] who investigated the optimal control of the dynamics of a solidifying thin liquid film on a solid flat plane in the context of pancake making. Whilst the physical system considered in this thesis differs from that studied by Boujo and Sellier [243], here we nonetheless devote significant attention to their work due to their comprehensive explanation of applying optimal control to fluid flow on a solid substrate. In their problem, the motion of the liquid film is influenced by factors such as temperature-dependent viscosity and changing gravity forces dependent on the orientation of the surface. Their aim was to optimise the uniform spreading of the liquid layer during its solidification process by controlling the movement of the underlying surface. They consider two methods for control: the first undergoes harmonic motion, for which Boujo and Sellier [243] determined the optimal parameters through the use of Monte Carlo simulations [258]. However, this approach is very computationally expensive whilst providing only modest improvement in uniformity over a stationary surface. A more efficient second approach is used, which treats the problem as an optimal control problem which consists of minimising a cost functional (denoted by $\mathcal{J}(t)$) which is the sum of the deviation of the film thickness from uniformity (denoted by $\mathcal{U}(t)$) and the associated cost of moving the surface (which is scaled by a parameter referred to as the "control weight", denoted in the notation of Boujo and Sellier [243] by γ, which imposes how strongly use of the control should be penalised). The minimisation problem is constrained by the governing PDEs and is solved using the conjugate gradient method. By varying the control weight, Boujo and Sellier [243] investigated how different balances between uniformity improvement and cost affect the optimisation results. Figure 1.36 shows optimisation results for different values of γ, showing the effect on $\mathcal{J}(t_\mathrm{f})$ and $\mathcal{U}(t_\mathrm{f})$ (where t_f is the final time). Small γ values indicate cheaper controls which, in this case, yield greater uniformity improvement, whilst higher γ values reflect more expensive controls which yield smaller uniformity improvement. In general, adjoint-based optimisation significantly improves uniformity, remaining more effective than uncontrolled cases up to $\gamma \approx 10^{-5}$. In general, they showed that optimal control can result in an up to 83% improvement in uniformity compared to the uncontrolled case, finding that the identified optimal controls mirror intuitive motions used in pancake making. Figure 1.37 shows the time evolution of the film thickness for $\gamma = 10^{-8}$: initially,

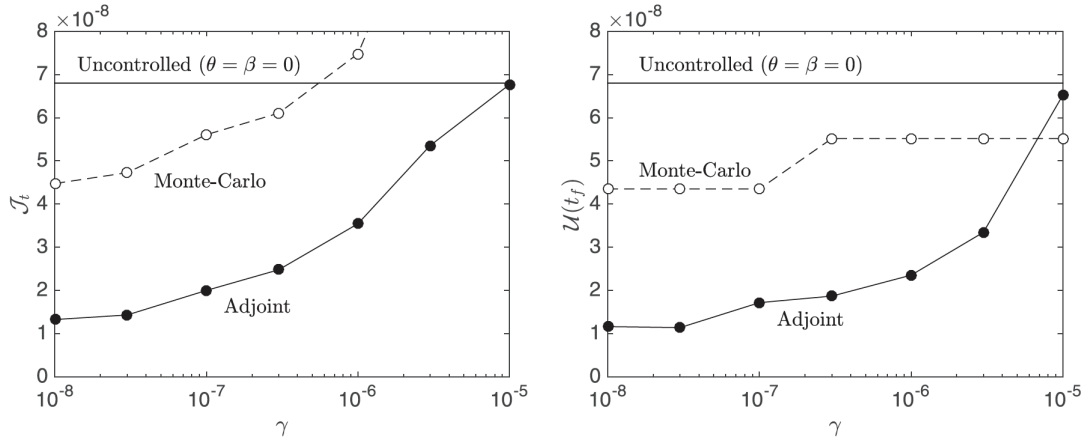

Figure 1.36: Results of optimal control calculations by Boujo and Sellier [243] showing (a) the cost functional $\mathcal{J}(t_\mathrm{f})$ and (b) the corresponding uniformity measure $\mathcal{U}(t_\mathrm{f})$ at the final time $t = t_\mathrm{f}$ plotted as functions of the control weight γ. Reprinted with permission from Boujo and Sellier [243]. Copyright 2019 by the American Physical Society.

the liquid is quickly pushed to the outer edge of the disk, thinning at the center; subsequent rotations distribute the liquid across the disk, enhancing uniformity, but to a lesser extent due to increased viscosity.

Recently, Wray *et al.* [244] investigated the optimal control of the Navier–Stokes equations governing a two-dimensional multi-phase flow involving a thin liquid film hanging beneath an inclined plane. An electric field is induced within the gas phase via a parallel electrode configuration, resulting in Maxwell stresses at the interface, which is used as the control mechanism. They use a model predictive control (MPC) framework, which consists of finding an updated control for a system at discrete time points during its evolution. Specifically, they perform optimal control calculations on their simplified second-order WRIBL model in order to yield the control inputs, whilst using DNS to re-initialise their WRIBL model (i.e., DNS is used to provide the measurements for the height h and flux q for use as the "initial" conditions), thereby enabling dynamic adjustments to the electric potential function. They showed that this method successfully yields precise control of fluid interface shapes towards a variety of desired target shapes. For example, Figure 1.38 shows the successful MPC of the fluid interface calculated from DNS using their WRIBL model towards (a), (d), (g) a uniform shape, (b),

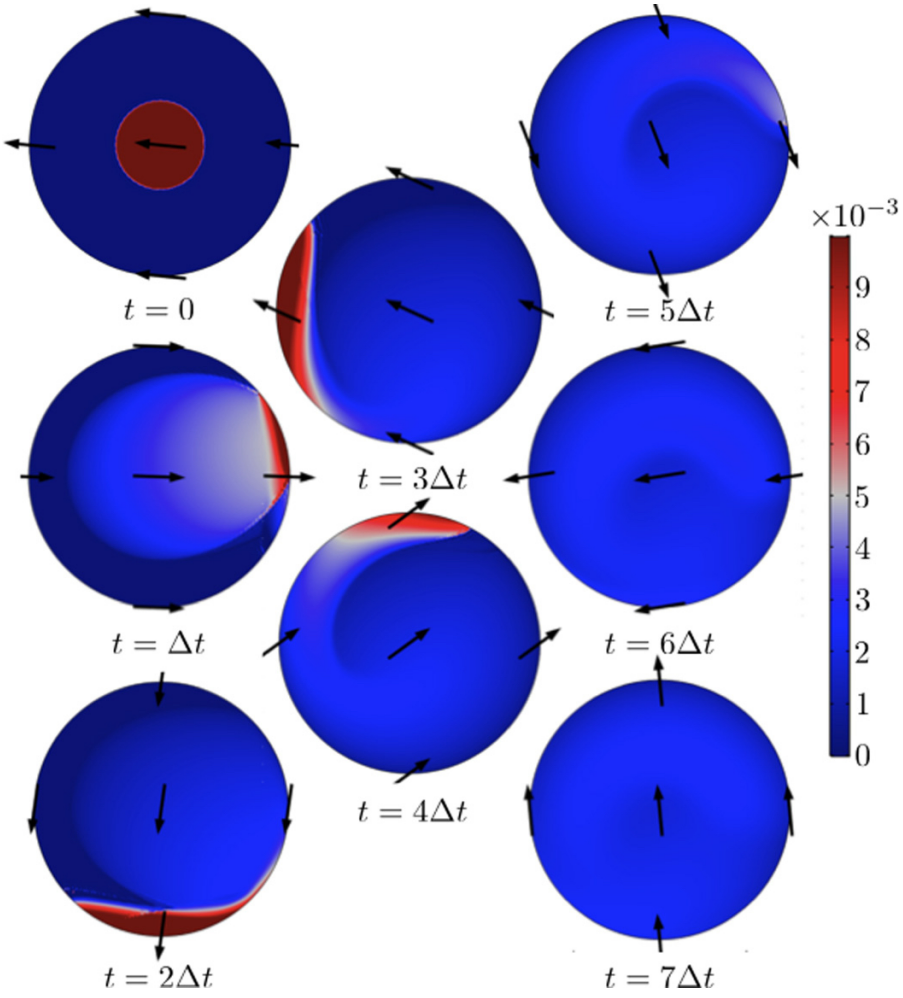

Figure 1.37: Results of the study by Boujo and Sellier [243] showing the time evolution of the film thickness for $\gamma = 10^{-8}$ from time $t = 0$ s to $t = 30.03$ s. Arrows represent the direction of the projection of the gravity vector on the surface plane, indicating the orientation of the substrate. Reprinted with permission from Boujo and Sellier [243]. Copyright 2019 by the American Physical Society.

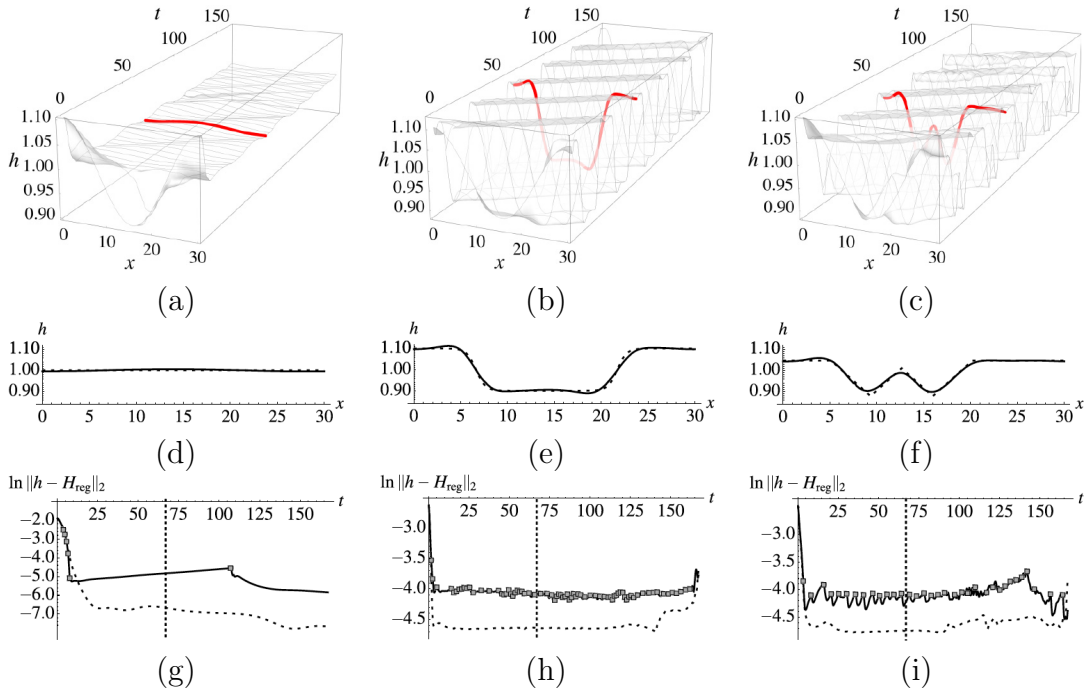

Figure 1.38: Results of calculations by Wray *et al.* [244] showing MPC of DNS using their WRIBL model towards (a), (d), (g) a uniform shape, (b), (e), (h) a "smoothed top-hat" shape, and (c), (f), (i) a "W-like" shape. (a), (b), (c) DNS interfaces over time. Highlighted in red is time $t = 0.4t_f$ where t_f is the final time. (d), (e), (f) DNS interface (solid) and target shape (dashed) at time $t = 0.4t_f$. (g), (h), (i) Log of the error over time calculated from their WRIBL model (dashed) and DNS (solid). The symbols indicate control recomputations. The vertical dotted line shows time $t = 0.4t_f$. Reprinted with permission from Wray *et al.* [244]. Copyright 2019 by the American Physical Society.

(e), (h) a "smoothed top-hat" shape, and (c), (f), (i) a "W-like" shape. The success of the control is particularly evident from Figures 1.38 (d)–(f), which show the DNS interface (solid) and target shape (dashed) at time $t = 0.4t_f$ where t_f is the final time (also shown as the solid red lines in Figures 1.38 (a)–(c)). The symbols in Figures 1.38 (g)–(i) indicate times at which the control was recomputed. Wray *et al.* [244] found that controlling the flow towards a flat state required a small number of recomputations. In particular, they found that only five initial recomputations are required to bring the interfacial (DNS) height close to a flat state, and only one more is required later. However, more recomputations are required for the more complex target shapes as the DNS and WRIBL model diverge

more rapidly.

The discussions in this section and those in Section 1.7.1 highlight a distinct omission from the existing literature on the active control of fluid flows that part of this thesis seeks to address, namely, that there have been no studies on controlling liquid film flows on a horizontal cylinder using an electric field.

1.8 Overview of thesis

This thesis concerns the mathematical modelling, analysis, and control of electrohydrodynamic flows on a horizontal circular cylinder. The primary objective of this thesis is twofold: firstly, to model and investigate the dynamics of a two-dimensional film of a perfectly conducting Newtonian liquid coating a horizontal circular electrode both in the cases in which the film is thin and in which it is thick, and secondly, to show that the dynamics of the flow can be successfully controlled using an electric field.

In Chapter 2, we introduce the system that we will be investigating, in particular obtaining and nondimensionalising the relevant governing equations and their respective boundary conditions. We derive two reduced-order models describing the flow: one that is valid for thin films and one that is valid for thick films. The thin-film system is analysed in Chapters 3 and 4, and the thick-film system is analysed in Chapters 5 and 6.

In Chapter 3, we consider thin-film draining flow in the absence of an electric field. We derive a complete description of the flow, both as an essential precursor to the thin-film electrostatic case considered in Chapter 4 and as an interesting (yet previously unsolved) problem in its own right.

In Chapter 4, we consider thin-film coating flow in the presence of an electric field. Motivated by the aim of understanding how electrostatic effects influence the dynamics of the well-understood thin-film coating flow system, we perform various analytical and numerical analyses on the model. In particular, we perform linear stability analyses on two analytically tractable special cases, a numerical parametric study, and a multiple-timescale analysis in order to elucidate the large-time dynamics of the system, as well as investigating the special case of electrostatic draining flow.

In Chapter 5, we consider thick-film coating flow in the presence of an electric field. The thick-film model is investigated numerically to reveal the evolution of

the film.

In Chapter 6, both feedback and optimal control of thick-film coating flow are considered. In particular, we show that the electric field can be successfully used as a mechanism by which to control the film towards complex target shapes.

In Chapter 7, we give our concluding remarks. In particular, we provide a summary of the analyses and main results within each chapter and discuss possible avenues for further study.

1.9 Presentations and publications

The results contained in this thesis have been published, or are in preparation for publication, in appropriate peer-reviewed journals and have been presented by me at various national and international meetings and conferences.

Aspects of the background theory surrounding the problem considered in this thesis detailed in Chapter 1 were presented in the form of a poster presentation at the Carnegie PhD Scholars' Gathering 2020 held in Dundee, UK.

The results detailed in Chapter 3 have recently been published in *Physical Review Fluids* (McKinlay *et al.* [259]) and were presented orally at the 63$^{\text{rd}}$ British Applied Mathematics Colloquium 2022 held in Loughborough, UK and at the 14$^{\text{th}}$ European Fluid Mechanics Conference 2022 held in Athens, Greece.

The results detailed in the first half of Chapter 2 and those in Chapter 4 are currently being prepared for publication. Early versions of these results were presented orally at the Joint Meeting of the British Mathematical Colloquium and the British Applied Mathematics Colloquium 2021 held in Glasgow, UK (virtual attendance) and at the 14$^{\text{th}}$ European Coating Symposium 2021 held in Brussels, Belgium (virtual attendance). More recent versions of these results were presented at the 63$^{\text{rd}}$ British Applied Mathematics Colloquium 2022 held in Loughborough, UK and at the 14$^{\text{th}}$ European Fluid Mechanics Conference 2022 held in Athens, Greece.

The results detailed in the second half of Chapter 2 and those in Chapters 5 and 6 are currently also being prepared for publication. Early versions of the results presented in Chapter 5 were presented orally at the 63$^{\text{rd}}$ British Applied Mathematics Colloquium 2022 held in Loughborough, UK and at the 14$^{\text{th}}$ European Fluid Mechanics Conference 2022 held in Athens, Greece. More recent versions of these results along with those in Chapter 6 were presented orally at the

75^{th} Annual Meeting of the American Physical Society Division of Fluid Dynamics 2022 held in Indianapolis, USA.

Chapter 2

Modelling

In this chapter, we begin in Section 2.1 by introducing the system that we will consider, in particular obtaining and nondimensionalising the relevant governing equations and their respective boundary conditions. In Section 2.2, we derive a model that is valid for thin films using a standard lubrication approximation. Finally, in Section 2.3, we derive a model that is valid for thick films using the long-wave methodology that was described in Section 1.4.2 together with the WRIBL method that was described in Section 1.2.5. Specifically, the electrostatic part of the thick-film model will be derived in Section 2.3.2 and the hydrodynamic part will be derived in Section 2.3.3.

2.1 Problem formulation

We consider the unsteady, two-dimensional flow of a film of an incompressible Newtonian liquid of constant density $\hat{\rho}$, viscosity $\hat{\mu}$, constant absolute permittivity $\hat{\epsilon}_{\mathrm{L}}$, and constant conductivity $\hat{\sigma}_{\mathrm{L}}$ on the outer surface of a circular cylinder of radius $\hat{R}_1$. The axis of the cylinder is aligned horizontally and gravitational acceleration $\hat{\mathbf{g}}$ acts vertically downwards. The cylinder is rotating with constant angular velocity $\hat{\Omega}$. The liquid film is surrounded by an inviscid, hydrodynamically passive gas (i.e., the density and viscosity of the gas are assumed to be negligible compared to those of the liquid, thus implying that the hydrodynamic flow equations are only relevant in the liquid) with constant pressure $\hat{p}_{\mathrm{a}}$, constant absolute permittivity $\hat{\epsilon}_{\mathrm{G}}$, and constant conductivity $\hat{\sigma}_{\mathrm{G}}$. The constant conductivity of the liquid is assumed to be to be significantly larger than the constant conductivity of the

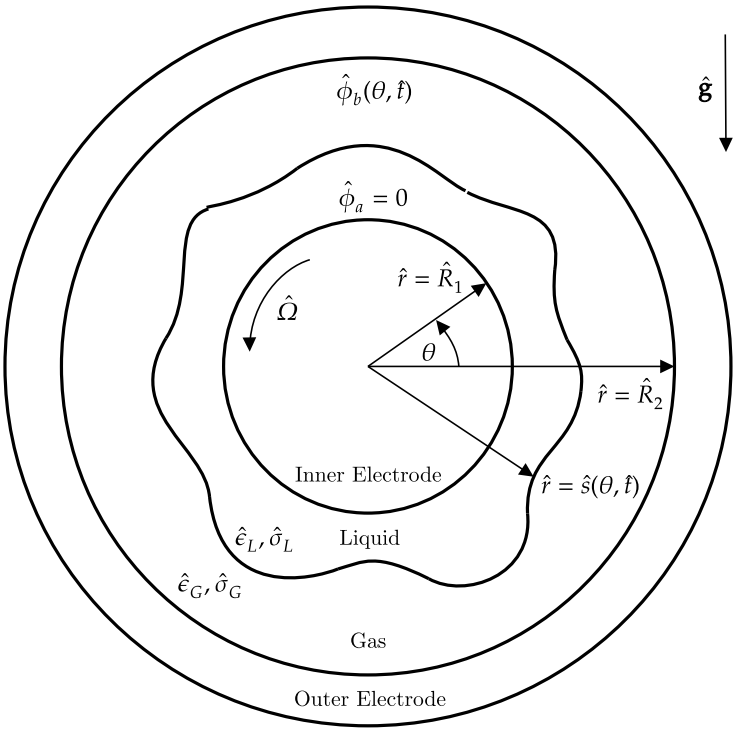

Figure 2.1: Geometry of the system considered in this thesis.

gas (i.e., we consider the case in which $\hat{\sigma}_{\mathrm{L}} \gg \hat{\sigma}_{\mathrm{G}}$) such that the liquid may be considered to be a perfect conductor. We use two-dimensional polar coordinates $(\hat{r}, \theta)$ centred on the axis of the cylinder with θ measured anticlockwise from the horizontal at the right-hand side of the cylinder. The film completely wets the cylinder, with the film thickness at time $\hat{t}$ denoted by $\hat{h} = \hat{h}(\theta, \hat{t})$, so that the liquid-gas interface is located at $\hat{r} = \hat{s}(\theta, \hat{t}) = \hat{R}_1 + \hat{h}(\theta, \hat{t})$ and the film has initial uniform thickness $\hat{h}|_{\hat{t}=0} = \hat{h}_0$. The interface has constant coefficient of surface tension $\hat{\sigma}$ and curvature $\hat{\kappa} = \hat{\kappa}(\theta)$. The liquid has pressure $\hat{p} = \hat{p}(\hat{r}, \theta)$ and velocity $\hat{\mathbf{u}}(\hat{r}, \theta) = \hat{u}(\hat{r}, \theta)\mathbf{e}_{\hat{r}} + \hat{v}(\hat{r}, \theta)\mathbf{e}_{\theta}$, where $\mathbf{e}_{\hat{r}}$ and $\mathbf{e}_{\theta}$ denote the unit vectors in the radial and azimuthal directions, respectively. The cylinder is an electrode (which we shall refer to hereafter as the "inner" electrode) held at a constant potential $\hat{\phi}_a$ which is set to zero without loss of generality, and there is a concentric cylindrical electrode of radius $\hat{R}_2$ enclosing the system (which we shall refer to hereafter as the "outer" electrode). We denote the potential at the outer electrode by $\hat{\phi}_b = \hat{\phi}_b(\theta, \hat{t})$ which is, in general, nonuniform, and its spatiotemporal distribution can be prescribed. The potential difference between the electrodes induces electrostatic forces at the liquid-gas interface. The geometry of the system is shown in Figure 2.1.

2.1.1 Governing equations and boundary conditions

To derive the governing equations, we use a special case of the Taylor–Melcher leaky-dielectric model [162, 163, 197, 198] (which was described in Section 1.6.1) in which one region is a perfect conductor and the other is a perfect dielectric. The assumption that the liquid is a perfect conductor is valid for many liquids surrounded by air, which has a very low dimensional conductivity of $\hat{\sigma}_{\mathrm{G}} \approx 1 \times 10^{-13}$ S m^{-1} at 25°C [215]. For example, brine (a concentrated sodium chloride solution in water with salinity higher than 3.5×10^4 mg L^{-1} total dissolved solids (TDS) [260]) has a dimensional conductivity of $\hat{\sigma}_{\mathrm{L}} = 2.3 \times 10^1$ S m^{-1} [261, 262] at 25°C, which is 14 orders of magnitude larger than that of air. Similarly, ultra-pure water (i.e., water of high purity used in, for example, the semiconductor and pharmaceutical industries to prevent contamination of products during manufacturing [263]) has a dimensional conductivity of $\hat{\sigma}_{\mathrm{L}} = 5.5 \times 10^{-6}$ S m^{-1} at 25°C [215, 263, 264], which is 7 orders of magnitude larger than that of air.

When considering the liquid to be a perfect conductor, its potential becomes equal to that of the electrode with which it is in contact. Hence, the liquid has zero potential everywhere and it follows that the system has non-zero potential in the gas only. As discussed in Section 1.6.1, the electric field, which we denote by $\hat{\mathbf{E}} = \hat{\mathbf{E}}(\hat{r}, \theta)$, satisfies [163]

$$\nabla \times \hat{\mathbf{E}} = \mathbf{0}, \quad \nabla \cdot \hat{\mathbf{E}} = 0. \tag{2.1.1}$$

In other words, equation (2.1.1) implies that the electric field has zero curl (i.e., the electric field is irrotational) and zero divergence. By the first equation in (2.1.1), the electric field can be expressed in terms of the gradient of the electric potential function $\hat{\phi} = \hat{\phi}(\hat{r}, \theta)$ (which we shall refer to hereafter as simply the "potential") such that

$$\hat{\mathbf{E}} = -\nabla\hat{\phi} = -\left(\mathbf{e}_{\hat{r}}\hat{\phi}_{\hat{r}} + \mathbf{e}_{\theta}\frac{\hat{\phi}_{\theta}}{\hat{r}}\right), \tag{2.1.2}$$

where the negative sign is consistent with the conventions used in the literature [163, 203]. By the second equation in (2.1.1), the potential $\hat{\phi}$ satisfies Laplace's equation,

$$\nabla^2\hat{\phi} = \hat{\phi}_{\hat{r}\hat{r}} + \frac{1}{\hat{r}}\hat{\phi}_{\hat{r}} + \frac{1}{\hat{r}^2}\hat{\phi}_{\theta\theta} = 0. \tag{2.1.3}$$

The difference in electrical material properties between the liquid and gas induces

electric (Maxwell) stresses at the interface. The total stress tensor $\hat{\underline{\underline{\mathbf{T}}}} = \hat{\underline{\underline{\mathbf{T}}}}(\hat{r}, \theta)$ is given by [25, 26, 162],

$$\hat{\underline{\underline{\mathbf{T}}}} = -\hat{p}\hat{\underline{\underline{\mathbf{I}}}} + \hat{\underline{\underline{\boldsymbol{\tau}}}} + \hat{\underline{\underline{\mathbf{M}}}}, \tag{2.1.4}$$

where $\hat{\underline{\underline{\mathbf{I}}}}$ is the identity tensor, $\hat{\underline{\underline{\boldsymbol{\tau}}}} = \hat{\underline{\underline{\boldsymbol{\tau}}}}(\hat{r}, \theta)$ is the viscous stress tensor,

$$\hat{\underline{\underline{\boldsymbol{\tau}}}} = \hat{\mu}\left(\nabla\hat{\mathbf{u}} + \nabla\hat{\mathbf{u}}^T\right) = \hat{\mu}\begin{bmatrix} 2\hat{u}_{\hat{r}} & \frac{1}{\hat{r}}\left(\hat{u}_\theta - \hat{v}\right) + \hat{v}_{\hat{r}} \\ \frac{1}{\hat{r}}\left(\hat{u}_\theta - \hat{v}\right) + \hat{v}_{\hat{r}} & \frac{2}{\hat{r}}\left(\hat{v}_\theta + \hat{u}\right) \end{bmatrix}, \tag{2.1.5}$$

where $\hat{\underline{\underline{\boldsymbol{\tau}}}} = 0$ in the hydrodynamically passive gas, and $\hat{\underline{\underline{\mathbf{M}}}} = \hat{\underline{\underline{\mathbf{M}}}}(\hat{r}, \theta)$ is the Maxwell stress tensor,

$$\hat{\underline{\underline{\mathbf{M}}}} = \hat{\epsilon}_{\mathrm{L,G}}\left(\hat{\mathbf{E}}\hat{\mathbf{E}} - \frac{1}{2}|\hat{\mathbf{E}}|^2\hat{\underline{\mathbf{I}}}\right). \tag{2.1.6}$$

Thus, by combining (2.1.4)–(2.1.6), the total stress tensor $\hat{\underline{\underline{\mathbf{T}}}}$ (2.1.4) is given by

$$\hat{\underline{\underline{\mathbf{T}}}} = \begin{bmatrix} -\hat{p} + 2\hat{\mu}\hat{u}_{\hat{r}} + \frac{\hat{\epsilon}_{\mathrm{L,G}}}{2}\left(\hat{\phi}_{\hat{r}}^2 - \frac{\hat{\phi}_\theta^2}{\hat{r}^2}\right) & \frac{\hat{\mu}}{\hat{r}}\left(\hat{u}_\theta - \hat{v}\right) + \hat{\mu}\hat{v}_{\hat{r}} + \frac{\hat{\epsilon}_{\mathrm{L,G}}\hat{\phi}_{\hat{r}}\hat{\phi}_\theta}{\hat{r}} \\ \frac{\hat{\mu}}{\hat{r}}\left(\hat{u}_\theta - \hat{v}\right) + \hat{\mu}\hat{v}_{\hat{r}} + \frac{\hat{\epsilon}_{\mathrm{L,G}}\hat{\phi}_{\hat{r}}\hat{\phi}_\theta}{\hat{r}} & \frac{2\hat{\mu}}{\hat{r}}\left(\hat{v}_\theta + \hat{u}\right) - \hat{p} + \frac{\hat{\epsilon}_{\mathrm{L,G}}}{2}\left(\frac{\hat{\phi}_\theta^2}{\hat{r}^2} - \hat{\phi}_{\hat{r}}^2\right) \end{bmatrix}. \tag{2.1.7}$$

As discussed in Section 1.6.1, under the assumptions of the leaky-dielectric model (i.e., that the characteristic timescale of electrostatic processes is large compared to that of magnetic processes, and the permittivities $\hat{\epsilon}_{\mathrm{L,G}}$ and conductivities $\hat{\sigma}_{\mathrm{L,G}}$ are constant) the divergence of the Maxwell stress tensor $\nabla \cdot \hat{\underline{\underline{\mathbf{M}}}}$ is identically zero everywhere in the system except at the liquid-gas interface. Consequently, the electric potential $\hat{\phi}$ does not appear in the Navier–Stokes equations which, as we recall from Section 1.1, are given by

$$\nabla \cdot \hat{\mathbf{u}} = 0, \tag{2.1.8}$$

$$\hat{\rho}\frac{\mathrm{D}\hat{\mathbf{u}}}{\mathrm{D}\hat{t}} = -\nabla\hat{p} + \hat{\mu}\nabla^2\hat{\mathbf{u}} + \hat{\rho}\hat{\mathbf{g}}. \tag{2.1.9}$$

Thus, the Navier–Stokes equations (2.1.8) and (2.1.9) govern the liquid pressure and velocity only. Instead, the coupling between hydrodynamics and electrostatics occurs solely through the interfacial boundary conditions, where the role of the Maxwell stress becomes significant. The electrostatic governing equation (2.1.3) (i.e., Laplace's equation) is complemented by suitable boundary conditions. Specif-

ically, we impose continuity of potential at the outer electrode and the interface,

$$\hat{\phi}|_{\hat{r}=\hat{R}_2} = \hat{\phi}_b(\theta, \hat{t}), \quad \hat{\phi}|_{\hat{r}=\hat{s}} = 0, \tag{2.1.10}$$

respectively, which we shall refer to hereafter as the "electrostatic boundary conditions". The hydrodynamic governing equations (2.1.8) and (2.1.9) are complemented by the no-slip and impermeability conditions at the surface of the inner electrode,

$$\hat{v}|_{\hat{r}=\hat{R}_1} = \hat{\Omega}\hat{R}_1, \quad \hat{u}|_{\hat{r}=\hat{R}_1} = 0, \tag{2.1.11}$$

respectively, along with the kinematic condition at the interface,

$$\left[\frac{\mathrm{D}}{\mathrm{D}\hat{t}}\left(\hat{r} - \hat{s}\right)\right]\Bigg|_{\hat{r}=\hat{s}} = 0, \tag{2.1.12}$$

and the balance of normal and tangential stresses at the interface $\hat{r} = \hat{s}$, given respectively by

$$\left[\hat{\mathbf{n}} \cdot \hat{\underline{\underline{\mathbf{T}}}} \cdot \hat{\mathbf{n}}\right]_{\mathrm{G}}^{\mathrm{L}} = -\hat{\sigma}\hat{\kappa}, \qquad \left[\hat{\mathbf{t}} \cdot \hat{\underline{\underline{\mathbf{T}}}} \cdot \hat{\mathbf{n}}\right]_{\mathrm{G}}^{\mathrm{L}} = 0, \tag{2.1.13}$$

where $[\cdot]_{\mathrm{G}}^{\mathrm{L}}$ represents the jump in the quantity across the liquid-gas interface, the interfacial curvature $\hat{\kappa}$ is given by

$$\hat{\kappa} = \nabla \cdot \hat{\mathbf{n}}, \tag{2.1.14}$$

and $\hat{\mathbf{n}}$ and $\hat{\mathbf{t}}$ are the unit outward-pointing normal and tangent vectors, given respectively by

$$\hat{\mathbf{n}} = \left(\hat{s}^2 + \hat{s}_\theta^2\right)^{-1/2}\left(\hat{s}\mathbf{e}_{\hat{r}} - \hat{s}_\theta \mathbf{e}_\theta\right), \tag{2.1.15}$$

$$\hat{\mathbf{t}} = \left(\hat{s}^2 + \hat{s}_\theta^2\right)^{-1/2}\left(\hat{s}_\theta \mathbf{e}_{\hat{r}} + \hat{s}\mathbf{e}_\theta\right). \tag{2.1.16}$$

The electrostatic contributions to the normal and tangential stress balances (2.1.13), which we denote by $E^N = E^N(\theta)$ and $E^T = E^T(\theta)$, respectively, describe the jump in value of the Maxwell stress across the interface. Tangential Maxwell stresses are present only when there is finite conductivity in both regions [162, 163, 197, 198]. Hence, the assumptions that the liquid is a perfect conductor and the gas is a perfect dielectric leads to $E^T = 0$. Therefore, for the purposes of this thesis we are concerned only with the normal Maxwell stress, namely,

$$E^N = \left[\hat{\mathbf{n}} \cdot \hat{\underline{\underline{\mathbf{M}}}} \cdot \hat{\mathbf{n}}\right]_{\mathrm{G}}^{\mathrm{L}}. \tag{2.1.17}$$

2.1.2 Nondimensionalisation

We nondimensionalise the system according to

$$\hat{\mathbf{u}} = \hat{U}_{\text{char}}\mathbf{u}, \quad \hat{r} = \hat{R}_1 r, \quad \hat{s} = \hat{R}_1 s, \quad \hat{h} = \hat{R}_1 h, \quad \hat{h}_0 = \hat{R}_1 h_0, \quad \hat{t} = \frac{\hat{R}_1}{\hat{U}_{\text{char}}} t,$$

$$\hat{p} - \hat{p}_a = \frac{\hat{\mu}\hat{U}_{\text{char}}}{\hat{R}_1} p, \quad \hat{\kappa} = \frac{1}{\hat{R}_1}\kappa, \quad \hat{\phi} = \hat{\phi}_{\text{char}}\phi, \quad \hat{\epsilon}_{\text{L,G}} = \hat{\epsilon}_0\epsilon_{\text{l,g}}, \quad \hat{q} = \hat{R}_1\hat{U}_{\text{char}} q, \tag{2.1.18}$$

where

$$\hat{U}_{\text{char}} = \frac{\hat{\rho}\hat{g}\hat{R}_1^2}{\hat{\mu}} \tag{2.1.19}$$

is a characteristic (drainage) velocity [102], $\hat{\epsilon}_0 = 8.85419 \times 10^{-12}$ F m^{-1} is the permittivity of free space [200], and $\hat{\phi}_{\text{char}}$ is a characteristic potential to be specified later. Upon applying the scalings (2.1.2), the continuity equation (2.1.8) becomes

$$(ru)_r + v_\theta = 0, \tag{2.1.20}$$

and the momentum equation (2.1.9) becomes

$$Re\left(u_t + uu_r + \frac{v}{r}u_\theta - \frac{v^2}{r}\right) = -p_r + \frac{1}{r}(ru_r)_r - \frac{u}{r^2} + \frac{1}{r^2}u_{\theta\theta} - \frac{2}{r^2}v_\theta - \sin\theta, \tag{2.1.21}$$

$$Re\left(v_t + uv_r + \frac{v}{r}v_\theta - \frac{uv}{r}\right) = -\frac{1}{r}p_\theta + \frac{1}{r}(rv_r)_r - \frac{v}{r^2} + \frac{1}{r^2}v_{\theta\theta} + \frac{2}{r^2}u_\theta - \cos\theta, \tag{2.1.22}$$

where

$$Re = \frac{\hat{\rho}\hat{U}_{\text{char}}\hat{R}_1}{\hat{\mu}} \tag{2.1.23}$$

is a Reynolds number, which is the ratio of inertial forces to viscous forces. The dimensionless initial condition is

$$h|_{t=0} = h_0 = \frac{\hat{h}_0}{\hat{R}_1}, \tag{2.1.24}$$

and the no-slip and impermeability conditions (2.1.11) become

$$v|_{r=1} = \omega, \quad u|_{r=1} = 0, \tag{2.1.25}$$

where

$$\omega = \frac{\hat{\Omega}\hat{R}_1}{\hat{U}_{\text{char}}} \tag{2.1.26}$$

is a dimensionless expression for the azimuthal rotation rate and $r = 1$ is a dimensionless expression for the radius of the inner electrode, respectively. At the interface $r = s(\theta, t) = 1 + h(\theta, t)$, the normal and tangential stress conditions (2.1.13) become

$$\left(p - \frac{\kappa}{Ca}\right)\left(s^2 + s_\theta^2\right) = 2\left[s^2 u_r + s_\theta(v - u_\theta - s v_r) + \frac{s_\theta^2}{s}(v_\theta + u)\right] - \tilde{E}_b E^N, \tag{2.1.27}$$

$$2 s_\theta \left[u_r - \frac{1}{s}\left(u + v_\theta\right)\right] + \left(1 - \frac{s_\theta^2}{s^2}\right)\left(s v_r - v + u_\theta\right) = 0, \tag{2.1.28}$$

respectively, where E^N (2.1.17) is given by

$$E^N = \frac{1}{2}\left(s^2 - s_\theta^2\right)\left(\phi_r^2 - \frac{\phi_\theta^2}{s^2}\right) - 2 s_\theta \phi_r \phi_\theta. \tag{2.1.29}$$

Furthermore,

$$Ca = \frac{\hat{\mu}\hat{U}_{\text{char}}}{\hat{\sigma}} \tag{2.1.30}$$

is a capillary number, which is the ratio of viscous forces to capillarity, and

$$\tilde{E}_b = \frac{\hat{\epsilon}_{\text{G}}\hat{\phi}_{\text{char}}^2}{\hat{\mu}\hat{U}_{\text{char}}\hat{R}_1} \tag{2.1.31}$$

is a dimensionless measure of the magnitude of the applied electric potential difference (referred to hereafter as simply the "electric potential difference"), and κ (2.1.14) is given by

$$\kappa = \frac{s^2 + 2 s_\theta^2 - s s_{\theta\theta}}{\left(s^2 + s_\theta^2\right)^{3/2}}. \tag{2.1.32}$$

The kinematic condition (2.1.12) becomes

$$\left(s_t + \frac{s_\theta}{s} v - u\right)\Big|_{r=s} = 0, \tag{2.1.33}$$

which may be written in the form

$$\frac{1}{2}\left(s^2\right)_t + q_\theta = 0, \tag{2.1.34}$$

where

$$q = \int_1^s v\,(\theta, r)\,\mathrm{d}r \tag{2.1.35}$$

is the dimensionless azimuthal volume flux per unit length (referred to hereafter as simply the "flux"). Laplace's equation (2.1.3) remains unchanged (dropping the hat decoration) and the electrostatic boundary conditions (2.1.10) become

$$\phi|_{r=d} = \phi_d(\theta, t), \quad \phi|_{r=s} = 0, \tag{2.1.36}$$

respectively, where

$$d = \frac{\hat{R}_2}{\hat{R}_1}, \quad \phi_d = \frac{\hat{\phi}_b}{\hat{\phi}_{\mathrm{char}}}, \tag{2.1.37}$$

are dimensionless expressions for the radius of the outer electrode and the potential at the outer electrode, respectively.

2.2 Thin-film modelling

In this section, we derive an equation governing the flow of the liquid layer described in the previous section in the case in which it is thin using the classical thin-film approximation. Specifically, as described in Section 1.4.1.1, we assume that the film thickness is small and introduce the thin-film aspect ratio $\epsilon = h_0 \ll 1$, where h_0 is given by (2.1.24). We introduce the standard thin-film scalings [95, 101, 102]

$$\begin{gathered} r = 1 + \epsilon\tilde{R}, \quad h = \epsilon\tilde{H}, \quad d = 1 + \epsilon\tilde{D}, \quad t = \epsilon^{-2}\tilde{T}, \quad p = \tilde{P}, \\ u = \epsilon^3\tilde{U}, \quad v = \epsilon^2\tilde{V}, \quad q = \epsilon^3\tilde{Q}, \quad \phi = \epsilon\tilde{\Phi}, \quad \phi_d = \epsilon\tilde{\Phi}_{\tilde{D}}, \end{gathered} \tag{2.2.1}$$

where we have introduced an appropriate timescale to capture the thin-film flow dynamics. Note that, by the rescaling of d with ϵ in (2.2.1), we consider the distinguished limit in which the gap between the inner and outer electrodes is thin. In what follows, we carry out a standard "lubrication" modelling procedure (see, for example, Pukhnachev [95], Reisfeld and Bankoff [101], and Evans *et al.* [102]). Specifically, we derive an expression for the azimuthal velocity $\tilde{V}$ in terms of the film thickness $\tilde{H}$, from which we evaluate the flux $\tilde{Q}$. Finally, substitution of $\tilde{Q}$ into the kinematic condition yields the final thin-film governing equation.

By (2.1.24), the initial condition becomes

$$\tilde{H}|_{\tilde{T}=0} = \tilde{H}_0 = 1. \tag{2.2.2}$$

Applying the thin-film scalings (2.2.1), Laplace's equation (2.1.3) becomes

$$\tilde{\Phi}_{\tilde{R}\tilde{R}} = 0 \tag{2.2.3}$$

to leading order in ϵ, and the electrostatic boundary conditions (2.1.36) become

$$\tilde{\Phi}|_{\tilde{R}=\tilde{D}} = \tilde{\Phi}_{\tilde{D}}, \quad \tilde{\Phi}|_{\tilde{R}=\tilde{H}} = 0. \tag{2.2.4}$$

We assume that the dimensionless potential at the outer electrode $\hat{\phi}_b$ is constant, and hence choose $\hat{\phi}_{\text{char}} = \hat{\phi}_b$, leading to $\phi_d = 1$ in the electrostatic boundary conditions (2.1.36), and hence $\tilde{\Phi}_{\tilde{D}} = 1$ in the thin-film electrostatic boundary conditions (2.2.4). Solving (2.2.3) subject to (2.2.4) yields the leading-order solution for the electric potential $\tilde{\Phi}$, namely,

$$\tilde{\Phi} = \frac{\tilde{R} - \tilde{H}}{\tilde{D} - \tilde{H}}. \tag{2.2.5}$$

The solution (2.2.5) is a linear function of $\tilde{R}$ which varies between $0 \leq \tilde{\Phi} \leq 1$ over the domain $\tilde{H} \leq \tilde{R} \leq \tilde{D}$. To leading order in ϵ, the hydrodynamic governing equations (2.1.20)–(2.1.22) become

$$\tilde{U}_{\tilde{R}} + \tilde{V}_{\theta} = 0, \tag{2.2.6}$$

$$\tilde{P}_{\tilde{R}} = 0, \tag{2.2.7}$$

$$\tilde{V}_{\tilde{R}\tilde{R}} = \tilde{P}_{\theta} + \cos\theta, \tag{2.2.8}$$

respectively. Applying the scalings (2.2.1) to the interfacial curvature (2.1.32) and retaining terms to first order in ϵ yields

$$\tilde{\kappa} = 1 - \epsilon(\tilde{H} + \tilde{H}_{\theta\theta}), \tag{2.2.9}$$

hence, to first order in ϵ, the normal stress condition (2.1.27) becomes

$$\tilde{P}|_{\tilde{R}=\tilde{H}} = \frac{1}{\epsilon\tilde{\gamma}}\left[1 - \epsilon(\tilde{H} + \tilde{H}_{\theta\theta})\right] - \frac{\tilde{E}_b}{2}\tilde{\Phi}^2_{\tilde{R}}, \tag{2.2.10}$$

where we have set

$$Ca = \epsilon\tilde{\gamma}, \tag{2.2.11}$$

in which $\tilde{\gamma} = O(1)$ in order to consider the distinguished limit in which $Ca = O(\epsilon)$ such that capillarity appears at leading order in ϵ alongside the electrostatic effects. Specifically, choosing to work in this distinguished limit ensures that capillarity has a significant influence on the flow dynamics and hence allows for a more accurate representation of the interplay between capillarity and the other forces. Evaluating (2.2.10) with $\tilde{\Phi}$ given by (2.2.5) yields

$$\tilde{P}|_{\tilde{R}=\tilde{H}} = \frac{1}{\epsilon\tilde{\gamma}}\left[1 - \epsilon(\tilde{H} + \tilde{H}_{\theta\theta})\right] - \frac{\tilde{E}_b}{2}\frac{1}{(\tilde{D} - \tilde{H})^2}. \tag{2.2.12}$$

To leading order in ϵ, the tangential stress condition (2.1.28) becomes

$$\tilde{V}_{\tilde{R}}|_{\tilde{R}=\tilde{H}} = 0. \tag{2.2.13}$$

The no-slip and impermeability conditions (2.1.25) become

$$\tilde{V}|_{\tilde{R}=1} = \bar{\omega}, \quad \tilde{U}|_{\tilde{R}=1} = 0, \tag{2.2.14}$$

where we have set

$$\omega = \epsilon^2\bar{\omega}, \tag{2.2.15}$$

in which $\bar{\omega} = O(1)$ in order to consider the distinguished limit in which $\omega = O(\epsilon^2)$ such that rotation appears at leading order in ϵ alongside the electrostatic and capillary effects. Specifically, choosing to work in this distinguished limit ensures that rotation speeds are comparable to flow speeds and hence ensures that the rotation does not dominate the dynamics of the system. Integrating the leading-order radial component of the momentum equation (2.2.7) subject to the normal stress condition (2.2.12) yields the solution for the pressure $\tilde{P}$ to first order in ϵ, namely,

$$\tilde{P} = \frac{1}{\epsilon\tilde{\gamma}}\left[1 - \epsilon(\tilde{H} + \tilde{H}_{\theta\theta})\right] - \frac{\tilde{E}_b}{2}\frac{1}{(\tilde{D} - \tilde{H})^2}. \tag{2.2.16}$$

Substituting the first-order solution for the pressure (2.2.16) into the leading-order azimuthal component of the momentum equation (2.2.8) and integrating twice with respect to $\tilde{R}$ subject to the no-slip condition (2.2.14) and the leading-order tan-

gential stress condition (2.2.13) yields the leading-order solution for the azimuthal velocity $\tilde{V}$, namely,

$$\tilde{V} = \bar{\omega} + \frac{1}{2}(\tilde{R}^2 - 2\tilde{R}\tilde{H}) \left[\cos\theta - \frac{1}{\tilde{\gamma}}(\tilde{H} + \tilde{H}_{\theta\theta})_\theta - \tilde{E}_b \frac{\tilde{H}_\theta}{(\tilde{D} - \tilde{H})^3} \right]. \tag{2.2.17}$$

To leading order in ϵ, the kinematic condition (2.1.34) becomes

$$\tilde{H}_{\tilde{T}} + \tilde{Q}_\theta = 0, \tag{2.2.18}$$

where, to leading order in ϵ, the flux (2.1.35) is given by

$$\tilde{Q} = \int_0^{\tilde{H}} \tilde{V}(\tilde{R}, \theta) \, \mathrm{d}\tilde{R}. \tag{2.2.19}$$

Evaluating the leading-order flux $\tilde{Q}$ (2.2.19) with the leading-order azimuthal velocity $\tilde{V}$ (2.2.17) and substituting the resulting expression for $\tilde{Q}$ into the leading-order kinematic condition (2.2.18) yields the governing equation for the thickness of a thin film on the outer surface of a rotating horizontal circular cylinder in the presence of an electric field, namely,

$$\tilde{H}_{\tilde{T}} + \left[\bar{\omega}\tilde{H} + \frac{\tilde{H}^3}{3} \left(-\cos\theta + \frac{1}{\tilde{\gamma}} \left(\tilde{H}_\theta + \tilde{H}_{\theta\theta\theta} \right) + \tilde{E}_b \frac{\tilde{H}_\theta}{(\tilde{D} - \tilde{H})^3} \right) \right]_\theta = 0. \tag{2.2.20}$$

In particular, the flux $\tilde{Q}$ (2.2.19) is

$$\tilde{Q} = \bar{\omega}\tilde{H} + \frac{\tilde{H}^3}{3} \left(-\cos\theta + \frac{1}{\tilde{\gamma}} \left(\tilde{H}_\theta + \tilde{H}_{\theta\theta\theta} \right) + \tilde{E}_b \frac{\tilde{H}_\theta}{(\tilde{D} - \tilde{H})^3} \right). \tag{2.2.21}$$

Equations (2.2.20) and (2.2.21) are the basis of all of the analysis contained within Chapter 3 and Section 4.3, in which we investigate the special case of a stationary cylinder, corresponding to $\bar{\omega} = 0$, in the absence and presence of an electric field, respectively.

To aid investigation of parameter space, we reduce the number of dimensionless parameters in the governing equation (2.2.20) and the flux (2.2.21) by one by

eliminating the dimensionless azimuthal rotation rate ω by imposing the scalings

$$\tilde{H} = \bar{\omega}^{1/2} H, \quad \tilde{D} = \bar{\omega}^{1/2} D, \quad \tilde{E}_b = \bar{\omega} E_b, \quad \tilde{\gamma} = \bar{\omega}^{1/2} \gamma, \quad \tilde{T} = \bar{\omega}^{-1} T, \quad \tilde{Q} = \bar{\omega}^{3/2} Q, \tag{2.2.22}$$

to yield

$$H_T + \left[H + \frac{H^3}{3} \left(-\cos\theta + \frac{1}{\gamma} \left(H_\theta + H_{\theta\theta\theta} \right) + E_b \frac{H_\theta}{(D-H)^3} \right) \right]_\theta = 0, \tag{2.2.23}$$

$$Q = H + \frac{H^3}{3} \left(-\cos\theta + \frac{1}{\gamma} \left(H_\theta + H_{\theta\theta\theta} \right) + E_b \frac{H_\theta}{(D-H)^3} \right), \tag{2.2.24}$$

respectively. The system is thus governed by four dimensionless groups, namely, the initial film thickness H_0, the capillary number γ, the electric potential difference E_b, and the distance between the inner and outer electrodes (referred to hereafter as simply the "electrode distance") D, given respectively by

$$H_0 = \left(\frac{\hat{\rho}\hat{g}}{\hat{\mu}\hat{\Omega}\hat{R}_1} \right)^{1/2} \hat{h}_0, \tag{2.2.25}$$

$$\gamma = \left(\frac{\hat{\rho}^3 \hat{g}^3 \hat{R}_1^5}{\hat{\mu}\hat{\sigma}^2\hat{\Omega}} \right)^{1/2}, \tag{2.2.26}$$

$$E_b = \frac{\hat{h}_0^2 \hat{\epsilon}_{\mathrm{G}} \hat{\phi}_b^2}{\hat{\mu}\hat{\Omega}\hat{R}_1^4}, \tag{2.2.27}$$

$$D = \left(\frac{\hat{R}_2}{\hat{R}_1} - 1 \right) \left(\frac{\hat{\rho}\hat{g}\hat{R}_1}{\hat{\mu}\hat{\Omega}} \right)^{1/2}. \tag{2.2.28}$$

Equations (2.2.23) and (2.2.24) are the basis of all of the analysis contained within Sections 4.1, 4.2, and 4.4, in which we investigate the case where $\bar{\omega}$ and E_b are both non-zero. Numerical solutions of the governing equations (2.2.20) and (2.2.23) are obtained using the numerical scheme outlined in Appendix A. Specifically, a uniform grid formulation is used to perform the numerical calculations in Sections 4.1, 4.2, and 4.4 and is outlined in Appendix A.1, and a nonuniform grid formulation is used to perform the numerical calculations in Chapter 3 and in Section 4.3 and is outlined in Appendix A.2. Note that, hereafter, when we refer to "the cylinder" we are referring specifically to the inner electrode rather than the outer electrode.

2.3 Thick-film modelling

In this section, we derive a model that is valid for thick films using the long-wave methodology described by Wray *et al.* [31, 56] in conjunction with the WRIBL method, both of which were described earlier in Sections 1.4.2 and 1.2.5, respectively. In particular, we generalise the thick-film model of Wray and Cimpeanu [31] (i.e., equation (1.4.28) and the integral form of the kinematic condition (1.2.9)), which was discussed earlier in Section 1.4.4, to incorporate electrostatic effects. As explained in Section 1.4.1.2, the fundamental assumption underlying the modelling of thick films is that the thickness of the film is assumed to be of the same order as the radius of curvature of the substrate. In line with the WRIBL method, we begin by deriving a boundary-layer equation for the hydrodynamic part of the problem in Section 2.3.1 before solving the electrostatic and hydrodynamic parts of the problem in Sections 2.3.2 and 2.3.3, respectively. Note that throughout this section, we assume that the potential at the outer electrode $\hat{\phi}_b$ varies spatially and hence define the characteristic potential $\hat{\phi}_{\text{char}} = \bar{\phi}_b$, where $\bar{\phi}_b$ is the mean potential at the outer electrode over the domain $0 \leq \theta \leq 2\pi$ measured at time $t = 0$.

2.3.1 Boundary-layer equation

In this section, we carry out the initial step of the WRIBL method which, as described in Section 1.2.5, is to derive a boundary-layer equation for the interfacial radius s and the azimuthal and radial velocities u and v, respectively. As discussed in Section 1.2.5, we employ the long-wave methodology by making the substitution [31, 56]

$$\partial_\theta = \varepsilon \partial_{\check{\theta}}, \tag{2.3.1}$$

which represents the assumption that variations in the azimuthal direction are small, where ε is an ordering parameter which is used to assert the expected relative magnitudes of particular terms and their derivatives during the calculations rather than having an explicit value of its own, and hence is set equal to unity in the final model [28, 29, 31, 37, 52–55, 64, 65]. Furthermore, balancing terms in the kinematic condition (1.2.13) and the continuity equation (2.1.20) suggests making the additional substitutions

$$t = \varepsilon^{-1}\check{t}, \quad u = \varepsilon \check{u}, \tag{2.3.2}$$

respectively.

Under the substitutions (2.3.1) and (2.3.2), the kinematic condition (2.1.34) and the no-slip and impermeability conditions (2.1.25) remain unchanged, whilst to $O(\varepsilon)$ the radial component of the momentum equation (2.1.21) becomes

$$p_r = Re\frac{v^2}{r} + \varepsilon\left[\left(\frac{1}{r}(r\check{u})_r\right)_r - \frac{2}{r^2}v_{\check{\theta}}\right] - \sin\theta + O(\varepsilon^2), \tag{2.3.3}$$

and the azimuthal component (2.1.22) becomes

$$Re\left(\varepsilon v_{\check{t}} + \varepsilon\check{u}v_r + \varepsilon\frac{v}{r}v_{\check{\theta}} + \varepsilon\frac{\check{u}v}{r}\right) = -\frac{\varepsilon}{r}p_{\check{\theta}} + \frac{1}{r}\left(rv_r\right)_r - \frac{v}{r^2} + \frac{\varepsilon^2}{r^2}v_{\check{\theta}\check{\theta}} + \frac{2\varepsilon^2}{r^2}\check{u}_{\check{\theta}} - \cos\theta. \tag{2.3.4}$$

Hence, by (2.3.4), the equation for the pressure (2.3.3) is sufficient for our present purposes as we only require an expression for p accurate to $O(\varepsilon)$ in order to obtain a boundary-layer equation accurate to $O(\varepsilon^2)$. The tangential stress condition (2.1.28) becomes

$$2\varepsilon s_{\check{\theta}}\left(\varepsilon\check{u}_r - \frac{\varepsilon}{s}(\check{u} + v_{\check{\theta}})\right) + \left(1 - \varepsilon^2\frac{s_{\check{\theta}}^2}{s^2}\right)(sv_r - v + \varepsilon^2\check{u}_{\check{\theta}}) = 0, \tag{2.3.5}$$

which, using the continuity equation (2.1.20), may be reduced to

$$v - sv_r = \varepsilon^2[\check{u}_{\check{\theta}} + 4s_{\check{\theta}}\check{u}_r] + O(\varepsilon^3). \tag{2.3.6}$$

The normal stress condition (2.1.27) becomes

$$\begin{aligned}\left(p - \frac{\kappa}{Ca}\right)(s^2 + \varepsilon^2 s_{\check{\theta}}^2) = 2\left[\varepsilon s^2\check{u}_r + \varepsilon s_{\check{\theta}}(v - \varepsilon^2\check{u}_{\check{\theta}} - sv_r) + \varepsilon^2\frac{s_{\check{\theta}}^2}{s^2}(\varepsilon v_{\check{\theta}} + \varepsilon\check{u})\right] \\ + \tilde{E}_b\left[2\varepsilon^2 s_{\check{\theta}}\phi_r\phi_{\check{\theta}} - \frac{1}{2}(s^2 - \varepsilon^2 s_{\check{\theta}}^2)\left(\phi_r^2 - \varepsilon^2\frac{\phi_{\check{\theta}}^2}{s^2}\right)\right],\end{aligned} \tag{2.3.7}$$

which to $O(\varepsilon)$ is

$$p|_{r=s} = \frac{\kappa}{Ca} + 2\varepsilon\check{u}_r|_{r=s} + \tilde{E}_b E^N + O(\varepsilon^2), \tag{2.3.8}$$

where we have used the tangential stress condition (2.3.6), and E^N is the normal

Maxwell stress, namely,

$$E^N = 2\varepsilon^2 \frac{s_{\check{\theta}}}{s^2}\phi_r\phi_{\check{\theta}} - \frac{1}{2}\left(1 - \varepsilon^2\frac{s_{\check{\theta}}^2}{s^2}\right)\left(\phi_r^2 - \varepsilon^2\frac{\phi_{\check{\theta}}^2}{s^2}\right), \tag{2.3.9}$$

where we have assumed that $\tilde{E}_b = O(1)$ (where $\tilde{E}_b$ is given by (2.1.31)). Integrating (2.3.3) with respect to the radial coordinate from r to s subject to the normal stress condition (2.3.8) yields an expression for the pressure p, namely,

$$\begin{aligned} p =& \frac{\kappa}{Ca} + 2\varepsilon\check{u}_r|_{r=s} + \tilde{E}_b E^N + \int_r^s \left(\frac{2\varepsilon}{x^2}v_{\check{\theta}} - Re\frac{v^2}{x}\right)\mathrm{d}x + (s-r)\sin\theta \\ & - \frac{\varepsilon}{r}v_{\check{\theta}} + \frac{\varepsilon}{s}v_{\check{\theta}}\bigg|_{r=s} + O(\varepsilon^2), \end{aligned} \tag{2.3.10}$$

where x is a dummy variable. Substituting (2.3.10) into (2.3.4) yields the boundary-layer equation, namely,

$$\begin{aligned} &\varepsilon Re\left(v_{\check{t}} + \check{u}v_r + \frac{v}{r}v_{\check{\theta}} + \frac{\check{u}v}{r}\right) = \frac{1}{r}\frac{\partial}{\partial r}\left(rv_r\right) - \frac{v}{r^2} + \frac{2\varepsilon^2}{r^2}\left(v_{\check{\theta}\check{\theta}} + \check{u}_{\check{\theta}}\right) - \frac{\varepsilon}{r}\Bigg[\frac{\kappa}{Ca} \\ &+ 2\varepsilon\check{u}_r|_{r=s} + s\sin\theta + \frac{\varepsilon}{s}v_{\check{\theta}}\bigg|_{r=s} + \int_r^s \left(\frac{2\varepsilon}{x^2}v_{\check{\theta}} - Re\frac{v^2}{x}\right)\mathrm{d}x\Bigg]_{\check{\theta}} - \frac{\varepsilon}{r}\tilde{E}_b E_{\check{\theta}}^N + O(\varepsilon^3), \end{aligned} \tag{2.3.11}$$

which is complemented by the no-slip and impermeability conditions (2.1.25), the kinematic condition (2.1.34), and the tangential stress condition at the interface (2.3.6).

We are now in a position to solve equations (2.1.25), (2.3.11), and (2.3.6) using the method of weighted residuals. Ahead of this, we first consider the electrostatic part of the problem in Section 2.3.2 in order to determine appropriate candidate models for the electric potential ϕ required to calculate the normal Maxwell stress E^N (2.3.9) for use in the boundary-layer equation (2.3.11). With candidate models derived, we solve the hydrodynamic part of the problem in Section 2.3.3.

2.3.2 Electrostatic modelling

In this section, we derive models governing the electrostatic part of the problem. Under the substitutions (2.3.1) and (2.3.2), Laplace's equation (2.1.3) becomes

$$\phi_{rr} + \frac{1}{r}\phi_r + \frac{\varepsilon^2}{r^2}\phi_{\tilde{\theta}\tilde{\theta}} = 0, \tag{2.3.12}$$

which is subject to the boundary conditions (2.1.36), which remain unchanged. To $O(\varepsilon)$, equation (2.3.12) becomes

$$\phi_{rr} + \frac{1}{r}\phi_r = 0, \tag{2.3.13}$$

which, when solved subject to (2.1.36), yields the leading-order solution for the electric potential ϕ, namely,

$$\phi = \underbrace{\phi_d - \phi_d \frac{\ln(r/d)}{\ln(s/d)}}_{\text{(a)}} = \underbrace{\phi_d \frac{\ln(r/s)}{\ln(d/s)}}_{\text{(b)}}, \tag{2.3.14}$$

which, notably, can be written in terms of either (a) $\ln(r/d)$ or (b) $\ln(r/s)$. To leading order, the normal Maxwell stress (2.3.9) is

$$E^N = -\frac{1}{2}(\phi_r|_{r=s})^2 + O(\varepsilon^2), \tag{2.3.15}$$

which, upon substitution of (2.3.14) into (2.3.15), becomes

$$E^N = -\frac{\phi_d^2}{2s^2 \ln^2(d/s)} + O(\varepsilon^2). \tag{2.3.16}$$

Note that the natural approach to solve the problem defined by (2.3.13) subject to (2.1.36) would be to perform a gradient expansion in powers of ε and solve order-by-order. However, various authors have shown that when disturbances vary towards the short-wave regime (as is often the case in applications involving electrostatic control, for example, which shall be discussed later in Section 5.1), WRIBL-type expansions yield significant improvements in accuracy when compared to classical gradient expansions [29, 56, 244]. Therefore, here we choose to adopt a WRIBL-type approach and proceed by seeking a solution for ϕ in the form of a series expansion based on a separation of variables (see Section 1.2.5).

In Sections 2.3.2.1–2.3.2.3, we derive three candidate models for the electric potential ϕ which are accurate to $O(\varepsilon^2)$. Two of the models will be obtained by projecting the solution for ϕ onto appropriate sets of basis functions. The first of these will be derived in Section 2.3.2.1, in which we derive what we shall refer to hereafter as the "electrode model" (since this model will satisfy the continuity of potential at the outer electrode (2.1.36) exactly). The second of these will be derived in Section 2.3.2.2, in which we derive what we shall refer to hereafter as the "interface model" (since this model will satisfy the continuity of potential at the interface (2.1.36) exactly). Finally, in Section 2.3.2.3, we perform a gradient expansion on both the electrode and interface models to yield a single simplified model which we shall refer to hereafter as the "thick-film gradient model".

2.3.2.1 Electrode model

In this section, we derive a model motivated by the leading-order solution (2.3.14) (a). In particular, this suggests projecting onto basis functions of the form $(r-d)^m \ln(r/d)^n$ so that the continuity of potential at the outer electrode (2.1.36) can be satisfied exactly. Specifically, this suggests using the form

$$\phi = f_0 + f_1 \ln\left(\frac{r}{d}\right) + \varepsilon^2 \underbrace{\sum_m^N \sum_n^N f_{m,n}(\theta)(r-d)^m \ln\left(\frac{r}{d}\right)^n}_{\Psi_{\text{outer}}} + O(\varepsilon^4), \tag{2.3.17}$$

where $f_{m,n}$ (for $n = 0, \ldots, N$ and $m = 0, \ldots, M$) are functions to be determined. Note that, due to the fact that the electrostatic governing equation (2.3.12) and the boundary conditions (2.1.36) contain only even powers of ε, coefficients of odd powers of ε in the expansion (2.3.21) would turn out to be zero, and are thus omitted. It is anticipated that all but finitely many of the $f_{m,n}$ will turn out to be zero. Whilst it is not, in general, necessary to determine a minimal set of basis polynomials *a priori*, here we do so in order to reduce the subsequent algebra. To that end, substitution of (2.3.17) into Laplace's equation (2.3.12) yields

$$\frac{1}{r}\left(r\frac{\partial \Psi_{\text{outer}}}{\partial r}\right)_r + \left[\frac{f_0}{r^2} + \frac{f_1}{r^2}\ln\left(\frac{r}{d}\right)\right]_{\check{\theta}\check{\theta}} = 0 \tag{2.3.18}$$

at $O(\varepsilon^2)$. Hence, we must consider what function Ψ_{outer} is required to balance the terms in equation (2.3.18). Therefore, we set

$$\frac{1}{r}\left(r\frac{\partial\Psi_{\text{outer}}}{\partial r}\right)_r = \frac{f_m}{r^2} + \frac{f_n}{r^2}\ln\left(\frac{r}{d}\right), \tag{2.3.19}$$

and solve for Ψ_{outer} to yield

$$\Psi_{\text{outer}} = \frac{1}{2}\left[f_m \ln^2\left(\frac{r}{d}\right) + \frac{f_n}{3}\ln^3\left(\frac{r}{d}\right)\right]. \tag{2.3.20}$$

Therefore, by (2.3.20), the form of the non-zero $O(\varepsilon^2)$ terms in the projection (2.3.17) is a polynomial in $\ln^2(r/d)$ and $\ln^3(r/d)$. Thus, we posit the projection

$$\phi = f_0 + f_1\ln\left(\frac{r}{d}\right) + \varepsilon^2\left[f_2\ln^2\left(\frac{r}{d}\right) + f_3\ln^3\left(\frac{r}{d}\right)\right] + O(\varepsilon^4). \tag{2.3.21}$$

As mentioned previously, choosing to project onto a polynomial in powers of $\ln(r/d)$ means that the boundary condition at the outer electrode (2.1.36) is satisfied exactly. Specifically, imposing continuity of potential at the outer electrode on the projection form of ϕ (2.3.21) yields

$$f_0 = \phi_d(\theta, \check{t}). \tag{2.3.22}$$

Evaluating the relevant partial derivatives of (2.3.21) yields

$$\phi_r = \frac{1}{r}f_1 + \varepsilon^2\left[\frac{2}{r}\ln\left(\frac{r}{d}\right)f_2 + \frac{3}{r}\ln^2\left(\frac{r}{d}\right)f_3\right] + O(\varepsilon^4), \tag{2.3.23}$$

$$\phi_{rr} = -\frac{1}{r^2}f_1 + \varepsilon^2\left\{\frac{2}{r^2}\left[1-\ln\left(\frac{r}{d}\right)\right]f_2 + \frac{3}{r^2}\left[2\ln\left(\frac{r}{d}\right) - \ln^2\left(\frac{r}{d}\right)\right]f_3\right\} + O(\varepsilon^4), \tag{2.3.24}$$

$$\phi_{\check{\theta}\check{\theta}} = f_{0\check{\theta}\check{\theta}} + f_{1\check{\theta}\check{\theta}}\ln\left(\frac{r}{d}\right) + \varepsilon^2\left[f_{2\check{\theta}\check{\theta}}\ln^2\left(\frac{r}{d}\right) + f_{3\check{\theta}\check{\theta}}\ln^3\left(\frac{r}{d}\right)\right] + O(\varepsilon^4). \tag{2.3.25}$$

Substituting (2.3.23)–(2.3.25) into Laplace's equation (2.3.12) gives

$$2f_2 + f_{0\check{\theta}\check{\theta}} + 6\ln\left(\frac{r}{d}\right)f_3 + \ln\left(\frac{r}{d}\right)f_{1\check{\theta}\check{\theta}} + O(\varepsilon^4) = 0. \tag{2.3.26}$$

Equating powers of $\ln(r/d)$ in (2.3.26) yields

$$f_2 = -\frac{1}{2}f_{0\check{\theta}\check{\theta}}, \qquad f_3 = -\frac{1}{6}f_{1\check{\theta}\check{\theta}}, \tag{2.3.27}$$

and hence, by (2.3.22), f_2 is

$$f_2 = -\frac{1}{2}\phi_{d\check{\theta}\check{\theta}}. \tag{2.3.28}$$

Substituting f_2 and f_3 into (2.3.21) gives

$$\phi = \phi_d(\theta, \check{t}) + f_1 \ln\left(\frac{r}{d}\right) + \varepsilon^2\left[-\frac{1}{2}\phi_{d\check{\theta}\check{\theta}} \ln^2\left(\frac{r}{d}\right) - \frac{1}{6} f_{1\check{\theta}\check{\theta}} \ln^3\left(\frac{r}{d}\right)\right] + O(\varepsilon^4), \tag{2.3.29}$$

where the unknown function f_1 can be determined by imposing the continuity of potential at the interface (2.1.36) on (2.3.29), giving

$$\phi_d(\theta, \check{t}) + f_1 \ln\left(\frac{s}{d}\right) + \varepsilon^2\left[-\frac{1}{2}\phi_{d\check{\theta}\check{\theta}} \ln^2\left(\frac{s}{d}\right) - \frac{1}{6} f_{1\check{\theta}\check{\theta}} \ln^3\left(\frac{s}{d}\right)\right] + O(\varepsilon^4) = 0. \tag{2.3.30}$$

Together (2.3.29) and (2.3.30) constitute the electrode model. In Chapter 5, we compare the performance of the electrode model against numerical solutions of Laplace's equation (2.1.3) and the two other candidate models, namely, the interface model and the thick-film gradient model, which we derive next in Sections 2.3.2.2 and 2.3.2.3, respectively.

2.3.2.2 Interface model

In this section, we derive a model motivated by the leading-order solution (2.3.14) (b). In particular, this suggests projecting onto basis functions of the form $(r-s)^m \ln(r/s)^n$ so that the continuity of potential at the interface (2.1.36) can be satisfied exactly. Specifically, this suggests using the form

$$\phi = g_0 + g_1 \ln\left(\frac{r}{d}\right) + \varepsilon^2 \sum_{m}^{N} \sum_{n}^{N} g_{m,n}(\theta)(r-s)^m \ln\left(\frac{r}{s}\right)^n + O(\varepsilon^4), \tag{2.3.31}$$

where $g_{m,n}$ (for $n = 0, \ldots, N$ and $m = 0, \ldots, M$) are functions to be determined. An analogous argument to that described earlier in Section 2.3.2.1 can be given to yield the appropriate projection as being

$$\phi = g_0 + g_1 \ln\left(\frac{r}{s}\right) + \varepsilon^2\left[g_2 \ln^2\left(\frac{r}{s}\right) + g_3 \ln^3\left(\frac{r}{s}\right)\right] + O(\varepsilon^4). \tag{2.3.32}$$

Choosing to project onto a polynomial in powers of $\ln(r/s)$ means that the boundary condition at the interface (2.1.36) is satisfied exactly. Specifically, imposing

continuity of potential at the interface on the projection form of ϕ (2.3.32) yields

$$g_0 = 0. \tag{2.3.33}$$

Evaluating the relevant partial derivatives of (2.3.32) yields

$$\phi_r = \frac{1}{r}g_1 + \varepsilon^2\left[\frac{2}{r}\ln\left(\frac{r}{s}\right)g_2 + \frac{3}{r}\ln^2\left(\frac{r}{s}\right)g_3\right] + O(\varepsilon^4), \tag{2.3.34}$$

$$\phi_{rr} = -\frac{1}{r^2}g_1 + \varepsilon^2\left\{\frac{2}{r^2}\left[1-\ln\left(\frac{r}{s}\right)\right]g_2 + \frac{3}{r^2}\left[2\ln\left(\frac{r}{s}\right) - \ln^2\left(\frac{r}{s}\right)\right]g_3\right\} + O(\varepsilon^4), \tag{2.3.35}$$

$$\phi_{\check{\theta}\check{\theta}} = g_{0\check{\theta}\check{\theta}} + g_{1\check{\theta}\check{\theta}}\ln\left(\frac{r}{s}\right) - 2g_{1\check{\theta}}\frac{s_{\check{\theta}}}{s} - g_1\left(\frac{s_{\check{\theta}}}{s}\right)_{\check{\theta}} + O(\varepsilon^2). \tag{2.3.36}$$

Substituting (2.3.34)–(2.3.36) into Laplace's equation (2.3.12) gives

$$2g_2 + g_{0\check{\theta}\check{\theta}} - 2g_{1\check{\theta}}\frac{s_{\check{\theta}}}{s} - g_1\left(\frac{s_{\check{\theta}}}{s}\right)_{\check{\theta}} + 6\ln\left(\frac{r}{s}\right)g_3 + \ln\left(\frac{r}{s}\right)g_{1\check{\theta}\check{\theta}} + O(\varepsilon^4) = 0. \tag{2.3.37}$$

Equating powers of $\ln(r/s)$ in (2.3.37) yields

$$g_2 = g_{1\check{\theta}}\frac{s_{\check{\theta}}}{s} + \frac{1}{2}g_1\left(\frac{s_{\check{\theta}}}{s}\right)_{\check{\theta}} - \frac{1}{2}g_{0\check{\theta}\check{\theta}}, \qquad g_3 = -\frac{1}{6}g_{1\check{\theta}\check{\theta}}, \tag{2.3.38}$$

and hence, by (2.3.33), g_2 is

$$g_2 = g_{1\check{\theta}}\frac{s_{\check{\theta}}}{s} + \frac{1}{2}g_1\left(\frac{s_{\check{\theta}}}{s}\right)_{\check{\theta}}. \tag{2.3.39}$$

Substituting g_2 and g_3 into (2.3.32) gives

$$\phi = g_1\left(1+\varepsilon^2\frac{s_{\check{\theta}}^2}{s^2}\right)\ln\left(\frac{r}{s}\right) - \frac{\varepsilon^2}{6}\left[g_1\ln^3\left(\frac{r}{s}\right)\right]_{\check{\theta}\check{\theta}} + O(\varepsilon^4), \tag{2.3.40}$$

where the unknown function g_1 can be determined by imposing continuity of potential at the outer electrode (2.1.36), giving

$$g_1\left(1+\varepsilon^2\frac{s_{\check{\theta}}^2}{s^2}\right)\ln\left(\frac{d}{s}\right) - \frac{\varepsilon^2}{6}\left[g_1\ln^3\left(\frac{d}{s}\right)\right]_{\check{\theta}\check{\theta}} + O(\varepsilon^4) = \phi_d(\theta,\check{t}). \tag{2.3.41}$$

The system (2.3.40) and (2.3.41) can be simplified by using the substitution

$$g = g_1 \left(1 + \varepsilon^2 \frac{s_{\check{\theta}}^2}{s^2}\right), \tag{2.3.42}$$

yielding

$$\phi = g \ln\left(\frac{r}{s}\right) - \frac{\varepsilon^2}{6}\left[g \ln^3\left(\frac{r}{s}\right)\right]_{\check{\theta}\check{\theta}} + O(\varepsilon^4), \tag{2.3.43}$$

$$g \ln\left(\frac{d}{s}\right) - \frac{\varepsilon^2}{6}\left[g \ln^3\left(\frac{d}{s}\right)\right]_{\check{\theta}\check{\theta}} = \phi_d(\theta, \check{t}) + O(\varepsilon^4). \tag{2.3.44}$$

Together (2.3.43) and (2.3.44) constitute the interface model.

2.3.2.3 Thick-film gradient model

In this section, we perform a classical gradient expansion on both the electrode model (given by (2.3.29) and (2.3.30)) and the interface model (given by (2.3.43) and (2.3.44)). This procedure helps us simplify the models by eliminating f_1 and g from the electrode and interface models, respectively, yielding explicit expressions for ϕ in terms of ϕ_d. In particular, we show that the two models actually coincide. We proceed by expanding f_1 and g as

$$f_1 = F_0 + \varepsilon^2 F_2 + O(\varepsilon^4), \quad g = G_0 + \varepsilon^2 G_2 + O(\varepsilon^4). \tag{2.3.45}$$

Note that, for the same reason as explained at the beginning of Section 2.3.2.1, we have omitted terms of odd powers of ε from (2.3.45). Substituting (2.3.45) into (2.3.30) and (2.3.44) yields

$$F_0 = G_0 = -\frac{\phi_d}{\ln(s/d)} \tag{2.3.46}$$

at $O(1)$, and using (2.3.46) yields

$$F_2 = \frac{1}{6}\ln\left(\frac{s}{d}\right)\left[3\phi_{d\check{\theta}\check{\theta}} - \ln\left(\frac{s}{d}\right)\left(\frac{\phi_d}{\ln(s/d)}\right)_{\check{\theta}\check{\theta}}\right], \quad G_2 = \frac{1}{6\ln(d/s)}\left[\ln^2\left(\frac{d}{s}\right)\phi_d\right]_{\check{\theta}\check{\theta}} \tag{2.3.47}$$

at $O(\varepsilon^2)$. Substituting (2.3.45) with (2.3.46) and (2.3.47) into (2.3.29) and (2.3.43) produces the same model, namely,

$$\phi = \frac{\ln(r/s)}{\ln(d/s)}\phi_d + \frac{\varepsilon^2}{6}\left[\frac{\ln(r/s)}{\ln(d/s)}\left(\ln^2\left(\frac{d}{s}\right)\phi_d\right)_{\check{\theta}\check{\theta}} - \left(\frac{\ln^3(r/s)}{\ln(d/s)}\phi_d\right)_{\check{\theta}\check{\theta}}\right] + O(\varepsilon^4), \tag{2.3.48}$$

which constitutes the thick-film gradient model. Analogous thin-film electrostatic models can be derived as limits of the thick-film electrostatic models derived in this section. Specifically, the thin-film gradient model, accompanied by thin-film electrode and interface models, are given in Appendix B.

Note that two additional candidate thick-film electrostatic models can be derived by instead using a weighted residual approach. These models are given in Appendix C, the derivation of which follows a method which is analogous to that used next in Section 2.3.3 to model the hydrodynamic part of the problem.

2.3.3 Hydrodynamic modelling

In this section, we model the hydrodynamic part of the problem. In particular, we use the boundary-layer equation (2.3.11) to develop a reduced-order model using the method of weighted residuals [29, 31, 55, 56]. We begin by deriving the leading-order solution for the azimuthal velocity v, which is determined by expanding v in powers of ε and solving order-by-order. At leading order, the dynamics of the flow are driven purely by the rotation induced by the substrate, rather than by gravity, pressure gradients, or electrostatic effects, all of which enter the solution at first order. In particular, by (2.3.6) and (2.3.11), the leading-order problem for the velocity v is

$$\frac{1}{r}\left(\frac{1}{r}\frac{\partial}{\partial r}(rv)\right) = 0, \quad v|_{r=1} = \omega, \quad (v - sv_r)|_{r=s} = 0, \tag{2.3.49}$$

which has the solution

$$v = \omega r, \tag{2.3.50}$$

corresponding to solid body rotation.

To obtain the solution for v to higher orders, we proceed by projecting v onto an appropriate set of basis functions $f_n = f_n(r)$ (for $n = 0, \ldots, N$) which have coefficients $a_n = a_n(\theta, \check{t})$ (for $n = 0, \ldots, N$) which account for the deviation of the velocity profile from solid body rotation for $n = 1, \ldots, N$ [31]. In other words, we

consider an expansion of the form

$$v(r,\theta,\check{t}) = a_0(\theta,\check{t})f_0(r) + \varepsilon\sum_{n=1}^{N} a_n(\theta,\check{t})f_n(r) + O(\varepsilon^2), \tag{2.3.51}$$

where the leading-order solution (2.3.50) requires choosing $f_0 = r$. In principle, the a_n can be determined by substituting the expansion (2.3.51) into the boundary-layer equation (2.3.11) and considering the terms at $O(\varepsilon)$ (indeed, this procedure is pursued by, for example, Ruyer–Quil and Manneville [29] and Oron and Heining [53]). However, this is, in general, an onerous process. As discussed in Section 1.2.5, Ruyer–Quil and Manneville [29] demonstrated that this procedure may be simplified significantly by the use of a weighted integral method in which we proceed by taking the inner product, defined by

$$\langle y_1, y_2\rangle = \int_1^s r y_1 y_2 \,\mathrm{d}r \tag{2.3.52}$$

[31, 56] for some functions $y_1 = y_1(r)$ and $y_2 = y_2(r)$, of the boundary-layer equation (2.3.11) (with v substituted by (2.3.51)) with a suitable weight function $w = w(r,\theta,\check{t})$, where w is the solution to the adjoint of the leading-order problem (2.3.49) (see Section 1.2.5.1). In what follows, we show that this particular choice of the weight w minimises the amount of algebra that is required to formulate the final model by removing the need to explicitly calculate the coefficients a_n and basis functions f_n, such that only the determination of a single equation for a_0 is required. As discussed earlier, in practice, it is more convenient to eliminate a_0 (which has no physical significance) in favour of the flux q (2.1.35) as this is a quantity which can be measured physically and, in addition, simplifies the resulting equation.

Integrating the expansion for v (2.3.51) across the film thickness and truncating at $O(\varepsilon)$ yields

$$q = a_0\int_1^s r \,\mathrm{d}r + \varepsilon\sum_{n=1}^{N} a_n\int_1^s f_n \,\mathrm{d}r, \tag{2.3.53}$$

where q is defined by (2.1.35). Equation (2.3.53) can be solved to find the leading-order coefficient a_0 in terms of q as

$$a_0 = \frac{q - \varepsilon\sum_{n=1}^{N} a_n\int_1^s f_n \,\mathrm{d}r}{\int_1^s r \,\mathrm{d}r}. \tag{2.3.54}$$

Substituting (2.3.54) into (2.3.51) yields

$$\begin{aligned} v &= \frac{q - \varepsilon \sum_{n=1}^{N} a_n(\theta, \check{t}) \int_1^s f_n(r)\ \mathrm{d}r}{\int_1^s r\ \mathrm{d}r} r + \varepsilon \sum_{n=1}^{N} a_n(\theta, \check{t}) f_n(r) \\ &= \frac{qr}{\int_1^s r\ \mathrm{d}r} + O(\varepsilon) \\ &= \frac{2q}{s^2 - 1} r + O(\varepsilon). \end{aligned} \tag{2.3.55}$$

In what follows, we write $\check{u}$ in terms of v using the continuity equation (2.1.20). Specifically, integrating (2.1.20) with respect to the radial coordinate from 1 to r yields

$$\check{u} = \left(\frac{q}{s^2 - 1} \right)_{\check{\theta}} \left(\frac{1 - r^2}{r} \right) + O(\varepsilon). \tag{2.3.56}$$

Taking the inner product of the boundary-layer equation (2.3.11) with the weight w yields

$$\begin{aligned} &\varepsilon Re \int_1^s \left(v_{\check{t}} + \check{u} v_r + \frac{v}{r} v_{\check{\theta}} + \frac{\check{u} v}{r} \right) wr\ \mathrm{d}r \\ &= \int_1^s \left(\frac{1}{r} (rv)_r \right)_r wr\ \mathrm{d}r + 2\varepsilon^2 \int_1^s \left(\frac{1}{r^2} v_{\check{\theta}\check{\theta}} + \frac{1}{r^2} \check{u}_{\check{\theta}} \right) wr\ \mathrm{d}r - \varepsilon \int_1^s \left[\frac{\kappa}{Ca} + 2\varepsilon \check{u}_r \Big|_{r=s} \right. \\ &\left. + s \sin\theta + \frac{\varepsilon}{s} v_{\check{\theta}} \Big|_{r=s} + \int_r^s \left(\frac{2\varepsilon}{x^2} v_{\check{\theta}} - Re \frac{v^2}{x} \right) dx \right]_{\check{\theta}} w\ \mathrm{d}r - \varepsilon \int_1^h \tilde{E}_b E_{\check{\theta}}^N w\ \mathrm{d}r + O(\varepsilon^3), \end{aligned} \tag{2.3.57}$$

where v is given by (2.3.55) and $\check{u}$ is given by (2.3.56). Terms involving the a_n for $n = 1, \ldots, N$ can only enter (2.3.57) at $O(\varepsilon)$ via the leading-order viscous term (i.e., the first term on the right-hand side of (2.3.57)). Hence, if this viscous term can be computed explicitly without the a_n then they will not appear anywhere in the problem, and hence the need to determine the a_n and f_n will have been completely avoided. In order to find a suitable weight function w for this purpose, we proceed by following the calculation described by Wray *et al.* [56]. In particular, we evaluate the inner product of the leading-order viscous term with the weight w

to yield

$$\int_1^s \left(\frac{1}{r}\left(rv\right)_r\right)_r wr \ \mathrm{d}r = \left[w\left(rv\right)_r - v\left(rw\right)_r\right]|_{r=s} + \left[v\left(rw\right)_r - w\left(rv\right)_r\right]|_{r=1} + \int_1^s \left(\frac{1}{r}\left(rw\right)_r\right)_r vr \ \mathrm{d}r, \tag{2.3.58}$$

where we have used two applications of integration by parts. Note that the first term on the right-hand side of (2.3.58) can be written as

$$\left[w\left(rv\right)_r - v\left(rw\right)_r\right]|_{r=s} = \left[w\left(rv_r - v\right)\right]|_{r=s} - \left[v\left(rw_r - w\right)\right]|_{r=s}. \tag{2.3.59}$$

By the second-order tangential stress condition (2.3.6), the first term on the right-hand side of (2.3.59) is zero to leading order. Hence, to leading order, (2.3.58) with (2.3.59) yields

$$\int_1^s \left(\frac{1}{r}\left(rv\right)_r\right)_r wr \ \mathrm{d}r = -\omega\left[\left(rw_r - w\right)\right]|_{r=s} + \omega\left[\left(rw\right)_r\right]|_{r=1} - \left[w\left(rv\right)_r\right]|_{r=1} + \int_1^s \left(\frac{1}{r}\left(rw\right)_r\right)_r vr \ \mathrm{d}r, \tag{2.3.60}$$

where we have used the no-slip condition (2.3.49). To remove the dependence of the right-hand side of (2.3.60) on the a_n, we choose w such that

$$\left(\frac{1}{r}\left(rw\right)_r\right)_r r = 1, \tag{2.3.61}$$

$$w|_{r=1} = 0, \tag{2.3.62}$$

$$\left[rw_r - w\right]|_{r=s} = 0, \tag{2.3.63}$$

where the first condition (2.3.61) is chosen such that the final term on the right-hand side of (2.3.60) reduces to exactly q, the second condition (2.3.62) is chosen such that the third term on the right-hand side of (2.3.60) is zero, and the third condition (2.3.63) is chosen such that the first term on the right-hand side of (2.3.60) is zero. Note that, as discussed previously, (2.3.61)–(2.3.63) is the adjoint of the leading-order problem (2.3.49). Solving (2.3.61) subject to (2.3.62) and (2.3.63) yields the weight function

$$w = \frac{r}{2}\ln r + \frac{s^2}{4r}(1 - r^2), \tag{2.3.64}$$

which is specific to the cylindrical geometry and hence is identical to equation (3.16) of Wray *et al.* [56] and equation (3.9) of Wray and Cimpeanu [31] up to differences in scalings.

Finally, evaluating (2.3.57) with the particular choice of weight function (2.3.64) yields the thick-film WRIBL governing equation (which we shall refer to hereafter as simply the "WRIBL equation"). In particular, evaluation of the leading-order viscous term (2.3.58) with the weight function (2.3.64) yields

$$\begin{aligned}\int_1^s \left(\frac{1}{r}\left(rv\right)_r\right)_r wr\ \mathrm{d}r &= \left[w\left(rv_r - v\right)\right]|_{r=s} + \omega\left[\left(rw\right)_r\right]|_{r=1} + q \\ &= -\varepsilon^2\left[rw_r\left(\check{u}_{\check{\theta}} + 4s_{\check{\theta}}\check{u}_r\right)\right]|_{r=s} + \frac{\omega}{2}\left(1-s^2\right) + q, \end{aligned} \tag{2.3.65}$$

to second order, where we have used the second-order tangential stress condition (2.3.6) along with the final condition (2.3.63) to obtain the first term on the second line (which we do not give in its expanded form for brevity). Hence, the WRIBL equation is given by

$$\begin{aligned}&\frac{\varepsilon}{8}(1-s^4+4s^2\ln s)\left[\underbrace{\frac{\kappa}{Ca}}_{\text{(a)}}\underbrace{+s\sin\theta}_{\text{(b)}}\underbrace{+\tilde{E}_b E^N}_{\text{(c)}}\underbrace{-2Re\frac{q^2}{s^2-1}}_{\text{(d)}}\right]_{\check{\theta}} = q\underbrace{+\frac{\omega}{2}(1-s^2)}_{\text{(e)}} \\ &\underbrace{-\varepsilon^2\frac{(1-s^2)^2(1+s^2)s_{\check{\theta}}}{2s^3}\left(\frac{q}{s^2-1}\right)_{\check{\theta}} + \varepsilon^2\frac{(1-s^2)(1+s^4+2s^2(\ln^2 s-1))}{4s^2}\left(\frac{q}{s^2-1}\right)_{\check{\theta}\check{\theta}}}_{\text{(f)}} \\ &\underbrace{+\varepsilon\frac{Re}{16}(-1+2s^2+2s^6-s^4(3+4\ln s))\left[\left(\frac{q}{s^2-1}\right)_{\check{t}} + \left(\frac{q^2}{(s^2-1)^2}\right)_{\check{\theta}}\right]}_{\text{(g)}}, \end{aligned} \tag{2.3.66}$$

where E^N is defined by (2.3.15). The terms in (2.3.66) represent (a) capillarity, (b) gravity, (c) Maxwell stress, (d) centrifugation, (e) rotation, (f) streamwise viscous dissipation, and (g) inertia. Equation (2.3.66) is coupled with the kinematic condition (2.1.34) and a suitable model for the electric potential ϕ to yield what we shall refer to hereafter as the "WRIBL model". Here, we choose to use one of the three candidate models for ϕ that we derived in Section 2.3.2, namely, the electrode model (2.3.29) and (2.3.30), the interface model (2.3.43) and (2.3.44), or the thick-film gradient model (2.3.48). The WRIBL model is governed by six dimensionless groups, namely, the initial film thickness h_0, the rotation rate ω, the

capillary number Ca, the Reynolds number Re, the electric potential difference $\tilde{E}_b$, and the radius of the outer electrode d, given respectively by

$$\begin{aligned} h_0 = \frac{\hat{h}_0}{\hat{R}_1}, \quad \omega = \frac{\hat{\Omega}\hat{R}_1}{\hat{U}_{\text{char}}} = \frac{\hat{\Omega}\hat{\mu}}{\hat{\rho}\hat{g}\hat{R}_1}, \quad Ca = \frac{\hat{\mu}\hat{U}_{\text{char}}}{\hat{\sigma}} = \frac{\hat{\rho}\hat{g}\hat{R}_1^2}{\hat{\sigma}}, \\ Re = \frac{\hat{\rho}\hat{U}_{\text{char}}\hat{R}_1}{\hat{\mu}} = \frac{\hat{\rho}^2\hat{g}\hat{R}_1^3}{\hat{\mu}^2}, \quad \tilde{E}_b = \frac{\hat{\epsilon}_{\text{G}}\hat{\phi}_{\text{char}}^2}{\hat{\mu}\hat{U}_{\text{char}}\hat{R}_1} = \frac{\hat{\epsilon}_{\text{G}}\hat{\phi}_{\text{char}}^2}{\hat{\rho}\hat{g}\hat{R}_1^3}, \quad d = \frac{\hat{R}_2}{\hat{R}_1}, \end{aligned} \tag{2.3.67}$$

where $\hat{U}_{\text{char}}$ is the characteristic drainage velocity (2.1.19).

The WRIBL model constitutes a closed system governing the evolution of the interface s, the flux q, and the electric potential ϕ. As mentioned previously, we compare the three candidate electrostatic models numerically in Chapter 5 in order to determine which model yields the greatest accuracy when compared to the numerical solution of Laplace's equation (2.1.3), and hence to decide which is most suited for use in the WRIBL model in practice.

The electric field contributes a normal stress at the interface which structurally enters the WRIBL equation (2.3.66) in the same manner as capillarity, gravity, and centrifugation. Upon setting $\tilde{E}_b = 0$, in the absence of an electric field the WRIBL equation (2.3.66) recovers equation (1.4.28) of Wray and Cimpeanu [31] up to differences in scalings. Specifically, Wray and Cimpeanu [31] use the different characteristic velocity scaling $\hat{U}_{\text{char}} = (\hat{R}_1\hat{g})^{1/2}$ and the different pressure scale $\hat{\rho}\hat{U}_{\text{char}}^2$, which together result in the gravity term in their equation (1.4.28) having a Reynolds number Re as a coefficient, unlike the corresponding gravitational term (b) in (2.3.66) which does not.

As discussed previously, ε is an ordering parameter and hence is set equal to unity in the final model. However, here we have chosen to retain it when displaying the WRIBL model for clarity regarding the positions of the ε. Note that the WRIBL model is formally a simplified second-order model: the WRIBL equation (2.3.66) contains second-order viscous terms, but only first-order inertial terms. This is because, as discussed earlier in Section 1.2.5, the complexity of full second-order WRIBL models often restricts their amenability to both analytical and numerical analysis, hence here we discard the second-order inertial terms for simplicity [29, 37]. Formally, this places a restriction on the range of validity of the Reynolds number Re, as this implies that Re should be small. However, Wray *et al.* [31, 56] showed that in practice, in the absence of an electric field, the model

still gives excellent agreement with DNS even for Re of order unity.

The thin-film governing equation (2.2.23) can be recovered as a special case of the WRIBL model (2.1.34) and (2.3.66) (along with a suitable model for the electric potential ϕ). To demonstrate this, in Section 2.3.3.1, we perform a gradient expansion on (2.3.66) to yield what we shall refer to hereafter as the "thick-film gradient model". In Section 2.3.3.2, we apply the thin-film scalings (2.2.1) to the thick-film gradient model, which in turn recovers the thin-film model (2.2.23) to leading order.

2.3.3.1 Thick-film gradient model

In this section, we perform a gradient expansion on q in the WRIBL model (2.1.34) and (2.3.66) (along with a suitable model for the electric potential ϕ). In particular, we expand q in powers of ε as

$$q = q_0 + \varepsilon q_1 + O(\varepsilon^2), \tag{2.3.68}$$

where ε is the same ordering parameter defined at the beginning of Section 2.3. Substituting (2.3.68) into the WRIBL equation (2.3.66) yields

$$q_0 = \frac{\omega}{2}(s^2 - 1) \tag{2.3.69}$$

at $O(1)$, and using (2.3.69) yields

$$q_1 = \frac{1}{8}(1 - s^4 + 4s^2 \ln s)\left[\frac{\kappa}{Ca} + s\sin\theta + \tilde{E}_b E^N - Re\ \omega^2 \frac{(s^2-1)}{2}\right]_{\check{\theta}} \tag{2.3.70}$$

at $O(\varepsilon)$. Substituting (2.3.68) with (2.3.69) and (2.3.70) into the kinematic condition (2.1.34) yields the thick-film gradient model, namely,

$$\begin{aligned}(s^2)_{\check{t}} = \Bigg\{&\omega(1-s^2) + \frac{\varepsilon}{4}(1 - s^4 + 4s^2\ln s) \\ &\times \left[Re\ \omega^2 \frac{(s^2-1)}{2} - \tilde{E}_b E^N - \frac{\kappa}{Ca} - s\sin\theta\right]_{\check{\theta}}\Bigg\}_{\check{\theta}} + O(\varepsilon^2).\end{aligned} \tag{2.3.71}$$

2.3.3.2 Thin-film gradient model

In this section, we derive the thin-film limit of the thick-film gradient model (2.3.71) and subsequently show that the thin-film governing equation (2.2.23) can

be recovered as a special case of the WRIBL model. We proceed by undoing the long-wave scalings (2.3.1) and (2.3.2) in the thick-film gradient model (2.3.71) and applying the thin-film scalings (2.2.1) to (2.3.71) (where $\epsilon = h_0 \ll 1$ is the same small aspect ratio defined at the beginning of Section 2.2) to yield what we shall refer to hereafter as the "thin-film gradient model", namely,

$$\begin{aligned}\epsilon^2(1+\epsilon\tilde{H})\tilde{H}_{\tilde{T}} = -\Bigg\{\omega\left(\tilde{H}+\frac{1}{2}\epsilon\tilde{H}^2\right) - \frac{\epsilon^2}{3}\tilde{H}^3\left[\cos\theta + \tilde{E}_b\tilde{E}^N_\theta\right] \\ + \epsilon^3\left[\frac{1}{3Ca}\tilde{H}^3(\tilde{H}_\theta + \tilde{H}_{\theta\theta\theta}) + \frac{1}{3}\omega^2 Re\tilde{H}^3\tilde{H}_\theta - \frac{1}{3}\tilde{H}^3\tilde{H}_\theta\sin\theta \right. \\ \left. - \frac{1}{2}\tilde{H}^4\cos\theta - \frac{1}{6}\tilde{H}^4\tilde{E}_b\tilde{E}^N_\theta\right]\Bigg\}_\theta + O(\epsilon^4), \end{aligned} \tag{2.3.72}$$

where $\tilde{E}^N$ is the leading order thin-film normal Maxwell stress, which is found by undoing the long-wave scalings (2.3.1) and (2.3.2) in (2.3.9) and applying the thin-film scalings (2.2.1), yielding

$$\tilde{E}^N = -\frac{1}{2}\tilde{\Phi}^2_{\tilde{R}} + O(\epsilon), \tag{2.3.73}$$

where $\tilde{\Phi}$ is the leading-order solution (2.2.5) to the leading-order thin-film Laplace equation, which was derived in Section 2.2.

The thin-film governing equation (2.2.23) can be recovered from the thin-film gradient model (2.3.72) to leading-order under the the rescalings (2.2.11) and (2.2.15) on ω and Ca which are required in order to ensure that electrostatic effects, rotation, and capillarity appear at the same order. Specifically, to second order, the thin-film gradient model (2.3.72) is

$$\epsilon^2\tilde{H}_{\tilde{T}} = -\left\{\epsilon^2\bar{\omega}\tilde{H} - \frac{\epsilon^2}{3}\tilde{H}^3\left[\cos\theta + \tilde{E}_b\tilde{E}^N_\theta\right] + \frac{\epsilon^2}{3\tilde{\gamma}}\tilde{H}^3(\tilde{H}_\theta + \tilde{H}_{\theta\theta\theta})\right\}_\theta, \tag{2.3.74}$$

which may be written as

$$\tilde{H}_{\tilde{T}} + \left[\bar{\omega}\tilde{H} + \frac{\tilde{H}^3}{3}\left(-\cos\theta + \frac{1}{\tilde{\gamma}}\left(\tilde{H}_\theta + \tilde{H}_{\theta\theta\theta}\right) + \tilde{E}_b\frac{\tilde{H}_\theta}{(\tilde{D}-\tilde{H})^3}\right)\right]_\theta = 0. \tag{2.3.75}$$

Equation (2.3.75) is identical to equation (2.2.23), showing that the thin-film governing equation can be derived as a special case of the WRIBL model.

2.4 Concluding remarks

In this chapter, we have introduced and modelled the system that we will investigate, namely, the flow of a perfectly conducting liquid coating a horizontal circular cylinder in the presence of an electric field.

In Section 2.1, we formulated the system (shown in Figure 2.1), describing the relevant governing equations and boundary conditions. In Section 2.2, we derived a model valid for thin films, namely, equation (2.2.20), using the classical lubrication approximation. In Section 2.3, we derived a model valid for thick films (referred to as the "WRIBL model") by applying the long-wave methodology [31, 56] in conjunction with the WRIBL method [29].

The electrostatic part of the thick-film problem was solved in Section 2.3.2, in which we derived three candidate models for the electric potential ϕ, namely, the electrode model (2.3.29) and (2.3.30), the interface model (2.3.43) and (2.3.44), and the thick-film gradient model (2.3.48). The electrode and interface models were obtained by projecting the solution for ϕ onto a polynomial in powers of $\ln(r/d)$ and $\ln(r/s)$, respectively, and the thick-film gradient model was obtained by performing a gradient expansion on these (with both resulting in the same model). The electrostatic models will be compared numerically in Chapter 5.

Subsequently, we solved the hydrodynamic part of the thick-film problem in Section 2.3.3, in which we derived the thick-film WRIBL model which incorporates the effects of capillarity, gravity, Maxwell stress, centrifugation, rotation, viscosity, and inertia. In particular, we derived the WRIBL equation (2.3.66) which is coupled with the kinematic condition (2.1.33) and a suitable model for the electric potential ϕ. We also derived two special cases of the WRIBL model, namely, the thick-film gradient model (2.3.71) and the thin-film gradient model (2.3.72), and showed that the thin-film model (2.2.20) can be recovered as a special case of the WRIBL model.

The thin-film model (2.2.20) will be investigated in Chapters 3 and 4, and the WRIBL model will be investigated in Chapters 5 and 6, with particular focus on its applications in electrostatic control.

Chapter 3

Thin-film draining flow in the absence of an electric field

Before investigating the influence that electrostatic effects have on the thin-film system that was described in Section 2.2, we must first undertake a comprehensive analysis of the case in the absence of an electric field.

The case in which the cylinder is rotating (i.e., coating flow) has been afforded considerable attention in the literature, and thus the reader is referred to the discussions in Section 1.4.4 for the full details of this problem.

As discussed in Section 1.4.3, the case in which the cylinder is stationary has been studied previously by many authors including Nusselt [34, 35], Reisfeld and Bankoff [101], Evans *et al.* [102], Takagi and Huppert [103], and Cachile *et al.* [104]. However, none of these studies attempted to obtain a complete description of the late-time behaviour of the film: each focused only on a specific feature (such as the draining near the top of the substrate, or the pendant drop formed near the bottom), and did not attempt to resolve how the different regions connected to one another. It is therefore for this reason that in this chapter we revisit the case in which the cylinder is stationary in the absence of an electric field as an essential precursor to the problem in the presence of an electric field.

In this chapter, we investigate the stationary case using an analogous method to that of Qin *et al.* [105] who, as discussed in Section 1.4.5, recently attempted to derive a complete description of the late-time behaviour of the flow of a thin film on the outer surface of a stationary sphere. We defer further discussion of this key paper until Section 3.3.

In Section 3.1, we formulate a special case of the thin-film governing equation (2.2.20) that was derived in Section 2.2 in the case of a stationary cylinder in the absence of an electric field. In Section 3.2, we obtain the asymptotic solution for the film thickness at early times, and in Sections 3.3–3.6, we obtain the leading-order asymptotic solution for the film thickness at late times. In Section 3.7, we draw our conclusions. We consider the case of a stationary cylinder in the presence of an electric field in Chapter 4.

3.1 Problem formulation

To consider the case in which the inner cylinder is stationary in the absence of an electric field, we begin by setting $\bar{\omega} = \tilde{E}_b = 0$ in the unrescaled governing equation (2.2.20) and the unrescaled flux (2.2.21), yielding

$$\tilde{H}_{\tilde{T}} + \left[-\frac{1}{3}\tilde{H}^3\cos\theta + \frac{1}{3\tilde{\gamma}}\tilde{H}^3\left(\tilde{H} + \tilde{H}_{\theta\theta}\right)_\theta\right]_\theta = 0, \tag{3.1.1}$$

$$\tilde{Q} = -\frac{1}{3}\tilde{H}^3\cos\theta + \frac{1}{3\tilde{\gamma}}\tilde{H}^3\left(\tilde{H} + \tilde{H}_{\theta\theta}\right)_\theta, \tag{3.1.2}$$

respectively, where

$$\tilde{\gamma} = \frac{\hat{\rho}\hat{g}\hat{R}_1^3}{\hat{h}_0\hat{\sigma}}, \tag{3.1.3}$$

by (2.2.11). The governing equation (3.1.1) is subject to the initial condition (2.2.2). In the absence of symmetry-breaking effects, throughout this chapter we assume that the flow has left-to-right symmetry and so we restrict our attention to the left-hand side of the cylinder and hence work in the domain $\pi/2 \leq \theta \leq 3\pi/2$. Note that whilst the governing equation (3.1.1) would normally be solved subject to periodic conditions, we instead exploit the symmetry of the system, which in particular, corresponds to imposing the symmetry conditions

$$\tilde{H}_\theta = \tilde{H}_{\theta\theta\theta} = 0 \quad \text{at} \quad \theta = \frac{\pi}{2} \quad \text{and} \quad \frac{3\pi}{2}. \tag{3.1.4}$$

Note that throughout this chapter we drop the tilde decoration in (2.2.2), (3.1.1), (3.1.2), and (3.1.4) hereafter for brevity. The geometry of the dimensionless system considered in this chapter is shown in Figure 3.1. Figure 3.1 also shows the three regions of qualitatively different behaviour that emerge at late times, which will

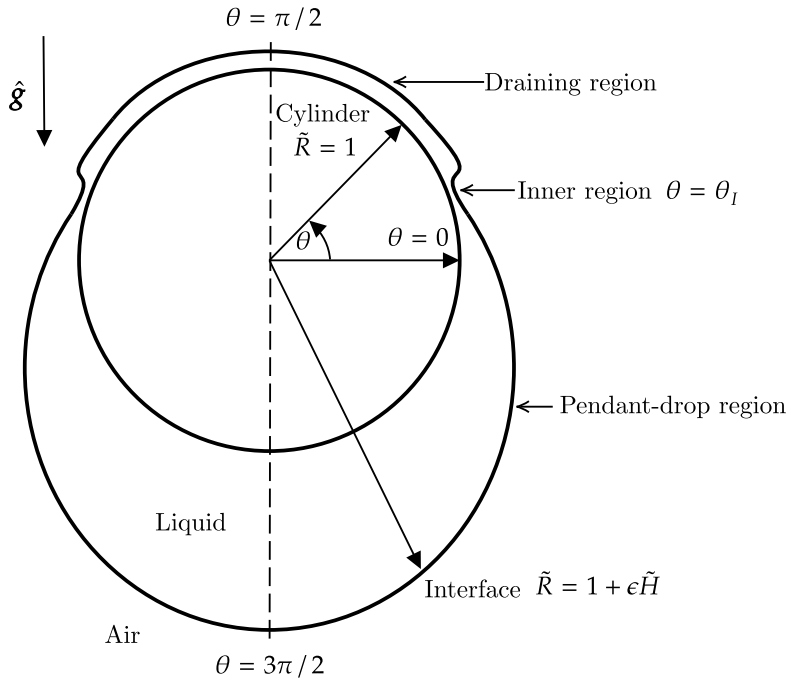

Figure 3.1: Geometry of the dimensionless system considered in Chapter 3.

be analysed in detail in Section 3.3.

Throughout this chapter, numerical solutions of (3.1.1) are obtained up to the longest final times of up to $T = O(10^{11})$ using the numerical scheme described in Appendix A.2.

3.2 Early-time draining

In this section, we describe the draining of the initially uniform film at early times. As in the corresponding problem of flow on a spherical substrate studied by Qin *et al.* [105], the asymptotic solution for the film thickness $H = H(\theta, T)$ at early times is found by expanding it in powers of $T \ll 1$ as

$$H = 1 + TH_1(\theta) + T^2 H_2(\theta) + O(T^3). \tag{3.2.1}$$

Substitution of (3.2.1) into the governing equation (3.1.1) and solving order-by-order yields

$$H = 1 - \frac{T}{3}\sin\theta - \frac{T^2}{6}\cos(2\theta) + O(T^3). \tag{3.2.2}$$

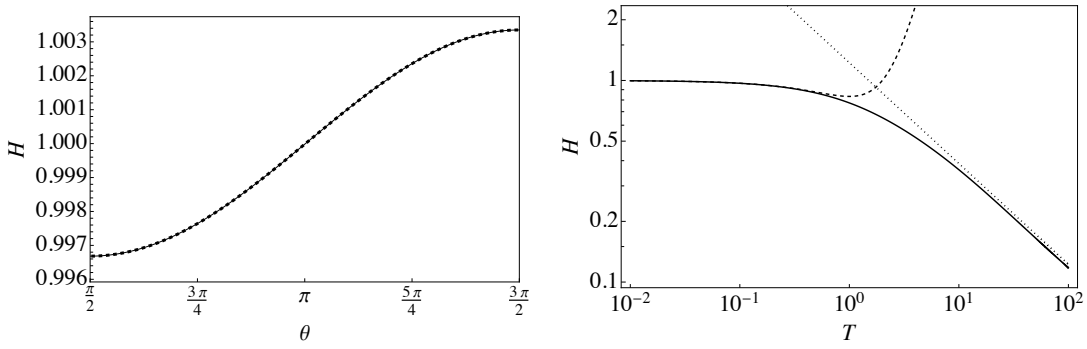

(a) (b)

Figure 3.2: (a) Film thickness for $\gamma = \gamma_\pi$ given by (3.2.3) at time $T = 10^{-2}$. The dashed line shows the early-time asymptotic solution (3.2.2) and the solid line shows the numerical solution of (3.1.1). Note that the two curves are almost indistinguishable from one another at this early time. (b) The evolution of the film thickness at the top of the cylinder for $\gamma = \gamma_\pi$ given by (3.2.3) until time $T = 10^2$. The solid line shows the numerical solution of (3.1.1), the dashed line shows the early-time asymptotic solution (3.2.2), and the dotted line shows the late-time asymptotic solution (3.4.8).

The absence of γ from (3.2.2) shows that, as expected given its small deviation from uniformity, at early times the evolution of the film is independent of capillarity up to, and including, at least $O(T^2) \ll 1$. Figure 3.2 (a) shows the film thickness at time $T = 10^{-2}$. Note that the value of γ has only a very weak effect on the numerical solution shown in Figure 3.2 (a). However, the value of γ will become important in the late-time dynamics discussed in Section 3.3, and so the particular value used here, namely,

$$\gamma = \gamma_\pi = \frac{8\pi}{\pi^2 - 8} \simeq 13.4428, \tag{3.2.3}$$

was chosen for consistency with that used subsequently. In particular, Figure 3.2 (a) shows that the asymptotic solution (3.2.2) is in excellent agreement with the numerical solution of the governing equation (3.1.1) at this early time. Figure 3.2 (b) shows the evolution of the film thickness at the top of the cylinder (i.e., at $\theta = \pi/2$) for $\gamma = \gamma_\pi$ given by (3.2.3) until time $T = 10^2$, and confirms that the early-time asymptotic solution (3.2.2) (shown with the dashed line) is valid at the top of the cylinder at early times. For completeness, Figure 3.2 (b) also

includes the corresponding late-time asymptotic solution (3.4.8) (shown as with the dotted line) which will be derived in Section 3.4, and confirms that it is valid at late times.

3.3 Late-time draining

As mentioned previously, and as sketched in Figure 3.1, three regions of qualitatively different behaviour emerge at late times. As in the corresponding problem of flow on a spherical substrate studied by Qin *et al.* [105], different balances of forces determine the dominant behaviour in each region, leading to different simplifications of the governing equation (3.1.1). Therefore, the overall evolution of the film at late times can be investigated by analysing each region separately and performing the appropriate asymptotic matching between them. On the upper part of the cylinder, gravity dominates capillarity, resulting in a draining flow which causes the film to thin, corresponding to the thin-film zone of Qin *et al.* [105] in the spherical case. We shall refer to this region hereafter as the "draining region" and it will be discussed in Section 3.4. On the other hand, on the lower part of the cylinder, gravity and capillarity balance, resulting in the formation of a quasi-static pendant drop, corresponding to the pendant-drop zone of Qin *et al.* [105] in the spherical case. We shall refer to this region hereafter as the "pendant-drop region" and it will be discussed in Section 3.5.

The draining and pendant-drop regions do not match directly with each other, but do so via a narrow intermediate region. We shall refer to this region hereafter as the "inner region". We will show that this inner region consists of an infinite sequence of alternating "dimples" (i.e., narrow regions in which the film thickness has a local minimum) and "ridges" (i.e., narrow regions in which the film thickness has a local maximum). The inner region, and, in particular, the qualitative difference between the structure of the inner region and that described by Qin *et al.* [105] in the spherical case, will be discussed in Section 3.6.

Figure 3.3 shows snapshots of the interface for $\gamma = \gamma_\pi$ given by (3.2.3) at various times. In Section 3.5 it will be shown that this value of γ leads to $\theta_{\rm I} = \pi$ (i.e., the inner region is located at the waist of the cylinder), and this is confirmed by the results shown in Figure 3.3. Figure 3.4 shows snapshots of the interface for various values of γ at time $T = 10^4$. In particular, Figure 3.4 shows that the effect of varying γ is mainly to change the location of the inner region $\theta_{\rm I}$ and,

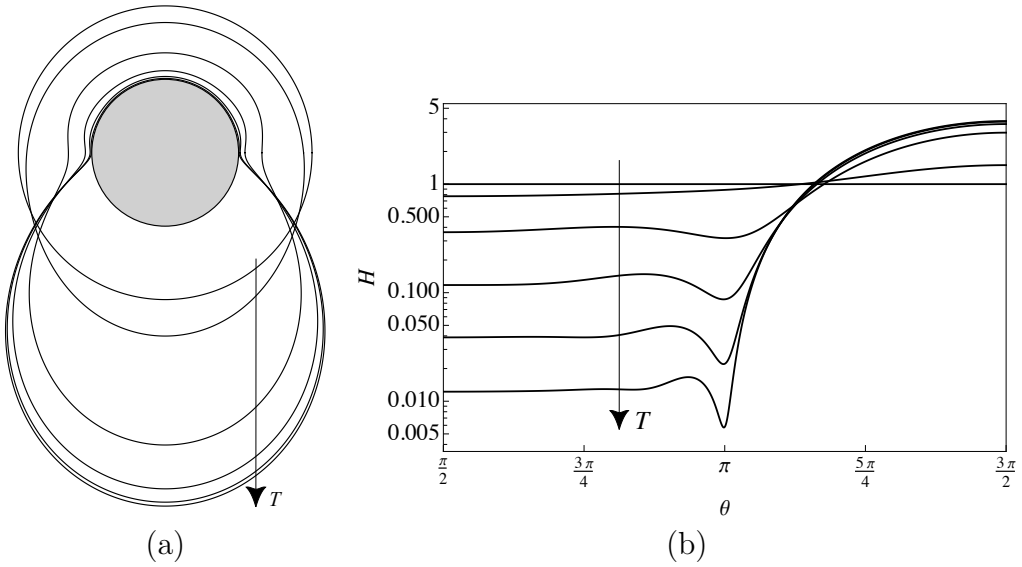

Figure 3.3: Snapshots of the interface for $\gamma = \gamma_\pi$ given by (3.2.3) at times $T = 0$, 10^0, 10^1, 10^2, 10^3, and 10^4. The arrows indicate the direction of increasing time. (a) Polar plot in which the film thickness has been exaggerated for illustrative purposes by using the artificial value $\epsilon = 1$. (b) Semi-log plot showing the film thickness H as a function of θ.

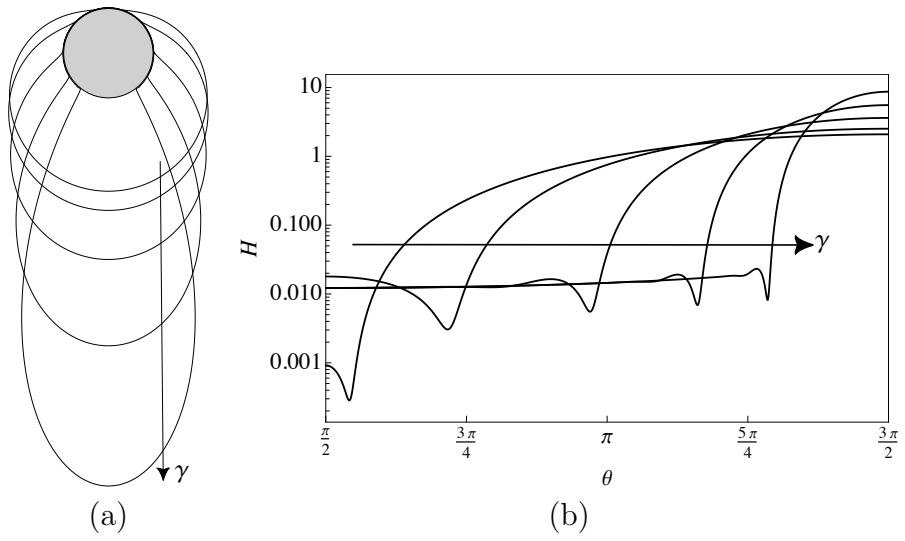

Figure 3.4: Snapshots of the interface for $\gamma = 10^{-1}$, 10^0, 10^1, 10^2, and 10^3 at time $T = 10^4$. The arrows indicate the direction of increasing γ. (a) Polar plot in which the film thickness has been exaggerated for illustrative purposes by using the artificial value $\epsilon = 1$. (b) Semi-log plot showing the film thickness H as a function of θ.

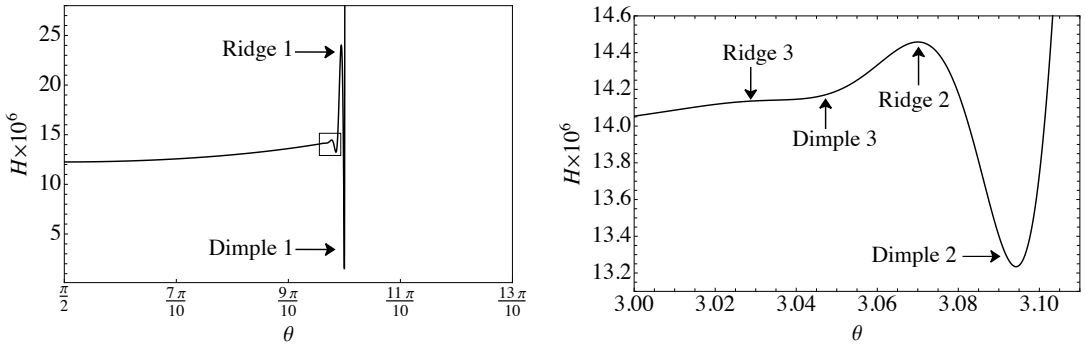

(a) (b)

Figure 3.5: The film thickness H for $\gamma = \gamma_\pi$ given by (3.2.3) at time $T = 10^{10}$. (a) Solution for $\pi/2 \leq \theta \leq 13\pi/10$. The rectangle indicates the location of the enlargement shown in (b). (b) Enlargement of (a) near $\theta = \theta_{\mathrm{I}} = \pi$.

correspondingly, the widths of the draining and pendant-drop regions. Specifically, decreasing the value of γ, corresponding to weakening gravity, results in a narrower draining region and a wider pendant-drop region, consistent with the numerical results of Reisfeld and Bankoff [101] discussed in Section 1.4.3. Figure 3.5 shows the film thickness H for $\gamma = \gamma_\pi$ given by (3.2.3) at time $T = 10^{10}$. In particular, whilst only the first dimple and ridge are immediately apparent in Figures 3.3, 3.4 and 3.5 (a), the second and third dimple and ridge are discernible in the enlargement of Figure 3.5 (a) near $\theta = \theta_{\mathrm{I}} = \pi$ shown in Figure 3.5 (b).

3.4 Draining region

In this section, we investigate the draining region. The results of our numerical calculations indicate that at late times the film becomes thin in the draining region. Therefore, we seek a late-time asymptotic solution in which $H \ll 1$, and hence at leading order the governing equation (3.1.1) becomes simply

$$H_T + \left(-\frac{1}{3}H^3\cos\theta\right)_\theta = 0. \tag{3.4.1}$$

We seek a separable solution to (3.4.1) of the form

$$H(\theta, T) = \eta(\theta)\, T^n, \tag{3.4.2}$$

and substitution of (3.4.2) into (3.4.1) yields

$$nT^{n-1}\eta + \left(-\frac{1}{3}T^{3n}\eta^3\cos\theta\right)_\theta. \tag{3.4.3}$$

Balancing powers of n in (3.4.3) yields $n = -1/2$, and hence (3.4.1) has a solution of the form

$$H(\theta, T) = \eta(\theta)T^{-1/2}, \tag{3.4.4}$$

where the function $\eta = \eta(\theta)$ satisfies the first-order ODE

$$\left(\eta^3\cos\theta\right)_\theta + \frac{3}{2}\eta = 0. \tag{3.4.5}$$

Solving (3.4.5) subject to the symmetry conditions (3.1.4) yields

$$\eta(\theta) = \begin{cases} \left(\dfrac{3}{2}\varphi(\theta)\right)^{1/2} & \text{for} \quad \dfrac{\pi}{2} \le \theta \le \pi, \\ \left(\dfrac{\sqrt{\pi}\,\Gamma\left(\frac{1}{3}\right)}{|\cos\theta|^{2/3}\,\Gamma\left(\frac{5}{6}\right)} - \dfrac{3}{2}\varphi(\theta)\right)^{1/2} & \text{for} \quad \pi \le \theta \le \dfrac{3\pi}{2}, \end{cases} \tag{3.4.6}$$

where $\varphi(\theta)$ is the hypergeometric function

$$\varphi(\theta) = {}_2F_1\left(\frac{1}{3}, \frac{1}{2}; \frac{4}{3}; (\cos\theta)^2\right). \tag{3.4.7}$$

Equation (3.4.4) shows that the film in the draining region thins as $T^{-1/2}$, consistent with the result of Takagi and Huppert [103] for a film with an advancing front discussed in Section 1.4.3, and that H is a monotonically increasing function of θ. In particular, this means that at any instant in time the leading-order film thickness in this region increases from a minimum value of

$$H|_{\theta=\pi/2} = \sqrt{\frac{3}{2}}T^{-1/2}. \tag{3.4.8}$$

at the top of the cylinder to a maximum value at $\theta = \theta_I$. As mentioned in Section 3.2, Figure 3.2 (b) shows the evolution of the film thickness at the top of the cylinder until time $T = 10^2$, and also confirms that (3.4.8) (shown with the dotted line) is indeed valid at the top of the cylinder at late times. Expanding (3.4.4) about $\theta = \pi/2$ shows that H is locally parabolic near the top of the cylinder,

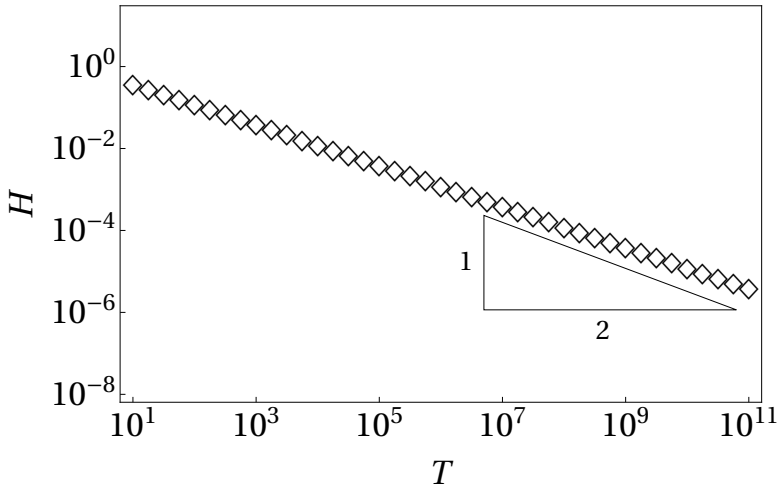

Figure 3.6: Log-log plot of H in the draining region, evaluated at the top of the cylinder for $\gamma = \gamma_\pi$ given by (3.2.3) as a function of T, and the corresponding late-time asymptotic scaling $T^{-1/2}$.

specifically

$$H = \left[\sqrt{\frac{3}{2}} + \frac{1}{16}\sqrt{\frac{3}{2}}\left(\theta - \frac{\pi}{2}\right)^2 + O\left(\left(\theta - \frac{\pi}{2}\right)^4\right)\right] T^{-1/2} \quad \text{as} \quad \theta \to \frac{\pi}{2}. \tag{3.4.9}$$

Substituting the solution for H in the draining region (3.4.4) into the flux (3.1.2) shows that the contributions to the flux due to gravity and capillarity are

$$Q_{\text{grav}} = -\frac{1}{3}H^3 \cos\theta = O(T^{-3/2}) \ll 1, \tag{3.4.10}$$

$$Q_{\text{cap}} = \frac{1}{3\gamma}H^3 \left(H + H_{\theta\theta}\right)_\theta = O(T^{-2}) \ll 1, \tag{3.4.11}$$

respectively. In particular, (3.4.10) and (3.4.11) show that $Q_{\text{cap}} \ll Q_{\text{grav}} \ll 1$ at late times, confirming the validity of neglecting capillarity in the draining region.

Figure 3.6 shows a log-log plot of H in the draining region, evaluated at the top of the cylinder obtained from the numerical solution of (3.1.1) for $\gamma = \gamma_\pi$ given by (3.2.3) as a function of T, and compares it with the corresponding late-time asymptotic scaling $T^{-1/2}$ obtained from (3.4.4). In particular, Figure 3.6 confirms that the interface has the predicted asymptotic behaviour at sufficiently late times. This conclusion is confirmed by the numerical values shown in Table 3.1, which shows that the asymptotic scaling is in excellent agreement with the slope of the

	Asymptotic scaling	Numerical result
H	-0.5	-0.5021

Table 3.1: The late-time asymptotic scaling for H in the draining region, evaluated at the top of the cylinder, and the slope of the corresponding line of best fit to the numerical results for $T \geq 10^{9/4}$ shown in Figure 3.6.

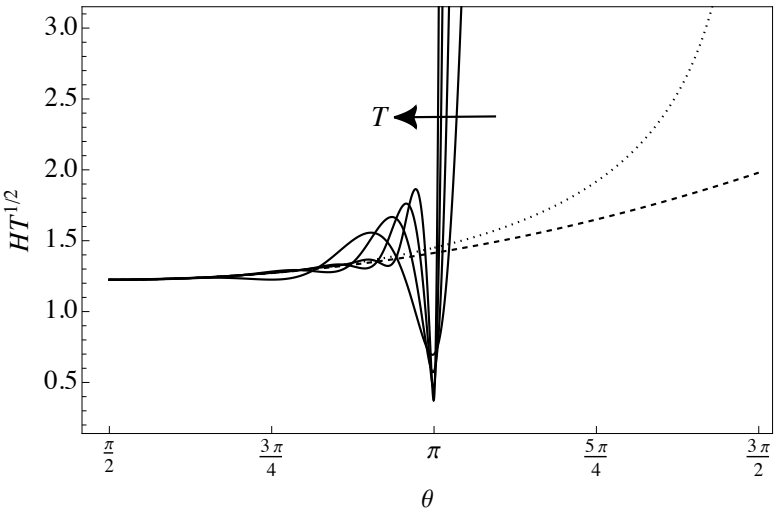

Figure 3.7: Snapshots of the scaled film thickness $\eta = HT^{1/2}$ for $\gamma = \gamma_\pi$ given by (3.2.3) at times $T = 10^3$, 10^4, 10^5, and 10^6. The arrow indicates the direction of increasing time. The dotted line shows the leading-order asymptotic solution in the draining region at late times (3.4.4) and the dashed line shows the asymptotic solution valid near the top of the cylinder (3.4.9).

corresponding line of best fit to the numerical results for $T \geq 10^{9/4}$ shown in Figure 3.6, which was calculated using the nonlinear curve fitting routine `FindFit[]` in Mathematica [265]. Note that $Q \equiv 0$ at the top of the cylinder. Specifically, $Q_{\text{grav}} \equiv 0$ (since $\cos(\pi/2) = 0$) and $Q_{\text{cap}} \equiv 0$ (as a consequence of the symmetry conditions (3.1.4)), and so all fluxes are omitted from both Figure 3.6 and Table 3.1.

Figure 3.7 shows snapshots of the scaled interface $\eta = HT^{1/2}$ for $\gamma = \gamma_\pi$ given by (3.2.3) at various times together with the leading-order asymptotic solution in the draining region (3.4.4), confirming that the interface does indeed approach the asymptotic solution at late times.

To perform the asymptotic matching with the inner region, it will be useful to determine the azimuthal volume flux out of the draining region, denoted by

$Q_{\text{drain}} = Q(\theta_{\text{I}}, T) = Q_{\text{drain}}(T)$. Integrating the governing equation (3.1.1) across the draining region gives an expression for Q_{drain}, namely

$$Q_{\text{drain}} = -\int_{\pi/2}^{\theta_{\text{I}}} H_T \, \mathrm{d}\theta, \tag{3.4.12}$$

where H is given by (3.4.4), and hence

$$Q_{\text{drain}} = \frac{1}{2} T^{-3/2} \int_{\pi/2}^{\theta_{\text{I}}} \eta(\theta) \, \mathrm{d}\theta, \tag{3.4.13}$$

showing that the flux out of the draining region decreases as $T^{-3/2}$ at late times.

3.5 Pendant-drop region

In this section, we investigate the pendant-drop region. The results of our numerical calculations indicate that at late times the pendant-drop region shown in Figures 3.3 (a) and 3.4 (a) is quasi-static so that $H = H(\theta)$ is independent of T. Hence, at leading order the governing equation (3.1.1) becomes

$$(H + H_{\theta\theta})_\theta = \gamma \cos\theta. \tag{3.5.1}$$

Equation (3.5.1) is a third-order ODE for the film thickness H which requires three boundary conditions. At the edge of the pendant-drop region, the interface approaches the surface of the cylinder tangentially, i.e., H satisfies the two boundary conditions

$$H|_{\theta=\theta_{\text{I}}} = 0, \tag{3.5.2}$$

$$H_\theta|_{\theta=\theta_{\text{I}}} = 0, \tag{3.5.3}$$

which together represent the assumption that at the boundary of the pendant drop there is an apparent contact line which is constrained by the requirement of a vanishing apparent contact angle due to the connection with a thin film (which has zero thickness to leading order). The third boundary condition is the symmetry condition at the bottom of the cylinder (3.1.4).

Solving (3.5.1) subject to (3.5.2), (3.5.3) and (3.1.4) yields the solution for H

in the pendant-drop region, namely

$$H = \frac{\gamma}{4}\left[(3\pi - 2\theta)\cos\theta - (3\pi - 2\theta_{\rm I})\cos\theta_{\rm I} + (\sin\theta - \sin\theta_{\rm I})\left(2 + (3\pi - 2\theta_{\rm I})\tan\theta_{\rm I}\right)\right], \tag{3.5.4}$$

which is valid for $\theta_{\rm I} \leq \theta \leq 3\pi/2$.

The solution (3.5.4) contains an unknown constant, namely, the azimuthal location of the inner region $\theta_{\rm I}$ (as shown in Figure 3.1), which can be determined by imposing global conservation of mass. To leading order, all of the liquid initially on the cylinder is contained within the pendant-drop region, so that

$$\int_{\theta_{\rm I}}^{3\pi/2} H \,{\rm d}\theta = \int_{\pi/2}^{3\pi/2} H(0)\,{\rm d}\theta = \pi. \tag{3.5.5}$$

Substituting the asymptotic solution for H given by (3.5.4) into the global mass conservation condition (3.5.5) and evaluating the integral yields an implicit equation for $\theta_{\rm I}$ in terms of γ, namely

$$\gamma = \frac{8\pi\cos\theta_{\rm I}}{4\left(1 + \cos(2\theta_{\rm I})\right) - (3\pi - 2\theta_{\rm I})\left(3\pi - 2\theta_{\rm I} + \sin(2\theta_{\rm I})\right)}. \tag{3.5.6}$$

Note that, unlike the corresponding equation in the spherical case obtained by Qin *et al.* [105], it is not possible to invert (3.5.6) to obtain an explicit expression for $\theta_{\rm I}$ in terms of γ. In particular, as mentioned in Section 3.3, (3.5.6) predicts that the inner region is located at $\theta_{\rm I} = \pi$ (i.e., the inner region is located at the waist of the cylinder) when $\gamma = \gamma_\pi$ is given by (3.2.3).

Figure 3.8 shows snapshots of the film thickness for $\gamma = \gamma_\pi$ given by (3.2.3) at various times together with the leading-order asymptotic solution in the pendant-drop region (3.5.4), confirming that the interface does indeed approach the asymptotic solution at late times. In particular, Figure 3.8 shows that the leading-order film thickness in this region increases from zero at $\theta_{\rm I} = \pi$ to a maximum value of

$$\begin{aligned} H\left(\frac{3\pi}{2}\right) &= -\frac{\gamma}{4}\left[(3\pi - 2\theta_{\rm I})\cos\theta_{\rm I} + \left\{2 + (3\pi - 2\theta_{\rm I})\tan\theta_{\rm I}\right\}(1 + \sin\theta_{\rm I})\right] \\ &= \frac{2\pi(\pi - 2)}{\pi^2 - 8} \simeq 3.8366 \end{aligned} \tag{3.5.7}$$

at the bottom on the cylinder.

Figure 3.9 shows the relationship between γ and $\theta_{\rm I}$. Specifically, Figure 3.9

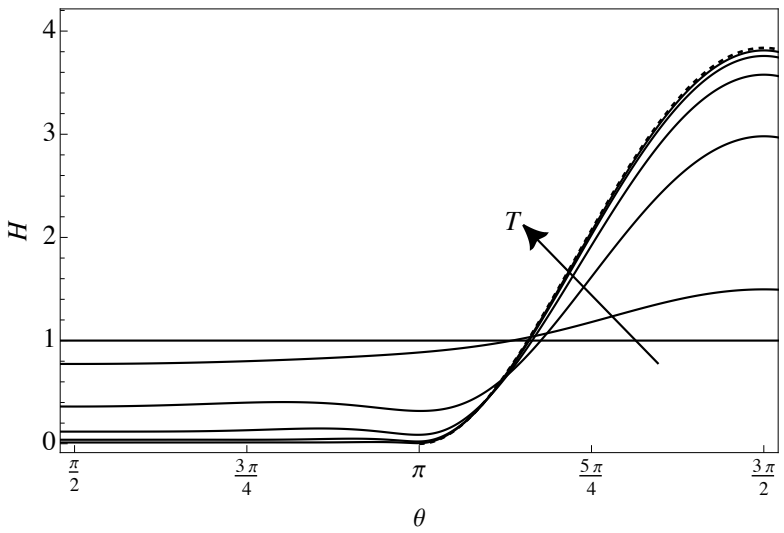

Figure 3.8: Snapshots of the film thickness for $\gamma = \gamma_\pi$ given by (3.2.3) at times $T = 0$, 10^0, 10^1, 10^2, 10^3, and 10^4. The arrow indicates the direction of increasing time. The (barely visible) dashed line shows the leading-order asymptotic solution in the pendant-drop region (3.5.4).

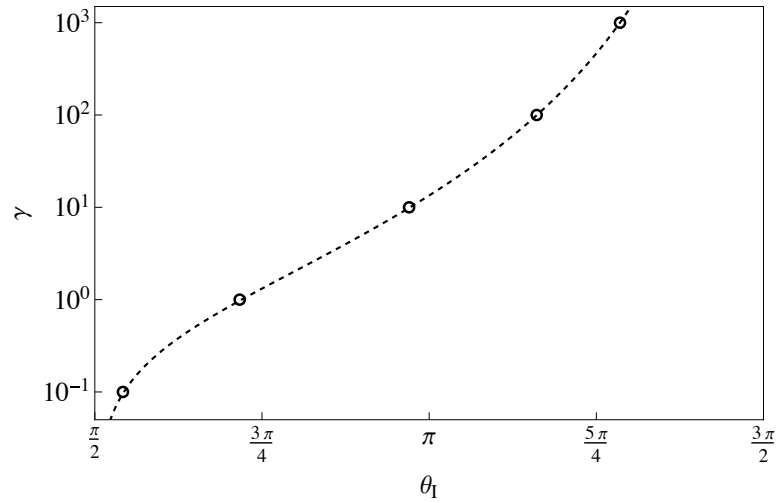

Figure 3.9: The relationship between γ and θ_I. The dashed line shows the asymptotic expression (3.5.6), and the circles show the position of the inner region calculated from numerical solutions of the governing equation (3.1.1) for $\gamma = 10^{-1}$, 10^0, 10^1, 10^2, and 10^3 at time $T = 10^4$.

shows that the asymptotic expression (3.5.6) is in very good agreement with the position of the inner region. Note that, to leading order, the position of the inner region is equivalent to the position of the minimum of dimple 1, which was located numerically in Mathematica [265] using the built-in function `FindPeaks[]`. Specifically, the position and height of the most dominant trough in the numerical solution of the governing equation (3.1.1) was calculated for five values of γ at time $T = 10^4$. In particular, Figure 3.9 shows that θ_{I} is a monotonically increasing function of γ, confirming that weakening gravity results in a narrower draining region and a wider pendant-drop region, consistent with the results shown in Figure 3.4.

Substituting (3.5.6) into (3.5.4) and taking the limit $\theta \to \theta_{\mathrm{I}}^+$ yields the local behaviour of the interface in the pendant-drop region as it approaches the inner region, namely

$$\begin{aligned} H =& \frac{\pi\left[2\theta_{\mathrm{I}} - 3\pi + \sin(2\theta_{\mathrm{I}})\right]}{4\left(1+\cos(2\theta_{\mathrm{I}})\right) - (3\pi - 2\theta_{\mathrm{I}})\left(3\pi - 2\theta_{\mathrm{I}} + \sin(2\theta_{\mathrm{I}})\right)}(\theta - \theta_{\mathrm{I}})^2 \\ &+ O\left((\theta-\theta_{\mathrm{I}})^3\right) \quad \text{as} \quad \theta \to \theta_{\mathrm{I}}^+. \end{aligned} \tag{3.5.8}$$

This result will be used in Section 3.6.1 when performing the asymptotic matching of the solution in the pendant-drop region to that in dimple 1.

3.6 Inner region

In this section, we investigate the inner region located at $\theta = \theta_{\mathrm{I}}$ which matches the draining and pendant-drop regions. Figure 3.10 shows a sketch of the asymptotic structure of the inner region, which, as mentioned above, consists of an infinite sequence of alternating dimples and ridges. This capillary-ripple structure (see Section 1.5) is qualitatively different from that of one dimple-ring zone and one ridge-ring zone described by Qin *et al.* [105] in the spherical case. In fact, we anticipate that a corresponding infinite sequence of alternating dimple-ring zones and ridge-ring zones (with, in particular, the same asymptotic scalings as those described subsequently in this chapter) also occurs in the spherical case. The flaw in the analysis of Qin *et al.* [105] is that the flux out of their thin-film zone is not, in fact, of the same order as the fluxes due to gravity and capillarity in their ridge-ring zone. This mismatch is not apparent in their numerical results

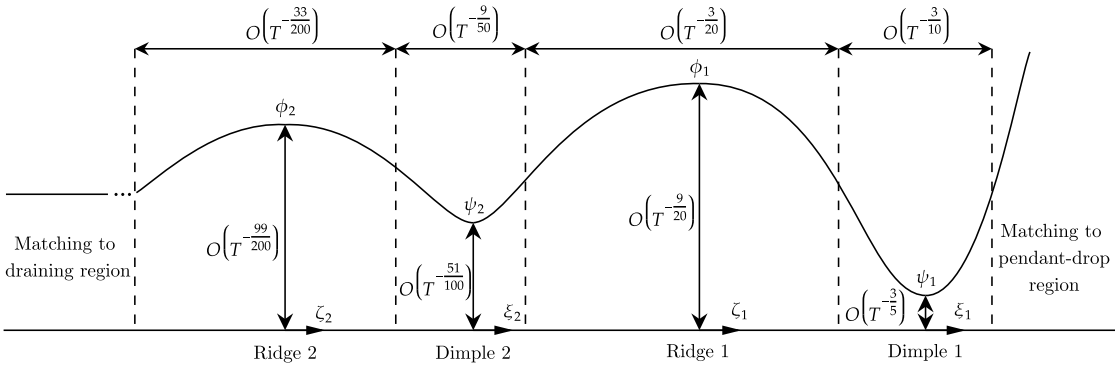

Figure 3.10: A sketch of the asymptotic structure of the inner region.

because they never computed beyond a final time of $T = O(10^5)$ (compared to a final time of $T = O(10^{11})$ used in this section), and (extrapolating from the behaviour of the present solution described in Section 3.6.3), the other dimple-ring and ridge-ring zones presumably only become apparent at larger values of T. However, as discussed in Section 1.5, capillary-ripple structures similar to that described here have been found in other situations, most famously by Jones and Wilson [156], who, as discussed earlier, showed that an infinite sequence of steady dimples and ridges is necessary to match a thin liquid film of uniform thickness flowing down a vertical wall to a quiescent pool of liquid. As discussed in Section 1.5, following this pioneering work, similar structures have been found in rimming flow [119], levitated drops [157], liquid films or drops on inclined planes [114, 158, 159], elastic-plated gravity currents [160], and Leidenfrost levitation of particles [161].

We will determine the asymptotic solutions for H in dimple 1 and ridge 1 in Sections 3.6.1 and 3.6.2, respectively. We will then generalise this analysis to determine the asymptotic solutions for H in dimple n and ridge n for $n = 2, 3, 4, \ldots$ in Section 3.6.3.

3.6.1 Dimple 1

The results of our numerical calculations indicate that, as Figure 3.5 illustrates, dimple 1 is narrow and thin (specifically, thinner than the draining region). Motivated by these numerical results, we seek a leading-order asymptotic solution for

H in the self-similar form

$$H = \frac{\psi_1(\xi_1)}{T^{\alpha_1}}, \quad \theta - \theta_\mathrm{I} = \frac{\xi_1}{T^{\beta_1}}, \tag{3.6.1}$$

where the exponents $\alpha_1 > 1/2$ and $\beta_1 > 0$ are positive constants which we shall determine.

In order to proceed, the solution in dimple 1 must be matched to the (known) solution in the pendant drop region in the downstream direction, and to the flux in the draining region (rather than the solution in ridge 1) in the upstream direction. This is because dimple 1 matches with ridge 1 in the upstream direction, whose solution cannot be determined until the solution in dimple 1 is known, therefore the fluxes must be matched rather than the film thickness.

In particular, equating the flux out of the draining region given by (3.4.13) with the flux in dimple 1 (obtained from substituting (3.6.1) into (3.1.2)) yields

$$T^{-3/2}K = -\frac{1}{3}\psi_1^3 T^{-3\alpha_1}\cos\theta_\mathrm{I} + \frac{1}{3\gamma}\psi_1^3\left[T^{-4\alpha_1+\beta_1}\psi_{1\xi_1} + T^{-4\alpha_1+3\beta_1}\psi_{1\xi_1\xi_1\xi_1}\right], \tag{3.6.2}$$

where

$$K = \frac{3\gamma}{2}\int_{\pi/2}^{\theta_\mathrm{I}} \eta(\theta)\,\mathrm{d}\theta > 0 \tag{3.6.3}$$

is a positive constant.

Considering the possible leading-order balances in (3.6.2) yields three possible equations relating α_1 and β_1, namely

$$-\frac{3}{2} = -4\alpha_1 + 3\beta_1, \quad -3\alpha_1 = -4\alpha_1 + 3\beta_1, \quad \text{and} \quad -\frac{3}{2} = -3\alpha_1. \tag{3.6.4}$$

The third of these equations may be immediately discarded on the basis that it yields $\alpha_1 = 1/2$, corresponding to the scaling of the film thickness in the draining region, and thus contradicting the assumption that dimple 1 is thinner than the draining region.

Another equation relating α_1 and β_1 arises from the asymptotic matching of dimple 1 with the pendant-drop region. Approaching dimple 1 from the pendant-drop region corresponds to taking the limit $\theta \to \theta_\mathrm{I}^+$, and approaching the pendant-drop region from dimple 1 corresponds to taking the limit $\xi_1 \to +\infty$. Thus, matching the solution for the film thickness in dimple 1 with that in the pendant-

drop region requires that

$$T^{-\alpha_1+2\beta_1}\psi_{1\xi_1\xi_1}|_{\xi_1\to+\infty} = H_{\theta\theta}|_{\theta\to\theta_{\mathrm{I}}^+}, \tag{3.6.5}$$

where H is given by (3.5.8). Equating the exponents of T in (3.6.5) yields

$$-\alpha_1 + 2\beta_1 = 0. \tag{3.6.6}$$

This allows us to discard the first equation in (3.6.4), as it yields $\alpha_1 = \beta_1 = 0$, corresponding to the scaling of the film thickness in the pendant-drop region. Therefore, the only relevant equation in (3.6.4) is $-3/2 = -4\alpha_1 + 3\beta_1$, yielding

$$\alpha_1 = \frac{3}{5}, \quad \beta_1 = \frac{3}{10}, \tag{3.6.7}$$

and hence the solution for H (3.6.1) becomes

$$H = \frac{\psi_1(\xi_1)}{T^{3/5}}, \quad \theta - \theta_{\mathrm{I}} = \frac{\xi_1}{T^{3/10}}, \tag{3.6.8}$$

where the function $\psi_1 = \psi_1(\xi_1)$ satisfies

$$\psi_1^3\psi_{1\xi_1\xi_1\xi_1} = K. \tag{3.6.9}$$

In particular, equation (3.6.8) shows that dimple 1 has the same asymptotic scalings as the dimple-ring zone in the spherical case found by Qin *et al.* [105]. Note that equation (3.6.9) (sometimes referred to as "the current equation") arises in a variety of other draining and coating flows (see, for example, Lamstaes and Eggers [266] and van Limbeek *et al.* [267]).

Substituting the solution for H (3.6.8) into the flux (3.1.2) shows that

$$Q_{\mathrm{grav}} = -\frac{1}{3}H^3\cos\theta = O(T^{-9/5}) \ll 1, \tag{3.6.10}$$

$$Q_{\mathrm{cap}} = \frac{1}{3\gamma}H^3\left(H + H_{\theta\theta}\right)_\theta = O(T^{-3/2}) \ll 1. \tag{3.6.11}$$

In particular, (3.6.10) and (3.6.11) show that $Q_{\mathrm{grav}} \ll Q_{\mathrm{cap}} \ll 1$ in dimple 1, confirming the consistency of neglecting gravity in dimple 1.

Figure 3.11 shows a log-log plot of H, Q_{grav}, Q_{cap}, and Q evaluated at the minimum of dimple 1 obtained from numerical solutions of (3.1.1) for $\gamma = \gamma_\pi$

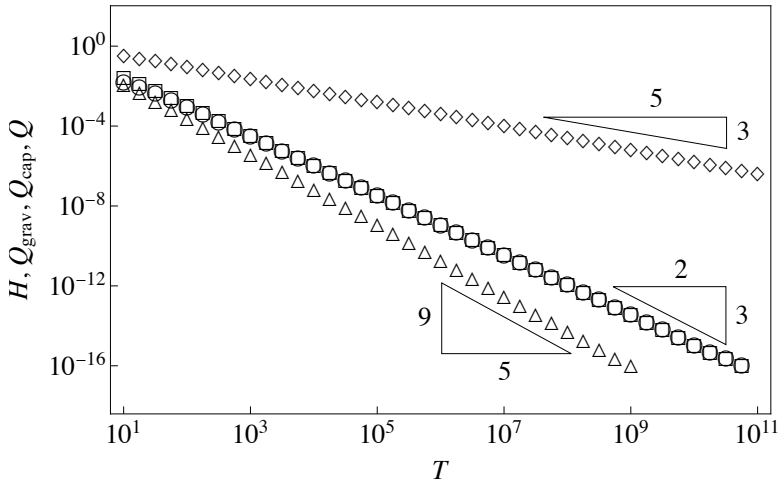

Figure 3.11: Log-log plot of H (diamonds), Q_{grav} (triangles), Q_{cap} (circles), and Q (squares) evaluated at the minimum of dimple 1 for $\gamma = \gamma_\pi$ given by (3.2.3) as functions of T, and the corresponding late-time asymptotic scalings $T^{-3/5}$, $T^{-9/5}$, $T^{-3/2}$, and $T^{-3/2}$. Note that the circles and the squares almost lie on top of each other.

	Asymptotic scaling	Numerical result
H	-0.6	-0.5974
Q_{grav}	-1.8	-1.7773
Q_{cap}	-1.5	-1.4877
Q	-1.5	-1.4953

Table 3.2: The late-time asymptotic scalings for H, Q_{grav}, Q_{cap}, and Q in dimple 1, and the slopes of the lines of best fit to the numerical results for $T \geq 10^{9/4}$ shown in Figure 3.11.

given by (3.2.3) as function of T, and compares them with the corresponding late-time asymptotic scalings $T^{-3/5}$, $T^{-9/5}$, $T^{-3/2}$, and $T^{-3/2}$ obtained from (3.6.8), (3.6.10), and (3.6.11). In particular, Figure 3.11 and Table 3.2 confirm that the interface has the predicted asymptotic behaviour at sufficiently late times.

The shape of the interface of dimple 1 is determined by solving (3.6.9) for ψ_1 subject to appropriate far-field and boundary conditions. As given by (3.6.5), the first condition arises from matching the solution in dimple 1 with that in the pendant-drop region, i.e.,

$$\psi_{1\xi_1\xi_1}|_{\xi_1\to+\infty} = L_0 := \frac{2\pi\left(2\theta_{\text{I}} - 3\pi + \sin(2\theta_{\text{I}})\right)}{4(1+\cos(2\theta_{\text{I}})) - (3\pi - 2\theta_{\text{I}})(3\pi - 2\theta_{\text{I}} + \sin(2\theta_{\text{I}}))}. \quad (3.6.12)$$

The second condition arises from matching dimple 1 with ridge 1, i.e.,

$$\psi_{1\xi_1\xi_1}|_{\xi_1\to-\infty} = 0. \tag{3.6.13}$$

Note that (3.6.12) and (3.6.13) mean that the leading-order film thickness in ridge 1 grows quadratically in the limit $\xi_1 \to +\infty$ but linearly in the limit $\xi_1 \to -\infty$. The third condition fixes the location of the minimum of ψ_1 at $\xi_1 = 0$, i.e.,

$$\psi_{1\xi_1}|_{\xi_1=0} = 0. \tag{3.6.14}$$

The constants K and L_0 can be scaled out of the problem (3.6.9) and (3.6.12)–(3.6.14) by setting

$$\psi_1 = c_1\tilde{\psi}, \quad \xi_1 = c_2\tilde{\xi}. \tag{3.6.15}$$

Substituting (3.6.15) into (3.6.9) and (3.6.12)–(3.6.14) yields

$$\tilde{\psi}^3\tilde{\psi}_{\tilde{\xi}\tilde{\xi}\tilde{\xi}} = \frac{c_2^3}{c_1^4}K, \tag{3.6.16}$$

$$\tilde{\psi}_{\tilde{\xi}}|_{\tilde{\xi}=0} = 0, \tag{3.6.17}$$

$$\tilde{\psi}_{\tilde{\xi}\tilde{\xi}}|_{\tilde{\xi}\to+\infty} = \frac{c_2^2}{c_1}L_0, \tag{3.6.18}$$

$$\tilde{\psi}_{\tilde{\xi}\tilde{\xi}}|_{\tilde{\xi}\to-\infty} = 0, \tag{3.6.19}$$

respectively. Solving $c_1^4/c_2^3 = K$ and $c_1/c_2^2 = L_0$ gives

$$\psi_1 = K^{2/5}L_0^{-3/5}\tilde{\psi}, \quad \xi_1 = K^{1/5}L_0^{-4/5}\tilde{\xi}. \tag{3.6.20}$$

Substitution of (3.6.20) into (3.6.9) and (3.6.12)–(3.6.14) yields the rescaled (parameter-free) problem

$$\tilde{\psi}^3\tilde{\psi}_{\tilde{\xi}\tilde{\xi}\tilde{\xi}} = 1, \tag{3.6.21}$$

$$\tilde{\psi}_{\tilde{\xi}\tilde{\xi}}|_{\tilde{\xi}\to+\infty} = 1, \tag{3.6.22}$$

$$\tilde{\psi}_{\tilde{\xi}\tilde{\xi}}|_{\tilde{\xi}\to-\infty} = 0, \tag{3.6.23}$$

$$\tilde{\psi}_{\tilde{\xi}}|_{\tilde{\xi}=0} = 0. \tag{3.6.24}$$

Figure 3.12 (a) shows the numerical solution of the rescaled problem (3.6.21)–

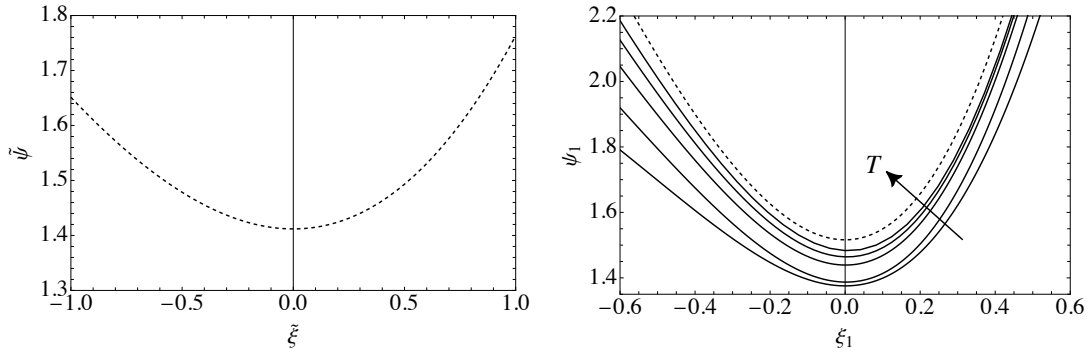

(a) (b)

Figure 3.12: (a) Solution of the rescaled problem (3.6.21)–(3.6.24) expressed in rescaled variables $\tilde{\xi}$ and $\tilde{\psi}$. (b) Snapshots of the film thickness for $\gamma = \gamma_\pi$ given by (3.2.3) at times $T = 10^2$, 10^3, 10^4, 10^5, and 10^6 expressed in scaled variables ξ_1 and ψ_1. The arrow indicates the direction of increasing time. The dashed line shows the leading-order asymptotic solution in dimple 1 (3.6.8).

(3.6.24) expressed in rescaled variables $\tilde{\xi}$ and $\tilde{\psi}$, and Figure 3.12 (b) shows snapshots of the film thickness for $\gamma = \gamma_\pi$ given by (3.2.3) at various times together with the leading-order asymptotic solution in dimple 1 (3.6.8) expressed in scaled variables ξ_1 and ψ_1, confirming that the interface does indeed approach the asymptotic solution at late times. In particular, the limiting value of the slope of the interface in the rescaled problem as $\tilde{\xi} \to -\infty$ is found to be

$$\tilde{\psi}|_{\tilde{\xi}\to-\infty} = -\tilde{m}, \tag{3.6.25}$$

where

$$\tilde{m} = 0.9626 \tag{3.6.26}$$

is found in solving the rescaled problem (3.6.21)–(3.6.24) numerically via a shooting method (see, for example, Edun *et al.* [268] or Meade *et al.* [269] for details). This result will be used in Section 3.6.2 when performing the asymptotic matching between dimple 1 and ridge 1, and again in Section 3.6.3 when performing the asymptotic matching between dimple n and ridge n.

3.6.2 Ridge 1

The results of our numerical calculations indicate that, as Figure 3.5 also illustrates, ridge 1 is narrow (but wider than dimple 1) and thin (but thicker than the draining region). Motivated by these numerical results, we seek a leading-order asymptotic solution for H in the self-similar form

$$H = \frac{\phi_1(\zeta_1)}{T^{\delta_1}}, \quad \theta - \theta_{\mathrm{I}} = \frac{\zeta_1}{T^{\lambda_1}}, \tag{3.6.27}$$

where the exponents $0 < \delta_1 < 1/2$ and $0 < \lambda_1 < \beta_1$ are positive constants which we shall determine.

Equating the flux out of the draining region given by (3.4.13) with the flux in ridge 1 (obtained from substituting (3.6.27) into (3.1.2)) yields

$$T^{-3/2}K = -\frac{1}{3}\phi_1^3 T^{-3\delta_1}\cos\theta_{\mathrm{I}} + \frac{1}{3\gamma}\phi_1^3\left[T^{-4\delta_1+\lambda_1}\phi_{1\zeta_1} + T^{-4\delta_1+3\lambda_1}\phi_{1\zeta_1\zeta_1\zeta_1}\right], \tag{3.6.28}$$

where the constant K is again given by (3.6.3).

Analogously to the corresponding analysis of dimple 1 described in Section 3.6.1, considering the possible leading-order balances in (3.6.28) yields three possible equations relating δ_1 and λ_1, namely

$$-\frac{3}{2} = -4\delta_1 + 3\lambda_1, \quad -3\delta_1 = -4\delta_1 + 3\lambda_1, \quad \text{and} \quad -\frac{3}{2} = -3\delta_1. \tag{3.6.29}$$

As before, the third of these may be discarded immediately on the basis that it yields $\delta_1 = 1/2$, corresponding to the scaling of the film thickness of the draining region, thus contradicting the assumption that ridge 1 is thicker than the draining region.

Imposing asymptotic matching of ridge 1 with dimple 1 yields

$$T^{-\delta_1+\lambda_1}\phi_{1\zeta_1}|_{\zeta_1\to+\infty} = T^{-3/10}\psi_{1\xi_1}|_{\xi_1\to-\infty}. \tag{3.6.30}$$

Equating exponents of T in (3.6.30) yields

$$-\delta_1 + \lambda_1 = -\frac{3}{10}, \tag{3.6.31}$$

which allows us to discard the first equation in (3.6.29) as it yields $\delta_1 = 3/5$ and $\lambda_1 = 3/10$, corresponding to the scaling of the thickness in dimple 1, contradicting

the assumption that ridge 1 is wider than dimple 1. Therefore, the only relevant equation in (3.6.29) is $-3\delta_1 = -4\delta_1 + 3\lambda_1$. It follows that δ_1 and λ_1 are given by

$$\delta_1 = \frac{9}{20}, \quad \lambda_1 = \frac{3}{20}, \tag{3.6.32}$$

respectively, and hence the solution for H given by (3.6.27) becomes

$$H = \frac{\phi_1(\zeta_1)}{T^{9/20}}, \quad \theta - \theta_{\mathrm{I}} = \frac{\zeta_1}{T^{3/20}}. \tag{3.6.33}$$

In particular, (3.6.33) shows that ridge 1 has the same asymptotic scalings as the ridge-ring zone in the spherical case found by Qin *et al.* [105].

By (3.6.33), (3.6.28) becomes

$$T^{-3/2}K = T^{-27/20}\left(-\frac{\phi_1^3}{3}\cos\theta_I + \gamma^{-1}\frac{\phi_1^3}{3}\phi_{1\zeta_1\zeta_1\zeta_1}\right), \tag{3.6.34}$$

and balancing (3.6.34) with the flux out of the draining region Q_{drain} (3.4.13) yields

$$-\frac{\phi_1^3}{3}\cos\theta_I + \gamma^{-1}\frac{\phi_1^3}{3}\phi_{1\zeta_1\zeta_1\zeta_1} = \frac{1}{2}T^{-3/20}\int_{\pi/2}^{\theta_I}\eta(\theta)\,\mathrm{d}\theta. \tag{3.6.35}$$

The right-hand side of (3.6.35) is negligible in the limit $T \to \infty$. Thus, to find the shape of ridge 1 at late times we must solve

$$\phi_{1\zeta_1\zeta_1\zeta_1} = \gamma\cos\theta_{\mathrm{I}}. \tag{3.6.36}$$

Substituting the solution for H given by (3.6.33) into the flux (3.1.2) shows that

$$Q_{\mathrm{grav}} = -\frac{1}{3}H^3\cos\theta = O(T^{-27/20}) \ll 1, \tag{3.6.37}$$

$$Q_{\mathrm{cap}} = \frac{1}{3\gamma}H^3\left(H + H_{\theta\theta}\right)_\theta = O(T^{-27/20}) \ll 1, \tag{3.6.38}$$

confirming that $Q_{\mathrm{grav}} \sim Q_{\mathrm{cap}} \ll 1$ in ridge 1, i.e., that gravity and capillarity are comparable in ridge 1.

Figure 3.13 shows a log-log plot of H, Q_{grav}, Q_{cap}, and Q evaluated at the maximum of ridge 1 obtained from numerical solutions of (3.1.1) for $\gamma = \gamma_\pi$ given by (3.2.3) as a function of T, and compares them with the corresponding late-time asymptotic scalings $T^{-9/20}$, $T^{-27/20}$, $T^{-27/20}$, and $T^{-3/2}$ obtained from (3.6.33),

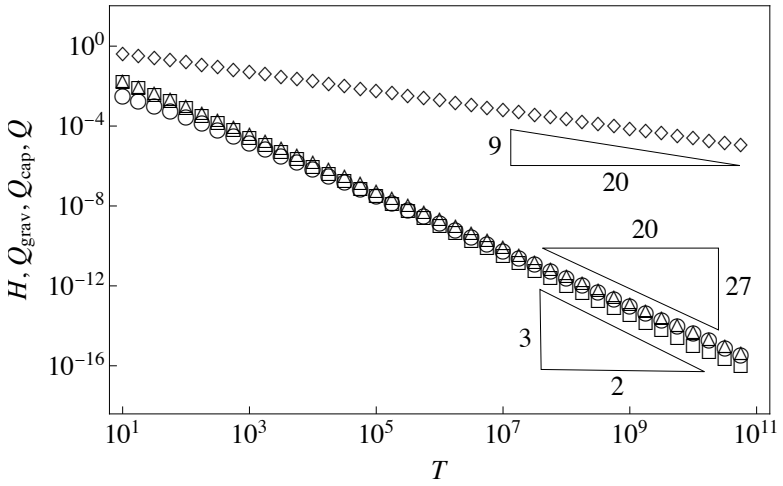

Figure 3.13: Log-log plot of H (diamonds), Q_{grav} (triangles), Q_{cap} (circles), and Q (squares) evaluated at the maximum of ridge 1 for $\gamma = \gamma_\pi$ given by (3.2.3) as functions of T, and the corresponding late-time asymptotic scalings $T^{-9/20}$, $T^{-27/20}$, $T^{-27/20}$, and $T^{-3/2}$. Note that the triangles, circles and the squares almost lie on top of each other.

	Asymptotic scaling	Numerical result
H	-0.45	-0.4736
Q_{grav}	-1.35	-1.4179
Q_{cap}	-1.35	-1.3658
Q	-1.50	-1.4828

Table 3.3: Late-time asymptotic scalings for H, Q_{grav}, Q_{cap}, and Q in ridge 1, and the slopes of the lines of best fit to the numerical results for $T \geq 10^{9/4}$ shown in Figure 3.13.

(3.6.37), and (3.6.38). In particular, Figure 3.13 and Table 3.3 confirm that the interface has the predicted asymptotic behaviour at sufficiently late times.

Since the $O(T^{-3/20}) \ll 1$ width of ridge 1 is asymptotically larger than both the $O(T^{-3/10}) \ll 1$ width of dimple 1 and the width of dimple 2 (which we determine in Section 3.6.3), the shape of the interface of ridge 1 is determined by solving (3.6.36) for ϕ_1 subject to appropriate boundary conditions on a finite (rather than an infinite) domain. Specifically, we solve (3.6.36) in the finite domain $\zeta_{1,0} \leq \zeta_1 \leq \zeta_{1,1}$, where the values of $\zeta_{1,0}$ and $\zeta_{1,1}$ are determined as part of the solution. The first boundary condition arises from matching the solution in ridge 1 with that in dimple

1 at $\zeta_1 = \zeta_{1,1}$, i.e.,

$$\phi_1|_{\zeta_1=\zeta_{1,1}} = 0 \quad \text{and} \quad \phi_{1\zeta_1}|_{\zeta_1=\zeta_{1,1}} = -m_1, \tag{3.6.39}$$

where m_1 is defined by

$$m_1 = \psi_{1\xi_1}|_{\xi_1\to-\infty}, \tag{3.6.40}$$

where by (3.6.20), (3.6.40) becomes

$$m_1 = \frac{c_{1,1}}{c_{1,2}}\tilde{\psi}_{\tilde{\xi}}|_{\tilde{\xi}\to-\infty} = K^{1/5}L_0^{1/5}\tilde{m}, \tag{3.6.41}$$

and the numerical value of $\tilde{m}$ is given by (3.6.26). The second boundary condition on (3.6.36) arises from matching the solution in ridge 1 with that in dimple 2 at $\zeta_1 = \zeta_{1,0}$, i.e.,

$$\phi_1|_{\zeta_1=\zeta_{1,0}} = 0 \quad \text{and} \quad \phi_{1\zeta_1}|_{\zeta_1=\zeta_{1,0}} = 0. \tag{3.6.42}$$

The final boundary condition fixes the location of the minimum of ϕ_1 at $\zeta_1 = 0$, i.e.,

$$\phi_{1\zeta_1}|_{\zeta_1=0} = 0. \tag{3.6.43}$$

Solving (3.6.36) subject to (3.6.39)–(3.6.43) yields the solution for the interface of ridge 1, namely

$$\phi_1 = \frac{8\sqrt{6}\left(K^{1/5}L_0^{1/5}\tilde{m}\right)^{3/2} - 9\gamma|\cos\theta_{\rm I}|\zeta_1^2\left[\sqrt{6}\left(K^{1/5}L_0^{1/5}\tilde{m}\right)^{1/2} + (\gamma|\cos\theta_{\rm I}|)^{1/2}\zeta_1\right]}{54(\gamma|\cos\theta_{\rm I}|)^{1/2}}, \tag{3.6.44}$$

where $\zeta_{1,0}$ and $\zeta_{1,1}$ are given by

$$\zeta_{1,0} = -\left(\frac{8K^{1/5}L_0^{1/5}\tilde{m}}{3\gamma|\cos\theta_{\rm I}|}\right)^{1/2} \quad \text{and} \quad \zeta_{1,1} = \left(\frac{2K^{1/5}L_0^{1/5}\tilde{m}}{3\gamma|\cos\theta_{\rm I}|}\right)^{1/2}, \tag{3.6.45}$$

respectively, γ and $\theta_{\rm I}$ are related by (3.5.6), and L_0 is given by (3.6.12). For example, the solution in ridge 1 for $\gamma = \gamma_\pi$ given by (3.2.3) is

$$\phi_1 = 0.5776 - 2.6949\zeta_1^2 - 2.2405\zeta_1^3. \tag{3.6.46}$$

Figure 3.14 shows snapshots of the film thickness for $\gamma = \gamma_\pi$ given by (3.2.3) at various times together with the leading-order asymptotic solution in ridge 1

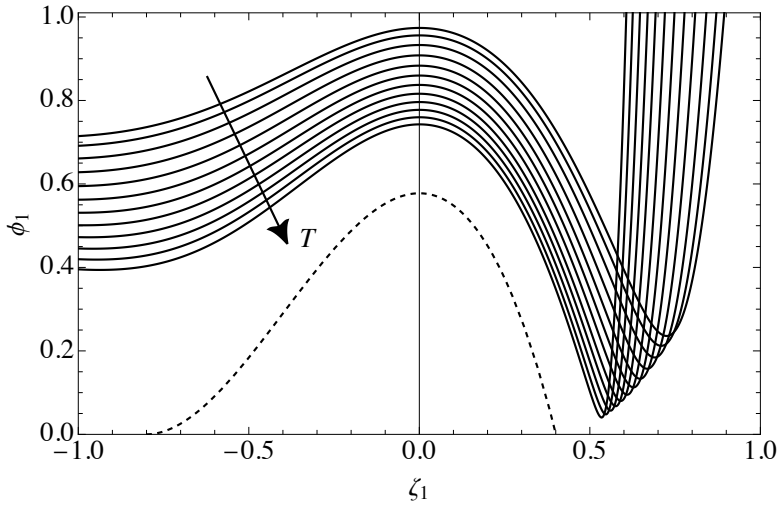

Figure 3.14: Snapshots of the film thickness for $\gamma = \gamma_\pi$ given by (3.2.3) at times $T = 10^5 + 10^{n/2}$ for $n = 10, 11, \ldots, 21$ expressed in scaled variables ζ_1 and ϕ_1. The arrow indicates the direction of increasing time. The dashed line shows the leading-order asymptotic solution in ridge 1 (3.6.46).

(3.6.46) expressed in scaled variables ζ_1 and ϕ_1, confirming that the interface does indeed approach the asymptotic solution at late times. Figure 3.14 also reveals that the convergence to the leading-order asymptotic solution in ridge 1 is significantly slower than the corresponding convergence in dimple 1 shown in Figure 3.12 (b): we return to this point in Section 3.6.3.

3.6.3 Dimple n and ridge n

As discussed previously, the inner region has a capillary-ripple structure consisting of an infinite sequence of dimples and ridges, and Figure 3.15 shows sketches of the leading-order asymptotic solutions in dimple n and ridge n for $n = 2, 3, 4, \ldots$. Fortunately, the asymptotic solutions for H in all of the dimples and ridges can be obtained by generalising the analysis for dimple 1 and ridge 1 described in Sections 3.6.1 and 3.6.2, respectively. Specifically, we seek leading-order asymptotic solutions for H in dimple n in the self-similar form

$$H = \frac{\psi_n(\xi_n)}{T^{\alpha_n}}, \quad \theta - \theta_{\mathrm{I}} = \frac{\xi_n}{T^{\beta_n}}, \tag{3.6.47}$$

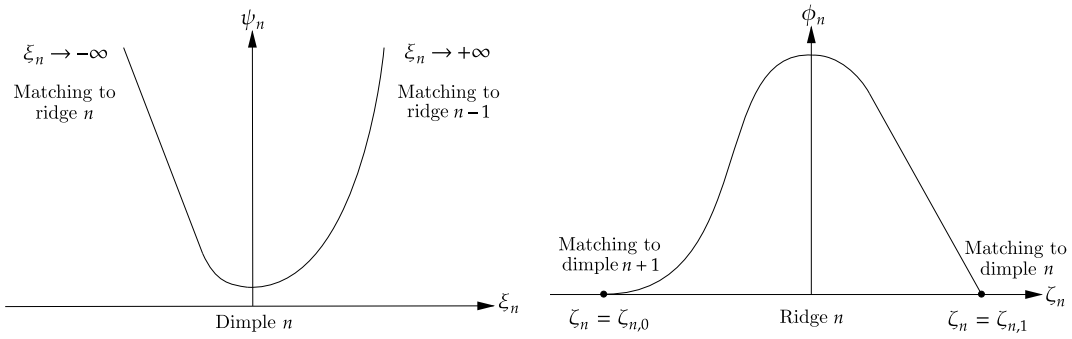

Figure 3.15: Sketches of the leading-order asymptotic solutions in (a) dimple n and (b) ridge n for $n = 2, 3, 4, \ldots$.

and for H in ridge n in the self-similar form

$$H = \frac{\phi_n(\zeta_n)}{T^{\delta_n}}, \quad \theta - \theta_{\mathrm{I}} = \frac{\zeta_n}{T^{\lambda_n}}, \tag{3.6.48}$$

where the exponents $\alpha_n > 1/2$, $\beta_n > 0$, $0 < \delta_n < 1/2$, and $0 < \lambda_n < \min(\beta_n, \beta_{n+1})$ are positive constants for which we will determine the general forms.

Equating the flux out of the draining region given by (3.4.13) with the flux in dimple n (obtained from substituting (3.6.47) into (3.1.2)) yields

$$T^{-3/2}K = -\frac{1}{3}\psi_n^3 T^{-3\alpha_n}\cos\theta_{\mathrm{I}} + \frac{1}{3\gamma}\psi_n^3\left[T^{-4\alpha_n+\beta_n}\psi_{n\xi_n} + T^{-4\alpha_n+3\beta_n}\psi_{n\xi_n\xi_n\xi_n}\right], \tag{3.6.49}$$

from which the relevant equation relating α_n and β_n is

$$-\frac{3}{2} = -4\alpha_n + 3\beta_n, \tag{3.6.50}$$

as per the analysis in Section 3.6.1. Matching dimple n with ridge $n-1$ requires

$$T^{2\beta_n-\alpha_n}\phi_{n\xi_n\xi_n}|_{\xi_n\to-\infty} = T^{2\lambda_{n-1}-\delta_{n-1}}\phi_{n-1\zeta_{n-1}\zeta_{n-1}}|_{\zeta_{n-1}\to+\infty}. \tag{3.6.51}$$

Equating exponents of T in (3.6.51), yields the second equation relating α_n and β_n, namely,

$$-\alpha_n + 2\beta_n = -\delta_{n-1} + 2\lambda_{n-1}. \tag{3.6.52}$$

Solving (3.6.50) and (3.6.52) yields

$$\alpha_n = \frac{3}{5} + \frac{1}{5}\left(-3\delta_{n-1} + 6\lambda_{n-1}\right), \quad \beta_n = \frac{3}{10} + \frac{1}{5}\left(-4\delta_{n-1} + 8\lambda_{n-1}\right). \tag{3.6.53}$$

On the other hand, equating the flux out of the draining region given by (3.4.13) with the flux in ridge n (obtained from substituting (3.6.48) into (3.1.2)) yields

$$T^{-3/2}K = -\frac{1}{3}\phi_1^3 T^{-3\delta_n}\cos\theta_{\mathrm{I}} + \frac{1}{3\gamma}\phi_n^3\left[T^{-4\delta_n+\lambda_n}\phi_{n\zeta_n} + T^{-4\delta_n+3\lambda_n}\phi_{n\zeta_n\zeta_n\zeta_n}\right], \tag{3.6.54}$$

from which the relevant equation relating δ_n and λ_n is

$$\delta_n - 3\lambda_n = 0, \tag{3.6.55}$$

as per the analysis in Section 3.6.2. Matching ridge n with dimple n requires

$$T^{2\beta_n-\alpha_n}\phi_{n\xi_n\xi_n}|_{\xi_n\to-\infty} = T^{2\lambda_{n-1}-\delta_{n-1}}\phi_{n-1\zeta_{n-1}\zeta_{n-1}}|_{\zeta_{n-1}\to+\infty}. \tag{3.6.56}$$

Equating exponents of T in (3.6.56) yields the second equation relating δ_n and λ_n, namely,

$$-\delta_n + \lambda_n = -\alpha_n + \beta_n. \tag{3.6.57}$$

Solving (3.6.55) and (3.6.57) yields

$$\delta_n = \frac{1}{2}\left(\alpha_n - \beta_n\right), \quad \lambda_n = \frac{3}{2}\left(\alpha_n - \beta_n\right). \tag{3.6.58}$$

By (3.6.7), (3.6.32), (3.6.53) and (3.6.58), the first five terms in the sequence of α_n β_n, δ_n, and λ_n are, respectively,

$$\begin{aligned}
\alpha_n &= \frac{3}{5}, \ \frac{51}{100}, \ \frac{501}{1000}, \ \frac{5001}{10000}, \ \frac{50001}{100000}, \dots \\
\beta_n &= \frac{3}{10}, \ \frac{9}{50}, \ \frac{21}{125}, \ \frac{417}{2500}, \ \frac{4167}{25000}, \dots \\
\delta_n &= \frac{9}{20}, \ \frac{99}{200}, \ \frac{999}{2000}, \ \frac{9999}{20000}, \ \frac{99999}{200000}, \dots \\
\lambda_n &= \frac{3}{20}, \ \frac{33}{200}, \ \frac{333}{2000}, \ \frac{3333}{20000}, \ \frac{33333}{200000}, \dots
\end{aligned} \tag{3.6.59}$$

To obtain the general form of α_n, we seek a recurrence relation of the form

$$\alpha_n = \begin{cases} \alpha_1 & n = 1, \\ a\alpha_{n-1} + b & n > 1, \end{cases} \tag{3.6.60}$$

where a and b are constants to be determined and $\alpha_1 = 3/5$ by (3.6.7). By (3.6.59) and (3.6.60), setting $n = 2$ and $n = 3$ yields, respectively,

$$\frac{51}{100} = \frac{3}{5}a + b, \quad \frac{501}{1000} = \frac{51}{100}a + b. \tag{3.6.61}$$

Solving (3.6.61) for a and b and substituting the solutions into (3.6.60) yields the recurrence relation

$$\alpha_n = \begin{cases} \dfrac{3}{5} & n = 1, \\ \dfrac{9}{20} + \dfrac{\alpha_{n-1}}{10} & n > 1. \end{cases} \tag{3.6.62}$$

Equation (3.6.62) is a nonhomogeneous, linear recurrence relation, for which the general solution α_n^{GS} has the form

$$\alpha_n^{\mathrm{GS}} = cr^n, \tag{3.6.63}$$

where r and c are constants to be determined. Substituting (3.6.63) into the homogeneous part of (3.6.62) and solving for r yields $r = 1/10$, thus the general solution is $\alpha_n^{\mathrm{GS}} = c10^{-n}$. The nonhomogeneous part of (3.6.62) is a constant, and so the particular solution α_n^{PS} has the form

$$\alpha_n^{PS} = d, \tag{3.6.64}$$

where d is a constant to be determined. Substituting (3.6.64) into (3.6.62) yields $d = 1/2$, thus

$$\alpha_n = \alpha_n^{\mathrm{GS}} + \alpha_n^{PS} = c10^{-n} + \frac{1}{2}. \tag{3.6.65}$$

Setting $n = 1$ in (3.6.65) and using $\alpha_1 = 3/5$ yields $c = 1$, therefore the general form of α_n is

$$\alpha_n = \frac{1}{2}(1 + 2 \times 10^{-n}). \tag{3.6.66}$$

Following through with analogous processes for β_n, δ_n, and λ_n yields the recurrence

relations

$$\beta_n = \begin{cases} \dfrac{3}{10} & n = 1, \\ \dfrac{3}{20} + \dfrac{\beta_{n-1}}{10} & n > 1, \end{cases} \tag{3.6.67}$$

$$\delta_n = \begin{cases} \dfrac{9}{20} & n = 1, \\ \dfrac{9}{20} + \dfrac{\delta_{n-1}}{10} & n > 1, \end{cases} \tag{3.6.68}$$

$$\lambda_n = \begin{cases} \dfrac{3}{20} & n = 1, \\ \dfrac{3}{20} + \dfrac{\lambda_{n-1}}{10} & n > 1, \end{cases} \tag{3.6.69}$$

respectively, from which the general forms of β_n, δ_n, and λ_n are found to be

$$\beta_n = \frac{1}{6}\left(1 + 8 \times 10^{-n}\right), \tag{3.6.70}$$

$$\delta_n = \frac{1}{2}\left(1 - 10^{-n}\right), \tag{3.6.71}$$

$$\lambda_n = \frac{1}{6}\left(1 - 10^{-n}\right). \tag{3.6.72}$$

Thus, the solution for H in dimple n (3.6.47) becomes

$$H = \frac{\psi_n(\xi_n)}{T^{(1+2\times 10^{-n})/2}}, \quad \theta - \theta_{\mathrm{I}} = \frac{\xi_n}{T^{(1+8\times 10^{-n})/6}}, \tag{3.6.73}$$

and the solution for H in ridge n (3.6.48) becomes

$$H = \frac{\phi_n(\zeta_n)}{T^{(1-10^{-n})/2}}, \quad \theta - \theta_{\mathrm{I}} = \frac{\zeta_n}{T^{(1-10^{-n})/6}}. \tag{3.6.74}$$

Note that setting $n = 1$ in (3.6.66) and (3.6.70)–(3.6.74) recovers the corresponding results for dimple 1 and ridge 1 obtained in Sections 3.6.1 and 3.6.2, respectively. Furthermore, we note that $\alpha_n \to 1/2^+$ and $\delta_n \to 1/2^-$ in the limit $n \to \infty$, confirming that an infinite sequence of dimples and ridges is required to achieve matching with the draining region. Moreover, as n increases these exponents approach their common asymptotic value rather quickly, as shown in Figure 3.16 which shows the progression of α_n (3.6.66), β_n (3.6.70), δ_n (3.6.71),

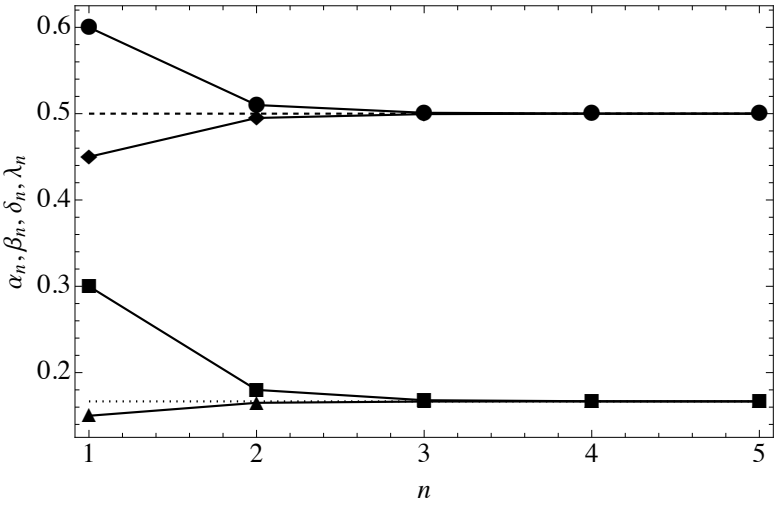

Figure 3.16: The exponents α_n (3.6.66) (circles), β_n (3.6.70) (squares), δ_n (3.6.71) (diamonds), and λ_n (3.6.72) (triangles) for $n = 1, 2, 3, 4$, and 5, where the symbols represent integer values of n. The horizontal lines show the asymptotic values of the limits as $n \to \infty$. The dashed line shows the value 1/2 and the dotted line shows the value 1/6.

and λ_n (3.6.72) for $n = 1, 2, 3, 4$, and 5. This explains why only the first three dimples and ridges are discernible in Figure 3.5 (b). This is also the reason why the $O(T^{-51/100})/O(T^{-9/20}) = O(T^{-3/50}) \ll 1$ convergence to the leading-order asymptotic solution in ridge 1 shown in Figure 3.14 is significantly slower than the corresponding $O(T^{-9/20})/O(T^{-3/5}) = O(T^{-3/20}) \ll 1$ convergence in dimple 1 shown in Figure 3.12 (b). In addition, note that the values of the exponents given in (3.6.66) and (3.6.70)–(3.6.72) mean that all of the dimples are narrower than all of the ridges (specifically, the width of dimple n is $O(T^{-\beta_n}) \ll 1$ and the width of ridge n is $O(T^{-\lambda_n}) \ll 1$, where $\beta_n > 1/6$ and $\lambda_n < 1/6$).

We can generalise the analysis described in Sections 3.6.1 and 3.6.2 for dimple n and ridge n, respectively. In dimple n, the function $\psi_n = \psi_n(\xi_n)$ satisfies

$$\psi_n^3 \psi_{n\xi_n\xi_n\xi_n} = K, \tag{3.6.75}$$

where K is again given by (3.6.3), subject to

$$\psi_{n\xi_n\xi_n}|_{\xi_n \to +\infty} = L_{n-1} := \phi_{n-1\zeta_{n-1}\zeta_{n-1}}|_{\zeta_{n-1} \to \zeta^+_{n-1,0}}, \tag{3.6.76}$$

$$\psi_{n\xi_n\xi_n}|_{\xi_n\to-\infty} = 0, \tag{3.6.77}$$

$$\psi_{n\xi_n}|_{\xi_n=0} = 0, \tag{3.6.78}$$

where the first condition (3.6.76) arises from matching dimple n to the pendant-drop region for $n = 1$ or to ridge $n-1$ for $n > 1$, the second condition (3.6.77) arises from matching dimple n with ridge n, and the third condition (3.6.78) fixes the maximum of ψ_n at $\xi_n = 0$.

In ridge n, the function $\phi_n = \phi_n(\zeta_n)$ satisfies

$$\phi_{n\zeta_n\zeta_n\zeta_n} = \gamma\cos\theta_{\mathrm{I}} \tag{3.6.79}$$

on the finite domain $\zeta_n \in [\zeta_{n,0}, \zeta_{n,1}]$ subject to

$$\phi_n|_{\zeta_n=\zeta_{n,1}} = 0 \quad \text{and} \quad \phi_{n\zeta_n}|_{\zeta_n=\zeta_{n,1}} = -m_n, \tag{3.6.80}$$

$$\phi_n|_{\zeta_n=\zeta_{n,0}} = 0 \quad \text{and} \quad \phi_{n\zeta_n}|_{\zeta_n=\zeta_{n,0}} = 0, \tag{3.6.81}$$

$$\phi_{n\zeta_n}|_{\zeta_n=0} = 0, \tag{3.6.82}$$

where the first condition (3.6.80) arises in matching ridge n to dimple n linearly by asserting that the gradient at $\zeta_n = \zeta_{n,1}$ matches that of the solution in dimple n, the second condition (3.6.81) arises in matching ridge n with dimple $n+1$ by asserting that the solution in ridge n approaches $\zeta_n = \zeta_{n,0}$ tangentially, and the third condition (3.6.82) fixes the location of the minimum of ϕ_n at $\zeta_n = 0$.

As before, the constants K and L_{n-1} can be scaled out of the problem (3.6.75)–(3.6.78) by setting

$$\psi_n = K^{2/5}L_{n-1}^{-3/5}\tilde{\psi}, \quad \xi_n = K^{1/5}L_{n-1}^{-4/5}\tilde{\xi}, \tag{3.6.83}$$

to exactly recover the rescaled problem (3.6.21)–(3.6.24) obtained in Section 3.6.2, and so m_n is given by

$$m_n = K^{1/5}L_{n-1}^{1/5}\tilde{m}, \tag{3.6.84}$$

where the numerical value of $\tilde{m}$ is again given by (3.6.26).

Solving (3.6.79) subject to (3.6.80)–(3.6.82) yields the solution for the interface

of ridge n, namely

$$\phi_n = \frac{8\sqrt{6}\left(K^{1/5}L_{n-1}^{1/5}\tilde{m}\right)^{3/2} - 9\gamma|\cos\theta_{\rm I}|\zeta_n^2\left[\sqrt{6}\left(K^{1/5}L_{n-1}^{1/5}\tilde{m}\right)^{1/2} + (\gamma|\cos\theta_{\rm I}|)^{1/2}\zeta_n\right]}{54(\gamma|\cos\theta_{\rm I}|)^{1/2}}, \tag{3.6.85}$$

where $\zeta_{n,0}$ and $\zeta_{n,1}$ are given by

$$\zeta_{n,0} = -\left(\frac{8K^{1/5}L_{n-1}^{1/5}\tilde{m}}{3\gamma|\cos\theta_{\rm I}|}\right)^{1/2}, \quad \zeta_{n,1} = \left(\frac{2K^{1/5}L_{n-1}^{1/5}\tilde{m}}{3\gamma|\cos\theta_{\rm I}|}\right)^{1/2}, \tag{3.6.86}$$

respectively, γ and $\theta_{\rm I}$ are again related by (3.5.6), and L_{n-1} is given by (3.6.76).

Using (3.6.76), we can obtain L_n terms of L_{n-1}, and hence inductively in terms of L_0. Differentiating (3.6.85) twice with respect to ζ_n and evaluating at $\zeta_n = \zeta_{n,0}$ (3.6.86) yields

$$L_n = \sqrt{\frac{2}{3}}\left(K^{1/5}L_{n-1}^{1/5}\tilde{m}\gamma|\cos\theta_{\rm I}|\right)^{1/2}, \tag{3.6.87}$$

which can be written in terms of L_0 (3.6.12) as

$$L_n = \left(\frac{2}{3}\tilde{m}\gamma|\cos\theta_{\rm I}|\right)^{x/2} K^y L_0^{10^{-n}}, \tag{3.6.88}$$

where the exponents x and y are given by

$$x = \sum_{i=1}^{n}\frac{1}{10^{i-1}} = \frac{10}{9}\left(1-10^{-n}\right), \quad y = \sum_{i=1}^{n}\frac{1}{10^i} = \frac{1}{9}\left(1-10^{-n}\right), \tag{3.6.89}$$

respectively.

The problem for ψ_n (which has to be solved numerically) and the solution for ϕ_n (given by (3.6.85) and (3.6.86)) are now given in terms of known constants, namely, K (3.6.3), L_0 (3.6.12), and $\tilde{m}$ (3.6.26), and so the leading-order shape of the interface can now be obtained throughout the inner region.

3.7 Concluding remarks

In this chapter, we have investigated the dynamics of a thin film on the outer surface of a horizontal circular cylinder in the case in which the cylinder is stationary in the absence of an electric field.

In Section 3.2, we showed that at early times, capillarity is negligible and the film thickness deviates from uniformity only slightly due to gravity

In Section 3.3, we showed that at late times, three regions of qualitatively different behaviour emerge, namely, a draining region on the upper part of the cylinder and a pendant-drop region on the lower part of the cylinder joined by a narrow inner region, as sketched in Figure 3.1.

The draining region was analysed in Section 3.4, in which gravity dominates capillarity, the flux decreases as $T^{-3/2} \ll 1$, and the film thins as $T^{-1/2} \ll 1$. The thickness of the film in the draining region is given by (3.4.7), which shows that at any instant in time the leading-order film thickness in this region increases from a minimum value given by (3.4.8) at the top of the cylinder to a maximum value at $\theta = \theta_{\rm I}$.

The pendant-drop region was analysed in Section 3.5 in which it was shown that there is a quasi-static balance between gravity and capillarity (where, to leading order, the pendant drop contains all of the liquid initially on the cylinder). The thickness of the film in the pendant-drop region is given by (3.5.4), which shows that the leading-order film thickness in this region increases from zero at $\theta_{\rm I} = \pi$ to a maximum value given by (3.5.7) at the bottom of the cylinder.

The solutions in the draining and pendant-drop regions match via the inner region which was analysed in Section 3.6, in which we showed that the location of the inner region $\theta_{\rm I}$ is given implicitly by (3.5.6). In particular, (3.5.6) shows that weakening the effect of gravity results in a narrower draining region and a wider pendant-drop region. Within the inner region the film has a capillary-ripple structure consisting of an infinite sequence of alternating dimples and ridges, as sketched in Figure 3.15. Gravity is negligible in the dimples, which are all thinner than the film in the draining region (specifically, the thickness of dimple n is $O(T^{-\alpha_n}) \ll 1$, where $\alpha_n > 1/2$). On the other hand, gravity and capillarity are comparable in the ridges, which are all thicker than the film in the draining region (specifically, the thickness of ridge n is $O(T^{-\delta_n}) \ll 1$, where $\delta_n < 1/2$). The dimples and the ridges are all asymmetric: specifically, the leading-order thickness of the dimples grows quadratically in the downstream direction but linearly in the upstream direction, whereas the leading-order thickness of the ridges goes to zero linearly in the downstream direction but quadratically in the upstream direction. Matching between the inner and the draining region is achieved in the limit $n \to \infty$, in which the exponents α_n and δ_n both approach their common asymptotic value of

1/2. The asymptotic solutions in the draining and pendant-drop regions, as well as those in dimple 1 and ridge 1 in the inner region, were verified by comparison with numerical solutions of the governing thin-film equation. As T increases the regions that have the largest deviation from the $O(T^{-1/2})$ thickness of the draining region (namely, dimple 1 followed by ridge 1) are the first to become discernible, with the other dimples and ridges subsequently becoming apparent in turn. However, since the exponents α_n and δ_n both approach 1/2 rather quickly as n increases (specifically, α_n and β_n both only differ from 1/2 by $O(10^{-n})$), the other dimples and ridges only become apparent for rather large values of T, i.e., only the first few dimples and ridges are likely to be discernible for large but finite times. This is presumably the reason why the corresponding infinite sequence of dimples and ridges was overlooked by Qin *et al.* [105] in their study of the corresponding problem on a spherical substrate.

Whilst several aspects of the structure of the late-time solution described in this chapter have been described by previous authors, such as the formation of a pendant drop on the lower part of the cylinder discussed by Reisfeld and Bankoff [101] and Evans *et al.* [102] and the thinning of the film on the upper part of the cylinder analysed by Takagi and Huppert [103], the work presented in this chapter is the first to provide a complete description of it. In particular, the work presented herein is the first to describe the surprisingly complicated capillary-ripple structure of the inner region which joins the draining and pendant-drop regions.

Note that the late times for which the present analysis is relevant may, in practice, correspond to only minutes or hours. For example, using the representative dimensional parameter values $\hat{R}_1 = 0.1\,\mathrm{m}$, $\hat{\rho} = 10^3\,\mathrm{kg\,m^{-3}}$, and $\hat{\mu} = 10^{-3}\,\mathrm{kg\,m^{-1}\,s^{-1}}$, together with $\epsilon = 0.1$, yields a characteristic timescale of $\hat{R}_1/(\epsilon^2\hat{U}_{\mathrm{char}}) = \hat{\mu}/(\epsilon^2\hat{\rho}\hat{g}\hat{R}_1) = O(10^{-4})\,\mathrm{s}$. Hence $T = O(10^6)$, for which the present late-time asymptotic solution already provides a good description of the flow, corresponds to about two minutes. Of course, as the film thins disjoining pressure effects, which are not included in the present analysis, will eventually become important. Specifically, for the representative parameter values used previously together with $\hat{\sigma} = 10^{-1}\,\mathrm{N\,m^{-1}}$ and Hamaker constant $\hat{A} = 10^{-20}\,\mathrm{J}$, disjoining pressure due to van der Waals forces (see, for example, Reisfeld and Bankoff [101]) becomes comparable to the pressure due to capillarity in dimple 1 (where the film is thinnest and $H = O(T^{-3/5})$) when $T = O(10^8)$, corresponding to about three hours. Hence, whilst the longest final times of up to $T = O(10^{11})$ required to validate the present asymptotic solution

correspond to around four months and are therefore almost certainly unphysical, there is likely to be a considerable period of time during which the present asymptotic solution provides a good description of the flow.

Finally, we note that the two-dimensional model described in this chapter can, of course, be readily extended to three dimensions, and we anticipate that the corresponding analysis of this problem would have many of the same features with that described in this chapter. However, the two-dimensional problem is an interesting problem in its own right and an essential first step towards understanding the three-dimensional problem and can be realised physically by preventing the occurrence of a three-dimensional instability in the axial direction by, for example, using a sufficiently short cylinder and/or imposing an axial electric field (see, for example, González *et al.* [270]).

Chapter 4

Thin-film coating flow in the presence of an electric field

In Chapter 3, we studied the thin-film system that was outlined in Section 2.2 in the absence of both rotation and electrostatic effects. It might be anticipated that the logical next step to understanding the dynamics of the system would be to introduce rotation prior to including electrostatic effects. However, as discussed in detail in Section 1.4.4, this system has already been extensively studied in the literature. Hence, in this chapter, we introduce rotation and electrostatic effects into the system simultaneously (although we return to the stationary case in Section 4.3). The geometry of the dimensionless system considered in this chapter is shown in Figure 4.1.

Firstly, we begin by considering the linear stability of steady states for the film thickness H in two analytically tractable special cases in Section 4.1. In Section 4.2, we conduct a numerical parametric study in (γ, E_b) parameter space in order to determine the full range of qualitatively different behaviours exhibited by the system and identify where in parameter space each of these behaviours occur, in addition to investigating each behaviour numerically. In Section 4.3, we consider the special case in which the cylinder is stationary, and in Section 4.4, we investigate the large-time dynamics of the system by means of a multiple-timescale analysis. Finally, we draw our conclusions in Section 4.5.

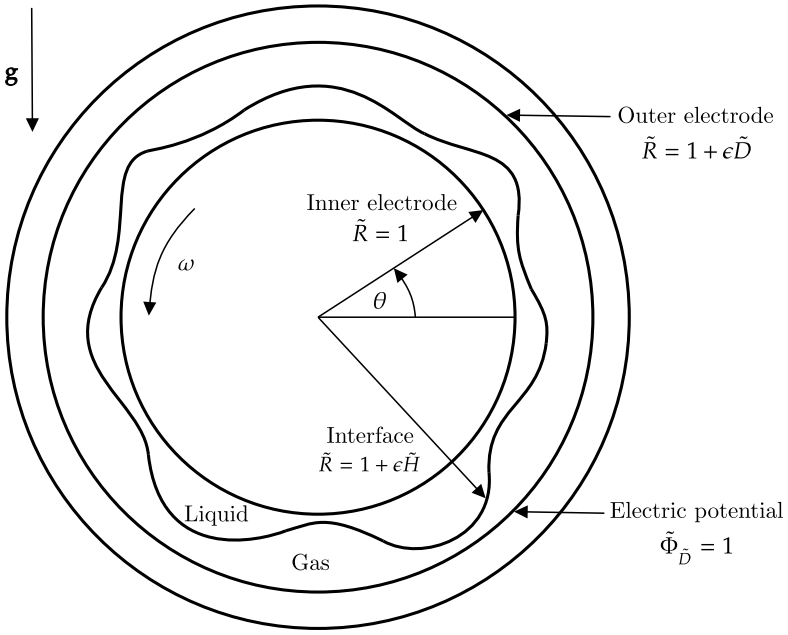

Figure 4.1: Geometry of the dimensionless system considered in Chapter 4.

4.1 Linear stability

In this section, we perform linear stability analyses of two analytically tractable special cases of the governing equation (2.2.23). We consider the stability of steady states with the aim of elucidating the mechanisms by which the flow is stabilised and destabilised. The linear stability of the coating flow problem in the absence of an electric field has been studied previously by many other authors, as discussed in Section 1.4.4. Hence, in this section we are interested primarily in the way in which electrostatic effects affect the stability of the flow.

Note that a full linear stability analysis of the general case would require a numerical approach due to the fact that, even for steady-state solutions, the governing equation (2.2.23) must, in general, be solved numerically. Hence, in this section, in order to proceed analytically we consider two analytically tractable special cases. The first is the case of zero gravity which is analysed in Section 4.1.1, which is analytically tractable owing to the fact that a uniform film is a solution of the governing equation (2.2.23) in the absence of the gravitational term $-H^3\cos\theta$. The second is the case in which both capillarity and electrostatic effects are weak which is analysed in Section 4.1.2. In this case, capillarity and electrostatic effects can be accounted for asymptotically, hence the problem is analytically tractable

owing to the fact that the leading-order solution is the known steady solution of Moffatt [106]. The linear stability of the steady state can then be analysed by following the method presented by Benilov and O'Brien [121], which was discussed in Section 1.4.4.

Note that throughout this section the symbol ω is chosen to represent the complex growth rate of small perturbations, and is not the dimensionless expression for the azimuthal rotation rate (2.1.26). This choice was made for consistency with the notation used by Benilov and O'Brien [121], but should not create any confusion since the rotation rate does not appear in the final governing equation (2.2.23) due to our choice of rescalings (2.2.22).

4.1.1 Zero-gravity case

In this section, we consider the case of zero gravity. In regimes in which electrostatic effects and capillarity are both strong, or when working in a microgravity environment, gravitational effects are dominated by electrostatic and capillary effects, thus gravitational effects may be neglected. Since $\hat{g}$ is used in the definition of $\hat{U}_{\text{char}}$ (2.1.19), this means that in the absence of gravity it is no longer appropriate to use the characteristic drainage velocity, and hence $\hat{U}_{\text{char}}$ must be redefined. In particular, we instead use the capillary velocity scale [56, 146, 151]

$$\hat{U}_{\text{char}} = \frac{\hat{\sigma}}{\hat{\mu}}, \tag{4.1.1}$$

leading to $Ca = 1$. Hence, when $\hat{g} = 0$, (2.2.23) yields

$$H_T + \left[H + \frac{H^3}{3} \left(\frac{1}{\gamma} \left(H_\theta + H_{\theta\theta\theta} \right) + E_b \frac{H_\theta}{(D-H)^3} \right) \right]_\theta = 0, \tag{4.1.2}$$

where H_0 (2.2.25), γ (2.2.26), and D (2.2.28) are redefined as

$$\gamma = \left(\frac{\hat{\sigma}}{\mu \hat{R}_1 \hat{\Omega}} \right)^{1/2}, \quad H_0 = \gamma \frac{\hat{h}_0}{\hat{R}_1}, \quad D = \gamma \left(\frac{\hat{R}_2}{\hat{R}_1} - 1 \right), \tag{4.1.3}$$

respectively, and E_b (2.2.27) remains unchanged. Note that γ still appears in (4.1.2) despite the fact that $Ca = 1$ due to the earlier rescalings (2.2.22). A uniform film $H = \bar{H}$, where $\bar{H}$ is a constant, is now a solution of the governing equation (4.1.2). We investigate the linear stability of this steady state by introducing a

small perturbation $\hat{H}$ by setting

$$H = \bar{H} + \xi \hat{H}(\theta, T), \tag{4.1.4}$$

where $\xi \ll 1$. We seek solutions of the form

$$\hat{H}(\theta, T) = \psi(\theta) \mathrm{e}^{-i\omega T}, \tag{4.1.5}$$

where $\omega = \omega(n)$ is the complex growth rate and $\psi(\theta) = \mathrm{e}^{in\theta}$ (corresponding to decomposition into normal modes) in which n is the wavenumber of the perturbation (which must be an integer due to the spatial periodicity of H). Substitution of (4.1.4) with (4.1.5) into the governing equation (4.1.2) and linearising with respect to ξ yields the dispersion relation,

$$\omega(n) = n + \frac{n^2}{3}\bar{H}^3 \left(\frac{E_b}{(D-\bar{H})^3} - \frac{1}{\gamma}(n^2-1) \right) i. \tag{4.1.6}$$

The imaginary component of (4.1.6) is the linear growth rate of the perturbations, namely,

$$\mathrm{Im}(\omega) = \frac{n^2}{3}\bar{H}^3 \left(\frac{E_b}{(D-\bar{H})^3} - \frac{1}{\gamma}(n^2-1) \right). \tag{4.1.7}$$

The steady state $\bar{H}$ is linearly unstable when $\mathrm{Im}(\omega) > 0$. Note that by (4.1.7), $\bar{H}$ is neutrally stable for $n = 0$. The cutoff wavenumber (i.e., the critical value of the wavenumber below which perturbations will grow, leading to instability), which we shall denote by n_c, is the value of n for which $\mathrm{Im}(\omega) = 0$, namely,

$$n_\mathrm{c} = \left\lfloor \left(1 + \frac{\gamma E_b}{(D-\bar{H})^3} \right)^{1/2} \right\rfloor, \tag{4.1.8}$$

where $\lfloor \cdot \rfloor$ represents the largest integer smaller than the argument. Perturbations with wavenumbers greater than n_c become damped due to the effect of capillarity and are hence stable, whereas perturbations with wavenumbers smaller than n_c grow in amplitude under the action of electrostatic effects and are hence unstable. The fastest growing wavenumber (i.e., the wavenumber at which small perturbations experience the largest amplification early in the evolution of the system),

which we shall denote by $n_{\max}$, is the value of n for which $[\mathrm{Im}(\omega)]_n = 0$, namely,

$$n_{\max} = \left[\frac{1}{\sqrt{2}} \left(1 + \frac{\gamma E_b}{(D - \bar{H})^3} \right)^{1/2} \right], \tag{4.1.9}$$

where $[\cdot]$ represents the integer closest to the argument. Substitution of (4.1.9) into (4.1.7) yields the most unstable growth rate, namely,

$$\mathrm{Im}\left(\omega_{\max}\right) = \frac{\bar{H}^3}{3} \left[\frac{1}{\sqrt{2}} \left(1 + \frac{\gamma E_b}{(D - \bar{H})^3} \right)^{1/2} \right]^2 \left(\frac{E_b}{(D - \bar{H})^3} - \frac{1}{\gamma}(n_{\max}^2 - 1) \right). \tag{4.1.10}$$

By (4.1.8) and (4.1.9), it is clear that increasing the electric potential difference E_b has a destabilising influence. Specifically, increasing the value of E_b results in both an increase in the cutoff wavenumber (resulting in a wider range of unstable wavenumbers) and an increase in the fastest growing wavenumber. This is demonstrated in Figure 4.2, which shows the growth rate $\mathrm{Im}(\omega)$ (4.1.7) calculated for various values of E_b with $\bar{H} = H_0 = 0.2$ and $\gamma = 30$, which correspond to the following dimensional quantities to three significant figures,

$$\begin{gathered} \hat{R}_1 = 1.00 \times 10^{-2} \text{ m}, \quad \hat{h}_0 = 6.67 \times 10^{-5} \text{ m}, \quad \hat{\sigma} = 1.80 \times 10^{-1} \text{ kg s}^{-2}, \\ \hat{\mu} = 8.00 \times 10^{-3} \text{ kg m}^{-1}\text{s}^{-1}, \quad \hat{\rho} = 1.00 \times 10^{3} \text{ kg m}^{-3}, \quad \hat{\Omega} = 2.5 \text{ rad s}^{-1}, \end{gathered} \tag{4.1.11}$$

for (a), (b) $D = 2$ and (c), (d) $D = 3$, which correspond to the outer electrode having dimensional radius $\hat{R}_2 = 1.10 \times 10^{-2}$ m and $\hat{R}_2 = 1.07 \times 10^{-2}$ m, respectively. Specifically, Figure 4.2 shows the growth rate calculated for $E_b = 0, 10, 20, 30, 40,$ and 50, which corresponds to varying the dimensional potential at the outer electrode over the range

$$0 \text{ V} \leq \hat{\phi}_b \leq 1.5 \text{ V}. \tag{4.1.12}$$

Note that the upper limit of $\hat{\phi}_b = 1.5$ V in (4.1.12) was chosen based on the results of the parametric study that will be discussed next in Section 4.2. Specifically, during our preliminary numerical investigations, we found that choosing $\hat{\phi}_b$ values greater than approximately 1.5 V does not allow the most interesting behaviours to arise for a (relatively small) dimensionless electrode distance of $D = 3$. Specifically, a phenomena termed as "outer contact", occurs early in time for larger values of

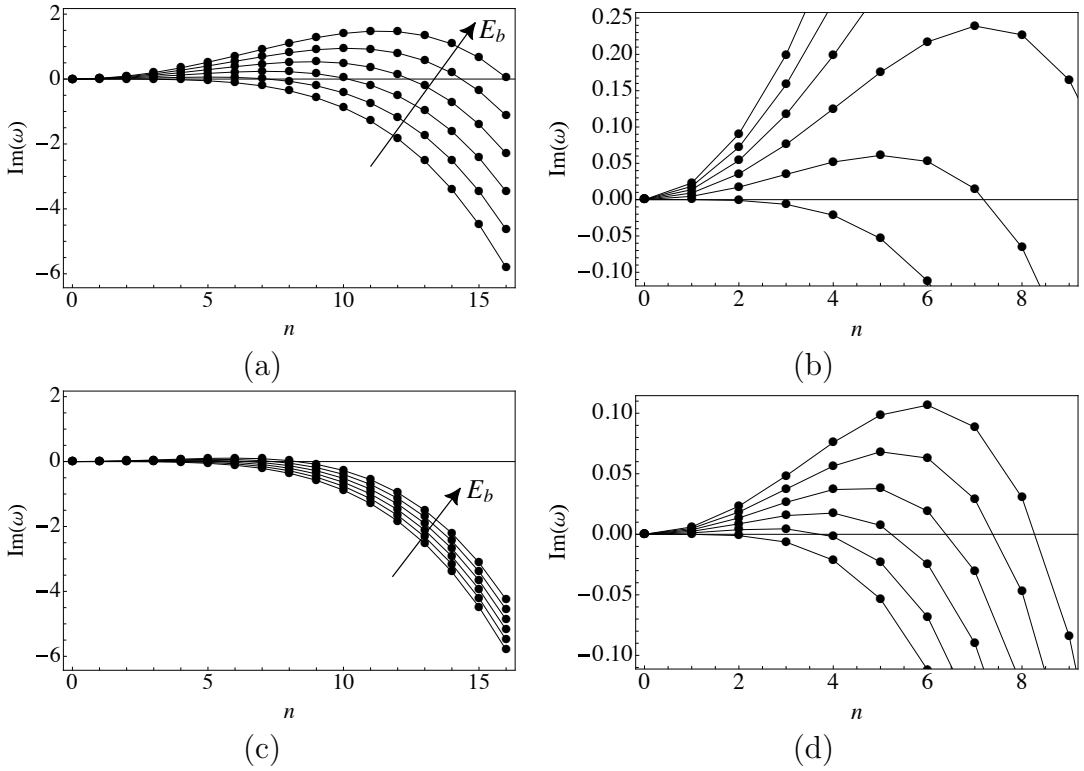

Figure 4.2: The growth rate $\mathrm{Im}(\omega)$ (4.1.7) calculated for (a), (b) $D = 2$ and (c), (d) $D = 3$ with $\bar{H} = 0.2$, $\gamma = 30$, and $E_b = 0, 10, 20, 30, 40$, and 50 over the range of wavenumbers (a), (c) $0 \leq n \leq 16$ and (b), (d) $0 \leq n \leq 8$. The arrow indicates the direction of increasing E_b and the filled circles correspond to integer values of n.

$\hat{\phi}_b$, which we shall discuss both later in this section and in further detail in Section 4.2.5. Additionally, 1.5 V is a reasonable and physically justifiable choice, yielding $\hat{\phi}_b/(\hat{R}_2 - \hat{R}_1) \approx 1.5 \times 10^3$ V m^{-1}, which is below the dielectric limit of air (which is approximately 3×10^6 V m^{-1} [271]). In addition, note that the dimensional quantities (4.1.1) are based on a water-glycerine mix [102, 272], however, we have chosen to use a higher coefficient of surface tension than the true physical value of a water-glycerine mix (which is 5.9×10^{-2} kg s^{-2} [102, 272]) in order to see the more complex behaviours that can arise.

Figure 4.2 shows that increasing the value of D (corresponding to moving the outer electrode further from the interface) decreases the destabilising effect of the electric field, reflected in the smaller range of unstable wavenumbers and lower growth rates in Figure 4.2 (c) compared to those in Figure 4.2 (a). It is clear from Figures 4.2 (b) and (d), which show a closer view near $\mathrm{Im}(\omega) = 0$, that solutions for $E_b = 0$ are neutrally stable for $n = 0$ and $n = 1$ and stable for $n > 1$ (in agreement with the result of Evans *et al.* [102] who, as discussed in Section 1.4.4, showed that the system is stable in the presence of capillarity in the absence of electrostatic effects and centrifugation).

Note that in the absence of an electric field, the evolution is periodic for the parameter values $H_0 = 0.2$ and $\gamma = 30$. However, the interface ultimately remains close to circular. This can be seen from Figure 4.3, which shows the numerical solution of the full governing equation (2.2.23) (i.e., with gravitational effects included) for $E_b = 0$. In particular, Figure 4.3 shows (a) the spatiotemporal evolution of the film thickness H, (b) the interfacial shape at the time $T = 44.6$ (by which time the system has reached a periodic state), and (c) the evolution of the maximum (black line) and minimum (solid line) film thicknesses over time, which we denote by $H_{\max} = H_{\max}(\theta)$ and $H_{\min} = H_{\min}(\theta)$, respectively.

The perturbation with the fastest-growing wavenumber (4.1.9) experiences the most rapid growth and is therefore the disturbance that is most likely to be observable in numerical and experimental results before nonlinear effects become significant. Whilst linear stability results provide valuable insights into only the initial stages of interface growth and development, they maintain significance in the nonlinear evolution due to the influence of dominant modes (in this case, the fastest-growing wavenumber (4.1.9)) persisting into the nonlinear regime. With this in mind, we now compare the results of our linear stability analysis with numerical solutions of the full governing equation (2.2.23). We use the parameter

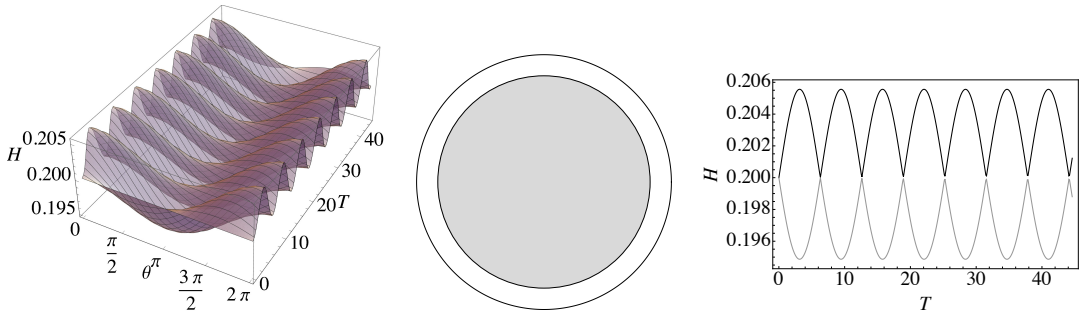

(a) (b) (c)

Figure 4.3: The numerical solution for the film thickness H calculated from the full governing equation (2.2.23) for $H_0 = 0.2$ and $\gamma = 30$ with $E_b = 0$. (a) The spatiotemporal evolution of H over the time interval $0 \leq T \leq 44.6$. (b) The interfacial shape at time $T = 44.6$. (Note that the film thickness has been exaggerated for illustrative purposes by using the artificial value $\epsilon = 1$). (c) The evolution of the maximum and minimum values of the film thickness $H_{\max}$ (black) and $H_{\min}$ (grey), respectively, over the time interval $0 \leq T \leq 44.6$.

values $H_0 = 0.2$ and $\gamma = 30$ with $E_b = 10, 30$, and 50. The results of these numerical calculations are shown in Figures 4.4 and 4.5 for $D = 2$ and $D = 3$, respectively. Our results indicate that as the film evolves, the destabilising electrostatic effects result in a growth in amplitude of initially small perturbations, ultimately leading to the formation of bulges of liquid separated by a thin film, which are approximately evenly spaced around the circumference of the cylinder. This behaviour can be seen in Figures 4.4 and 4.5 (a)–(c), which show the spatiotemporal evolution of the film thickness. This behaviour is qualitatively similar to that described by Evans *et al.* [102] who, as discussed in Section 1.4.4, found that for the zero-gravity case in the absence of an electric field but in the presence of centrifugal effects, small perturbations grow due to centrifugation which results in the formation of bulges of liquid around the cylinder. It follows that, physically, the value of the fastest growing wavenumber $n_{\max}$ (4.1.9) corresponds to the number of bulges that are most likely to be observable in the numerical calculations. The electric field exerts a normal Maxwell stress on the interface which results in the film being "pulled" towards the outer electrode. Our results indicate that when the electric potential difference is large or capillarity is weak, the interface can evolve to touch the outer electrode in a finite time; we shall refer to this behaviour hereafter as "outer contact", of which we defer a detailed discussion until

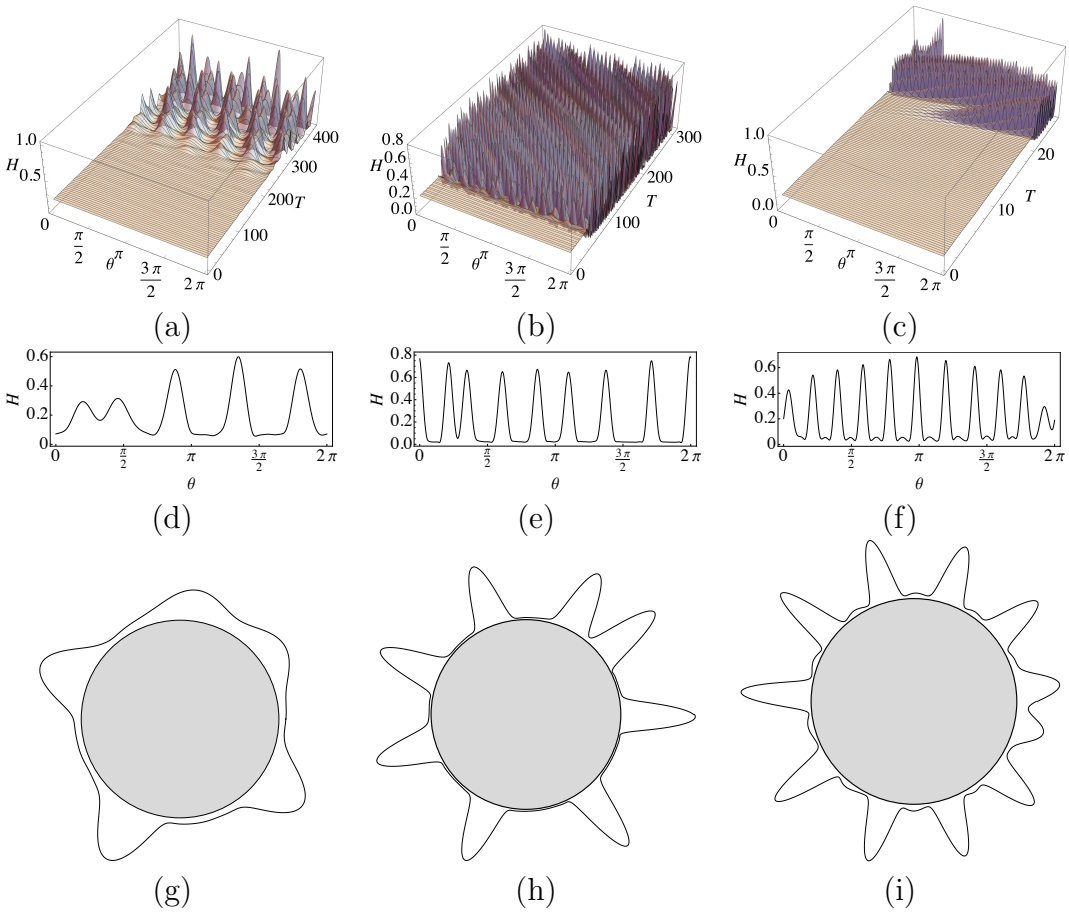

Figure 4.4: The numerical solution for the film thickness H calculated from the full governing equation (2.2.23) for $D = 2$ with (a), (d), (g) $E_b = 10$, (b), (e), (h) $E_b = 30$, and (c), (f), (i) $E_b = 50$. (a)–(c) The spatiotemporal evolution of H over the time interval $0 \leq T \leq T_c$ where $T_c = 426.782, 310.878$, and 26.3979, respectively. (d)–(f) The film thickness H and (g)–(i) the interfacial shape shown at times $T = 328.4, 310$, and 25 for $E_b = 10, 30$, and 50, respectively. (Note that the film thickness has been exaggerated for illustrative purposes by using the artificial value $\epsilon = 1$).

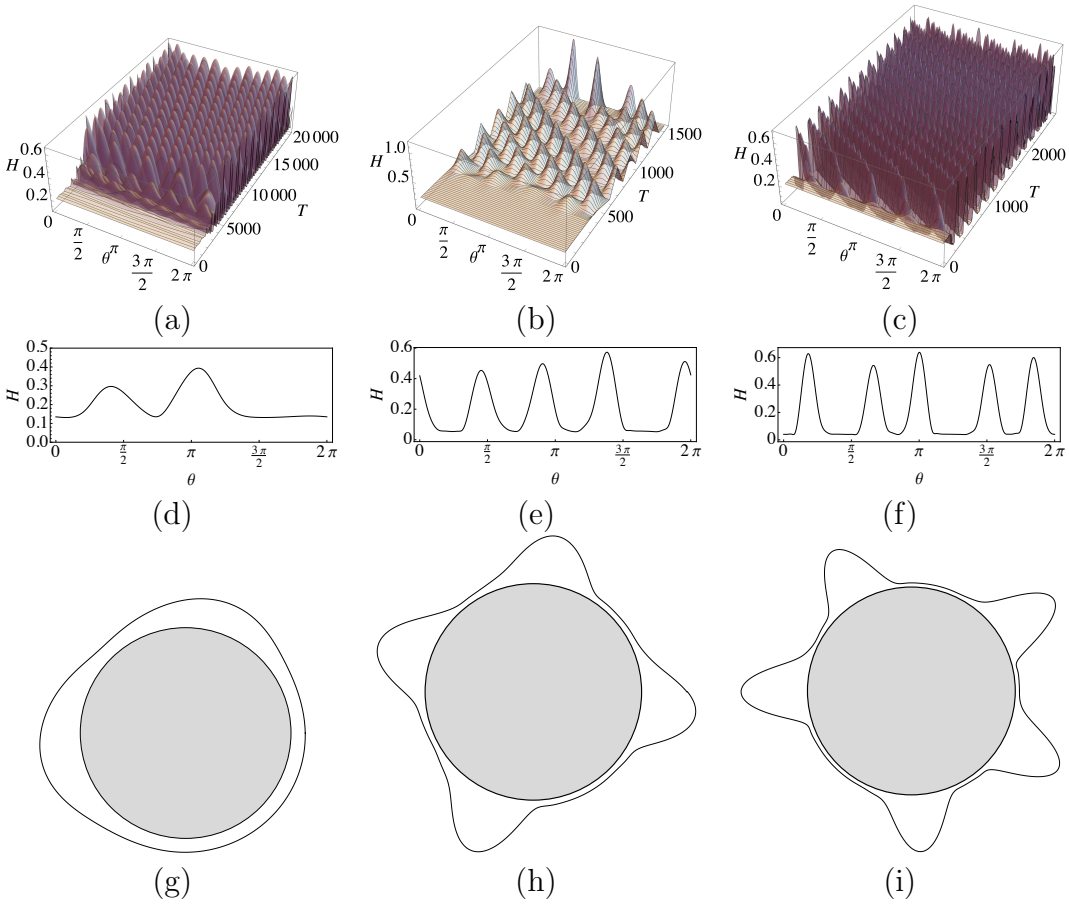

Figure 4.5: The numerical solution for the film thickness H calculated from the full governing equation (2.2.23) for $D = 3$ with (a), (d), (g) $E_b = 10$, (b), (e), (h) $E_b = 30$, and (c), (f), (i) $E_b = 50$. (a)–(c) The spatiotemporal evolution of H over the time interval (a) $0 \leq T \leq 20000$, (b) $0 \leq T \leq T_c$ where $T_c = 1550.93$, and (c) $0 \leq T \leq T_c$ where $T_c = 2789.31$. (d)–(f) The film thickness H and (g)–(i) the interfacial shape shown at times $T = 3671, 851.1$, and 2289.5, respectively. (Note that the film thickness has been exaggerated for illustrative purposes by using the artificial value $\epsilon = 1$).

Section 4.2.5. Hereafter, we denote the time at which outer contact occurs as T_c. Note that it is extremely difficult to calculate T_c exactly. Hence, in the numerical results presented throughout this thesis, T_c is in fact the final time at which the code converges before outer contact, rather than the exact time at which it occurs. Note that all of the qualitatively different behaviours that the system exhibits will be examined and discussed in detail in Section 4.2.

By (4.1.9), the linear stability analysis predicts that the fastest growing wavenumbers for $D = 2$ with $E_b = 10, 30$, and 50 are $n_{\max} \approx [5.12056] = 5$, $n_{\max} \approx [8.81252] = 9$, and $n_{\max} \approx [11.3623] = 11$, respectively. Figures 4.4 (d) and (g), (e) and (h), and (f) and (i) show that $5, 8$, and 11 distinct bulges of liquid have formed around the cylinder in the numerical solution by the late times $T = 328.4, 310$, and 25 for $E_b = 10, 30$, and 50, respectively, all of which eventually coalesce as the system evolves towards outer contact behaviour by times $T_c = 426.782, 310.878$, and 26.3979, respectively. For $D = 3$, the linear stability analysis predicts that the fastest growing wavenumbers for $E_b = 10, 30$, and 50 are $n_{\max} \approx [2.70797] = 3$, $n_{\max} \approx [4.58250] = 5$, and $n_{\max} \approx [5.88774] = 6$, respectively. Figures 4.5 (d) and (g), (e) and (h), and (f) and (i) show that $2, 4$, and 5 distinct bulges have formed around the cylinder in the numerical solution by the late times $T = 3671, 851.1$, and 2289.5 for $E_b = 10, 30$, and 50, respectively. For $E_b = 10$, the two bulges coalesce and the system eventually evolves towards a periodic state (of which we defer a detailed discussion until Section 4.2.4), whereas for $E_b = 30$ and $E_b = 50$, the bulges coalesce as the system evolves towards outer contact behaviour by times $T_c = 1550.93$ and $T_c = 2789.31$, respectively. Thus, we conclude that the linear theory in the zero-gravity case yields an accurate prediction of the behaviour of the complete system (i.e., in the presence of gravity) at later times in the evolution.

4.1.2 Weak capillarity and weak electrostatic effects

In this section, we examine the linear stability of the nonuniform steady state $H(\theta, T) = \bar{H}(\theta)$ (which, as we will show, is the known solution to the steady equation (1.4.5) analysed by Moffatt [106]) of the governing equation (2.2.23) in the case in which both capillarity and electrostatic effects are weak. We proceed by following the method of Benilov and O'Brien [121] who, as discussed in Section 1.4.4, investigated how the stability of normal modes in thin-film rimming flow is affected by weak inertia, hydrostatic pressure gradient, and capillarity, which arise

as higher-order terms in the lubrication model. They found that inertia always destabilises the system, the effect of capillarity is weak but stabilising, and that the hydrostatic pressure gradient has no effect on the stability. The aim of this section is to examine how the inclusion of weak electrostatic effects impacts the stability of the nonuniform steady state $\bar{H}(\theta)$, whilst also considering the influence of weak capillarity.

We investigate the linear stability of the steady state $\bar{H}(\theta)$ by introducing a small perturbation by setting

$$H(\theta, T) = \bar{H}(\theta) + \xi \tilde{H}(\theta, T), \tag{4.1.13}$$

where $\xi \ll 1$. Substituting (4.1.13) into (2.2.24) and linearising with respect to ξ yields

$$\tilde{H}_T + \left[A(\theta)\tilde{H}_\theta + B(\theta)\left(\tilde{H}_\theta + \tilde{H}_{\theta\theta\theta}\right) + C(\theta)\tilde{H} \right]_\theta = 0, \tag{4.1.14}$$

where $A(\theta)$, $B(\theta)$, and $C(\theta)$ are

$$A(\theta) = \frac{E_b}{3}\left(\frac{\bar{H}}{D - \bar{H}}\right)^3, \tag{4.1.15}$$

$$B(\theta) = \frac{1}{3\gamma}\bar{H}^3, \tag{4.1.16}$$

$$C(\theta) = 1 - \cos\theta \bar{H}^2 + \frac{1}{\gamma}\bar{H}^2(\bar{H}_\theta + \bar{H}_{\theta\theta\theta}) + DE_b \frac{\bar{H}^2}{(D - \bar{H})^4}\bar{H}_\theta, \tag{4.1.17}$$

respectively. We proceed by seeking solutions of the form

$$\tilde{H}(\theta, T) = \psi(\theta)\mathrm{e}^{-i\omega T}, \tag{4.1.18}$$

where $\omega = \omega(n)$ is the complex growth rate of the perturbations. It follows that steady solutions $\bar{H}(\theta)$ are neutrally stable for $\mathrm{Im}(\omega) = 0$, stable for $\mathrm{Im}(\omega) < 0$, and unstable for $\mathrm{Im}(\omega) > 0$. Substitution of (4.1.18) into (4.1.14) yields

$$\left[A(\theta)\psi_\theta + B(\theta)(\psi_\theta + \psi_{\theta\theta\theta}) + C(\theta)\psi \right]_\theta - i\omega\psi = 0. \tag{4.1.19}$$

Equation (4.1.19), together with the periodicity condition

$$\psi(\theta + 2\pi) = \psi(\theta), \tag{4.1.20}$$

together constitute an eigenvalue problem involving the eigenfunction $\psi(\theta)$ and eigenvalue ω.

In order to proceed analytically, we work in the distinguished limit in which both capillarity and electrostatic effects are weak by setting

$$E_b = \gamma^{-1}\hat{E}_b, \tag{4.1.21}$$

where $\gamma^{-1} \ll 1$ and $\hat{E}_b = O(1)$, which will allow us to examine a nonuniform steady state $\bar{H}(\theta)$ which can be expressed in an analytical form. The steady state $\bar{H}(\theta)$ in this special case can now be determined. Expanding $\bar{H}$ in powers of γ^{-1} yields

$$\bar{H}(\theta) = \bar{H}_0 + \gamma^{-1}\bar{H}_1 + O(\gamma^{-2}), \tag{4.1.22}$$

where $\bar{H}_0 = \bar{H}_0(\theta)$ satisfies

$$\bar{H}_0 - \frac{1}{3}\bar{H}_0^3\cos\theta = Q. \tag{4.1.23}$$

As discussed in Section 1.4.4, equation (4.1.23) was analysed by Moffatt [106] who showed that the system admits full-film solutions only if Q remains within the range $0 < Q \leq Q_{\text{crit}}$ where $Q_{\text{crit}} = 2/3$. Subsequently, the solution $\bar{H}_0$ was shown to be neutrally stable by O'Brien [127]. As discussed previously, full-film solutions $\bar{H}_0$ (as derived by Duffy and Wilson [100]) are shown in Figure 1.12 for two subcritical values of Q and for the critical flux $Q = Q_{\text{crit}}$. In this section, we shall denote the critical solution by $\bar{H}_{0\text{crit}}$. Note that throughout this analysis we only require the steady solution $\bar{H}$ to leading order in γ^{-1}, but that higher-order terms of the expansion (4.1.22) can be calculated in the usual way by solving order-by-order. For example, at first order, substitution of (4.1.22) into the flux equation (2.2.24) and solving for $\bar{H}_1$ yields

$$\bar{H}_1 = -\frac{1}{3}\frac{\bar{H}_0^3}{(1-\bar{H}_0^2\cos\theta)}\left[\bar{H}_{0\theta} + \bar{H}_{0\theta\theta\theta} + \hat{E}_b\frac{\bar{H}_{0\theta}}{(D-\bar{H}_0)^3}\right]. \tag{4.1.24}$$

The aim of this section is to determine the linear growth rate of the perturbations, denoted by ω. To achieve this, we utilise the method presented by Benilov and O'Brien [121]. Specifically, we begin by expanding the eigenfunction ψ and eigenvalue ω in (4.1.14) as a series in powers of γ^{-1}. Next, we solve the resulting ODE at leading order to obtain the leading-order solutions for ψ and ω. As demon-

strated by Benilov and O'Brien [121], this analysis reveals that the disturbance is neutrally stable at leading order. At first order, capillarity and electrostatic effects become significant. Therefore, we must consider the first-order problem to understand their impact on the stability. To proceed, we solve the ODE arising at first order to find the first-order solution for ω. Note that the method crucially facilitates the analytical tractability of computing the first-order solution for ω by removing the requirement to compute the first-order solution for ψ (which is a difficult calculation) by instead calculating its adjoint (which is a significantly simpler calculation) [121]. Finally, we examine the imaginary component of ω to determine the linear growth rate at first order in γ^{-1}, enabling us to understand how capillarity and electrostatic effects influence the stability.

Substituting (4.1.22) with (4.1.23) and (4.1.24) into (4.1.15)–(4.1.17) yields

$$A(\theta) = \gamma^{-1}A_1 + O(\gamma^{-2}), \tag{4.1.25}$$

$$B(\theta) = \gamma^{-1}B_1 + O(\gamma^{-2}), \tag{4.1.26}$$

$$C(\theta) = C_0 + \gamma^{-1}C_1 + O(\gamma^{-2}), \tag{4.1.27}$$

where $A_1(\theta)$, $B_1(\theta)$, $C_0(\theta)$, and $C_1(\theta)$ are

$$A_1 = \frac{\hat{E}_b}{3}\left(\frac{\bar{H}_0}{D-\bar{H}_0}\right)^3, \tag{4.1.28}$$

$$B_1 = \frac{1}{3}\bar{H}_0^3, \tag{4.1.29}$$

$$C_0 = 1 - \bar{H}_0^2\cos\theta, \tag{4.1.30}$$

$$C_1 = -2\bar{H}_0\bar{H}_1\cos\theta + \bar{H}_0^2\left[\bar{H}_{0\theta} + \bar{H}_{0\theta\theta\theta} + D\hat{E}_b\frac{\bar{H}_{0\theta}}{(D-\bar{H}_0)^4}\right], \tag{4.1.31}$$

respectively. Thus, substituting (4.1.25)–(4.1.27) into (4.1.19) yields

$$\left\{C_0\psi + \gamma^{-1}\left[C_1\psi + A_1\psi_\theta + B_1(\psi_\theta + \psi_{\theta\theta\theta})\right]\right\}_\theta - i\omega\psi + O(\gamma^{-2}) = 0. \tag{4.1.32}$$

We seek a solution of (4.1.32) by expanding the eigenfunction ψ and eigenvalue ω, respectively, as

$$\psi(\theta) = \psi_0(\theta) + \gamma^{-1}\psi_1(\theta) + O(\gamma^{-2}), \tag{4.1.33}$$

$$\omega = \omega_0 + \gamma^{-1}\omega_1 + O(\gamma^{-2}). \tag{4.1.34}$$

To leading order, substituting (4.1.33) and (4.1.34) into (4.1.32) yields the first-order ODE for ψ_0, namely,

$$[C_0\psi_0]_\theta - i\omega_0\psi_0 = 0, \tag{4.1.35}$$

which has the exact solution

$$\psi_0 = \frac{1}{C_0(\theta)} \exp\left[i\omega_0 \int_0^\theta \frac{\mathrm{d}\theta}{C_0(\theta)}\right]. \tag{4.1.36}$$

For ψ_0 to be periodic in θ with period 2π we require

$$\omega_0 = \frac{2\pi n}{\displaystyle\int_0^{2\pi} \frac{\mathrm{d}\theta}{C_0(\theta)}}, \tag{4.1.37}$$

where n is the integer mode number. By (4.1.18), the stability of $\bar{H}$ is determined from the imaginary part of ω. By (4.1.37), $\mathrm{Im}(\omega) = 0$ to leading order, corresponding to the neutral stability of the leading-order solution given by Moffatt [106, 127]. Hence, as alluded to previously, we must go to first order to understand how capillarity and electrostatic effects affect the stability.

At first order, substitution of (4.1.33) and (4.1.34) into (4.1.32) yields the ODE for ψ_1, namely,

$$[C_0\psi_1]_\theta - i\omega_0\psi_1 = i\omega_1\psi_0 - \left[C_1\psi_0 + A_1\psi_{0\theta} + B_1(\psi_{0\theta} + \psi_{0\theta\theta\theta})\right]_\theta. \tag{4.1.38}$$

As explained by Benilov and O'Brien [121], equation (4.1.38) has a periodic solution for ψ_1 if and only if its right-hand side is orthogonal to the adjoint solution $\psi_1^+ = \psi_1^+(\theta)$. We proceed as in [121] by multiplying (4.1.38) by ψ_1^+ and integrating over the domain $0 \le \theta \le 2\pi$, yielding

$$\begin{aligned} &\int_0^{2\pi} \psi_1^+ \Big\{ [C_0\psi_1]_\theta - i\omega_0\psi_1 \Big\}\, \mathrm{d}\theta \\ &= \int_0^{2\pi} \psi_1^+ \Big\{ i\omega_1\psi_0 - \Big[C_1\psi_0 + A_1\psi_{0\theta} + B_1(\psi_{0\theta} + \psi_{0\theta\theta\theta})\Big]_\theta \Big\}\, \mathrm{d}\theta. \end{aligned} \tag{4.1.39}$$

Considering the left-hand side of (4.1.39), we have

$$\int_0^{2\pi} \psi_1^+ \Big\{ [C_0\psi_1]_\theta - i\omega_0\psi_1 \Big\} \,\mathrm{d}\theta = \int_0^{2\pi} \psi_1^+ [C_0\psi_1]_\theta \,\mathrm{d}\theta - \int_0^{2\pi} i\omega_0\psi_1\psi_1^+ \,\mathrm{d}\theta$$
$$= [C_0\psi_1\psi_1^+]_0^{2\pi} - \int_0^{2\pi} \psi_1\{i\omega_0\psi_1^+ + C_0(\psi_1^+)_\theta\} \,\mathrm{d}\theta, \tag{4.1.40}$$

where the second line is obtained by performing integration by parts on the first term on the right-hand side of the first line. Since ψ_1 is assumed to be 2π-periodic by the periodicity condition (4.1.20), we find that $[C_0\psi_1\psi_1^+]_0^{2\pi} = 0$. Hence, for the right-hand side of (4.1.39) to be equal to zero (and, consequently, for the right-hand side of (4.1.38) to be orthogonal to the adjoint solution ψ_1^+), we require that the integrand on the second line is equal to zero. Setting $i\omega_0\psi_1^+ + C_0(\psi_1^+)_\theta = 0$ and solving for ψ_1^+ yields the adjoint solution,

$$\psi_1^+ = \exp\bigg[- i\omega_0 \int_0^\theta \frac{\mathrm{d}\theta}{C_0(\theta)} \bigg], \tag{4.1.41}$$

which is 2π-periodic by (4.1.37). It follows that the right-hand side of (4.1.39) is equal to zero, i.e.,

$$\int_0^{2\pi} \psi_1^+ \Big\{ i\omega_1\psi_0 - \Big[C_1\psi_0 + A_1\psi_{0\theta} + B_1(\psi_{0\theta} + \psi_{0\theta\theta\theta}) \Big]_\theta \Big\} \,\mathrm{d}\theta = 0, \tag{4.1.42}$$

where ψ_1^+ is given by (4.1.41) and ψ_0 is given by (4.1.36). The benefit of this method is now clear: it allows us to eliminate the unknown function ψ_1 from the problem, thus leaving us in a position to be able to obtain ω_1 in terms of the known functions ψ_0 (4.1.36) and ψ_1^+ (4.1.41). Equation (4.1.42) can be written as

$$\underbrace{i\omega_1 \int_0^{2\pi} \psi_1^+\psi_0 \,\mathrm{d}\theta}_{I_1} \underbrace{- \int_0^{2\pi} \psi_1^+ \Big[C_1\psi_0 + A_1\psi_{0\theta} + B_1(\psi_{0\theta} + \psi_{0\theta\theta\theta}) \Big]_\theta \,\mathrm{d}\theta}_{I_2} = 0, \tag{4.1.43}$$

where the first integral I_1 can be expressed as

$$I_1 = i\omega_1 \int_0^{2\pi} \frac{\mathrm{d}\theta}{C_0}, \tag{4.1.44}$$

and the second integral I_2 can be expressed (via an application of integration by parts) as

$$\begin{aligned} I_2 &= \left[\psi_1^+\left\{C_1\psi_0 + A_1\psi_{0\theta} + B_1(\psi_{0\theta} + \psi_{0\theta\theta\theta})\right\}\right]_0^{2\pi} \\ &\quad - \int_0^{2\pi}\left[C_1\psi_0(\psi_1^+)_\theta + A_1\psi_{0\theta}(\psi_1^+)_\theta + B_1(\psi_{0\theta}(\psi_1^+)_\theta + \psi_{0\theta\theta\theta}(\psi_1^+)_\theta)\right]\,\mathrm{d}\theta \\ &= -\int_0^{2\pi}\left[C_1\psi_0(\psi_1^+)_\theta + A_1\psi_{0\theta}(\psi_1^+)_\theta + B_1(\psi_{0\theta}(\psi_1^+)_\theta + \psi_{0\theta\theta\theta}(\psi_1^+)_\theta)\right]\,\mathrm{d}\theta, \end{aligned} \tag{4.1.45}$$

where the terms on the first line are identically zero by periodicity of the adjoint solution ψ_1^+. The final expression for I_2 is thus given by

$$\begin{aligned} I_2 = -\int_0^{2\pi}\frac{i\omega_0}{C_0}\Bigg\{&\frac{C_1}{C_0} + \left[\left(C_0^{-1}\right)_\theta - \frac{i\omega_0}{C_0^2}\right]A_1 + \Bigg[\left(C_0^{-1}\right)_{\theta\theta\theta} - \frac{4i\omega_0}{C_0}\left(C_0^{-1}\right)_{\theta\theta} \\ &- 3i\omega_0\left(C_0^{-1}\right)_\theta^2 - \frac{6\omega_0^2}{C_0^2}\left(C_0^{-1}\right)_\theta + \frac{i\omega_0^3}{C_0^4} + \left(C_0^{-1}\right)_\theta - \frac{i\omega_0}{C_0^2}\Bigg]B_1\Bigg\}\,\mathrm{d}\theta. \end{aligned} \tag{4.1.46}$$

It follows from (4.1.44) and (4.1.46) that

$$\begin{aligned} 0 &= I_1 - I_2 \\ &= i\omega_1\int_0^{2\pi}\frac{\mathrm{d}\theta}{C_0} + \int_0^{2\pi}\Bigg\{B_1\Bigg[\left(C_0^{-1}\right)_{\theta\theta\theta} - \frac{4i\omega_0}{C_0}\left(C_0^{-1}\right)_{\theta\theta} - 3i\omega_0\left(C_0^{-1}\right)_\theta^2 \\ &\quad - \frac{6\omega_0^2}{C_0^2}\left(C_0^{-1}\right)_\theta + \frac{i\omega_0^3}{C_0^4} + \left(C_0^{-1}\right)_\theta - \frac{i\omega_0}{C_0^2}\Bigg] + \frac{C_1}{C_0} + A_1\Bigg[\left(C_0^{-1}\right)_\theta - \frac{i\omega_0}{C_0^2}\Bigg]\Bigg\}\frac{i\omega_0}{C_0}\,\mathrm{d}\theta. \end{aligned} \tag{4.1.47}$$

Solving (4.1.47) for ω_1 and taking the imaginary part yields

$$\begin{aligned} \mathrm{Im}(\omega_1) = &\left(\int_0^{2\pi}\frac{\mathrm{d}\theta}{C_0}\right)^{-1} \\ &\times\left[\omega_0^2\int_0^{2\pi}\left\{\frac{B_1}{C_0^3}\left(1 - \frac{1}{C_0^2}\left[\omega_0^2 + 4C_0\left(C_0\right)_{\theta\theta} - 11\left(C_0\right)_\theta^2\right]\right) + \frac{A_1}{C_0^3}\right\}\,\mathrm{d}\theta\right]. \end{aligned} \tag{4.1.48}$$

Equation (4.1.48) is the main result of this section. Note that since $\mathrm{Im}\left(\omega_0\right) = 0$, the steady state $\bar{H}(\theta)$ is unstable for $\mathrm{Im}(\omega_1) > 0$. Electrostatic effects only enter the stability calculation via A_1 (4.1.28). Note that an electrostatic term also arises in the expression for C_1 (4.1.31), however, since this only appears in the real part of ω_1, it does not contribute to the stability. We can recover equation (24) of

Benilov and O'Brien [121] from (4.1.48) by setting $\hat{E}_b = 0$, such that $A_1 = 0$. Benilov and O'Brien [121] showed that in the absence of an electric field, $\mathrm{Im}(\omega)$ is negative for all Q, showing that capillarity is always a stabilising influence[1].

Throughout this section, the terms in (4.1.48) were calculated numerically using the symbolic computational system Mathematica [265]. Firstly, values of the solution of the leading-order steady problem (4.1.23) $\bar{H}_0$ were calculated over the range $0 \leq \theta \leq 2\pi$. The computed values were then utilised to construct an interpolation using the built-in function `Interpolation[]` by applying a third-order spline method. Using this, the integrals in (4.1.48) were calculated numerically using the built-in function `NIntegrate[]`. Values of these integrals were calculated over the range $0 \leq Q \leq Q_{\mathrm{crit}}$ and were then interpolated again using `Interpolation[]` by applying a fifth-order spline method. Figure 4.6 shows $\mathrm{Im}(\omega)$ (4.1.53) with $D = 2$ and $\gamma^{-1} = 0.1$ plotted as a function of Q over the range $0 \leq Q \leq Q_{\mathrm{crit}}$ for the first five modes for $\hat{E}_b = 2, 4, 6$, and 8 (corresponding to $E_b = 0.2, 0.4, 0.6$, and 0.8). In particular, Figure 4.6 shows that increasing the electric potential difference increases the value of $\mathrm{Im}(\omega)$ and the range of unstable wavenumbers, and thus has a destabilising effect on the system.

To make clear how capillarity and electrostatic effects affect the growth rate, we may decompose (4.1.48) into the form

$$\mathrm{Im}(\omega_1) = n^2 F_1 + n^4 F_2 + n^2 \hat{E}_b F_3, \tag{4.1.49}$$

where $F_1 = F_1(Q)$ and $F_2 = F_2(Q)$ are

$$\begin{aligned} F_1 &= 4\pi^2 \left(\int_0^{2\pi} \frac{\mathrm{d}\theta}{C_0} \right)^{-3} \int_0^{2\pi} \left[\frac{B_1}{C_0^3} - 4\frac{B_1}{C_0^4} C_{0_{\theta\theta}} + 11\frac{B_1}{C_0^5} \left(C_{0_\theta}\right)^2 \right] \mathrm{d}\theta \qquad (4.1.50) \\ &= \frac{4\pi^2}{3} \left(\int_0^{2\pi} \frac{\mathrm{d}\theta}{1 - \bar{H}_0^2 \cos\theta} \right)^{-3} \int_0^{2\pi} \left[\left(\frac{\bar{H}_0}{1 - \bar{H}_0^2 \cos\theta} \right)^3 \right. \\ &\quad \left. - 4\frac{\bar{H}_0^3}{(1 - \bar{H}_0^2 \cos\theta)^4} \left[1 - \bar{H}_0^2 \cos\theta\right]_{\theta\theta} + 11\frac{\bar{H}_0^3}{(1 - \bar{H}_0^2 \cos\theta)^5} \left(\left[1 - \bar{H}_0^2 \cos\theta\right]_\theta \right)^2 \right] \mathrm{d}\theta, \end{aligned}$$

[1]Benilov and O'Brien [121] investigated disturbances of the form $\eta'(\theta, t) = \phi(\theta) \mathrm{e}^{i\omega t}$ and concluded that steady-state flows are unstable when their equation (24) yields a positive value. However, upon careful examination, this leads us to believe that their expression for the disturbance $\eta'(\theta, t)$ may contain a typographical error, specifically, an omission of a negative sign in the exponent.

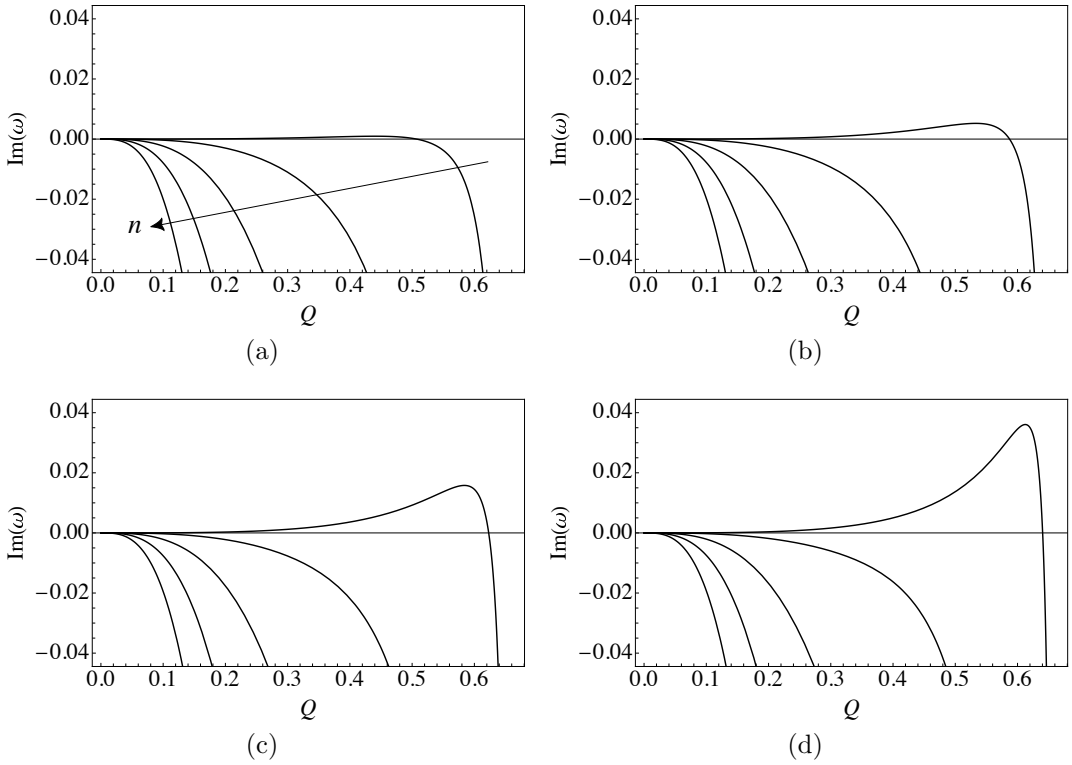

Figure 4.6: $\mathrm{Im}(\omega)$ (4.1.53) over the range $0 \leq Q \leq Q_{\mathrm{crit}}$ for the first five modes for $D = 2$ and $\gamma^{-1} = 0.1$ with (a) $\hat{E}_b = 2$, (b) $\hat{E}_b = 4$, (c) $\hat{E}_b = 6$, and (d) $\hat{E}_b = 8$. The arrow indicates the direction of increasing n for $n = 1, 2, 3, 4$, and 5.

$$F_2 = -16\pi^4 \left(\int_0^{2\pi} \frac{\mathrm{d}\theta}{C_0} \right)^{-3} \int_0^{2\pi} \frac{B_1}{C_0^5} \left(\int_0^{2\pi} \frac{\mathrm{d}\theta}{C_0} \right)^{-2} \tag{4.1.51}$$
$$= -\frac{16\pi^4}{3} \left(\int_0^{2\pi} \frac{\mathrm{d}\theta}{1 - \bar{H}_0^2 \cos\theta} \right)^{-5} \int_0^{2\pi} \frac{\bar{H}_0^3}{(1 - \bar{H}_0^2 \cos\theta)^5} \, \mathrm{d}\theta,$$

respectively, and together represent the effect of capillarity (which, as discussed previously, was shown by Benilov and O'Brien [121] to be a stabilising influence). Note that F_1 (4.1.50) and F_2 (4.1.51) are independent of both $\hat{E}_b$ and D. The final term $F_3 = F_3(Q)$ is

$$F_3 = \frac{4\pi^2}{3} \left(\int_0^{2\pi} \frac{\mathrm{d}\theta}{1 - \bar{H}_0^2 \cos\theta} \right)^{-3} \int_0^{2\pi} \left[\frac{\bar{H}_0}{(D - \bar{H}_0)(1 - \bar{H}_0^2 \cos\theta)} \right]^3 \mathrm{d}\theta, \tag{4.1.52}$$

and represents the electrostatic effects (which we shall often refer to hereafter as the "electrostatic term" for clarity in later discussions). Note that F_3 (4.1.52) is independent of $\hat{E}_b$ but is dependent on D. Since $\mathrm{Im}(\omega_0) = 0$ by (4.1.37), it follows from (4.1.49) that to $O(\gamma^{-1})$ the growth rate is

$$\mathrm{Im}(\omega) = \gamma^{-1} n^2 [F_1 + n^2 F_2 + \hat{E}_b F_3] + O(\gamma^{-2}). \tag{4.1.53}$$

For $n = 0$ the system is neutrally stable to $O(\gamma^{-1})$. From (4.1.53), we obtain the instability criterion, namely, that for mode n steady solutions $\bar{H}$ are unstable if

$$\hat{E}_b > -\left(\frac{F_1 + n^2 F_2}{F_3} \right). \tag{4.1.54}$$

The components of the growth rate, F_1 (4.1.50), F_2 (4.1.51), and F_3 (4.1.52), depend on the flux Q via the solution $\bar{H}_0$ of the leading-order steady problem (4.1.23). Figure 4.7 shows F_1 (4.1.50), F_2 (4.1.51), and F_3 (4.1.52) plotted as functions of Q over the range $0 \leq Q \leq Q_{\mathrm{crit}}$ for $\gamma^{-1} = 0.1$ with (a) $D = 2$ and (b) $D = 4$. The electrostatic term F_3 is always positive (and monotonically increasing), indicating that electrostatic effects have a destabilising influence, which becomes stronger for increasing Q. One of the two capillary terms, F_2, is always negative (and monotonically decreasing), indicating that this term has an overall stabilising influence. Figure 4.7 also shows that the other capillary term, F_1, changes sign and is thus either stabilising or destabilising depending on the value of Q. To

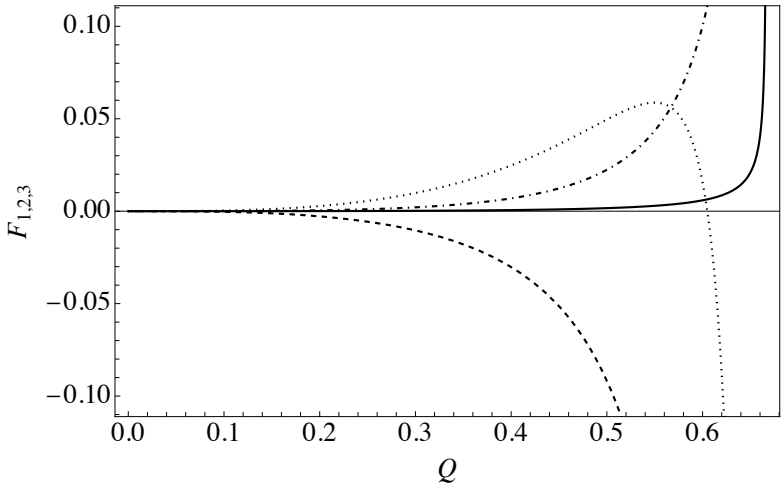

Figure 4.7: Individual contributions to the growth rate (4.1.53) over the range $0 \leq Q \leq Q_{\text{crit}}$: F_1 (4.1.50) (dotted line), F_2 (4.1.51) (dashed line), and F_3 (4.1.52) for $D = 2$ (dot-dashed line) and $D = 4$ (solid line).

see which term is causing the change in signs, we decompose F_1 into three terms, namely, F_{11}, F_{12}, and F_{13}, which can be written as

$$F_1(Q) = \underbrace{\frac{4\pi^2}{3}\left(\int_0^{2\pi} \frac{\mathrm{d}\theta}{1-\bar{H}_0^2\cos\theta}\right)^{-3} \int_0^{2\pi} \left(\frac{\bar{H}_0}{1-\bar{H}_0^2\cos\theta}\right)^3 \mathrm{d}\theta}_{F_{11}}$$
$$\underbrace{-\frac{16\pi^2}{3}\left(\int_0^{2\pi} \frac{\mathrm{d}\theta}{1-\bar{H}_0^2\cos\theta}\right)^{-3} \int_0^{2\pi} \frac{\bar{H}_0^3}{(1-\bar{H}_0^2\cos\theta)^4}\left[1-\bar{H}_0^2\cos\theta\right]_{\theta\theta} \mathrm{d}\theta}_{F_{12}}$$
$$\underbrace{+\frac{44\pi^2}{3}\left(\int_0^{2\pi} \frac{\mathrm{d}\theta}{1-\bar{H}_0^2\cos\theta}\right)^{-3} \int_0^{2\pi} \frac{\bar{H}_0^3}{(1-\bar{H}_0^2\cos\theta)^5}\left(\left[1-\bar{H}_0^2\cos\theta\right]_{\theta}\right)^2 \mathrm{d}\theta}_{F_{13}}. \tag{4.1.55}$$

Figure 4.8 shows the three terms F_{11}, F_{12}, and F_{13} given by (4.1.55) plotted as functions of Q over the range $0 \leq Q \leq Q_{\text{crit}}$. In particular, Figure 4.8 shows that F_{12} is always negative (and monotonically decreasing) and is thus stabilising, whereas the other two terms, F_{11} and F_{13}, are always positive (and monotonically increasing) and are thus destabilising.

Note that, as indicated by Benilov and O'Brien [121], the growth rate $\mathrm{Im}(\omega)$

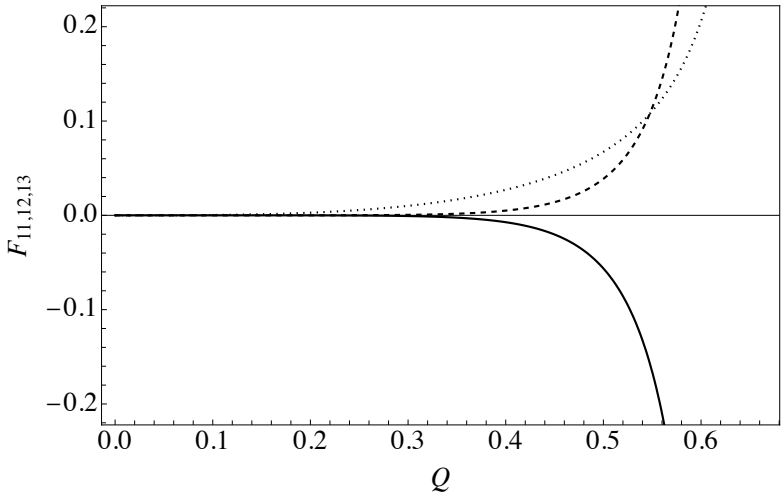

Figure 4.8: Individual contributions to F_1 (4.1.50) given by (4.1.55) over the range $0 \leq Q \leq Q_{\text{crit}}$: F_{11} (dotted line), F_{12} (solid line), and F_{13} (dashed line).

(4.1.53) depends on the mode number n only through the ω_0 (4.1.37) in the numerator of $\text{Im}(\omega_1)$ (4.1.48), which grows with n. It follows that higher modes (i.e, $n \geq 2$) grow only if the first mode (i.e., $n = 1$) grows. Hence, the flow is unstable if and only if the stability criterion (4.1.54) is satisfied for the first mode. We investigate what happens to the stability of the first mode when we vary the electric potential difference $\hat{E}_b$. Figure 4.9 shows plots of the growth rate of the first mode calculated from (4.1.53) over the range $0 \leq Q \leq Q_{\text{crit}}$ for $\gamma^{-1} = 0.1$ and $\hat{E}_b = 0, 2, 4, 6$, and 8 (corresponding to $E_b = 0, 0.2, 0.4, 0.6$, and 0.8) with (a) $D = 2$ and (b) $D = 4$. Figure 4.9 shows that smaller electric potential differences (i.e., smaller values of $\hat{E}_b$) lead to a wider range of Q values that correspond to a stable system. As $\hat{E}_b$ is increased, $\text{Im}(\omega)$ is increasingly more positive over a wider range of Q values, corresponding to the system being increasingly more unstable. The outer electrode is closer to the film in Figure 4.9 (a) than in Figure 4.9 (b), leading to a stronger electric field and thus producing a more unstable system. Larger values of $\hat{E}_b$ are required to induce instability for larger D. This makes sense physically, as we would expect that a stronger electric field is required to induce the same destabilising effect when the outer electrode is further away from the interface.

Figure 4.10 shows regions of instability (shown as the shaded regions) for the first mode in $(\hat{E}_b, Q)$ parameter space calculated for $\gamma^{-1} = 0.1$ with (a) $D = 2$ and (b) $D = 4$. Specifically, Figure 4.10 reveals that, as observed by Benilov and

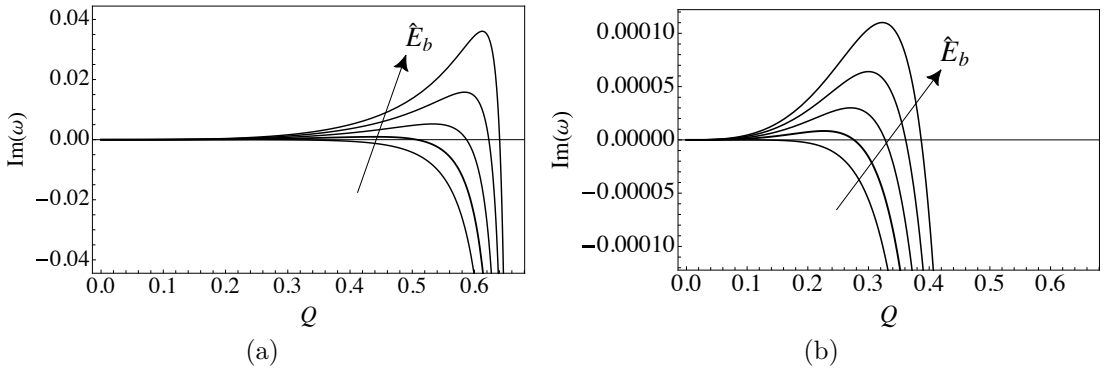

Figure 4.9: $\mathrm{Im}(\omega)$ (4.1.53) over the range $0 \leq Q \leq Q_{\mathrm{crit}}$ for the first mode (i.e., $n = 1$) with $\gamma^{-1} = 0.1$, $\hat{E}_b = 0, 2, 4, 6$, and 8 and (a) $D = 2$ and (b) $D = 4$. The arrow indicates the direction of increasing $\hat{E}_b$.

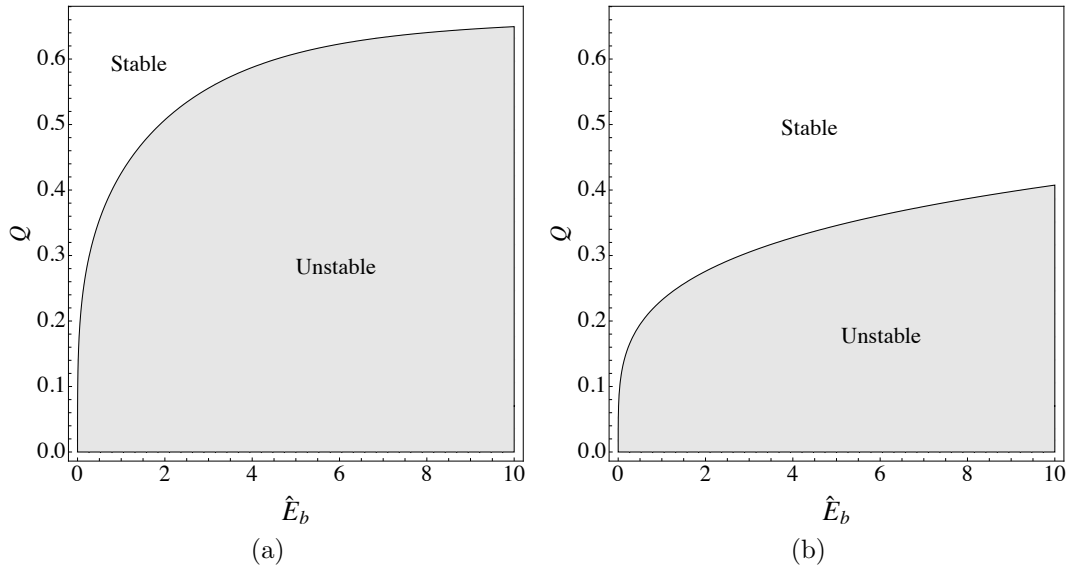

Figure 4.10: Regions of instability (shaded) in $(\hat{E}_b, Q)$ parameter space for the first mode (i.e., $n = 1$) calculated from (4.1.53) for $\gamma^{-1} = 0.1$ for (a) $D = 2$ and (b) $D = 4$.

O'Brien [121] (as mentioned earlier in Section 1.4.4), thicker films (i.e., flows with larger Q) are more stable than thinner films. As seen above, larger values of $\hat{E}_b$ are required to induce instability in Figure 4.10 (b) (in which $D = 4$) compared to in Figure 4.10 (a) (in which $D = 2$).

Ultimately, the preceding analysis of the growth rate (4.1.53) reveals two important features of the stability: firstly, the steady state $\bar{H}(\theta)$ is more stable when the outer electrode is further from the interface (i.e., for larger values of D), and secondly, the steady state is (perhaps counter-intuitively) more stable for thicker films. To investigate these behaviours in more detail, we consider the limiting cases in which D is large in Section 4.1.2.1, in which Q is small in Section 4.1.2.2, and finally, in Section 4.1.2.3, we consider the case in which Q approaches the critical value Q_{crit}.

4.1.2.1 Limiting case: $D \to \infty$

In this section, we consider the limiting case of large D. Large values of D correspond to the outer electrode being located far from the interface, which, as shown in Figures 4.9 and 4.10, requires a stronger electric field to induce instability. However, note that, strictly speaking, the investigation of this limit breaks the asymptotic assumption under which the thin-film governing equation (2.2.23) was derived (i.e., that the gap between the electrodes is also thin). Thus, the analysis in this section should be treated as a statement regarding the equation for the growth rate (4.1.53) itself, rather than one regarding the original physical system.

Taking the limit $D \to \infty$ in the electrostatic term F_3 (4.1.52), yields

$$\begin{aligned} F_3 &= \frac{4\pi^2}{3}\left(\int_0^{2\pi} \frac{\mathrm{d}\theta}{1-\bar{H}_0^2\cos\theta}\right)^{-3}\int_0^{2\pi}\left[\frac{\bar{H}_0}{(D-\bar{H}_0)(1-\bar{H}_0^2\cos\theta)}\right]^3 \mathrm{d}\theta \\ &= \frac{4\pi^2}{3}\left(\int_0^{2\pi} \frac{\mathrm{d}\theta}{1-\bar{H}_0^2\cos\theta}\right)^{-3}\int_0^{2\pi}\left[\frac{\bar{H}_0}{D(1-\bar{H}_0^2\cos\theta)}\right]^3 \left(1-\frac{\bar{H}_0}{D}\right)^{-3} \mathrm{d}\theta \\ &= \frac{4\pi^2}{3}\left(\int_0^{2\pi} \frac{\mathrm{d}\theta}{1-\bar{H}_0^2\cos\theta}\right)^{3}\int_0^{2\pi}\frac{1}{D^3}\left[\frac{\bar{H}_0}{1-\bar{H}_0^2\cos\theta}\right]^3 \mathrm{d}\theta + O(D^{-4}) \\ &= \frac{F_{11}}{D^3} + O(D^{-4}), \end{aligned} \tag{4.1.56}$$

where F_{11} is given by (4.1.55). Thus, in the limit of large D, $\mathrm{Im}(\omega)$ is

$$\mathrm{Im}(\omega) = \gamma^{-1}\left\{n^2\left[F_{11}(Q)\left(1+\frac{\hat{E}_b}{D^3}\right)+F_{12}(Q)+F_{13}(Q)\right]+n^4F_2(Q)\right\} + O(D^{-4},\gamma^{-2}). \tag{4.1.57}$$

In order to retain electrostatic effects at leading order in $D^{-1} \ll 1$, we choose to work in the distinguished limit in which the electric potential difference is large by setting

$$\hat{E}_b = D^3\bar{E}_b, \tag{4.1.58}$$

where $\bar{E}_b = O(1)$. Then, in the limit of large D, $\mathrm{Im}(\omega)$ becomes

$$\mathrm{Im}(\omega) = \gamma^{-1}\left\{n^2\left[F_{11}(Q)\left(1+\bar{E}_b\right)+F_{12}(Q)+F_{13}(Q)\right]+n^4F_2(Q)\right\}+O(D^{-1},\gamma^{-2}), \tag{4.1.59}$$

where F_{11}, F_{12}, and F_{13} are given by (4.1.55). In this limiting case, the growth rate is dominated by the (overall stabilising) capillary terms F_1 (4.1.50) and F_2 (4.1.51). Electrostatic effects enhance the effect of F_{11}, which, as seen above, is one of the destabilising components of the capillary term F_1.

4.1.2.2 Limiting case: $Q \to 0$

In this section, we consider the limiting case of small Q. This choice is motivated by our previous observation that the steady state is more unstable for thinner films, and hence it is instructive to investigate our results in the limit $Q \to 0$. In the limit $Q \to 0$, the equation for the leading-order steady solution $\bar{H}_0$ (4.1.23) can be solved by expanding $\bar{H}_0$ as

$$\bar{H}_0 = \bar{H}_{00} + Q\bar{H}_{01} + \ldots + Q^7\bar{H}_{07} + O(Q^8), \tag{4.1.60}$$

where $Q \ll 1$, and solving order-by-order to yield [112, 121]

$$\bar{H}_0 = Q + \frac{1}{3}Q^3\cos\theta + \frac{1}{3}Q^5\left(\cos\theta\right)^2 + \frac{4}{9}Q^7\left(\cos\theta\right)^3 + O(Q^9). \tag{4.1.61}$$

Note that equation (4.1.61) shows that in the small-Q limit, $\bar{H}_0 = Q$ to leading order in Q. The formula for the growth rate (4.1.53) can thus be simplified in the

small-Q limit by substituting (4.1.61) into (4.1.50)–(4.1.52) to yield

$$F_1 = \frac{1}{3}Q^3 - \frac{5}{10}Q^7 + O(Q^{11}), \tag{4.1.62}$$

$$F_2 = -\frac{1}{3}Q^3 - \frac{49}{18}Q^7 + O(Q^{11}), \tag{4.1.63}$$

$$F_3 = \frac{1}{3D^3}Q^3 + \frac{1}{D^4}Q^4 + \frac{2}{D^5}Q^5 + \frac{10}{3D^6}Q^6 + \left(\frac{5}{D^7} + \frac{11}{9D^3}\right)Q^7 + O(Q^8). \tag{4.1.64}$$

Thus, in the limit of small Q, the growth rate $\mathrm{Im}(\omega)$ is

$$\mathrm{Im}(\omega) = \gamma^{-1}\left\{\left(\frac{n^2}{3} + \frac{\hat{E}_b n^2}{3D^3} - \frac{n^4}{3}\right)Q^3 + \frac{\hat{E}_b n^2}{D^4}Q^4 + \frac{2\hat{E}_b n^2}{D^5}Q^5 + \frac{10\hat{E}_b n^2}{3D^6}Q^6 + \left(\frac{5\hat{E}_b n^2}{D^7} + \frac{11\hat{E}_b n^2}{9D^3} - \frac{5}{18}n^2\right)Q^7\right\} + O(\gamma^{-2}, Q^8). \tag{4.1.65}$$

Upon setting $\hat{E}_b = 0$, equation (4.1.65) recovers the small-Q solution for $\mathrm{Im}(\omega_1)$ of Benilov and O'Brien [121] (i.e., their equation (30)), namely,

$$\mathrm{Im}(\omega_1) = -\frac{1}{3}n^2\left(n^2 - 1\right)Q^3 - \frac{1}{18}n^2\left(49n^2 + 5\right)Q^7 + O(Q^8). \tag{4.1.66}$$

Benilov and O'Brien [121] found that in the absence of an electric field the growth rate of the first mode is $O(Q^7)$, which is much smaller than the growth rates of higher modes which are $O(Q^3)$. Thus, in the absence of an electric field, the first mode is always the first to become unstable. However, when $\hat{E}_b$ is non-zero, electrostatic terms appear at all orders starting from $O(Q^3)$, as shown in (4.1.65). Thus, when electrostatic effects are present, the growth rate of both the first mode and all higher modes is $O(Q^3)$, a significant difference from the case in the absence of an electric field. In the limit of small Q, the instability criterion (4.1.54) can be simplified. Setting $n = 1$ in (4.1.65) yields

$$\mathrm{Im}(\omega) = \gamma^{-1}\left\{\frac{\hat{E}_b}{3D^3}Q^3 + \frac{\hat{E}_b}{D^4}Q^4 + \frac{2\hat{E}_b}{D^5}Q^5 + \frac{10\hat{E}_b}{3D^6}Q^6 + \left(\frac{5\hat{E}_b}{D^7} + \frac{11\hat{E}_b}{9D^3} + \frac{5}{18}\right)Q^7\right\}. \tag{4.1.67}$$

Thus, to $O(\gamma^{-1})$ the first mode is unstable for

$$\hat{E}_b > 0. \tag{4.1.68}$$

In other words, in the limit of small Q, the flow is unstable for all non-zero values of $\hat{E}_b$, which is in agreement with the results shown in Figure 4.10. As discussed by Benilov and O'Brien [121], investigation of the small-Q limit also reveals why thicker films (i.e., flows with larger Q) are more stable than thinner films. The contribution of capillarity to the growth rate of the first mode (4.1.67) is proportional to Q^7, whereas the contribution of electrostatic effects is proportional to Q^3. Therefore, the stabilising effect of capillarity has a stronger dependence on Q (and hence the film thickness) than electrostatic effects, which explains the stabilisation of the flow for large Q.

4.1.2.3 Limiting case: $Q \to Q_{\mathbf{crit}}$

In this section, we consider the limiting case in which Q approaches the critical value Q_{crit}. Once again, we are motivated by the observation that the steady state is more unstable for thinner films. Therefore, it is of interest to investigate the behaviours of F_1 (4.1.50), F_2 (4.1.51), and F_3 (4.1.52) in the limit $Q \to Q_{\text{crit}}$ to gain insight into the dominant behaviour close to the critical value Q_{crit}. We proceed by setting $Q = Q_{\text{crit}} - \lambda$ and evaluating (4.1.50)–(4.1.52) over the range $0 < \lambda \leq Q_{\text{crit}}$ to understand the behaviour of the system as Q moves further away from Q_{crit}. As a form of validation, we use two different methods to compute (4.1.50)–(4.1.52). Firstly, as discussed in Section 1.4.4, the solution $\bar{H}_0$ to the leading-order steady problem (4.1.23) can be calculated near $Q = Q_{\text{crit}}$ by using the composite critical solution given by Tougher *et al.* [112], which we denote here by $\bar{H}_{0\text{comp}}$, namely,

$$\bar{H}_{0\text{comp}} = \bar{H}_{0\text{crit}} + \lambda \left(\frac{\sqrt{6}}{2|\theta|} - \frac{1}{1 - \bar{H}_{0\text{crit}}^2 \cos\theta} \right) + \frac{|\theta|}{6} - \sqrt{\lambda + \frac{\theta^2}{6}} \quad \text{as} \quad \lambda \to 0^+, \tag{4.1.69}$$

where, as explained in Section 1.4.4, $\bar{H}_{0\text{crit}}$ is the critical solution for $\bar{H}_0$ when $Q = Q_{\text{crit}}$. Figure 4.11 shows the solutions for (a), (b) F_1, (c), (d) F_2, and (e), (f) F_3 for $Q = Q_{\text{crit}} - \lambda$, where Figures 4.11 (b), (d), and (f) show the solutions on a log-log scale. The solid line shows the solutions calculated using the solution $\bar{H}_0$ to the leading-order steady problem (4.1.23), and the dashed line shows the solutions calculated using the composite critical solution $\bar{H}_{0\text{comp}}$ (4.1.69), plotted over the range $0 < \lambda \leq Q_{\text{crit}}$.

Note that, unlike F_2 (4.1.51) and F_3 (4.1.52), the solution for F_1 (4.1.50) cannot be calculated numerically using the composite critical solution (4.1.69). This

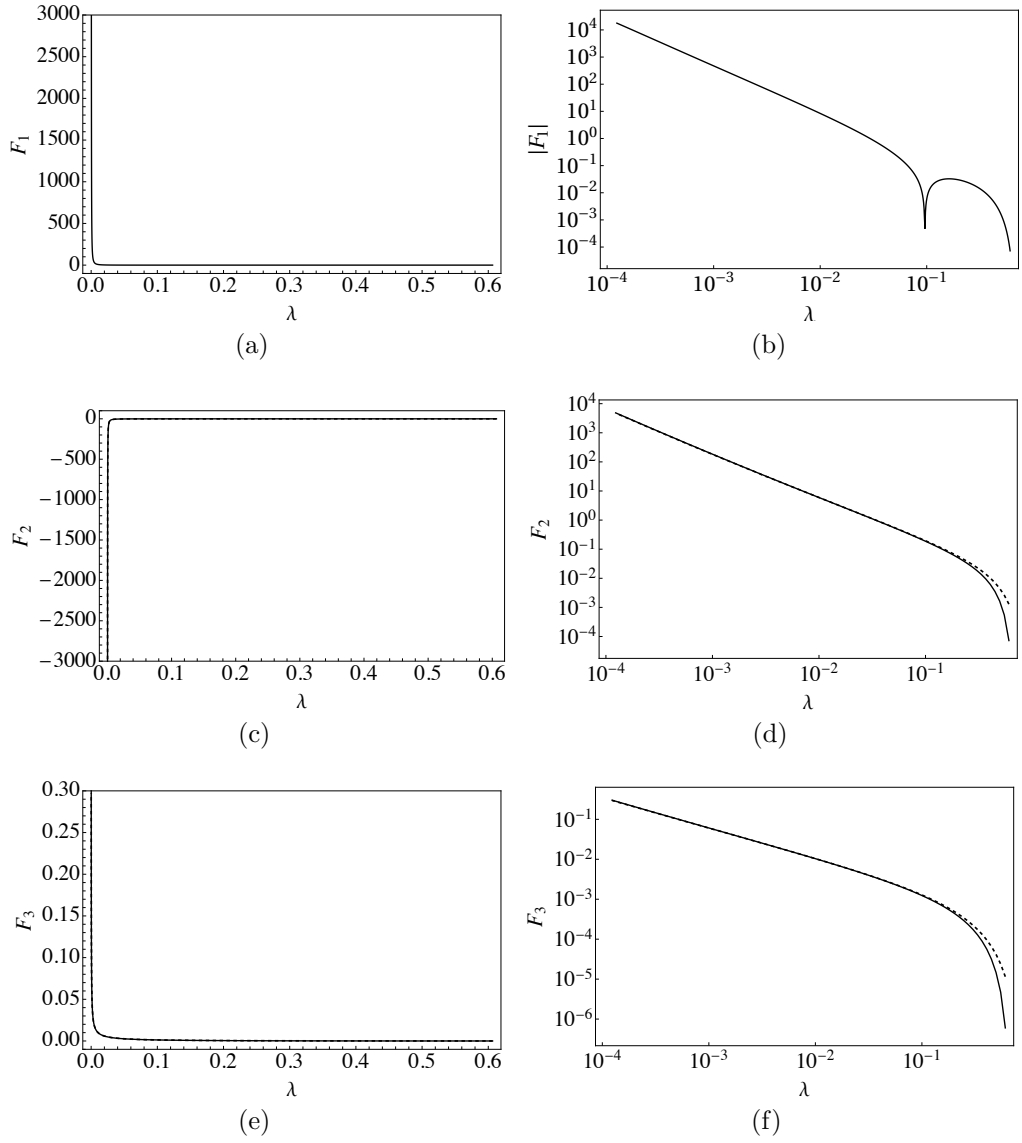

Figure 4.11: (a), (b) F_1 (4.1.50), (c), (d) F_2 (4.1.51), and (e), (f) F_3 (4.1.52) for $Q = Q_{\text{crit}} - \lambda$ over the range $0 < \lambda \leq Q_{\text{crit}}$ with $\bar{H}_0$ calculated using either the solution to the leading-order steady problem (4.1.23) (dashed line) or the composite critical solution of Tougher *et al.* [112] (solid line). (a), (c), (d) F_1, F_2, and F_3 as functions of λ. (b), (d), and (f) show the results in (a), (c), and (e) on a log-log scale. Note that (b) shows the absolute value of F_1 due to the fact that F_1 changes signs.

limitation arises due to the fact that derivatives of the term $1 - \bar{H}_{0\text{crit}} \cos\theta$ are nonintegrable. Specifically, when evaluating this term using the composite critical solution, one needs to take derivatives of a numerical interpolation of $\bar{H}_{0\text{crit}}$, which belongs to the function space C^0. The C^0 function space encompasses functions that are continuous on a given domain and vanish at infinity, but their derivatives are not necessarily continuous. In the case of the numerical interpolation of $\bar{H}_{0\text{crit}}$, its derivatives with respect to θ involve delta functions (which exhibit singular behavior at specific points) and derivatives thereof, resulting in an integral which is divergent. It is due to this nonintegrability of the derivatives of $1 - \bar{H}_{0\text{crit}} \cos\theta$ that the solution for F_1 cannot be obtained directly using the composite critical solution (4.1.69), hence precluding its inclusion in Figure 4.11. Instead, F_1 was independently calculated twice using different numerical implementations as an alternative means of validation. Specifically, two distinct numerical approaches were employed to compute $\bar{H}_0$ separately, and both methods exhibited excellent agreement.

Figures 4.11 (b), (d), and (f) show that $\log(|F_1|)$, $\log(F_2)$, and $\log(F_3)$ each have a linear relationship with $\log(\lambda)$ as $\log(\lambda) \to 0$. Note that the behaviour of $\log(|F_1|)$ around $\lambda = 10^{-1}$ in Figure 4.11 (b) is a reflection of the fact that F_1 changes signs from negative to positive as Q is decreased from Q_{crit}, as can be seen from the dotted line in Figure 4.7. The slopes of the corresponding lines of best fit to the numerical results for $\log(|F_1|)$, $\log(F_2)$, and $\log(F_3)$ for $\lambda \leq 10^{-2}$ were calculated numerically using the built-in nonlinear curve fitting routine `FindFit[]` in Mathematica [265]. These were found to be -1.73658, -1.52376, and -0.76407, respectively, indicating that the stabilising effect of capillarity dominates as $Q \to Q_{\text{crit}}$ and the solution becomes stable, thus explaining the reason why the growth rate (4.1.53) changes sign from positive to negative as Q nears the critical value Q_{crit} (see, for example, Figure 4.9).

4.2 Parametric study

In this section, we examine the qualitatively different behaviours exhibited by the system by carrying out a numerical parametric study on the full governing equation (2.2.23). The parametric study was performed by numerically solving (2.2.23) for the film thickness H. The behaviour that the system exhibits depends on the initial uniform film thickness H_0 (2.2.25), the capillary number γ (2.2.26),

the electric potential difference E_b (2.2.27), and the electrode distance D (2.2.28). The full parameter space is large, and hence to reduce the dimensionality of the problem the electrode distance was fixed at $D = 5$ and a numerical investigation of (γ, E_b) parameter space was performed for 8 different initial film thicknesses H_0. The results of the numerical study revealed that the system exhibits four distinct behaviours, namely, steady states, periodic states, outer contact, and transient states. These behaviours are defined in a physical sense for the present system respectively as follows:

1. Steady-state behaviour: a bulge is held in place;
2. Periodic-state behaviour: a bulge is carried around the cylinder periodically in time;
3. Outer contact behaviour: the interface touches the outer electrode in a finite time;
4. Transient-state behaviour: none of the criteria for the other three behaviours are met.

The four behaviours listed above and the corresponding metrics used in the code to identify them will be discussed in detail in Sections 4.2.3, 4.2.4, 4.2.5 and 4.2.6, respectively. As explained in Section 4.1.1, we again denote the final time at which the code converges before outer contact occurs by T_c. Note that when the outer electrode was positioned too close to the initial uniform interface (for example, for $D = 2$) we did not observe any periodic states for the chosen set of parameter values, and only a small number of steady states for small values of both γ and E_b. This is because the strength of the electric field increases as the distance between the interface and the outer electrode decreases, thus leading to more instances of outer contact occurring within the chosen range of parameter values. Hence, the fixed value of $D = 5$ was chosen to ensure that the outer electrode was positioned far enough away from the initial uniform interface to allow the richest variety of behaviours.

The dimensional quantities used in the parametric study are given in Section 4.2.1. In Section 4.2.2, we give an overview of the results, followed by a detailed discussion of the individual behaviours in Sections 4.2.3–4.2.6, each of which begins with a description of the classification criteria within the code for the behaviour

Quantity	Symbol	Value
Inner electrode radius	$\hat{R}_1$	0.01 m
Outer electrode radius	$\hat{R}_2$	0.0335801 m
Gravity	$\hat{g}$	9.81 m s^{-2}
Density	$\hat{\rho}$	1100 kg m^{-3}
Viscosity	$\hat{\mu}$	0.8 kg m^{-1} s^{-1}
Permittivity of gas region	$\hat{\epsilon}_G$	1.0006 F m^{-1}
Angular velocity	$\hat{\Omega}$	30 rad s^{-1}

Symbol	Definition	Value
$\hat{U}_{\text{char}}$	$\hat{\rho}\hat{g}\hat{R}_1^2/\hat{\mu}$	1.34888 m s^{-1}
Re	$\hat{\rho}\hat{U}_{\text{char}}\hat{R}_1/\hat{\mu}$	18.547

Table 4.1: Dimensional quantities based on a water-glycerine mix [102, 272] for $D = 5$.

at each point in (γ, E_b) parameter space. Points in (γ, E_b) parameter space close to the transitions between behaviours and at extrema were checked to validate the classifications. Specifically, the spatiotemporal evolution of the interface shape and evolution of the maximum and minimum film thicknesses over time were plotted in order to provide a qualitative check on the behaviour.

4.2.1 Dimensional quantities

The dimensional quantities used in this section are listed in Table 4.1 and are based on a water-glycerine mix [102, 272]. The dimensionless initial uniform film thickness H_0 is explored over the range

$$0.1 \leq H_0 \leq 1.5, \tag{4.2.1}$$

in increments of 0.2, corresponding to varying the dimensional initial uniform film thickness $\hat{h}_0$ over the range

$$0.47 \text{ mm} \leq \hat{h}_0 \leq 7.07 \text{ mm}. \tag{4.2.2}$$

For each choice of H_0, the capillary number γ is explored over the range

$$1 \leq \gamma \leq 50, \tag{4.2.3}$$

in increments of 1, corresponding to varying the dimensional surface tension coefficient $\hat{\sigma}$ over the range

$$0.0457633 \text{ kg s}^{-2} \leq \hat{\sigma} \leq 2.28816 \text{ kg s}^{-2}, \tag{4.2.4}$$

and the dimensionless electric potential difference E_b is explored over the range

$$0 \leq E_b \leq 50, \tag{4.2.5}$$

in increments of 1. Since E_b depends on $\hat{h}_0$ by (2.2.27), the range over which the dimensional potential at the outer electrode $\hat{\phi}_b$ is explored is different for each value of H_0. For the smallest value of H_0 considered in the present study (i.e., for $H_0 = 0.1$), $\hat{\phi}_b$ is varied over the range

$$0 \text{ V} \leq \hat{\phi}_b \leq 7.343204 \text{ V}, \tag{4.2.6}$$

whereas for the largest value of H_0 considered in the present study (i.e., for $H_0 = 1.5$), $\hat{\phi}_b$ is varied over the range

$$0 \text{ V} \leq \hat{\phi}_b \leq 0.489547 \text{ V}. \tag{4.2.7}$$

Note that the chosen upper limit of $\hat{\phi}_b = 7.343204$ V in (4.2.6) yields $\hat{\phi}_b/(\hat{R}_2 - \hat{R}_1) \approx 311$ V m^{-1}, which is significantly below the dielectric limit of air (which, as mentioned previously, is approximately 3×10^6 V m^{-1} [271]).

Finally, the increment sizes for H_0, γ, and E_b were chosen such that an accurate visualisation of parameter space is obtained without taking a prohibitively large amount of computational time to do so.

4.2.2 Results

In this section, we provide an overview of the results of the parametric study which are depicted in Figure 4.12, which shows the parameter planes for (a) $H_0 = 0.1$, (b) $H_0 = 0.3$, (c) $H_0 = 0.5$, (d) $H_0 = 0.7$, (e) $H_0 = 0.9$, (f) $H_0 = 1.1$, (g) $H_0 = 1.3$, and (h) $H_0 = 1.5$. Steady states, periodic states, outer contact, and transient states are represented by dark grey squares, light grey circles, grey triangles, and black diamonds, respectively, and the corresponding regions in parameter space are indicated by the letters "S", "P", "O", and "T", respectively. In general, a bulge

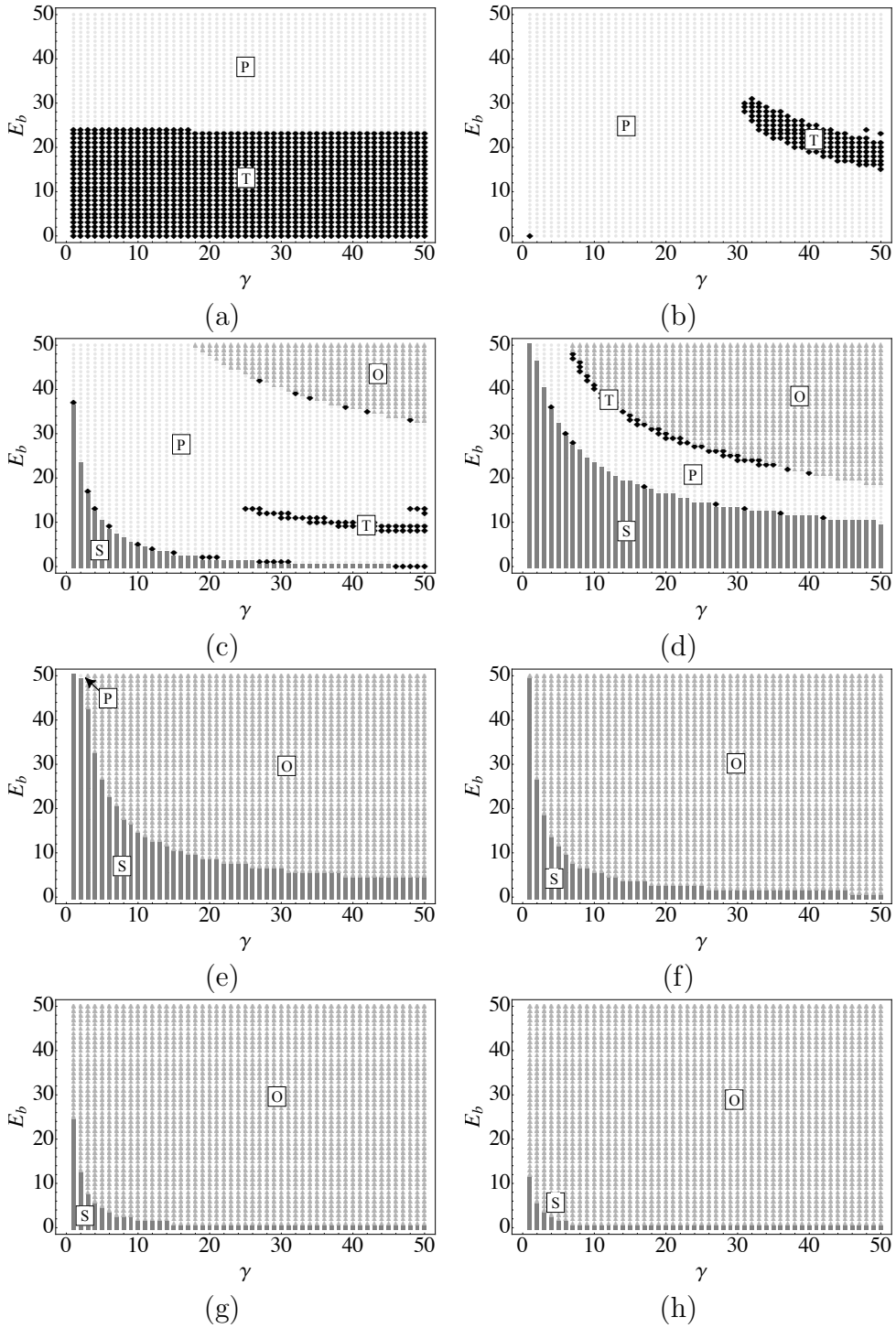

Figure 4.12: Parameter planes for $D = 5$, $1 \leq \gamma \leq 50$, $0 \leq E_b \leq 50$ and (a) $H_0 = 0.1$, (b) $H_0 = 0.3$, (c) $H_0 = 0.5$, (d) $H_0 = 0.7$, (e) $H_0 = 0.9$, (f) $H_0 = 1.1$, (g) $H_0 = 1.3$, and (h) $H_0 = 1.5$. Steady ("S"), periodic ("P"), outer contact ("O"), and transient ("T") states are represented by dark grey squares, light grey circles, grey triangles, and black diamonds, respectively.

forms as the liquid drains towards the lower part of the cylinder due to gravity and is supported by capillarity. Rotation drives the bulge in the anticlockwise direction (i.e., in the direction of rotation), and electrostatic effects pull the interface towards the outer electrode most strongly where the film is thickest.

4.2.2.1 Overview of parameter space

In this section, we provide an overview of the parameter space, in particular, highlighting the regions where each behavior is observed. Within the chosen range of parameter values, as H_0 increases there is a wider array of parameters in (γ, E_b) space for which outer contact occurs, and the location of the grey triangles (indicating where outer contact occurs in parameter space) moves downwards and to the left (i.e., outer contact occurs for a wider range of parameter values), as shown in Figures 4.12 (c)–(h). Physically, this is because as the film thickness increases whilst the position of the outer electrode remains fixed, the interface will be closer to the outer electrode. As mentioned previously, the strength of the electric field increases as the distance between the interface and the outer electrode decreases. Therefore, we expect the region in parameter space associated with outer contact to expand as H_0 increases. As a result, there is a narrower array of parameters for which any of the other behaviours occur. In general, smaller values of γ and E_b more readily admit steady or periodic states, with the locations of the dark grey squares and the light grey circles (corresponding to steady and periodic states, respectively) being concentrated in the bottom left-hand corner of the parameter planes shown in Figures 4.12 (c)–(h).

For very thin films, no steady states or instances of outer contact occur within the chosen range of parameter values, as shown in Figures 4.12 (a) and (b). In this case, the most common behaviour is either periodic states or transient states. Periodic states arise for very thin films due to the fact that the electric field is very weak when the interface is far from the outer electrode, and hence the dominant force is that due to rotation. We defer discussion of the transient states until Section 4.2.6. For thin (but not very thin) films, in general, increasing E_b over the range $0 \leq E_b \leq 50$ results in a transition in parameter space from steady states to periodic states, and then a transition from periodic states to outer contact, as shown in Figures 4.12 (c) and (d). For very small values of γ, the stabilising effect of capillarity dominates the behaviour and hence outer contact does not

occur within the chosen range of parameter values, as shown in the left-hand side of Figures 4.12 (c) and (d). For slightly larger values of γ, outer contact occurs only for the largest values of E_b. For large γ, the stabilising effect of capillarity is weak and hence the destabilising effect of the electric field can dominate the behaviour. Therefore, outer contact can occur for smaller values of E_b, as shown in the right-hand side of Figures 4.12 (c) and (d).

The effects of increasing E_b for a fixed value of γ and increasing γ for a fixed value of E_b for the chosen range of parameter values are shown in Figures 4.13 and 4.14, respectively. In particular, Figure 4.13 shows the evolution of both the minimum film thickness $H_{\min}$ and the maximum film thickness $H_{\max}$ (shown as the grey and black lines, respectively) along with the spatiotemporal evolution of the film thickness H for $H_0 = 0.7$ (corresponding to Figure 4.12 (d)) for $\gamma = 10$ and $E_b = 23, 24$, and 44, resulting in the emergence of a steady state, a periodic state, and outer contact, respectively. Similarly, Figure 4.14 shows the evolution of $H_{\min}$ and $H_{\max}$ and the spatiotemporal evolution of the film thickness for $H_0 = 0.5$ (corresponding to Figure 4.12 (c)) for $E_b = 36$ and $\gamma = 1, 25$, and 50, resulting in the emergence of a steady state, a periodic state, and outer contact, respectively.

4.2.2.2 Prediction of number of bulges

In this section, we discuss the number of bulges that are expected to arise in our numerical results within the chosen range of parameter values. In Section 4.1.1, we established that the number of bulges that are expected to appear at later times in the evolution can be accurately predicted by the most unstable mode $n_{\max}$ (4.1.9). Figure 4.15 shows regions in (γ, E_b) parameter space in which the number of bulges that arise is predicted by (4.1.9) to be greater than $0, 1, 2, 3$, and 4 for (a) $H_0 = 0.5$, (b) $H_0 = 0.7$, (c) $H_0 = 0.9$, and (d) $H_0 = 1.1$ (corresponding to Figures 4.12 (c)–(f), respectively). In particular, Figure 4.15 shows that, within the chosen range of parameter values, more than 4 bulges are expected to appear only for the thickest films considered for large values of γ and E_b. This is in contrast to the results shown in Section 4.1.1 in which we considered the smaller values $D = 2$ and $D = 3$ which yielded much higher values of $n_{\max}$ (see, for example, Figures 4.4 and 4.5 which showed up to 11 and 5 bulges forming in the numerical solution, respectively). In the present study, the maximum value of $n_{\max}$ is $n_{\max} \approx [5.4456] = 5$ which occurs for the largest values of H_0, γ, and E_b that

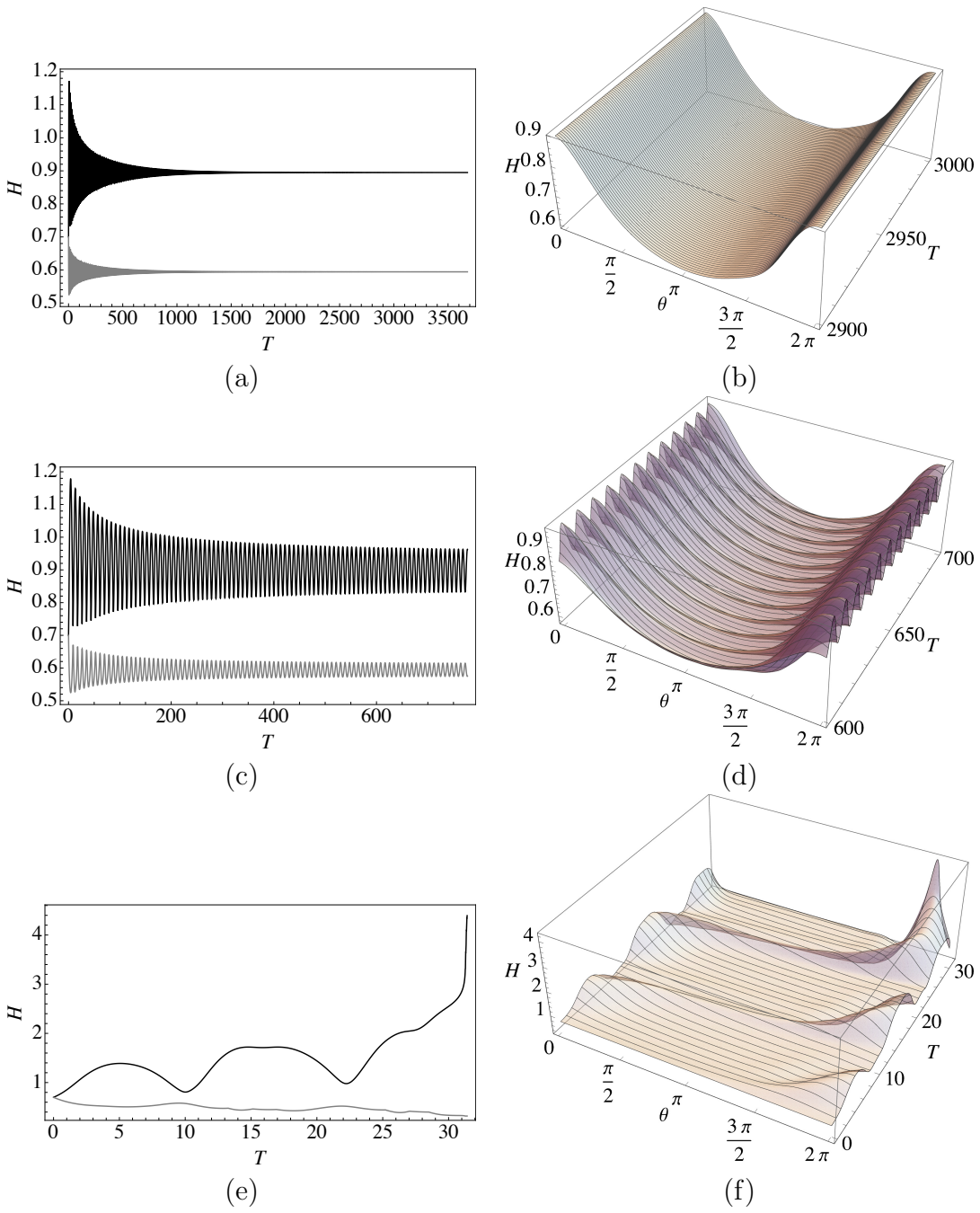

Figure 4.13: (a), (c), (e) The time evolution of the minimum film thickness $H_{\min}$ (grey lines) and maximum film thickness $H_{\max}$ (black lines) for $H_0 = 0.7$, $\gamma = 10$, and (a) $E_b = 23$ (steady), (c) $E_b = 24$ (periodic), and (e) $E_b = 44$ (outer contact), respectively. (b), (d), (f) Spatiotemporal evolution of the film thickness H with (b) $E_b = 23$ for $T = [2900, 3000]$, (d) $E_b = 24$ for $T = [600, 700]$, and (f) $E_b = 44$ for $T = [0, T_c]$ where $T_c = 31.4064$.

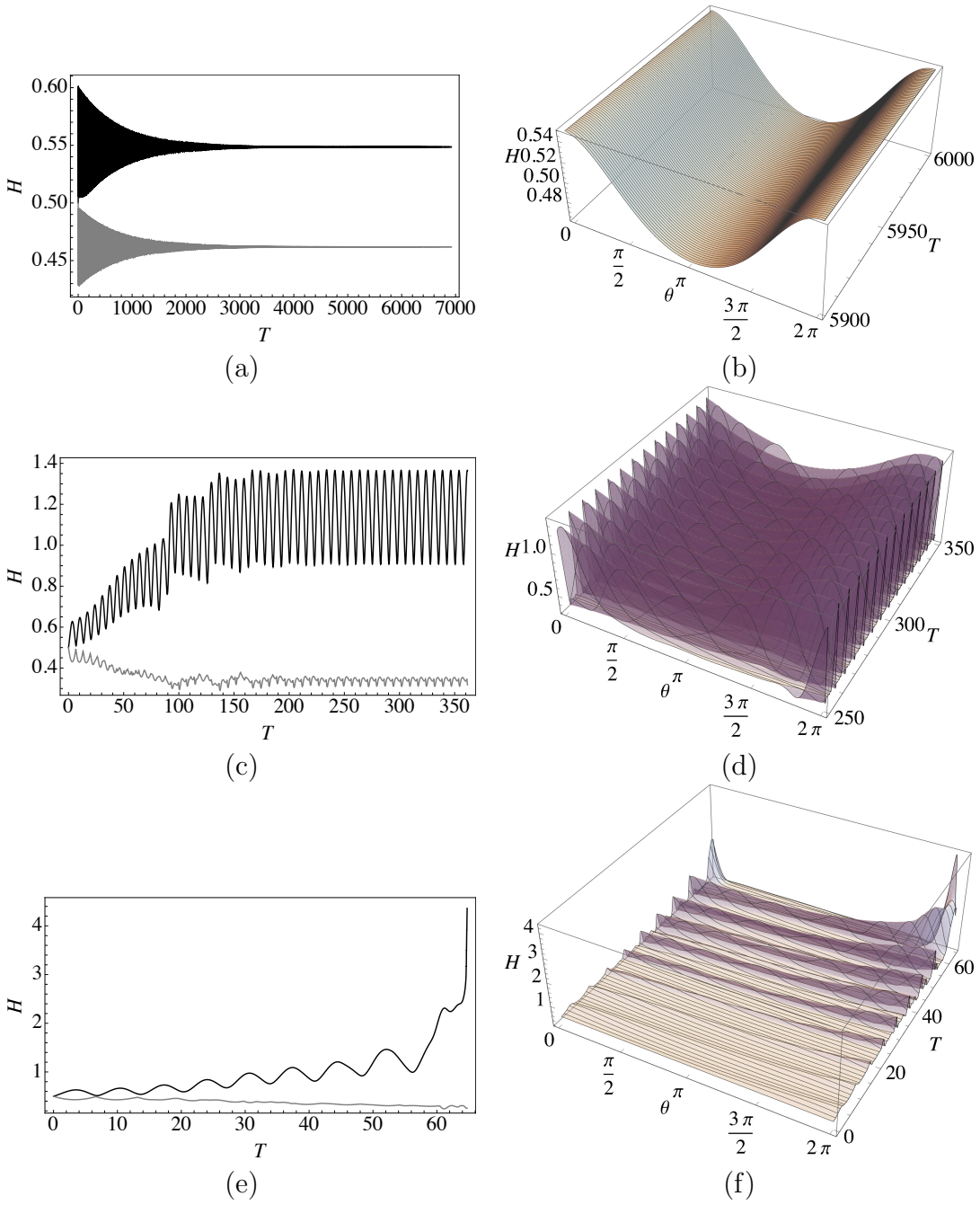

Figure 4.14: (a), (c), (e) The time evolution of the minimum film thickness $H_{\min}$ (grey lines) and maximum film thickness $H_{\max}$ (black lines) for $H_0 = 0.5$, $E_b = 36$, and (a) $\gamma = 1$ (steady), (c) $\gamma = 25$ (periodic), and (e) $\gamma = 50$ (outer contact), respectively. (b), (d), (f) Spatiotemporal evolution of the film thickness H with (b) $\gamma = 1$ for $T = [5900, 6000]$, (d) $\gamma = 25$ for $T = [250, 350]$, and (f) $\gamma = 50$ for $T = [0, T_c]$ where $T_c = 64.7323$.

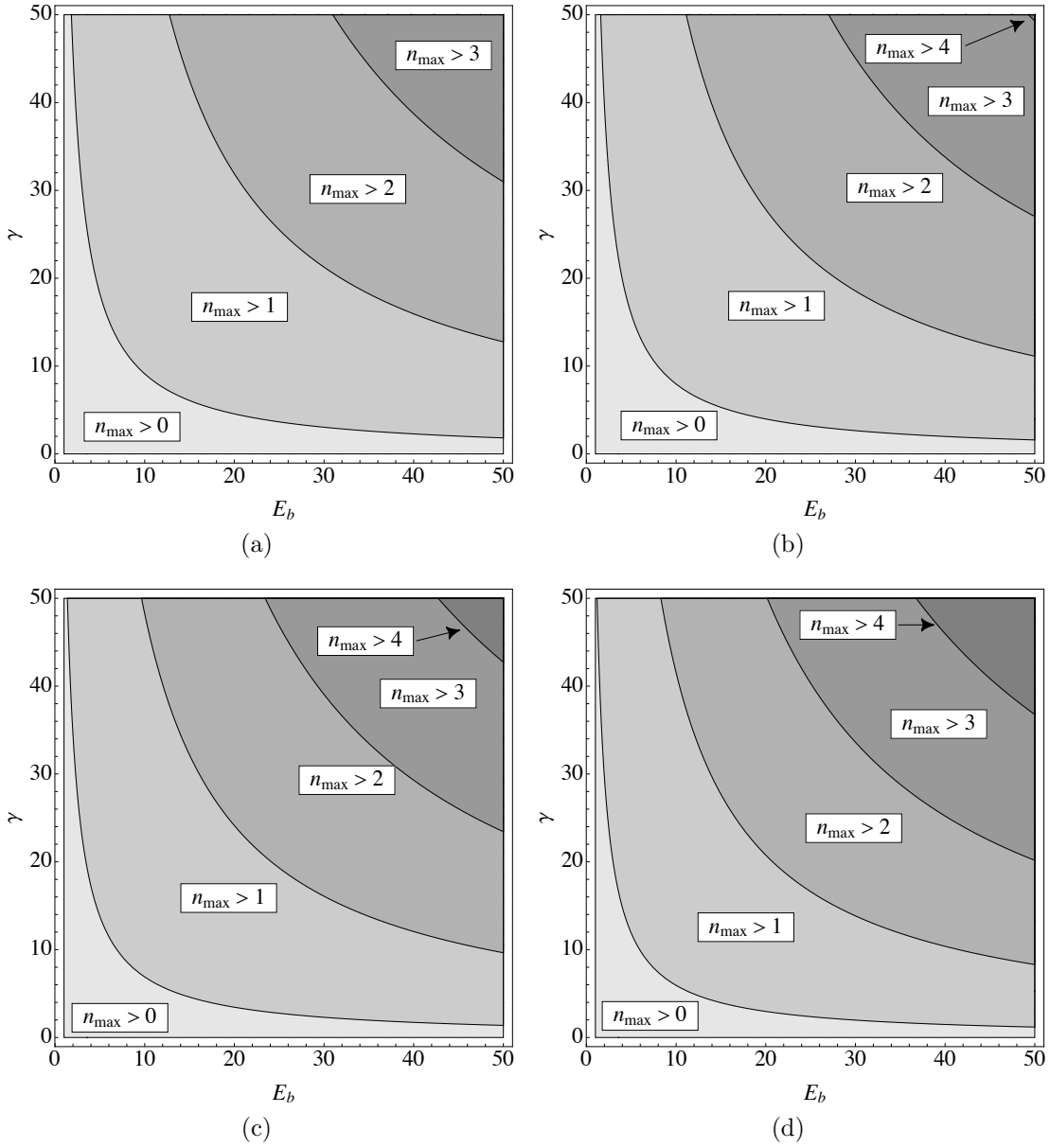

Figure 4.15: Regions in (γ, E_b) parameter space in which the number of bulges that are expected to appear at late times in the evolution is predicted by $n_{\max}$ (4.1.9) to be greater than $0, 1, 2, 3$, and 4 represented by the lightest to darkest grey regions in ascending order. (a) $H_0 = 0.5$, (b) $H_0 = 0.7$, (c) $H_0 = 0.9$, and (d) $H_0 = 1.1$.

we consider, namely, $H_0 = 1.5$, $\gamma = 50$, and $E_b = 50$. However, outer contact occurs so quickly for these parameter values (at time $T = T_c = 0.196685$) that in practice there is not enough time for the bulges to form. We observed at most four bulges in our numerical investigations, all instances of which arose during the evolution of the system towards outer contact behaviour. This is to be expected given that, in general, the regions corresponding to $n_{\max} > 3$ shown in Figure 4.15 overlap with the regions corresponding to outer contact in Figures 4.12 (c)–(f). The periodic states that we observed in our investigations had at most two bulges arise throughout their evolution, and the steady states always contained only one bulge, which is also to be expected given that, in general, the regions in Figure 4.15 in which $n_{\max} < 2$ overlap with those in Figure 4.12 which correspond to steady states. We defer a detailed discussion of these results until Sections 4.2.5, 4.2.4 and 4.2.3, and respectively.

4.2.3 Steady-state behaviour

The numerical solution is classified as a steady state when the values of H at each gridpoint vary by less than 10^{-5} over 1 dimensionless time. In states classified as steady, a bulge is typically held in place on the lower right-hand side of the cylinder due to a balance of gravitational, rotational, capillary, and electrostatic forces. Figure 4.12 shows that steady states are typically achieved by a combination of sufficiently large H_0 along with either strong capillarity (i.e., small γ) or weak electrostatic effects (i.e., small E_b). This observation aligns with physical intuition: for small H_0, the system is mainly dominated by rotation, leading to periodic states resembling solid body rotation. On the other hand, larger H_0 values allow capillarity to dominate, resulting in steady states, provided that the influence of electrostatic effects is not strong enough to induce outer contact.

As mentioned in Section 4.2.2, the steady states that we observed in our investigations always contained only one bulge, as predicted by the linear theory described in Section 4.1.1 and shown in Figure 4.15, which predicts that one bulge is most likely to be observable in the numerical solution in parameter regimes which induce steady states. Figure 4.16 shows the effect of (a), (c) increasing E_b for a fixed value of γ and (b), (d) increasing γ for a fixed value of E_b on a representative steady state for $H_0 = 0.9$ (corresponding to Figure 4.12 (e)). In particular, Figures 4.16 (a) and (c) show the effect of increasing E_b from $E_b = 0$ to $E_b = 10$ for

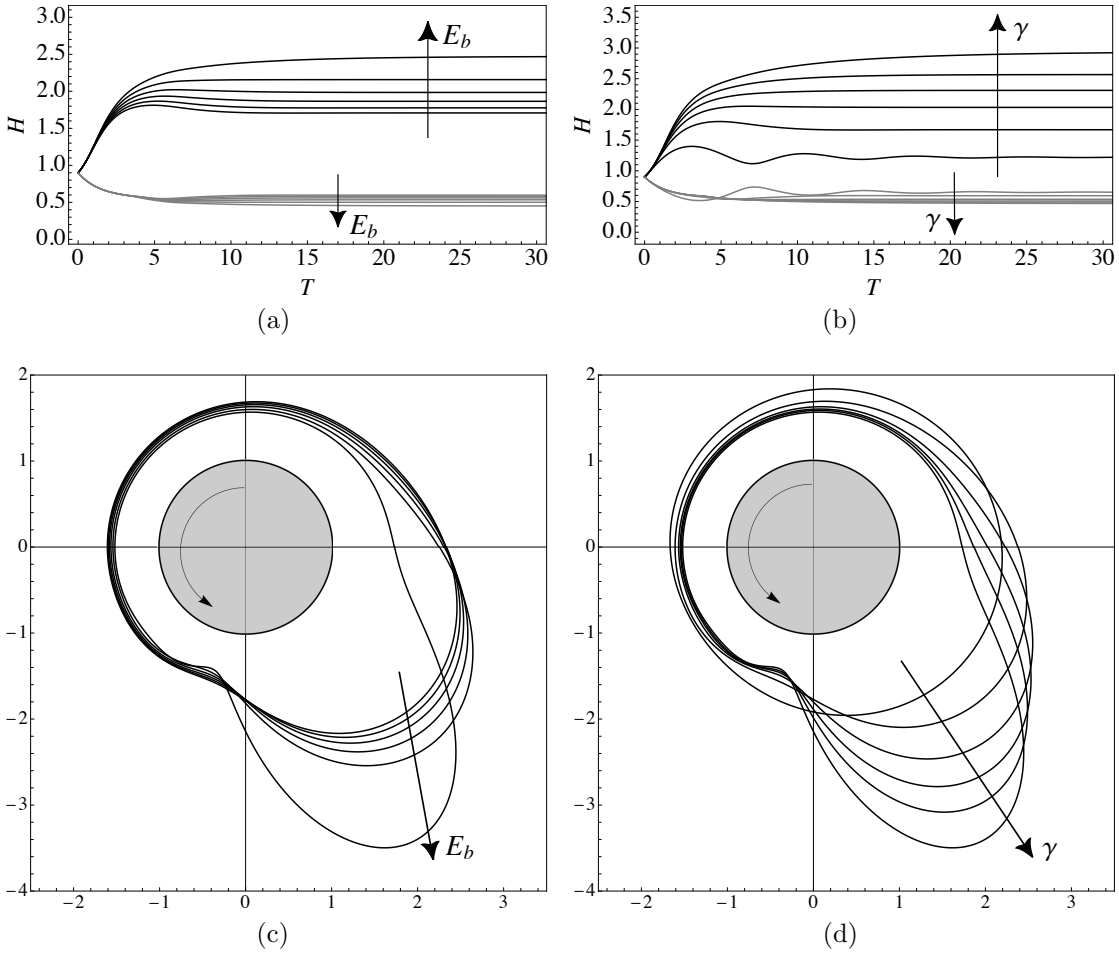

Figure 4.16: Steady states for $H_0 = 0.9$ and (a), (c) $\gamma = 15$ with $E_b = 0, 2, 4, 6, 8,$ and 10, and (b), (d) $E_b = 4$ with $\gamma = 1, 10, 20, 30, 40,$ and 50. (a), (c) The time evolution of the minimum film thicknesses $H_{\min}$ (grey lines) and maximum film thicknesses $H_{\max}$ (black lines). (c), (d) Steady interface profiles for increasing (c) E_b and (d) γ. The straight arrows represent the direction of (a) increasing E_b and (b) increasing γ. The curved arrows represent the direction of rotation. Note that the film thickness has been exaggerated in (c) and (d) for illustrative purposes by using the artificial value $\epsilon = 1$.

the fixed value $\gamma = 15$. By (4.1.9) the linear theory predicts that for $0 \leq E_b \leq 10$, only one bulge will arise ($n_{\max}$ is calculated to be $n_{\max} \approx [1.26024] = 1$ for the largest value $E_b = 10$), which agrees with the numerical results shown in Figure 4.16 (c). Similarly, Figures 4.16 (b) and (d) show the effect of increasing γ from $\gamma = 1$ to $\gamma = 50$ for the fixed value $E_b = 4$. For these parameter values, by (4.1.9) the linear theory predicts that for $1 \leq \gamma \leq 50$, only one bulge will arise ($n_{\max}$ is calculated to be $n_{\max} \approx [1.39676] = 1$ for the largest value $\gamma = 50$) in agreement with the numerical results shown in Figure 4.16 (d).

For small (but not very small) values of H_0, the system typically reaches a steady state at late times. The bulge forms on the lower part of the cylinder due to gravity, is pulled towards the outer electrode by electrostatic effects, and is carried around the cylinder by the rotation. This behaviour results in the oscillatory behaviour of $H_{\max}$ and $H_{\min}$ which is shown in Figure 4.13 (a) and Figure 4.14 (a) which, as described previously, show the time evolution of $H_{\min}$ and $H_{\max}$ for two different systems which evolve towards a steady state for the small values $H_0 = 0.7$ and $H_0 = 0.5$, respectively. The oscillations are damped by viscosity and eventually a steady state is reached as shown in Figure 4.13 (b) and Figure 4.14 (b), respectively.

For large H_0, the system typically reaches a steady state before the bulge completes a full period of rotation around the cylinder: the bulge forms on the lower part of the cylinder due to gravity, is driven anticlockwise by the rotation, pulled towards the outer electrode by electrostatic effects, and ultimately held in place as the forces balance. This behaviour is shown in Figures 4.16 (a) and (b) which show that for the large value $H_0 = 0.9$, in most cases, $H_{\max}$ and $H_{\min}$ level out to constant values before any oscillations occur. In some cases, the bulge does oscillate around the cylinder before the steady state is reached, as shown in Figure 4.16 (b) which shows that for $E_b = 4$ and $\gamma = 1$ there is a slight oscillation in $H_{\max}$ and $H_{\min}$ before the steady state is reached. Our results indicate that this initial oscillatory behaviour tends to require small values of both γ and E_b in which case the behaviour is dominated by the rotation and strong capillarity, resulting in small oscillations in $H_{\max}$ and $H_{\min}$ (such as those shown in Figure 4.16 (b)) which are quickly damped. The location of the bulge in the steady interface profiles shown in Figures 4.16 (c) and (d) migrates downwards with increasing γ (i.e., weakening capillarity) or increasing E_b (i.e., strengthening electrostatic effects), respectively. Correspondingly, increasing either γ or E_b leads to an increase in $H_{\max}$ (and hence

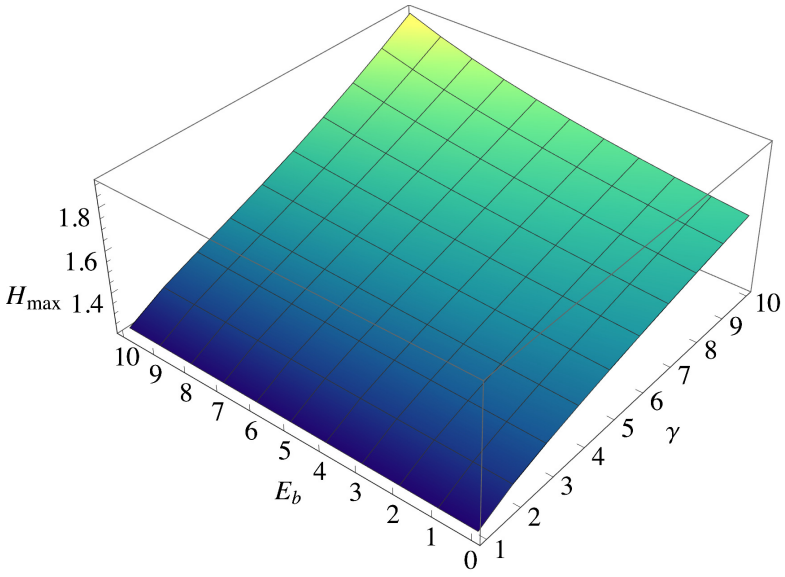

Figure 4.17: Surface plot showing how the maximum film thickness $H_{\max}$ of steady states varies for $H_0 = 0.9$, $0 \leq E_b \leq 10$, and $1 \leq \gamma \leq 10$.

a decrease in $H_{\min}$) as shown in Figures 4.16 (a) and (b). Increasing E_b from $E_b = 0$ to $E_b = 10$ for $\gamma = 15$ (as shown in Figure 4.16 (a)) yields an increase in the maximum film thickness from $H_{\max} = 1.70812$ to $H_{\max} = 2.47154$. Similarly, increasing γ from $\gamma = 1$ to $\gamma = 50$ for $E_b = 4$ (as shown in Figure 4.16 (b)) yields an increase in the maximum film thickness from $H_{\max} = 1.21986$ to $H_{\max} = 2.94165$. This is also demonstrated by Figure 4.17 which shows a surface plot of $H_{\max}$ in a region of (γ, E_b) parameter space in which the behaviour is steady for $H_0 = 0.9$ (located in the bottom left-hand corner of Figure 4.12 (e)). Figure 4.17 shows that the maximum film thickness increases from $H_{\max} = 1.21626$ for $\gamma = 1$ and $E_b = 0$ to $H_{\max} = 1.91085$ for $\gamma = 10$ and $E_b = 10$.

4.2.4 Periodic-state behaviour

In our numerical calculations, we track the locations and heights of spatiotemporal maxima (i.e., values of $H(\theta, T)$ that are locally maximal in both space and time). The numerical solution is classified as periodic when the code detects that these maxima approach temporal periodicity. Specifically, an array is stored that records each instance there is such a maximum, along with its associated thickness and the time at which it occurred. These parameters are monitored over 10 oscillations and the algorithm evaluates if the variations in thickness are less than 10^{-3} and

whether the time intervals between successive maxima remain constant down to time step accuracy. If these conditions are met, the numerical solution is classified as periodic.

In states classified as periodic, a bulge is typically carried around the cylinder periodically by the rotation. Figures 4.12 (a) and (b) show that for very thin films, solid body rotation behaviour dominates and periodic states occur. Figures 4.12 (c) and (d) show that for thin (but not very thin) films, a band of periodic states occurs between steady states and outer contact.

As mentioned in Section 4.2.2, the periodic states that we observed in our investigations contained at most two bulges throughout their evolution, in agreement with the linear theory described in Section 4.1.1 and shown in Figure 4.15. When two bulges arise, they coalesce before the final periodic state is reached, which always consists of only one bulge. Figure 4.18 shows an example of this behaviour, in particular, showing snapshots of the interface for $H_0 = 0.5$ (corresponding to Figure 4.12 (c)), $\gamma = 25$, and $E_b = 40$ during two different stages of the evolution: (a)–(d) as the system evolves towards the periodic state (during which time two bulges have formed and are oscillating around the cylinder) and (e)–(h) once the system has reached its final periodic state (by which point the two bulges have coalesced). For these parameter values, by (4.1.9) the linear theory predicts that 2 bulges will arise (specifically, $n_{\max}$ is calculated to be $n_{\max} \approx [2.44683] = 2$), which is in agreement with the numerical results.

The effect of increasing E_b for a fixed value of γ on a representative periodic state for $H_0 = 0.5$ (corresponding to Figure 4.12) (c)) is shown in Figure 4.19. Specifically, Figure 4.19 shows (a), (b) the evolution of the maximum and minimum film thicknesses over time and (c), (d) the periodic interface profiles for $\gamma = 10$ with (a), (c) $E_b = 10$ and (b), (d) $E_b = 40$. Note that Figures 4.19 (b) and (d) correspond to the same system that is shown in Figure 4.18 and is discussed above. For $E_b = 10$, the linear theory predicts that one bulge will arise (specifically, $n_{\max} \approx [1.36812] = 1$), which is in agreement with the numerical results shown in Figure 4.18 (c). As before, increasing the electric potential difference results in an increase in $H_{\max}$ (and, correspondingly, a decrease in $H_{\min}$) as the bulge is pulled closer to the outer electrode by electrostatic effects. Increasing the electric potential difference from $E_b = 10$ to $E_b = 40$ almost triples the maximum film thickness from $H_{\max} = 0.631839$ to $H_{\max} = 1.71866$.

Similarly, the effect of increasing γ for a fixed value of E_b is shown in Figure

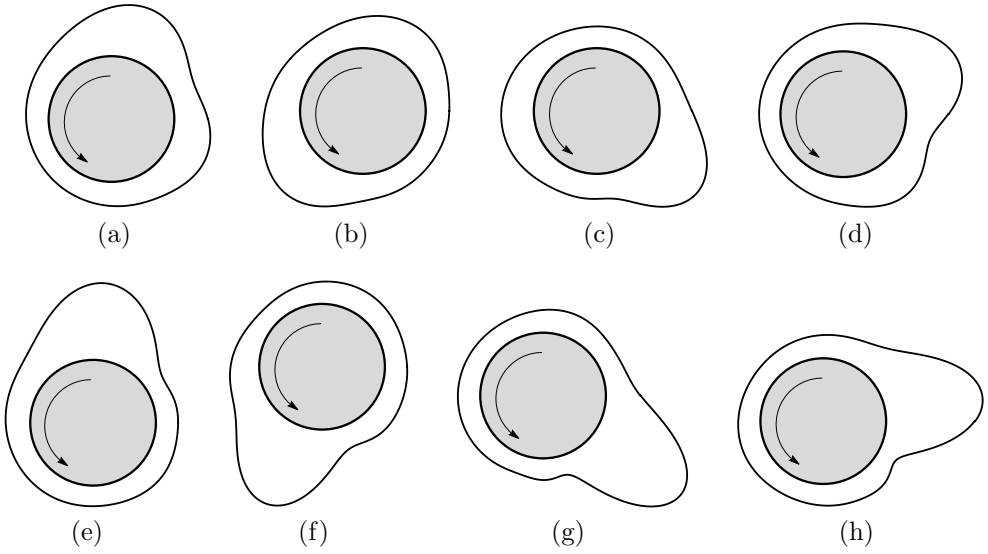

Figure 4.18: Snapshots of the interface for $H_0 = 0.5$, $\gamma = 25$, and $E_b = 40$ at times (a) $T = 60$, (b) $T = 62$, (c) $T = 64$, and (d) $T = 66$ and at the later times (e) $T = 300$, (f) $T = 302$, (g) $T = 304$, and (h) $T = 306$. The curved arrows represent the direction of rotation. Note that the film thickness has been exaggerated for illustrative purposes by using the artificial value $\epsilon = 1$.

4.20. In particular, Figure 4.20 shows that, as we have seen previously, weakening capillarity has a qualitatively similar effect on the system as increasing E_b, yielding an increase in the maximum film thickness. For these parameter values, by (4.1.9) the linear theory predicts that 1 and 2 bulges will arise for $\gamma = 10$ and $\gamma = 40$, respectively, in agreement with the numerical results. Specifically, the two-bulge configuration for $\gamma = 40$ is qualitatively similar to that shown in Figure 4.18 and thus is not displayed for brevity. As before, the bulge is pulled closer to the outer electrode by electrostatic effects which can have a more prominent effect on the system when the stabilising effect of capillarity is weak. Increasing the capillary number from $\gamma = 10$ to $\gamma = 40$ increases the maximum film thickness from $H_{\max} = 0.735154$ to $H_{\max} = 1.05773$. Hence, in general, increasing either γ or E_b increases in the maximum film thickness as demonstrated in Figure 4.21 which shows a surface plot of $H_{\max}$ in a region of (γ, E_b) parameter space in which the behaviour is periodic for $H_0 = 0.5$ (located roughly in the middle of the periodic region in Figure 4.12 (c)). Figure 4.21 shows that the maximum film thickness increases from $H_{\max} = 0.695663$ for $\gamma = 10$ and $E_b = 20$ to $H_{\max} = 1.91532$ for

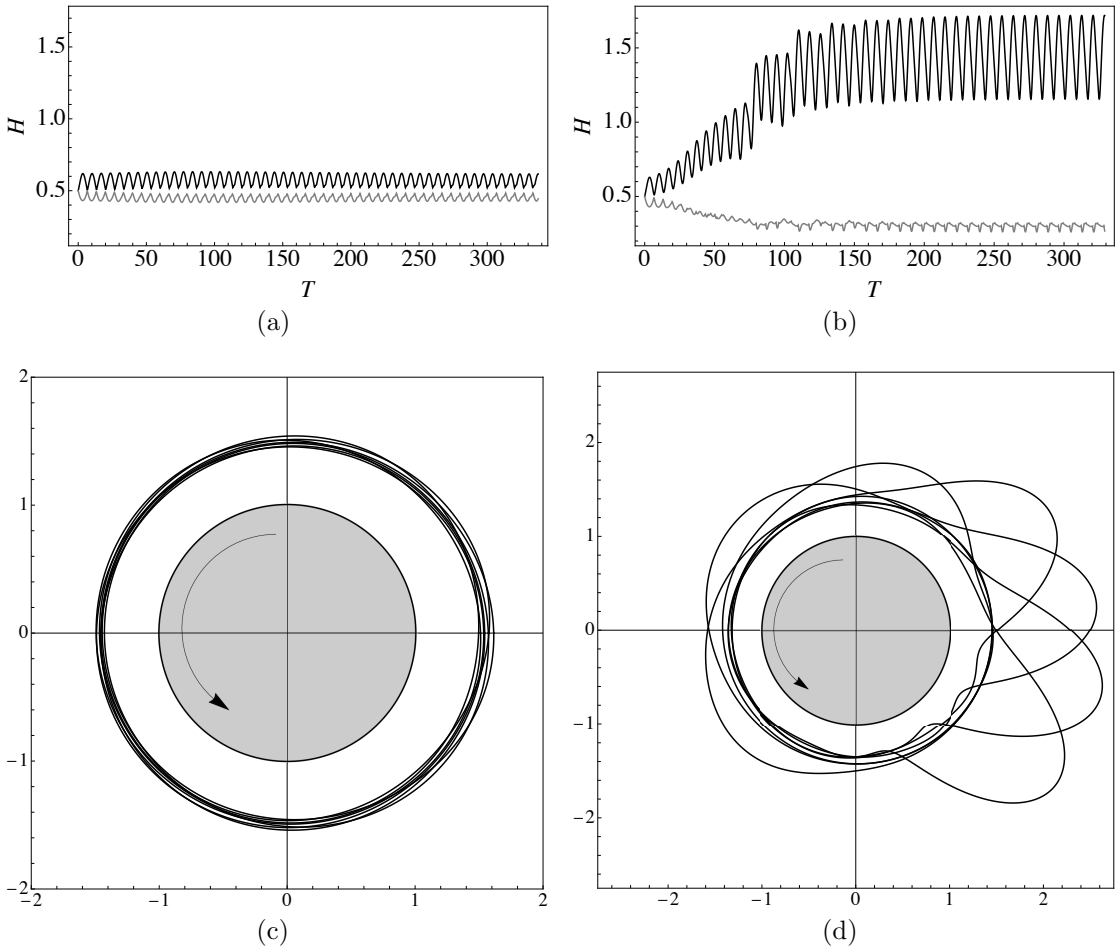

Figure 4.19: Periodic states for $H_0 = 0.5$, $\gamma = 25$, and (a), (c) $E_b = 10$ and (b), (d) $E_b = 40$. (a), (b) The time evolution of the minimum film thickness $H_{\min}$ (grey lines) and maximum film thicknesses $H_{\max}$ (black lines). (c), (d) Periodic interface profiles at times (c) $T = 328.6, 329.6, 330.6, 331.6, 332.6, 333.6$, and 334.6 and (d) $T = 320.3, 321.3, 322.3, 323.3, 324.3, 325.3$, and 326.3. The curved arrows represent the direction of rotation. Note that the film thickness has been exaggerated in (c) and (d) for illustrative purposes by using the artificial value $\epsilon = 1$.

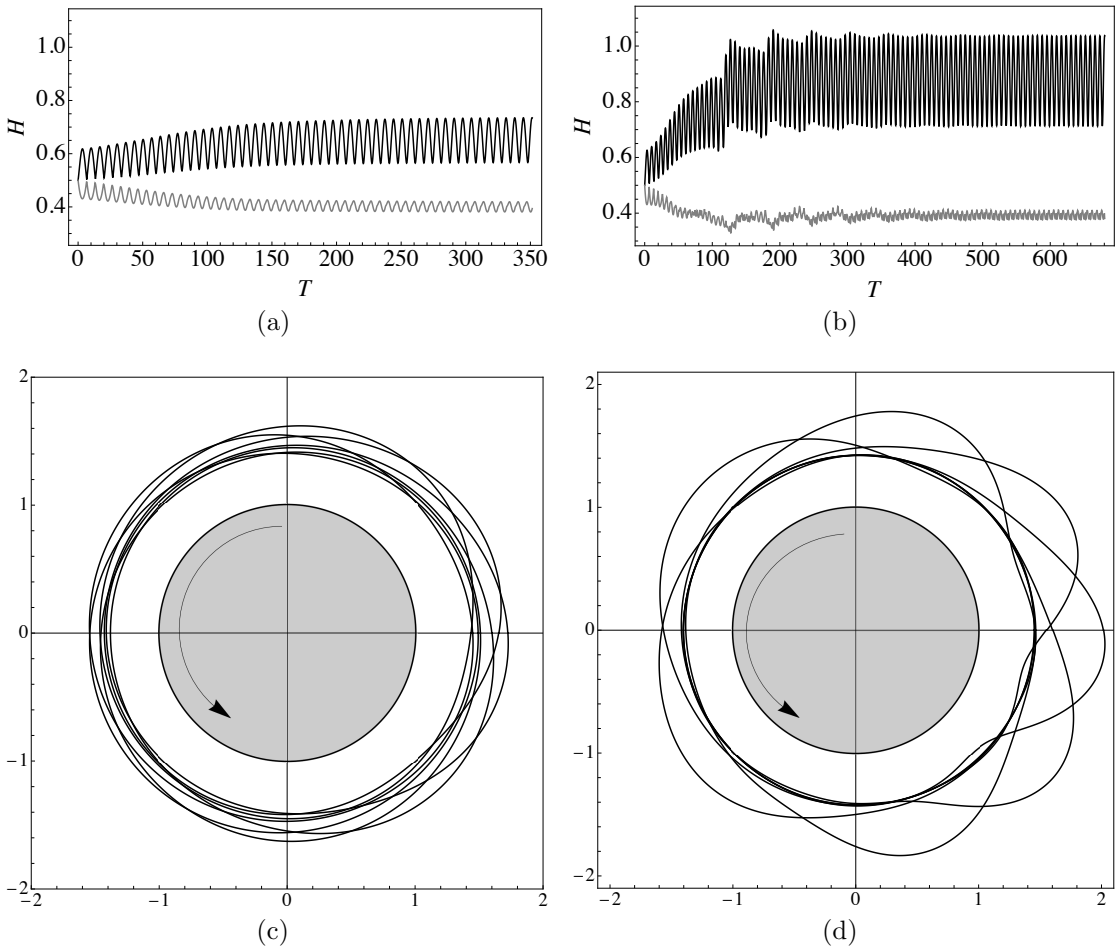

Figure 4.20: Periodic states for $H_0 = 0.5$, $E_b = 25$, and (a), (c) $\gamma = 10$ and (b), (d) $\gamma = 40$. (a), (b) The time evolution of the minimum film thickness $H_{\min}$ (grey lines) and maximum film thicknesses $H_{\max}$ (black lines). (c), (d) Periodic interface profiles at times (c) $T = 342.6, 343.6, 344.6, 345.6, 346.6, 347.6$, and 348.6 and (d) $T = 671.8, 672.8, 673.8, 674.8, 675.8, 676.8$, and 677.8. The curved arrows represent the direction of rotation. Note that the film thickness has been exaggerated in (c) and (d) for illustrative purposes by using the artificial value $\epsilon = 1$.

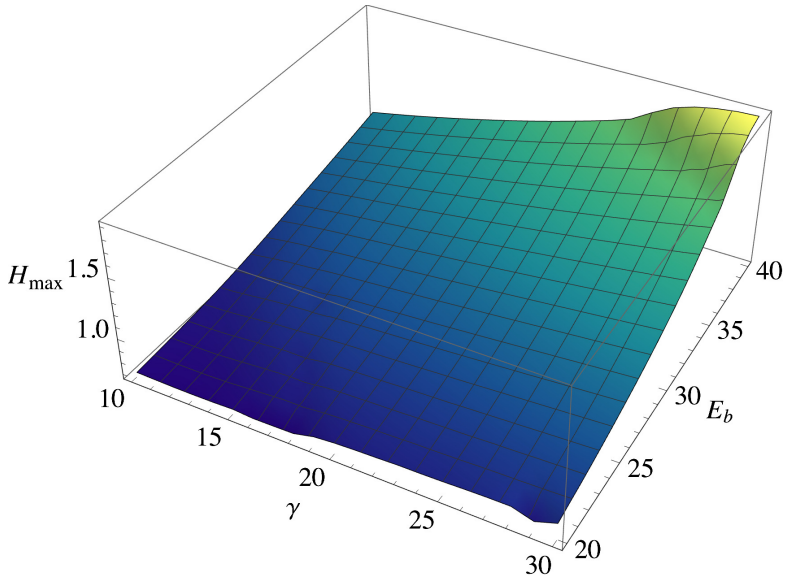

Figure 4.21: Surface plot showing how the maximum film thickness $H_{\max}$ of periodic states varies for $H_0 = 0.5$, $20 \leq E_b \leq 40$, and $10 \leq \gamma \leq 30$.

$\gamma = 30$ and $E_b = 40$.

4.2.5 Outer contact behaviour

Outer contact occurs when the interface touches the outer electrode in a finite time as illustrated by Figure 4.22 which shows outer contact occurring for the parameter values $H_0 = 0.7$, $\gamma = 10$, and $E_b = 44$ (corresponding to Figures 4.13 (e) and (f)). Specifically, Figure 4.22 (a) shows the evolution of the film thickness H over the final 10 time steps on the approach to outer contact, in which the solid horizontal lines indicate the location of the inner and outer electrodes and the dashed horizontal line indicates the initial condition $H_0 = 0.7$. Figure 4.22 (b) shows snapshots of the interface over the final 10 time steps. Outer contact corresponds to a singularity of the governing equation (2.2.23) which occurs when $H = D$, thus the final term in (2.2.23) diverges on the approach to outer contact as $H_{\max} \to D^-$. The interface accelerates as it approaches the outer electrode, which requires successively smaller time steps in order to ensure that the backwards Euler iteration converges in the time-stepping procedure (see Section 1.3.3 and Appendix A for details). Hence, the numerical solution is classified as outer contact behaviour if the time step $\Delta T < 10^{-6}$ (where ΔT is as defined in Section 1.3.3). Whilst this alone is sufficient to verify outer contact behaviour as such convergence issues do

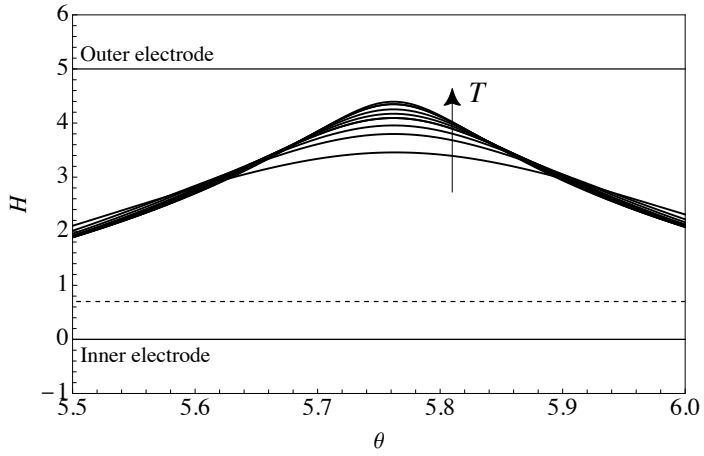

(a)

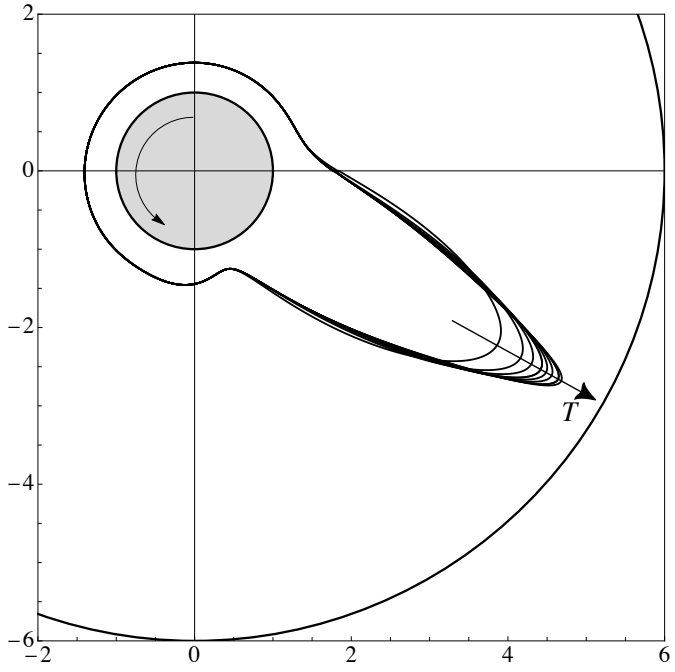

(b)

Figure 4.22: Outer contact for the parameter values $H_0 = 0.7$, $\gamma = 10$, and $E_b = 44$. (a) The evolution of the film thickness H over the final 10 time steps from $T = 31.4059$ until $T_c = 31.4064$. The horizontal lines indicate the location of the inner and outer electrodes (solid) and the initial condition $H_0 = 0.7$ (dashed). (b) Snapshots of the interface over the final 10 time steps. Note that the film thickness and the electrode distance have been exaggerated in (b) for illustrative purposes by using the artificial value $\epsilon = 1$. The straight arrow indicates the direction of increasing T and the curved arrow represents the direction of rotation.

not occur in any other regime, we have also verified that $(H_{\max}-1)/(D-1) > 0.9$ at the final time $T_{\rm c}$ for which the backwards Euler iteration converges. Note that outer contact behaviour is analogous to the "upper contact" behaviour which occurs in the case of a perfectly conducting thin film bounded between two parallel electrodes which was recently described by Keith [214] (see Section 1.6.2 for further details).

4.2.5.1 Bulge formation

As mentioned in Section 4.2.2, we observed at most 4 bulges in systems which evolved towards outer contact behaviour, in agreement with the linear theory described in Section 4.1.1 and shown in Figure 4.15. As discussed briefly in Section 4.2.2, more than 3 bulges are only expected to appear in outer contact states for large values of γ and E_b. However, in general, these are the parameter values for which outer contact occurs early in time (often as early as before $T = 1$ for large values of H_0). Hence, in many instances of outer contact behaviour there is not enough time in practice for the bulges to form. It is for this reason that at most 2 bulges arise in most of the outer contact states identified in the present study in practice. As discussed previously in Section 4.1.1, when more than one bulge does arise throughout the evolution, they often coalesce on the approach to outer contact as $H_{\max} \to D^-$. Figure 4.23 shows an example of this behaviour, in particular, showing snapshots of the interface for $H_0 = 0.5$, $\gamma = 50$, and $E_b = 50$ as the system evolves towards outer contact. For these parameter values, by (4.1.9) the linear theory predicts that 4 bulges will arise (specifically, $n_{\max}$ is calculated to be $n_{\max} \approx [3.7706] = 4$). Initially, 1 bulge forms (see Figures 4.23 (a) and (b)) which then separates into 3 bulges by time $T = 23.5$ (see Figure 4.23 (f)). At late times, the largest bulge continues to increase in height whilst two smaller bulges shrink until eventually the bulges coalesce as $H_{\max} \to D^-$ and outer contact occurs at time $T_{\rm c} = 30.9025$.

4.2.5.2 Transitions and parameter space analysis

Our results indicate that outer contact behaviour occurs in two different cases in parameter space: the first occurs through a transition from a region of periodic states for small (but not very small) H_0 (see Figures 4.12 (c) and (d)), and the second occurs through a transition from a region of steady states for large H_0 (see

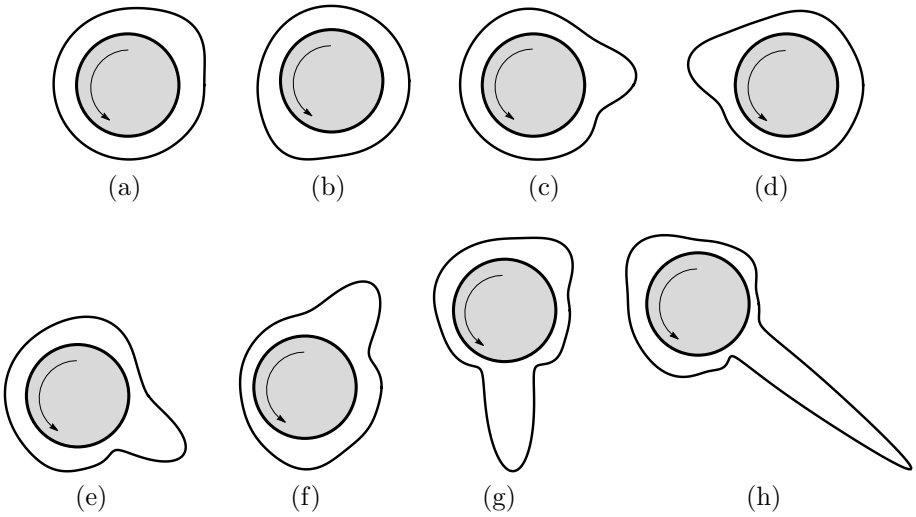

Figure 4.23: Snapshots of the interface for $H_0 = 0.5$, $\gamma = 50$, and $E_b = 50$ at times (a) $T = 11.5$, (b) $T = 14.5$, (c) $T = 17.5$, (d) $T = 20.5$, (e) $T = 23.5$, (f) $T = 26.5$, (g) $T = 29.5$, and (h) $T = T_c$ where $T_c = 30.9025$. The curved arrows represent the direction of rotation. Note that the film thickness has been exaggerated for illustrative purposes by using the artificial value $\epsilon = 1$.

Figures 4.12 (e)–(h)).

In instances in which outer contact occurs through a transition from periodic states, $H_{\max}$ increases whilst the bulge (or bulges) oscillates around the cylinder. As we have seen previously, the electric field is strongest where the film is closest to the outer electrode, hence this behaviour eventually leads to outer contact. Representative systems demonstrating this behaviour are shown in Figures 4.13 (e) and (f) and Figures 4.14 (e) and (f) which, as described in Section 4.2.2, show the time evolution of $H_{\max}$ and $H_{\min}$ and the spatiotemporal evolution of H as the respective systems evolve towards outer contact. In particular, Figures 4.13 (e) and (f) show that for $H_0 = 0.7$, $\gamma = 10$, and $E_b = 44$ outer contact occurs on the third oscillation at time $T_c = 31.4064$. Figure 4.24 shows snapshots of the interface during the final oscillation on the approach to outer contact for these parameter values. By (4.1.9), the linear theory predicts that 2 bulges will arise, whilst Figure 4.24 shows that in practice 1 bulge arises in the numerical solution. Similarly, Figures 4.14 (e) and (f) show that for $H_0 = 0.5$, $\gamma = 50$, and $E_b = 36$ outer contact occurs on the ninth oscillation at time $T_c = 64.7323$. Figure 4.25 shows snapshots of the interface during the final oscillation on the approach to

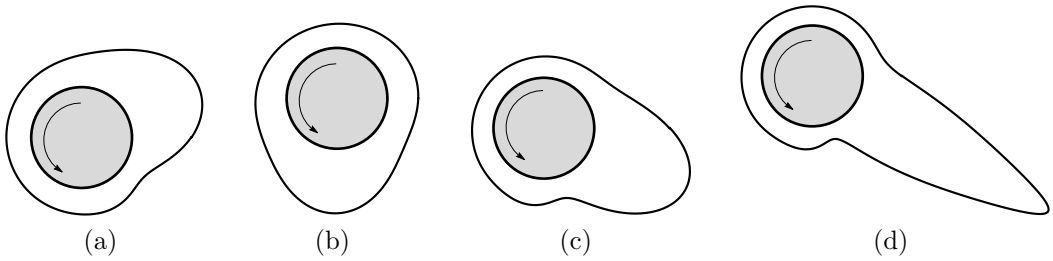

Figure 4.24: Snapshots of the interface for $H_0 = 0.7$, $\gamma = 10$, and $E_b = 44$ at times (a) $T = 19.56$, (b) $T = 23.56$, (c) $T = 27.56$, and (d) T_c where $T_c = 31.4064$. The curved arrows represent the direction of rotation. Note that the film thickness has been exaggerated for illustrative purposes by using the artificial value $\epsilon = 1$.

outer contact for these parameter values. By (4.1.9), the linear theory predicts that 3 bulges will arise, whilst Figure 4.25 shows that in practice 2 bulges arise (in particular, see Figures 4.25 (c)–(f)) before coalescing on the approach to outer contact as $H_{\max} \to D^-$ (see Figure 4.25 (h)).

Close to the transition between periodic-state behaviour and outer contact behaviour, the oscillations are less regular in the sense that there is not a steady (albeit oscillatory) increase in $H_{\max}$ like those shown in Figure 4.16 (e) and Figure 4.14 (e). Rather, the behaviour is more erratic, reflecting a more complex interplay between rotation, capillarity, and electrostatic effects. The effect of increasing E_b for a fixed value of γ on a representative outer contact state close to the transition between periodic-state behaviour and outer contact behaviour for $H_0 = 0.7$ (corresponding to Figure 4.12 (d)) is shown in Figure 4.26. In particular, Figure 4.26 shows (a), (b) the spatiotemporal evolution of the film thickness, (c), (d) the evolution of $H_{\max}$ and $H_{\min}$ over time, and (e), (f) the interface profiles over the final 10 time steps before outer contact for $H_0 = 0.7$ and $\gamma = 24$ with (a), (c), (e) $E_b = 28$ and (b), (d), (f) $E_b = 38$. By (4.1.9) the linear theory predicts that 2 bulges will arise for both $E_b = 28$ and $E_b = 38$. In practice, only 1 bulge arises in the numerical solution in both cases. Near the transition point from the region of periodic states (i.e., for $E_b = 28$), the rotational motion attempts to carry the bulge around the cylinder. However, the movement of the bulge is hindered by the influence of electrostatic effects, causing it to be temporarily held at the bottom right-hand side of the cylinder during each rotation. This behavior is depicted in Figures 4.26 (a) and (c). Specifically, this behavior corresponds to the semi-flat

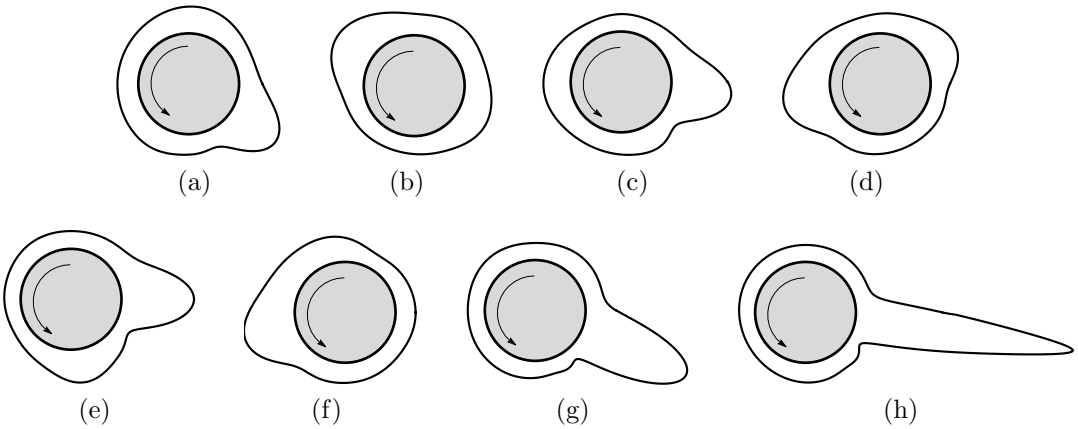

Figure 4.25: Snapshots of the interface for $H_0 = 0.5$, $\gamma = 50$, and $E_b = 36$ at times (a) $T = 36.89$, (b) $T = 40.89$, (c) $T = 44.89$, (d) $T = 48.89$, (e) $T = 52.89$, (f) $T = 56.89$, (g) $T = 60.89$, and (h) $T = T_c$ where $T_c = 64.7323$. The curved arrows represent the direction of rotation. Note that the film thickness has been exaggerated for illustrative purposes by using the artificial value $\epsilon = 1$.

regions depicted in Figure 4.26 (c), which persist for an extended duration during each rotation. The reason behind this behavior lies in the combined influence of rotation, gravity, and electrostatic effects on the lower part of the cylinder, where the film thickness is greatest, consequently intensifying the strength of the electric field. Eventually, when $H_{\max}$ attains a significant magnitude, the dominance of electrostatic effects becomes prominent, leading to the occurrence of outer contact after three rotations at time $T_c = 101.591$. Figures 4.26 (b) and (d) show the effect of increasing E_b to $E_b = 38$, which shows that the bulge does not complete a full oscillation around the cylinder and outer contact occurs at the much earlier time $T_c = 5.91194$. The approach to outer contact described above is shown in Figure 4.27 which shows snapshots of the interface at times $T = 2.927, 3.927, 4.927$, and T_c.

The effect of increasing γ for a fixed value of E_b on a representative outer contact state close to the transition between periodic-state behaviour and outer contact behaviour for $H_0 = 0.7$ is shown in Figure 4.28. In particular, Figure 4.28 shows (a), (b) the spatiotemporal evolution of the film thickness, (c), (d) the evolution of $H_{\max}$ and $H_{\min}$ over time, and (e), (f) the interface profiles over the final 10 time steps before outer contact for $H_0 = 0.7$ and $E_b = 30$ with (a), (c), (e) $\gamma = 21$ and (b), (d), (f) $\gamma = 31$. By (4.1.9) the linear theory predicts that 2 bulges

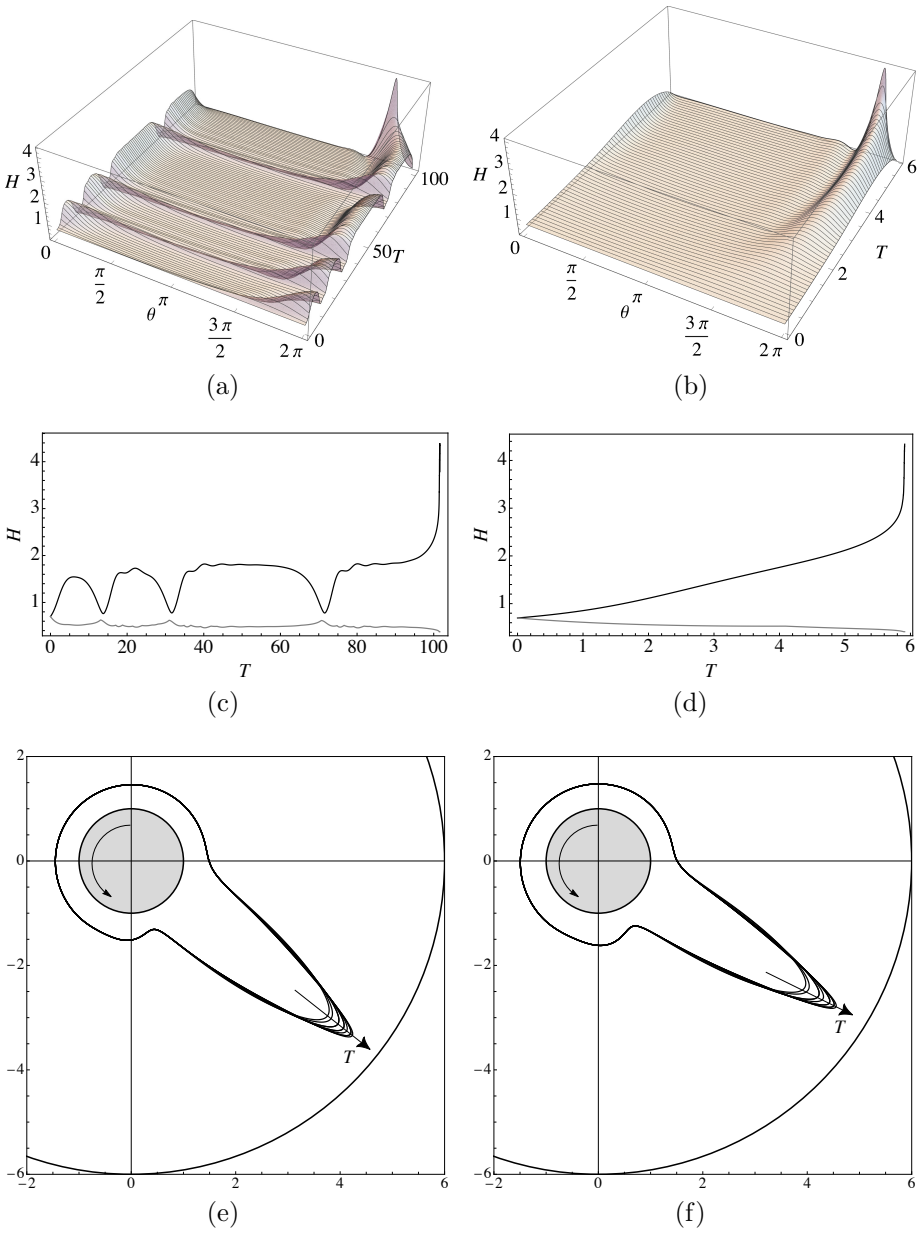

Figure 4.26: Outer contact for $H_0 = 0.7$, $\gamma = 24$, and (a), (c), (e) $E_b = 28$, and (b), (d), (f) $E_b = 38$. (a), (b) Spatiotemporal evolution of the film thickness H for $T = [0, T_c]$ where (c) $T_c = 101.591$ and (d) $T_c = 5.91194$. (c), (d) The time evolution of the minimum film thickness $H_{\min}$ (grey lines) and maximum film thicknesses $H_{\max}$ (black lines). (e), (f) Interface profiles over the final 10 time steps before outer contact from time (e) $T = 101.590$ and (f) $T = 5.91151$. Note that the film thickness and the electrode distance have been exaggerated in (e) and (f) for illustrative purposes by using the artificial value $\epsilon = 1$. The straight arrows indicate the direction of increasing T and the curved arrows represent the direction of rotation.

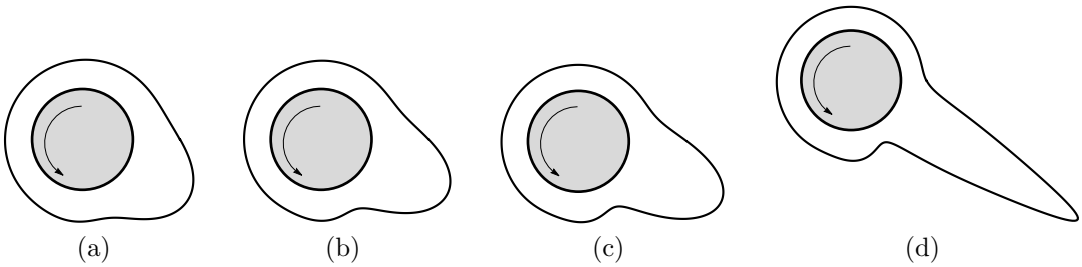

Figure 4.27: Snapshots of the interface for $H_0 = 0.7$, $\gamma = 24$, and $E_b = 38$ at times $T = 2.927, 3.927, 4.927$, and T_c where $T_c = 5.91194$. The curved arrows represent the direction of rotation. Note that the film thickness has been exaggerated for illustrative purposes by using the artificial value $\epsilon = 1$.

will arise for both $\gamma = 21$ and $\gamma = 31$, however, in practice, only 1 bulge arises in the numerical solution in both cases. The effect of increasing γ is qualitatively the same as that of increasing E_b which was described above. Specifically, for values of γ close to the transition (see, for example, Figures 4.28 (a) and (c)), the bulge oscillates around the cylinder before outer contact occurs, whereas for larger values of γ (see, for example, Figure 4.28 (b) and (d)) the bulge does not complete a full rotation around the cylinder before outer contact occurs. This is due to the fact that, as described previously, the destabilising electrostatic effects dominate when capillarity is weak. As before, it is for this reason that the time at which outer contact occurs decreases from $T_c = 75.9406$ for $\gamma = 21$ to $T_c = 7.13897$ for $\gamma = 31$.

In instances in which outer contact occurs through a transition from a region of steady states, the behaviour is qualitatively the same as that described above for large E_b or large γ as shown in Figures 4.26 (b) and (d), Figures 4.28 (b) and (d), and in Figure 4.27. Specifically, as described previously, for large H_0 the bulge does not complete a full rotation around the cylinder before outer contact occurs because electrostatic effects dominate the behaviour so quickly.

In general, as we have seen, increasing either γ or E_b decreases the time at which outer contact occurs. This is demonstrated in Figure 4.29 which shows a surface plot of T_c in a region of (γ, E_b) parameter space in which outer contact behaviour occurs for $H_0 = 0.5$ (located roughly in the top right-hand corner of the outer contact region in Figure 4.12 (d)). Figure 4.29 shows that the time at which outer contact occurs decreases from $T_c = 1.91532$ for $\gamma = 30$ and $E_b = 40$ to $T_c = 0.69566$ for $\gamma = 10$ and $E_b = 20$. Note that the surface shown in Figure 4.29 is

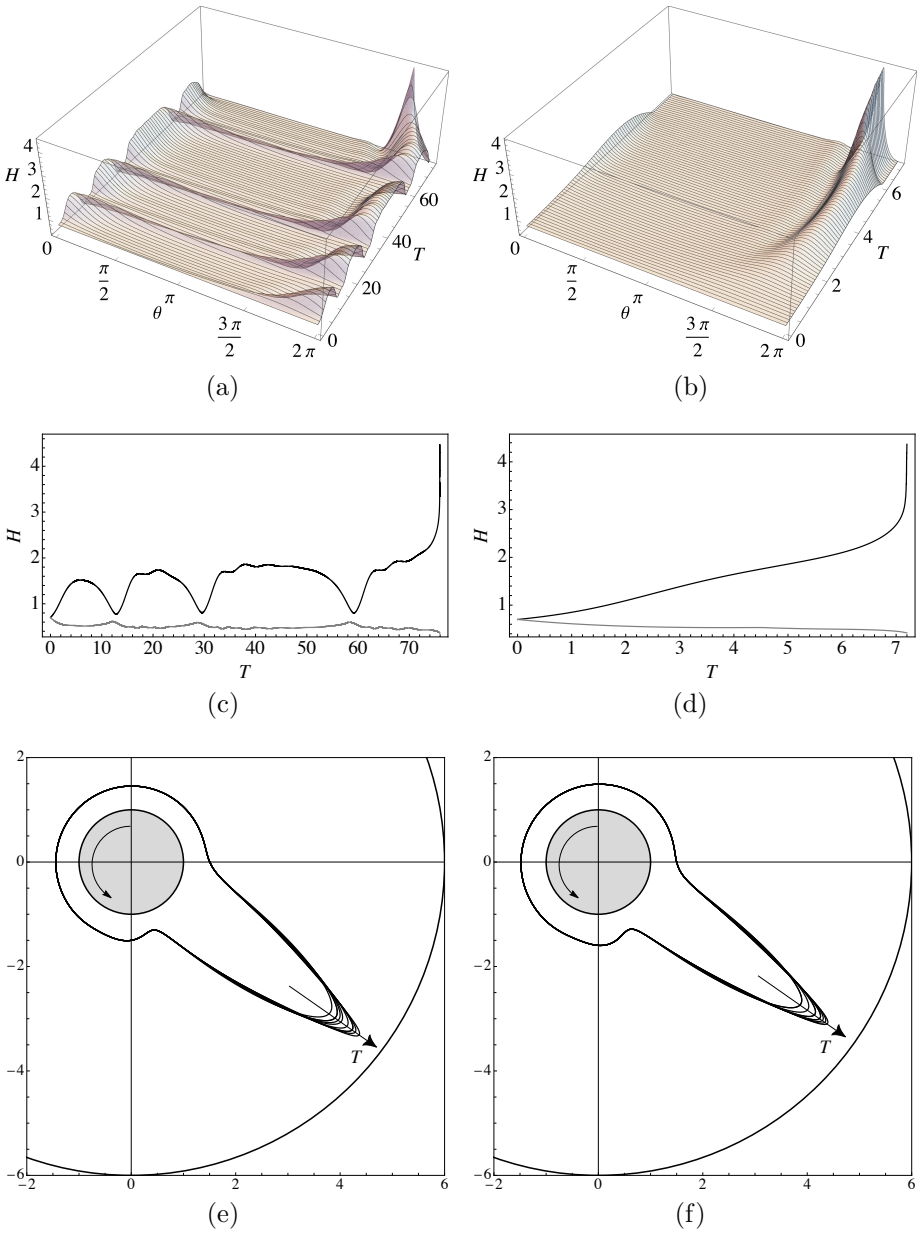

Figure 4.28: Outer contact for $H_0 = 0.7$, $E_b = 30$, and (a), (c), (e) $\gamma = 21$, and (b), (d), (f) $\gamma = 31$. (a), (b) Spatiotemporal evolution of the film thickness H for $T = [0, T_c]$ where (c) $T_c = 75.9406$ and (d) $T_c = 7.13897$. (c), (d) The time evolution of the minimum film thickness $H_{\min}$ (grey lines) and maximum film thicknesses $H_{\max}$ (black lines). (e), (f) Interface profiles over the final 10 time steps before outer contact from time (e) $T = 75.9404$ and (f) $T = 7.13894$. Note that the film thickness and the electrode distance have been exaggerated in (e) and (f) for illustrative purposes by using the artificial value $\epsilon = 1$. The straight arrows indicate the direction of increasing T and the curved arrows represent the direction of rotation.

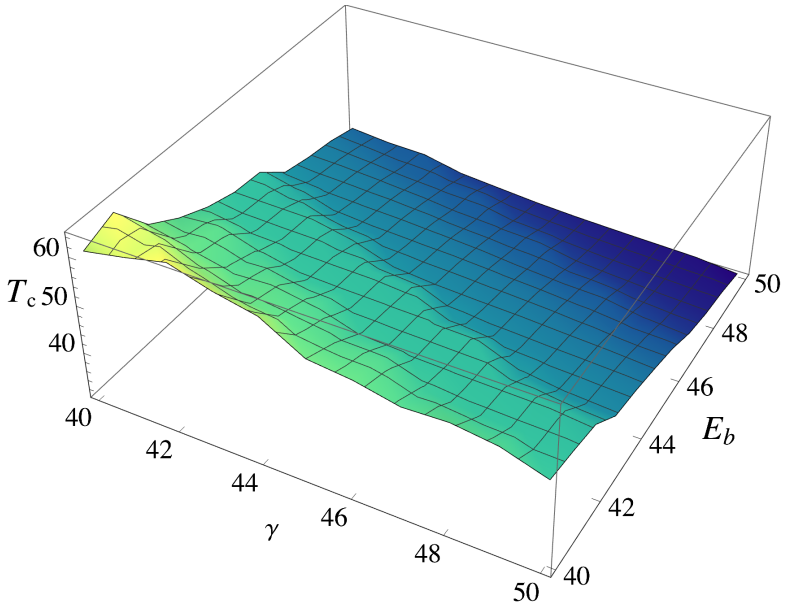

Figure 4.29: Surface plot showing how T_c varies for $H_0 = 0.5$, $40 \leq E_b \leq 50$, and $40 \leq \gamma \leq 50$.

not smooth, which we suspect is due to the variation in the number of oscillations that the bulge completes around the cylinder before outer contact occurs.

Note that an analytical investigation of outer contact behaviour could be an interesting and fruitful avenue for future study. We anticipate such an analysis to be tractable via the use of similarity solutions as shown recently by Keith [214] for the corresponding "upper contact" behaviour in the planar case.

4.2.6 Transient-state behaviour

The behaviour is classified as transient if $T > 10^4$ and none of the criteria for the other three behaviours described in the previous three sections has been met, representing temporary or transitional states that do not exhibit consistent or recurring patterns. Figure 4.12 shows that transient-state behaviour only occurs for relatively small values of H_0 and that the size of the transient region increases as H_0 decreases. For larger values of H_0, the transient states lie primarily on the transition between two other states. For example, Figure 4.12 (d) shows that for $H_0 = 0.7$, transient states occur near the transitions between steady states and periodic states and between periodic states and outer contact states. On the other hand, for very small values of H_0, large regions of transient-state behaviour

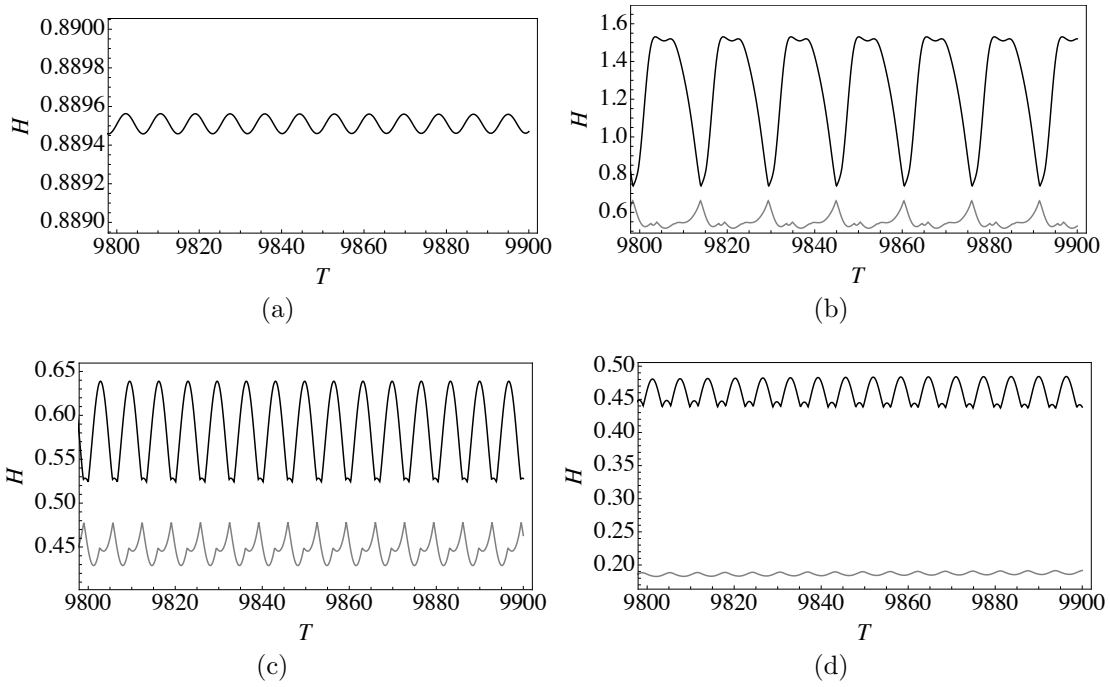

Figure 4.30: The time evolution of the minimum film thickness $H_{\min}$ (grey lines) and maximum film thickness $H_{\max}$ (black lines) of transient states over the time interval $9800 \leq T \leq 9900$ for (a) $H_0 = 0.7$ with $\gamma = 7$ and $E_b = 28$, (b) $H_0 = 0.7$ with $\gamma = 37$ and $E_b = 22$, (c) $H_0 = 0.5$ with $\gamma = 40$ and $E_b = 10$, and (d) $H_0 = 0.3$ with $\gamma = 48$ and $E_b = 19$.

which do not lie on a transition between states can also arise. For example, Figure 4.12 (b) shows that for $H_0 = 0.3$, a region of transient states occurs for large values of γ with moderate values of E_b.

Figure 4.30 shows the evolution of the maximum and minimum film thickness over the time interval $9800 \leq T \leq 9900$ for a selection of transient states. Specifically, Figures 4.30 (a) and (b) show transient states for $H_0 = 0.7$ near the transitions between steady states and periodic states, and between periodic states and outer contact states, respectively. The behavior illustrated in Figure 4.30 (a) exhibits very small oscillations, deviating only slightly from steady-state behaviour (note that only $H_{\max}$ is visible due to the scale required to discern the oscillations). Similarly, Figure 4.30 (b) demonstrates small deviations from periodic-state behaviour which are not obviously discernible. Figures 4.30 (c) and (d) show transient states for (c) $H_0 = 0.5$ and (d) $H_0 = 0.3$, respectively, which belong to the large

transient regions shown in Figures 4.12 (b) and (c), respectively. As before, the behaviour deviates only slightly from periodic-state behaviour. Whilst this deviation might not be readily apparent in Figure 4.30 (c), it becomes slightly more discernible when observing $H_{\max}$ in Figure 4.30 (d).

Time constraints prohibit us from running the code for longer than $T = 10^4$ per each run, which has a run-time of approximately 1.37 hours in wall-clock time. Therefore, calculation of the 1217 transient states shown in Figure 4.12 (a), for example, to $T = 10^4$ required a cumulative run-time of approximately 1667.29 hours in wall-clock time (equivalent to approximately 2.3 months of back-to-back calculations). It is therefore possible that, in some instances (for example, on the transition between different behaviours, such as those described above) states which appear to be transient may actually settle down to one of the other three behaviour classifications at much later times. For example, those on the transition between periodic-state behaviour and steady-state behaviour may eventually settle to a steady state, and those on the transition between periodic-state behavior and outer contact behaviour may eventually evolve to touch the outer electrode. In these cases, the states which are classified in this study as transient could actually be instances of complex, large-time dynamics which are difficult to capture numerically. Hence, it is possible that their presence in Figure 4.12 may represent the technical limitations of the current numerical approach. Indeed, this observation is similar to that of Hinch and Kelmanson [73] who, as discussed earlier in Section 1.4.4, found that when the film is very thin, the dynamics of the coating flow system (in absence of electrostatic effects) at large times evolve on four different time scales. In this case, numerical simulations of the Navier–Stokes equations become very computationally expensive, hence they performed a multiple-timescale analysis in order to elucidate the large-time dynamics of the system. Motivated by this observation, we discuss and investigate the large-time dynamics of the system considered in this chapter in Section 4.4.

4.3 Draining flow

In this section, we consider the special case in which the inner electrode is stationary by generalising the analysis presented in Chapter 3 to incorporate electrostatic effects. We proceed by setting the dimensionless rotation rate $\bar{\omega}$ to zero in the gov-

erning equation (2.2.20) to yield

$$\tilde{H}_{\tilde{T}} + \tilde{Q}_{\theta} = 0, \tag{4.3.1}$$

where $\tilde{Q} = \tilde{Q}(\theta, \tilde{T})$ is defined by

$$\tilde{Q} = -\frac{1}{3}\tilde{H}^3 \cos\theta + \frac{1}{3\tilde{\gamma}}\tilde{H}^3 \left(\tilde{H} + \tilde{H}_{\theta\theta}\right)_{\theta} + \frac{\tilde{E}_b}{3}\left(\frac{\tilde{H}}{\tilde{D} - \tilde{H}}\right)^3 \tilde{H}_{\theta}. \tag{4.3.2}$$

As in Chapter 3, throughout this section, we assume that the flow has left-to-right symmetry, and so restrict our attention to the left-hand side of the cylinder and hence work in the domain $\pi/2 \leq \theta \leq 3\pi/2$. Equation (4.3.1) is again subject to the initial condition (2.2.2) and the symmetry conditions (3.1.4). Note that throughout this section we drop the tilde decoration in (2.2.2), (3.1.4), (4.3.1), and (4.3.2) hereafter for brevity and for consistency with the analysis presented in Chapter 3.

The geometry of the dimensionless system considered in this section is shown in Figure 4.31, along with the three distinct regions of qualitatively different behaviour which emerge at late times which are qualitatively the same as those described in Chapter 3. Due to the similarities with the system analysed in Chapter 3, throughout this section we focus our attention on the differences between the draining problems in the absence and presence of an electric field, respectively, and will not repeat equations, definitions, and discussions which are the same as those given in Chapter 3. As before, numerical solutions of the governing equation (4.3.1) have been obtained up to late times (specifically, up to $T = O(10^{11})$) using the numerical scheme described in Appendix A.2.

Note that incorporating leading-order electrostatic effects into the dynamics in the pendant-drop region is a challenging problem owing to the fact that electrostatic effects can cause outer contact to occur. In instances of outer contact, it is not possible to generalise the analytical approach used before in Chapter 3, which relies on the assumption that the pendant drop is quasi-static at late times. Our results indicate that when electrostatic effects are weak (i.e., when either E_b is small or when outer electrode is far from the interface such that the electric field is weak), the system reaches a quasi-steady state. However, the limit of small E_b is not analytically tractable due to the fact that an analytical solution cannot be obtained in the pendant-drop region at first order. Therefore, we instead choose to

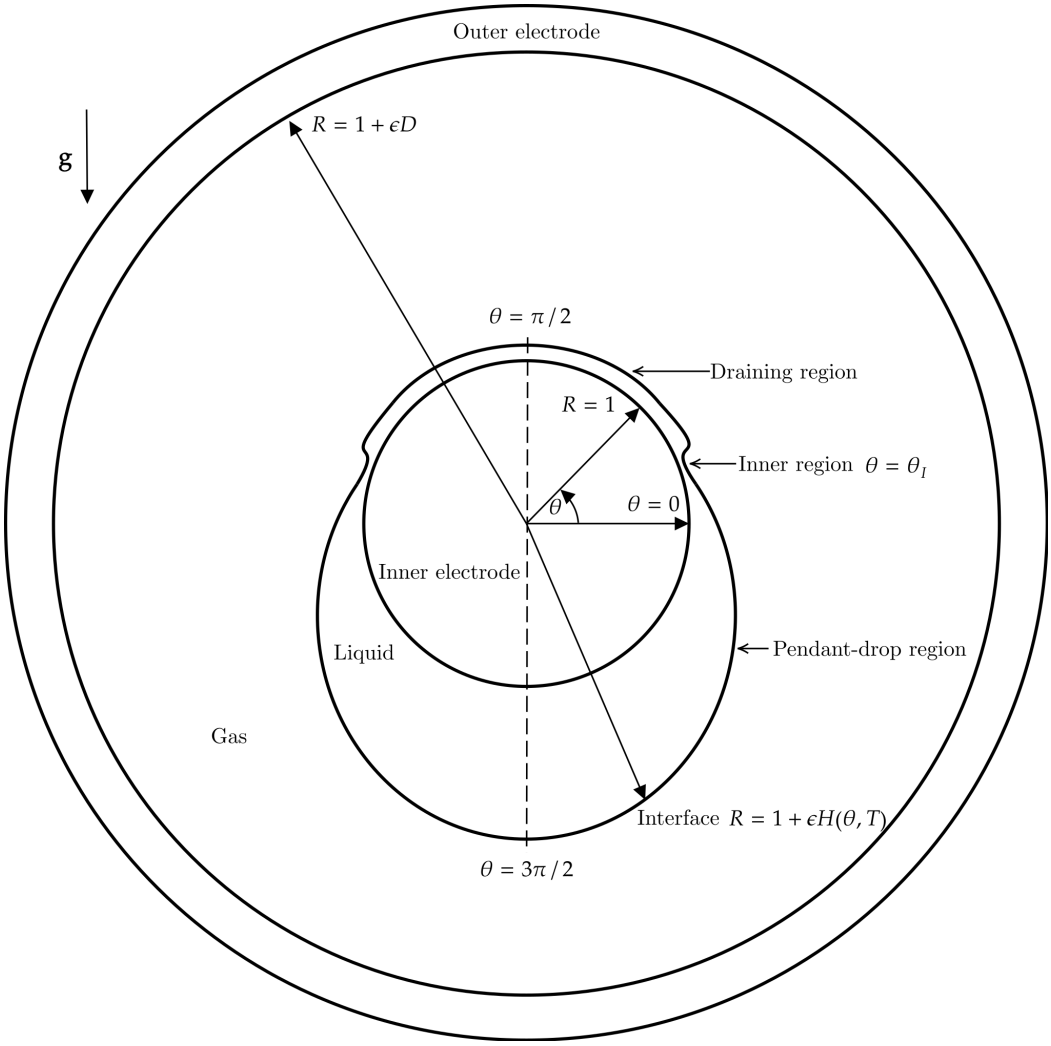

Figure 4.31: Geometry of the dimensionless system considered in Section 4.3.

consider the limit of large D in the pendant-drop region to ensure that the electric field is weak (such that outer contact does not occur) as a sensible first step to understanding the full problem. As we shall see, this choice simplifies the nonlinearities that arise in the governing equation in the pendant-drop region and hence allows us to generalise the approach described in Section 3.5 for the problem in the absence of an electric field. Note that we do not need to consider the limit of large D in the draining and inner regions because, as will be shown in Sections 4.3.3 and 4.3.5, respectively, these regions are unaffected by leading-order electrostatic effects due to the fact that the film is extremely thin in these regions. As a result, many of the figures presented throughout this section are rather similar to the corresponding figures in the absence of an electric field given in Chapter 3. Nevertheless, we include these to validate this fact by comparing the asymptotic results with numerical solutions of the governing equation (4.3.1) for non-zero values of E_b.

As before, we discuss first the early-time dynamics in Section 4.3.1, before investigating the late-time dynamics in Section 4.3.2.

4.3.1 Early-time draining

In this section, we describe the draining of the initially uniform film in the presence of an electric field at early times. As in Section 3.2, substitution of the expansion (3.2.1) into the governing equation (4.3.1) and solving order-by-order yields

$$H = 1 - \frac{1}{3}T\sin\theta - \frac{1}{6}T^2\underbrace{\left(\cos(2\theta) + \frac{E_b\sin\theta}{3(D-1)^3}\right)}_{H_2} + O(T^3). \tag{4.3.3}$$

Upon setting $E_b = 0$, equation (4.3.3) recovers equation (3.2.2). Figure 4.32 shows the second-order terms in (4.3.3), which we denote by $H_2 = H_2(\theta)$, for $D = 4$ with $E_b = 0$ (shown as the solid line) and $E_b = 10$ (shown as the dashed line). Electrostatic effects exert normal stress on the film everywhere, however, as we have seen previously, the electric field is stronger where the film is thicker, and hence its effect is most pronounced in the pendant-drop region. This is shown in Figure 4.32, confirming that H_2 is largest at the bottom of the cylinder (i.e., at $\theta = 3\pi/2$). Figure 4.33 (a) shows the film thickness at time $T = 10^{-2}$ for $E_b = 5$,

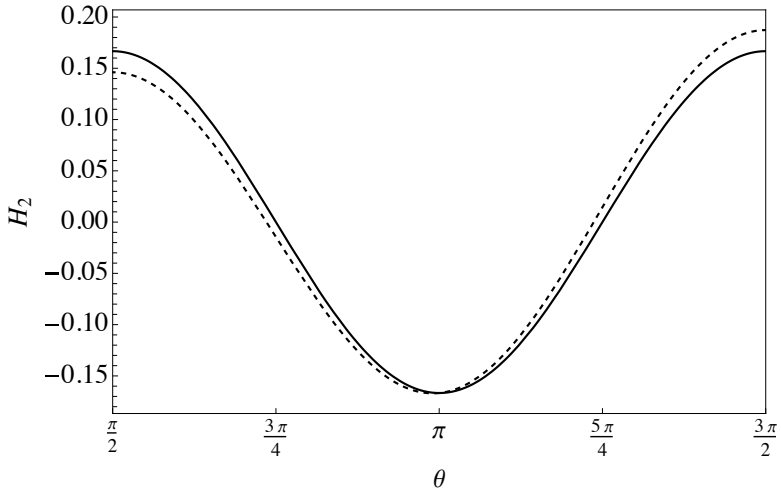

Figure 4.32: The second-order terms H_2 in the early-time asymptotic solution (4.3.3) for $D = 4$ with $E_b = 0$ (solid line) and $E_b = 10$ (dashed line).

$D = 8$ and the specific value

$$\gamma = \gamma_\pi(5, 8) \simeq 12.8785, \tag{4.3.4}$$

which was chosen for consistency with that used subsequently, where $\gamma_\pi = \gamma_\pi(E_b, D)$ is the value of γ required to have the inner region located at $\theta_{\rm I} = \pi$ for particular choices of E_b and D. This result will be shown and discussed in detail in Section 4.3.2. Note that the value (4.3.4) is smaller than the corresponding value $\gamma_\pi = 13.4428$ (3.2.3) that was used in Chapter 3 in the absence of an electric field, a point which we discuss in Section 4.3.4. In particular, Figure 4.33 (a) shows that the asymptotic solution (4.3.3) is in excellent agreement with the numerical solution of the governing equation (4.3.1) at this early time. Figure 4.33 (b) shows the evolution of the film thickness at the top of the cylinder (i.e., at $\theta = \pi/2$) plotted against time until $T = 10^2$ for $E_b = 5$, $D = 8$, and $\gamma = \gamma_\pi(5, 8)$ given by (4.3.4) until time $T = 10^2$, and confirms that (4.3.3) is valid at the top of the cylinder at early times. As in Section 3.2, for completeness, Figure 4.33 (b) also includes the corresponding late-time asymptotic solution (3.4.8) (shown with the dotted line) which was derived in Section 3.4, which will be shown in Section 4.3.3 to also be the solution in the draining region in the presence of an electric field.

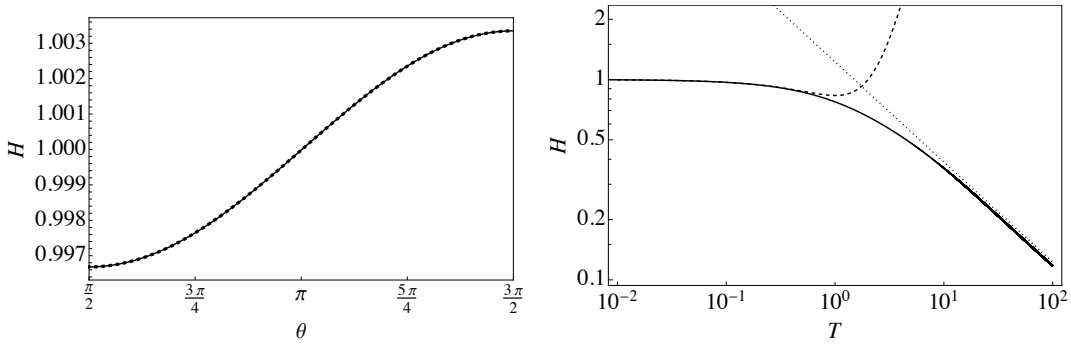

(a) (b)

Figure 4.33: (a) Film thickness for $E_b = 5$, $D = 8$, and $\gamma = \gamma_\pi(5, 8)$ given by (4.3.4) at time $T = 10^{-2}$. The dashed line shows the early-time asymptotic solution (4.3.3) and the solid line shows the numerical solution of (4.3.1). Note that the two curves are almost indistinguishable from one another at this early time. (b) The evolution of the film thickness at the top of the cylinder for $E_b = 5$, $D = 8$, and $\gamma = \gamma_\pi(5, 8)$ given by (4.3.4). The solid line shows the numerical solution of (4.3.1), the dashed line shows the early-time asymptotic solution (4.3.3), and the dotted line shows the late-time asymptotic solution (3.4.8).

4.3.2 Late-time draining

At late times, three distinct regions of behaviour emerge which are qualitatively the same as those in the absence of an electric field that were described in Section 3.3 and as sketched in Figure 4.31, namely, a draining region on the upper part of the cylinder, a pendant-drop region on the lower part of the cylinder, and a narrow inner region which joins the other two regions.

Figure 4.34 shows snapshots of the interface for $\gamma = \gamma_\pi(5, 8)$ given by (4.3.4) with $E_b = 5$ for (a), (b) $D = 4$ and (c), (d), $D = 8$. At late times, outer contact occurs for large values of E_b or small values of D. Figures 4.34 (a) and (b) show that for $D = 4$, a quasi-static pendant drop does not form as the destabilising electrostatic effects dominate the behaviour and lead to outer contact. However, Figures 4.34 (c) and (d) show that a quasi-static pendant drop forms at late times for the larger value $D = 8$.

Similarly to the effect of varying γ as discussed in Section 3.3, the effect of varying E_b is also mainly to vary the location of θ_I and, correspondingly, the widths of the draining and pendant-drop regions. Increasing the value of E_b results in a

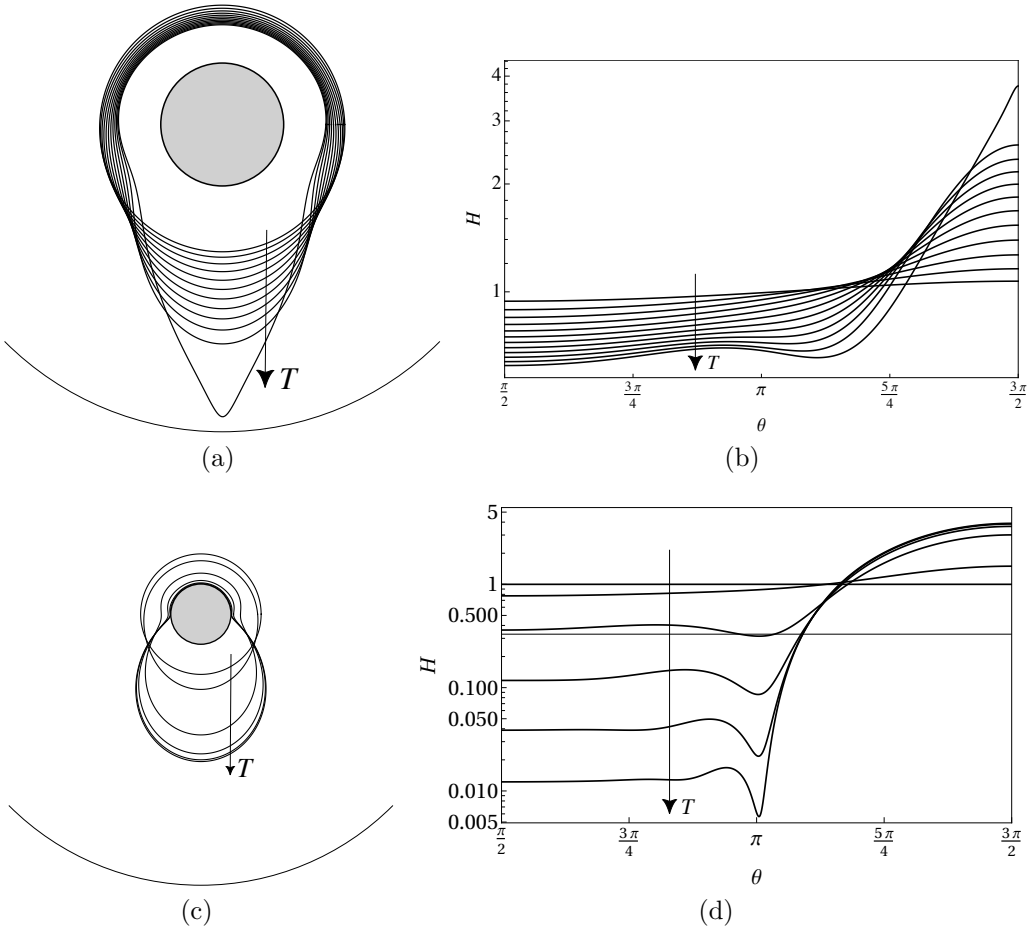

Figure 4.34: Snapshots of the interface for $\gamma = \gamma_\pi(5, 8)$ given by (4.3.4) and $E_b = 5$ with (a), (b) $D = 4$ at times $T = 0.192 + 0.193n$ for $n = 0, 1, \ldots, 10$ and at $T_c = 2.30001$, and (c), (d) $D = 8$ at times $T = 0, 10^0, 10^1, 10^2, 10^3$, and 10^4. The arrows indicate the direction of increasing time. (a), (c) Polar plots in which the film thickness and the electrode distance have been exaggerated for illustrative purposes by using the artificial value $\epsilon = 1$. (b), (d) Semi-log plots showing the film thickness H as a function of θ.

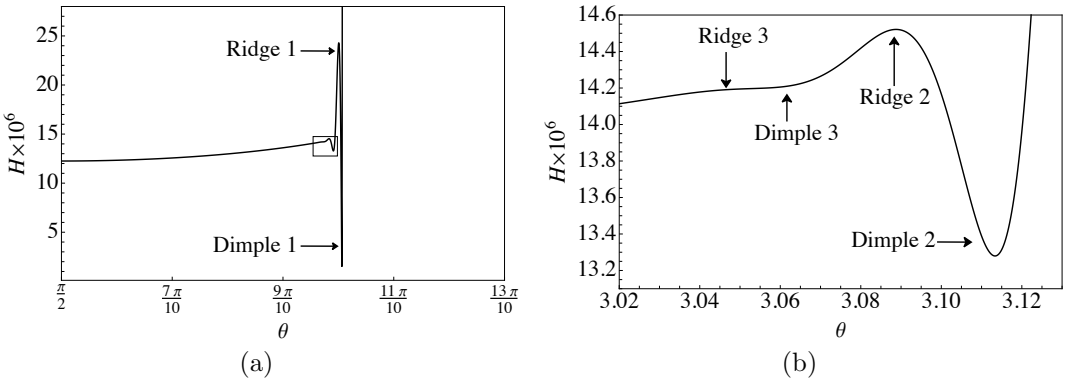

(a) (b)

Figure 4.35: The film thickness H for $E_b = 5$, $D = 8$, and $\gamma = \gamma_\pi(5, 8)$ given by (4.3.4) at time $T = 10^{10}$. (a) Solution for $\pi/2 \leq \theta \leq 13\pi/10$. The rectangle indicates the location of the enlargement shown in (b). (b) Enlargement of (a) near $\theta = \theta_{\rm I} = \pi$.

wider draining region and a narrower pendant-drop region as the pendant drop is pulled towards the outer electrode. However, note that when appropriate E_b and D values are selected in order to prevent outer contact from occurring for a particular choice of γ, the visual difference resulting from this adjustment is not readily discernible when compared to the interface depicted in Figures 4.34 (c) and (d). Therefore, we have not presented it here for visual comparison. We return to this point in Section 4.3.4.

Figure 4.35 shows the film thickness H calculated for $E_b = 5$, $D = 8$, and $\gamma = \gamma_\pi(5, 8)$ given by (4.3.4) at time $T = 10^{10}$. As described in Chapter 3, whilst only the first dimple and ridge are immediately apparent in Figures 4.34 and 4.35 (a), the second and third dimple and ridge are discernible in the enlargement of Figure 4.35 (a) near $\theta = \theta_{\rm I} = \pi$, shown in Figure 4.35 (b).

In Sections 4.3.3–4.3.5, we will show that electrostatic effects only affect the dynamics at leading order in the pendant-drop region and can be neglected in the draining region and in the inner region. In particular, it will be shown that electrostatic effects influence the calculations in the inner region only through matching dimple 1 with the pendant-drop region. The presence of an electric field introduces the term

$$Q_{\rm elec} = \frac{E_b}{3}\left(\frac{H}{D-H}\right)^3 H_\theta, \tag{4.3.5}$$

in each region which, analogous to the terms $Q_{\rm grav}$ and $Q_{\rm cap}$ introduced in Section

3.3, represents the contribution to the flux Q (4.3.2) due to electrostatic effects. In Sections 4.3.3 and 4.3.5, respectively, we show that Q_{elec} is of higher order in the draining and inner regions and so can be neglected. Note that, as mentioned previously, we will not make any assumptions on the size of D in the draining and inner regions in order to verify that they are unaffected by leading-order electrostatic effects. In Section 4.3.4, we derive the asymptotic solution in the pendant-drop region in which leading-order electrostatic effects are significant. In particular, in this region we consider the asymptotic limit of large D in which the electric field is weak: the problem is thus made analytically tractable and can be approached by generalising the method that was described previously in Section 3.5.

4.3.3 Draining region

In this section, we investigate the draining region in the presence of an electric field. As in Section 3.4, we seek a late-time asymptotic solution in which $H \ll 1$, in which case, to leading order, the governing equation (4.3.1) becomes the same as the governing equation in the draining region in the absence of an electric field (3.4.1). Therefore, the analysis in the draining region in the presence of an electric field is identical to that in the absence of an electric field given in Section 3.4. The solution in the draining region in the presence of an electric field is thus (3.4.4) where η is given by (3.4.6) with (3.4.7).

Figure 4.33 (b) shows the evolution of the film thickness at the top of the cylinder (i.e., at $\theta = \pi/2$) plotted against time until $T = 10^2$ for $E_b = 5$, $D = 8$, and $\gamma = \gamma_\pi(5, 8)$ given by (4.3.4) until time $T = 10^2$, and confirms that (3.4.4) is valid at the top of the cylinder at late times in the presence of electrostatic effects.

Substituting the solution for H in the draining region (3.4.4) into the flux (4.3.2) shows that the contribution to the flux due to electrostatic effects in the draining region is

$$Q_{\text{elec}} = \frac{E_b}{3}\left(\frac{H}{D-H}\right)^3 H_\theta = O(T^{-2}) \ll 1. \tag{4.3.6}$$

The contributions to the flux in the draining region due to gravity and capillarity are given in Section 3.4 as (3.4.10) and (3.4.11), respectively. In particular, (3.4.10), (3.4.11), and (4.3.6) show that $Q_{\text{cap}} \sim Q_{\text{elec}} \ll Q_{\text{grav}}$ at late times, con-

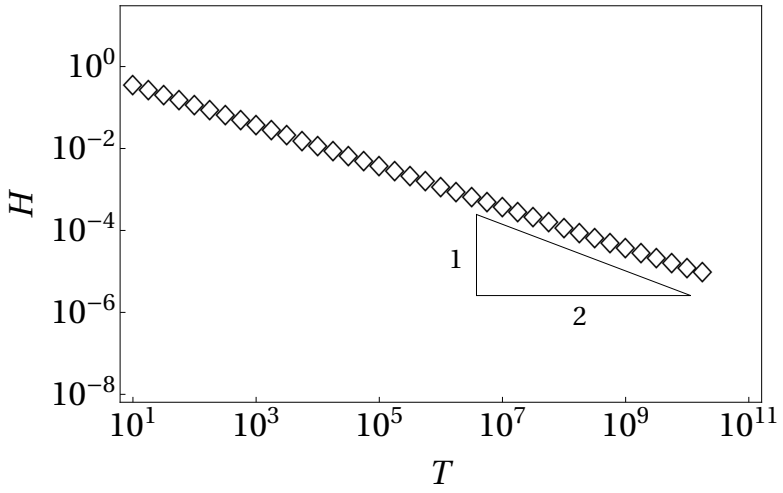

Figure 4.36: Log-log plot of H in the draining region, evaluated at the top of the cylinder for $E_b = 5$, $D = 8$, and $\gamma = \gamma_\pi(5, 8)$ given by (4.3.4) as a function of T, and the corresponding late-time asymptotic scaling $T^{-1/2}$.

	Asymptotic scaling	Numerical result
H	-0.5	-0.4984

Table 4.2: The late-time asymptotic scaling for H in the draining region, evaluated at the top of the cylinder, and the slope of the corresponding line of best fit to the numerical result for $T \geq 10^{9/4}$ shown in Figure 4.36.

firming the consistency of neglecting capillarity and electrostatic effects in the draining region.

Figure 4.36 shows a log-log plot of H in the draining region, evaluated at the top of the cylinder, obtained from the numerical solutions of (4.3.1) for $E_b = 5$, $D = 8$, and $\gamma = \gamma_\pi(5, 8)$ given by (4.3.4) as a function of T, and compares them with the corresponding late-time asymptotic scaling $T^{-1/2}$ obtained from (3.4.4). In particular, Figure 4.36 confirms that the interface has the predicted asymptotic behaviour at sufficiently late times. This conclusion is confirmed by the numerical values shown in Table 4.2, which shows that the asymptotic scaling is in good agreement with the slope of the corresponding line of best fit to the numerical results for $T \geq 10^{9/4}$ shown in Figure 4.36. Note that $Q \equiv 0$ at the top of the cylinder. Specifically, $Q_{\text{grav}} \equiv 0$ (since $\cos(\pi/2) = 0$) and $Q_{\text{cap}} = Q_{\text{elec}} \equiv 0$ (as a consequence of the symmetry conditions (3.1.4)), and so all fluxes are omitted from both Figure 4.36 and Table 4.2.

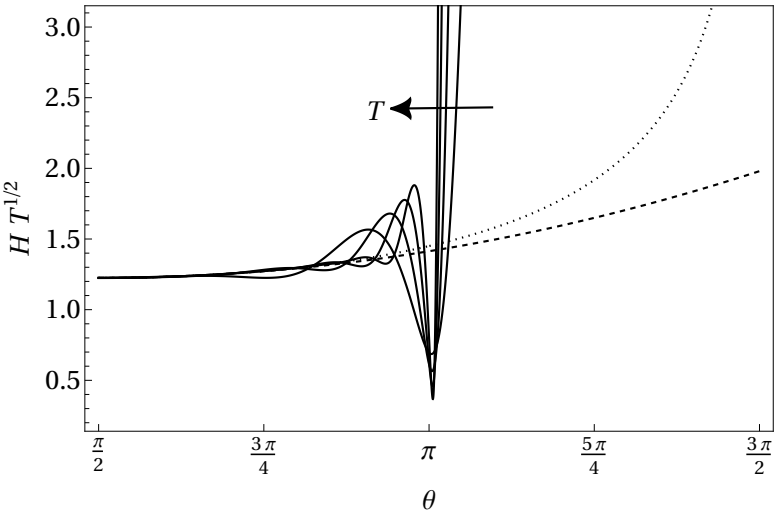

Figure 4.37: Snapshots of the scaled film thickness $\eta = HT^{1/2}$ for $E_b = 5$, $D = 8$, and $\gamma = \gamma_\pi(5, 8)$ given by (4.3.4) at times $T = 10^3, 10^4, 10^5$, and 10^6. The arrow indicates the direction of increasing time. The dotted line shows the leading-order asymptotic solution in the draining region at late times (3.4.6) and the dashed line shows the asymptotic solution valid near the top of the cylinder (3.4.9).

Figure 4.37 shows snapshots of the scaled film thickness $\eta = HT^{1/2}$ calculated at various times for $E_b = 5$, $D = 8$, and $\gamma = \gamma_\pi(5, 8)$ given by (4.3.4) together with the self-similar solution in the draining region (3.4.6) (dotted line) and the asymptotic solution near the top of the cylinder (3.4.9) (dashed line), confirming that (3.4.6) and (3.4.9) are valid in the draining region at late times.

4.3.4 Pendant-drop region

In this section, we investigate the pendant-drop region in the presence of an electric field. The results of our numerical calculations indicate that electrostatic effects are significant at leading order in the pendant-drop region. As mentioned before, at late times when the outer electrode is far enough from the interface, a quasi-static pendant drop forms on the lower part of the cylinder, as shown in Figure 4.34 (c).

In order to investigate the behaviour of the model (4.3.1) (which was derived by assuming that $D = O(1)$) in the distinguished limit in which D is large, we

assume that $D^{-1} \ll 1$ such that the governing equation (4.3.1) becomes

$$(H + H_{\theta\theta})_\theta + \gamma \bar{E}_b H_\theta + O(D^{-1}) = \gamma \cos\theta, \tag{4.3.7}$$

where we have set

$$E_b = D^3 \bar{E}_b, \tag{4.3.8}$$

where $\bar{E}_b = O(1)$ so as to retain electrostatic effects at leading order in D^{-1}. As discussed previously, the problem is analytically tractable in the limit $D^{-1} \ll 1$ by generalising the approach described in Section 3.5 for the problem in the absence of an electric field.

Solving (4.3.7) subject to the symmetry condition at the bottom of the cylinder (3.1.4) and the boundary conditions (3.5.2) and (3.5.3) yields the leading-order solution for H in the pendant-drop region in the presence of an electric field in the limit of large D, namely,

$$\begin{aligned} H =& \bar{E}_b^{-1} \Bigg\{ \sin\theta - \sin\theta_{\mathrm{I}} \\ &+ A^{-1} \left[2\cos\theta_{\mathrm{I}} \csc\left(\frac{1}{2}A\left(3\pi - 2\theta_{\mathrm{I}}\right)\right) \sin\left(\frac{1}{2}A\left(\theta - \theta_{\mathrm{I}}\right)\right) \sin\left(\frac{1}{2}A\left(\theta - 3\pi + \theta_{\mathrm{I}}\right)\right) \right] \Bigg\}, \end{aligned} \tag{4.3.9}$$

which is valid for $\theta_{\mathrm{I}} \leq \theta \leq 3\pi/2$, where A is defined as

$$A = \sqrt{1 + \gamma \bar{E}_b}. \tag{4.3.10}$$

In the limit $\bar{E}_b \to 0$, equation (4.3.9) with (4.3.10) recovers equation (3.5.4) in the absence of an electric field. Note that equation (4.3.9) contains the term $\bar{E}_b^{-1}$ and hence we cannot directly set $\bar{E}_b = 0$.

Analogous to Section 3.5, substitution of the asymptotic solution for H in the pendant-drop region (4.3.9) with (4.3.10) into the global mass conservation condition (3.5.5) and evaluating the integral yields an implicit equation for θ_{I} in terms of γ and $\bar{E}_b$, namely

$$\begin{aligned} &2\bar{E}_b\pi + (3\pi - 2\theta_{\mathrm{I}})\sin\theta_{\mathrm{I}} \\ &+ \frac{1}{A^2}\cos\theta_{\mathrm{I}} \left[-2\bar{E}_b\gamma + A\left(2\theta_{\mathrm{I}} - 3\pi\right)\cot\left(\frac{1}{2}A\left(3\pi - 2\theta_{\mathrm{I}}\right)\right) \right] = 0. \end{aligned} \tag{4.3.11}$$

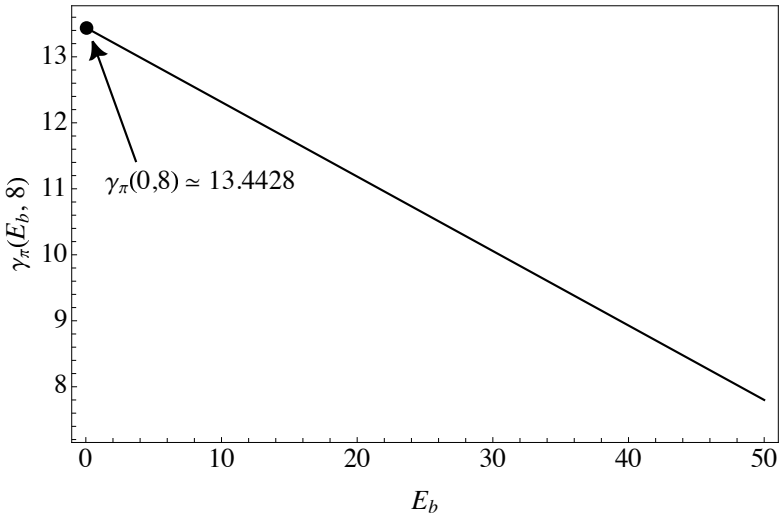

Figure 4.38: The linear relationship between $\gamma_\pi(E_b, D)$ and E_b to leading order in $\bar{E}_b$ with $D = 8$ for $0 \leq E_b \leq 50$ (corresponding to $0 \leq \bar{E}_b \leq 0.0976$) calculated from (4.3.12).

Note that it is not possible to invert equation (4.3.11) to obtain an explicit expression for γ, $\bar{E}_b$, or $\theta_{\rm I}$. Therefore, to make analytical progress, we consider the limit in which $\bar{E}_b$ is small by expanding γ in powers of $\bar{E}_b \ll 1$ in (4.3.11) as

$$\gamma = \gamma_0 + \bar{E}_b \gamma_1 + O(\bar{E}_b^2). \tag{4.3.12}$$

Solving order-by-order, (4.3.11) with (4.3.12) yields

$$\begin{aligned} \gamma_0 &= -\frac{8\pi \cos\theta_{\rm I}}{(3\pi - 2\theta_{\rm I})(2\pi - 2\theta_{\rm I} + \sin(2\theta_{\rm I})) - 8(\cos\theta_{\rm I})^2}, \\ \gamma_1 &= \frac{\begin{array}{c}\big[16\pi^2 \cos\theta_{\rm I}(3\,(-8 + (3\pi - 2\theta_{\rm I})^2)\cos\theta_{\rm I} - 8\cos(3\theta_{\rm I}) \\ + (3\pi - 2\theta_{\rm I})(3 + (3\pi - 2\theta_{\rm I})^2 + 3\cos(2\theta_{\rm I}))\sin\theta_{\rm I})\big]\end{array}}{(-4 + (3\pi - 2\theta_{\rm I})^2 - 4\cos(2\theta_{\rm I}) + (3\pi - 2\theta_{\rm I})\sin(2\theta_{\rm I}))^3}. \end{aligned} \tag{4.3.13}$$

Setting $\bar{E}_b = 0$ in (4.3.12) with (4.3.13) recovers equation (3.5.6). In particular, (4.3.12) with (4.3.13) predicts that the inner region is located at $\theta_{\rm I} = \pi$ when $\gamma = \gamma_\pi(5, 8)$ given by (4.3.4) for $E_b = 5$ and $D = 8$ (such that $\bar{E}_b = E_b/D^3 = 0.0976$). The value (4.3.4) of $\gamma_\pi(E_b, D)$ is smaller than the corresponding value γ_π (3.2.3) in the absence of an electric field. Figure 4.38 shows the linear relationship between $\gamma_\pi(E_b, D)$ and E_b to leading-order in $\bar{E}_b$ with $D = 8$ for $0 \leq E_b \leq 50$ (corresponding to $0 \leq \bar{E}_b \leq 0.0976$) calculated from (4.3.12) with (4.3.13). Figure 4.38 shows that

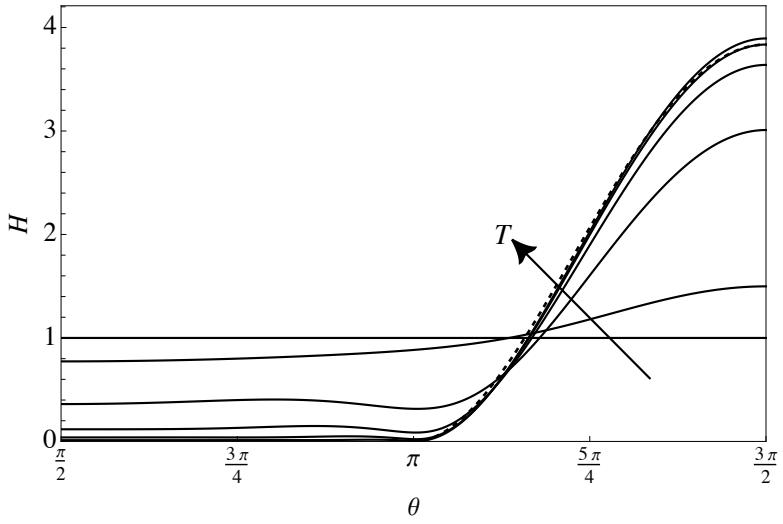

Figure 4.39: Snapshots of the film thickness for $E_b = 5$, $D = 8$, and $\gamma = \gamma_\pi(5, 8)$ given by (4.3.4) at times $T = 0, 10^0, 10^1, 10^2, 10^3$, and 10^4. The arrow indicates the direction of increasing time and the dashed line shows the leading-order asymptotic solution in the pendant-drop region (4.3.9).

as the value of E_b is increased, the value of γ_π decreases. This reflects the fact that electrostatic effects work against capillarity to pull the pendant drop towards the outer electrode, hence stronger capillarity is required to counter the destabilising effect of the electric field.

Figure 4.39 shows snapshots of the film thickness for $E_b = 5$, $D = 8$, and $\gamma = \gamma_\pi(5, 8)$ given by (4.3.4) at various times together with the leading-order asymptotic solution in the pendant-drop region (4.3.9), confirming that the interface does indeed approach the asymptotic solution at late times. In particular, Figure 4.39 shows that the leading-order film thickness in this region increases from zero at $\theta_{\rm I} = \pi$ to a maximum value of

$$H\left(\frac{3\pi}{2}\right) = -\bar{E}_b^{-1}\left\{1 + \sin\theta_{\rm I} + A^{-1}\cos\theta_{\rm I}\tan\left(\frac{1}{4}A\left(3\pi - 2\theta_{\rm I}\right)\right)\right\} \simeq 3.8351 \tag{4.3.14}$$

at the bottom of the cylinder, which is very close to the corresponding value $H(3\pi/2) \simeq 3.8366$ (3.5.7) calculated in the absence of an electric field. The values are expected to be close since in both cases there is the same volume of liquid initially on the cylinder, and both (4.3.14) and (3.5.7) are calculated using the values of γ that are required to have the inner region located at $\theta_{\rm I} = \pi$, thus

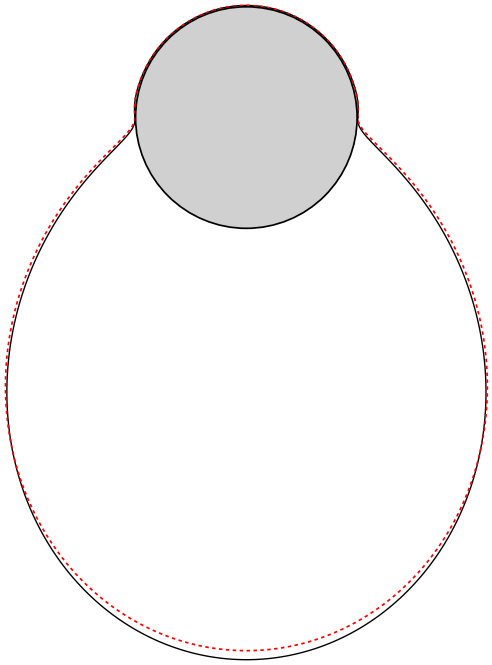

Figure 4.40: The interface at time $T = 10^4$ for $\gamma = \gamma_\pi(5, 8)$ given by (4.3.4) with $E_b = 5$ and $D = 8$ (solid black line), and for $\gamma = \gamma_\pi$ given by (3.2.3) with $E_b = 0$ (dashed red line). The film thickness has been exaggerated for illustrative purposes by using the artificial value $\epsilon = 1$

resulting in a pendant drop of approximately the same height and width. Figure 4.40 shows the interface both for $\gamma = \gamma_\pi(5, 8)$ given by (4.3.4) with $E_b = 5$ and $D = 8$ (solid black line), and for $\gamma = \gamma_\pi$ given by (3.2.3) with $E_b = 0$ (dashed red line) at time $T = 10^4$. In particular, Figure 4.40 shows that the pendant drop is slightly longer and narrower in the presence of an electric field compared that in the absence of an electric field due to the electrostatic effects pulling the film towards the outer electrode.

Figure 4.41 shows the relationship between γ and $\theta_{\rm I}$ as predicted by (4.3.12) with (4.3.13) for $E_b = 5$ and $D = 16$ (such that $\bar{E}_b = E_b/D^3 = 0.0012$). Note that the value $D = 8$ was not used in Figure 4.41 because outer contact occurs for γ values larger than $\gamma = O(10)$, hence the final position of the inner region for these large values of γ cannot be seen unless the outer electrode is far enough away. Specifically, Figure 4.41 shows that the asymptotic expression (4.3.12) is in very good agreement with the position of the inner region calculated from numerical solutions of the governing equation (4.3.1) for five values of γ at time $T = 10^4$.

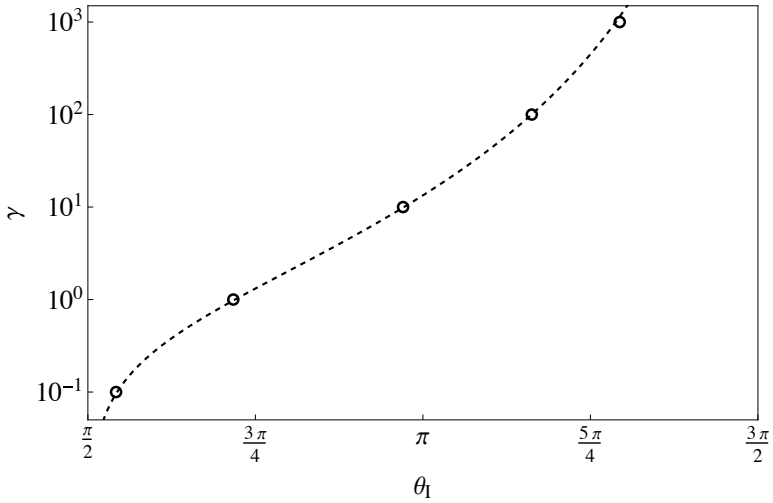

Figure 4.41: The relationship between γ and θ_{I} for $E_b = 5$ and $D = 16$. The dashed line shows the asymptotic expression (4.3.12) and the circles show the position of the inner region calculated from numerical solutions of the governing equation (4.3.1) for $\gamma = 10^{-1}, 10^0, 10^1, 10^2$, and 10^3.

It is worth noting that, as mentioned earlier, when suitable E_b and D values are selected to prevent outer contact occurring for a particular choice of γ, the visual distinction resulting from the variation of E_b is not readily apparent. In such cases, the position of θ_{I} will exhibit considerably less variation compared to the range illustrated in Figure 4.41 for varying γ due to the narrow range of E_b values that permit a quasi-static pendant drop. Consequently, this particular effect is not displayed here.

Substituting (4.3.12) with (4.3.13) into (4.3.9) and taking the limit $\theta \to \theta_{\mathrm{I}}^+$, yields the local behaviour of the interface in the pendant-drop region as it approaches the inner region, namely,

$$H|_{\theta\to\theta_{\mathrm{I}}} = -\frac{1}{2}\bar{E}_b^{-1}\left[\sin\theta_{\mathrm{I}} + \cos\theta_{\mathrm{I}}\cot\left(\frac{1}{2}\left(-3\pi + 2\theta_{\mathrm{I}}\right)B\right)B\right](\theta-\theta_{\mathrm{I}})^2 + O\left((\theta-\theta_{\mathrm{I}})^3\right), \tag{4.3.15}$$

where B is defined as

$$B = \left(1 + \gamma_0\bar{E}_b + \gamma_1\bar{E}_b^2\right)^{1/2}. \tag{4.3.16}$$

Note that (4.3.15) holds for general θ_{I} and γ and is not specific to the particular case in which $\theta_{\mathrm{I}} = \pi$. In the limit $\bar{E}_b \to 0$, equation (4.3.15) recovers equation (3.5.8). We will make use of (4.3.15) with (4.3.16) in Section 4.3.5 when performing the

asymptotic matching of the solution in the pendant-drop region to that in dimple 1. As we shall see in Section 4.3.5, it is only through (4.3.15) that the electric field influences the calculations in the inner region, which is otherwise unaffected by electrostatic effects.

4.3.5 Inner region

In this section, we investigate the inner region located at $\theta = \theta_{\mathrm{I}}$ in the presence of an electric field. It transpires that electrostatic effects can be neglected in the inner region. Hence, the calculations for the asymptotic scalings in dimple n and ridge n are identical to those given in Section 3.6.3. The solutions in dimple n and ridge n in the presence of an electric field are thus given by (3.6.73) and (3.6.74), respectively. We will show that electrostatic effects only enter the calculations in the inner region through matching dimple 1 to the pendant-drop region.

Substituting the solution for H in dimple 1 (3.6.8) into the flux (4.3.2) shows that the contribution to the flux due electrostatic effects in dimple 1 is

$$Q_{\mathrm{elec}} = \frac{E_b}{3}\left(\frac{H}{D-H}\right)^3 H_\theta = O(T^{-21/10}) \ll 1. \tag{4.3.17}$$

The contributions to the flux due to gravity and capillarity in dimple 1 are given in Section 3.6.1 as (3.6.10) and (3.6.11), respectively. In particular, (3.6.10), (3.6.11), and (4.3.17) show that $Q_{\mathrm{elec}} \ll Q_{\mathrm{grav}} \ll Q_{\mathrm{cap}} \ll 1$ at late times, confirming the consistency of neglecting gravitational and electrostatic effects in dimple 1. Specifically, since Q_{elec} is smaller than both Q_{cap} and Q_{grav}, we infer that the leading-order balance in (3.6.8) is still valid, hence confirming that the asymptotic scalings in dimple 1 in the absence of an electric field (3.6.8) are also valid in the presence of an electric field.

Figure 4.42 shows a log-log plot of H, Q_{grav}, Q_{cap}, and Q evaluated at the minimum of dimple 1 obtained from the numerical solution of (4.3.1) for $E_b = 5$, $D = 8$, and $\gamma = \gamma_\pi(5, 8)$ given by (4.3.4) as functions of T, and compares them with the corresponding late-time asymptotic scalings $T^{-3/5}$, $T^{-9/5}$, $T^{-3/2}$, and $T^{-3/2}$ obtained from (3.6.8), (3.6.10), (3.6.11), and (3.4.13), respectively. In particular, Figure 4.42 and Table 4.3 confirm that the interface has the predicted asymptotic behaviour at sufficiently late times. Note that $Q_{\mathrm{elec}} \equiv 0$ at the minimum of the dimples, and so is omitted from both Figure 4.42 and Table 4.3.

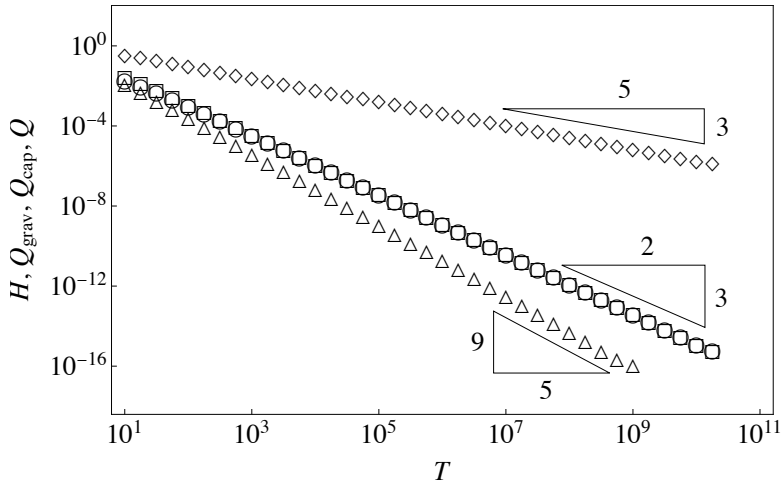

Figure 4.42: Log-log plot of H (diamonds), Q_{grav} (triangles), Q_{cap} (circles), and Q (squares) evaluated at the minimum of dimple 1 for $E_b = 5$, $D = 8$, and $\gamma = \gamma_\pi(5, 8)$ given by (4.3.4) as functions of T, and the corresponding asymptotic scalings $T^{-3/5}$, $T^{-9/5}$, $T^{-3/2}$, and $T^{-3/2}$. Note that the circles and squares almost overlay each other.

	Asymptotic scaling	Numerical result
H	-0.6	-0.5940
Q_{grav}	-1.8	-1.7784
Q_{cap}	-1.5	-1.4883
Q	-1.5	-1.4962

Table 4.3: The late-time asymptotic scalings for H, Q_{grav}, Q_{cap}, and Q in dimple 1, and the slopes of the lines of best fit to the numerical results for $T \geq 10^{9/4}$ shown in Figure 4.42.

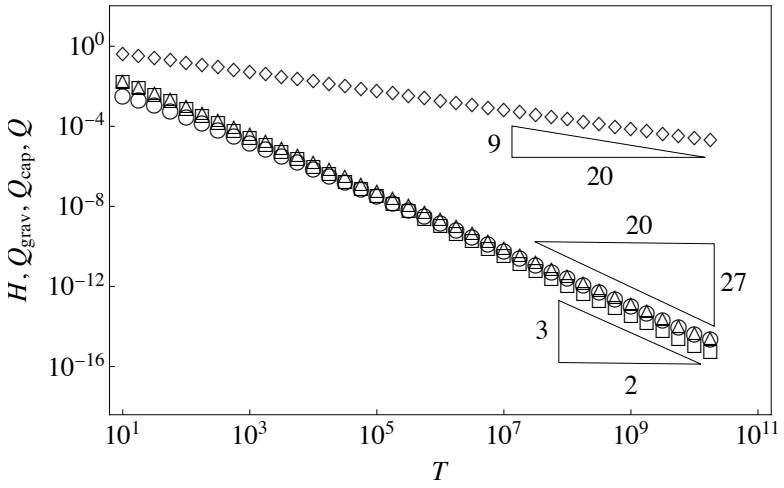

Figure 4.43: Log-log plot of H (diamonds), Q_{grav} (triangles), Q_{cap} (circles), and Q (squares) evaluated at the maximum of ridge 1 for $E_b = 5$, $D = 8$, and $\gamma = \gamma_\pi(5, 8)$ given by (4.3.4) as functions of T, and the corresponding asymptotic scalings $T^{-9/20}$, $T^{-27/20}$, $T^{-27/20}$, and $T^{-3/2}$. Note that the triangles, circles, and squares almost overlay each other.

Substituting the solution for H in ridge 1 (3.6.33) into the flux (4.3.2) shows that the contribution to the flux due to electrostatic effects in ridge 1 is

$$Q_{\text{elec}} = \frac{E_b}{3}\left(\frac{H}{D-H}\right)^3 H_\theta = O(T^{-33/20}) \ll 1. \tag{4.3.18}$$

The contributions to the flux due to gravity and capillarity in ridge 1 are given in Section 3.6.2 as (3.6.37) and (3.6.38), respectively. In particular, (3.6.37), (3.6.38), and (4.3.18) show that $Q_{\text{elec}} \ll Q_{\text{grav}} \sim Q_{\text{cap}} \ll 1$ in ridge 1 at late times, confirming the consistency of neglecting electrostatic effects in ridge 1. As was the case in dimple 1 described above, since Q_{elec} is smaller than Q_{cap} and Q_{grav}, we infer that the leading-order balance in (3.6.33) is still valid, hence confirming that the asymptotic scalings in ridge 1 in the absence of an electric field (3.6.33) are also valid in the presence of an electric field.

Figure 4.43 shows a log-log plot of H, Q_{grav}, Q_{cap}, and Q in ridge 1 obtained from the numerical solution of (4.3.1) for $E_b = 5$, $D = 8$, and $\gamma = \gamma_\pi(5, 8)$ given by (4.3.4) as functions of T, and compares them with the corresponding late-time asymptotic scalings $T^{-9/20}$, $T^{-27/20}$, $T^{-27/20}$, and $T^{-3/2}$ obtained from (3.6.33), (3.6.37), (3.6.38), and (3.4.13), respectively. In particular, Figure 4.43 and Table

	Asymptotic scaling	Numerical result
H	-0.45	-0.4730
Q_{grav}	-1.35	-1.4165
Q_{cap}	-1.35	-1.3620
Q	-1.50	-1.4850

Table 4.4: The late-time asymptotic scalings for H, Q_{grav}, Q_{cap}, and Q in ridge 1 and the slopes of the lines of best fit to the numerical results for $T \geq 10^{9/4}$ shown in Figure 4.43.

4.4 confirm that the interface has the predicted asymptotic behaviour at sufficiently late times. Note that $Q_{\text{elec}} \equiv 0$ at the maximum of the ridges, and so is omitted from both Figure 4.43 and Table 4.4.

As explained in Section 3.6.3, the problem in dimple n has to be solved numerically and is given by (3.6.21)–(3.6.24) where ψ_n and ξ_n are scaled by the constants K and L_{n-1} as (3.6.83) where, as before, K is given by (3.6.3) and L_{n-1} is given by (3.6.76). The solution in ridge n is given by (3.6.85) and (3.6.86) where γ, θ_{I}, and $\bar{E}_b$ are related by (4.3.12) with (4.3.13).

As in Section 3.6, L_n can be written in terms of L_{n-1} and hence inductively in terms of L_0 as (3.6.88), where the exponents x and y are given by (3.6.89). In the presence of an electric field, L_0 is given by the second derivative of equation (4.3.15), namely,

$$L_0 = H_{\theta\theta}|_{\theta\to\theta_{\text{I}}^+} = -\bar{E}_b^{-1}\left[\sin\theta_{\text{I}} + \cos\theta_{\text{I}}\cot\left(\frac{1}{2}\left(-3\pi + 2\theta_{\text{I}}\right)B\right)B\right], \qquad (4.3.19)$$

where B is given by (4.3.16). As mentioned in Section 4.3.4, it is through (4.3.15), and hence, through L_0 (4.3.19), that electrostatic effects influence the calculations in the inner region, which otherwise remains unaffected by electrostatic effects.

Figure 4.44 shows snapshots of the film thickness for $E_b = 5$, $D = 8$, and $\gamma = \gamma_\pi(5, 8)$ given by (4.3.4) at various times together with the leading-order asymptotic solution in dimple 1 expressed in the scaled variables ψ_1 and ξ_1, confirming that the interface does indeed approach the asymptotic solution at late times.

The solution in ridge 1 for $E_b = 5$, $D = 8$, and $\gamma = \gamma_\pi(5, 8)$ given by (4.3.4) is

$$\phi_1 = 0.5807 - 2.6236\zeta_1^2 - 2.1464\zeta_1^3. \qquad (4.3.20)$$

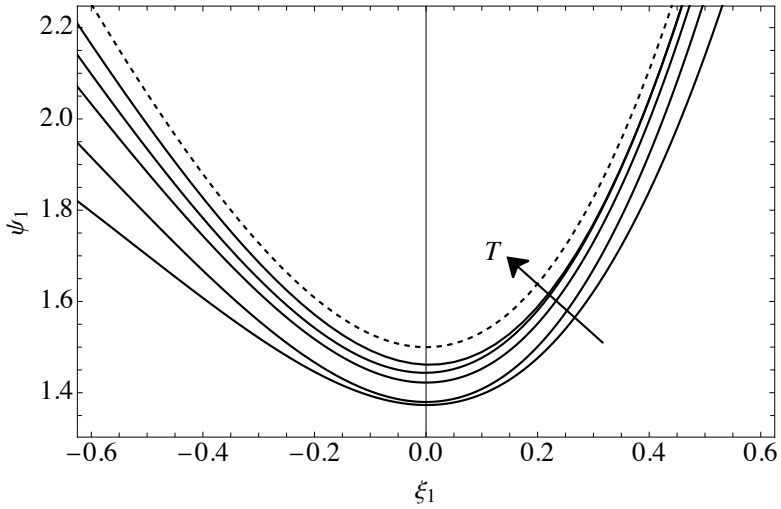

Figure 4.44: Snapshots of the film thickness for $E_b = 5$, $D = 8$, and $\gamma = \gamma_\pi(5, 8)$ given by (4.3.4) at times $T = 10^2, 10^3, 10^4, 10^5$, and 10^6 expressed in scaled variables ξ_1 and ψ_1. The arrow indicates the direction of increasing time. The dashed line shows the leading-order asymptotic solution in dimple 1 (3.6.8).

Upon comparison with the solution in ridge 1 in the absence of an electric field (3.6.46), equation (4.3.20) is different but the coefficients remain close in value, owing to the small-D limit under which (4.3.15) was derived. Figure 4.45 shows snapshots of the film thickness for $E_b = 5$, $D = 8$, and $\gamma = \gamma_\pi(5, 8)$ given by (4.3.4) at various times together with the leading-order asymptotic solution in ridge 1 (4.3.20) expressed in scaled variables ζ_1 and ϕ_1, confirming that the interface does indeed approach the asymptotic solution at late times. Figure 4.45 also reveals, as discussed previously in Section 3.6.2, that the convergence to the leading-order asymptotic solution in ridge 1 is significantly slower than the corresponding convergence in dimple 1 shown in Figure 4.44.

4.4 Multiple-timescale analysis of large-time dynamics

In this section, we return to the case in which the rotation rate is non-zero in order to investigate the large-time dynamics of the system. We anticipate the analysis in this section to be applicable to many of the states that were classified as transient in the nonlinear parametric study which was analysed in Section 4.2.

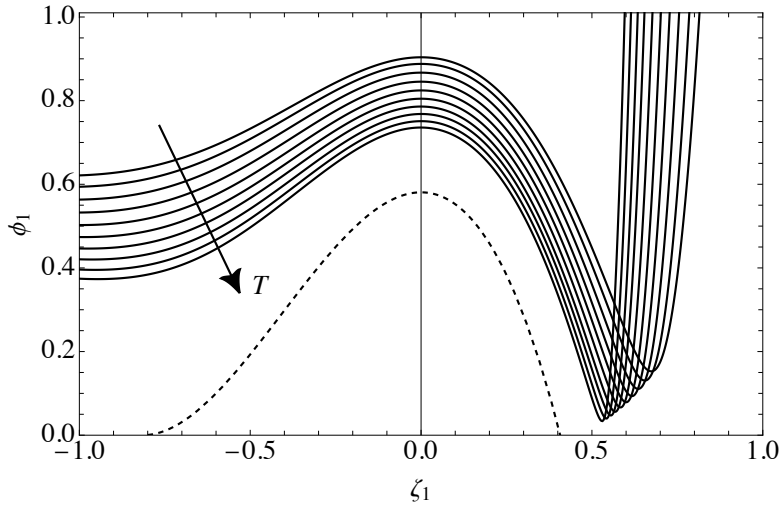

Figure 4.45: Snapshots of the film thickness for $E_b = 5$, $D = 8$, and $\gamma = \gamma_\pi(5, 8)$ given by (4.3.4) at times $T = 10^{n/2}$ for $n = 13, 14, \ldots, 22$. The arrow indicates the direction of increasing time. The dashed line shows the leading-order asymptotic solution in ridge 1 (4.3.20).

In particular, as discussed in Section 4.2.6, it is possible that states which were classified as transient could be instances of complex, large-time dynamics which are difficult to capture numerically, and hence the forthcoming analysis could provide an insight into the large-time evolution of such states.

We generalise the asymptotic analysis of Hinch and Kelmanson [73] (which was discussed in Section 1.4.4) to incorporate electrostatic effects. To proceed, we follow the same approach as Hinch and Kelmanson [73] and Mitchell *et al.* [130] and so, for the purposes of comparing directly with their results, we apply the usual thin-film scalings (2.2.1) and nondimensionalise according to [73, 130]

$$\begin{aligned} \tilde{\mathbf{U}} =& \hat{U}_{\text{char}}\mathbf{U}, \quad \tilde{R} = \hat{R}_1 R, \quad \tilde{S} = \hat{R}_1 S, \quad \tilde{H} = \hat{R}_1 H, \quad \tilde{H}_0 = \hat{R}_1 H_0, \\ & \tilde{T} = \frac{\epsilon^2}{\hat{\Omega}} T, \quad \tilde{P} - \hat{P}_a = \hat{\rho}\hat{g}\hat{R}_1 P, \quad \tilde{\Phi} = \hat{\phi}_b \Phi, \quad \tilde{Q} = \hat{U}_{\text{char}}\hat{R}_1 Q, \end{aligned} \tag{4.4.1}$$

where $\hat{U}_{\text{char}} = \hat{\Omega}\hat{R}_1$ is a characteristic velocity based on rotation (which we note is different from the characteristic velocity based on drainage used in Section 2.1.2). Hence, the governing equation (2.2.23) becomes

$$H_T + \left[H - \beta H^3 \cos\theta + \alpha H^3 \left(H_\theta + H_{\theta\theta\theta} \right) + \check{\delta} \left(\frac{H}{D - H} \right)^3 H_\theta \right]_\theta = 0, \tag{4.4.2}$$

where α, β, and $\check{\delta}$ represent an inverse capillary number, dimensionless gravity parameter, and dimensionless electric potential difference, respectively, namely,

$$\alpha = \frac{\epsilon^3 \hat{\sigma}}{3\hat{\mu}\hat{\Omega}\hat{R}_1}, \quad \beta = \frac{\epsilon^2 \hat{\rho}\hat{g}\hat{R}_1}{3\hat{\mu}\hat{\Omega}}, \quad \check{\delta} = \frac{\epsilon^2 \hat{\epsilon}_{\mathrm{G}} \hat{\phi}_{\mathrm{char}}^2}{3\hat{\mu}\hat{\Omega}\hat{R}_1^2}. \tag{4.4.3}$$

Note that we have chosen not to denote the dimensionless gravity parameter by γ (which was the notation used by Hinch and Kelmanson [73] and Mitchell *et al.* [130]) as this symbol has already been used to denote a capillary number elsewhere in this thesis. Hence, to avoid confusion, throughout this section the parameter β is the same as the parameter γ of Hinch and Kelmanson [73] and Mitchell *et al.* [130], whilst the parameter α used in this section is the same as the parameter α used in the aforementioned studies. Hence, upon setting $\check{\delta} = 0$, equation (4.4.2) recovers equation (2.4) of Hinch and Kelmanson [73] and equation (8) of Mitchell *et al.* [130] in the absence of an airflow.

As discussed in Section 1.4.4, Hinch and Kelmanson [73] and Mitchell *et al.* [130] analysed the evolution of the flow in the case in which gravitational and capillary effects are both weak by requiring that $\alpha \ll 1$ and $\beta \ll 1$ (specifically, they worked in the regime $\beta^2 \ll \alpha \ll \beta \ll 1$). In this section, we work in the same regime as Hinch and Kelmanson [73] and Mitchell *et al.* [130], and therefore will also require that electrostatic effects are weak to ensure that they do not overwhelm the dynamics of the system. We proceed by rescaling the electric potential difference $\check{\delta}$ with the gravity parameter $\beta \ll 1$ such that

$$\check{\delta} = \beta\delta, \tag{4.4.4}$$

where δ is no larger than $O(\beta^{-1})$. We follow Hinch and Kelmanson [73] and Mitchell *et al.* [130] and allow α to be as large as $O(1)$ despite the formal restrictions stated above, based on the assumption that in the presence of an electric field the film thickness H is again only weakly dependent on α. To make the subsequent calculations simpler, we move into the co-rotating frame by making the substitutions

$$\tau = T, \quad \phi = \theta - T, \tag{4.4.5}$$

such that

$$\frac{\partial}{\partial T} = \frac{\partial}{\partial \tau} - \frac{\partial}{\partial \phi}, \quad \frac{\partial}{\partial \theta} = \frac{\partial}{\partial \phi}. \tag{4.4.6}$$

Substituting (4.4.5) and (4.4.4) into (4.4.2) yields the final governing equation which we analyse throughout this section, namely,

$$H_\tau + \left[-\beta H^3 \cos(\phi + \tau) + \alpha H^3 \left(H_\phi + H_{\phi\phi\phi} \right) + \beta\delta \left(\frac{H}{D - H} \right)^3 H_\phi \right]_\phi = 0. \quad (4.4.7)$$

4.4.1 Naïve expansion

In this section, we show that performing the natural naïve expansion for H

$$H_N(\phi, \tau) = \sum_{i=1}^{N} \epsilon^i H_i(\phi, \tau), \quad (4.4.8)$$

where, as before, $\epsilon = \hat{h}_0 / \hat{R}_1 \ll 1$, on the governing equation (4.4.7) results in the emergence of secular terms (i.e., terms which grow linearly in time). Note that, in this subsection only, we remove the assumptions $\beta^2 \ll \alpha \ll \beta \ll 1$ and $\delta \ll 1$ and instead assume that $\alpha = O(1)$, $\beta = O(1)$, and $\delta = O(1)$ for the purposes of performing the naïve expansion.

In contrast to Hinch and Kelmanson [73], who found that secularity first arises at $O(\epsilon^7)$, in the presence of an electric field secularity first arises at $O(\epsilon^6)$. Solving order-by-order subject to the initial conditions $H_1(\phi, 0) = 1$ and $H_i(\phi, 0) = 0$ for $i \geq 2$ yields

$$\begin{aligned}
\frac{\partial H_1}{\partial \tau} &= 0, \quad & H_1 &= 1, \quad (4.4.9)\\
\frac{\partial H_2}{\partial \tau} &= 0, \quad & H_2 &= 0,\\
\frac{\partial H_3}{\partial \tau} &= \beta \sin(\phi + \tau), \quad & H_3 &= \beta \left(\cos\phi - \cos(\phi + \tau) \right),\\
\frac{\partial H_4}{\partial \tau} &= 0, \quad & H_4 &= 0,\\
\frac{\partial H_5}{\partial \tau} &= -6\beta^2 \cos\left(2\phi + \frac{3}{2}\tau \right) \sin\left(\frac{\tau}{2} \right), \quad & H_5 &= -6\beta^2 \cos(2\phi + \tau) \sin^2\left(\frac{\tau}{2} \right)
\end{aligned}$$

to $O(\epsilon^5)$, in which we note that there are no secular terms. However, at $O(\epsilon^6)$ the equation for H_6 is

$$\frac{\partial H_6}{\partial \tau} = \frac{\beta^2 \delta}{D^3} \left(\cos\phi - \cos(\phi + \tau) \right), \quad (4.4.10)$$

which yields the solution

$$H_6 = \frac{\beta^2\delta}{D^3}\left(\tau\cos\phi + \sin\phi - \sin(\phi+\tau)\right). \tag{4.4.11}$$

The solution for H_6 (4.4.11) exhibits a resonance effect due to the fact that the right-hand side of (4.4.10) contains the term $\cos\phi$, which is part of the complementary function for H_6, and thus results in the secular term $\tau\cos\phi$ arising in (4.4.11). Thus, the naïve expansion is nonuniform, failing when $T = O(\epsilon^{-1})$. We calculated the naïve expansion up to $O(\epsilon^{17})$ (which was chosen as this is the order to which Hinch and Kelmanson [73] calculated their naïve expansion) and found that secular terms arise in the solutions for all H_i for $i = 6, \ldots, 17$. The solutions for the H_i are omitted here for brevity, which rapidly become too long and cumbersome with increasing i to be presented here.

4.4.2 The method of multiple scales

In this section, we adopt the approach used by Hinch and Kelmanson [73] and Mitchell *et al.* [130] and use the method of multiple scales to remove the secularities (as discussed earlier in Section 1.3.2). However, in contrast to these analyses [73, 130], it will transpire that three (rather than two) timescales are required to resolve the secularities that arise when an electric field is present. Hence, we proceed by proposing an $(N+1)$-term, three-timescale expansion for the film thickness H, namely,

$$H_{N+1}^{(3\tau)}(\phi,\tau) = 1 + \sum_{i=1}^{N}\beta^i\psi_i\left(\phi,\tau_0,\tau_1,\tau_2\right), \tag{4.4.12}$$

where

$$\tau_0 = \tau, \quad \tau_1 = \beta\tau, \quad \tau_2 = \beta^2\tau, \tag{4.4.13}$$

such that

$$\frac{\partial}{\partial\tau} = \frac{\partial}{\partial\tau_0} + \beta\frac{\partial}{\partial\tau_1} + \beta^2\frac{\partial}{\partial\tau_2}. \tag{4.4.14}$$

Hence, the governing equation in the co-rotating frame (4.4.7) becomes

$$\begin{aligned} &H_{\tau_0} + \beta H_{\tau_1} + \beta^2 H_{\tau_2} \\ &+ \left[-\beta H^3\cos\left(\phi+\tau_0\right) + \alpha H^3\left(H_\phi + H_{\phi\phi\phi}\right) + \beta\delta\left(\frac{H}{D-H}\right)^3 H_\theta\right]_\phi = 0, \end{aligned} \tag{4.4.15}$$

where H is given by (4.4.12). For brevity, throughout this section we hereafter adopt the notation

$$c_{j,k} = \cos\left(j\phi - k\tau_0\right), \quad s_{j,k} = \sin\left(j\phi - k\tau_0\right). \tag{4.4.16}$$

It will also be of use to define the linear operator $\mathcal{L}$ as introduced by Hinch and Kelmanson [73] (transformed into the co-rotating frame), namely,

$$\mathcal{L} = \frac{\partial}{\partial\tau_0} + \alpha\left(\frac{\partial^2}{\partial\phi^2} + \frac{\partial^4}{\partial\phi^4}\right). \tag{4.4.17}$$

As explained by Hinch and Kelmanson [73], the 2π-periodic solutions $\psi_i(\phi, \tau_0, \tau_1, \tau_2)$ of the homogeneous equation $\mathcal{L}\psi_i = 0$ are of the form

$$\psi_i(\phi, \tau_0, \tau_1, \tau_2) = \sum_{n=1}^{\infty} \left[A_{i,n}(\tau_1, \tau_2)c_{n,0} + B_{i,n}(\tau_1, \tau_2)s_{n,0}\right] \mathrm{e}^{-\alpha n^2(n^2-1)\tau_0}, \tag{4.4.18}$$

where n is the integer mode number and $A_{i,n}(\tau_1, \tau_2)$ and $B_{i,n}(\tau_1, \tau_2)$ are arbitrary functions of τ_1 and τ_2. Equation (4.4.18) shows that the first modes $c_{1,0}$ and $s_{1,0}$ (i.e., for $n = 1$) can only decay via $A_{i,1}(\tau_1, \tau_2)$ and $B_{i,1}(\tau_1, \tau_2)$ on the slow timescales $\tau_1 = \beta\tau_0$ and $\tau_2 = \beta^2\tau_0$, whilst higher modes ($n = 2, 3, 4, \ldots$) decay exponentially on the faster timescale $\alpha\tau_0$.

The principal aims of this section are twofold: the first is to determine the growth rate of the first (sometimes referred to as "fundamental" [73]) modes $c_{1,0}$ and $s_{1,0}$ (and hence, the growth rate of the film thickness H, since the overall decay rate is dictated by that of only the first modes [73]) in order to understand how the presence of an electric field affects the evolution of the film. To do this, it will be necessary to determine the solutions for ψ_1 at $O(\beta)$ and ψ_2 at $O(\beta^2)$ and the equation for ψ_3 at $O(\beta^3)$ in order to identify and remove the secular terms. Secularities arise at $O(\beta^2)$ and $O(\beta^3)$ and must be removed before the growth rate at $O(\beta)$ can be determined. Throughout this process, it shall become clear that the reason that three timescales are required is because the complementary function for ψ_1 creates secularities at two different orders, namely, at $O(\beta^2)$ by interacting with the electrostatic term, and at $O(\beta^3)$ by interacting with the gravity term. The second aim is to determine the third-order three-timescale asymptotic solution for the film thickness $H_4^{(3\tau)}(\phi, \tau)$ and to compare this with numerical solutions of the governing equation (4.4.7), for which we must also determine the solution for ψ_3.

The algebraic manipulations involved in obtaining the following analytical results are extensive and cumbersome, and hence were performed using Mathematica [265]. Throughout the present analysis, we verify that in the absence of an electric field (i.e., for $\delta = 0$) the results obtained reduce to those of Hinch and Kelmanson [73] and of Mitchell *et al.* [130] in the absence of an airflow.

4.4.3 Solution for ψ_1

At $O(\beta)$, substitution of (4.4.12) into (4.4.15) yields

$$\mathcal{L}\psi_1 = -s_{1,-1}. \tag{4.4.19}$$

The particular solution of (4.4.19) is $\psi_{1\text{part}} = c_{1,-1}$ and, by (4.4.18), the complementary function of (4.4.19) is

$$\psi_{1\text{comp}} = \sum_{n=1}^{\infty} \left[A_{1,n}(\tau_1, \tau_2)c_{n,0} + B_{1,n}(\tau_1, \tau_2)s_{n,0}\right] \mathrm{e}^{-\alpha n^2(n^2-1)\tau_0}, \tag{4.4.20}$$

where the initial condition $H(\phi, 0) = 1$ requires that $A_{1,n}(\tau_1, \tau_2)$ and $B_{1,n}(\tau_1, \tau_2)$ satisfy

$$A_{1,1}(0,0) = -1, \quad B_{1,1}(0,0) = 0 \tag{4.4.21}$$

for the first mode (i.e., for $n = 1$), and $A_{1,n}(0,0) = B_{1,n}(0,0) = 0$ for all higher modes (i.e., for $n \geq 2$). As explained by Mitchell *et al.* [130], the contributions from the higher modes are only nonnegligible for small times (since they decay exponentially on the fast timescale $\alpha\tau_0$). Therefore, we can replace $A_{1,n}(\tau_1, \tau_2)$ and $B_{1,n}(\tau_1, \tau_2)$ with $A_{1,n}(0,0)$ and $B_{1,n}(0,0)$ for $n \geq 2$, but not for $n = 1$. Thus, the complementary function (4.4.20) becomes

$$\psi_{1\text{comp}} = A_{1,1}(\tau_1, \tau_2)c_{1,0} + B_{1,1}(\tau_1, \tau_2)s_{1,0}. \tag{4.4.22}$$

Hence, the general solution $\psi_1 = \psi_{1\text{part}} + \psi_{1\text{comp}}$ of (4.4.19) for ψ_1 is

$$\psi_1(\phi, \tau_0, \tau_1, \tau_2) = c_{1,-1} + A_{1,1}(\tau_1, \tau_2)c_{1,0} + B_{1,1}(\tau_1, \tau_2)s_{1,0}, \tag{4.4.23}$$

where $A_{1,1}(\tau_1, \tau_2)$ and $B_{1,1}(\tau_1, \tau_2)$ satisfy the initial condition (4.4.21). Note that upon converting back to the fixed frame, the solution for ψ_1 given by equation

(4.4.23) is in agreement with equation (3.3) of Hinch and Kelmanson [73] and equation (22) of Mitchell *et al.* [130] in the absence of an airflow.

We will determine $A_{1,1}(\tau_1,\tau_2)$ and $B_{1,1}(\tau_1,\tau_2)$ as part of the analyses in Sections 4.4.4 and 4.4.5 combined by eliminating the secular terms which arise at $O(\beta^2)$ and $O(\beta^3)$. Determination of $A_{1,1}(\tau_1,\tau_2)$ and $B_{1,1}(\tau_1,\tau_2)$ will yield the growth rate of the first modes, which, as we recall, is the first of the two principal aims of this section.

4.4.4 Solution for ψ_2

At $O(\beta^2)$, substitution of (4.4.12) into (4.4.15) yields

$$\begin{aligned}\mathcal{L}\psi_2 = &-3s_{2,-2}+3s_{2,-1}A_{1,1}(\tau_1,\tau_2)+3c_{2,-1}B_{1,1}(\tau_1,\tau_2)-c_{1,0}\frac{\partial A_{1,1}(\tau_1,\tau_2)}{\partial\tau_1}\\ &-s_{1,0}\frac{\partial B_{1,1}}{\partial\tau_1}(\tau_1,\tau_2)+S_0\left[c_{1,-1}+c_{1,0}A_{1,1}(\tau_1,\tau_2)+s_{1,0}B_{1,1}(\tau_1,\tau_2)\right],\end{aligned}\tag{4.4.24}$$

where ψ_1 is given by (4.4.23) and the real constant S_0 is given by

$$S_0=\frac{\delta}{(D-1)^3}\geq 0,\tag{4.4.25}$$

and arises due to the electrostatic term in (4.4.15). One of the key points of this section is that, in contrast to the corresponding equations for ψ_2 given by Hinch and Kelmanson [73] and Mitchell *et al.* [130], equation (4.4.24) contains the terms $c_{1,0}$ and $s_{1,0}$ which arise due to electrostatic effects and will generate secular terms unless their coefficients are zero. Hence, to eliminate the secularities, we proceed by setting the coefficients of the $c_{1,0}$ and $s_{1,0}$ to zero in (4.4.24) to yield a pair of separable ODEs for $A_{1,1}(\tau_1,\tau_2)$ and $B_{1,1}(\tau_1,\tau_2)$, namely,

$$\frac{\partial A_{1,1}(\tau_1,\tau_2)}{\partial\tau_1}=S_0A_{1,1}(\tau_1,\tau_2),\tag{4.4.26}$$

$$\frac{\partial B_{1,1}(\tau_1,\tau_2)}{\partial\tau_1}=S_0B_{1,1}(\tau_1,\tau_2),\tag{4.4.27}$$

where S_0 is defined by (4.4.25). Solving (4.4.26) and (4.4.27) for $A_{1,1}(\tau_1,\tau_2)$ and $B_{1,1}(\tau_1,\tau_2)$, respectively, yields

$$A_{1,1}(\tau_1,\tau_2)=a_1(\tau_2)\mathrm{e}^{S_0\tau_1},\qquad B_{1,1}(\tau_1,\tau_2)=b_1(\tau_2)\mathrm{e}^{S_0\tau_1}.\tag{4.4.28}$$

To determine the initial conditions on $a_1(\tau_2)$ and $b_1(\tau_2)$, we set $\tau = 0$ such that τ_1 and τ_2 are identically zero in (4.4.28) and use the initial conditions on $A_{1,1}(\tau_1, \tau_2)$ and $B_{1,1}(\tau_1, \tau_2)$ (4.4.21) to yield

$$a_1(0) = -1, \qquad b_1(0) = 0. \tag{4.4.29}$$

The particular solution $\psi_{2\text{part}}$ of (4.4.24) is thus

$$\begin{aligned}\psi_{2\text{part}} = {} & \frac{3c_{2,-2}}{2(36\alpha^2+1)} - \frac{9\alpha s_{2,-2}}{36\alpha^2+1} + \frac{3\left[A_{1,1}(\tau_1,\tau_2) + 12\alpha B_{1,1}(\tau_1,\tau_2)\right]c_{2,-1}}{144\alpha^2+1} \\ & - \frac{3\left[12\alpha A_{1,1}(\tau_1,\tau_2) - B_{1,1}(\tau_1,\tau_2)\right]s_{2,-1}}{144\alpha^2+1} + S_0 s_{1,-1},\end{aligned} \tag{4.4.30}$$

where $A_{1,1}(\tau_1, \tau_2)$ and $B_{1,1}(\tau_1, \tau_2)$ are given by (4.4.28). By (4.4.18), the complementary function $\psi_{2\text{comp}}$ of (4.4.24) is

$$\psi_{2\text{comp}} = \sum_{n=1}^{\infty} \left[A_{2,n}(\tau_1,\tau_2)c_{n,0} + B_{2,n}(\tau_1,\tau_2)s_{n,0}\right] \mathrm{e}^{-\alpha n^2(n^2-1)\tau_0}. \tag{4.4.31}$$

The initial condition $H(\phi, 0) = 1$ requires that $A_{2,n}(\tau_1, \tau_2)$ and $B_{2,n}(\tau_1, \tau_2)$ satisfy

$$A_{2,1}(0,0) = 0, \qquad B_{2,1}(0,0) = -S_0 \tag{4.4.32}$$

for the first mode,

$$A_{2,2}(0,0) = -\frac{3}{2(36\alpha^2+1)} + \frac{3}{144\alpha^2+1}, \quad B_{2,2}(0,0) = \frac{9\alpha}{36\alpha^2+1} - \frac{36\alpha}{144\alpha^2+1} \tag{4.4.33}$$

for the second mode (in agreement with equation (3.6) of Hinch and Kelmanson [73]), and $A_{2,n}(0,0) = B_{2,n}(0,0) = 0$ for all higher modes (i.e., for $n \geq 3$). Following the same reasoning as described in Section 4.4.3, we can replace $A_{2,n}(\tau_1, \tau_2)$ and $B_{2,n}(\tau_1, \tau_2)$ with $A_{2,n}(0,0)$ and $B_{2,n}(0,0)$ for $n \geq 2$. The general solution of (4.4.24) for ψ_2 is therefore

$$\begin{aligned}\psi_2(\phi,\tau_0,\tau_1,\tau_2) = {} & \frac{3c_{2,-2}}{2(36\alpha^2+1)} - \frac{9\alpha s_{2,-2}}{36\alpha^2+1} + \frac{3\left[A_{1,1}(\tau_1,\tau_2) + 12\alpha B_{1,1}(\tau_1,\tau_2)\right]c_{2,-1}}{144\alpha^2+1} \\ & - \frac{3\left[12\alpha A_{1,1}(\tau_1,\tau_2) - B_{1,1}(\tau_1,\tau_2)\right]s_{2,-1}}{144\alpha^2+1} + S_0 s_{1,-1} \\ & + A_{2,1}(\tau_1,\tau_2)c_{1,0} + B_{2,1}(\tau_1,\tau_2)s_{1,0} + \left[A_{2,2}c_{2,0} + B_{2,2}s_{2,0}\right]\mathrm{e}^{-12\alpha\tau_0},\end{aligned} \tag{4.4.34}$$

where $A_{1,1}(\tau_1,\tau_2)$ and $B_{1,1}(\tau_1,\tau_2)$ are given by (4.4.28), $A_{2,2}$ and $B_{2,2}$ are given by (4.4.33), and $a_1(\tau_2)$, $b_1(\tau_2)$, $A_{2,1}(\tau_1,\tau_2)$, and $B_{2,1}(\tau_1,\tau_2)$ will be determined in Section 4.4.5. Note that in the absence of an electric field, upon converting back to the fixed frame equation (4.4.34) is in agreement with the solution for ψ_2 given by equation (3.5) of Hinch and Kelmanson [73] and equations (23) and (24) of Mitchell *et al.* [130] in the absence of an airflow.

4.4.5 Solution for ψ_3

At $O(\beta^3)$, substitution of (4.4.12) into (4.4.15) yields

$$\begin{aligned}\mathcal{L}\psi_3 = {} & 3\left(c_{1,-1} - 2\alpha\frac{\partial\psi_1}{\partial\phi}\right)\frac{\partial\psi_2}{\partial\phi} - 3\left(\psi_1^2+\psi_2\right)\left[s_{1,-1} + \alpha\left(\frac{\partial^2\psi_1}{\partial\phi^2}+\frac{\partial^4\psi_1}{\partial\phi^4}\right)\right] \\ & - 3\psi_1\left[2\alpha\frac{\partial\psi_1}{\partial\phi} - 2\frac{\partial\psi_1}{\partial\phi}\left(c_{1,-1}-\alpha\frac{\partial^3\psi_1}{\partial\phi^3}\right) + \alpha\left(\frac{\partial^2\psi_2}{\partial\phi^2}+\frac{\partial^4\psi_2}{\partial\phi^4}\right)\right] \\ & - \alpha\left[\frac{\partial^2\psi_3}{\partial\phi^2} + 3\frac{\partial\psi_2}{\partial\phi}\frac{\partial^3\psi_1}{\partial\phi^3} + 3\frac{\partial\psi_1}{\partial\phi}\frac{\partial^3\psi_2}{\partial\phi^3} + \frac{\partial^4\psi_3}{\partial\phi^4}\right] \\ & - \frac{S_0}{(D-1)}\left[3D\left(\left(\frac{\partial\psi_1}{\partial\phi}\right)^2 + \psi_1\frac{\partial^2\psi_1}{\partial\phi^2}\right) + (D-1)\frac{\partial^2\psi_2}{\partial\phi^2}\right] \\ & - \frac{\partial\psi_1}{\partial\tau_2} - \frac{\partial\psi_2}{\partial\tau_1}, \end{aligned} \tag{4.4.35}$$

where S_0 is defined by (4.4.25), ψ_1 and ψ_2 are given by (4.4.23) and (4.4.34), respectively, with $A_{1,1}(\tau_1,\tau_2)$ and $B_{1,1}(\tau_1,\tau_2)$ given by (4.4.28) and $A_{2,2}$ and $B_{2,2}$ given by (4.4.33). The expanded form of (4.4.35) contains 143 terms and is thus omitted for brevity, but notably involves the terms $c_{1,0}$ and $s_{1,0}$ which will, as before, generate secular terms unless their coefficients are zero. Henceforth, we follow Hinch and Kelmanson [73] and Mitchell *et al.* [130] in neglecting higher modes (i.e., $n \geq 2$) when we consider higher-order terms in β since they decay exponentially on the fast timescale $\alpha\tau_0$. In addition, due to the fact that $\tau_2 = \beta^2\tau_0$ is a much slower timescale than $\tau_1 = \alpha\tau_0$, in what follows we may consider $A_{2,1}(\tau_1,\tau_2)$ and $B_{2,1}(\tau_1,\tau_2)$ to be functions of τ_1 only in order to obtain a solution for H which is accurate to $O(\beta^3)$.

A particular solution for (4.4.35) cannot be obtained until the functions $a_1(\tau_2)$ and $b_1(\tau_2)$ in (4.4.28) arising at $O(\beta)$ and $A_{2,1}(\tau_1)$ and $B_{2,1}(\tau_1)$ arising at $O(\beta^2)$, are determined, which we now do through removing the secularities. We proceed as before and set the coefficients of the terms $c_{1,0}$ and $s_{1,0}$ to zero in (4.4.35) to

yield

$$\begin{aligned}\frac{\mathrm{d}a_1(\tau_2)}{\mathrm{d}\tau_2} - S_1 a_1(\tau_2) - S_2 b_1(\tau_2) + \mathrm{e}^{-S_0\tau_1}\left[-S_0 A_{2,1}(\tau_1) + \frac{\mathrm{d}A_{2,1}(\tau_1)}{\mathrm{d}\tau_1}\right] = 0,\\ \frac{\mathrm{d}b_1(\tau_2)}{\mathrm{d}\tau_2} + S_2 a_1(\tau_2) - S_1 b_1(\tau_2) + \mathrm{e}^{-S_0\tau_1}\left[-S_0 B_{2,1}(\tau_1) + \frac{\mathrm{d}B_{2,1}(\tau_1)}{\mathrm{d}\tau_1}\right] = 0,\end{aligned} \tag{4.4.36}$$

where S_1 and S_2 are real constants, given by

$$S_1 = -\frac{81\alpha}{144\alpha^2+1}, \qquad S_2 = \frac{3\left(5+72\alpha^2\right)}{2\left(144\alpha^2+1\right)}, \tag{4.4.37}$$

which are in agreement, respectively, with equations (3.10) and (3.11) of Hinch and Kelmanson [73] and equations (29) and (30) of Mitchell *et al.* [130] in the absence of an airflow. From (4.4.36), we obtain two sets of equations: the first set will allow us to determine $A_{2,1}(\tau_1)$ and $B_{2,1}(\tau_1)$ and the second set will allow us to determine $a_1(\tau_2)$ and $b_1(\tau_2)$. Note that equations (4.4.36) can be written as

$$\begin{aligned}\frac{\mathrm{d}a_1(\tau_2)}{\mathrm{d}\tau_2} - S_1 a_1(\tau_2) - S_2 b_1(\tau_2) = -\mathrm{e}^{-S_0\tau_1}\left[-S_0 A_{2,1}(\tau_1) + \frac{\mathrm{d}A_{2,1}(\tau_1)}{\mathrm{d}\tau_1}\right] = X,\\ \frac{\mathrm{d}b_1(\tau_2)}{\mathrm{d}\tau_2} + S_2 a_1(\tau_2) - S_1 b_1(\tau_2) = -\mathrm{e}^{-S_0\tau_1}\left[-S_0 B_{2,1}(\tau_1) + \frac{\mathrm{d}B_{2,1}(\tau_1)}{\mathrm{d}\tau_1}\right] = Y,\end{aligned} \tag{4.4.38}$$

where X and Y are separation constants which depend on neither τ_1 nor τ_2. There are not enough constraints on the equations (4.4.36) to solve for $A_{2,1}(\tau_1)$, $B_{2,1}(\tau_1)$, $a_1(\tau_2)$, and $b_1(\tau_2)$ in the usual way; this is a common feature of multiple-timescale analyses which involve more than two timescales, in which an extra degree of freedom is introduced by the third timescale, resulting in ambiguities [273]. Hence, to proceed we assume without loss of generality (see, for example, Section 11.2 and Problem 11.7 of Bender *et al.* [273]) that the separation constants X and Y in (4.4.38) are identically zero. Considering the equations in terms of τ_1 in (4.4.38) yields a pair of separable ODEs for $A_{2,1}(\tau_1)$ and $B_{2,1}(\tau_1)$, namely,

$$\frac{\partial A_{2,1}(\tau_1)}{\partial \tau_1} = S_0 A_{2,1}(\tau_1), \tag{4.4.39}$$

$$\frac{\partial B_{2,1}(\tau_1)}{\partial \tau_1} = S_0 B_{2,1}(\tau_1). \tag{4.4.40}$$

Solving (4.4.39) and (4.4.40) together subject to the initial conditions on $A_{2,1}(\tau_1, \tau_2)$ and $B_{2,1}(\tau_1, \tau_2)$ (4.4.32) yields

$$A_{2,1}(\tau_1) = 0, \qquad B_{2,1}(\tau_1) = -S_0 \mathrm{e}^{S_0 \tau_1}. \tag{4.4.41}$$

Next, considering the equations in terms of τ_2 in (4.4.38) yields a pair of ODEs for $a_1(\tau_2)$ and $b_1(\tau_2)$, namely,

$$\frac{\mathrm{d}a_1(\tau_2)}{\mathrm{d}\tau_2} = S_1 a_1(\tau_2) + S_2 b_1(\tau_2), \tag{4.4.42}$$

$$\frac{\mathrm{d}b_1(\tau_2)}{\mathrm{d}\tau_2} = -S_2 a_1(\tau_2) + S_1 b_1(\tau_2), \tag{4.4.43}$$

which are in agreement, respectively, with equations (3.8) and (3.9) of Hinch and Kelmanson [73] and equations (27) and (28) of Mitchell *et al.* [130] in the absence of an airflow. Solving (4.4.42) and (4.4.43) subject to the initial conditions on $a_1(\tau_2)$ and $b_1(\tau_2)$ (4.4.29) yields

$$a_1(\tau_2) = -\mathrm{e}^{S_1 \tau_2} \cos(S_2 \tau_2), \qquad b_1(\tau_2) = \mathrm{e}^{S_1 \tau_2} \sin(S_2 \tau_2). \tag{4.4.44}$$

Thus, by (4.4.28) and (4.4.44), $A_{1,1}(\tau_1, \tau_2)$ and $B_{1,1}(\tau_1, \tau_2)$ are

$$A_{1,1}(\tau_1, \tau_2) = -\mathrm{e}^{S_0 \tau_1 + S_1 \tau_2} \cos(S_2 \tau_2), \quad B_{1,1}(\tau_1, \tau_2) = \mathrm{e}^{S_0 \tau_1 + S_1 \tau_2} \sin(S_2 \tau_2). \tag{4.4.45}$$

Setting $\delta = 0$ in (4.4.45) recovers equation (3.12) of Hinch and Kelmanson [73] and equations (31) and (32) of Mitchell *et al.* [130] in the absence of an airflow. The expressions for $A_{1,1}(\tau_1, \tau_2)$ and $B_{1,1}(\tau_1, \tau_2)$ (4.4.45) yield the growth rate of the first modes, the determination of which was the first of the two principal aims of this section. We discuss this result in detail in Section 4.4.6.

With $A_{1,1}(\tau_1, \tau_2)$ and $B_{1,1}(\tau_1, \tau_2)$ determined, the solution of (4.4.35) for ψ_3 can now be found, namely,

$$\psi_3(\phi, \tau_0, \tau_1, \tau_2) = \psi_{3\mathrm{part}} + \sum_{n=1}^{N} \left[A_{3,n}(\tau_1, \tau_2) c_{n,0} + B_{3,n}(\tau_1, \tau_2) s_{n,0} \right] \mathrm{e}^{-\alpha n^2 \left(n^2 - 1\right) \tau_0}, \tag{4.4.46}$$

where $\psi_{3\mathrm{part}}$ is the particular solution of ψ_3, which is extremely cumbersome (containing 2353 terms in its expanded form) and is thus omitted here for brevity. The initial condition $H(\phi, 0) = 1$ requires that $A_{3,n}(\tau_1, \tau_2)$ and $B_{3,n}(\tau_1, \tau_2)$ satisfy

the initial conditions given in Appendix D. Following the same reasoning as in Sections 4.4.3 and 4.4.4, we may replace $A_{3,n}$ and $B_{3,n}$ in (4.4.46) with $A_{3,n}(0,0)$ and $B_{3,n}(0,0)$ for $n \geq 2$. In addition, due to the fact that $\tau_2 = \beta^2\tau_0$ and $\tau_1 = \beta\tau_0$ are slower timescales than τ_0, in order to obtain a solution for H which is accurate to $O(\beta^3)$ we may also consider $A_{3,1}(\tau_1, \tau_2)$ and $B_{3,1}(\tau_1, \tau_2)$ to be the constants $A_{3,1}(0,0)$ and $B_{3,1}(0,0)$. Hence, we have achieved the second of the two principal aims of this section, which was to determine the third-order three-timescale asymptotic solution for the film thickness $H_4^{(3\tau)}(\phi, \tau)$. We compare $H_4^{(3\tau)}(\phi, \tau)$ against numerical solutions of the governing equation (4.4.7) in Section 4.4.7.

4.4.6 Growth rate ω

It follows from (4.4.45) that to $O(\beta^3)$ the growth rate of first modes, which we denote here by ω, is

$$\omega = S_0\tau_1 + S_1\tau_2, \tag{4.4.47}$$

where S_0 is given by (4.4.25) and S_1 is given by (4.4.37). Equation (4.4.47) yields the main result of this section, namely, that for $\delta > 0$, the growth rate will be dominated by that of the $O(\beta)$ term in the asymptotic limit as $\beta \to 0$, thus to leading order the growth rate is

$$\omega = S_0 > 0, \tag{4.4.48}$$

which is always positive. Equation (4.4.48) indicates that the solution (4.4.52) is unconditionally unstable, growing exponentially like $\exp(S_0\tau_1)$ and blowing up at large times. Note that for $\delta = 0$, the growth rate reduces to the $O(\beta^2)$ term, S_1, recovering equation (3.10) of Hinch and Kelmanson [73] and equation (29) of Mitchell *et al.* [130] in the absence of an airflow, namely,

$$\omega = S_1 = -\frac{81\alpha}{144\alpha^2 + 1} \leq 0. \tag{4.4.49}$$

Equation (4.4.49) shows that in the absence of an electric field, the solution decays to a steady state at large times for $\alpha > 0$ on the timescale $\tau_2 = \beta^2\tau$ (which is slow compared to the timescales $\tau_1 = O(\beta)$ and $\tau_0 = O(1)$), and that for $\alpha = 0$ the system is neutrally stable [73, 130].

4.4.7 Evolution of the film thickness

From (4.4.12), (4.4.23), and (4.4.45), the film thickness H to $O(\beta)$ is $H = 1+\beta\psi_1$, i.e.,

$$H = 1 + \beta\Big[\cos(\phi+\tau_0) - \mathrm{e}^{S_0\tau_1+S_1\tau_2}\cos(S_2\tau_2)\cos\phi + \mathrm{e}^{S_0\tau_1+S_1\tau_2}\sin(S_2\tau_2)\sin\phi\Big]. \tag{4.4.50}$$

Converting (4.4.50) back to the fixed frame yields

$$H = 1 \;+\; \beta\Big[\cos\theta \;-\; \mathrm{e}^{S_0T_1+S_1T_2}\cos(S_2T_2)\cos(\theta-T) + \;\mathrm{e}^{S_0T_1+S_1T_2}\sin(S_2T_2)\sin(\theta-T_0)\Big], \tag{4.4.51}$$

where we define $T_n = \tau_n$ for $n = 0, 1, 2$, and 3 (since $\tau_n = \beta^n\tau = \beta^n T$ by (4.4.13) and (4.4.5)). Note that (4.4.51) may be written as

$$H = 1 + \beta\Big[\cos\theta - \mathrm{e}^{S_0T_1+S_1T_2}\cos[\theta-(T_0-S_2T_2)]\Big], \tag{4.4.52}$$

then, to $O(\epsilon\beta)$, the interface has the form $r = 1+\epsilon(1+\beta\psi_1)$, that is,

$$r = 1 + \epsilon + \epsilon\beta\Big[\cos\theta - \mathrm{e}^{S_0T_1+S_1T_2}\cos[\theta-(T_0-S_2T_2)]\Big]. \tag{4.4.53}$$

As explained by Hinch and Kelmanson [73] and Mitchell *et al.* [130], the interface (4.4.53) is a circle of radius $1+\epsilon$, with centre offset from the axis of the rotating cylinder by the Cartesian displacement

$$\epsilon\beta\left(1 + A_{1,1}\cos T_0 - B_{1,1}\sin T_0,\, A_{1,1}\sin T_0 + B_{1,1}\cos T_0\right), \tag{4.4.54}$$

where $A_{1,1} = A_{1,1}(T_1, T_2)$ and $B_{1,1} = B_{1,1}(T_1, T_2)$ are given by (4.4.45). When both $\delta = 0$ (i.e., in the absence of an electric field) and $\alpha > 0$, the centre of the circular interface spirals around the point $(\epsilon\beta, 0)$ and approaches it as $T \to \infty$. On the other hand, when $\delta > 0$ (i.e., in the presence of an electric field), the centre of the circular interface spirals away from the point $(\epsilon\beta, 0)$ as $T \to \infty$ as the electric field destabilises the system. The behaviour of the term $\exp(S_0T_1)$ in (4.4.53) dictates the behaviour of the system. The electric field destabilises the system on the slow timescale $T_1 = \beta T$, resulting in the interface being pulled closer to the

outer electrode, as we have seen previously.

In the following results, we use the value $D = 5$ with $\beta = 0.0532$ and $\alpha = 0.0048$, which are chosen to be consistent with the corresponding choices of γ and α used by Hinch and Kelmanson [73] in order to offer a direct comparison with their results. Figure 4.46 shows plots of the maximum values of the film thickness, which we again denote by $H_{\max}$, calculated from both the third-order three-timescale asymptotic solution $H_4^{(3\tau)}(\phi, \tau)$ (4.4.12) (converted back to the fixed frame) and numerical solutions of the governing equation (4.4.7) for $\beta = 0.0532$, $\alpha = 0.0048$, and (a), (b) $\delta = 0$, (c), (d) $\delta = 2$, and (e), (f) $\delta = 4$ over the time interval $T = [0, 500]$. This time interval was chosen as the asymptotic solution for the film thickness H (4.4.12) is valid until time $T = O(\beta^{-2})$ which, for the value $\beta = 0.0523$, corresponds to $T \approx 350$. Figures 4.46 (a) and (b) show stability of the solution in the absence of an electric field, in agreement with the results of Hinch and Kelmanson [73] and Mitchell *et al.* [130]. Figures 4.46 (c) and (d) and Figures 4.46 (e) and (f) show growth of the maximum film thickness within the asymptotically valid time interval due to electrostatic effects destabilising the system. Increasing the electric potential difference corresponds to faster exponential growth of the maximum film thickness. Note that the value of δ can be at most $O(\beta^{-1})$ to remain asymptotically consistent with (4.4.4), which corresponds to $\delta \approx 20$ for the value $\beta = 0.0523$.

Figure 4.47 demonstrates the convergence of the third-order three-timescale asymptotic solution $H_4^{(3\tau)}(\phi, \tau)$ (4.4.12) (converted back to the fixed frame) at $\theta = 0$ for $N = 1, 2$, and 3 to the numerical solution of the governing equation (4.4.7) for $\beta = 0.0532$, $\alpha = 0.0048$, and (a)–(c) $\delta = 0$, (d)–(f) $\delta = 2$, and (g)–(i) $\delta = 4$ over the time intervals (a), (d), (g) $T = [0, 10]$, (b), (e), (f) $T = [190, 200]$, and (c), (f), (i) $T = [490, 500]$. Specifically, Figures 4.47 (a), (d), and (g) show that there is close agreement between $H_4^{(3\tau)}(0, \tau)$ and the numerical results in the time interval $T = [0, 10]$. This agreement remains close in the time interval $T = [190, 200]$ as shown in Figures 4.47 (b), (e), and (h). However, at larger times (i.e., beyond $T = O(\beta^{-2}) \approx O(350)$), the accuracy of the third-order three-timescale asymptotic solution is expected to deteriorate, as shown in Figures 4.47 (c), (f), and (i) in which it is evident by the separation between the solid line and any of the dotted, dashed, or dot-dashed lines that the asymptotic solution has drifted away from the numerical solution. Figures 4.47 (f) and (i) also show that increasing the electric potential difference leads to an increase in the amplitude of the maximum film

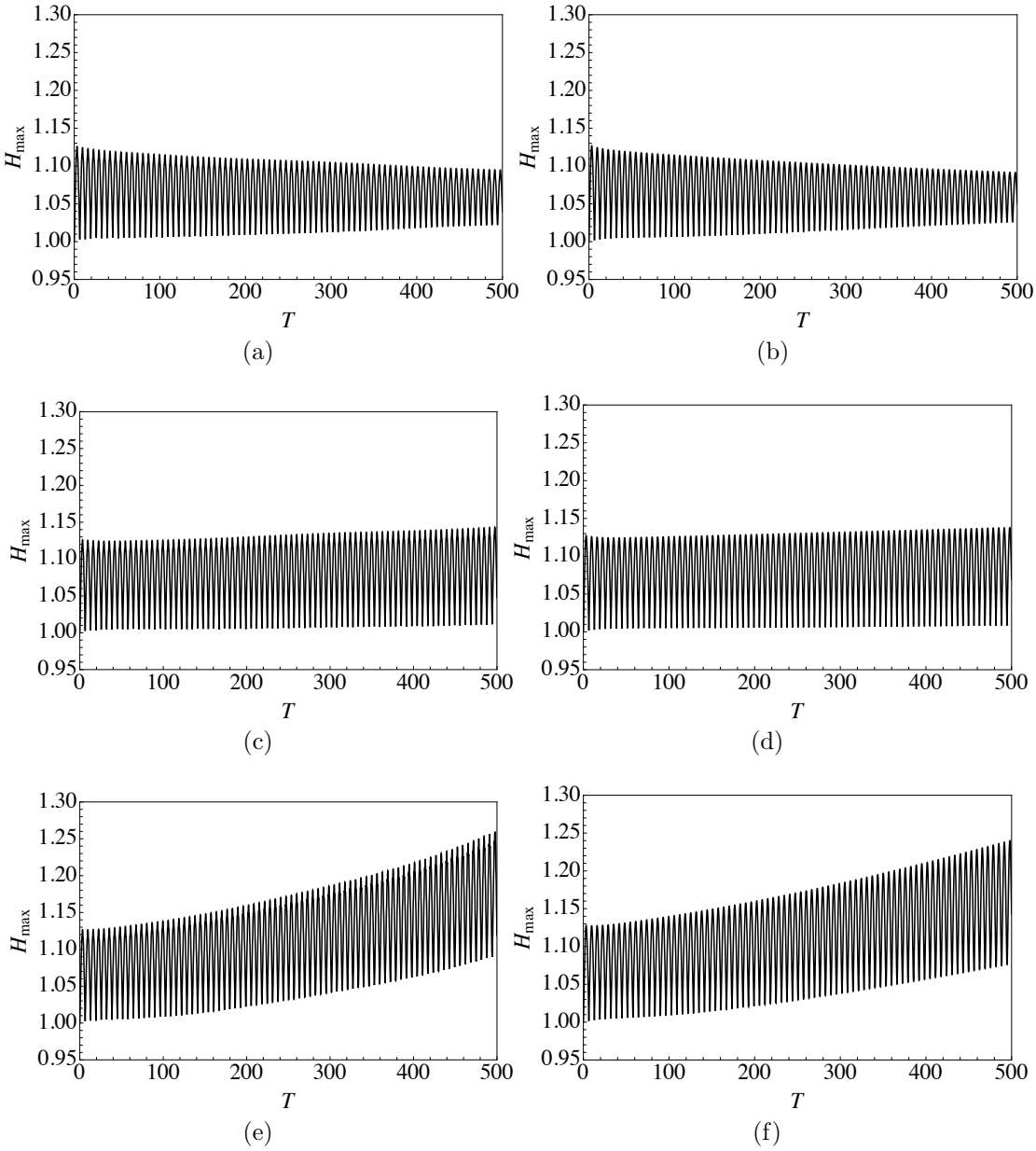

Figure 4.46: Maximum values of the film thickness $H_{\max}$ for $D = 5$, $\beta = 0.0532$, and $\alpha = 0.0048$ over the time interval $T = [0, 500]$, calculated from (a), (c), (e) the third-order three-timescale asymptotic solution $H_4^{(3\tau)}(\phi, \tau)$ (4.4.12) (converted back to the fixed frame) and (b), (d), (f) the numerical solution of the governing equation (4.4.7) for (a), (b) $\delta = 0$, (c), (d) $\delta = 2$, and (e), (f) $\delta = 4$.

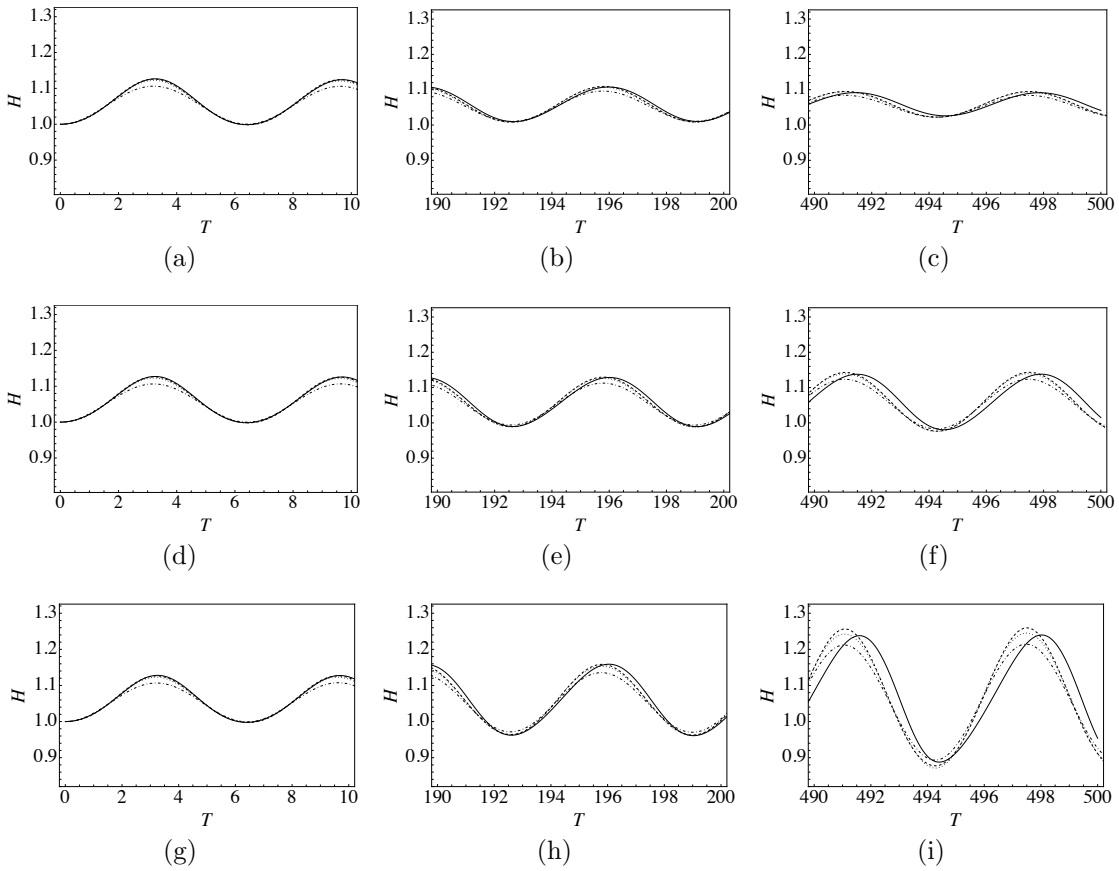

Figure 4.47: The third-order three-timescale asymptotic solution $H_4^{(3\tau)}(\phi,\tau)$ (4.4.12) (converted back to the fixed frame) at $\theta = 0$ at for $N = 1, 2$, and 3 (dot-dashed, dotted, and dashed lines, respectively) compared with the numerical solution of the governing equation (4.4.7) (solid line) for $D = 5$, $\beta = 0.0532$, $\alpha = 0.0048$, and (a)–(c) $\delta = 0$, (d)–(f) $\delta = 2$, and (g)–(i) $\delta = 4$ over the time intervals (a), (d), (g) $T = [0, 10]$, (b), (e), (h) $T = [190, 200]$, and (c), (f), (i) $T = [490, 500]$.

thickness.

Figure 4.48 shows convergence of the third-order three-timescale asymptotic solution $H_4^{(3\tau)}(\phi,\tau)$ (4.4.12) (converted back to the fixed frame) for $N = 1, 2$, and 3 to the numerical solution of the governing equation (4.4.7) for $\beta = 0.0532$, $\alpha = 0.0048$, and (a)–(c) $\delta = 0$, (d)–(f) $\delta = 2$, and (g)–(i) $\delta = 4$ at times $T = 10, 100$, and 500, demonstrating further that increasing the electric potential difference δ results in an increase in the maximum film thickness.

In summary, the third-order three-timescale asymptotic solution for the film thickness $H_4^{(3\tau)}(\phi,\tau)$ agrees well with the numerical solution within the asymptotically valid time interval. Our numerical and asymptotic results confirm that, as predicted by the growth rate (4.4.48), when $\delta = O(1)$ the solution for H to $O(\beta^3)$ blows up at large times, manifesting physically as the interface being pulled closer to the outer electrode by the destabilising electrostatic effects.

4.4.8 Limiting case: $O(\beta^2)$ electrostatic effects

The preceding analysis is valid for cases not only in which electrostatic effects are $O(\beta)$, but also for those in which particular choices of parameter values are such that electrostatic effects are $O(\beta^2)$. Hence, to investigate further the interplay between electrostatic, gravitational, and capillary effects without the impediment of the overwhelming destabilising effect of the electric field, in this section we use (4.4.45) to investigate the limit in which $\delta = O(\beta)$ such that the electrostatic term in the governing equation (4.4.7) is $O(\beta^2)$. Note that, formally, this approach is asymptotically inconsistent due to the fact that the asymptotic order of S_0 changes. However, we proceed in this manner in order to study the result that would arise if we had assumed that $\delta = O(\beta)$ from the beginning of this section.

4.4.8.1 Growth rate ω

To determine the growth rate, we proceed by setting $\delta = \beta\hat{\delta}$ such that

$$S_0\tau_1 = \frac{\delta}{(D-1)^3}\beta\tau_0 = \frac{\hat{\delta}}{(D-1)^3}\beta^2\tau_0 := \hat{S}_0\tau_2. \tag{4.4.55}$$

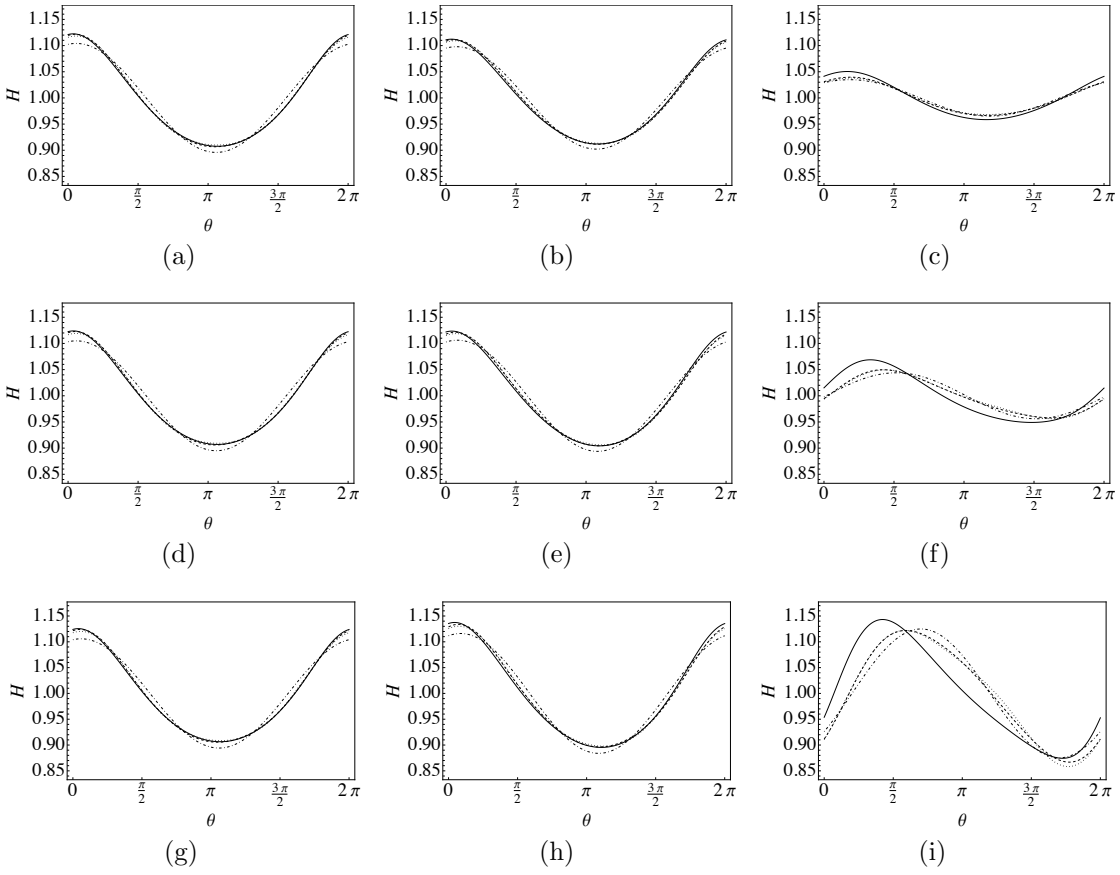

Figure 4.48: The third-order three-timescale asymptotic solution $H_4^{(3\tau)}(\phi,\tau)$ (4.4.12) (converted back to the fixed frame) for $N = 1, 2$, and 3 (dot-dashed, dotted, and dashed lines, respectively) compared with the numerical solution of the governing equation (4.4.7) (solid line) for $D = 5$, $\beta = 0.0532$, $\alpha = 0.0048$, and (a)–(c) $\delta = 0$, (d)–(f) $\delta = 2$, and (g)–(i) $\delta = 4$ at times (a), (d), (g) $T = 10$, (b), (e), (h) $T = 100$, and (c), (f), (i) $T = 500$.

Thus, in this case, the growth rate (4.4.47) is $O(\beta^2)$ and is given by

$$\omega = \hat{S}_0 + S_1 = \frac{\hat{\delta}}{(D-1)^3} - \frac{81\alpha}{144\alpha^2+1}, \tag{4.4.56}$$

from which we find that the solution (4.4.12) for the film thickness H to $O(\beta^3)$ is stable for

$$\hat{\delta} < \frac{81\alpha\,(D-1)^3}{144\alpha^2+1} \coloneqq \hat{\delta}_{\text{crit}}. \tag{4.4.57}$$

Hence, in the case in which electrostatic effects are $O(\beta^2)$, the flow is conditionally unstable in the sense that the solution for the film thickness grows for certain values of the physical parameters. The interplay between electrostatic, gravitational, and capillary effects is discussed in Section 4.4.8.2, in which we analyse the evolution of the film in the case in which electrostatic effects are $O(\beta^2)$.

4.4.8.2 Evolution of the film thickness

As discussed in Section 4.4.8, in the case in which electrostatic effects are $O(\beta^2)$, the electrostatic term in (4.4.52) no longer dominates but instead enters at the same order as capillarity, also working on the slower timescale $T_2 = \beta^2 T$. In this case, to $O(\beta)$ the film thickness is

$$H = 1 + \beta\left[\cos\theta - \mathrm{e}^{\left(\hat{S}_0+S_1\right)T_2}\cos\left[\theta - (T_0 - S_2T_2)\right]\right], \tag{4.4.58}$$

and thus, to $O(\epsilon\beta)$ the interface has the form

$$r = 1 + \epsilon + \epsilon\beta\left[\cos\theta - \mathrm{e}^{\left(\hat{S}_0+S_1\right)T_2}\cos\left[\theta - (T_0 - S_2T_2)\right]\right]. \tag{4.4.59}$$

The term $\cos\left[\theta - (T_0 - S_2T_2)\right]$ shows that the phase of the interface drifts away from the phase of the solid cylinder by the amount S_2T_2 on the slower timescale $T_2 = \beta^2 T$. The $\exp\left(S_1T_2\right)$ term represents the effect of capillarity, which works to decay the amplitude of the fundamental modes $\cos\left(\theta - T_0\right)$ and $\sin\left(\theta - T_0\right)$ on the very slow timescale $T_2 = \beta^2 T$, whilst the $\exp(\hat{S}_0T_2)$ term represents electrostatic effects, which work on the same timescale to increase the amplitude of the fundamental modes. There is a complex interplay between electrostatic and capillary effects, in which electrostatic effects are able to dominate and destabilise the system subject to the stability criterion $\hat{\delta} > \hat{\delta}_{\text{crit}}$ (4.4.57). For example, for the

parameter values $D = 5$ and $\alpha = 0.0048$, solutions for the film thickness H will be stable for $\hat{\delta} < \hat{\delta}_{\text{crit}} = 24.8009$.

In the following results, we again use the value $D = 5$ with $\beta = 0.0532$ and $\alpha = 0.0048$. Figure 4.49 shows plots of the maximum values of the film thickness $H_{\max}$ calculated from both the third-order three-timescale asymptotic solution $H_4^{(3\tau)}(\phi, \tau)$ (4.4.7) (converted back to the fixed frame) in the case in which $\delta = \beta\hat{\delta}$ and the numerical solution of the governing equation (4.4.7) for $\beta = 0.0532$, $\alpha = 0.0048$, and (a), (b) $\hat{\delta} = 14.8009$, (c), (d) $\hat{\delta} = \hat{\delta}_{\text{crit}} = 24.8009$, and (e), (f) $\hat{\delta} = 34.8009$ over the time interval $T = [0, 500]$. Note that the values $\hat{\delta} = 14.8009$, $\hat{\delta} = 24.8009$, and $\hat{\delta} = 34.8009$ were chosen to investigate a stable solution, a neutrally stable solution, and an unstable solution, respectively. Specifically, the values $\hat{\delta} = 14.8009$ and $\hat{\delta} = 34.8009$ were chosen to be equidistant either side of the stability threshold, from which they were chosen to be far enough away so as to show an appreciable difference over the time interval $T = [0, 500]$ when compared to the neutrally stable case. Figures 4.49 (a) and (b) show that the maximum film thickness decreases over the asymptotically valid time interval, indicating stability of the system for $\hat{\delta} = 14.8009$. Figures 4.49 (c) and (d) show neutral stability of the system, as predicted from the stability criterion (4.4.57). Figures 4.49 (e) and (f) show that the maximum film thickness is increasing over the asymptotically valid time interval, indicating instability of the system for $\hat{\delta} = 34.8009 > \hat{\delta}_{\text{crit}}$, as expected.

Figure 4.50 demonstrates the convergence of the third-order three-timescale asymptotic solution $H_4^{(3\tau)}(\phi, \tau)$ (4.4.12) in the case in which $\delta = \beta\hat{\delta}$ (converted back to the fixed frame) at $\theta = 0$ at for $N = 1, 2$, and 3 to the numerical solution of the governing equation (4.4.7) for $\beta = 0.0532$, $\alpha = 0.0048$ and (a), (b) $\hat{\delta} = 14.8009$, (c), (d) $\hat{\delta} = \hat{\delta}_{\text{crit}} = 24.8009$, and (e), (f) $\hat{\delta} = 34.8009$ over the time intervals (a), (d), (g) $T = [0, 10]$, (b), (e), (f) $T = [190, 200]$, and (c), (f), (i) $T = [490, 500]$. Figures 4.50 (c), (f), and (i) show that the expansion has drifted from the numerical solution, and that increasing the electric potential difference leads to an increase in the amplitude of the maximum film thickness.

Figure 4.51 shows convergence of the third-order three-timescale asymptotic solution $H_4^{(3\tau)}(\phi, \tau)$ (4.4.12) in the case in which $\delta = \beta\hat{\delta}$ (converted back to the fixed frame) for $N = 1, 2$, and 3 to the numerical solution of the governing equation (4.4.7) for $\beta = 0.0532$, $\alpha = 0.0048$ and (a)–(c) $\hat{\delta} = 14.8009$, (d)–(f) $\hat{\delta} = \hat{\delta}_{\text{crit}} = 24.8009$, and (g)–(i) $\hat{\delta} = 34.8009$, demonstrating further that increasing the electric

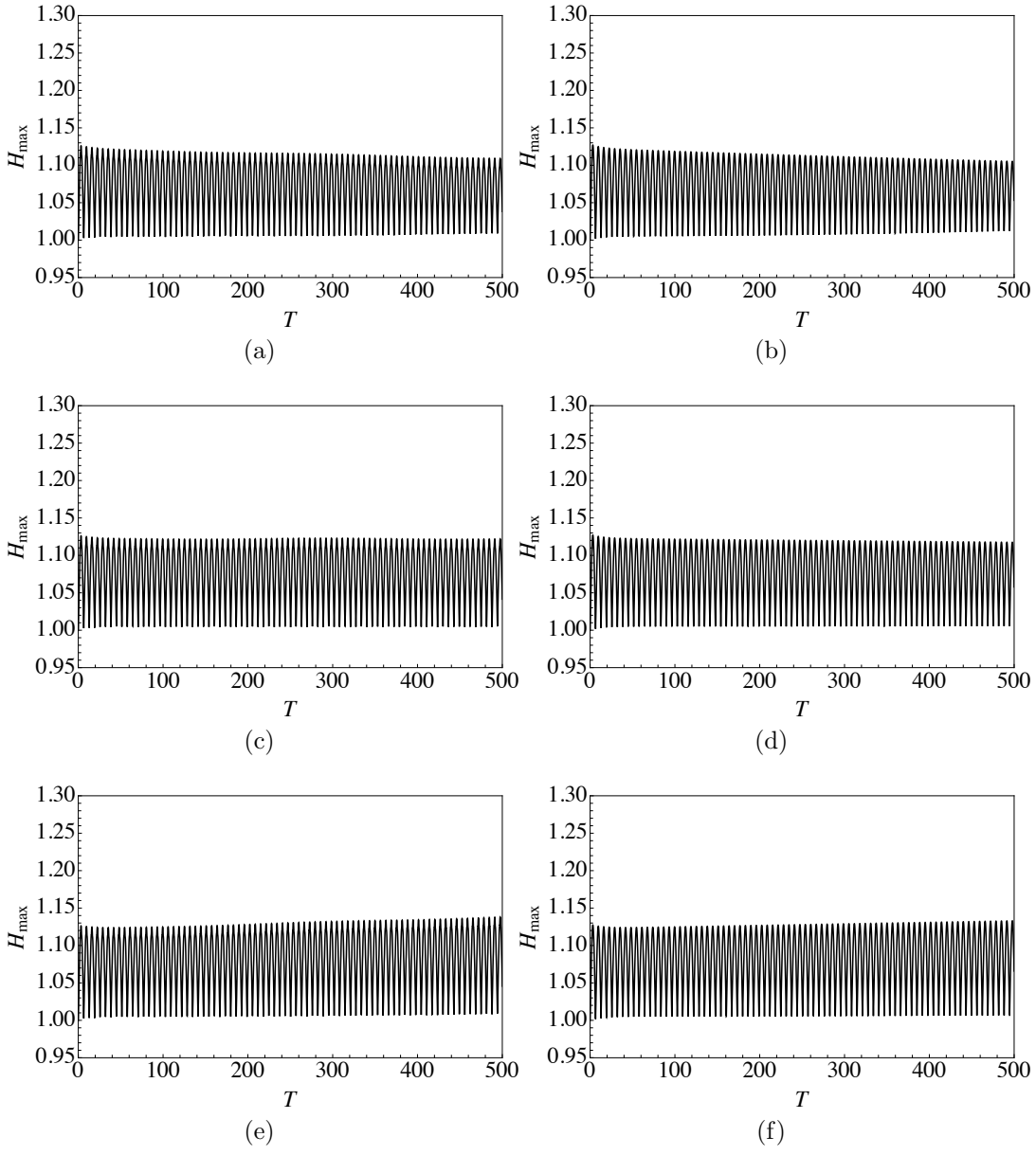

Figure 4.49: Maximum values of the film thickness $H_{\max}$ for $D = 5$, $\beta = 0.0532$, and $\alpha = 0.0048$, calculated from (a), (c), (e) the third-order three-timescale asymptotic solution $H_4^{(3\tau)}(\phi, \tau)$ (4.4.12) (with $\delta = \beta\hat{\delta}$ and converted back to the fixed frame) and (b), (d), (f) the numerical solution of the governing equation (4.4.7) for (a), (b) $\hat{\delta} = 14.8009$ (stability), (c), (d) $\hat{\delta} = \hat{\delta}_{\text{crit}} = 24.8009$ (neutral stability), and (e), (f) $\hat{\delta} = 34.8009$ (instability) over the time interval $T = [0, 500]$.

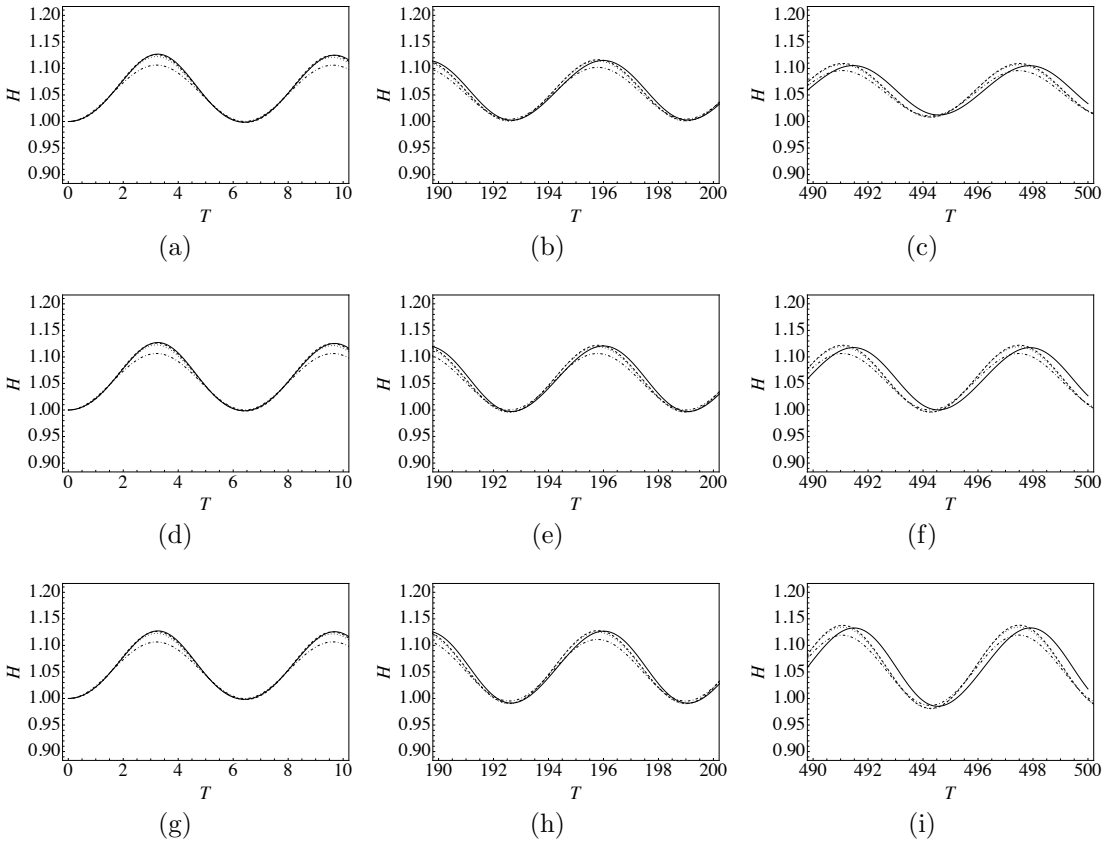

Figure 4.50: The third-order three-timescale asymptotic solution $H_4^{(3\tau)}(\phi,\tau)$ (4.4.12) (converted back to the fixed frame) in the case where $\delta = \beta\hat{\delta}$ such that the electric field is $O(\beta^2)$, shown at $\theta = 0$ at for $N = 1, 2$, and 3 (dot-dashed, dotted, and dashed lines, respectively) compared with the numerical solution of the governing equation (4.4.7) (solid line) for $D = 5$, $\beta = 0.0532$, $\alpha = 0.0048$, and (a), (b) $\hat{\delta} = 14.8009$ (stable), (c), (d) $\hat{\delta} = 24.8009$ (neutrally stable), and (e), (f) $\hat{\delta} = 34.8009$ (unstable) over the time intervals (a), (d), (g) $T = [0, 10]$, (b), (e), (h) $T = [190, 200]$, and (c), (f), (i) $T = [490, 500]$.

potential difference results in an increase in the maximum film thickness.

In summary, when $\delta = O(\beta)$ such that electrostatic effects and capillarity are both $O(\beta^2)$, the third-order, three-timescale asymptotic solution for the film thickness $H_4^{(3\tau)}(\phi, \tau)$ agrees well with the numerical solution within the asymptotically valid time interval. Our numerical and asymptotic results confirm that, as predicted by the stability criterion (4.4.57), capillarity stabilises the flow, whilst electrostatic effects destabilise the flow at sufficiently large electric potential differences. This is evident in the fact that the maximum film thickness $H_{\max}$ decreases in time for values of $\hat{\delta}$ below the stability threshold, and increases in time for values of $\hat{\delta}$ above the stability threshold as the interface is pulled closer to the outer electrode as seen previously.

4.5 Concluding remarks

In this chapter, we have undertaken a detailed analysis of coating flow on a horizontal circular cylinder in the presence of an electric field.

Firstly, in Section 4.1, we considered the linear stability of steady states in two analytically tractable special cases: the case of zero gravity in Section 4.1.1, and the case in which capillarity and electrostatic effects are weak in Section 4.1.2. In both cases, it was shown that electrostatic effects destabilise the system. In the case of zero gravity, the stability of uniform steady states was considered. The dispersion relation was derived, from which the most unstable mode $n_{\max}$ was found. The linear stability results were compared with numerical solutions of the full governing equation which indicate that, as the film evolves, the destabilising electrostatic effects lead to the formation of bulges of liquid around the circumference of the cylinder. It was shown that the number of bulges expected to appear in the nonlinear numerical results can be accurately predicted by $n_{\max}$. In the case in which capillarity and electrostatic effects are both weak, it was shown that nonuniform steady states are unstable to $O(\gamma^{-1})$ for $\hat{E}_b > -(F_1 + n^2 F_2)/F_3$. Electrostatic effects were shown to cause instability, as increasing $\hat{E}_b$ contributes to increasing the growth rate, whilst capillarity was shown to be a stabilising influence. It was found that steady solutions are more stable in cases involving either thicker films or when there is a greater distance between the outer electrode and the interface. In such cases, capillarity is the dominant behaviour and stabilises the flow.

Next, the qualitatively different behaviours that the system exhibits were iden-

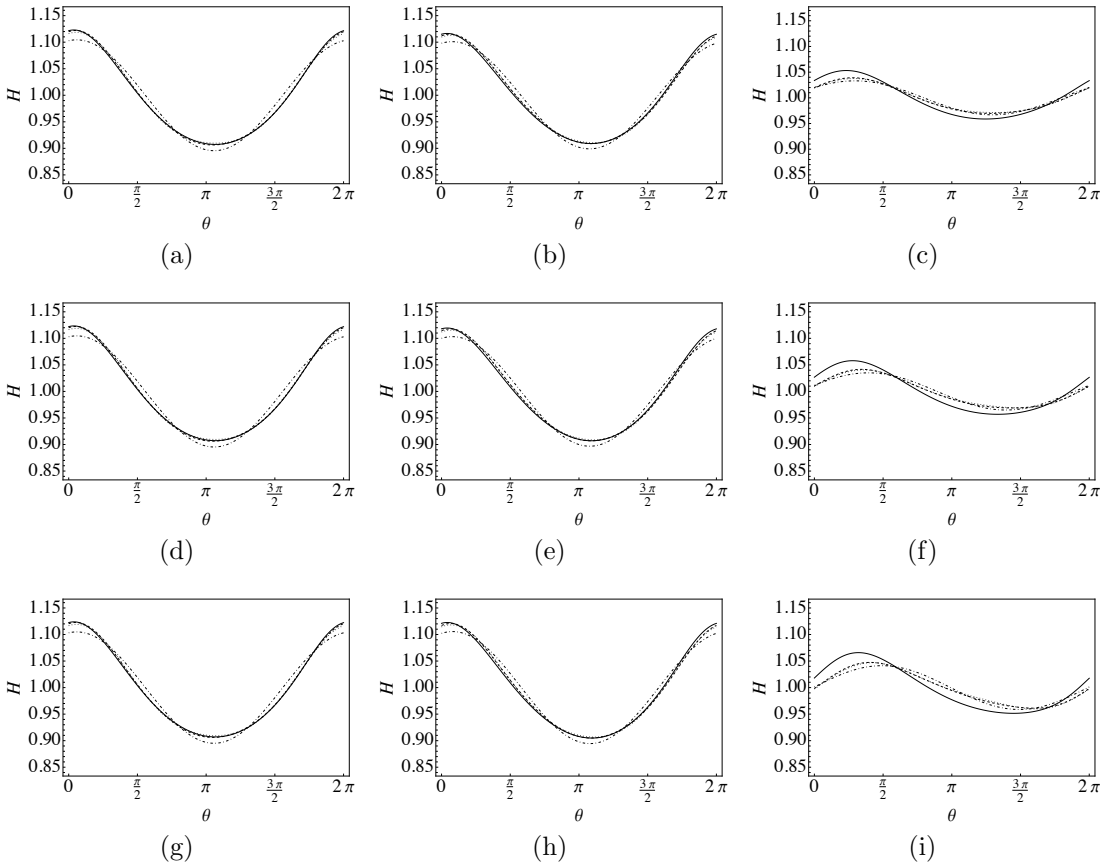

Figure 4.51: The third-order three-timescale asymptotic solution $H_4^{(3\tau)}(\phi,\tau)$ (4.4.12) (converted back to the fixed frame) for $N = 1, 2$, and 3 (dot-dashed, dotted, and dashed lines, respectively) compared with the numerical solution of the governing equation (4.4.2) (solid line) for $\beta = 0.0532$, $\alpha = 0.0048$ and (a)–(c) $\hat{\delta} = 14.8009$ (stable), (d)–(f) $\hat{\delta} = 24.8009$ (neutrally stable), and (g)–(i) $\hat{\delta} = 34.8009$ (unstable) at times $T = 10, 100$, and 500.

tified and analysed in Section 4.2 by means of a numerical parametric study in (γ, E_b) parameter space. It was found that the system exhibits four distinct behaviours: steady states, periodic states, outer contact, and transient states. For very thin films, only transient and periodic states arise due to the fact that the effect of the electric field is very weak when the interface is far from the outer electrode, and hence the dominant force is that due to rotation. For thin (but not very thin) films, increasing γ or E_b results in a transition in parameter space from steady states to periodic states and then a transition from periodic states to outer contact. For the thickest films, the interface is closer to the outer electrode and hence the electric field is stronger, leading to more instances of outer contact occurring. Steady-state behaviour was described in Section 4.2.3 and arises for all but the smallest initial film thicknesses when γ or E_b are small enough. Typically, one bulge forms and is held in place on the lower right-hand side of the cylinder as the forces balance, and increasing γ or E_b increases the maximum thickness of the bulge. Periodic-state behaviour was described in Section 4.2.4 and occurs for thin and very thin films. At most two bulges form in periodic states, which coalesce as the system approaches the final periodic state in which a single bulge is typically carried around the cylinder periodically by the rotation. In general, increasing either γ or E_b results in an increase in the maximum film thickness. Outer contact behaviour was described in Section 4.2.5 and occurs when the interface touches the outer electrode in a finite time. For small H_0, outer contact behaviour arises in parameter space through a transition from periodic states in which typically up to four bulges form and oscillate around the cylinder whilst the maximum film thickness increases until eventually the bulges coalesce on the approach to outer contact. For large H_0, outer contact behaviour arises in parameter space through a transition from a region of steady states. Typically, there is only enough time for one bulge to form. This bulge does not complete a full rotation around the cylinder before outer contact occurs due to the increased strength of the electric field because the interface is closer to the outer electrode. In general, increasing either γ or E_b decreases the time taken for outer contact to occur. Transient-state behaviour was described in Section 4.2.6, and occurs for small and very small values of H_0. We hypothesise that, in some instances (for example, on the transition between different behaviours), states which appear to be transient could actually be instances of complex, large-time dynamics which are difficult to capture numerically and may settle down to one of the other three behaviour classifications

at much later times.

The analysis presented in Chapter 3 was generalised in Section 4.3 to include electrostatic effects. At early times, electrostatic effects are weak, entering the solution at second order. At late times, it was found that the same three distinct regions of behaviour arise as in the absence of an electric field, as described in Chapter 3. Electrostatic effects are only significant in the pendant-drop region due to the fact that the film is extremely thin at late times in the remaining regions. In this region, electrostatic effects are strongest (since this is where the film is thickest) which can lead to outer contact when the outer electrode is positioned too close to the interface. When the outer electrode is far enough away such that outer contact does not occur, there is a quasi-static balance between capillarity, gravity, and electrostatic effects in the pendant-drop region. In this case, the asymptotic solution for the film thickness to leading order in D^{-1} was found and validated against numerical solutions of the governing equation. It was shown that electrostatic effects influence the calculations in the inner region only through the matching condition L_0 (4.3.19) which is required to match dimple 1 to the pendant-drop region. The qualitative behaviour and structure of the inner region remains unchanged when compared to the problem described in Chapter 3. The solutions in dimple 1 and ridge 1 were found and validated against numerical solutions of the governing equation for non-zero E_b.

Finally, the large-time dynamics of the system were investigated in Section 4.4, in which we generalised the asymptotic analysis of Hinch and Kelmanson [73] to incorporate electrostatic effects in the case in which gravity and electrostatic effects are weak. It was found that three timescales (rather than two) are required to resolve the secularities that arise. The third-order three-timescale asymptotic solution $H_4^{(3\tau)}(\phi, \tau)$ was derived and was shown to yield very close agreement with the numerical solution within the asymptotically valid time interval. In the case in which $\delta = O(1)$, for $\delta > 0$, the growth rate $\omega = S_0$ is always positive, indicating that the solution for H to $O(\beta^3)$ is unconditionally unstable and blows up like $\exp(S_0\tau_1)$ at late times. In this case, the electric field destabilises the system on the slow timescale $\tau_1 = \beta\tau$, resulting in the interface being pulled closer to the outer electrode as we have seen previously. In the case in which $\delta = O(\beta)$, electrostatic effects no longer dominate the evolution, instead entering at the same order as capillarity. Capillarity stabilises the flow [73, 130] whilst electrostatic effects destabilise the flow at sufficiently large electric potential differences, specifically

when $\hat{\delta} > 81\alpha\,(D-1)^3\,/\,(144\alpha^2+1)$.

Chapter 5

Thick-film coating flow in the presence of an electric field

In this chapter, we refocus our attention on the WRIBL model for thick-film coating flow in the presence of an electric field, which was derived earlier in Section 2.3 and consists of the WRIBL equation (2.3.66) and the kinematic condition (2.1.34) together with either the electrode model (2.3.29) and (2.3.30), the interface model (2.3.43) and (2.3.44), or the thick-film gradient model (2.3.48). The aims of this chapter are twofold: firstly, we aim to determine which of the three candidate electrostatic models offers the greatest accuracy and hence is the most suitable for use in the WRIBL model. Secondly, with a suitable electrostatic model chosen, we aim to build upon the recent study by Wray and Cimpeanu [31] (who, as discussed in Section 1.4.4, investigated the thick-film coating flow system in the absence of an electric field) to understand how the incorporation of an electric field with a constant potential influences the dynamics of the system.

Firstly, in Section 5.1, we compare the three candidate electrostatic models numerically to determine which yields the greatest accuracy when compared to the numerical solution of Laplace's equation (2.1.3). Next, in Section 5.2, we investigate the evolution of the film in order to understand how electrostatic effects induced by an electric field with a constant potential influence the dynamics of the system, in particular, investigating flows which are either steady or periodic in the absence of an electric field in Sections 5.2.1 and 5.2.2, respectively. Finally, in Section 5.3, we draw our conclusions.

5.1 Comparison of the electrostatic models

In this section, we compare the electrode model (2.3.29) and (2.3.30), the interface model (2.3.43) and (2.3.44), and the thick-film gradient model (2.3.48) for the purpose of determining which of these offers the greatest accuracy and hence is the most suitable for use in the WRIBL model. The quantity that is of interest in this section is the normal Maxwell stress E^N (2.3.9), which, as we recall, is given by

$$E^N = 2\varepsilon^2 \frac{s_{\check{\theta}}}{s^2}\phi_r\phi_{\check{\theta}} - \frac{1}{2}\left(1 - \varepsilon^2\frac{s_{\check{\theta}}^2}{s^2}\right)\left(\phi_r^2 - \varepsilon^2\frac{\phi_{\check{\theta}}^2}{s^2}\right),$$

where, as before, ε is an ordering parameter. As we recall, E^N enters the WRIBL equation (2.3.66) at first order in ε. Hence, in order to obtain a WRIBL model that is accurate to second order in ε, terms which are second order and higher in (2.3.9) can be disregarded. Hence, in what follows, it will be appropriate to compare the performance of the three aforementioned models in calculating E^N (2.3.9) to leading order against the full fourth-order expression for E^N (2.3.9) calculated from the numerical solution of Laplace's equation (2.1.3) which is solved subject to the boundary conditions (2.1.36). The solutions for f_1 in the electrode model, g in the interface model, and the numerical solution of Laplace's equation (2.1.3) are all obtained in Mathematica [265] using the built-in function `NDSolve[]` which implements the finite element method.

Substitution of equation (2.3.43) of the interface model into E^N (2.3.9) yields the following simple form of the normal Maxwell stress,

$$E^N = -\frac{g^2}{2s^2} + O(\varepsilon^4). \tag{5.1.1}$$

Similarly, substitution of equation (2.3.29) of the electrode model into E^N (2.3.9) yields

$$E^N = -\frac{f_1^2}{2s^2} + O(\varepsilon^2). \tag{5.1.2}$$

Note that (5.1.1) is accurate up to third order in ε, whereas (5.1.2) is only accurate to first order. Thus, we expect that the interface model will perform better than the electrode model *a priori*. At leading order, substitution of the thick-film gradient model (2.3.48) into (2.3.9) recovers the expression for E^N calculated from the leading-order solution to Laplace's equation (2.3.14), namely, equation (2.3.16)

which, as we recall, is given by

$$E^N = -\frac{\phi_d^2}{2s^2 \ln^2(d/s)}.$$

Note that the electrode model (2.3.29) and (2.3.30) and the interface model (2.3.43) and (2.3.44) better preserve the elliptic nature of the underlying Laplace equation [244]. These models accurately represent the behavior of the electric potential ϕ as it propagates in all directions whilst gradually decreasing in intensity. In contrast, in lubrication models such as the thick-film gradient model (2.3.48), the electric potential ϕ is solely dependent on the local values of ϕ_d and its derivatives. As a result, these models introduce artificial locality, meaning that the normal Maxwell stress is limited to the region where the potential is applied and becomes exactly zero beyond that region.

In what follows, we compare the performance of (2.3.16), (5.1.1), and (5.1.2) using two stringent tests: a sharply varying potential at the outer electrode ϕ_d (for constant interfacial radius s) in Section 5.1.1, and a sharply varying interfacial radius s (for constant potential ϕ_d) in Section 5.1.2. Note that comparing the performance of models derived under a long-wave assumption in the short-wave regime might appear unconventional *a priori*. However, it is anticipated that these models can still be applicable outside of the long-wave regime. Previous investigations in optimal control problems [244] have revealed that whilst the waves remain long, precise adjustments in the control parameter are often necessary to achieve the desired behavior, particularly during the initial stages. Therefore, there is an expectation for favorable agreement in the short-wave regime, which would be valuable for practical applications.

5.1.1 Sharply varying potential

In this section, we compare the performance of the three electrostatic models in the case in which the potential at the outer electrode ϕ_d can vary sharply with θ whilst the position of the interfacial radius s remains constant. We consider first a step-function shape for ϕ_d, before considering functions with sinusoidal shapes of high frequency for ϕ_d, which have both been deliberately chosen so as to be outside the regime of asymptotic applicability of the long-wave approximation in order to provide a stringent test. Throughout this section, we use the values $d = 3$

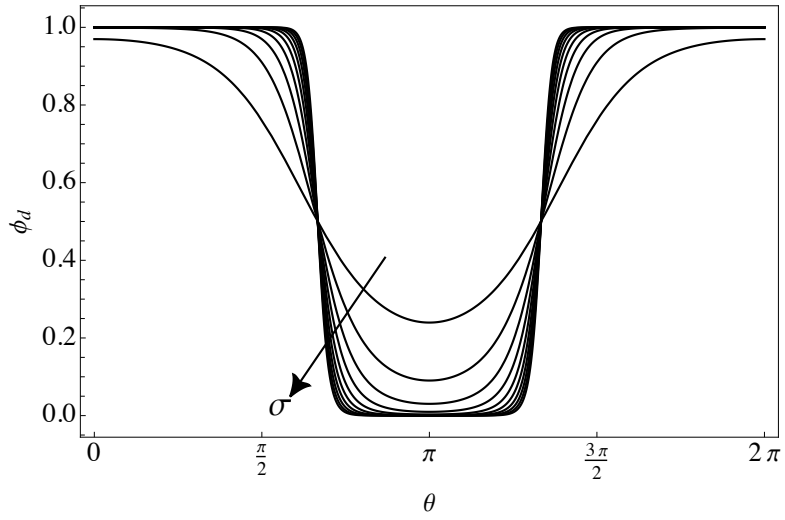

Figure 5.1: The potential at the outer electrode ϕ_d (5.1.3) for $\sigma = 1, 2, \ldots, 10$. The arrow indicates the direction of increasing σ.

and $s = 2$.

To consider potentials with a step-function shape we choose ϕ_d to be of the form [67]

$$\phi_d = \frac{1}{2}\left[1 + \tanh\left\{\frac{\sigma(\cos(m\theta) - \cos(mX)}{m\sin(mX)}\right\}\right], \tag{5.1.3}$$

which is appropriate for a periodic domain of length $2\pi/m$, where the parameter σ controls the "sharpness" of the function (i.e., how steep the gradients are) and the parameter X controls the width of the region in which the potential is (approximately) constant. Throughout this section, we consider the function (5.1.3) with the values $m = 1$ and $X = 2\pi/3$, so that the domain has length 2π and the potential is approximately constant in a region of width $4\pi/3$, and close to zero outside of this region. Figure 5.1 shows (5.1.3) for $\sigma = 1, 2, \ldots, 10$. Figure 5.2 shows the numerical solution of Laplace's equation (2.1.3) calculated subject to the boundary conditions (2.1.36) with ϕ_d given by (5.1.3) with $\sigma = 10$ (corresponding to a very sharp potential). Figure 5.3 shows plots of the solutions for (a) f_1 and (b) g calculated from the electrode model (2.3.30) and the interface model (2.3.44), respectively, with ϕ_d given by (5.1.3) with $\sigma = 10$.

Figure 5.4 shows the leading-order normal Maxwell stress E^N calculated from the electrode model (5.1.2), the interface model (5.1.1), and the thick-film gradient model (2.3.16) compared with the full expression for E^N (2.3.9) calculated from the numerical solution of Laplace's equation (2.1.3). In particular, Figure 5.4

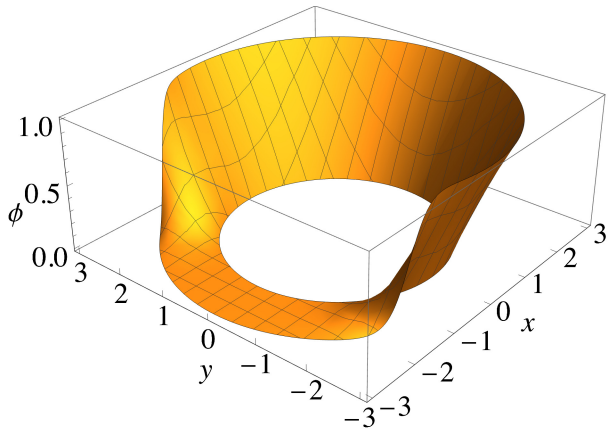

Figure 5.2: Numerical solution of Laplace's equation (2.1.3) calculated subject to the boundary conditions (2.1.36) with ϕ_d given by (5.1.3) with $\sigma = 10$.

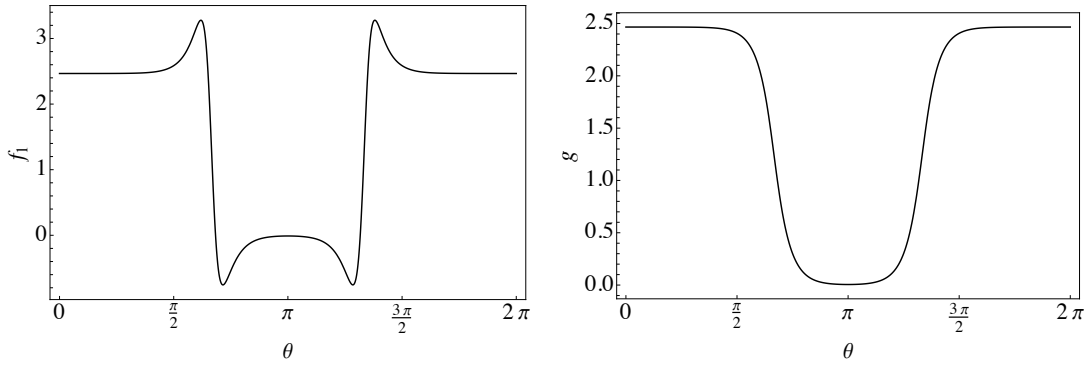

Figure 5.3: Solutions for (a) f_1 calculated from (2.3.30) and (b) g calculated from (2.3.44) with ϕ_d given by (5.1.3) with $\sigma = 10$.

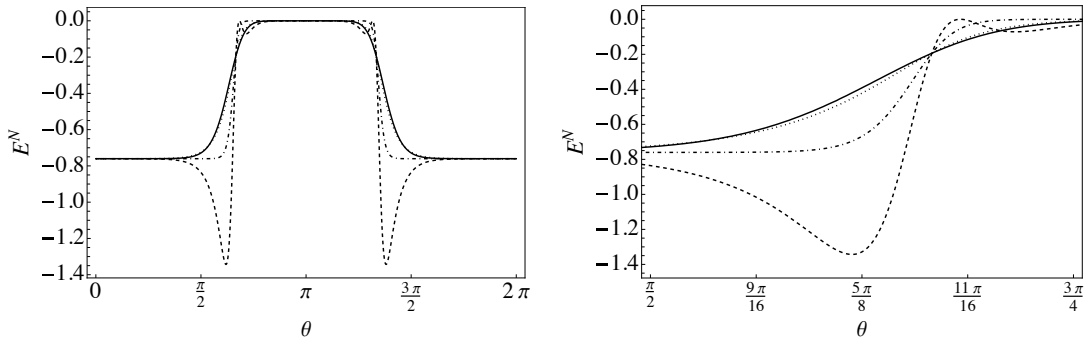

(a) (b)

Figure 5.4: The leading-order normal Maxwell stress E^N calculated from the electrode model (5.1.2) (dashed line), the interface model (5.1.1) (dotted line), and the thick-film gradient model (2.3.16) (dot-dashed line) compared with the full expression for E^N (2.3.9) calculated from the numerical solution of Laplace's equation (2.1.3) (solid line), calculated with ϕ_d given by (5.1.3) with $\sigma = 10$. (a) Solution for $0 \leq \theta \leq 2\pi$. (b) Enlargement of (a) close to $\theta = 5\pi/8$.

shows that the interface model (2.3.43) and (2.3.44) (shown as the dotted line) performs best, the thick-film gradient model (2.3.48) (shown as the dot-dashed line) performs less well, and the electrode model (2.3.29) and (2.3.30) (shown as the dashed line) performs the poorest.

It is instructive to investigate the performance of the models as the parameter σ is varied in (5.1.3) to understand how the performance of the models changes as the wavelength of the potential is varied. We compare the performance of the models by calculating their integral absolute error, defined by

$$\chi = \int_0^{2\pi} |E^N_{\text{num}} - E^N_{\text{model}}| \, \mathrm{d}\theta, \tag{5.1.4}$$

where E^N_{num} and E^N_{model} represent E^N (2.3.9) calculated from the numerical solution of Laplace's equation (2.1.3) and from any of the three electrostatic models whose solution we wish to compare with, respectively.

We proceed by setting $\sigma = 1, 2, \ldots, 10$, as shown in Figure 5.1. Figure 5.5 (a) shows a semi-log plot of χ (5.1.4) calculated for the interface model (5.1.1), the electrode model (5.1.2), and the thick-film gradient model (2.3.16) compared to the full expression for E^N (2.3.9) calculated from the numerical solution of Laplace's equation (2.1.3). In particular, Figure 5.5 (a) shows that the accuracy of each of

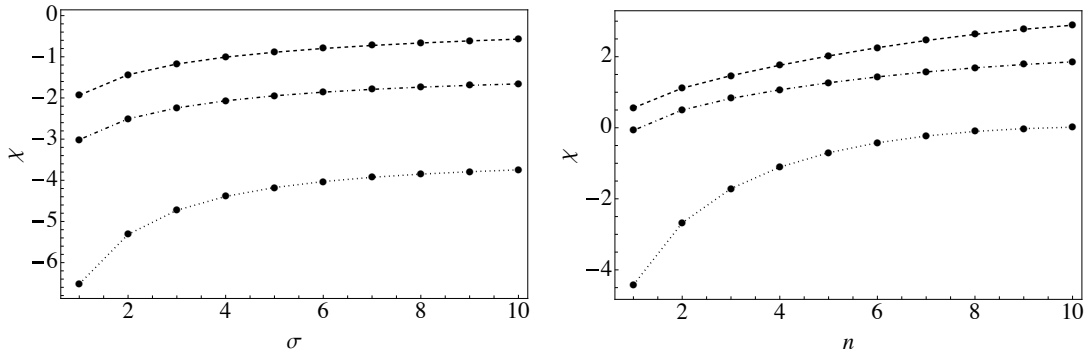

Figure 5.5: Semi-log plots of the integral absolute error χ (5.1.4) of the leading-order normal Maxwell stress E^N calculated numerically from comparing the electrode model (5.1.2) (dashed line), the interface model (5.1.1) (dotted line), and the thick-film gradient model (2.3.16) (dot-dashed line) with the full expression for E^N (2.3.9) calculated from the numerical solution of Laplace's equation (2.1.3) with ϕ_d given by (a) (5.1.3) for $1 \leq \sigma \leq 10$ and (b) (5.1.5) for $1 \leq n \leq 10$. Filled circles represent values of (a) σ and (b) n.

the models decreases as σ is increased (i.e., as the variation in ϕ_d gets sharper), as expected. Figure 5.5 (a) also shows that the interface model (5.1.1) (shown as the dotted line) is the most accurate, followed by the thick-film gradient model (2.3.16) (shown as the dot-dashed line), and that the electrode model (5.1.2) (shown as the dashed line) performs the poorest.

To consider potentials with sinusoidal shapes of high frequency, we choose ϕ_d to be of the form

$$\phi_d = \sin(n\theta) \tag{5.1.5}$$

for wavenumbers $n = 1, 2, 3$, and 4. Figure 5.6 shows the numerical solution of Laplace's equation (2.1.3) calculated subject to the boundary conditions (2.1.36) with ϕ_d given by (5.1.5) for (a) $n = 1$, (b) $n = 2$, (c) $n = 3$, and (d) $n = 4$.

Figure 5.7 shows the leading-order normal Maxwell stress E^N calculated from the electrode model (5.1.2), the interface model (5.1.1), and the thick-film gradient model (2.3.16) compared with the full expression for E^N (2.3.9) calculated from the numerical solution of Laplace's equation (2.1.3) calculated for ϕ_d given by (5.1.5) with (a) $n = 1$, (b) $n = 2$, (c) $n = 3$, and (d) $n = 4$. In particular, Figure 5.7 shows that the interface model (2.3.43) and (2.3.44) (shown as the dotted line)

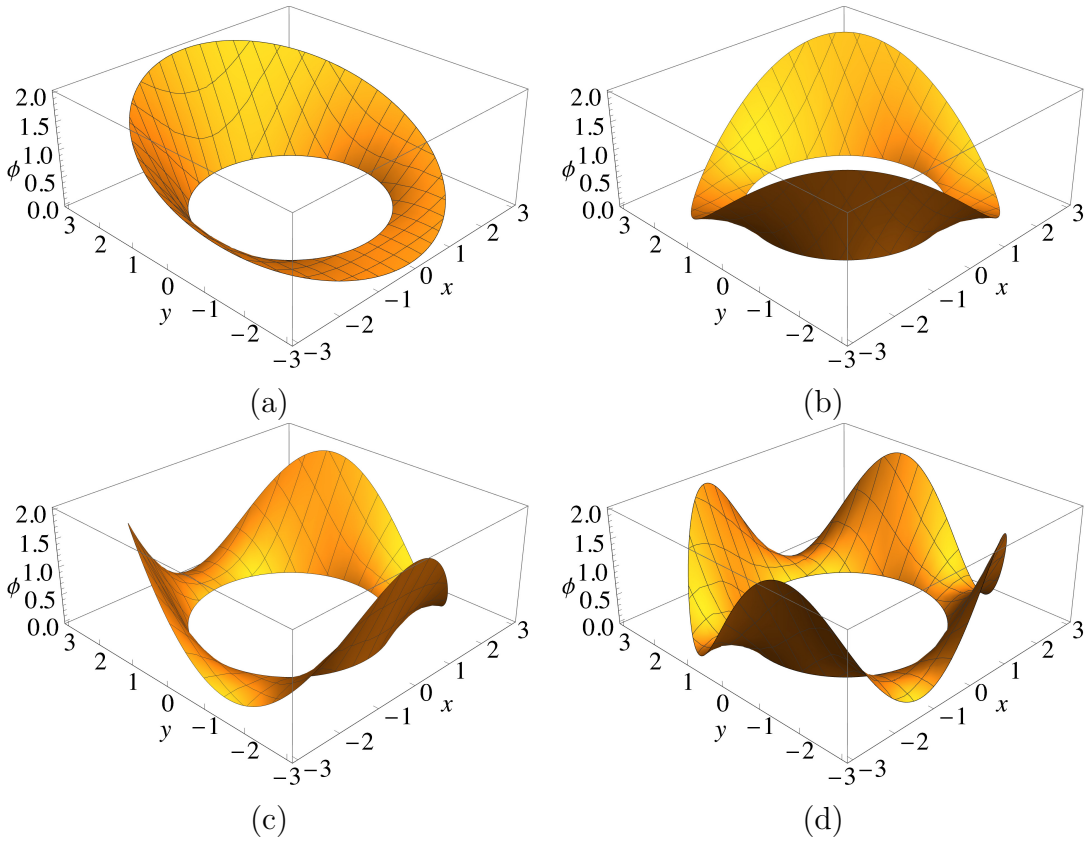

Figure 5.6: Numerical solution of Laplace's equation (2.1.3) calculated subject to the boundary conditions (2.1.36) with ϕ_d given by (5.1.5) with (a) $n = 1$, (b) $n = 2$, (c) $n = 3$, and (d) $n = 4$.

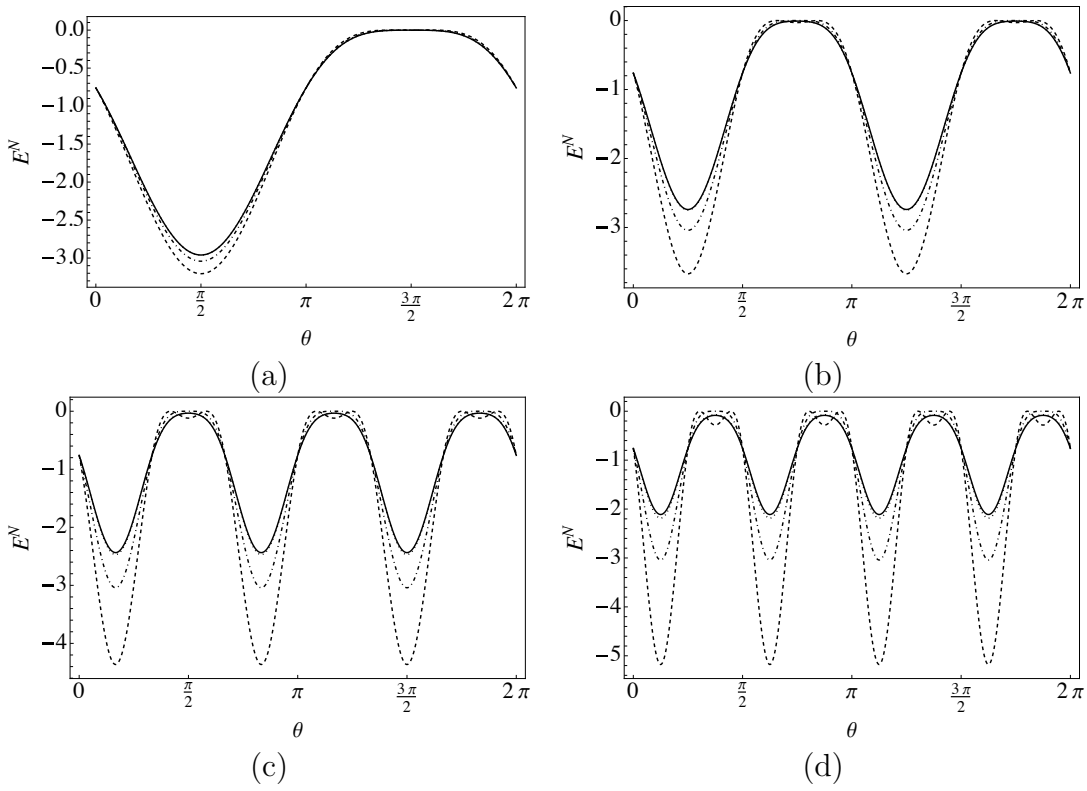

Figure 5.7: The leading-order normal Maxwell stress E^N calculated from the electrode model (5.1.2) (dashed line), the interface model (5.1.1) (dotted line), and the thick-film gradient model (2.3.16) (dot-dashed line) compared with the full expression for E^N (2.3.9) calculated from the numerical solution of Laplace's equation (2.1.3) (solid line), calculated with ϕ_d given by (5.1.5) with (a) $n = 1$, (b) $n = 2$, (c) $n = 3$, and (d) $n = 4$.

performs best, the thick-film gradient model (2.3.48) performs less well (shown as the dot-dashed line) and the electrode model (2.3.29) and (2.3.30) (shown as the dashed line) performs the poorest.

Figure 5.5 (b) shows a semi-log plot of χ (5.1.4) calculated for the interface (5.1.1), electrode (5.1.2), and gradient expansion (2.3.16) models with $1 \leq n \leq 10$ compared to the full expression for E^N (2.3.9) calculated from the numerical solution of Laplace's equation (2.1.3). In particular, Figure 5.5 (b) shows that the accuracy of all models decreases as n is increases (i.e., as the wavelengths become shorter), as expected due to the fact that the models were derived under the long-wave assumption. Figure 5.5 (b) also shows that the interface model (5.1.1) (shown as the dotted line) remains the most accurate, followed by the thick-film gradient model (2.3.16) (shown as the dot-dashed line), and that the electrode model (5.1.2) (shown as the dashed line) performs the poorest.

In summary, the interface model (2.3.43) and (2.3.44) affords the most accurate solution for the normal Maxwell stress E^N (2.3.9) in situations in which the interfacial radius s is constant and the potential ϕ_d varies spatially, even for functions of ϕ_d which vary sharply with θ. As discussed at the beginning of this section, this is to be expected *a priori* due to the fact that the expression obtained for the normal Maxwell stress E^N calculated from the interface model (5.1.1) is accurate up to third order in ε, whereas that calculated from the electrode model (5.1.2) is only accurate to first order.

5.1.2 Sharply varying interfacial radius

In this section, we compare the performance of the three electrostatic models in the case in which the interfacial radius s can vary sharply with θ whilst the potential at the outer electrode ϕ_d remains constant. We first consider a step-function shape for s, before considering functions with sinusoidal shapes of high frequency for s. As in Section 5.1.1, all of the functions for s have been deliberately chosen so as to be outside of the regime of asymptotic applicability of the long-wave approximation in order to provide a stringent test. In this section, numerical solutions of Laplace's equation (2.1.3) were calculated via remapping the (r, θ) domain onto a rectangular one to allow for easy discretisation in space, as described in Appendix E. Throughout this section, we use the values $d = 3$ and $\phi_d = 1$.

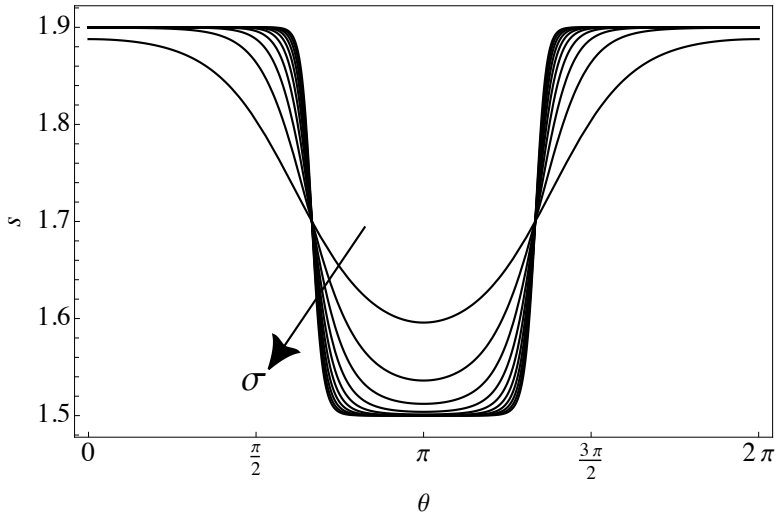

Figure 5.8: The interfacial radius s (5.1.6) for $\sigma = 1, 2, \ldots, 10$. The arrow indicates the direction of increasing σ.

Similarly to before, we first select the interfacial radius s to be of the form [67]

$$s = 1.5 + 0.2\left[1 + \tanh\left\{\frac{\sigma(\cos(m\theta) - \cos(mX)}{m\sin(mX)}\right\}\right], \tag{5.1.6}$$

where, as in Section 5.1.1, we select $m = 1$ and $X = 2\pi/3$. Figure 5.8 shows (5.1.6) for $\sigma = 1, 2, \ldots, 10$. Figure 5.9 shows the numerical solution of Laplace's equation (2.1.3) calculated subject to the boundary conditions (2.1.36) remapped onto a rectangular domain with s given by (5.1.6) for (a) $\sigma = 1$ and (b) $\sigma = 5$. Figure 5.10 shows the leading-order normal Maxwell stress E^N calculated from the electrode model (5.1.2), the interface model (5.1.1), and the thick-film gradient model (2.3.16) compared with the full expression for E^N (2.3.9) calculated from the numerical solution of Laplace's equation (2.1.3) with s given by (5.1.6) for (a) $\sigma = 1$ and (b) $\sigma = 5$. In particular, Figure 5.10 shows that the interface model (2.3.43) and (2.3.44) (shown as the dotted line) performs best, the thick-film gradient model (2.3.48) performs less well (shown as the dot-dashed line) and the electrode model (2.3.29) and (2.3.30) (shown as the dashed line) performs the poorest. However, note that the overall agreement with the numerical solution in the case of a sharply varying interfacial radius s is poorer than for a sharply varying potential ϕ_d as shown in Section 5.1.1. Figure 5.10 (a) shows that for $\sigma = 1$ (i.e., when the gradients of the interfacial radius are gentle) the interface model

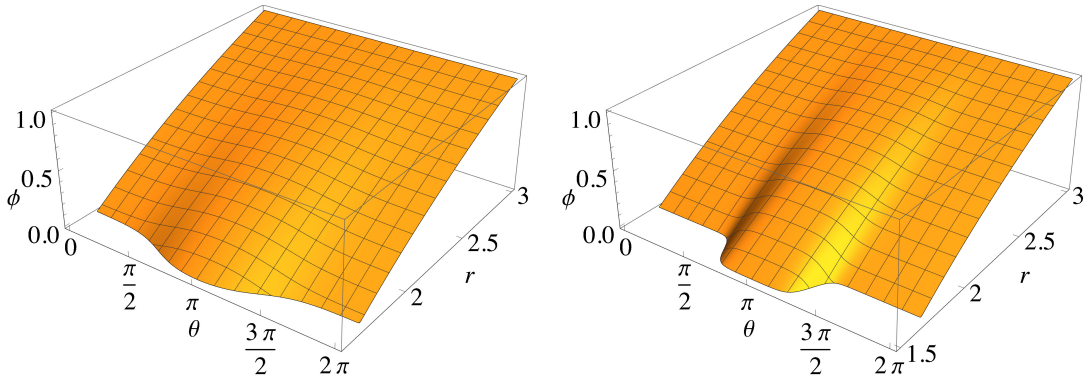

Figure 5.9: Numerical solution of Laplace's equation (2.1.3) calculated subject to the boundary conditions (2.1.36) remapped onto a rectangular domain with s given by (5.1.6) for (a) $\sigma = 1$ and (b) $\sigma = 5$.

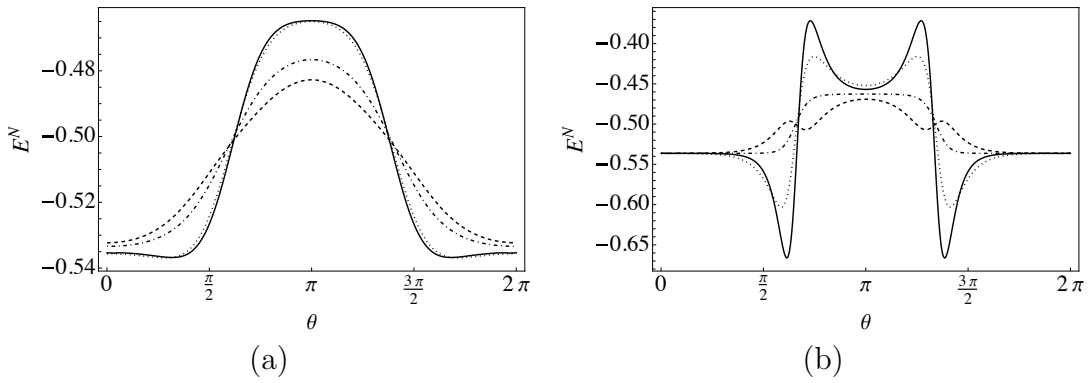

Figure 5.10: The leading-order normal Maxwell stress E^N calculated from the electrode model (5.1.2) (dashed line), the interface model (5.1.1) (dotted line), and the thick-film gradient model (2.3.16) (dot-dashed line) compared with the full expression for E^N (2.3.9) calculated from the numerical solution of Laplace's equation (2.1.3) (solid line), with s given by (5.1.6) for (a) $\sigma = 1$ and (b) $\sigma = 5$.

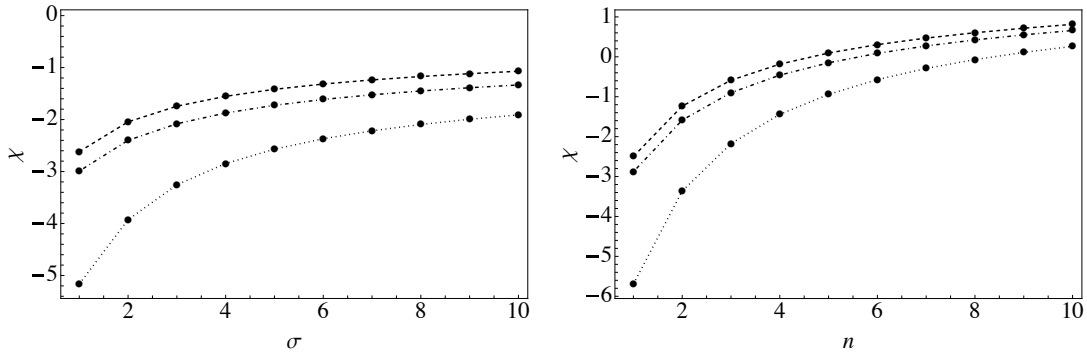

(a) (b)

Figure 5.11: Semi-log plots of the integral absolute error χ (5.1.4) of the leading-order normal Maxwell stress E^N calculated numerically from comparing the electrode model (5.1.2) (dashed line), the interface model (5.1.1) (dotted line), and the thick-film gradient model (2.3.16) (dot-dashed line) with the full expression for E^N (2.3.9) calculated from the numerical solution of Laplace's equation (2.1.3) with s given by (a) (5.1.6) for $1 \leq \sigma \leq 10$ and (b) (5.1.7) for $1 \leq n \leq 10$. Filled circles represent values of (a) σ and (b) n.

performs fairly well, whereas Figure 5.10 (b) shows that for $\sigma = 5$ the accuracy of all three models decreases significantly. Figure 5.11 (a) shows a semi-log plot of χ (5.1.4) calculated for the interface model (5.1.1), the electrode model (5.1.2), and the thick-film gradient model (2.3.16) compared to the full expression for E^N (2.3.9) calculated from the numerical solution of Laplace's equation (2.1.3). In particular, Figure 5.5 (a) shows that, as before, the accuracy of each of the models decreases as σ is increased, and that the interface model (5.1.1) is the most accurate, followed by the thick-film gradient model, and that the electrode model performs the poorest.

Similarly to before, to consider functions with sinusoidal shapes of high frequency, we select the interfacial radius s to be of the form

$$s = 1.5 + 0.1\cos(n\theta) \tag{5.1.7}$$

for wavenumbers $n = 1, 2, 3$, and 4. Figure 5.12 shows the numerical solution of Laplace's equation (2.1.3) calculated subject to the boundary conditions (2.1.36) remapped onto a rectangular domain with s given by (5.1.7) for (a) $n = 1$, (b) $n = 2$, (c) $n = 3$, and (d) $n = 4$. Figure 5.13 shows the leading-order normal Maxwell

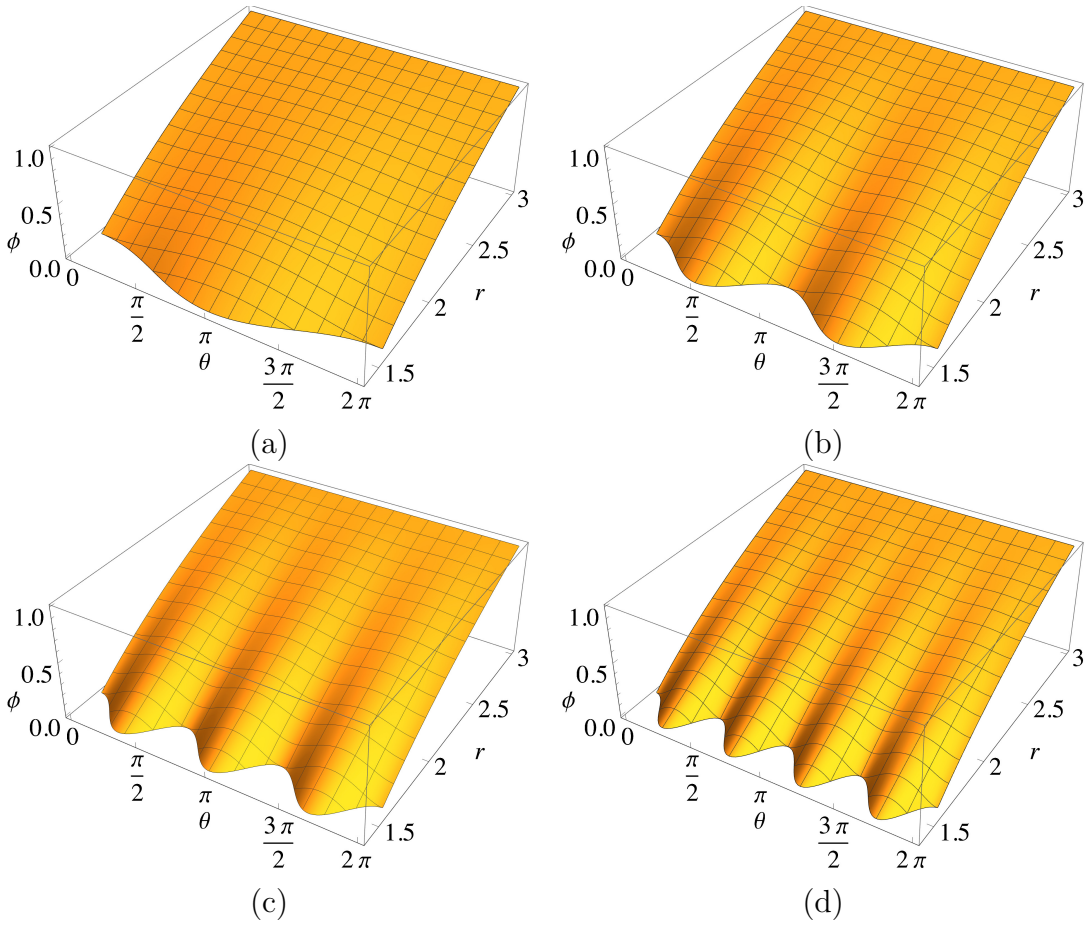

Figure 5.12: Numerical solution of Laplace's equation (2.1.3) calculated subject to the boundary conditions (2.1.36) remapped onto a rectangular domain with s given by (5.1.7) with (a) $n = 1$, (b) $n = 2$, (c) $n = 3$, and (d) $n = 4$.

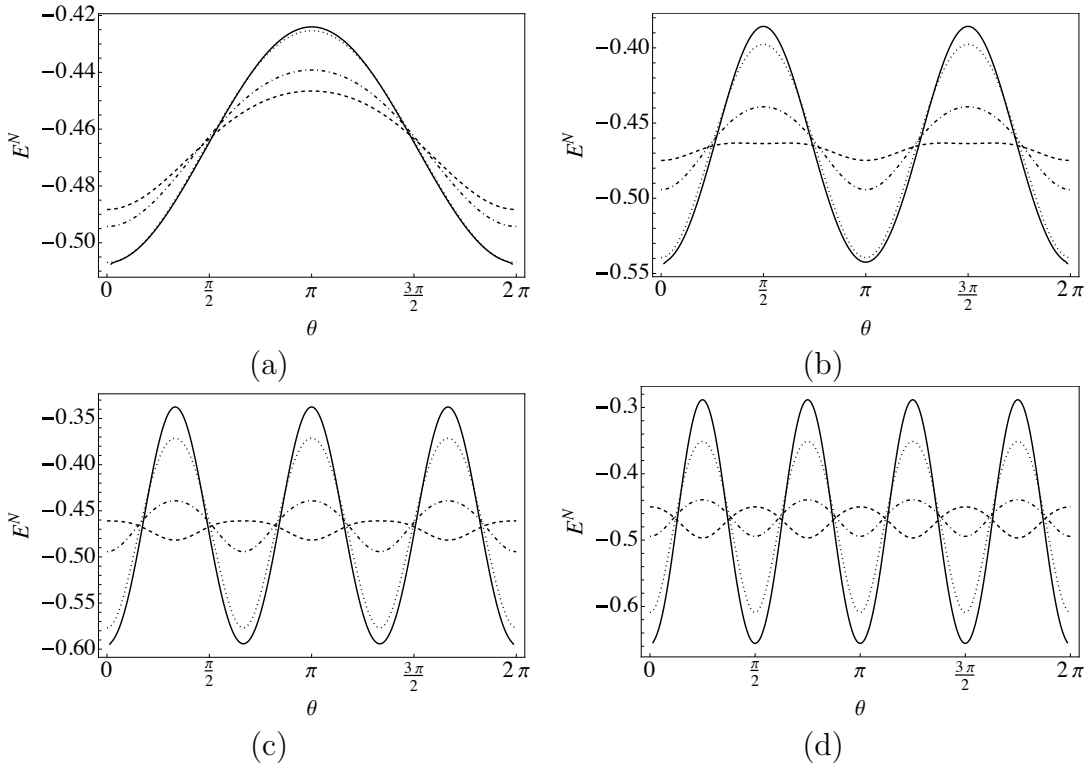

Figure 5.13: The leading-order normal Maxwell stress E^N calculated from the electrode model (5.1.2) (dashed line), the interface model (5.1.1) (dotted line), and the thick-film gradient model (2.3.16) (dot-dashed line) compared with the full expression for E^N (2.3.9) calculated from the numerical solution of Laplace's equation (2.1.3) (solid line), calculated with ϕ_d given by (5.1.5) with (a) $n = 1$, (b) $n = 2$, (c) $n = 3$, and (d) $n = 4$.

stress E^N calculated from the electrode model (5.1.2), the interface model (5.1.1), and the thick-film gradient model (2.3.16) compared with the full expression for E^N (2.3.9) calculated from the numerical solution of Laplace's equation (2.1.3) with s given by (5.1.7) with (a) $n = 1$, (b) $n = 2$, (c) $n = 3$, and (d) $n = 4$. Figure 5.11 (b) shows a semi-log plot of χ (5.1.4) calculated for the interface model (5.1.1), the electrode model (5.1.2), and the thick-film gradient model (2.3.16) compared to the full expression for E^N (2.3.9) calculated from the numerical solution of Laplace's equation (2.1.3). Together, Figure 5.13 and Figure 5.11 (b) show that, as before, the accuracy of all three models decreases significantly as n is increased, as expected, and that the interface model (5.1.1) is the most accurate, followed by the thick-film gradient model, with the electrode model performing the poorest. As

before, the overall agreement with the numerical solution in the case of a sharply varying interfacial radius s is poorer than for a sharply varying potential ϕ_d as shown in Section 5.1.1.

In summary, the interface model (2.3.43) and (2.3.44) affords the most accurate solution for the normal Maxwell stress E^N (2.3.9) in situations in which ϕ_d is constant and the interfacial radius s varies spatially, even for functions of s which vary sharply with θ. As discussed previously, this is to be expected *a priori* due to the fact that the expression obtained for the normal Maxwell stress E^N calculated from the interface model (5.1.1) is accurate up to third order in ε, whereas that calculated from the electrode model (5.1.2) is only accurate to first order. Hence, we conclude that the interface model is most suitable for use in the WRIBL model.

5.2 Evolution of the film

In this section, we investigate the evolution of the film in order to understand how electrostatic effects influence the dynamics of the thick-film coating flow system. In Section 5.1, we showed that the interface model (2.3.43) and (2.3.44) affords the most accurate solution for the normal Maxwell stress E^N (2.3.9) overall. Hence, hereafter, we exclusively use the interface model in the WRIBL model alongside the WRIBL equation (2.3.66) and the kinematic condition (2.1.34). Specifically, when calculating the normal Maxwell stress E^N, we use the leading-order expression calculated from the interface model (5.1.1).

The thick-film coating flow system in the absence of an electric field was studied recently by Wray and Cimpeanu [31] who, as discussed in Section 1.4.4, discovered that the system exhibits three different behaviours, namely, steady states, periodic states, and multivalued states (which potentially includes interfacial rupture). As discussed earlier in Section 1.4.4, multivaluedness and rupture cannot be modelled using the WRIBL model due to the fact that we have parameterised by the azimuthal angle θ, in addition to the fact that the long-wave approximation is no longer valid because the interfacial slopes are so large. Hence, these behaviours must be analysed via DNS of the Navier–Stokes equations (2.1.21) and (2.1.22) [31]. Thus, for the purposes of the present thesis (in which we do not perform DNS), the states which are of interest are steady states and periodic states. The investigation of multivalued states and interfacial rupture in the presence of an electric field using DNS could be an interesting direction for future study.

In Chapter 4, we showed that, for a constant potential in the thin-film case, electrostatic effects destabilise the film. In particular, in Section 4.2, we discussed the effect that increasing the electric potential difference has on states which are steady or periodic, and showed that electrostatic effects can result in outer contact behaviour (which, as we recall, is when the film touches the outer electrode in a finite time). Our results indicate that in the thick-film case, the system exhibits behaviours that are qualitatively the same as those observed in the thin-film case. Hence, in what follows we give only a handful of representative results demonstrating the effect that the incorporation of an electric field with a constant potential has on the system in the thick-film case. Specifically, we examine the effect that the electric field has on systems which are steady in Section 5.2.1 and on those which are periodic in Section 5.2.2.

In the following results, the values

$$Re = 3.76, \quad Ca = 0.157, \quad d = 2.5 \tag{5.2.1}$$

are chosen in order to consider a qualitatively similar region of (Re, Ca) parameter space as that which was investigated by Wray and Cimpeanu [31]. Specifically, the value $Re = 3.76$ was chosen to ensure that inertia is significant but not dominant, and the value $Ca = 0.157$ was chosen to ensure that capillarity is strong enough to allow for steady states to be observed [31]. The outer electrode was chosen to be located at $d = 2.5$ so as to ensure that the electric field has a significant effect on the behaviour of the system, without prematurely inducing outer contact and hence preventing other behaviors from manifesting. In Sections 5.2.1 and 5.2.2, we select values of the rotation rate ω and the initial uniform interfacial radius s_0 that support steady and periodic states, respectively, and will thereafter vary the electric potential difference $\tilde{E}_b$ in order to investigate the effect that the electric field has on these configurations.

Throughout this section, solutions to the WRIBL model are obtained using the numerical scheme outlined in Appendix A.1. The dimensional quantities used in this section are listed in Table F.1 of Appendix F, and correspond approximately to some ratio of water-syrup mix [102, 272]. Note that, analogous to the variable T_c used in Chapter 4, the time at which outer contact occurs is denoted here, and in Chapter 6, by t_c.

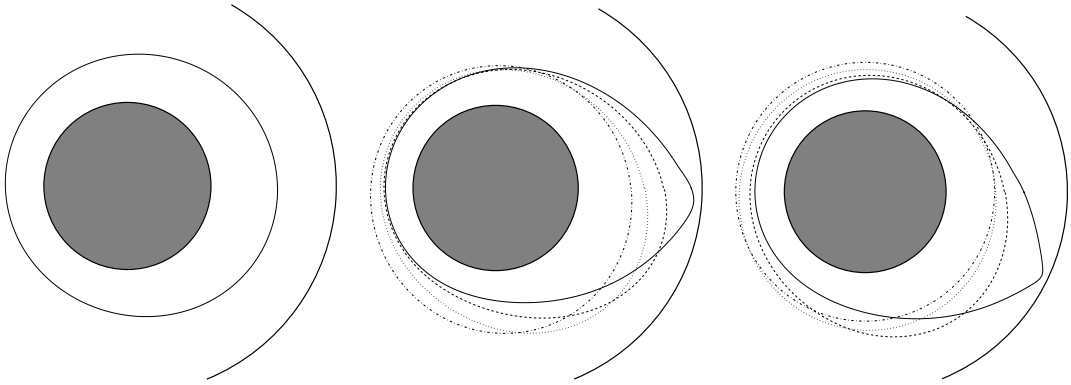

Figure 5.14: Interface profiles for $\omega = 0.5$, $s_0 = 1.6$, and (a) $\tilde{E}_b = 0$, (b) $\tilde{E}_b = 0.6$, and (c) $\tilde{E}_b = 1$. (a) Steady state in the absence of an electric field. (b), (c) Evolution to outer contact at time $t = t_c$ where $t_c = 8.78$ and 6.05, respectively. The interfacial radius is shown at times (b) $t = 2.78, 4.78, 6.78$, and t_c, (c) $t = 0.05, 2.05, 4.05$, and t_c. In ascending order, the times are shown by the dot-dashed, dotted, dashed, and solid lines, respectively.

5.2.1 Steady states

In the absence of an electric field, Wray and Cimpeanu [31] showed that for a thick film of initial uniform interfacial radius 1.6 with a low dimensionless rotation rate of 0.5 for the values (5.2.1) of Ca and Re, their system exhibits a steady state (see Figure 1.20 (a)). Hence, in this section we choose the same values $\omega = 0.5$ and $s_0 = 1.6$ in order to analyse the effect that electrostatic effects have on a steady state. Figure 5.14 (a) shows the final shape of the steady state for $\tilde{E}_b = 0$. The bulge of liquid is largest on the right-hand side of the cylinder, where rotation and gravity act in opposition to one another. In this case, capillarity dominates, and hence the interfacial radius remains nearly circular. In the absence of an electric field, the system reaches a steady state before time $t = 500$, as shown in Figure 5.15, which shows the evolution of the maximum interfacial radius $s_{\max}$ over the time interval $1 \leq t \leq 1000$ for $\tilde{E}_b = 0, 0.2, 0.4, 0.6, 0.8$, and 1. For the chosen set of parameter values, outer contact occurs for $\tilde{E}_b$ values greater than approximately 0.5. Figures 5.14 (b) and (c) show the interface profiles for $\tilde{E}_b = 0.6$ and $\tilde{E}_b = 1$, respectively, in which the interface touches the outer electrode at times $t_c = 8.78$ and $t_c = 6.05$, respectively (shown as the solid lines). For sufficiently large $\tilde{E}_b$, electrostatic effects dominate the behaviour of the system, with outer contact

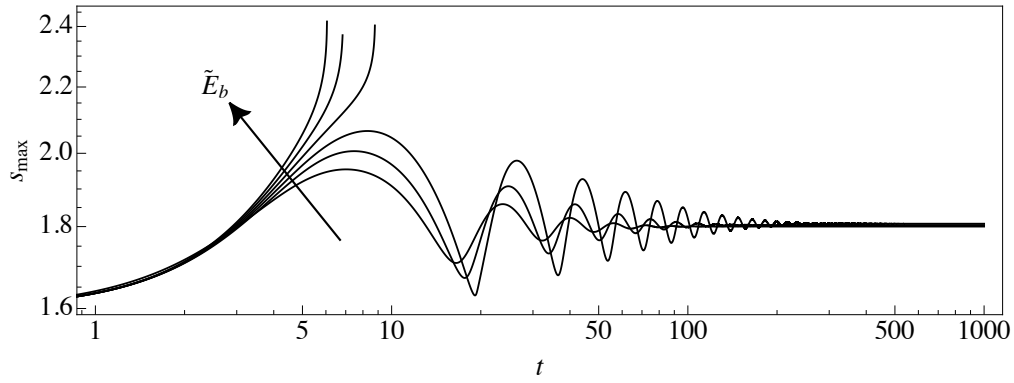

Figure 5.15: Evolution of the maximum interfacial radius $s_{\max}$ on a log-log scale over the time interval $1 \leq t \leq 1000$ for $\omega = 0.5$, $s_0 = 1.6$, and $\tilde{E}_b = 0, 0.2, 0.4, 0.6, 0.8$, and 1. The arrow indicates the direction of increasing $\tilde{E}_b$.

occurring earlier in time for larger $\tilde{E}_b$. For $\tilde{E}_b = 0.6, 0.8$, and 1, the system is driven towards outer contact before time $t = 10$, as shown in Figure 5.15. For $\tilde{E}_b = 0.2$ and $\tilde{E}_b = 0.4$, Figure 5.15 shows that electrostatic effects result in a significant increase in $s_{\max}$ at earlier times (i.e., before around $t = 100$), but overall result in negligible change to the value of $s_{\max}$ once the system has reached a steady state. Moreover, the final steady state shapes for $\tilde{E}_b = 0.2$ and $\tilde{E}_b = 0.4$ are qualitatively the same as the steady state shown for $\tilde{E}_b = 0$ in Figure 5.14 (a), and are thus not shown. Indeed, it is due to the fact that the interface remains nearly circular in the absence of an electric field (as shown in Figure 5.14 (a)) that the effect of the electric field on the final steady state shapes is small, but is most noticeable at earlier times in which the deviations from circularity are larger. The present results indicate that, in general, increasing the electric potential difference leads to outer contact.

5.2.2 Periodic states

In the absence of an electric field, Wray and Cimpeanu [31] showed that for a thick film of initial uniform interfacial radius 1.3 with a moderate dimensionless rotation rate of 1 for the values (5.2.1) of Ca and Re, their system exhibits a periodic state (see Figure 1.20 (a)). Hence, in this section we choose the same values $\omega = 1$ and $s_0 = 1.3$ in order to analyse the effect that electrostatic effects have on a periodic state. The periodic state that emerges in the absence of an electric field

is shown in Figure 5.16 (a) at times $t = 9997, 9998, 9999$, and 10000 (shown as the dot-dashed, dotted, dashed, and solid lines, respectively). The bulge of liquid is carried around the cylinder by rotation, initially increasing in size before settling to a periodic state after around $t = 10^3$. This can be understood from the line furthest to the right-hand side in Figure 5.17, which shows the evolution of the maximum interfacial radius $s_{\max}$ over the time interval $0 \leq t \leq 10^4$ for increasing values of $\tilde{E}_b$. The evolution of the interfacial radius in the absence of an electric field is shown in Figure 5.18 over the time interval $0 \leq t \leq 20$, indicating that s is sinusoidal at time $t = 20$. Note that we have chosen to consider this particular time interval in this section to remain consistent with the forthcoming calculations in Section 6.2, in which we perform optimal control calculations over the time interval $0 \leq t \leq t_f$ where $t_f = 20$.

Increasing $\tilde{E}_b$ can result in outer contact: Figures 5.16 (b), (c), and (d) show the interfacial radius for $\tilde{E}_b = 1, 5$, and 10, respectively, for which the interfacial radius touches the outer electrode at time $t = t_c$ where $t_c = 161.45, 53.14$, and 26.83, respectively. The first, second, and third lines closest to the left-hand side of Figure 5.17 show $s_{\max}$ over time for $\tilde{E}_b = 1, 5$, and 10, respectively. In a qualitatively similar manner to the thin-film case discussed in Section 4.2.4, the bulge of liquid oscillates around the cylinder and grows in size whilst doing so, before eventually being pulled towards the outer electrode where the film is thickest, resulting in outer contact which occurs earlier in time and with fewer complete periods traversed around the cylinder as $\tilde{E}_b$ increases. For the chosen parameter values, for $\tilde{E}_b$ values that are small enough that they do not induce outer contact, the overall change to the final periodic state is small and is not obviously discerned when comparing the interface shape directly with the interface shape for $\tilde{E}_b = 0$ shown in Figure 5.16 (a), and so are not shown here. This difference can, however, be seen in Figure 5.19, which shows $s_{\max}$ over the time interval $950 \leq t \leq 1000$ for $\tilde{E}_b = 0$ and $\tilde{E}_b = 0.1$, shown respectively as the solid and dashed lines. For $\tilde{E}_b = 0.1$, the maximum value of $s_{\max}$ is 2.09136, compared to 2.05463 in the absence of an electric field.

5.3 Concluding remarks

In this chapter, we have analysed the electrostatic modelling and dynamics of thick-film coating flow in the presence of an electric field.

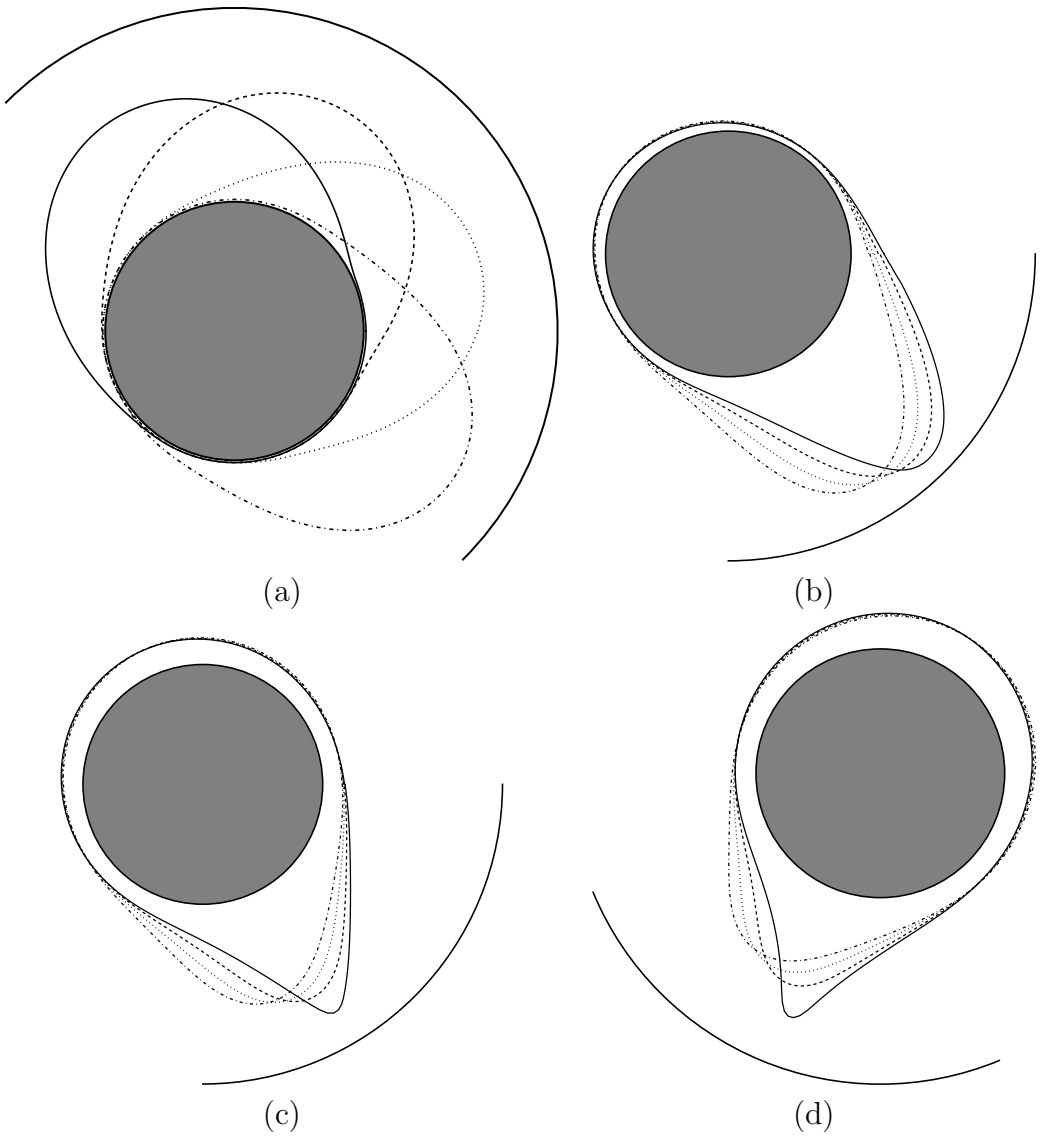

Figure 5.16: Interface profiles for $\omega = 1$, $s_0 = 1.3$, and (a) $\tilde{E}_b = 0$, (b) $\tilde{E}_b = 1$, (c) $\tilde{E}_b = 5$, and (d) $\tilde{E}_b = 10$. (a) Periodic state in the absence of an electric field shown at times $t = 9997, 9998, 9999$, and 10000. (b), (c), (d) Evolution to outer contact at time $t = t_c$ where $t_c = 161.45, 53.14$, and 26.83, respectively. The interfacial radius is shown at times (b) $t = 161.15, 161.25, 161.35$, and t_c, (c) $t = 52.84, 52.94, 53.04$, and t_c, and (d) $t = 26.53, 26.63, 26.73$, and t_c. In ascending order, the times are shown by the dot-dashed, dotted, dashed, and solid lines, respectively.

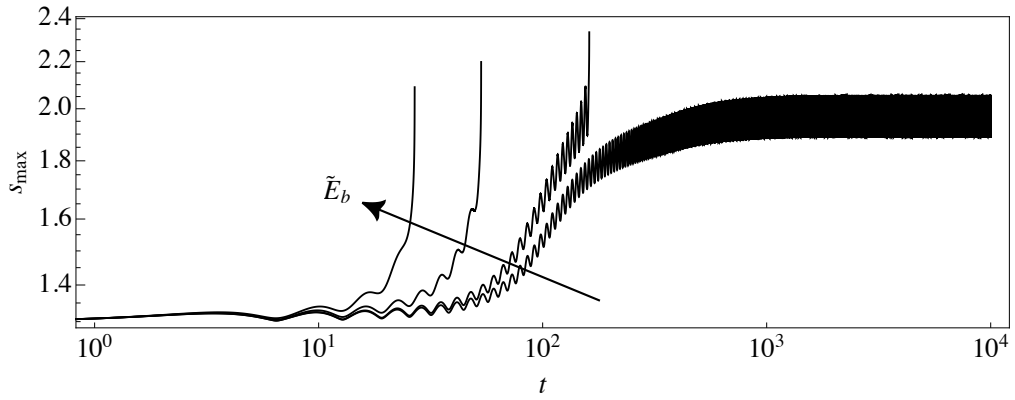

Figure 5.17: Evolution of the maximum interfacial radius $s_{\max}$ on a log-log scale over the time interval $1 \leq t \leq 10^4$ for $\omega = 1$, $s_0 = 1.3$, and $\tilde{E}_b = 0, 1, 5$, and 10. The arrow indicates the direction of increasing $\tilde{E}_b$.

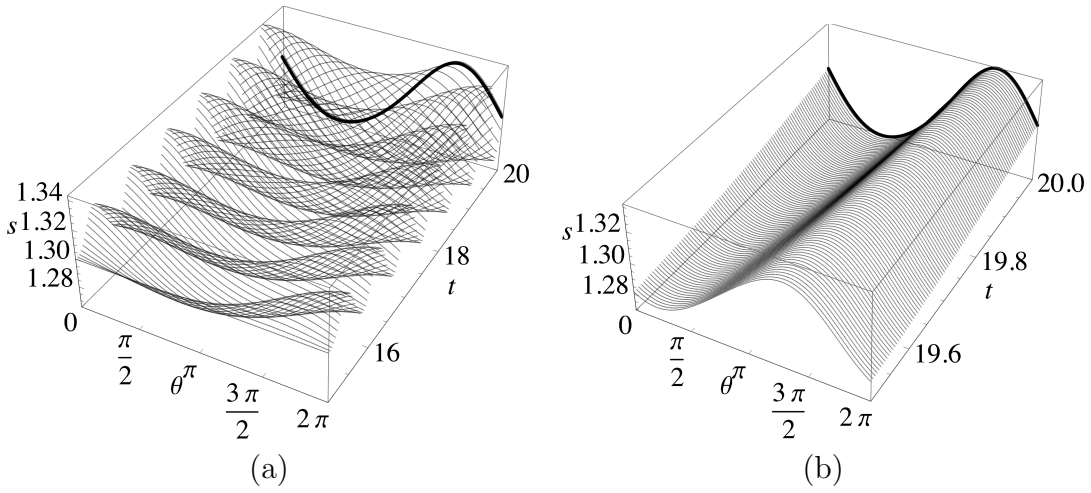

Figure 5.18: Evolution of the interfacial radius for $\omega = 1$, $s_0 = 1.3$, and $\tilde{E}_b = 0$ over the time intervals (a) $0 \leq t \leq 20$ shown at times $t = 31n/200$ for $n = 0, 1, \ldots, 129$ and (b) $19.5 \leq t \leq 20$ shown at times $t = 19.5, 19.505, 19.510, \ldots, 20$. The thick black line shows the interfacial radius at the time $t = 20$.

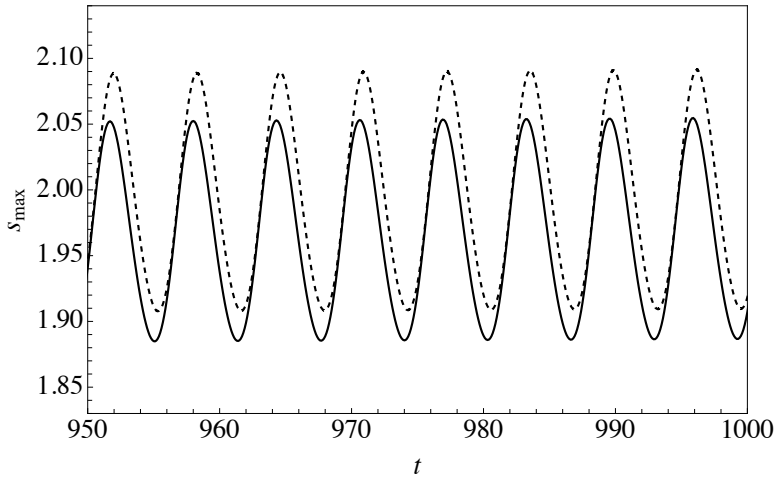

Figure 5.19: Evolution of the maximum interfacial radius $s_{\max}$ over the time interval $950 \leq t \leq 1000$ for $\omega = 1$ and $s_0 = 1.3$ with $\tilde{E}_b = 0$ (solid line) and $\tilde{E}_b = 0.1$ (dashed line).

Firstly, in Section 5.1, we compared numerically the three candidate electrostatic models for the potential ϕ that we derived in Section 2.3.2, namely, the electrode model (2.3.29) and (2.3.30), the interface model (2.3.43) and (2.3.44), and the thick-film gradient model (2.3.48), and determined that the interface model affords the most accurate solution for the normal Maxwell stress E^N (2.3.9) overall. Hence, we concluded that the interface model is most suitable for use in the WRIBL model alongside the WRIBL equation (2.3.66) and the kinematic condition (2.1.34). In particular, we decided that hereafter we shall exclusively use the leading-order expression for the normal Maxwell stress calculated from the interface model (5.1.1) in the WRIBL model.

Once the most suitable choice of electrostatic model was established, the evolution of the film in the presence of an electric field with a constant potential was analysed in Section 5.2. The analysis in Section 5.2 built upon the recent study by Wray and Cimpeanu [31] and showed that, in general, an electric field with a constant potential destabilises the system (as expected in light of the analyses of the thin-film case given in Chapter 4). States that are qualitatively the same as those which were shown by Wray and Cimpeanu [31] to be steady or periodic in the absence of an electric field were analysed in Sections 5.2.1 and 5.2.2, respectively, and it was shown that, in both cases, increasing the electric potential difference $\tilde{E}_b$ can lead to outer contact. When outer contact does not occur, increasing $\tilde{E}_b$

results in an increase in the maximum interfacial radius $s_{\max}$, corresponding to an increase in the maximum height of the liquid bulge that forms.

Note that in Chapter 6, we analyse the optimal control of films which are periodic in the absence of any control mechanisms using the same parameter values that were used in Section 5.2.2, namely, the values (5.2.1) of Re and Ca along with $\omega = 1$ and either $s_0 = 1.3$ exactly or some value of s_0 close to 1.3. Therefore, the analysis presented in Section 5.2.2 is essential to better understand the dynamics of the flow when it is not under the influence of any control mechanisms.

Chapter 6

Electrostatic control of thick-film coating flow

As described in Sections 1.6 and 1.7, the control of fluid systems using electric fields has been afforded significant attention in the literature to date, owing to the plentiful industrial applications that arise such as those in pattern formation [5, 163, 190, 193–195, 274–276] and in chemical engineering processes [178, 179, 184, 185]. In this chapter, we aim to build upon these existing studies by analysing both the feedback and optimal electrostatic control of thick-film coating flow. In particular, the aim of this chapter is to show that it is possible to exert fine control over the thick-film system using the WRIBL model (2.1.34), (2.3.66), (2.3.43), and (2.3.44) which was derived in Section 2.3 and analysed in Chapter 5.

We first investigate feedback control of the film in Section 6.1, with the aim of constructing a potential which controls the interfacial shape towards a uniform state. Secondly, in Section 6.2, we investigate controlling the film towards specified target shapes in an optimal sense. Specifically, we develop the optimal control framework in Section 6.2.1 before conducting an investigation into controlling the interfacial shape towards several challenging target shapes in Sections 6.2.2–6.2.5. Finally, we draw our conclusions in Section 6.3.

In this chapter, we drop the check decoration from the WRIBL model (which, as we recall, arises from the long-wave scalings (2.3.1) and (2.3.2)) hereafter for brevity. As in Section 5.2, solutions to the WRIBL model are obtained using the numerical scheme outlined in Appendix A.1, and the dimensional quantities used in this section are listed in Table F.1 of Appendix F.

6.1 Feedback control

In this section, we apply feedback control to the WRIBL model by which we aim to produce a uniform interface. In other words, we aim to control the interface towards the target shape

$$s_{\text{targ}} = s_0, \tag{6.1.1}$$

where, as before, s_0 is the initial uniform interfacial radius. To achieve this, we use information regarding the interfacial radius s at every time step in order to construct a suitable potential ϕ_d. As discussed in Section 1.7, controlling towards a uniform interface can be beneficial in many industrial applications of coating flow in which a flat state is needed in order to achieve specific functional, aesthetic, or performance-related requirements [230–232].

As we have established in Chapters 4 and 5, when the potential is uniform, electrostatic effects pull the film towards the outer electrode most strongly where it is thickest because this is where the electric field is strongest. This action results in an increase in the maximum interfacial radius $s_{\max}$ and, simultaneously, a decrease in the minimum interfacial radius $s_{\min}$. It is therefore sensible to expect imposing an electric field on only the thinnest regions of the film to be of benefit when one desires to achieve a uniform interface: pulling the thinner regions towards the outer electrode will in turn result in the film thickness shrinking in the thicker regions due to mass conservation, overall resulting in a more uniform interface. To this end, we define

$$\phi_d = \begin{cases} 0 & \text{for} \quad s(\theta,t) > s_{\text{cutoff}}, \\ (s_{\text{cutoff}} - s(\theta,t))^2 & \text{for} \quad s(\theta,t) \leq s_{\text{cutoff}}, \end{cases} \tag{6.1.2}$$

where in our calculations we choose $s_{\text{cutoff}} = s_{\text{targ}} - 0.001$. In other words, the electric field is "switched on" where the interfacial radius s is more than 0.001 dimensionless units below the target shape (6.1.1). Throughout this section, in our calculations we use the parameter values (5.2.1) for Ca, Re, and d with

$$\omega = 1, \quad s_0 = 1.5, \quad \tilde{E}_b = 5000. \tag{6.1.3}$$

Figure 6.1 shows the evolution of the maximum interfacial radius $s_{\max}$ in both the case in which $\tilde{E}_b = 0$ (which we shall refer to hereafter as the "“uncontrolled"

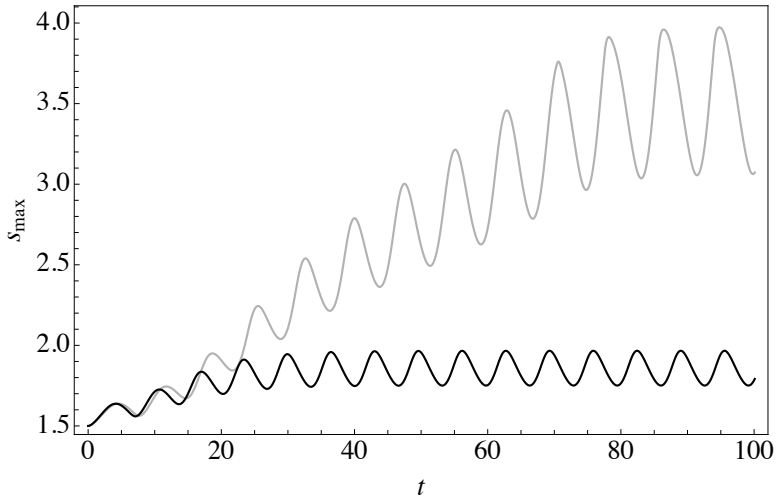

Figure 6.1: Evolution of the maximum interfacial radius $s_{\max}$ in the uncontrolled (grey) and controlled (black) cases for the parameter values (5.2.1) of Ca, Re, and d with (6.1.3).

case) and in the controlled case, which are represented by the grey and black lines, respectively. In particular, Figure 6.1 shows that the control mechanism successfully results in the maximum interfacial radius $s_{\max}$ being reduced. Within the time interval $0 \leq t \leq 100$, $s_{\max}$ does not exceed the value 2.0392 in the controlled case, which is significantly lower than the maximum value of 3.9854 attained in the uncontrolled case. Figure 6.2 shows the interface in the (a) uncontrolled and (b) controlled cases at times $t = 97.7, 98.5, 99.3$, and 100, shown as the dot-dashed, dotted, dashed, and solid lines, respectively. In the uncontrolled case, the bulge of liquid continues to increase in size as it oscillates around the cylinder, eventually settling to a periodic state. On the other hand, in the controlled case, the bulge of liquid remains significantly smaller owing to the feedback control mechanism.

The controlled interface shown in Figure 6.2 (b) is closer to uniform than the uncontrolled interface shown in Figure 6.2 (a); however, a genuinely uniform film has not been achieved using the feedback control mechanism (6.1.2). The performance of the feedback control mechanism could potentially be improved by tweaking the imposed potential ϕ_d (6.1.2) or by increasing the potential difference $\tilde{E}_b$. However, such trial-and-error approaches are not efficient and are unlikely to yield a significant advantage over the current values of ϕ_d and $\tilde{E}_b$. Instead, in Section 6.2, we formulate and implement a more robust control framework using optimal control theory which will allow us to exert fine control over the

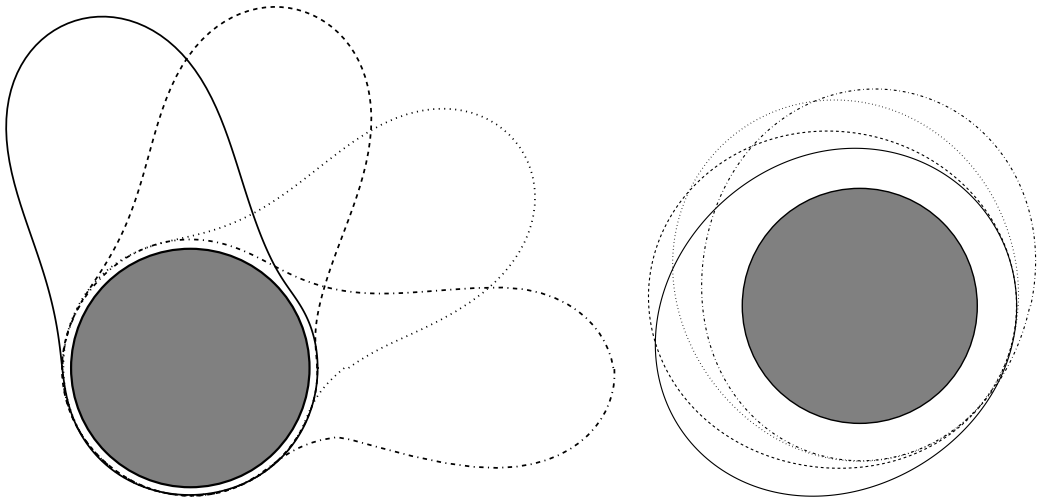

(a) (b)

Figure 6.2: The interface s calculated for the parameter values (5.2.1) of Ca, Re, and d with (6.1.3) at times $t = 97.7$ (dot-dashed line), $t = 98.5$ (dotted line), $t = 99.3$ (dashed line), and $t = 100$ (solid line) in the (a) uncontrolled and (b) controlled cases.

WRIBL model. In particular, in Section 6.2.3, we use optimal control to control the interface towards its initial uniform shape in an optimal sense.

6.2 Optimal control

In this section, we formulate and implement a robust optimal control framework designed to finely control the interfacial radius towards some specified target shape. We describe the framework of the optimal control problem at hand in Section 6.2.1 and present our results in Sections 6.2.2–6.2.5. Specifically, we demonstrate that we can successfully control the interfacial radius towards a uniform shape in Section 6.2.3, before conducting a parametric study into the success of the control mechanism when controlling towards a family of sinusoidal shapes in Section 6.2.4. We then investigate the control of the interface towards a square shape in Section 6.2.5. Finally, in Section 6.2.6, we discuss instances in which the control mechanism may have an unsuccessful outcome.

6.2.1 Framework of the optimal control problem

We aim to find a potential ϕ_d which minimises a measure of the difference between the interfacial radius s and some target shape, which we denote by $s_{\text{targ}} = s_{\text{targ}}(\theta, t)$. We wish to achieve the target shape at minimal control cost (i.e., in this case, by applying the minimum required voltage to deform the interface). To proceed, we introduce the cost functional $\mathcal{J}_{\text{t,r}}$ (sometimes referred to as the "scalar objective function" [243]),

$$\mathcal{J}_{\text{t,r}} = \mathcal{U}_{\text{t,r}} + \mathcal{C}_{\phi}, \tag{6.2.1}$$

where the subscripts "t" and "r" in (6.2.1)–(6.2.3) represent "terminal" and "regulation" control (to be defined shortly), respectively, $\mathcal{C}_{\phi}$ (which we shall refer to hereafter as the "cost" of the control mechanism) is given by

$$\mathcal{C}_{\phi} = \gamma_{\phi} \int_{t=0}^{t_{\text{f}}} \int_{\theta=0}^{2\pi} \phi_d(\theta, t)^2 \, \mathrm{d}\theta \, \mathrm{d}t, \tag{6.2.2}$$

and $\mathcal{U}_{\text{t,r}}$ (which we shall refer to hereafter as the "deviation measure") is given by

$$\mathcal{U}_{\text{t,r}} = \delta_{\text{t}} \int_{\theta=0}^{2\pi} \left[s(\theta, t_{\text{f}}) - s_{\text{targ}}(\theta) \right]^2 \, \mathrm{d}\theta + \delta_{\text{r}} \int_{t=0}^{t_{\text{f}}} \int_{\theta=0}^{2\pi} \left[s(\theta, t) - s_{\text{targ}}(\theta, t) \right]^2 \, \mathrm{d}\theta \, \mathrm{d}t. \tag{6.2.3}$$

The control weights δ_{t} and δ_{r} in (6.2.3) are taken to be $(\delta_{\text{t}}, \delta_{\text{r}}) = (1, 0)$ or $(\delta_{\text{t}}, \delta_{\text{r}}) = (0, 1)$ depending on whether we are imposing terminal or regulation control, respectively. Specifically, the deviation measure (6.2.3) penalises based on the deviation of s from the target shape s_{targ}: the first term in (6.2.3) penalises based on the deviation at the final time $t = t_{\text{f}}$ only (i.e., terminal control), whereas the second term in (6.2.3) penalises based on the deviation weighted uniformly across the entire time interval $t = [0, t_{\text{f}}]$ (i.e., regulation control). The final term in (6.2.1) penalises based on the integral square potential at the outer electrode, where the control weight $\gamma_{\phi} \geq 0$ represents the weighting of the cost of the control (i.e., it allows us to choose how much the control should be penalised). Small values of γ_{ϕ} correspond to "cheap" controls (i.e., large values of ϕ_d are not penalised as they have a weak effect on $\mathcal{J}_{\text{t,r}}$), and large values of γ_{ϕ} correspond to "expensive" controls (i.e., large values of ϕ_d are penalised as they have a strong effect on $\mathcal{J}_{\text{t,r}}$).

Note that we have not introduced any constraints on ϕ_d here due to the fact that traversing the parameter space is already challenging due to its non-smooth nature (of which we defer a detailed discussion until Section 6.2.6). However, in

practice, the constraint $\phi_d \leq k\phi_{d_{\max}}$ should be imposed in order to prevent the electric field from violating the dielectric limit (as done by Wray *et al.* [244]), where the constant $k < 1$ is a "saturation constant" and $\phi_{d_{\max}}$ is the dimensionless constant potential at the outer electrode that would induce an electric field in the gas region in the dielectric limit (which, as mentioned previously, is approximately 3×10^6 V m^{-1} [271]).

Whilst we have outlined the present optimal control problem to be readily applicable to both terminal and regulation control, hereafter, we have chosen to focus our attention on terminal control only. Terminal control is less restrictive compared to regulation control as it allows for poorer short-term performance provided that it yields long-term advantages [243, 277]. Nevertheless, it is important to recognise that in real-world scenarios, such as in numerous industrial applications, the target shape is not generally time-independent. Simply achieving the target shape isn't sufficient; rather, it must be maintained throughout the entire industrial process. Hence, regulation control often proves more pragmatic as it measures the deviation of the interfacial shape from the target shape across the entire time interval, rather than solely at the final time. However, regulation control is more difficult to implement and more computationally expensive, and so we focus on terminal control in this thesis as an important first step to understanding the optimal control problem at hand.

We proceed by setting $(\delta_{\mathrm{t}}, \delta_{\mathrm{r}}) = (1, 0)$ in (6.2.3), and so the cost functional (6.2.1) becomes

$$\mathcal{J}_{\mathrm{t}} = \mathcal{U}_{\mathrm{t}} + \mathcal{C}_{\phi}, \tag{6.2.4}$$

where $\mathcal{U}_{\mathrm{t}}$ is referred to hereafter as the "terminal deviation measure" and is given by

$$\mathcal{U}_{\mathrm{t}} = \int_{\theta=0}^{2\pi} \left[s(\theta, t_{\mathrm{f}}) - s_{\mathrm{targ}}(\theta)\right]^2 \, \mathrm{d}\theta. \tag{6.2.5}$$

The constrained optimisation problem is then

$$\min_{\phi_d(\theta,t)} \mathcal{J}_{\mathrm{t}} \;\text{ subject to }\; (2.1.34), (2.3.44), \text{ and } (2.3.66), \tag{6.2.6}$$

subject to the initial condition $s|_{t=0} = s_0$. As discussed in Section 1.7.2, to solve the optimisation problem (6.2.6), we compute the direction in which the cost functional $\mathcal{J}_{\mathrm{t}}$ decreases most steeply with respect to the control (i.e., the descent direction). To achieve this, we need to compute the negative of the gradient of the

cost functional with respect to the control, i.e.,

$$-\frac{\mathrm{d}\mathcal{J}_\mathrm{t}}{\mathrm{d}\phi_d}. \tag{6.2.7}$$

As explained by Boujo and Sellier [243], given the infinite number of degrees of freedom in the control ϕ_d, evaluation of the gradient (6.2.7) numerically via a finite-difference approach would require that the value of $\mathcal{J}_\mathrm{t}$ is repeatedly evaluated for each degree of freedom, one at a time. Clearly, this has a prohibitive computational cost and so, as discussed in Section 1.7.2, it is common in the literature to use an adjoint-based approach to compute the gradient (6.2.7) efficiently [229, 243, 244].

As discussed in Section 1.7.2, solving constrained optimisation problems such as (6.2.6) is substantially more difficult than solving unconstrained optimisation problems. We therefore proceed by converting the constrained problem (6.2.6) into an unconstrained problem by introducing the Lagrangian,

$$\begin{aligned}
\mathcal{L} =& \mathcal{J}_\mathrm{t} - \int_{t=0}^{t_\mathrm{f}}\int_{\theta=0}^{2\pi} \lambda^s \left\{ \frac{1}{2}\left(s^2\right)_t + q_\theta \right\} \,\mathrm{d}\theta\,\mathrm{d}t \\
&- \int_{t=0}^{t_\mathrm{f}}\int_{\theta=0}^{2\pi} \lambda^g \left\{ g\ln\left(\frac{d}{s}\right) - \frac{\epsilon^2}{6}\left[g\ln^3\left(\frac{d}{s}\right)\right]_{\theta\theta} - \phi_d \right\} \,\mathrm{d}\theta\,\mathrm{d}t \\
&- \int_{t=0}^{t_\mathrm{f}}\int_{\theta=0}^{2\pi} \lambda^q \Bigg\{ q + \frac{\omega}{2}(1-s^2) - \varepsilon^2 \frac{(1-s^2)^2(1+s^2)s_\theta}{2s^3}\left(\frac{q}{s^2-1}\right)_\theta \\
&+ \varepsilon^2 \frac{(1-s^2)(1+s^4+2s^2(\ln^2 s-1))}{4s^2}\left(\frac{q}{s^2-1}\right)_{\theta\theta} \\
&+ \varepsilon\frac{Re}{16}(-1+2s^2+2s^6-s^4(3+4\ln s))\left[\left(\frac{q}{s^2-1}\right)_t + \left(\frac{q^2}{(s^2-1)^2}\right)_\theta\right] \\
&- \frac{\varepsilon}{8}(1-s^4+4s^2\ln s)\left[\frac{\kappa}{Ca} + s\sin\theta + \tilde{E}_b E^N - 2Re\frac{q^2}{s^2-1}\right]_\theta \Bigg\} \,\mathrm{d}\theta\,\mathrm{d}t,
\end{aligned} \tag{6.2.8}$$

where $\lambda^s(\theta,t)$, $\lambda^g(\theta,t)$, and $\lambda^q(\theta,t)$ are Lagrange multipliers which enforce the governing equations (2.1.34), (2.3.44), and (2.3.66), respectively. Then, the optimisation problem becomes

$$\min_{\phi_d(\theta,t)} \mathcal{L}, \tag{6.2.9}$$

which can be solved using standard unconstrained optimisation techniques.

We take derivatives on functional spaces to be Fréchet derivatives, which we

denote for a function $f(\nu)$ of a scalar or vector quantity ν as

$$\frac{\partial f(\nu)}{\partial \nu}\delta\nu = \lim_{\varepsilon\to 0}\frac{f(\nu+\varepsilon\delta\nu - f(\nu))}{\varepsilon} \tag{6.2.10}$$

for all $\delta\nu$ [243]. By the chain rule, the total derivative of the Lagrangian (6.2.8) with respect to the control ϕ_d is

$$\frac{\mathrm{d}\mathcal{L}}{\mathrm{d}\phi_d} = \frac{\partial\mathcal{L}}{\partial\phi_d} + \frac{\partial\mathcal{L}}{\partial s}\frac{\mathrm{d}h}{\mathrm{d}\phi_d} + \frac{\partial\mathcal{L}}{\partial q}\frac{\mathrm{d}q}{\mathrm{d}\phi_d} + \frac{\partial\mathcal{L}}{\partial g}\frac{\mathrm{d}g}{\mathrm{d}\phi_d} + \frac{\partial\mathcal{L}}{\partial\lambda^s}\frac{\mathrm{d}\lambda^s}{\mathrm{d}\phi_d} + \frac{\partial\mathcal{L}}{\partial\lambda^q}\frac{\mathrm{d}\lambda^q}{\mathrm{d}\phi_d} + \frac{\partial\mathcal{L}}{\partial\lambda^g}\frac{\mathrm{d}\lambda^g}{\mathrm{d}\phi_d}, \tag{6.2.11}$$

which reduces to

$$\frac{\mathrm{d}\mathcal{L}}{\mathrm{d}\phi_d} = \frac{\partial\mathcal{L}}{\partial\phi_d}, \tag{6.2.12}$$

when the following conditions are satisfied,

$$\frac{\partial\mathcal{L}}{\partial\lambda^s} = 0, \quad \frac{\partial\mathcal{L}}{\partial\lambda^g} = 0, \quad \frac{\partial\mathcal{L}}{\partial\lambda^q} = 0, \tag{6.2.13}$$

$$\frac{\partial\mathcal{L}}{\partial s} = 0, \quad \frac{\partial\mathcal{L}}{\partial g} = 0, \quad \frac{\partial\mathcal{L}}{\partial q} = 0. \tag{6.2.14}$$

The conditions (6.2.13) are simply the governing equations (2.1.34), (2.3.44), and (2.3.66). Evaluation of the conditions (6.2.14) yields the adjoint equations for the adjoint variables λ^s, λ^g, and λ^q: two initial-value PDEs for λ^s and λ^q, and one boundary-value PDE for λ^g. The adjoint equations (6.2.14) are dependent on the solutions s, q, and g to the governing equations (6.2.13). Their expanded forms contain 413, 70, and 8 terms, respectively, and are thus omitted here for brevity. If the conditions (6.2.13) and (6.2.14) are satisfied, then $\mathcal{L} = \mathcal{J}_\mathrm{t}$ and hence the negative of the gradient of the cost functional with respect to the control (6.2.7) becomes simply

$$-\frac{\mathrm{d}\mathcal{J}_\mathrm{t}}{\mathrm{d}\phi_d} = -\frac{\partial\mathcal{L}}{\partial\phi_d}. \tag{6.2.15}$$

Evaluating (6.2.15) yields the descent direction,

$$-\frac{\mathrm{d}\mathcal{J}_\mathrm{t}}{\mathrm{d}\phi_d} = -\frac{\partial\mathcal{L}}{\partial\phi_d} = -\big(2\gamma_\phi\phi_d(\theta,t) + \lambda^g\big). \tag{6.2.16}$$

Evaluation of (6.2.16) requires the solution for λ^g. This is found by solving the adjoint equations (6.2.14) which must be integrated backwards in time from $t = t_\mathrm{f}$ to $t = 0$ subject to periodicity conditions on λ_g and terminal conditions for λ^s, λ^q,

and λ^g which are found from the constraints

$$\frac{\partial \mathcal{L}}{\partial s(\theta, t_\mathrm{f})} = 0, \quad \frac{\partial \mathcal{L}}{\partial q(\theta, t_\mathrm{f})} = 0, \quad \frac{\partial \mathcal{L}}{\partial g(\theta, t_\mathrm{f})} = 0, \tag{6.2.17}$$

the evaluation of which yields

$$\lambda^s(\theta, t_\mathrm{f}) = 2\gamma_\phi(s(\theta, t_\mathrm{f}) - s_\mathrm{targ}), \quad \lambda^q(\theta, t_\mathrm{f}) = 0, \quad \lambda^g(\theta, t_\mathrm{f}) = 0. \tag{6.2.18}$$

We are now in a position to outline the iterative optimal control procedure, a schematic of which is shown in Figure 6.3 for iteration n. At the first iteration (i.e., $n = 0$) we choose an initial guess for ϕ_d, which we denote by ϕ_{d_0}. In Step 1, given ϕ_{d_0}, we solve the governing equations (6.2.13) to obtain the solutions for s, q, and g. In Step 2, we determine the terminal conditions on s, q, and g for use in Step 3. In Step 3, given ϕ_{d_0} with s, q, and g obtained in Step 1, we solve the adjoint equations (6.2.14) subject to the terminal conditions obtained in Step 2 to obtain the solutions for λ^s, λ^q, and λ^g. In Step 4, given λ^g obtained in Step 3, we evaluate the gradient (6.2.15) to yield the descent direction. In Step 5, given the gradient from Step 4, we update the control $\phi_{d_n}(\theta, t) \to \phi_{d_{n+1}}(\theta, t)$ using a suitable gradient-based method. Finally, we return to Step 1 and iterate the procedure until convergence.

6.2.2 Results

In this section, we give an overview of the calculations that are performed to obtain the results that will be presented next in Sections 6.2.3–6.2.5.

Throughout this section, in our numerical calculations we use the parameter values (5.2.1) of Ca, Re, and d with $\omega = 1$ and $\tilde{E}_b = 10$. Numerical solutions of the governing equations (6.2.13) and the adjoint equations (6.2.14) are obtained using the numerical scheme described in Appendix A.1. To update the control in Step 4, either a Polak-Ribière [245] (in Sections 6.2.3 and 6.2.4) or a steepest descent (in Section 6.2.5) conjugate gradient method is used to determine the descent direction, and a golden section method [247] is used to perform the line search to determine the descent distance (see Sections 1.7.2.2–1.7.2.4).

The initial guess ϕ_{d_0} is fixed as $\phi_{d_0} = 0.02$, which was chosen to be small to ensure that electrostatic effects do not overwhelm the system, and non-zero in order for the control mechanism to be able to calculate the normalisation on

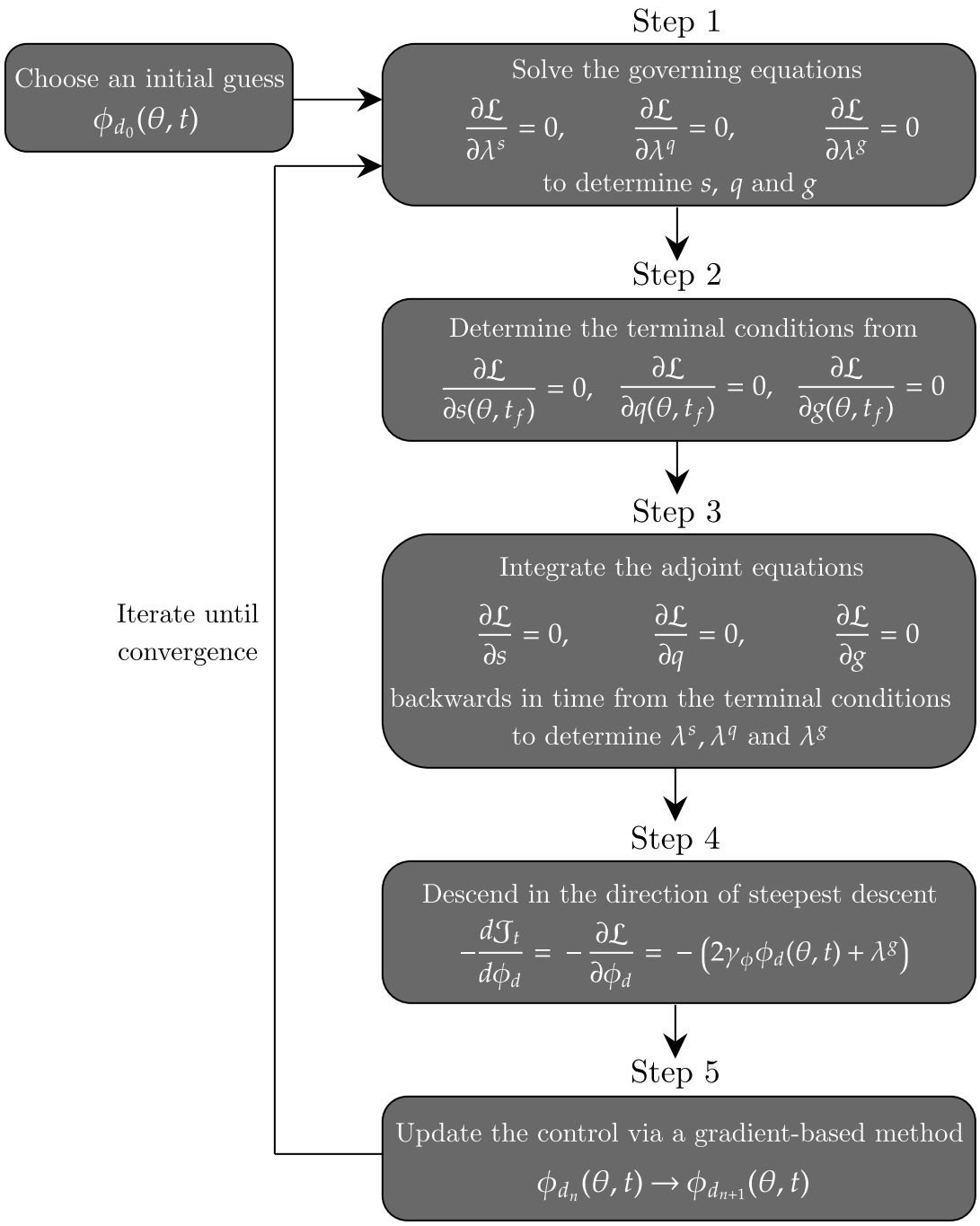

Figure 6.3: The iterative optimal control procedure described in Section 6.2.1.

the first iteration (which involves division by ϕ_{d_0}). Note that, in theory, it is possible that the outcome of the control could be improved by a "better" choice of ϕ_{d_0}. However, as it is not possible to know if the control mechanism has converged towards a global minimum or a local minimum (in which the gradient methods may remain trapped), trial-and-error choices of ϕ_{d_0} are unlikely to yield a significant advantage. Alternatively, one may use a Monte Carlo method to infer a promising choice of ϕ_{d_0}, as used by Boujo and Sellier [243] (see earlier discussion in Section 1.7.2). However, we have chosen not to adopt this approach because it has a high computational cost due to that fact that it randomly samples the parameter space.

The iterative optimal control procedure illustrated in Figure 6.3 is performed until the convergence criterion is reached, namely, that $\mathcal{L}$ does not vary by more than 10^{-10} across 10 iterations. In our calculations, each iteration is performed over the time interval $0 \leq t \leq t_\mathrm{f}$, where $t_\mathrm{f} = 20$. The value $t_\mathrm{f} = 20$ was chosen to be fairly small due to the fact that, as shall be shown throughout this section, terminal control acts only near the end of the time interval (hence there is no benefit in running the mechanism for long times), but also large enough such that the electric field has enough time to act on the system. We use the value $\gamma_\phi = 10^{-13}$ for the control weight, which could be considered small compared to the control weights used by other authors in other contexts (for example, Boujo and Sellier [243] considered control weights within the range $[10^{-8}, 10^{-5}]$). This value was initially chosen to test the feasibility of our control methodology. However, we subsequently chose to retain this value after finding that the controls that result from it are always realisable. In particular, in Sections 6.2.3–6.2.5, we show that the resulting controls do not come close to the dimensionless potential which would break the dielectric limit of air for the parameter values used in this section, which is computed to be

$$\begin{aligned}
\phi_{d\max} &= \frac{(\hat{R}_2 - \hat{R}_1)\left(3 \times 10^6 \text{ V m}^{-1}\right)}{\hat{\phi}_\mathrm{char}} \\
&= \frac{(3 \times 10^{-3}\text{m})\left(3 \times 10^6 \text{ V m}^{-1}\right)}{2.8 \times 10^{-2} \text{ V}} \\
&\approx 3.2 \times 10^5. \qquad (6.2.19)
\end{aligned}$$

Hence, at present, it is not necessary to increase γ_ϕ. Analysing the effect of varying the value of the control weight could be an interesting direction for future study.

Note that when choosing a target shape s_{targ}, it is crucial to ensure that the total liquid volume is preserved. In other words, we should not attempt to control the interfacial radius towards a target shape which would require a change in the total mass of the system. With this in mind, in our calculations we have ensured conservation of the liquid volume by choosing the initial (uniform) interfacial radius s_0 based on the desired target shape. Specifically, conservation of the liquid volume requires

$$V_{\text{targ}} = V|_{t=0}, \tag{6.2.20}$$

where V_{targ} is the volume of the target shape and $V|_{t=0}$ is the initial liquid volume, given respectively by

$$V_{\text{targ}} = \int_0^{2\pi} \int_1^{s_{\text{targ}}} r \, \mathrm{d}r \, \mathrm{d}\theta = \frac{1}{2} \int_0^{2\pi} \left(s_{\text{targ}}^2 - 1 \right) \, \mathrm{d}\theta, \tag{6.2.21}$$

$$V_0 = \int_0^{2\pi} \int_1^{s_0} r \, \mathrm{d}r \, \mathrm{d}\theta = \frac{1}{2} \int_0^{2\pi} \left(s_0^2 - 1 \right) \, \mathrm{d}\theta. \tag{6.2.22}$$

Solving (6.2.21) and (6.2.22) together for s_0 yields

$$s_0 = \left(\frac{1}{2\pi} \int_0^{2\pi} s_{\text{targ}}^2 \, \mathrm{d}\theta \right)^{1/2}. \tag{6.2.23}$$

It is straight-forward to see that the liquid volume is automatically conserved for the uniform target shape $s_{\text{targ}} = s_0$ (which will be considered in Section 6.2.3). However, if we choose a nonuniform target shape such as, for example,

$$s_{\text{targ}} = 1.3 + 0.02 \sin(2\theta), \tag{6.2.24}$$

(which will be considered in Section 6.2.4), then by (6.2.23), we must choose the initial interfacial radius to be $s_0 = 1.30008$.

Note that all of the figures throughout the remainder of this chapter are from the final iteration. It will be useful to define the deviation $\mathcal{U} = \mathcal{U}(t)$ of the interfacial radius s from the target shape s_{targ} at any given time t as

$$\mathcal{U} = \left|\left| s(\theta, t) - s_{\text{targ}}(\theta) \right|\right|_2, \tag{6.2.25}$$

where $|| \cdot ||_2$ denotes the usual L^2-norm.

$\mathcal{J}_t$	$\mathcal{U}_\mathrm{t}$	$\mathcal{U}_\mathrm{t}$ $(\tilde{E}_b = 0)$	$\mathcal{C}_\phi$	Iterations
1.19302×10^{-8}	1.19299×10^{-8}	3.55705×10^{-3}	3.35583×10^{-13}	83

Table 6.1: Results for controlling towards the target shape (6.2.26): the total cost of the control (6.2.4), the terminal deviation measure $\mathcal{U}_\mathrm{t}$ (6.2.5), the uncontrolled terminal deviation measure, the cost of the control mechanism (6.2.2), and the number of iterations required to determine the optimal control.

6.2.3 Uniform target shape

In this section, we revisit the problem of controlling the interfacial radius towards its initial uniform shape which was discussed earlier in the context of feedback control in Section 6.1. Specifically, in this case, we choose

$$s_\mathrm{targ} = s_0, \tag{6.2.26}$$

where $s_0 = 1.3$. The entries in Table 6.1 contain the total cost of the control (6.2.4), the terminal deviation measure $\mathcal{U}_\mathrm{t}$ (6.2.5), the uncontrolled terminal deviation measure (i.e., for $\tilde{E}_b = 0$), the cost of the control mechanism (6.2.2), and the number of iterations required to determine the optimal control, respectively. In this instance, the optimal control procedure successfully converged after 83 iterations, which had a runtime of approximately 0.55 hours in wall-clock time. The deviation measure (6.2.5) at the final time $t = t_\mathrm{f}$ was calculated to be $\mathcal{U}_\mathrm{t} = 1.19299 \times 10^{-8}$ in the controlled case, which is five orders of magnitude smaller than the terminal deviation measure in the uncontrolled case, $\mathcal{U}_\mathrm{t} = 3.55705 \times 10^{-3}$. The total control cost required to achieve the target shape was $\mathcal{J}_\mathrm{t} = 1.19302 \times 10^{-8}$.

Figure 6.4 shows the final approach of the interfacial radius towards the target shape (6.2.26) (shown as the thick red line) at times $t = 20 - n/20$ (for $n = 0, 1, \ldots, 20$) (shown as the solid black lines). The interfacial radius at the final time $t = t_\mathrm{f}$ is shown in Figure 6.5 (a) as the dashed black line, which is in excellent agreement with the desired target shape (6.2.26), shown as the thick red line. The electric potential ϕ_d at the final time $t = t_\mathrm{f}$ is shown in Figure 6.5 (b), indicating that ϕ_d is weakest on the lower part of the cylinder. This is perhaps counter intuitive, as one might have anticipated the electric field to instead be stronger where the interfacial radius is least uniform (i.e., in this system, typically near where the bulge of liquid naturally forms on the lower part of the cylinder). On

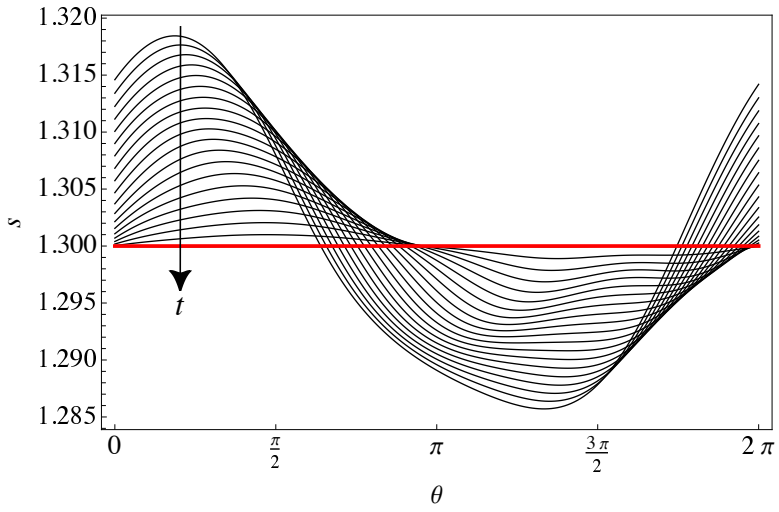

Figure 6.4: The interfacial radius s at times $t = 20 - n/20$ for $n = 0, 1, \ldots, 20$ (solid black lines) and the target shape (6.2.26) (thick red line). The arrow indicates the direction of increasing time.

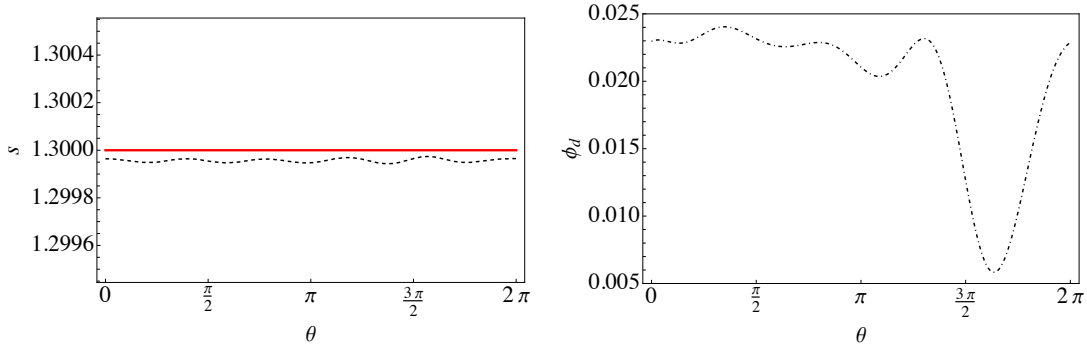

Figure 6.5: (a) The interfacial radius s at the final time $t = t_{\mathrm{f}}$ (dashed black line) and the target shape (6.2.26) (solid red line). (b) The electric potential ϕ_d at the final time $t = t_{\mathrm{f}}$.

the contrary, as discussed earlier in Section 6.1, a stronger electric field where the film is thinnest is of benefit, as this pulls these thinner regions towards the outer electrode, thus shrinking the bulge of liquid as desired due to mass conservation.

Figure 6.6 shows the controlled evolution of s and ϕ_d over time, where the thick red line highlights the final time $t = t_{\mathrm{f}}$. Note that Figures 6.6 (a) and (b) show the same system as in Figure 5.18, which shows that for the same parameter values the system exhibits a sinusoidal shape by time $t = t_{\mathrm{f}}$ in the uncontrolled case. Figures 6.6 (a) and (b) show the evolution of s over the entire time interval and close to the final time, respectively, revealing that the interface converges towards the target shape (6.2.26) quickly as t approaches t_{f}. Similarly, Figures 6.6 (c) and (d) show the evolution of the electric potential ϕ_d over the entire time interval and close to the final time $t = t_{\mathrm{f}}$, respectively, showing that terminal control acts during the latter stages of the time interval. Additionally, Figure 6.6 (c) also shows that the absolute value of ϕ_d never exceeds, or even comes close to, $\phi_{d\max}$ (6.2.19).

Figure 6.7 (a) shows the deviation (6.2.25) of the interfacial radius from the target shape (6.2.26) over time in both the uncontrolled (shown as the dotted line) and the controlled (shown as the dashed line) cases, along with the average of the electric potential ϕ_d at each time step, which we denote by ϕ_{avg}, plotted over time (shown as the dot-dashed line). The small value of the deviation (6.2.25) at time $t = t_{\mathrm{f}}$ in Figure 6.7 (a) confirms that the interface has been successfully controlled towards the target shape, in particular, showing that the deviation measure decreases sharply as t approaches t_{f}. This demonstrates a key feature of the terminal control process: there is less value in reaching the target shape early in the time interval and holding it there until the final time than there is in keeping the control weak until t approaches t_{f}. Figure 6.7 (b) shows the evolution of the maximum interfacial radius $s_{\max}$ over time in both the uncontrolled (shown as the dotted line) and the controlled (shown as the dashed line) cases. The maximum interfacial radius reaches a final value of $s_{\max} = 1.33697$ in the uncontrolled case by time $t = t_{\mathrm{f}}$ compared to $s_{\max} = 1.29997$ at time $t = t_{\mathrm{f}}$ in the controlled case. It can be seen from Figure 6.7 (a) that ϕ_{avg} increases as t approaches t_{f}, and decreases again before t_{f} is reached. As we shall see throughout the rest of this chapter, qualitatively similar behaviour occurs in all of our results, and thus requires an explanation. At present, we are not aware of any similar studies with which to directly compare our results. Hence, we are not aware of any accepted explanation for the observed sharp decrease in ϕ_{avg}. We hypothesise two possibilities: the first

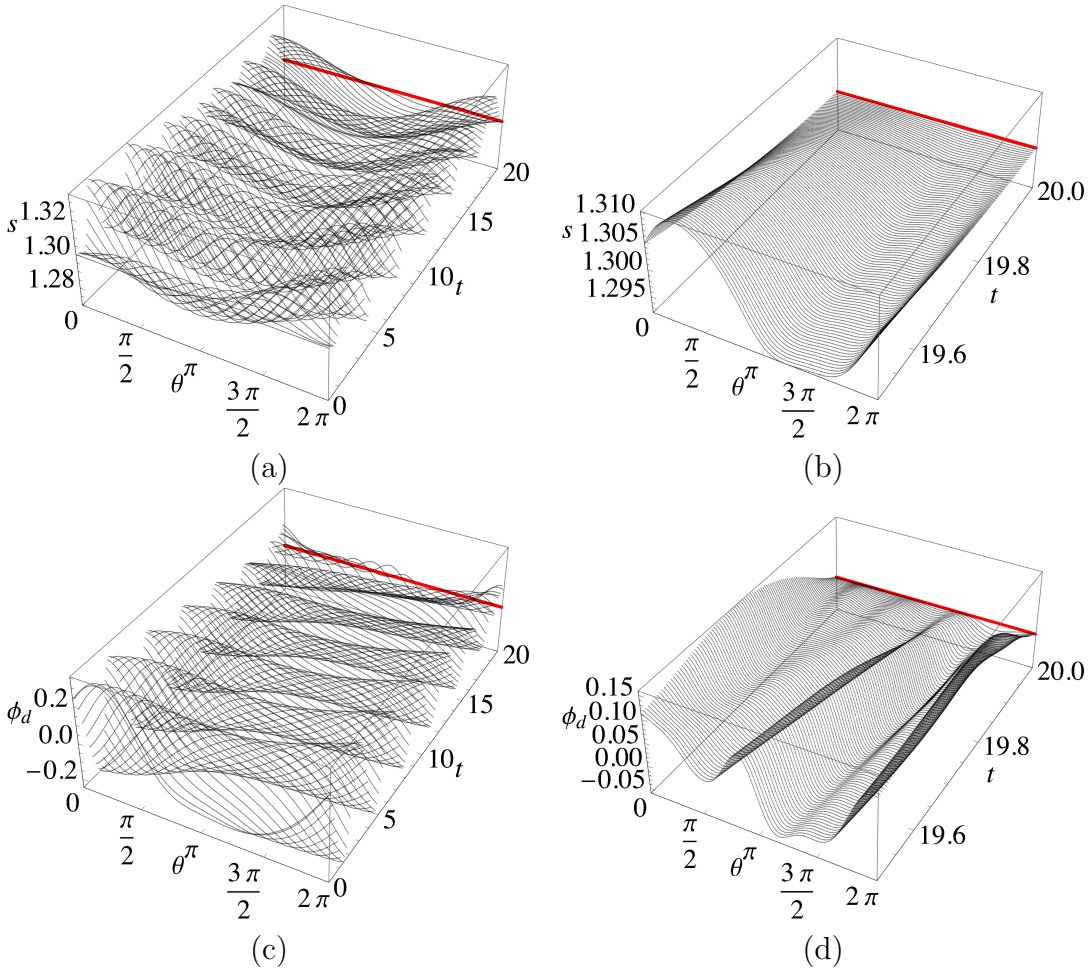

Figure 6.6: Terminal control of the thick-film WRIBL model towards the target shape (6.2.26). The solid black lines show the evolution of (a), (b) the interfacial radius s and (c), (d) the electric potential ϕ_d for (a), (c) $0 \leq t \leq t_{\rm f}$ shown at times $t = 31n/200$ for $n = 0, 1, \ldots, 129$ and (b), (d) $19.5 \leq t \leq t_{\rm f}$ shown at times $t = 19.500, 19.505, \ldots, t_{\rm f}$. The thick red line highlights the final time $t = t_{\rm f}$.

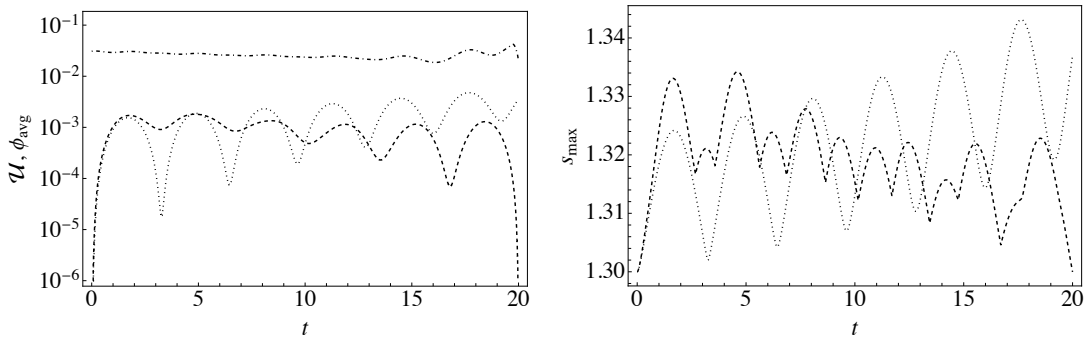

(a) (b)

Figure 6.7: (a) Semi-log plot of the deviation (6.2.25) of the uncontrolled interfacial radius (dotted line) and the controlled interfacial radius (dashed line) from the target shape (6.2.26) and the average of the electric potential ϕ_{avg} (dot-dashed line) over time. (b) Evolution of the maximum interfacial radius $s_{\max}$ in the uncontrolled (dotted line) and the controlled (6.2.26) (dashed line) cases.

is that the control mechanism first gets the interfacial radius into a form that is close enough to the target shape that capillarity can then naturally drive the interfacial radius towards the target shape over the final time steps, hence the strength of ϕ_{avg} can be reduced near $t = t_{\text{f}}$. Note that we anticipate this reasoning being particularly relevant for control towards the uniform target shape (6.2.26), as capillarity favours a uniform interfacial radius. The second possibility, which we consider to be the more likely explanation, is that there is a time lag between the imposition of a particular control and the effect that it has. This is partially due to the fact that the interface cannot transition instantaneously, and so transitions smoothly from the point at which the control at imposed, but also due to the effect of inertia, which exacerbates this time lag.

It instructive to consider what effect varying the parameters Ca, d, and $\tilde{E}_b$ from the original values $Ca = 0.157$, $d = 2.5$, and $\tilde{E}_b = 10$ has on the convergence of the control mechanism. The entries in Table 6.2 contain the total cost of the control (6.2.4), the terminal deviation measure $\mathcal{U}_{\text{t}}$ (6.2.5), the uncontrolled terminal deviation measure, the cost of the control mechanism (6.2.2), and the number of iterations required to determine the optimal control, respectively, for various values of the parameters Ca, d, and $\tilde{E}_b$. Note that the results for the original parameter values $Ca = 0.157$, $d = 2.5$, and $\tilde{E}_b = 10$ are given in the middle row for each parameter and are highlighted in bold. Our results show that decreasing

	Value	$\mathcal{J}_\mathrm{t}$	$\mathcal{U}_\mathrm{t}$	$\mathcal{U}_\mathrm{t}$ $(\tilde{E}_b = 0)$	$\mathcal{C}_\phi$	Iterations
	0.03925	1.45504×10^{-9}	1.45422×10^{-9}	3.81860×10^{-3}	8.18592×10^{-13}	65
	0.0785	4.02836×10^{-9}	4.02779×10^{-9}	3.51721×10^{-3}	5.74171×10^{-13}	85
Ca	**0.1570**	$\mathbf{1.19302 \times 10^{-8}}$	$\mathbf{1.19299 \times 10^{-8}}$	$\mathbf{3.55705 \times 10^{-3}}$	$\mathbf{3.35583 \times 10^{-13}}$	**83**
	0.3140	6.39463×10^{-9}	6.39448×10^{-9}	3.72525×10^{-3}	1.55297×10^{-13}	74
	0.6280	2.71162×10^{-8}	2.71160×10^{-8}	4.06327×10^{-3}	1.74321×10^{-13}	174
	1.5	1.47659×10^{-10}	1.47648×10^{-10}	3.55705×10^{-3}	1.07036×10^{-14}	22
	2	3.28732×10^{-9}	3.28722×10^{-9}	3.55705×10^{-3}	1.00299×10^{-13}	76
d	**2.5**	$\mathbf{1.19302 \times 10^{-8}}$	$\mathbf{1.19299 \times 10^{-8}}$	$\mathbf{3.55705 \times 10^{-3}}$	$\mathbf{3.35583 \times 10^{-13}}$	**83**
	3	3.00835×10^{-8}	3.00827×10^{-8}	3.55705×10^{-3}	7.51303×10^{-13}	102
	3.5	5.42654×10^{-8}	5.42640×10^{-8}	3.55705×10^{-3}	1.32845×10^{-12}	126
	1	6.20071×10^{-8}	6.20022×10^{-8}	3.55705×10^{-3}	4.97087×10^{-12}	125
	5	2.56403×10^{-8}	2.56395×10^{-8}	3.55705×10^{-3}	8.04266×10^{-13}	91
$\tilde{E}_b$	**10**	$\mathbf{1.19302 \times 10^{-8}}$	$\mathbf{1.19299 \times 10^{-8}}$	$\mathbf{3.55705 \times 10^{-3}}$	$\mathbf{3.35583 \times 10^{-13}}$	**83**
	15	7.25095×10^{-9}	7.25075×10^{-9}	3.55705×10^{-3}	2.00087×10^{-13}	82
	20	4.67908×10^{-9}	4.67895×10^{-9}	3.55705×10^{-3}	1.34609×10^{-13}	64

Table 6.2: Results for controlling towards the target shape (6.2.26) for various values of Ca, d, and $\tilde{E}_b$: the total cost of the control (6.2.4), the terminal deviation measure $\mathcal{U}_\mathrm{t}$ (6.2.5), the uncontrolled terminal deviation measure, the cost of the control mechanism (6.2.2), and the number of iterations required to determine the optimal control. The results for the original parameter values $Ca = 0.157$, $d = 2.5$, and $\tilde{E}_b = 10$ are highlighted in bold.

Ca (corresponding to strengthening capillarity) or decreasing d (corresponding to moving the outer electrode closer to the interface) both result in more successful control, as reflected in the general decrease in the terminal deviation measures shown in Table 6.2. In these instances, the number of iterations required to reach convergence and the total cost of the control decreases. Capillarity favours the cylindrical shape and so strengthening it assists the control mechanism. To a certain point, decreasing d helps the control mechanism, as the proximity of the outer electrode diminishes the diffusive effect of Laplace's equation making fine control of the system easier. However, if d is too small, outer contact can occur, in which case the algorithm fails at Step 1 and the iterative process is terminated. Although instances of such failures due to small d do not appear in Table 6.2, they (along with other instances of unsuccessful control) will be shown in Section 6.2.5 and discussed in detail in Section 6.2.6. Increasing $\tilde{E}_b$ (corresponding to increasing the electric potential difference) yields more successful control, as reflected in the decrease in the terminal deviation measures shown in Table 6.2. In this case, the total cost of the control and the number of iterations both decrease for increasing $\tilde{E}_b$. Table 6.2 indicates that, for the parameters considered, the most successful

and computationally efficient control could be attained by choosing $Ca = 0.1570$, $\tilde{E}_b = 10$, and $d = 1.5$, resulting in the lowest terminal deviation measure ($\mathcal{U}_\mathrm{t} = 1.47659 \times 10^{-10}$), the lowest cost of the control mechanism ($\mathcal{C}_\phi = 1.07036 \times 10^{-14}$), and the fewest iterations required for convergence (22).

6.2.4 Parametric study

In this section, we aim to obtain a clearer understanding of the capabilities of the control mechanism, especially into the short-wave regime. To this end, we investigate control of the interface towards nonuniform sinusoidal target shapes of the form

$$s_\mathrm{targ} = 1.3 + m\sin(n\theta) \tag{6.2.27}$$

by conducting an investigation in (m, n) parameter space. Not only is this a stringent test, but is also of industrial interest as control towards nonuniform shapes results in an increase in the interfacial area which has numerous applications in the enhancement of heat and mass transfer rates and in micro-manufacturing (see Sections 1.6 and 1.7). We consider the amplitude m over the range $0.02 \leq m \leq 0.12$ with step size 0.02, and the wavelength n over the range $1 \leq n \leq 10$ with step size 1. The results are given in Table 6.3, wherein hyphens indicate calculations which were unsuccessful. Unsuccessful calculations can correspond to a variety of issues, which will be discussed in detail in Section 6.2.6. For now, we note that in this section it was found that the control mechanism is successful so long as the target shape does not deviate too far from what the underlying physics are capable of supporting (i.e., it is difficult to successfully control towards target shapes with short wavelengths and large amplitudes). For example, Table 6.3 shows that the attempt to control towards the target shape (6.2.27) for $m = 0.10$ and $n = 10$ was unsuccessful. Note that, in an attempt to control successfully towards some of these more difficult target shapes, an alternative reformulation of the Lagrangian was used as described in Appendix G. Calculations which used the reformulation are identified by asterisks in Table 6.3.

Figure 6.8 shows the values of the terminal deviation measure given in Table 6.3 plotted over n for each value of m. The control mechanism was most successful for the smallest amplitude considered ($m = 0.02$) and least successful for the largest amplitude considered ($m = 0.12$). In general, the terminal deviation measure increases for all m as the wavelength n increases, as one would expect.

	n	$\mathcal{J}_\mathrm{t}$	$\mathcal{U}_\mathrm{t}$	$\mathcal{C}_\phi$	Iterations
0.02	1	9.34113×10^{-8}	9.34108×10^{-8}	5.45361×10^{-13}	109
	2	1.77872×10^{-8}	1.77868×10^{-8}	4.29601×10^{-13}	68
	3	1.34795×10^{-8}	1.34791×10^{-8}	3.88311×10^{-13}	89
	4	1.42257×10^{-8}	1.42254×10^{-8}	3.83567×10^{-13}	76
	5	1.42400×10^{-8}	1.42396×10^{-8}	3.86654×10^{-13}	90
	6	1.68849×10^{-8}	1.68845×10^{-8}	4.01219×10^{-13}	143
	7	2.07032×10^{-8}	2.07028×10^{-8}	4.15929×10^{-13}	132
	8	2.38134×10^{-8}	2.38129×10^{-8}	4.44689×10^{-13}	160
	9	4.78229×10^{-8}	4.78224×10^{-8}	4.67620×10^{-13}	92
	10	7.88358×10^{-8}	7.88353×10^{-8}	4.89232×10^{-13}	111
0.04	1	3.15947×10^{-7}	3.15947×10^{-7}	6.82613×10^{-13}	72
	2	8.15724×10^{-8}	8.15717×10^{-8}	6.68179×10^{-13}	74
	3	1.37178×10^{-7}	1.37177×10^{-7}	7.09756×10^{-13}	90
	4	8.94006×10^{-8}	8.94000×10^{-8}	6.14789×10^{-13}	60
	5	4.04862×10^{-8}	4.04857×10^{-8}	4.70868×10^{-13}	76
	6	4.71222×10^{-8}	4.71217×10^{-8}	4.58772×10^{-13}	104
	7	5.91715×10^{-8}	5.91710×10^{-8}	4.36156×10^{-13}	143
	8	1.19042×10^{-7}	1.19042×10^{-7}	5.02048×10^{-13}	180
	9	2.21278×10^{-7}	2.21277×10^{-7}	5.62364×10^{-13}	2878
	10	3.85946×10^{-7}	3.85946×10^{-7}	6.32153×10^{-13}	8492
0.06	1	8.87659×10^{-7}	8.87658×10^{-7}	7.99855×10^{-13}	85
	2	1.46008×10^{-6}	1.46008×10^{-6}	1.42045×10^{-12}	79
	3	1.31177×10^{-6}	1.31177×10^{-6}	1.28134×10^{-12}	64
	4	2.15929×10^{-6}	2.15929×10^{-6}	1.34388×10^{-12}	63
	5	1.58377×10^{-6}	1.58377×10^{-6}	1.21328×10^{-12}	71
	6	2.49147×10^{-7}	2.49146×10^{-7}	6.16372×10^{-13}	76
	7	3.73202×10^{-7}	3.73201×10^{-7}	5.51196×10^{-13}	134
	8	7.68039×10^{-7}	7.68039×10^{-7}	4.87538×10^{-13}	92
	9	1.41831×10^{-4}	1.41831×10^{-4}	6.48910×10^{-13}	31
	10	3.67676×10^{-3}	3.67676×10^{-3}	8.15632×10^{-13}	33
0.08	1	2.00446×10^{-6}	2.00446×10^{-6}	8.95598×10^{-13}	74
	2	5.21239×10^{-6}	5.21239×10^{-6}	1.97452×10^{-12}	116
	3	3.68830×10^{-6}	3.68829×10^{-6}	1.72911×10^{-12}	64
	4	4.00660×10^{-6}	4.00659×10^{-6}	1.60223×10^{-12}	55
	5	5.74503×10^{-6}	5.74503×10^{-6}	1.64981×10^{-12}	65
	6	5.46700×10^{-6}	5.46700×10^{-6}	1.54826×10^{-12}	69
	7	1.71350×10^{-6}	1.71350×10^{-6}	6.75996×10^{-13}	82
	8	3.86916×10^{-6}	3.86916×10^{-6}	6.15693×10^{-13}	102
	9	1.15858×10^{-2}	1.15858×10^{-2}	7.84220×10^{-13}	24
	10	3.67850×10^{-3}	3.67850×10^{-3}	6.83406×10^{-13}	19
0.10	1	3.89112×10^{-6}	3.89112×10^{-6}	1.01693×10^{-12}	76
	2	7.40558×10^{-6}	7.40558×10^{-6}	2.10519×10^{-12}	181
	3	1.88780×10^{-2}	1.88780×10^{-2}	1.98450×10^{-12}	18
	4	6.85408×10^{-6}	6.85408×10^{-6}	1.90372×10^{-12}	95
	5	8.79466×10^{-6}	8.79466×10^{-6}	1.81896×10^{-12}	125
	6	1.76596×10^{-5}	1.76596×10^{-5}	2.10087×10^{-12}	1735
	7	6.33742×10^{-6}	6.33742×10^{-6}	1.26146×10^{-12}	105
	8*	3.67502×10^{-5}	3.67502×10^{-5}	2.34995×10^{-12}	58
	9	6.02524×10^{-3}	6.02524×10^{-3}	7.89339×10^{-13}	17
	10	–	–	–	–
0.12	1	1.28327×10^{-4}	1.28327×10^{-4}	1.17056×10^{-12}	44
	2	1.79064×10^{-5}	1.79064×10^{-5}	2.40604×10^{-12}	79
	3*	3.24800×10^{-2}	3.24800×10^{-2}	2.54683×10^{-12}	21
	4*	1.49700×10^{-2}	1.49700×10^{-2}	3.59810×10^{-12}	14
	5	–	–	–	–
	6	1.48516×10^{-5}	1.48516×10^{-5}	2.02872×10^{-12}	5736
	7	2.19513×10^{-5}	2.19513×10^{-5}	1.85548×10^{-12}	422
	8	–	–	–	–
	9	8.82820×10^{-3}	8.82820×10^{-2}	7.53121×10^{-13}	19
	10	1.67698×10^{-2}	1.67698×10^{-2}	8.50459×10^{-13}	17

Table 6.3: Results of the parametric study in (m, n) parameter space in controlling towards the target shape (6.2.27): the total cost of the control (6.2.4), the terminal deviation measure $\mathcal{U}_\mathrm{t}$ (6.2.5), the cost of the control mechanism (6.2.2), and the number of iterations required to determine the optimal control. Hyphens indicate unsuccessful calculations and asterisks indicate calculations which utilised the alternative form of the Lagrangian in Appendix G.

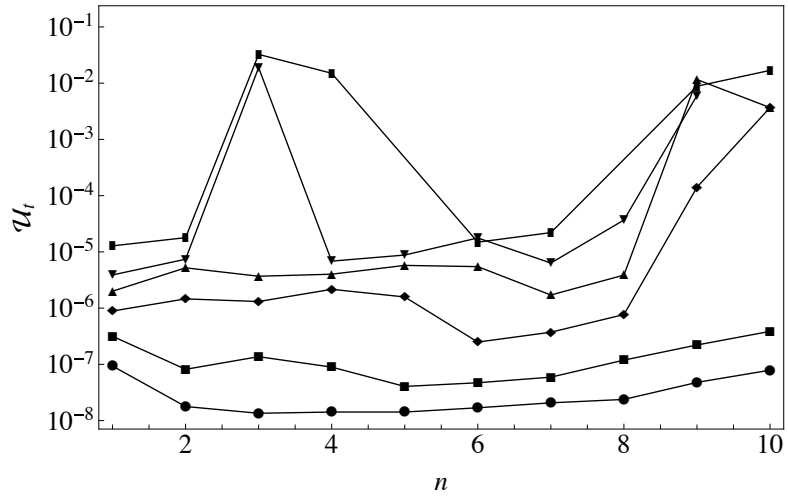

Figure 6.8: The terminal deviation measure $\mathcal{U}_{\mathrm{t}}$ (6.2.5) for $1 \leq n \leq 10$ with $m = 0.02$ (circles), $m = 0.04$ (squares), $m = 0.06$ (diamonds), $m = 0.08$ (triangles), $m = 0.10$ (inverse triangles), and $m = 0.12$ (rectangles). Symbols represent integer values of n.

In order to gain a clearer understanding of parameter space, we investigate first the effect of increasing n for a fixed m in Section 6.2.4.1, before considering the effect of increasing m for a fixed n in Section 6.2.4.2. Although in what follows we analyse specific examples, note that we found that the trends that will be described throughout this section for increasing m and n were consistent with what we found for other values of m and n.

6.2.4.1 Varying n

In this section, we investigate the effect of varying n for a fixed m on the success of the control. We first consider control towards the target shape (6.2.27) for $m = 0.02$ (as this was the amplitude value that corresponds to the most successful control shown in Table 6.3) for increasing wavenumbers $n = 2, 4, 6,$ and 8. The entries in Table 6.4 contain the wavenumber n, the total cost of the control (6.2.4), the terminal deviation measure $\mathcal{U}_{\mathrm{t}}$ (6.2.5), the uncontrolled terminal deviation measure, the cost of the control mechanism (6.2.2), and the number of iterations required to determine the optimal control. As n increases, as does the number of iterations and the terminal deviation measure, as expected given the increasingly shorter wavelengths. The terminal deviation measures for all n given in Table 6.4 are five orders of magnitude smaller than the deviation measures in

n	$\mathcal{J}_{\mathrm{t}}$	$\mathcal{U}_{\mathrm{t}}$	$\mathcal{U}_{\mathrm{t}}$ $(\tilde{E}_b = 0)$	$\mathcal{C}_\phi$	Iterations
2	1.77872×10^{-8}	1.77868×10^{-8}	5.19732×10^{-3}	4.29601×10^{-13}	68
4	1.42257×10^{-8}	1.42254×10^{-8}	4.82170×10^{-3}	3.83567×10^{-13}	76
6	1.68849×10^{-8}	1.68845×10^{-8}	4.82333×10^{-3}	4.01219×10^{-13}	143
8	2.38134×10^{-8}	2.38129×10^{-8}	4.82418×10^{-3}	4.44689×10^{-13}	160

Table 6.4: Results for controlling towards the target shape (6.2.27) for $m = 0.02$ and $n = 2, 4, 6$, and 8: the total cost of the control (6.2.4), the terminal deviation measure $\mathcal{U}_{\mathrm{t}}$ (6.2.5), the uncontrolled terminal deviation measure, the cost of the control mechanism (6.2.2), and the number of iterations required to determine the optimal control.

their corresponding uncontrolled cases. Figure 6.9 shows (a), (c), (e), (g) the interfacial radius s at the final time $t = t_{\mathrm{f}}$ (shown as the dashed black line) with the target shape (6.2.27) (shown as the thick red line) and (b), (d), (f), (h) the electric potential ϕ_d at the final time $t = t_{\mathrm{f}}$ (shown as the dashed black line) for (a), (b) $n = 2$, (c), (d) $n = 4$, (e), (f) $n = 6$, and (g), (h) $n = 8$. At the final time, the electric potential ϕ_d approximately mirrors the target shape. In general, a stronger electric potential is required for larger n, and is strongest in each system where the maxima in the target shape are located in order to pull the film towards the outer electrode to the desired amplitude. For the same reason that was described in Section 6.2.3, ϕ_d is smaller on the lower part of the cylinder where the liquid accumulates into a bulge.

Figure 6.10 shows the evolution of (a), (c), (e), (g) the interfacial radius s and (b), (d), (f), (h) the electric potential ϕ_d for $19.5 \leq t \leq t_{\mathrm{f}}$ for (a), (b) $n = 2$, (c), (d) $n = 4$, (e), (f) $n = 6$, and (g), (h) $n = 8$, where the thick red line highlights the final time $t = t_{\mathrm{f}}$. As established in Section 6.2.3, the control mechanism acts only near the end of the time interval, therefore it is instructive to observe the evolution close to $t = t_{\mathrm{f}}$. Hence, throughout the rest of this section, we focus our attention near $t = t_{\mathrm{f}}$. Figure 6.10 shows that the interface converges towards the target shape (6.2.27) quickly as t approaches t_{f}. Additionally, Figures 6.10 (b), (d), (f), and (h) show that the absolute value of ϕ_d never exceeds, or even comes close to, $\phi_{d\max}$ (6.2.19).

Figure 6.11 shows the deviation (6.2.25) of the interfacial radius from the target shape (6.2.27) over time in both the uncontrolled (shown as the dotted line) and the controlled (shown as the dashed line) cases, along with ϕ_{avg} (shown as the dot-

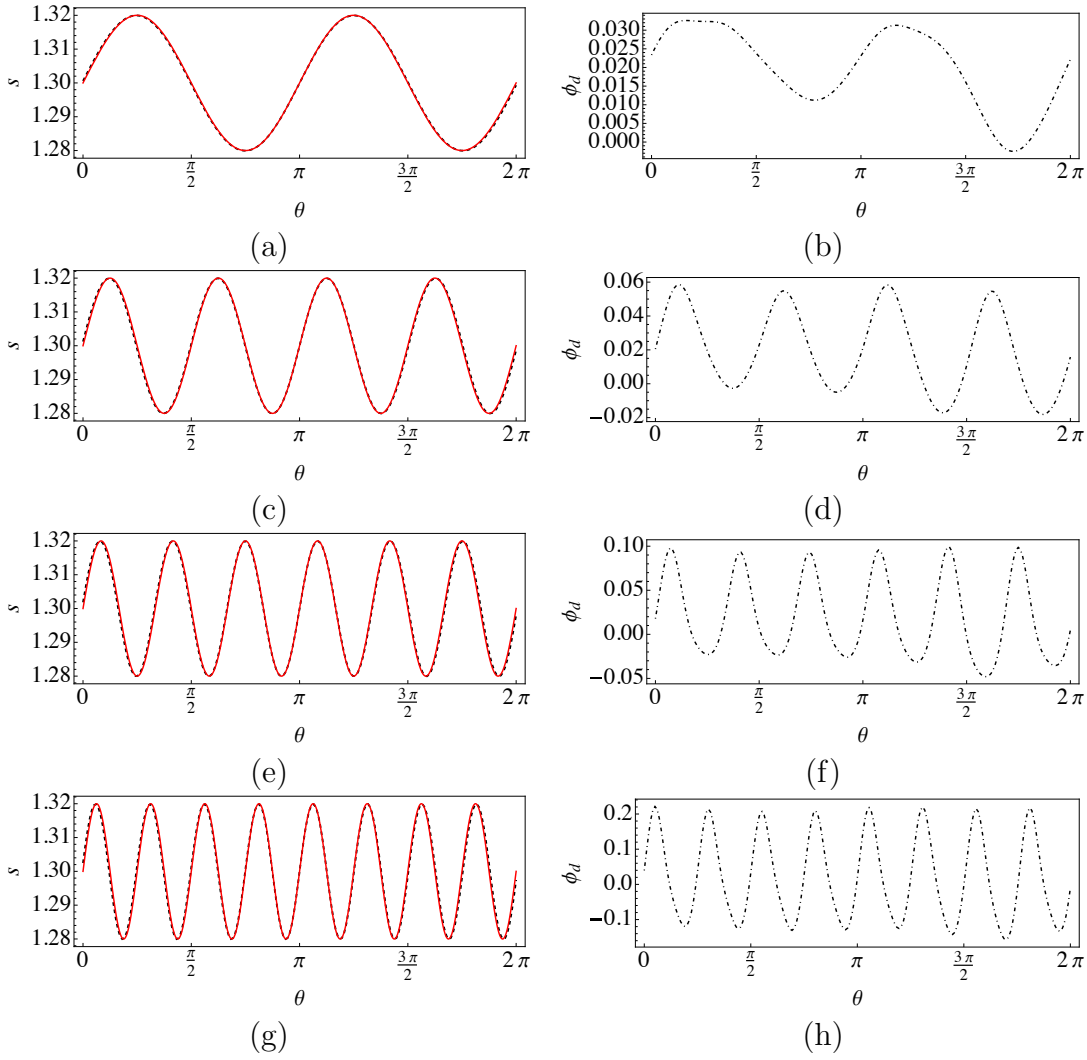

Figure 6.9: (a), (c), (e), (g) The interfacial radius s (dashed black line) with the target shape (6.2.27) (solid red line) and (b), (d), (f), (h) the electric potential ϕ_d (dot-dashed black line) shown at the final time $t = t_{\mathrm{f}}$ for $m = 0.02$ and (a), (b) $n = 2$, (c), (d) $n = 4$, (e), (f) $n = 6$, and (g), (h) $n = 8$.

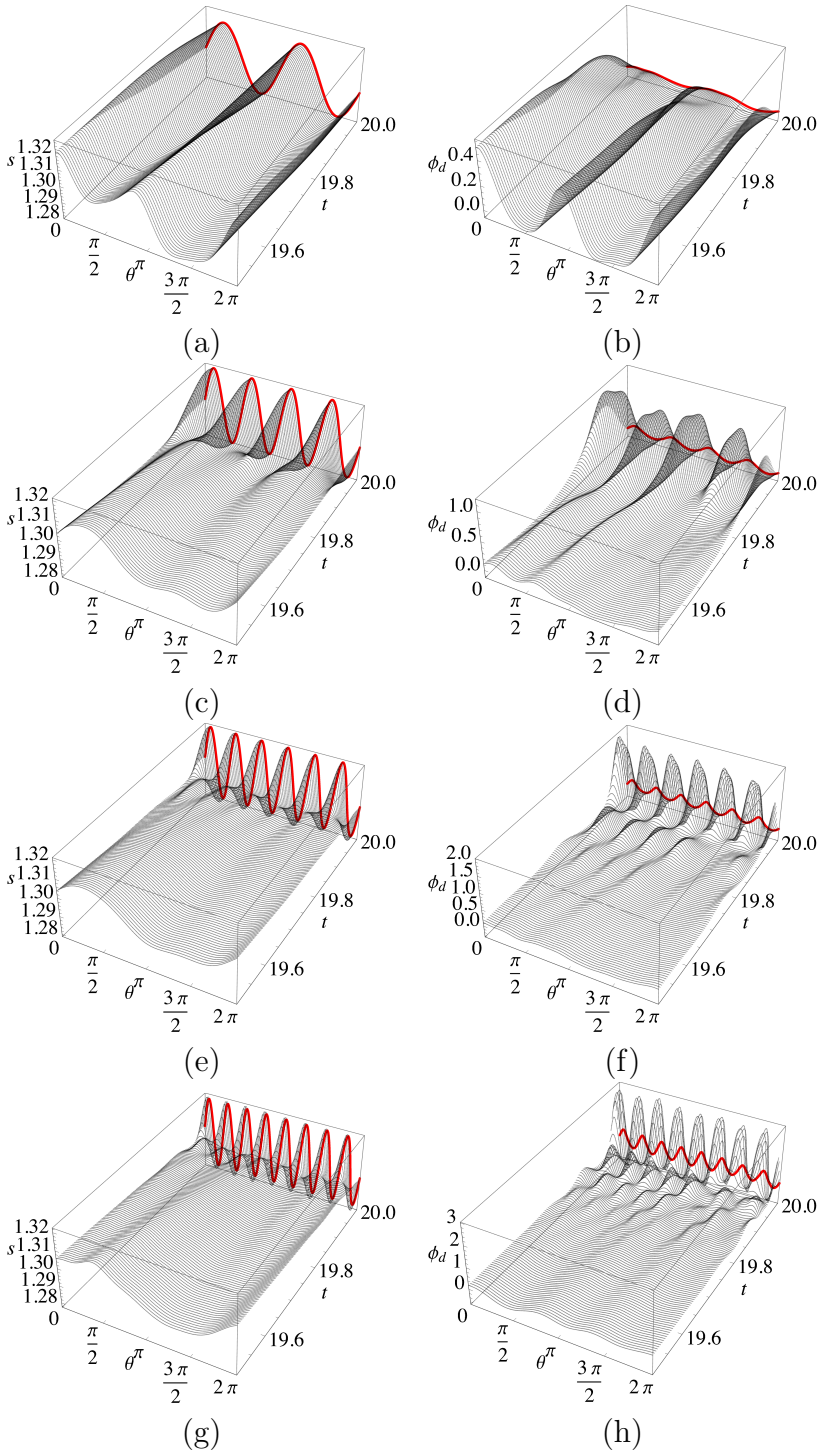

Figure 6.10: Terminal control of the thick-film WRIBL model towards the target shape (6.2.27) shown for $19.5 \leq t \leq t_{\mathrm{f}}$ at times $t = 19.500, 19.505, \ldots, t_{\mathrm{f}}$. The solid black lines show the evolution of (a), (c), (e), (g) the interfacial radius s and (b), (d), (f), (h) the electric potential ϕ_d for $m = 0.02$ and (a), (b) $n = 2$, (c), (d) $n = 4$, (e), (f) $n = 6$, and (g), (h) $n = 8$. The thick red line highlights the final time $t = t_{\mathrm{f}}$.

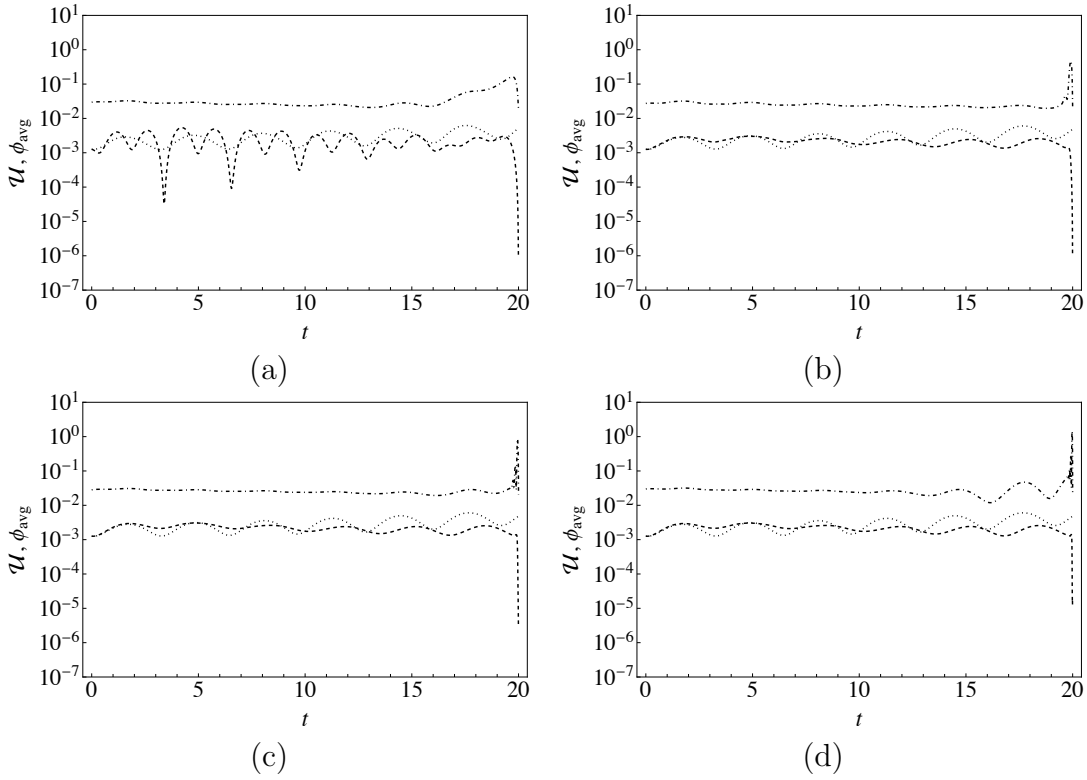

Figure 6.11: Semi-log plots of the deviation (6.2.25) of the uncontrolled interfacial radius (dotted line) and the controlled interfacial radius (dashed line) from the target shape (6.2.27) and the average of the electric potential ϕ_{avg} (dot-dashed line) over time for $m = 0.02$ and (a) $n = 2$, (b) $n = 4$, (c) $n = 6$, and (d) $n = 8$.

dashed line) for (a) $n = 2$, (b) $n = 4$, (c) $n = 6$, and (d) $n = 8$. The small values of the deviation (6.2.25) at the final time $t = t_{\text{f}}$ confirm that the interface has been successfully controlled towards the respective desired target shapes. Note that the more erratic nature of the deviation measure for $n = 2$ seen in Figure 6.11 (a) is a reflection of the fact that the $n = 2$ mode is frequently a natural shape for the interfacial radius to take whilst the liquid oscillates around the cylinder. As n increases, the average potential ϕ_{avg} increases: for $n = 2, 4, 6$, and 8, the maximum values of ϕ_{avg} over the entire time interval are 0.5633, 1.2029, 2.0044, and 3.0364, respectively. In particular, Figure 6.11 shows that, as discussed in Section 6.2.3, ϕ_{avg} peaks before the end of the time interval and decreases sharply over the final time steps.

Figure 6.12 illustrates the successful control of the interface towards the target shape (6.2.27) (shown as the red line) for $m = 0.02$ and $n = 8$ at times (a) $t = 0$

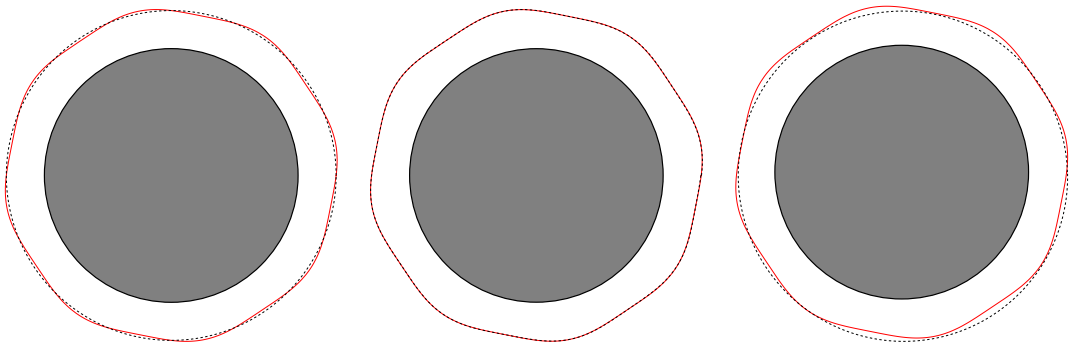

(a) (b) (c)

Figure 6.12: Terminal control of the interface s (dashed black line) towards the target shape (6.2.26) (solid red line) for $m = 0.02$ and $n = 8$ shown at times (a) $t = 0$ and (b) $t = t_{\mathrm{f}}$. (c) The uncontrolled interface s shown at time $t = t_{\mathrm{f}}$.

and (b) $t = t_{\mathrm{f}}$. Figure 6.12 (c) shows the uncontrolled system at time $t = t_{\mathrm{f}}$, at which time a bulge of liquid is oscillating around the cylinder. Note that the bulge is not immediately obvious in Figure 6.12 (c), but can be seen in a qualitatively similar situation in Figure 5.18 (in which $s_0 = 1.3$, compared to $s_0 = 1.30008$ for $m = 0.02$ and $n = 8$ by (6.2.23)).

As in Section 6.2.3, it is instructive to consider what effect varying the parameters Ca, d, and $\tilde{E}_b$ have on the success of the control mechanism. We consider control towards (6.2.27) for $m = 0.02$ and $n = 8$, the results for which are shown in Table 6.5 for various parameter values. Our results show that, as elucidated in Section 6.2.3, decreasing d results in more successful control, as reflected in the decrease in the terminal deviation measures shown in Table 6.5. As before, increasing $\tilde{E}_b$ yields more successful control whilst the total control cost of the control mechanism decreases overall. For this choice of target shape, varying Ca does not significantly increase nor decrease the terminal deviation measure, owing to the fact that we are considering a small amplitude ($m = 0.02$) which results in a small curvature. Hence, varying the strength of capillarity should not be expected to have a significant effect on the outcome of the control. As in the case of a uniform target shape described in Section 6.2.3, Table 6.5 indicates that for control towards (6.2.27) with $m = 0.02$ and $n = 8$, the most successful and computationally efficient control is afforded by choosing $Ca = 0.1570$, $\tilde{E}_b = 10$, and $d = 1.5$, resulting in the lowest terminal deviation measure ($\mathcal{U}_{\mathrm{t}} = 5.71670 \times 10^{-9}$), the lowest total control cost ($\mathcal{J}_{\mathrm{t}} = 5.71668 \times 10^{-9}$), and the fewest iterations required for

	Value	$\mathcal{J}_{\mathrm{t}}$	$\mathcal{U}_{\mathrm{t}}$	$\mathcal{U}_{\mathrm{t}}$ $(\tilde{E}_b = 0)$	$\mathcal{C}_\phi$	Iterations
Ca	0.03925	4.63569×10^{-8}	4.63558×10^{-8}	5.08644×10^{-3}	1.13583×10^{-12}	173
	0.0785	2.99222×10^{-8}	2.99215×10^{-8}	4.78354×10^{-3}	7.47456×10^{-13}	103
	0.1570	$\mathbf{2.38134 \times 10^{-8}}$	$\mathbf{2.38129 \times 10^{-8}}$	$\mathbf{4.82418 \times 10^{-3}}$	$\mathbf{4.44689 \times 10^{-13}}$	**160**
	0.3140	8.65348×10^{-8}	8.65326×10^{-9}	4.99219×10^{-3}	2.21438×10^{-13}	104
	0.6280	5.91139×10^{-8}	5.91137×10^{-8}	5.33214×10^{-3}	2.33224×10^{-13}	2509
d	1.5	5.71670×10^{-9}	5.71668×10^{-9}	4.82418×10^{-3}	1.16942×10^{-14}	73
	2	1.02333×10^{-8}	1.02332×10^{-8}	4.82418×10^{-3}	1.19602×10^{-13}	178
	2.5	$\mathbf{2.38134 \times 10^{-8}}$	$\mathbf{2.38129 \times 10^{-8}}$	$\mathbf{4.82418 \times 10^{-3}}$	$\mathbf{4.44689 \times 10^{-13}}$	**160**
	3	6.53168×10^{-8}	6.53156×10^{-8}	4.82418×10^{-3}	1.19687×10^{-12}	108
	3.5	9.50412×10^{-8}	9.50392×10^{-8}	4.82418×10^{-3}	1.97266×10^{-12}	104
$\tilde{E}_b$	1	9.44317×10^{-8}	9.44256×10^{-8}	4.82418×10^{-3}	6.11802×10^{-12}	221
	5	4.57904×10^{-8}	4.57894×10^{-8}	4.82418×10^{-3}	1.00164×10^{-12}	252
	10	$\mathbf{2.38134 \times 10^{-8}}$	$\mathbf{2.38129 \times 10^{-8}}$	$\mathbf{4.82418 \times 10^{-3}}$	$\mathbf{4.44689 \times 10^{-13}}$	**160**
	15	1.98683×10^{-8}	1.98680×10^{-8}	4.82418×10^{-3}	2.65672×10^{-13}	278
	20	1.28750×10^{-8}	1.28748×10^{-8}	4.82418×10^{-3}	1.86087×10^{-13}	180

Table 6.5: Results for controlling towards the target shape (6.2.27) for $m = 0.02$ and $n = 8$ for various values of Ca, d, and $\tilde{E}_b$: the total cost of the control (6.2.4), the terminal deviation measure $\mathcal{U}_{\mathrm{t}}$ (6.2.5), the uncontrolled terminal deviation measure, the cost of the control mechanism (6.2.2), and the number of iterations required to determine the optimal control. The results for the original parameter values $Ca = 0.157$, $d = 2.5$, and $\tilde{E}_b = 10$ are highlighted in bold.

convergence (73).

6.2.4.2 Varying m

In this section, we investigate the effect of varying m for a fixed n on the success of the control. Table 6.3 shows that $n = 8$ is one of the highest wavenumbers which affords successful control for all amplitudes m that we have considered (in the sense that the control mechanism is successful for all m considered and does not diverge). Hence, to investigate the effect of increasing the amplitude m, we fix the wavenumber n as $n = 8$ and consider amplitudes $m = 0.02, 0.04, 0.06$, and 0.08. The entries in Table 6.6 contain the amplitude m, the terminal deviation measure $\mathcal{U}_{\mathrm{t}}$ (6.2.5), the uncontrolled terminal deviation measure, the total cost of the control $\mathcal{J}_{\mathrm{t}}$ (6.2.4), and the number of iterations required to determine the optimal control. Increasing m results in an increase in the terminal deviation measure as expected, which is at least four orders of magnitude smaller than the deviation measure in the corresponding uncontrolled cases for all m considered. Increasing m also results in an increase in the total control cost. Figures 6.13 (a)

m	$\mathcal{J}_\mathrm{t}$	$\mathcal{U}_\mathrm{t}$	$\mathcal{U}_\mathrm{t}$ $(\widetilde{E}_b = 0)$	$\mathcal{C}_\phi$	Iterations
0.02	2.38134×10^{-8}	2.38129×10^{-8}	4.82333×10^{-3}	4.44689×10^{-13}	160
0.04	1.19042×10^{-7}	1.19042×10^{-7}	8.62278×10^{-3}	5.02048×10^{-13}	180
0.06	7.68039×10^{-7}	7.68039×10^{-7}	1.49572×10^{-2}	4.87538×10^{-13}	92
0.08	3.86916×10^{-6}	3.86916×10^{-6}	2.38296×10^{-2}	6.15693×10^{-13}	102

Table 6.6: Results for controlling towards the target shape (6.2.27) for $n = 8$ with $m = 0.02, 0.04, 0.06$, and 0.08: the total cost of the control (6.2.4), the terminal deviation measure $\mathcal{U}_\mathrm{t}$ (6.2.5), the uncontrolled terminal deviation measure, the cost of the control mechanism (6.2.2), and the number of iterations required to determine the optimal control.

and (c) show the interfacial radius s (shown as the dashed black line) with the target shape (6.2.27) (shown as the thick red line), and Figures 6.13 (b), and (d) show ϕ_d at the final time $t = t_\mathrm{f}$ (shown as the dashed black line) for (a), (b) $m = 0.04$ and (c), (d) $m = 0.08$. In particular, Figures 6.13 (b) and (d) show that control towards target shapes with larger amplitudes requires a larger electric potential difference.

Figure 6.14 shows the evolution of (a), (b) the interfacial radius s and (c), (d) the electric potential ϕ_d for $n = 8$ and $m = 0.08$ over the time intervals (a), (c) $19.5 \leq t \leq t_\mathrm{f}$ and (b), (d) $19.955 \leq t \leq t_\mathrm{f}$, where the thick red line highlights the final time $t = t_\mathrm{f}$. Figures 6.14 (b) and (d) show s and ϕ_d at the final 10 time steps, respectively. In particular, Figure 6.14 shows that s converges successfully towards the desired target shape as t approaches t_f, and ϕ_d peaks before the end of the time interval before subsequently decreasing.

Figure 6.15 shows the deviation (6.2.25) of the interfacial radius from the target shape (6.2.27) over time in both the uncontrolled (shown as the dotted line) and the controlled (shown as the dashed line) cases, along with ϕ_avg (shown as the dot-dashed line) for $n = 8$ with (a) $m = 0.04$ and (b) $m = 0.08$. The small values of the deviation (6.2.25) at time $t = t_\mathrm{f}$ confirm that the interface has been successfully controlled towards the desired target shapes. In particular, Figure 6.15 shows that the deviation measures are higher for $m = 0.08$. Likewise, as m increases, the maximum value of ϕ_avg increases from 4.1138 for $m = 0.04$ to 4.8753 for $m = 0.08$. The successful control of the interface towards the target shape (6.2.27) is shown in Figure 6.16 for $n = 8$ and (a)–(c) $m = 0.04$ and (d)–(f) $m = 0.08$ at times (a), (d) $t = 0$ and (b), (e) $t = t_\mathrm{f}$. Figures 6.16 (c) and (f) show the uncontrolled system

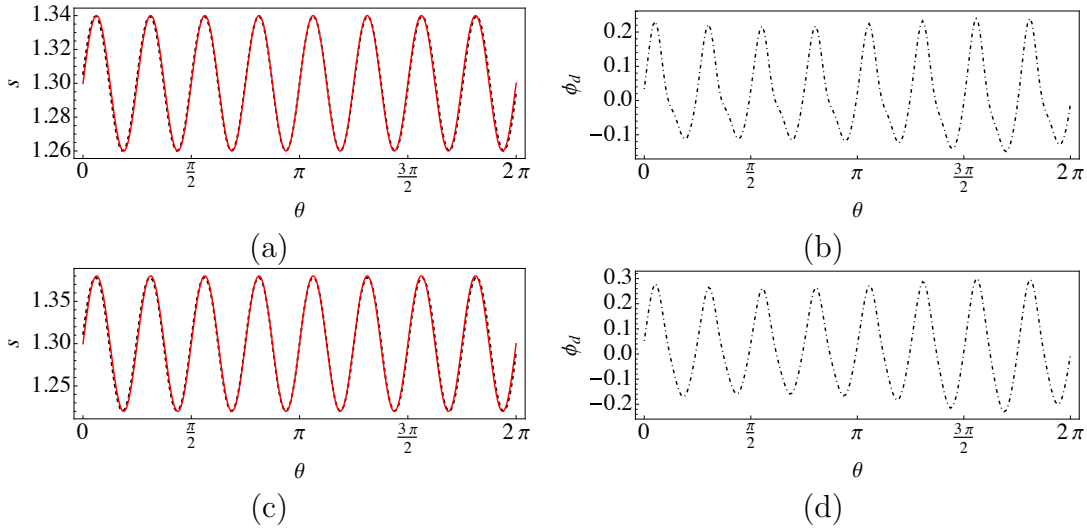

Figure 6.13: (a), (c) The interfacial radius s (dashed black line) and the target shape (6.2.27) (solid red line) and (b), (d) the electric potential ϕ_d (dot-dashed black line) shown at the final time $t = t_{\mathrm{f}}$ for $n = 8$ and (a), (b) $m = 0.04$ and (c), (d) $m = 0.08$.

at time $t = t_{\mathrm{f}}$.

6.2.5 Square target shape

In this section, we demonstrate the extent of the capabilities of the control mechanism by controlling the interfacial radius towards a square target shape. In particular, we choose

$$s_{\mathrm{targ}} = 1.2 \sec\left(\frac{1}{2}\arcsin\left[\sin\left(2\theta\right)\right]\right), \tag{6.2.28}$$

which represents a square with sides of length 2.4 which do not touch the surface of the cylinder. In order to increase the likelihood of the control mechanism being successful, throughout this section in our calculations we use the alternative reformulation of the Lagrangian described in Appendix G. In addition, we do not use the Polak-Ribière method to determine the descent direction because in our numerical investigations we found that it was resulting in many unsuccessful calculations. Instead, we use the method of steepest descent as described in Section 1.7.2.2. There is no clear explanation for the unfavourable outcome when using the Polak-Ribière method, other than the fact that, as explained in Section 1.7.2.3, its derivation is heuristic, and hence there is no guarantee that it will be of benefit

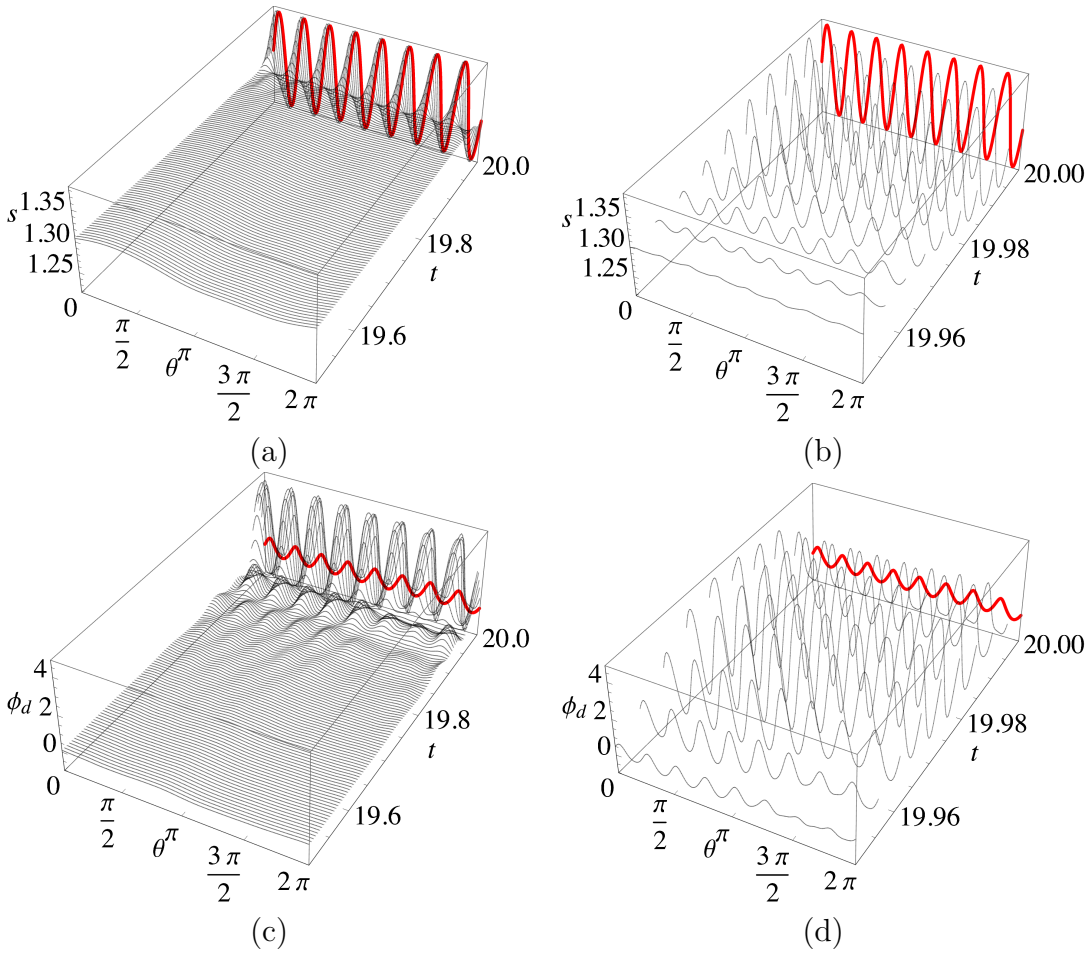

Figure 6.14: Terminal control of the thick-film WRIBL model towards the target shape (6.2.27) for $m = 0.08$ and $n = 8$. The solid black lines show the evolution of (a), (b) the interfacial radius s and (c), (d) the electric potential ϕ_d for (a), (c) $19.5 \leq t \leq t_{\rm f}$ and (b), (d) $19.955 \leq t \leq t_{\rm f}$ at times $t = 19.500, 19.505, \ldots, t_{\rm f}$. The thick red line highlights the final time $t = t_{\rm f}$.

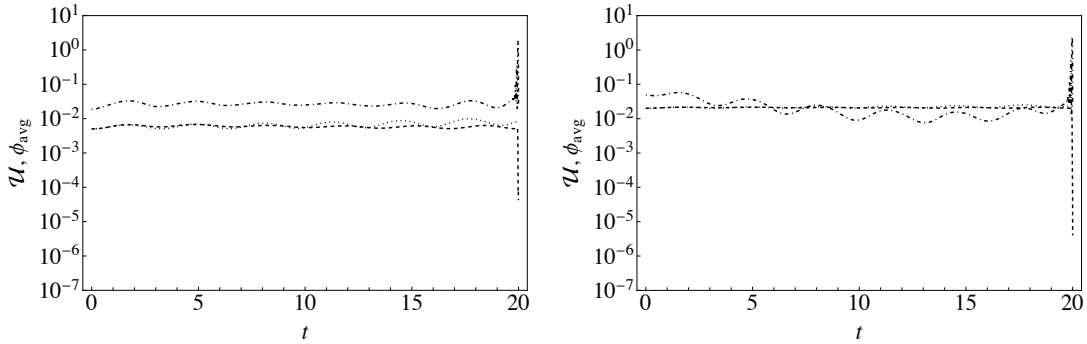

Figure 6.15: Semi-log plots of the deviation (6.2.25) of the uncontrolled interfacial radius (dotted line) and the controlled interfacial radius (dashed line) from the target shape (6.2.27) and the average of the electric potential ϕ_{avg} (dot-dashed line) over time for $n = 8$ and (a) $m = 0.04$ and (b) $m = 0.08$.

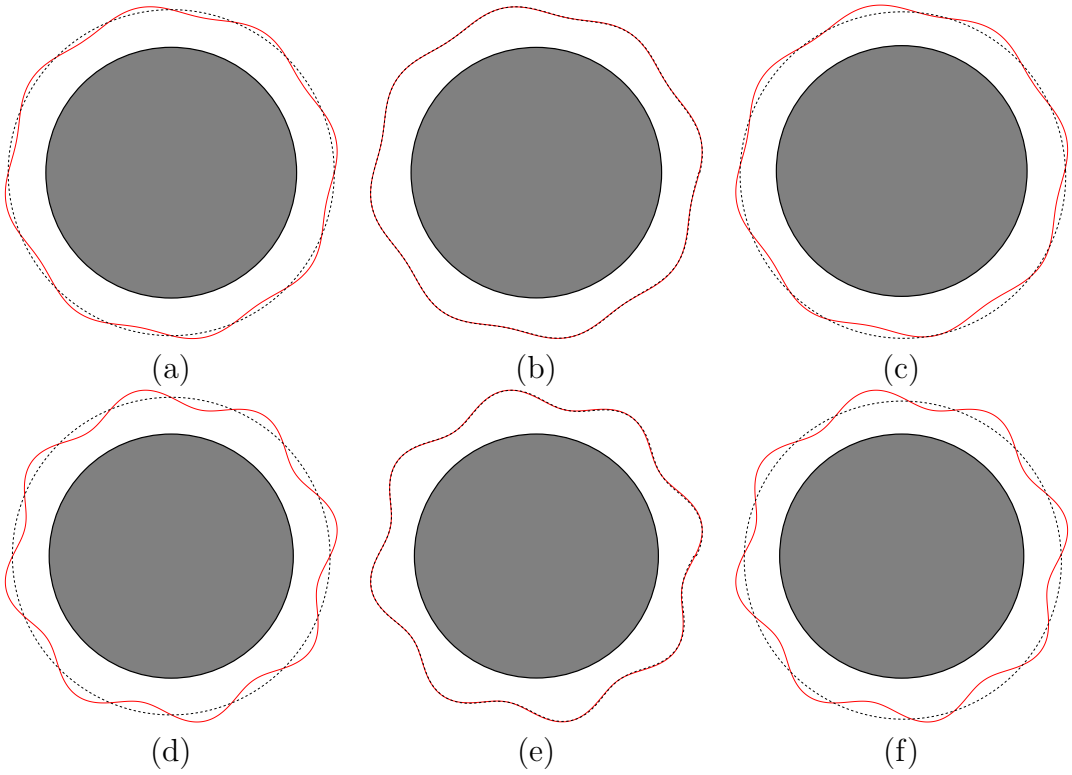

Figure 6.16: Terminal control of the interface s (dashed black line) towards the target shape (6.2.27) (solid red line) for $n = 8$ and (a)–(c) $m = 0.04$ and (d)–(f) $m = 0.08$, shown at times (a), (d) $t = 0$ and (b), (e) $t = t_{\text{f}}$. (c), (f) The uncontrolled interface s at time $t = t_{\text{f}}$.

$\mathcal{J}_{\mathrm{t}}$	$\mathcal{U}_{\mathrm{t}}$	$\mathcal{U}_{\mathrm{t}}$ $(\tilde{E}_b = 0)$	$\mathcal{C}_\phi$	Iterations
1.71545×10^{-3}	1.71545×10^{-3}	1.50986×10^{-1}	6.54644×10^{-13}	134

Table 6.7: Results for controlling towards the target shape (6.2.28): the total cost of the control (6.2.4), the terminal deviation measure $\mathcal{U}_{\mathrm{t}}$ (6.2.5), the uncontrolled terminal deviation measure, the cost of the control mechanism (6.2.2), and the number of iterations required to determine the optimal control.

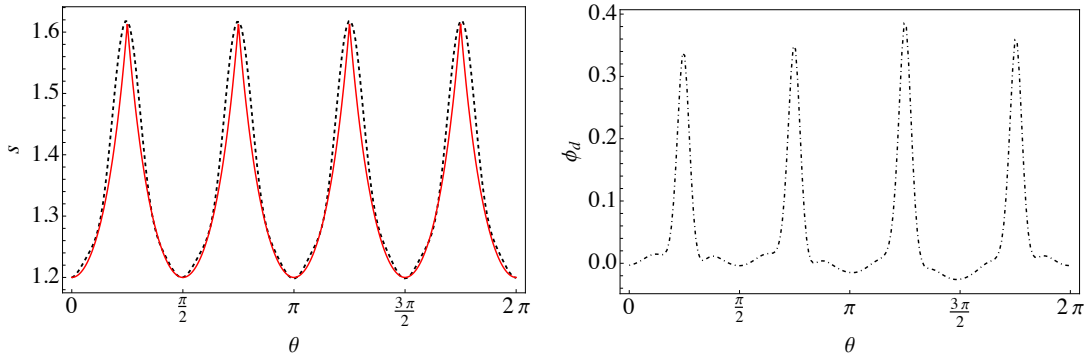

(a) (b)

Figure 6.17: (a) The interfacial radius s at the final time $t = t_{\mathrm{f}}$ (dashed black line) and the target shape (6.2.28) (solid red line). (b) The electric potential ϕ_d (dot-dashed black line) at the final time $t = t_{\mathrm{f}}$.

in any particular situation [245].

The results are given in Table 6.7. In this instance, the optimal control procedure converged after 134 iterations, which had a runtime of approximately 1.51 hours in wall-clock time. The total control cost was $\mathcal{J}_{\mathrm{t}} = 1.71545 \times 10^{-3}$ and the terminal deviation measure was $\mathcal{U}_{\mathrm{t}} = 1.71545 \times 10^{-3}$, an improvement upon the terminal deviation measure in the uncontrolled case which was $\mathcal{U}_{\mathrm{t}} = 1.50985 \times 10^{-1}$. The terminal deviation measure is at least three orders of magnitude larger than the terminal deviation measures for all of the cases considered in Sections 6.2.3 and 6.2.4, owing to the significantly more difficult target shape considered in this section due to the sharp corners that are required by the square. The interfacial radius at the final time $t = t_{\mathrm{f}}$ is shown in Figure 6.17 (a) as the dashed black line along with the target shape (6.2.28) which is shown as the thick red line. The match with the target shape is imperfect, as expected given that corner configurations are not easily supported by capillarity and electrostatic effects. Despite this, the control is fairly successful, clearly replicating the general form of the square.

The electric potential ϕ_d at the final time $t = t_\mathrm{f}$ is shown in Figure 6.17 (b), which has sharp peaks corresponding to where the corners are desired.

Figure 6.18 shows the evolution of (a), (b) the interfacial radius s and (c), (d) the electric potential ϕ_d over the time intervals (a), (c) $19.5 \leq t \leq t_\mathrm{f}$ and (b), (d) $19.955 \leq t \leq t_\mathrm{f}$, where the thick red line highlights the final time $t = t_\mathrm{f}$. Additionally, Figures 6.18 (c) and (d) show that the absolute value of ϕ_d never exceeds, or even comes close to, $\phi_{d\mathrm{max}}$ (6.2.19). The deviation measures (6.2.25) for both the uncontrolled (shown as the dotted line) and the controlled (shown as the dashed line) interfacial radius are shown in Figures 6.19 (a) and (b), respectively. As before, the terminal control mechanism acts only near the end of the time interval. This can be seen from Figure 6.19 (b) which shows that the deviation measure begins a steep decline to its final value after $t \approx 19.8$. Similarly, Figures 6.19 (c) and (d) show the average electric potential ϕ_avg over time, demonstrating its sharp increase close to $t = t_\mathrm{f}$, followed by the sharp decline before the final time is reached. The system is shown in Figure 6.20 at times (a) $t = 0$ and (b) $t = t_\mathrm{f}$, compared with the desired target shape (shown as the red line). As discussed previously, the match is imperfect, as the control mechanism struggles to reproduce the sharp corners of the square. However, it is still a significant improvement upon the uncontrolled interfacial radius at time $t = t_\mathrm{f}$, as shown in Figure 6.20 (c) in which the bulge of liquid is rotating around the cylinder.

Table 6.8 contains the results of the control mechanism for various values of Ca, d, and $\tilde{E}_b$, wherein hyphens indicate instances in which the control mechanism was unsuccessful. As elucidated in Section 6.2.3, to a certain point, decreasing d helps the control mechanism as this results in an increase in the strength of the electric field. However, when d is too small, outer contact can occur (see, for example, the unsuccessful control for $d = 1.5$ in Table 6.8). Note that there are other instances of unsuccessful control in Table 6.8 for which there is not such a clear explanation. We endeavour to explain these in Section 6.2.6.

6.2.6 Discussion of unsuccessful control calculations

In this section, we discuss some of the possible causes of unsuccessful control calculations which were identified in Sections 6.2.3–6.2.5

Unsuccessful control can correspond to a variety of issues in which the Newton–Raphson iteration procedure for the time-stepping (see Appendix A) does not

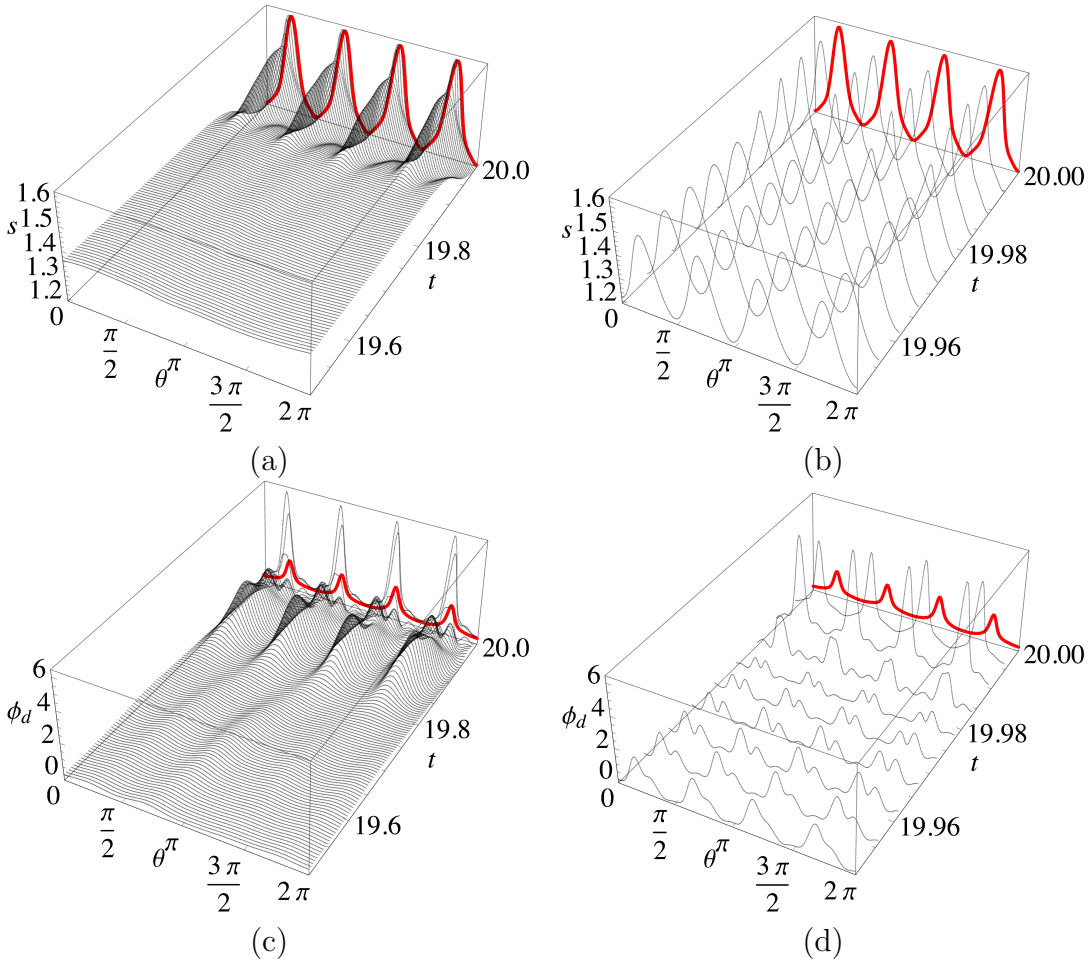

Figure 6.18: Terminal control of the thick-film WRIBL model towards the target shape (6.2.28). The solid black lines show the evolution of (a), (b) the interfacial radius s and (c), (d) the electric potential ϕ_d for (a), (c) $19.5 \leq t \leq t_{\rm f}$ at times $t = 19.500, 19.505, \ldots, t_{\rm f}$ and (b), (d) $19.955 \leq t \leq t_{\rm f}$ at times $t = 19.955, 19.660, \ldots, t_{\rm f}$. The thick red line highlights the final time $t = t_{\rm f}$.

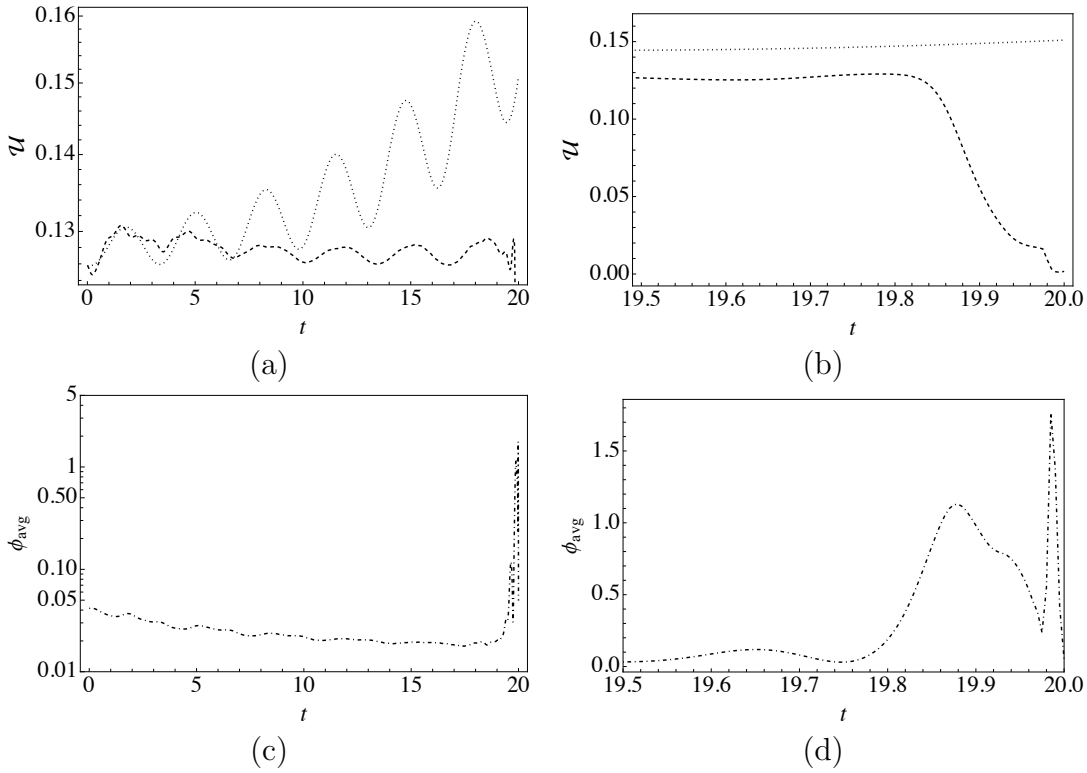

Figure 6.19: (a), (b) The deviation (6.2.25) of the uncontrolled interfacial radius (dotted line) and the controlled interfacial radius (dashed line) from the target shape (6.2.28) over time. (c), (d) The average of the electric potential ϕ_{avg} (dot-dashed line) over time. Evolution shown at times (a), (c) $0 \leq t \leq t_{\text{f}}$ and (b), (d) $19.5 \leq t \leq t_{\text{f}}$.

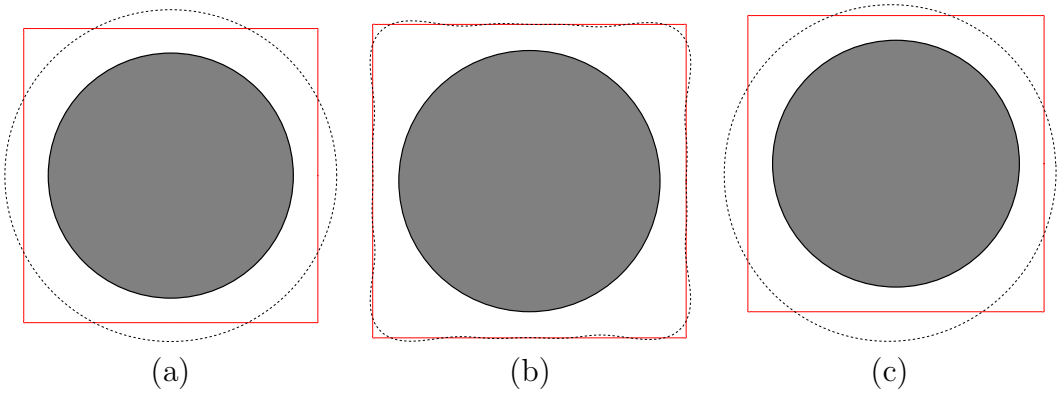

Figure 6.20: Terminal control of the interface s (dashed black line) towards the target shape (6.2.28) (solid red line) shown at times (a) $t = 0$ and (b) $t = t_{\text{f}}$. (c) The uncontrolled interface s at time $t = t_{\text{f}}$.

	Value	$\mathcal{J}_\mathrm{t}$	$\mathcal{U}_\mathrm{t}$	$\mathcal{U}_\mathrm{t}$ ($\tilde{E}_b = 0$)	$\mathcal{C}_\phi$	Iterations
	0.03925	1.89810×10^{-2}	1.60514×10^{-1}	1.89810×10^{-2}	1.43589×10^{-12}	75
	0.0785	6.35178×10^{-3}	1.53180×10^{-1}	6.35178×10^{-3}	1.01627×10^{-12}	77
Ca	**0.1570**	$\mathbf{1.71545 \times 10^{-3}}$	$\mathbf{1.50986 \times 10^{-1}}$	$\mathbf{1.71545 \times 10^{-3}}$	$\mathbf{6.54644 \times 10^{-13}}$	**134**
	0.3140	–	–	–	–	–
	0.6280	4.82623×10^{-2}	1.67989×10^{-1}	4.82623×10^{-2}	2.34934×10^{-13}	30
	1.5	–	–	–	–	–
	2	6.47903×10^{-2}	1.50986×10^{-1}	6.47903×10^{-2}	1.22684×10^{-13}	43
d	**2.5**	$\mathbf{1.71545 \times 10^{-3}}$	$\mathbf{1.50986 \times 10^{-1}}$	$\mathbf{1.71545 \times 10^{-3}}$	$\mathbf{6.54644 \times 10^{-13}}$	**134**
	3	1.70838×10^{-3}	1.50986×10^{-1}	1.70838×10^{-3}	1.64956×10^{-12}	297
	3.5	3.69771×10^{-3}	1.50986×10^{-1}	3.69771×10^{-3}	3.06797×10^{-12}	151
	1	2.23722×10^{-3}	1.50986×10^{-1}	2.23722×10^{-3}	4.70667×10^{-12}	116
	5	–	–	–	–	–
$\tilde{E}_b$	**10**	$\mathbf{1.71545 \times 10^{-3}}$	$\mathbf{1.50986 \times 10^{-1}}$	$\mathbf{1.71545 \times 10^{-3}}$	$\mathbf{6.54644 \times 10^{-13}}$	**134**
	15	–	–	–	–	–
	20	1.67844×10^{-3}	1.50986×10^{-1}	1.67844×10^{-3}	3.90000×10^{-13}	155

Table 6.8: Results for controlling towards the target shape (6.2.28) for various values of Ca, d, and $\tilde{E}_b$: the total cost of the control (6.2.4), the terminal deviation measure $\mathcal{U}_\mathrm{t}$ (6.2.5), the uncontrolled terminal deviation measure (i.e., for $\tilde{E}_b = 0$), the cost of the control mechanism (6.2.2), and the number of iterations required to determine the optimal control. The results for the original parameter values $Ca = 0.157$, $d = 2.5$, and $\tilde{E}_b = 10$ are highlighted in bold.

converge. In our calculations, we have observed two distinct instances of this occurring: the first case is when the algorithm outlined in Figure 6.3 fails at one of the steps and is subsequently terminated, and the second case is when the iteration becomes trapped in a local minimum.

In the latter case, the unsuccessful calculations could be reflective of an initial guess ϕ_{d_0} that is too far from the true solution, or in an unfavorable region of parameter space, in which the gradient descent calculations remain trapped and cannot subsequently converge towards the global minimum (or a more suitable local minimum). On the other hand, the inability to converge towards the target shape (but still remaining relatively close) could simply be a representation of the fact that not all target shapes are attainable. It is, of course, to be expected that the convergence becomes worse for target shapes with sharper interfaces due to the fact that there are many regularisation mechanisms present in the WRIBL model (e.g., capillarity) which render it difficult for the control mechanism to produce sharp interfaces.

In the former case, the rationale is less straightforward. Whilst we cannot, at this stage, definitively exclude the possibility that these instances of unsuccessful

control are due to an error in our code, we note that traversing this parameter space is challenging due to its non-smooth nature (as mentioned previously, certain controls can cause outer contact and consequential failure of the forwards simulation) and it is possible that solutions exist that the gradient descent method is unable to find. The gradient descent calculations can end up in a region of parameter space in which the adjoint calculation is not stable. Notably, the adjoint equations are linear, and so can have catastrophic instabilities. The optimal control problem considered in this chapter is a novel problem of a difficulty which has not been observed in other systems due to their simpler state spaces and governing equations (see, for example, Boujo and Sellier [243] and Wray *et al.* [244]). Indeed, whilst the governing PDEs themselves (a coupled triplet of two initial value and one boundary value problems) are both extremely stiff (which renders it difficult to obtain an accurate and stable solution using explicit time-stepping methods) and highly nonlinear (resulting in their computation being challenging, especially to solve on the sub-second timescale required), it is actually the unusual complexity of our state space that proves most problematic. The system exhibits a variety of modes of failure (including the potential for multivaluedness, outer contact, and even changes in topology) which result in the state space being not only non-smooth, but actually not simply-connected. Due to the complexity of the state space of the problem at hand, it is not, as yet, possible to directly relate individual instances of termination to the occurrence of any of these individual failure modes with certainty. In contrast, the parameter regime of Wray *et al.* [244] was carefully chosen so as to avoid the worst of these issues. Our algorithm traverses state space via a standard conjugate gradient method, which had to be modified specially to cope with the absence of smoothness. For example, this proves problematic in line searches where the existence of a local minimum is no longer guaranteed. We are unaware of any comparably complicated state spaces having been explored previously.

6.3 Concluding remarks

In this chapter, we have shown that the electric field can be utilised as a mechanism by which to successfully control the thick-film system governed by the WRIBL model that was derived in Chapter 2 and analysed in Chapter 5. In particular, the fast computations afforded by the WRIBL model have allowed us to solve

complex, challenging optimisation problems rapidly, which could have important consequences for applications in industrial settings.

Feedback control was applied to the system in Section 6.1, in which it was demonstrated that the electric field can be used to reduce the maximum interfacial radius, with the aim of controlling the interfacial shape towards a uniform state. The control was imposed by employing a potential which dictates that the electric field is switched on only where the interfacial radius deviates from the initial interfacial radius by more than a certain tolerance. Our results showed that the control mechanism significantly reduces the value of the maximum interfacial radius compared to the uncontrolled case.

Optimal control was applied to the system in Section 6.2, in which we formulated and implemented a robust control framework designed to finely control the interfacial radius towards some specified target shapes. The framework of the general optimal control problem was formulated in Section 6.2.1 and was subsequently specialised to focus on terminal control. We demonstrated that, in general, the terminal control mechanism acts only near the end of the time interval, as there is less value in reaching the target shape early in the time interval than there is in keeping the controls weak until t approaches t_{f}. One of the key results of this section is the fact that the average of the electric potential at the outer electrode ϕ_{avg} decreases sharply near the final time, for which we hypothesised two possibilities. The first possibility is that near the end of the time interval the control mechanism has manipulated the interfacial radius into a shape which is close enough to the target that capillarity can drive the interfacial radius towards the target over the final time steps. The second possibility, which we consider to be the more likely explanation, is that there is a time lag between the imposition of a particular control and the effect that it has, which we believe is partially due to the fact that the interface cannot transition instantaneously and so transitions smoothly from the point at which the control is imposed, but also due to the effect of inertia which exacerbates this time lag.

The iterative optimisation procedure was found to be successful in general in controlling towards the three different types of target shapes that we considered, namely, a uniform shape in Section 6.2.3, a family of nonuniform shapes in Section 6.2.4, and a square shape in Section 6.2.5. We demonstrated successful control of the interface towards its initial uniform radius in Section 6.2.3, yielding a terminal deviation measure five orders of magnitude smaller than in the uncontrolled case.

The potential is required to be stronger where the film is thinner, in turn reducing the maximum height of the bulge of liquid due to mass conservation. A parametric study in (m, n) parameter space was conducted in Section 6.2.4, in which we demonstrated that increasing m or n both result in less successful control. Overall, the control mechanism was shown to be very successful even for wavelengths far into the challenging short-wave regime. Finally, in Section 6.2.5, we demonstrated control of the interface towards a square shape. This final section was the most stringent test of the control mechanism thus far, in which it was shown that the match with the target shape is imperfect (as expected, given that corner structures are not easily supported by capillary and electrostatic effects). Nevertheless, the control was deemed successful as it effectively achieved a shape that can be described as approximately square, still resulting in an overall decrease in the terminal deviation measure by two orders of magnitude compared to the uncontrolled case. In general, it was found that weakening capillarity, increasing the electric potential difference, or moving the outer electrode closer to the interface all result in more successful control.

Finally, we conclude by reiterating that the optimal control problem at hand is a novel problem of a difficulty which has not been observed in other systems [243, 244] due to the unusual complexity of our state space. The thick-film coating flow system in the presence of an electric field exhibits a variety of modes of failure, including potentially multivaluedness, outer contact, and changes in topology, all of which result in the state space being both non-smooth and not simply-connected. We are unaware of any comparably complicated state spaces having been explored previously. Further investigation of this complex optimal control problem is anticipated to be an intriguing and potentially fruitful avenue for future study.

Chapter 7

Conclusions and further work

In this chapter, we conclude the work presented in this thesis. In particular, in Section 7.1, we summarise the main results and conclusions of each chapter, and in Section 7.2, we outline some possible directions for further study.

7.1 Conclusions

This thesis has considered the reduced-order modelling of electrohydrodynamic flows on a circular cylinder. Specifically, we have modelled and investigated the dynamics of a two-dimensional film of a perfectly conducting Newtonian liquid coating a horizontal circular electrode in the cases both in which the film is thin and in which it is thick.

We began by formulating and modelling the system in Chapter 2. In the first half of Chapter 2, we used the classical lubrication approximation to derive the equation governing the system in the case in which the film is thin, which incorporates the effects of rotation, gravity, viscosity, capillarity, and Maxwell stress. We subsequently analysed the dynamics of the thin-film system in Chapters 3 and 4. In the second half of Chapter 2, we used the long-wave methodology in conjunction with the WRIBL method to derive a model (referred to throughout this thesis as the WRIBL model) which is valid for the case in which the film is thick, along with three candidate models for the electric potential. The WRIBL model incorporates the effects of rotation, gravity, viscosity, capillarity, Maxwell stress, streamwise viscous dissipation, and inertia (including centrifugation). The dynamics of the thick-film system, including analysis of the candidate electrostatic

models, were subsequently analysed in Chapters 5 and 6.

As an essential precursor to the thin-film electrostatic case, a complete description of thin-film draining flow in the absence of an electric field was derived in Chapter 3. We found that at early times, capillarity is negligible and the film thickness deviates from uniformity only slightly due to gravity. At late times, three regions of qualitatively different behaviour emerge, namely, a draining region on the upper part of the cylinder (in which capillarity is negligible and the film thins due to gravity) and a pendant-drop region on the lower part of the cylinder (in which there is a quasi-static balance between gravity and capillarity), joined by a narrow inner region. We showed that the matching between the draining and pendant-drop regions occurs via the inner region, in which the film has a capillary-ripple structure consisting of an infinite sequence of alternating dimples (in which gravity is negligible) and ridges (in which gravity and capillarity are comparable). The dimples and ridges become apparent in turn as the draining proceeds, and only the first few dimples and ridges are likely to be discernible for large but finite times. However, we have shown that there is likely to be a considerable period of time during which the present asymptotic solution provides a good description of the flow.

In Chapter 4, we devoted our attention to analysing the dynamics of thin-film coating flow in the presence of an electric field. Linear stability analyses were performed in two analytically tractable special cases, through which it was shown that electrostatic effects cause instability. We found that, as the film evolves, the destabilising electrostatic effects lead to the formation of bulges of liquid around the circumference of the cylinder. A parametric study in (γ, E_b) parameter space was performed which identified the four distinct behaviours of the system: steady states, periodic states, outer contact, and transient states. The regions in parameter space in which different behaviours occur were identified, and a numerical investigation of the interfacial dynamics of each behaviour was performed. We showed that a strong electric field or large electric potential difference can drive the system towards outer contact, in which the interface touches the outer electrode in a finite time. Draining flow was analysed by means of a generalisation of the analysis presented in Chapter 3 to include electrostatic effects. At early times, electrostatic effects are weak, and at late times, the same three distinct regions of behaviour arise as in the absence of an electric field. Electrostatic effects are significant only in the pendant-drop region, in which there is a quasi-static bal-

ance between capillarity, gravity, and electrostatic effects when the electric field is weak. Finally, the large-time dynamics of the system were investigated in the case in which gravity and capillarity are both weak by means of a multiple-timescale analysis. It was found that when electrostatic effects enter the system at the same order as gravity, the solution is unconditionally unstable. However, when electrostatic effects are further weakened (such that they arise in the growth rate at the same order as capillarity) electrostatic effects destabilise the system only for sufficiently large electric potential differences.

In Chapter 5, we analysed the electrostatic modelling and dynamics of thick-film coating flow in the presence of an electric field. The candidate electrostatic models were compared numerically, from which we established that the interface model affords the most accurate solution for the electric potential. The evolution of the thick film in the presence of an electric field with a constant potential was studied, from which it was shown that (as in the case in which the film is thin) electrostatic effects destabilise the system, with a strong electric field or large electric potential difference driving the interface towards outer contact.

Finally, in Chapter 6, we analysed both the feedback and optimal electrostatic control of thick-film coating flow. In the former case, we demonstrated that a particular choice of potential can be used to significantly reduce the maximum interfacial radius. In the latter case, we formulated and implemented a robust optimal control framework designed to finely control the interfacial radius towards some specified target shape. We considered only terminal control, for which we found the iterative optimisation procedure to be successful in controlling towards a variety of uniform and nonuniform target shapes, even far into the challenging short-wave regime. The optimal control problem at hand has an unusually complex state space, owing to the fact that the present system exhibits a variety of modes of failure (such as, for example, potential multivaluedness, outer contact, and changes in topology), all of which yield a state space which is both non-smooth and not simply-connected. Further investigation into the use of an electric field as a control mechanism in the present system is vital at this early stage. However, the results presented in this chapter are highly promising.

7.2 Further work

The work presented in this thesis suggests many possible avenues for further study, some of which we now outline and discuss in detail.

Firstly, the models derived in Chapter 2 are all based on the assumption that the liquid is a perfect conductor, a simplified situation which is particularly amenable to analytical analysis. The system, and hence, the results obtained in this thesis, could therefore be made more general by considering both fluids to be leaky dielectrics. In this case, a non-zero electric field would also be present in the liquid region, and so one would be required to solve the electrostatic problem in both fluids due to the fact that the liquid would no longer simply obtain the potential of the inner electrode. As a result, tangential Maxwell stresses would be present. Specifically, a non-zero tangential Maxwell stress $E^T = E^T(\theta)$ (analogous to the normal Maxwell stress used throughout this thesis, E^N) would be included in all of the models derived in Chapter 2 (see, for example, Craster and Matar [203], Papageorgiou [163], and Keith [214]).

It would be of interest to examine the weighted residual formulation of the electrostatic models, preliminary calculations of which which are outlined in Appendix C. Due to time constraints, the performance of the two models derived in Appendix C has not yet been compared to that of the interface, electrode, and thick-film gradient models that were derived in Chapter 2, nor to numerical solutions of Laplace's equation (2.1.3). Further work should seek to carry out these comparisons in order to determine if the weighted residual electrostatic models offer greater accuracy in calculating the normal Maxwell stress.

The governing equations derived in Chapter 2 provide the basis for several obvious extensions. For example, it would be of interest to investigate what effect an electric field has on the dynamics of coating flow on other geometries, such as elliptical cylinders [150, 151], and to explore where in parameter space each behaviour occurs. Moreover, the two-dimensional model described in this thesis can be readily extended to three dimensions, which is an important step towards deriving a model which is more suitable for practical applications. This is particularly relevant for applications in electrostatic control, which, as discussed previously, undoubtedly has the potential to lend itself to a variety of industrial processes [178, 179, 184, 185]. Due to its increased complexity, the investigation of a three-dimensional system would likely have to be carried out numerically,

and would certainly have a significant computational cost. Nonetheless, all of the possible behaviours could be determined numerically, and it would be interesting to carry out a systematic parametric investigation (analogous to that which was carried out in Chapter 4) of where each behaviour occurs in parameter space in order to provide insights into the qualitative structure of the parameter space in comparison to that of the two-dimensional system.

The incorporation of other physical effects into the system could be another promising step towards making the model more general for use in industrial contexts, which often involve a multitude of other physical effects such as, for example, thermocapillary effects, viscosity stratification, multiphase flows, and chemical reactions. Thermocapillary effects have previously been incorporated in a planar weighted residual context by Ruyer–Quil *et al.* [278], but it would be non-trivial to extend these results to the cylindrical geometry considered in this thesis. The resulting model would be of particular interest because there are a number of industrially-relevant problems that will be immediately accessible: for example, many falling-film reactors require careful treatment of thermal effects. In addition, systems involving dissolved solute are ubiquitous in biochemical systems, however, the typical modelling (based on the work of Jensen and Grotberg [279]) relies on the assumption that the solute rapidly diffuses in the vertical direction. Instead, it is well-known that this does not happen in many physical processes, which actually exhibit significant vertical stratification (see, for example, Maki and Kumar [280]). It is anticipated that an appropriate application of the method of weighted residuals would provide an accurate model incorporating this vertical stratification.

Perhaps the most obvious direction for further work would be to compare the results of our numerical calculations with those from DNS. Of course, systematic parametric studies would be impractical as they would have a prohibitive computational cost. However, it would certainly be of great interest to investigate each individual behaviour further using DNS. In particular, it would be insightful to analyse how the approach to outer contact compares to that inferred from the models derived in this thesis. In addition, the investigation of multivalued states and interfacial rupture in the thick-film case in the presence of an electric field (both of which cannot currently be modelled using the WRIBL model) using DNS could be an interesting and insightful direction for further study. It would also be of particular interest to see to what extent the results presented in Chapter

3 for draining flow in the absence of an electric field still hold for non-thin films governed by the full Navier–Stokes equations.

It must be acknowledged that there is an obvious analytical investigation that we have neglected to carry out in this thesis, which is that of outer contact behaviour in the thin-film case. Indeed, in Chapter 4 (and, more generally, throughout this thesis), we have investigated outer contact behaviour only in a numerical sense. An analytical investigation of outer contact behaviour would be of interest, and is almost certainly tractable. It is anticipated that as the maximum film thickness approaches the outer electrode, the interface exhibits self-similar behaviour, and hence the investigation would be analytically tractable through the use of similarity solutions. Indeed, a related calculation was recently performed successfully by Keith [214] for the analogous "upper contact" behaviour in the planar case.

The results presented in Chapter 6 regarding the optimal electrostatic control of the system are perhaps those with the greatest scope for further work. The optimal control framework outlined in Section 6.2.1 was derived to be readily applicable to both terminal and regulation control; an obvious direction for further study is to investigate how the results obtained in Sections 6.2.3–6.2.5 differ when one instead uses regulation control. It is anticipated that such results will bear qualitative resemblance to those of Wray *et al.* [244] who, as discussed previously, considered an analogous optimal control problem in the planar case. In addition, as discussed previously, in future calculations the constraint $\phi_d \leq k\phi_{d_{\max}}$ should be imposed on the potential in order to prevent the electric field from violating the dielectric limit [244]. Throughout the optimal control calculations presented in this thesis, the control weight γ_ϕ was kept constant; it could therefore be of interest to analyse the effect of varying the value of the control weight on the outcome of the control (see, for example, Boujo and Sellier [243]). In addition, control to various other target shapes should be investigated in future studies. In particular, with industrial applications in mind, the optimal control framework presented in this thesis could be reformulated to maximise the interfacial area with the aim of optimising heat and/or mass transfer. It could also be of interest to instead use the rotation rate of the cylinder as the control mechanism. We anticipate the reformulation of the optimal control framework in this case to be a relatively straightforward process, owing to the fact that the dimensionless rotation rate ω could be allowed to vary temporally without requiring any other changes to the WRIBL model.

Finally, at present, we are unaware of any previous physical experiments against which the theoretical results derived in this thesis can be validated. We therefore hope that the work presented in this thesis might inspire such experiments in the future.

In summary, we believe that the results described in this thesis constitute a valuable contribution to the existing literature on coating flow, electrohydrodynamics, and control theory. However, there remains, of course, a plethora of interesting open questions which further work should endeavour to address.

Appendix A

Numerical schemes

In this appendix, we give the details of the code that was used to obtain numerical solutions of the thin-film governing equation (2.2.23) in Chapters 3 and 4, the WRIBL model (2.1.34), (2.3.66), (2.3.43) and (2.3.44) in Chapters 5 and 6, and the adjoint equations (6.2.14) in Chapter 6.

The code was implemented in C++ and is based on an existing implementation developed by one of the author's supervisors (Dr A. W. Wray), by whom previous iterations of this code have been successfully used to solve other problems (see, for example, [56] and [31]). It imposes periodic boundary conditions and uses the method of lines, in which the governing PDEs are discretised into a system of nonlinear ODEs using a second-order implicit centered-finite-difference method in space. For time integration, a combination of first-order (backwards Euler) and second-order (trapezoidal rule) methods was used. The Eigen C++ template library for linear algebra [281] was used to perform the linear algebra required to compute the Newton–Raphson iterations for the fully-implicit time-stepping.

In Section A.1, we give details of the uniform grid formulation of the code which was used in Sections 4.1, 4.2, and 4.4 and in Chapters 5 and 6. In Section A.2, we give details of the nonuniform grid formulation of the code which was used in Chapter 3 and in Section 4.3.

A.1 Uniform grid formulation

In this section, we outline the uniform grid formulation of the code that was used to obtain numerical solutions of the thin-film governing equation in Sections 4.1,

4.2, and 4.4 and the WRIBL model and adjoint equations in Chapters 5 and 6.

When solving the thin-film governing equation (2.2.23), the trapezoidal rule was used for the time integration. This method was chosen because it offers higher (second-order) accuracy when compared to the backwards Euler method (which offers only first-order accuracy) and is hence beneficial when solving the thin-film governing equation to late times, as is required in this thesis. A uniform grid was used with 1200 grid points, which was chosen to ensure that the calculations had converged spatially. The initial time step was set to be 0.001 and an adaptive time-stepping method was used to speed up the calculations. Specifically, after each time step (which we denote by ΔT), if H changed by less than 1% and $\Delta T < 0.01$, the time step was increased by 50%.

When solving the WRIBL model (2.1.34), (2.3.66), (2.3.43), and (2.3.44) and when solving the adjoint equations (6.2.14), the backwards Euler method was used for the time integration. This method was chosen because it offers greater numerical stability and is simpler to implement when compared to the trapezoidal rule when solving stiff and complex equations. In addition, we can afford a trade-off between stability and accuracy as we do not require solutions to the long-wave equations to be calculated to final times as late as those required when solving the thin-film model (see, for example, Chapter 6, in which the long-wave equations are solved until time $t_{\mathrm{f}} = 20$ compared to the final time $T = 10^4$ used in the thin-film parametric study in Section 4.2). A uniform grid was used with 300 grid points, chosen to ensure that the calculations had converged spatially, and 4000 time steps of fixed length 5×10^{-3}.

The spatial convergence of both the thin-film and long-wave versions of the code was verified. In particular, the number of grid points M was doubled and it was verified that the numerical results for M grid points differ imperceptibly, on the presented scale, from those of the simulation using $2M$ grid points. As an example, Figure A.1 shows the grid dependence for demonstrative examples of (a), (b) the thin-film variant of the code and (c), (d) the long-wave variant of the code. In particular, Figures A.1 (a) and (b) show the numerical solution of the thin-film governing equation (2.2.23) for the values $H_0 = 0.9$, $\gamma = 15$, $E_b = 10$, and $D = 5$ at time $T = 40$ (by which time the behaviour is classified as steady), corresponding, in particular, to the steady case shown in Figures 4.16 (a) and (c) for $E_b = 10$. Similarly, Figures A.1 (c) and (d) show the numerical solution of the WRIBL model (2.1.34), (2.3.66), (2.3.43), and (2.3.44) for the values $\omega = 0.5$,

$Ca = 0.157$, $\tilde{E}_b = 0.2$, $d = 2.5$, $Re = 3.76$, and $h_0 = 1.6$ at time $t = 1000$ (by which time a steady state is reached), corresponding, in particular, to the steady case shown in Figure 5.15 for $\tilde{E}_b = 0.2$. The insets in Figures 5.15 (b) and (d) show that the numerical results for M and $2M$ grid points are almost indistinguishable at the scale of interest in both the thin-film and long-wave variants of the code, and hence that the code has converged spatially to the desired level of accuracy for the respective problems.

A.2 Nonuniform grid formulation

In this section, we outline the nonuniform grid formulation of the code that was used in Chapter 3 and in Section 4.3 to enable computations to be performed up to late times (specifically, up to $T = O(10^{11})$) whilst still resolving the fine spatial structures that occur. The version of the code described above in which the trapezoidal rule was used for the time integration was altered to use a standard nonuniform grid formulation. The grid spacing was reduced smoothly from 5×10^{-3} in the bulk of the domain to 10^{-6} within $\pi/18$ of the inner region (located at $\theta = \theta_{\mathrm{I}}$), with a smooth tanh interpolation between the two resolutions, resulting in 6879 grid points.

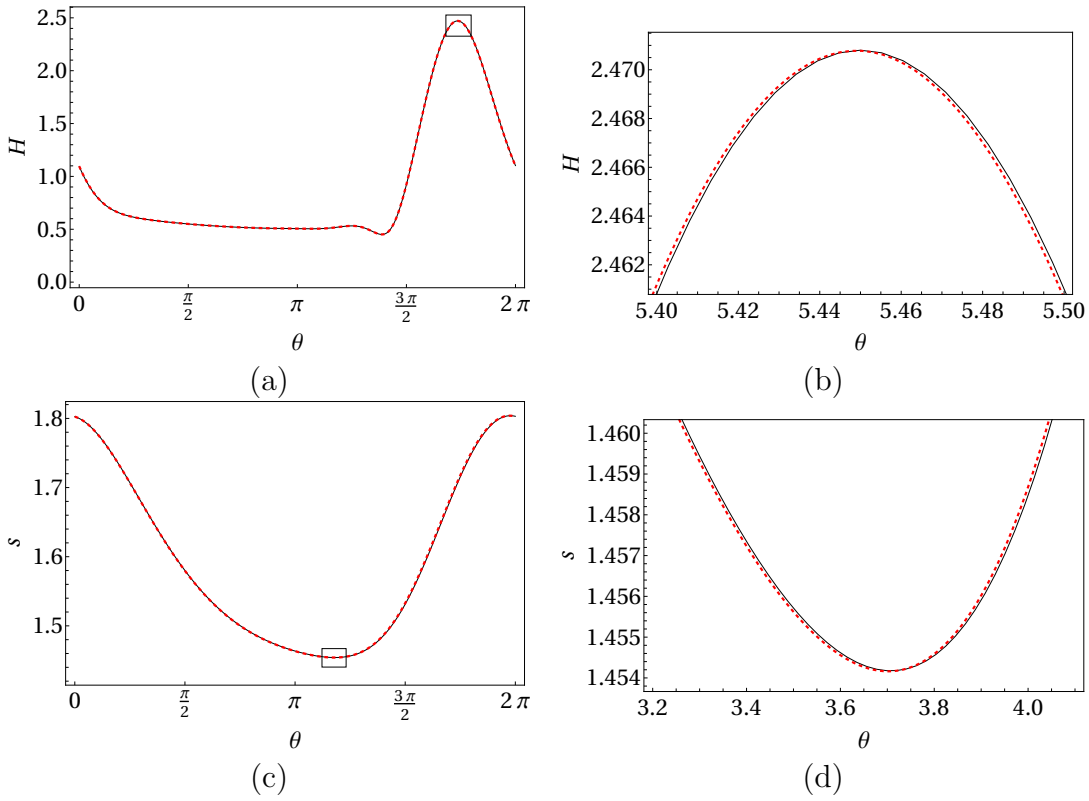

Figure A.1: Numerical solutions of (a) the thin-film governing equation (2.2.23) for the values $H_0 = 0.9$, $\gamma = 15$, $E_b = 10$, and $D = 5$ at time $T = 40$ and (b) the WRIBL model (2.1.34), (2.3.66), (2.3.43), and (2.3.44) for the values $\omega = 0.5$, $Ca = 0.157$, $\tilde{E}_b = 0.2$, $d = 2.5$, $Re = 3.76$, and $h_0 = 1.6$ at time $t = 1000$. The solid black lines correspond to the numerical solutions calculated using (a), (b) $M = 1200$ grid points and (c), (d) $M = 300$ grid points and the dashed red lines correspond to the numerical solutions for $2M$ grid points. The rectangles in (a) and (c) indicate the location of the enlargements shown in (b) and (d), respectively.

Appendix B

Thin-film electrostatic models

In this appendix, we derive thin-film versions of the electrostatic models derived in Section 2.3.2, namely, the electrode model, interface model, and thick-film gradient model.

We undo the long-wave scalings (2.3.1) and (2.3.2) and apply the thin-film scalings (2.2.1) to the electrode model (2.3.29) and (2.3.30) and the interface model (2.3.43) and (2.3.44), yielding the thin-film electrode model, namely,

$$\tilde{\Phi} = \tilde{\Phi}_D + (\tilde{R} - \tilde{D})f_1 + \frac{\epsilon}{2}(\tilde{D}^2 - \tilde{R}^2)f_1 + \frac{\epsilon^2}{6}(\tilde{R} - \tilde{D})\Big\{2(\tilde{D}^2 + \tilde{R}\tilde{D} + \tilde{R}^2)f_1 + (\tilde{D} - \tilde{R})\left[(\tilde{R} - \tilde{D})f_{1_{\theta\theta}} + 3\tilde{\Phi}_{D_{\theta\theta}}\right]\Big\} + O(\epsilon^3), \tag{B.0.1}$$

$$0 = \tilde{\Phi}_D + (\tilde{H} - \tilde{D})f_1 + \frac{\epsilon}{2}(\tilde{D}^2 - \tilde{H}^2)f_1 + \frac{\epsilon^2}{6}(\tilde{H} - \tilde{D})\Big\{2(\tilde{D}^2 + \tilde{H}\tilde{D} + \tilde{H}^2)f_1 + (\tilde{D} - \tilde{H})\left[(\tilde{H} - \tilde{D})f_{1_{\theta\theta}} + 3\tilde{\Phi}_{D_{\theta\theta}}\right]\Big\} + O(\epsilon^3), \tag{B.0.2}$$

and the thin-film interface model, namely,

$$\begin{aligned}\tilde{\Phi} &= (\tilde{R}-\tilde{H})g - \frac{\epsilon}{2}(\tilde{R}^2-\tilde{H}^2)g \\ &\quad + \frac{\epsilon^2}{6}(\tilde{R}-\tilde{H})\Big\{(\tilde{R}-\tilde{H})\left[6\tilde{H}_\theta g_\theta - (\tilde{R}-\tilde{H})g_{\theta\theta}\right] \\ &\quad + g\left[2(\tilde{R}^2+\tilde{H}\tilde{R}+\tilde{H}^2-3\tilde{H}_\theta^2)+3(\tilde{R}-\tilde{H})\tilde{H}_{\theta\theta})\right]\Big\} + O(\epsilon^3), \end{aligned} \tag{B.0.3}$$

$$\begin{aligned}\tilde{\Phi}_D &= (\tilde{D}-\tilde{H})g - \frac{\epsilon}{2}(\tilde{D}^2-\tilde{H}^2)g \\ &\quad + \frac{\epsilon^2}{6}(\tilde{D}-\tilde{H})\Big\{(\tilde{D}-\tilde{H})\left[6\tilde{H}_\theta g_\theta - (\tilde{D}-\tilde{H})g_{\theta\theta}\right] \\ &\quad + g\left[2(\tilde{D}^2+\tilde{H}\tilde{D}+\tilde{H}^2-3\tilde{H}_\theta^2)+3(\tilde{D}-\tilde{H})\tilde{H}_{\theta\theta})\right]\Big\} + O(\epsilon^3). \end{aligned} \tag{B.0.4}$$

We proceed as in Section 2.3.3.1 and perform a classical gradient expansion on both the thin-film electrode model (B.0.1) and (B.0.2) and the thin-film interface model (B.0.3) and (B.0.4) by expanding f_1 and g, respectively, as

$$f_1 = M_0 + \epsilon M_1 + \epsilon^2 M_2 + O(\epsilon^3), \quad g = N_0 + \epsilon M_1 + \epsilon^2 N_2 + O(\epsilon^3). \tag{B.0.5}$$

Note that, contrary to the expansions (2.3.45) used in Section 2.3.3.1, here we do include terms of odd power in ϵ since these do not turn out to be zero under the thin-film approximation. Substituting (B.0.5) into (B.0.2) and (B.0.4) yields

$$M_0 = N_0 = \frac{\tilde{\Phi}_D}{(\tilde{D}-\tilde{H})} \tag{B.0.6}$$

at $O(1)$, and using (B.0.6) yields

$$M_1 = N_1 = \frac{(\tilde{D}+\tilde{H})\tilde{\Phi}_D}{2(\tilde{D}-\tilde{H})} \tag{B.0.7}$$

at $O(\epsilon)$. Finally, using (B.0.6) and (B.0.7) yields

$$M_2 = \frac{1}{12}\left(4\tilde{H}_\theta\tilde{\Phi}_{D_\theta} + \tilde{\Phi}_D\left[\tilde{H} - \tilde{D} + \frac{4\tilde{H}_\theta^2}{\tilde{D}-\tilde{H}} + 2\tilde{H}_{\theta\theta}\right] + 4(\tilde{H}-\tilde{D})\tilde{\Phi}_{D_{\theta\theta}}\right),$$
$$N_2 = \frac{1}{12}\left(-8\tilde{H}_\theta\tilde{\Phi}_{D_\theta} + \tilde{\Phi}_D\left[\tilde{H} - \tilde{D} + \frac{4\tilde{H}_\theta^2}{\tilde{D}-\tilde{H}} - 4\tilde{H}_{\theta\theta}\right] - 2(\tilde{H}-\tilde{D})\tilde{\Phi}_{D_{\theta\theta}}\right) \tag{B.0.8}$$

at $O(\epsilon^2)$. Substituting (B.0.5) with (B.0.6)–(B.0.8) into (B.0.1) and (B.0.3) produces the same model, namely,

$$\begin{aligned}\tilde{\Phi} = &\left(\frac{\tilde{R}-\tilde{H}}{\tilde{D}-\tilde{H}}\right)\tilde{\Phi}_D + 3\epsilon\frac{(\tilde{D}-\tilde{R})(\tilde{R}-\tilde{H})}{\tilde{D}-\tilde{H}}\tilde{\Phi}_D \\ &+ \frac{\epsilon^2}{2}\frac{(\tilde{D}-\tilde{R})(\tilde{R}-\tilde{H})}{(\tilde{D}-\tilde{H})^3}\Big\{4(\tilde{D}-\tilde{H})(2\tilde{D}-\tilde{R}-\tilde{H})\tilde{H}_\theta\tilde{\Phi}_{D_\theta} \\ &+ \tilde{\Phi}_D\Big[\tilde{D}^2(\tilde{D}-4\tilde{R}) + \tilde{H}^3 + \tilde{H}^2(4\tilde{R}-\tilde{D}+2\tilde{H}_{\theta\theta}) + 2(2\tilde{D}-\tilde{R})(2\tilde{H}_\theta^2 + \tilde{D}\tilde{H}_{\theta\theta}) \\ &- \tilde{H}(\tilde{D}(\tilde{D}+8\tilde{R}) + 4\tilde{H}_\theta^2 + (6\tilde{D}-2\tilde{R})\tilde{H}_{\theta\theta})\Big] - 2(\tilde{D}+\tilde{R}-2\tilde{H})(\tilde{D}-\tilde{H}^2)\tilde{\Phi}_{D_{\theta\theta}}\Big\} \\ &+ O(\epsilon^3).\end{aligned} \tag{B.0.9}$$

Appendix C

Electrostatic modelling using a weighted residual approach

In this appendix, we derive two candidate electrostatic models using a weighted residual approach. The method followed in this section is analogous to that which was used in Section 2.3.3 to model the hydrodynamic problem.

As we recall, the leading-order problem for the potential ϕ is given by (2.1.36) and (2.3.13), namely,

$$\phi_{rr} + \frac{1}{r}\phi_r = 0, \quad \phi|_{r=d} = \phi_d, \quad \phi|_{r=s} = 0, \tag{C.0.1}$$

which has the solution (2.3.14), namely,

$$\phi = \phi_d \frac{\ln(r/s)}{\ln(d/s)}. \tag{C.0.2}$$

To obtain the solution for ϕ to higher orders, we project the solution for ϕ onto an appropriate set of basis functions $f_n(r)$ (for $n = 0, \ldots, N$), which have coefficients b_n (for $n = 0, \ldots, N$). We seek a solution for ϕ in the form of a series expansion based on a separation of variables,

$$\phi(r, \theta, \check{t}) = b_0(\theta, \check{t}) f_0(r) + \varepsilon^2 \sum_{n=2}^{N} b_n(\theta, \check{t}) f_n(r) + O(\varepsilon^4), \tag{C.0.3}$$

where we note that odd powers of ε are not included in (C.0.3) for the same reason as was outlined in Section 2.3.2. As explained previously, both in Section 1.2.5

and in Section 2.3.3, the key step in the method of weighted residuals is to take the inner product (2.3.52) of Laplace's equation (2.3.12) with a suitable weight function, which we denote here by $w_{\text{elec}} = w_{\text{elec}}(r, \theta, \check{t})$, which will be determined as part of the solution. In particular, this yields

$$\int_s^d r\, w_{\text{elec}} \left[\underbrace{\frac{1}{r}\left(r\phi_r\right)_r}_{(a)} + \underbrace{\varepsilon^2 \frac{1}{r^2}\phi_{\check{\theta}\check{\theta}}}_{(b)} \right] \mathrm{d}r = 0, \tag{C.0.4}$$

where term (b) can be calculated once the weight w_{elec} is determined. Evaluating term (a) in (C.0.4) yields

$$\begin{aligned}\int_s^d r\, w_{\text{elec}} \frac{1}{r}\left(r\phi_r\right)_r \mathrm{d}r = &\underbrace{w_{\text{elec}} r\phi_r|_{r=d}}_{(c)} - \underbrace{w_{\text{elec}} r\phi_r|_{r=s}}_{(d)} - \underbrace{\phi r (w_{\text{elec}})_r|_{r=d}}_{(e)} \\ &+ \underbrace{\phi r (w_{\text{elec}})_r|_{r=s}}_{(f)} + \underbrace{\int_s^d r\phi \frac{1}{r}\left[r(w_{\text{elec}})_r\right]_r \mathrm{d}r}_{(g)},\end{aligned} \tag{C.0.5}$$

where we have used two applications of integration by parts. By the continuity of potential at the interface (2.1.36), term (f) is exactly zero. Term (e) can be calculated once w_{elec} is determined. Analogous to the hydrodynamic problem, in which we choose to base our calculations on the physical quantity q rather than a_0 (see equations (2.3.53)–(2.3.55)), here it will be appropriate to base our calculations on the quantity

$$\Psi \equiv \phi_r|_{r=s}, \tag{C.0.6}$$

owing to the fact that the leading order Maxwell stress $-\left(\phi_r|_{r=s}\right)^2/2$ (2.3.15) is the quantity of interest. To remove the dependence of the term (a) on the b_n, we choose w_{elec} such that

$$\left(\frac{1}{r}\left(r w_{\text{elec}}\right)_r\right)_r = 0, \tag{C.0.7}$$

$$w_{\text{elec}}|_{r=d} = 0, \tag{C.0.8}$$

$$w_{\text{elec}}|_{r=s} = 1, \tag{C.0.9}$$

where the first condition (C.0.7) is chosen such that term (g) is zero, the second condition (C.0.8) is chosen such that term (c) is zero, and the final condition

(C.0.9) is chosen such that term (d) reduces to exactly Ψ. Solving (C.0.7) subject to (C.0.8) and (C.0.9) yields the weight function

$$w_{\text{elec}} = \frac{\ln(d/r)}{\ln(d/s)}. \tag{C.0.10}$$

In order to evaluate term (d) exactly, we write

$$\Psi \equiv \phi_r|_{r=s} = \frac{b_1}{s} + \epsilon^2 \sum_{n=2}^{N} b_n(\theta, \check{t})[(f_n)_r]_{r=s} + O(\varepsilon^4), \tag{C.0.11}$$

hence ϕ (C.0.3) is given by

$$\phi = b_0 + \left[\Psi - \epsilon^2 \sum_{n=2}^{N} b_n[(f_n)_r]_{r=s}\right] s \ln r + \varepsilon^2 \sum_{n=2}^{N} b_n(\theta, \check{t}) f_n + O(\varepsilon^4). \tag{C.0.12}$$

To eliminate the unknown b_0, we can choose to impose the continuity of potential at either the outer electrode or the interface (2.1.36) on (C.0.12) to derive what we shall refer to hereafter as the "weighted residual electrode model" and the "weighted residual interface model", respectively.

C.1 Weighted residual electrode model

In this section, we impose the continuity of potential at the outer electrode $\phi|_{r=d} = \phi_d$ (2.1.36) on (C.0.12) to yield

$$b_0 = \phi_d - s\left[\Psi - \varepsilon^2 \sum_{n=2}^{N} b_n (f_n)_r\right] \ln d + O(\varepsilon^2), \tag{C.1.1}$$

hence, ϕ (C.0.3) is given by

$$\phi = \phi_d + s\left[\Psi - \varepsilon^2 \sum_{n=2}^{N} b_n (f_n)_r\right] \ln\left(\frac{r}{d}\right) + \varepsilon^2 \sum_{n=2}^{N} b_n(\theta, \check{t}) f_n + \mathcal{O}\left(\epsilon^4\right). \tag{C.1.2}$$

Then, evaluating (C.0.4) with the particular choice of weight function (C.0.10) and (C.1.2) yields

$$\begin{aligned} 0 &= -w_{\text{elec}} r\phi_r|_{r=s} - \phi r[(w_{\text{elec}})_r]_{r=d} + \varepsilon^2 \int_s^d \frac{w_{\text{elec}}}{r}\phi_{\check{\theta}\check{\theta}}\,\mathrm{d}r + O(\varepsilon^4) \\ &= -s\Psi + \frac{\phi_d}{\ln(d/s)} + \varepsilon^2\Bigg\{\frac{1}{2}\ln\left(\frac{d}{s}\right)\left[\phi_{d\check{\theta}\check{\theta}} - \ln d\,(s\Psi)_{\check{\theta}\check{\theta}}\right] \\ &+ \frac{1}{6}(s\Psi)_{\check{\theta}\check{\theta}}\ln\left(\frac{d}{s}\right)\ln\left(ds^2\right)\Bigg\} + O(\varepsilon^4), \end{aligned} \tag{C.1.3}$$

which can be simplified to

$$\phi_d + s\Psi\ln\left(\frac{s}{d}\right) - \varepsilon^2\left\{-\frac{1}{2}\phi_{d\check{\theta}\check{\theta}}\ln^2\left(\frac{s}{d}\right) - \frac{1}{3}\ln^2\left(\frac{s}{d}\right)(s\Psi)_{\check{\theta}\check{\theta}}\right\} + O(\varepsilon^4) = 0. \tag{C.1.4}$$

Equation (C.1.4) for Ψ is the weighted residual electrode model.

C.2 Weighted residual interface model

In this section, we impose the continuity of potential at the outer electrode $\phi|_{r=s} = 0$ (2.1.36) on (C.0.12 to yield

$$b_0 = -s\left[\Psi - \varepsilon^2\sum_{n=2}^{N} b_n(f_n)_r\right]\ln s + O(\epsilon^2), \tag{C.2.1}$$

hence, ϕ (C.0.3) is given by

$$\phi = s\left[\Psi - \varepsilon^2\sum_{n=2}^{N} b_n(f_n)_r\right]\ln\left(\frac{r}{s}\right) + \varepsilon^2\sum_{n=2}^{N} b_n(\theta,\check{t})f_n + \mathcal{O}\left(\epsilon^4\right). \tag{C.2.2}$$

Then, evaluating (C.0.5) with the particular choice of weight function (C.0.10) and (C.1.2) yields

$$\begin{aligned} 0 &= -w_{\text{elec}} r\phi_r|_{r=s} - \phi r[(w_{\text{elec}})_r]_{r=d} + \varepsilon^2\int_s^d \frac{w_{\text{elec}}}{r}\phi_{\check{\theta}\check{\theta}}\,\mathrm{d}r \\ &= -s\Psi + \frac{\phi_d}{\ln(d/s)} + \varepsilon^2\left[(\Psi s)_{\check{\theta}\check{\theta}}\frac{1}{6}\ln\left(\frac{d}{s}\right)\ln(ds^2) - \frac{1}{2}\ln\left(\frac{d}{s}\right)(\Psi s\ln s)_{\check{\theta}\check{\theta}}\right], \end{aligned} \tag{C.2.3}$$

which can be simplified to

$$
\begin{aligned}
&-\phi_d + s\Psi \ln\left(\frac{d}{s}\right) \\
&+\varepsilon^2\left\{\frac{1}{2}\ln^2\left(\frac{d}{s}\right)[\Psi s \ln s]_{\tilde{\theta}\tilde{\theta}} - \frac{1}{6}\ln^2\left(\frac{d}{s}\right)\ln\left(ds^2\right)(\Psi s)_{\tilde{\theta}\tilde{\theta}}\right\} + O(\varepsilon^4) = 0.
\end{aligned}
\tag{C.2.4}
$$

Equation (C.2.4) for Ψ is the weighted residual interface model.

Appendix D

Initial conditions on $A_{3,n}(\tau_1, \tau_2)$ and $B_{3,n}(\tau_1, \tau_2)$ in Section 4.4.5

In this appendix, we state the initial conditions on $A_{3,n}(\tau_1, \tau_2)$ and $B_{3,n}(\tau_1, \tau_2)$ (defined in equation (4.4.46)) for $n = 1, 2$, and 3 required for the analysis in Section 4.4.5.

The initial condition $H(\phi, 0) = 1$ requires that $A_{3,n}(\tau_1, \tau_2)$ and $B_{3,n}(\tau_1, \tau_2)$ satisfy

$$A_{3,1}(0,0) = \frac{9}{8} - \frac{27}{288\alpha^2 + 8} - \frac{9}{576\alpha^2 + 4} + \frac{\delta^2}{(D-1)^6}, \tag{D.0.1}$$

$$B_{3,1}(0,0) = \frac{27\alpha\,(576\alpha^2 + 7)}{20736\alpha^4 + 720\alpha^2 + 4}, \tag{D.0.2}$$

for the first mode,

$$\begin{aligned} A_{3,2}(0,0) =& \frac{1}{4\alpha\big(5184\alpha^4 + 180\alpha^2 + 1\big)^2\big(D-1\big)^4} \\ & \Bigg\{12\alpha(1+36\alpha^2)(D-1)^4\Bigg[-12(\alpha+144\alpha^3)B_{2,1}(0,0) + 24\alpha\frac{\partial A_{1,1}(0,0)}{\partial \tau_1} \\ & - (1-144\alpha^2)\frac{\partial B_{1,1}(0,0)}{\partial \tau_1}\Bigg] + \delta\Bigg[108\alpha^2\Bigg\{8D - 9 - 12\alpha^2\Bigg[23 - 29D \\ & + 288\alpha^2(72\alpha^2(D-1) + 6D - 7)\Bigg]\Bigg\} - D\Bigg]\Bigg\}, \end{aligned} \tag{D.0.3}$$

$$B_{3,2}(0,0) = -\frac{1}{2(5184\alpha^4+180\alpha^2+1)^2(D-1)^4}$$
$$\Big\{6(1+36\alpha^2)(D-1)^4\Big[-(1+144\alpha^2)B_{2,1}(0,0)+(1-144\alpha^2\frac{\partial A_{1,1}(0,0)}{\partial\tau_1}$$
$$+24\alpha\frac{\partial B_{1,1}(0,0)}{\partial\tau_1}\Big]+3\delta\Big[8D-1-108\alpha^2\Big\{8D-13$$
$$+166\alpha^2(48\alpha^2(D-1)-8+7D)\Big\}\Big]\Big\}, \tag{D.0.4}$$

for the second mode,

$$A_{3,3}(0,0) = \frac{3}{80}\left(\frac{22}{36\alpha^2+1}-\frac{99}{144\alpha^2+1}-\frac{120}{576\alpha^2+1}+\frac{393}{1296\alpha^2+1}-\frac{96}{5184\alpha^2+1}\right), \tag{D.0.5}$$

$$B_{3,3}(0,0) = \frac{9\alpha}{20}\left(-\frac{11}{36\alpha^2+1}+\frac{99}{144\alpha^2+1}+\frac{240}{576\alpha^2+1}-\frac{1179}{1296\alpha^2+1}+\frac{576}{5184\alpha^2+1}\right), \tag{D.0.6}$$

for the third mode, and $A_{3,n}(0,0) = B_{3,n}(0,0) = 0$ for all higher modes (i.e., for $n \geq 4$).

Appendix E

Remapping onto a rectangular domain in Section 5.1.2

In this appendix, we show that using the rescalings

$$R = \frac{r-s}{d-s}, \quad \Theta = \theta, \tag{E.0.1}$$

where $0 \leq R \leq 1$ and $0 \leq \Theta \leq 2\pi$, allows us to remap the (r, θ) domain onto a rectangular domain, which allows for easy discretisation in space.

Use of the chain rule yields the first-order derivatives,

$$\partial_r = \frac{1}{d-s}\partial_R, \quad \partial_\theta = \partial_\Theta + s_\Theta \left(\frac{R-1}{d-s}\right)\partial_R. \tag{E.0.2}$$

The second-order derivatives are thus given by,

$$\partial_{rr} = \frac{1}{(d-s)^2}\partial_{RR}, \tag{E.0.3}$$

$$\partial_{\theta\theta} = \partial_{\Theta\Theta} + 2s_\Theta \partial_{R\Theta} + 2s_\Theta^2 \frac{R-1}{(d-s)^2}\partial_R + s_\Theta^2 \left(\frac{R-1}{d-s}\right)^2 \partial_{RR} + s_{\Theta\Theta}\left(\frac{R-1}{d-s}\right)\partial_R. \tag{E.0.4}$$

It follows that reformulating Laplace's equation (2.1.3) into (R, Θ) coordinates

yields

$$\begin{aligned} 0 =& \Big[(s + R(d-s))^2 + s_\Theta^2 (R-1)^2 \Big] \phi_{RR} + 2(R-1)(d-s) s_\Theta \phi_{R\Theta} \\ &+ (d-s)^2 \phi_{\Theta\Theta} + \Big[(d-s)((s + R(d-s)) \\ &+ (R-1)(2s_\Theta^2 + s_{\Theta\Theta}(d-s)) \Big] \phi_R. \end{aligned} \tag{E.0.5}$$

Hence, to leading order in ε, the normal Maxwell stress (2.3.9) becomes

$$E^N = -\frac{1}{2} \left(\phi_r |_{r=s} \right)^2 = -\frac{1}{2} \left(\frac{1}{d-s} \phi_R \right)^2 . \tag{E.0.6}$$

Appendix F

Summary of parameter values used in Chapters 5 and 6

In this appendix, we give the parameter values used in Chapters 5 and 6. Specifically, the parameters used in Section 5.2.1, Section 5.2.2, Section 6.1 and Section 6.2.2 are summarised in Table F.1. The dimensional quantities used correspond approximately to some ratio of water-syrup mix [102, 272]. Note that all values of $\bar{\phi}_b$ are less than 1 V, a typical voltage used in experiments [203].

Symbol	**Formula**	**Section 5.2.1**	**Section 5.2.2**	**Section 6.1**	**Section 6.2.2**
Re	$\hat{\rho}\hat{U}_{\text{ref}}\hat{R}_1/\hat{\mu}$	3.76	3.76	3.76	3.76
Ca	$\hat{\mu}\hat{U}_{\text{ref}}/\hat{\sigma}$	0.157	0.157	0.157	$\{3.93, 7.85, 15.7, 31.4, 62.8\}\times10^{-2}$
$\bar{E}_b$	$\hat{\epsilon}_{\text{G}}\hat{\phi}_b^2/(\hat{\mu}\hat{U}_{\text{ref}}\hat{R}_1)$	$\{0.2, 0.4, 0.6, 0.8, 1\}$	$\{0.1, 1, 5, 10\}$	5000	$\{1, 5, 10, 15, 20\}$
d	$\hat{R}_2/\hat{R}_1$	2.5	2.5	2.8	$\{1.5, 2, 2.5, 3, 3.5\}$
ω	$\hat{\Omega}\hat{R}_1/\hat{U}_{\text{ref}}$	0.5	1	1	1
$\hat{U}_{\text{ref}}$	$\hat{\rho}\hat{g}\hat{R}_1^2/\hat{\mu}$	0.272 m s^{-1}	0.272 m s^{-1}	0.272 m s^{-1}	0.272 m s^{-1}
Quantity	**Symbol (unit)**				
Inner radius	$\hat{R}_1$ (m)	0.002	0.002	0.002	0.002
Outer radius	$\hat{R}_2$ (m)	0.005	0.005	0.0056	$\{3, 4, 5, 6, 7\}\times10^{-3}$
Gravity	$\hat{g}$ (m s^{-2})	9.81	9.81	9.81	9.81
Density	$\hat{\rho}$ (kg m^{-3})	1000	1000	1000	1000
Viscosity	$\hat{\mu}$ (kg m^{-1} s^{-1})	0.144	0.144	0.144	0.144
Permittivity	$\hat{\epsilon}_{\text{G}}$ (F m^{-1})	1.0006	1.0006	1.0006	1.0006
Surface tension	$\hat{\sigma}$ (kg s^{-2})	0.25	0.25	0.25	$\{1, 0.5, 0.25, 0.12, 0.06\}$
Angular velocity	$\hat{\Omega}$ (rad s^{-1})	67.9	135.8	135.8	135.8
Mean potential	$\hat{\phi}_b$ (V)	$\{3.7, 5.6, 6.9, 7.9, 8.9\}\times10^{-3}$	$\{2.8, 8.9, 20, 28\}\times10^{-3}$	0.0626	$\{8.9, 19, 28, 34, 40\}\times10^{-3}$

Table F.1: Summary of the dimensional and dimensionless parameter values used in Sections 5.2.1, 5.2.2, 6.1, and 6.2.2.

Appendix G

Reformulation of the Lagrangian (6.2.8)

In this section, we derive a simplified form of the Lagrangian (6.2.8) in an attempt to better control towards some of the more difficult target shapes in Section 6.2.4 and towards the challenging square target shape in Section 6.2.5.

A simplified version of the curvature κ (2.1.32) is used, obtained by applying the long-wave scalings (2.3.1) and (2.3.2) to (2.1.32) to yield

$$\kappa = \frac{1}{s} + \frac{\epsilon^2}{2s^3}\left(s_\theta^2 - 2ss_{\theta\theta}\right) + O(\epsilon^3). \tag{G.0.1}$$

In addition, we introduce the parameter $m = m(\theta, t)$ where

$$m = \frac{q}{s^2 - 1}, \tag{G.0.2}$$

to further simplify the equation by removing the explicit dependence on the flux q. Substitution of (G.0.1) and (G.0.2) into the Lagrangian (6.2.8) yields the simplified

Lagrangian,

$$
\begin{aligned}
\mathcal{L} =& \mathcal{J}_{\mathrm{t}} - \int\int \lambda^s \left\{ \frac{1}{2}\left(s^2\right)_t + \left[m\left(s^2-1\right)\right]_\theta \right\} \,\mathrm{d}\theta\,\mathrm{d}t \\
& - \int\int \lambda^g \left\{ g\ln\left(\frac{d}{s}\right) - \frac{\epsilon^2}{6}\left[g\ln^3\left(\frac{d}{s}\right)\right]_{\theta\theta} - \phi_d \right\} \,\mathrm{d}\theta\,\mathrm{d}t \\
& - \int\int \lambda^q \Bigg\{ m\left(s^2-1\right) + \frac{\omega}{2}(1-s^2) - \varepsilon^2 \frac{(1-s^2)^2(1+s^2)s_\theta}{2s^3} m_\theta \\
& + \varepsilon^2 \frac{(1-s^2)(1+s^4+2s^2(\ln^2 s-1))}{4s^2} m_{\theta\theta} \\
& + \varepsilon \frac{Re}{16}(-1+2s^2+2s^6-s^4(3+4\ln s))\left[m_t + \left(m^2\right)_\theta\right] \\
& - \frac{\varepsilon}{8}(1-s^4+4s^2\ln s)\Bigg[\frac{1}{Ca}\left(\frac{1}{s} + \frac{\epsilon^2}{2s^3}\left(s_\theta^2 - 2ss_{\theta\theta}\right)\right) \\
& + s\sin\theta + \tilde{E}_b E^N - 2Re\; m^2\left(s^2-1\right)\Bigg]_\theta \Bigg\} \,\mathrm{d}\theta\,\mathrm{d}t. \qquad \text{(G.0.3)}
\end{aligned}
$$

Bibliography

[1] R. W. Yeung, "Numerical methods in free-surface flows", *Annual Review of Fluid Mechanics*, **14**, 395–442, 1982.

[2] W.-T. Tsai and D. K. P. Yue, "Computation of nonlinear free-surface flows", *Annual Review of Fluid Mechanics*, **28**, 249–278, 1996.

[3] J. Eggers, "Nonlinear dynamics and breakup of free-surface flows", *Reviews of Modern Physics*, **69**(3), 865–929, 1997.

[4] A. Oron, S. H. Davis, and S. G. Bankoff, "Long-scale evolution of thin liquid films", *Reviews of Modern Physics*, **69**(3), 931–980, 1997.

[5] R. V. Craster and O. K. Matar, "Dynamics and stability of thin liquid films", *Reviews of Modern Physics*, **81**(3), 1131–1198, 2009.

[6] R. W. Griffiths, "The dynamics of lava flows", *Annual Review of Fluid Mechanics*, **32**, 477–518, 2000.

[7] E. J. Hopfinger, "Snow avalanche motion and related phenomena", *Annual Review of Fluid Mechanics*, **15**, 47–76, 1983.

[8] H. E. Huppert, "Gravity currents: a personal perspective", *Journal of Fluid Mechanics*, **554**, 299–322, 2006.

[9] K. H. Jensen, K. Berg-Sørensen, H. Bruus, N. M. Holbrook, J. Liesche, A. Schulz, M. A. Zwieniecki, and T. Bohr, "Sap flow and sugar transport in plants", *Reviews of Modern Physics*, **88**(3), 035007, 2016.

[10] J. Best, "The fluid dynamics of river dunes: a review and some future research directions", *Journal of Geophysical Research*, **110**(F4), F04S02, 2005.

[11] R. S. Johnson, "Application of the ideas and techniques of classical fluid mechanics to some problems in physical oceanography", *Philosophical Transactions A*, **376**(2111), 20170092, 2018.

[12] C. Schoof, I. J. Hewitt, and M. A. Werder, "Flotation and free surface flow in a model for subglacial drainage. Part 1. Distributed drainage", *Journal of Fluid Mechanics*, **702**, 126–156, 2012.

[13] I. J. Hewitt, C. Schoof, and M. A. Werder, "Flotation and free surface flow in a model for subglacial drainage. Part 2. Channel flow", *Journal of Fluid Mechanics*, **702**, 157–187, 2012.

[14] J. L. Hammack, "A note on tsunamis: their generation and propagation in an ocean of uniform depth", *Journal of Fluid Mechanics*, **60**(4), 769–799, 1973.

[15] E. McLean, R. Bowles, B. Scheichl, and J.-M. Vanden–Broeck, "Improved calculations of waterfalls and weir flows", *Journal of Fluid Mechanics*, **941**, A27, 2022.

[16] B. Bäuerlein and K. Avila, "Phase lag predicts nonlinear response maxima in liquid-sloshing experiments", *Journal of Fluid Mechanics*, **925**, A22, 2021.

[17] T. M. Squires and S. R. Quake, "Microfluidics: Fluid physics at the nanoliter scale", *Reviews of Modern Physics*, **77**(3), 977–1026, 2005.

[18] N. Lamarque, B. Zoppé, O. Lebaigue, Y. Dolias, M. Bertrand, and F. Ducros, "Large-eddy simulation of the turbulent free-surface flow in an unbaffled stirred tank reactor", *Chemical Engineering Science*, **65**(15), 4307–4322, 2010.

[19] P. Krata, "The impact of sloshing liquids on ship stability for various dimensions of partly filled tanks", *The International Journal on Marine Navigation and Safety of Sea Transportation*, **7**(4), 481–489, 2013.

[20] S. Fontanesi, G. Cicalese, and G. De Pasquale, "A methodology for the reduction of numerical diffusion in sloshing analyses through automated mesh adaptation", *Energy Procedia*, vol. **81**: *69th Conference of the Italian Thermal Engineering Association 2014*, 2015, 856–865.

[21] E. W. Graham and A. M. Rodriguez, "The characteristics of fuel motion which affect airplane dynamics", *ASME Journal of Applied Mechanics*, **19**(3), 381–388, 1952.

[22] O. M. Faltinsen and A. N. Timokha, "An adaptive multimodal approach to nonlinear sloshing in a rectangular tank", *Journal of Fluid Mechanics*, **432**, 167–200, 2001.

[23] A. S. Kozelkov, M. A. Pogosyan, D. Y. Strelets, and N. V. Tarasova, "Application of mathematical modeling to solve the emergency water landing task in the interests of passenger aircraft certification", *Aerospace Systems*, **4**, 75–89, 2021.

[24] J. Chen, T. Xiao, M. Wang, Y. Lu, and M. Tong, "Numerical study of wave effect on aircraft water-landing performance", *Applied Sciences*, **12**(5), 2561, 2022.

[25] G. K. Batchelor, *"An Introduction to Fluid Dynamics"*, 2nd ed., Cambridge University Press, 1967.

[26] D. J. Acheson, *"Elementary Fluid Dynamics"*, 1st ed., Oxford University Press, 1991.

[27] C. L. Fefferman, *"Existence and Smoothness of the Navier–Stokes Equation"*, Clay Mathematics Institute, 2006, 57–67.

[28] S. Kalliadasis, C. Ruyer-Quil, B. Scheid, and M. G. Velarde, *"Falling Liquid Films"*, vol. 176, Springer Science and Business Media, 2012.

[29] C. Ruyer-Quil and P. Manneville, "Improved modeling of flows down inclined planes", *The European Physical Journal B*, **15**(2), 357–369, 2000.

[30] A. W. Wray, "Interfacial fluid dynamics in the presence of electric fields", PhD thesis, Imperial College of Science, Technology and Medicine, London, 2014.

[31] A. W. Wray and R. Cimpeanu, "Reduced-order modelling of thick inertial flows around rotating cylinders", *Journal of Fluid Mechanics*, **898**, A1, 2020.

[32] D. J. Benney, "Long waves on liquid films", *Journal of Mathematical Physics*, **45**(1–4), 150–155, 1966.

[33] P. L. Kapitza, "Wave flow of thin layers of a viscous liquid", *Journal of Experimental and Theoretical Physics*, **18**, 261–272 (in Russian), 1948.

[34] W Nusselt, "Die oberflächenkondensation des wasserdampfes", *Vereines Deutscher Ingenieure Z*, **60**(7), 541–546 (in German), 1916.

[35] W Nusselt, "Die oberflächenkondensation des wasserdampfes", *Vereines Deutscher Ingenieure Z*, **60**(7), 569–575 (in German), 1916.

[36] A. Pumir, P. Manneville, and Y. Pomeau, "On solitary waves running down an inclined plane", *Journal of Fluid Mechanics*, **135**, 27–50, 1983.

[37] B. Scheid, C. Ruyer-Quil, and P. Manneville, "Wave patterns in film flows: modelling and three-dimensional waves", *Journal of Fluid Mechanics*, **562**, 183–222, 2006.

[38] B. Scheid, C. Ruyer-Quil, U. Thiele, O. A. Kabov, J. C. Legros, and P. Colinet, "Validity domain of the Benney equation including the Marangoni effect for closed and open flows", *Journal of Fluid Mechanics*, **527**, 303–335, 2005.

[39] S. P. Lin, "Finite amplitude side-band stability of a viscous film", *Journal of Fluid Mechanics*, **63**(3), 417–429, 1974.

[40] A. Oron and O. Gottlieb, "Subcritical and supercritical bifurcations of the first- and second-order Benney equations", *Journal of Engineering Mathematics*, **50**(2), 121–140, 2004.

[41] Y. Kuramoto, "Diffusion-induced chaos in reaction systems", *Progress of Theoretical Physics Supplement*, **64**, 346–367, 1978.

[42] G. I. Sivashinsky, "Nonlinear analysis of hydrodynamic instability in laminar flames – I. Derivation of basic equations", *Acta Astronautica*, **4**(11), 1177–1206, 1977.

[43] G. I. Sivashinsky and D. Michelson, "On irregular wavy flow of a liquid film down a vertical plane", *Progress of Theoretical Physics*, **63**(6), 2112–2114, 1980.

[44] A. P. Hooper and R. Grimshaw, "Nonlinear instability at the interface between two viscous fluids", *Physics of Fluids*, **28**(1), 37–45, 1985.

[45] D. T. Papageorgiou, C. Maldarelli, and D. S. Rumschitzki, "Nonlinear interfacial stability of core-annular film flows", *Physics of Fluids A*, **2**(3), 340–352, 1990.

[46] S. N. Gomes, D. T. Papageorgiou, and G. A. Pavliotis, "Stabilizing nontrivial solutions of the generalized Kuramoto–Sivashinsky equation using feedback and optimal control", *IMA Journal of Applied Mathematics*, **82**(1), 158–194, 2017.

[47] R. J. Tomlin and S. N. Gomes, "Point-actuated feedback control of multidimensional interfaces", *IMA Journal of Applied Mathematics*, **84**(6), 1112–1142, 2019.

[48] M. S. Jolly, R. Rosa, and R. Temam, "Evaluating the dimension of an inertial manifold for the Kuramoto-Sivashinsky equation", *Advances in Differential Equations*, **5**(1–3), 31–66, 2000.

[49] I. G. Kevrekidis, B. Nicolaenko, and J. C. Scovel, "Back in the saddle again: a computer assisted study of the Kuramoto–Sivashinsky equation", *SIAM Journal on Applied Mathematics*, **50**(3), 760–790, 1990.

[50] D. T. Papageorgiou and Y. S. Smyrlis, "The route to chaos for the Kuramoto–Sivashinsky equation", *Theoretical and Computational Fluid Dynamics*, **3**(1), 15–42, 1991.

[51] V. Y. Shkadov, "Wave flow regimes of a thin layer of viscous fluid subject to gravity", *Fluid Dynamics*, **2**(1), 29–34, 1967.

[52] C. Ruyer-Quil, P. Treveleyan, F. Giorgiutti-Dauphiné, C. Duprat, and S. Kalliadasis, "Modelling film flows down a fibre", *Journal of Fluid Mechanics*, **603**, 431–462, 2008.

[53] A. Oron and C. Heining, "Weighted-residual integral boundary-layer model for the nonlinear dynamics of thin liquid films falling on an undulating vertical wall", *Physics of Fluids*, **20**(8), 082102, 2008.

[54] S. Kalliadasis, E. A. Demekhin, C. Ruyer-Quil, and M. G. Velarde, "Thermocapillary instability and wave formation on a film falling down a uniformly heated plane", *Journal of Fluid Mechanics*, **492**, 303–338, 2003.

[55] A. W. Wray, O. K. Matar, and D. T. Papageorgiou, "Accurate low-order modeling of electrified falling films at moderate Reynolds number", *Physical Review Fluids*, **2**(6), 063701, 2017.

[56] A. W. Wray, D. T. Papageorgiou, and O. K. Matar, "Reduced models for thick liquid layers with inertia on highly curved substrates", *SIAM Journal on Applied Mathematics*, **77**(3), 881–904, 2017.

[57] M. Amaouche, A. Djema, and L. Bourdache, "A modified Shkadov's model for thin film flow of a power law fluid over an inclined surface", *Comptes Rendus Mécanique*, **337**(1), 48–52, 2009.

[58] C. Ruyer-Quil and P. Manneville, "Modeling film flows down inclined planes", *The European Physical Journal B*, **6**, 277–292, 1998.

[59] J.-J. Lee and C. C. Mei, "Stationary waves on an inclined sheet of viscous fluid at high Reynolds and moderate Weber numbers", *Journal of Fluid Mechanics*, **307**, 191–229, 1996.

[60] T. Prokopiou, M. Cheng, and H.-C. Chang, "Long waves on inclined films at high Reynolds number.", *Journal of Fluid Mechanics*, **222**, 665–691, 1991.

[61] M. Amaouche, A. Djema, and H. Ait Abderrahmane, "Film flow for power-law fluids: modeling and linear stability", *European Journal of Mechanics – B/Fluids*, **34**, 70–84, 2012.

[62] C. Ruyer–Quil and P. Manneville, "Further accuracy and convergence results on the modeling of flows down inclined planes by weighted-residual approximations", *Physics of Fluids*, **14**(1), 170–183, 2002.

[63] C. Ruyer-Quil and P. Manneville, "On the speed of solitary waves running down a vertical wall", *Journal of Fluid Mechanics*, **531**, 181–190, 2005.

[64] A. B. Thompson, D. Tseluiko, and D. T. Papageorgiou, "Falling liquid films with blowing and suction", *Journal of Fluid Mechanics*, **787**, 292–330, 2016.

[65] A. B. Thompson, S. N. Gomes, G. A. Pavliotis, and D. T. Papageorgiou, "Stabilising falling liquid film flows using feedback control", *Physics of Fluids*, **28**(1), 012107, 2016.

[66] S. Chakraborty, P.-K. Nguyen, C. Ruyer-Quil, and V. Bontozoglou, "Extreme solitary waves on falling liquid films", *Journal of Fluid Mechanics*, **745**, 564–591, 2014.

[67] A. B. Thompson, S. N. Gomes, F. Denner, M. C. Dallaston, and S. Kalliadasis, "Robust low-dimensional modelling of falling liquid films subject to variable wall heating", *Journal of Fluid Mechanics*, **877**, 844–881, 2019.

[68] R. Cimpeanu, S. N. Gomes, and D. T. Papageorgiou, "Active control of liquid film flows: beyond reduced-order models", *Nonlinear Dynamics*, **104**, 267–287, 2021.

[69] K. Zakaria and M. Sirwah, "Nonlinear dynamics of a liquid film flow over a solid substrate in the presence of external shear stress and electric field", *The European Physical Journal Plus*, **137**(9), 1087, 2022.

[70] A. Georgescu, *"Hydrodynamic Stability Theory"*, 2nd ed., Dordrecht, Springer, 1986.

[71] N. E. Sanchez, "The method of multiple scales: asymptotic solutions and normal forms for nonlinear oscillatory problems", *Journal of Symbolic Computation*, **21**(2), 245–252, 1996.

[72] A. H. Nayfeh, *"Perturbation Methods"*, John Wiley and Sons, Inc., 2000.

[73] E. J. Hinch and M. A. Kelmanson, "On the decay and drift of free-surface perturbations in viscous thin-film flow exterior to a rotating cylinder", *Proceedings of the Royal Society of London A*, **459**(2033), 1193–1213, 2003.

[74] R. J. Leveque, *"Finite Difference Methods for Ordinary and Partial Differential Equations"*, Society for Industrial and Applied Mathematics, 2007.

[75] A. Iserles, *"A First Course in the Numerical Analysis of Differential Equations"*, 2nd ed., Cambridge Texts in Applied Mathematics. Cambridge University Press, 2008.

[76] H. Sundqvist and G. Veronis, "A simple finite-difference grid with non-constant intervals", *Tellus*, **22**(1), 26–31, 1970.

[77] M. R. Moore, D. Vella, and J. M. Oliver, "The nascent coffee ring: how solute diffusion counters advection", *Journal of Fluid Mechanics*, **920**, A54, 2021.

[78] S. F. Kistler and P. M. Schweizer, *"Liquid Film Coating"*, Dordrecht, Springer, 1997.

[79] R. J. Braun, R. Usha, G. B. McFadden, T. A. Driscoll, L. P. Cook, and P. E. King-Smith, "Thin film dynamics on a prolate spheroid with application to the cornea", *Journal of Engineering Mathematics*, **73**(1), 121–138, 2012.

[80] J. B. Grotberg, "Pulmonary flow and transport phenomena", *Annual Review of Fluid Mechanics*, **26**, 529–571, 1994.

[81] V. Mihalca, A. D. Kerezsi, A. Weber, C. Gruber-Traub, J. Schmucker, D. C. Vodnar, F. V. Dulf, S. A. Socaci, A. Fărcaș, C. I. Mureșan, R. Suharoschi, and O. L. Pop, "Protein-based films and coatings for food industry applications", *Polymers*, **13**(5), 769, 2021.

[82] L. Liang, Y. Chen, B. Zhang, X. Zhang, J. Liu, C. Shen, Y. Cui, and X. D. Guo, "Optimization of dip-coating methods for the fabrication of coated microneedles for drug delivery", *Journal of Drug Delivery Science and Technology*, **55**, 101464, 2020.

[83] N. K. Akafuah, S. Poozesh, A. Salaimeh, G. Patrick, K. Lawler, and K. Saito, "Evolution of the automotive body coating process – a review", *Coatings*, **6**(2), 24, 2016.

[84] R. Smedley, *Testing explained: Rob Smedley on flow-vis paint*, `https://www.formula1.com/en/latest/article.testing-explained-rob-smedley-%20on-flow-vis.7nU2VePGlVrhIGa8wgCoLE.html`, Accessed: 2023-25-07.

[85] S. Ristic, "Flow visualisation techniques in wind tunnels Part I – Non optical methods", *Scientific Technical Review*, **57**(1), 39–50, 2007.

[86] A. S. H. Makhlouf, *"Nanocoatings and Ultra-Thin Films"*, Woodhead Publishing, 2011.

[87] B. W. Minifie, *"Chocolate, Cocoa and Confectionery: Science and Technology"*, 3rd ed., Chapman and Hall, 1989.

[88] S. Kumar, "Liquid transfer in printing processes: liquid bridges with moving contact lines", *Annual Review of Fluid Mechanics*, **47**, 67–94, 2015.

[89] Z. Liu, H. Ma, L. Zhou, Y. Liu, Z. Huang, X. Liao, and Y. Zhao, "DEM-DDM investigation of the tablet coating process using different particle shape models", *Industrial and Engineering Chemistry Research*, **62**(1), 829–840, 2023.

[90] J. Vetter, *"Coating Technology for Vehicle Applications"*, Springer International Publishing, 2015.

[91] E. Vural and S. Özer, "Thermal analysis of a piston coated with SiC and $MgOZrO_2$ thermal barrier materials", *International Journal of Scientific and Technological Research*, **1**(7), 43–51, 2015.

[92] G. Ribatski and A. M. Jacobi, "Falling-film evaporation on horizontal tubes – a critical review", *International Journal of Refrigeration*, **28**(5), 635–653, 2005.

[93] D. L. Chandler, *Thin coating on condensers could make power plants more efficient*, `https://news.mit.edu/2015/graphene-coating-more-efficient-power-plants-0529`, Accessed: 2023-25-07.

[94] R. C. Peterson, P. K. Jimack, and M. A. Kelmanson, "On the stability of viscous free-surface flow supported by a rotating cylinder", *Proceedings of the Royal Society of London A*, **457**(2010), 1427–1445, 2001.

[95] V. V. Pukhnachev, "Motion of a liquid film on the surface of a rotating cylinder in a gravitational field", *Journal of Applied Mechanics and Technical Physics*, **18**(3), 344–351, 1977.

[96] E. B. Hansen and M. A. Kelmanson, "Steady, viscous, free-surface flow on a rotating cylinder", *Journal of Fluid Mechanics*, **272**, 91–107, 1994.

[97] S. D. R. Wilson, "The drag-out problem in film coating theory", *Journal of Engineering Mathematics*, **16**, 209–221, 1982.

[98] P. Rosenau, A. Oron, and J. M. Hyman, "Bounded and unbounded patterns of the Benney equation", *Physics of Fluids A: Fluid Dynamics*, **4**(6), 1102–1104, 1992.

[99] I. L. Kliakhandler, S. H. Davis, and S. G. Dankoff, "Viscous beads on vertical fibre", *Journal of Fluid Mechanics*, **429**, 381–390, 2001.

[100] B. R. Duffy and S. K. Wilson, "Thin-film and curtain flows on the outside of a rotating horizontal cylinder", *Journal of Fluid Mechanics*, **394**, 29–49, 1999.

[101] B. Reisfeld and S. G. Bankoff, "Non-isothermal flow of a liquid film on a horizontal cylinder", *Journal of Fluid Mechanics*, **236**, 167–196, 1992.

[102] P. L. Evans, L. W. Schwartz, and R. V. Roy, "Steady and unsteady solutions for coating flow on a rotating horizontal cylinder: two-dimensional theoretical and numerical modeling", *Physics of Fluids*, **16**(8), 2742, 2004.

[103] D. Takagi and H. E. Huppert, "Flow and instability of thin films on a cylinder and sphere", *Journal of Fluid Mechanics*, **647**, 221–238, 2010.

[104] M. Cachile, M. A. Aguirre, M. Lenschen, and A. Calvo, "Flow of a thin liquid film coating a horizontal stationary cylinder", *Physical Review E*, **88**(6), 063005, 2013.

[105] J. Qin, Y. Xia, and P. Gao, "Axisymmetric evolution of gravity-driven thin films on a small sphere", *Journal of Fluid Mechanics*, **907**, A4, 2021.

[106] H. K. Moffatt, "Behaviour of a viscous film on the outer surface of a rotating cylinder", *Journal de Mécanique*, **16**(5), 651–673, 1977.

[107] V. V. Pukhnachov, "On the equation of a rotating film", *Siberian Mathematical Journal*, **46**(5), 913–924, 2005.

[108] V. V. Pukhnachov, "Capillary/gravity film flows on the surface of a rotating cylinder", *Journal of Mathematical Sciences*, **130**(4), 4871–4883, 2005.

[109] G. Seiden and P. J. Thomas, "Complexity, segregation, and pattern formation in rotating-drum flows", *Reviews of Modern Physics*, **83**(4), 1323–1365.

[110] K. J. Ruschak, "Coating flows", *Annual Review of Fluid Mechanics*, **17**, 65–89, 1985.

[111] S. J. Weinstein and K. J. Ruschak, "Coating flows", *Annual Review of Fluid Mechanics*, **36**, 29–53, 2004.

[112] C. H. Tougher, S. K. Wilson, and B. R. Duffy, "On the approach to the critical solution in leading order thin-film coating and rimming flow", *Applied Mathematics Letters*, **22**(6), 882–886, 2009.

[113] L. Preziosi and D. D. Joseph, "The run-off condition for coating and rimming flows", *Journal of Fluid Mechanics*, **187**, 99–113, 1988.

[114] E. S. Benilov, M. S. Benilov, and N. Kopteva, "Steady rimming flows with surface tension", *Journal of Fluid Mechanics*, **597**, 91–118, 2008.

[115] A. v. B. Lopes, U. Thiele, and A. L. Hazel, "On the multiple solutions of coating and rimming flows on rotating cylinders", *Journal of Fluid Mechanics*, **835**, 540–574, 2018.

[116] M. Tirumkudulu and A. Acrivos, "Coating flows within a rotating horizontal cylinder: lubrication analysis, numerical computations, and experimental measurements", *Physics of Fluids*, **13**(1), 14–19, 2001.

[117] E. A. Karabut, "Two regimes of liquid film flow on a rotating cylinder", *Journal of Applied Mechanics and Technical Physics*, **48**(1), 55–64, 2007.

[118] M. A Kelmanson, "Theoretical and experimental analyses of the maximum-supportable fluid load on a rotating cylinder", *Journal of Engineering Mathematics*, **29**(3), 271–285, 1995.

[119] J. Ashmore, A. E. Hosoi, and H. A. Stone, "The effect of surface tension on rimming flows in a partially filled rotating cylinder", *Journal of Fluid Mechanics*, **479**, 65–98, 2003.

[120] A. E. Hosoi and L. Mahadevan, "Axial instability of a free-surface front in a partially filled horizontal rotating cylinder", *Physics of Fluids*, **11**(1), 97–106, 1999.

[121] E. S. Benilov and S. O'Brien, "Inertial instability of a liquid film inside a rotating horizontal cylinder", *Physics of Fluids*, **17**(5), 052106, 2005.

[122] E. S. Benilov and V. N. Lapin, "Inertial instability of flows on the inside or outside of a rotating horizontal cylinder", *Journal of Fluid Mechanics*, **736**, 107–129, 2013.

[123] P. L. Evans, L. W. Schwartz, and R. V. Roy, "Three-dimensional solutions for coating flow on a rotating horizontal cylinder: theory and experiment", *Physics of Fluids*, **17**(7), 072102, 2005.

[124] M. A. Kelmanson, "On inertial effects in the Moffatt–Pukhnachov coating-flow problem", *Journal of Fluid Mechanics*, **633**, 327–353, 2009.

[125] S. K. Wilson, R. Hunt, and B. R. Duffy, "On the critical solutions in coating and rimming flow on a uniformly rotating horizontal cylinder", *The Quarterly Journal of Mechanics and Applied Mathematics*, **55**(3), 357–383, 2002.

[126] X. Xu, U. Thiele, and T. Qian, "A Variational approach to thin film hydrodynamics of binary mixtures", *Journal of Physics: Condensed Matter*, **27**(8), 085005, 2015.

[127] S. B. G. O'Brien, "Linear stability of rimming flow", *Quarterly of Applied Mathematics*, **60**(2), 201–211, 2002.

[128] S. B. G. O'Brien, "A mechanism for linear instability in two-dimensional rimming flow", *Quarterly of Applied Mathematics*, **60**(2), 283–299, 2002.

[129] A. J. Mitchell, B. R. Duffy, and S. K. Wilson, "Coating flow on a rotating cylinder in the presence of an irrotational airflow with circulation", *Journal of Fluid Mechanics*, **932**, A33, 2022.

[130] A. J. Mitchell, B. R. Duffy, and S. K. Wilson, "Unsteady coating flow on a rotating cylinder in the presence of an irrotational airflow with circulation", *Physics of Fluids*, **34**(4), 043105, 2022.

[131] C. M. Groh and M. A. Kelmanson, "Multiple-timescale asymptotic analysis of transient coating flows", *Physics of Fluids*, **21**(9), 091702, 2009.

[132] C. M. Groh and M. A. Kelmanson, "Computer-algebra multiple-timescale method for spatially periodic thin-film viscous-flow problems", *International Journal for Numerical Methods in Fluids*, **68**(11), 1457–1470, 2012.

[133] C. M. Groh and M. A. Kelmanson, "Inertially induced cyclic solutions in thin-film free-surface flows", *Journal of Fluid Mechanics*, **755**, 628–653, 2014.

[134] B. R. Duffy and S. K. Wilson, "Large-Biot-number non-isothermal flow of a thin film on a stationary or rotating cylinder", *The European Physical Journal Special Topics*, **166**(1), 147–150, 2009.

[135] G. A. Leslie, S. K. Wilson, and B. R. Duffy, "Non-isothermal flow of a thin film of fluid with temperature-dependent viscosity on a stationary horizontal cylinder", *Physics of Fluids*, **23**(6), 062101, 2011.

[136] G. A. Leslie, S. K. Wilson, and B. R. Duffy, "Thermoviscous Coating and Rimming Flow", *The Quarterly Journal of Mechanics and Applied Mathematics*, **66**(4), 483–511, 2012.

[137] U. Thiele, "On the depinning of a drop of partially wetting liquid on a rotating cylinder", *Journal of Fluid Mechanics*, **671**, 121–136, 2011.

[138] T.-S. Lin, S. Rogers, D. Tseluiko, and U. Thiele, "Bifurcation analysis of the behavior of partially wetting liquids on a rotating cylinder", *Physics of Fluids*, **28**(8), 082102, 2016.

[139] D. E. Weidner, "Suppression and reversal of drop formation on horizontal cylinders due to surfactant convection", *Physics of Fluids*, **25**(8), 082110, 2013.

[140] W. Li and S. Kumar, "Thin-film coating of surfactant-laden liquids on rotating cylinders", *Physics of Fluids*, **27**(7), 072106, 2015.

[141] D. E. Weidner, "Drop formation in a magnetic fluid coating a horizontal cylinder carrying an axial electric current", *Physics of Fluids*, **29**(5), 052103, 2017.

[142] D. E. Weidner, L. W. Schwartz, and M. H. Eres, "Simulation of coating layer evolution and drop formation on horizontal cylinders", *Journal of Colloid and Interface Science*, **187**(1), 243–258, 1997.

[143] C. K. Lin, C. C. Hwang, and T. C. Ke, "Three-dimensional nonlinear rupture theory of thin liquid films on a cylinder", *Journal of Colloid and Interface Science*, **256**(2), 480–482, 2002.

[144] E. S. Benilov, "Explosive instability in a linear system with neutrally stable eigenmodes. Part 2. Multi-dimensional disturbances", *Journal of Fluid Mechanics*, **501**, 105–124, 2004.

[145] C. J. Noakes, J. R. King, and D. S. Riley, "On the development of rational approximations incorporating inertial effects in coating and rimming flows: a multiple-scales approach", *The Quarterly Journal of Mechanics and Applied Mathematics*, **59**(2), 163–190, 2006.

[146] A. K. Sahu and S. Kumar, "Thin-liquid-film flow on a topographically patterned rotating cylinder", *Physics of Fluids*, **26**(4), 042102, 2014.

[147] W. Li, M. S. Carvalho, and S. Kumar, "Liquid-film coating on topographically patterned rotating cylinders", *Physical Review Fluids*, **2**(2), 024001, 2017.

[148] C. Parrish, L. Pham, and S. Kumar, "Thin-liquid-film flow on three-dimensional topographically patterned rotating cylinders", *Journal of Fluid Mechanics*, **918**, A12, 2021.

[149] C. Parrish, M. S. Carvalho, and S. Kumar, "Thin-film flows on rotating non-circular cylinders with large curvature variations", *Physical Review Fluids*, **7**(5), 054002, 2022.

[150] R. Hunt, "Numerical solution of the free-surface viscous flow on a horizontal rotating elliptical cylinder", *Numerical Methods for Partial Differential Equations*, **24**(4), 1094–1114, 2008.

[151] W. Li, M. S. Carvalho, and S. Kumar, "Viscous free-surface flows on rotating elliptical cylinders", *Physical Review Fluids*, **2**(9), 094005, 2017.

[152] A. Lee, P. T. Brun, J. Marthelot, G. Balestra, F. Gallaire, and P. M. Reis, "Fabrication of slender elastic shells by the coating of curved surfaces", *Nature Communications*, **7**(1), 11155, 2016.

[153] G. Balestra, D. M. P. Nguyen, and F. Gallaire, "Rayleigh–Taylor instability under a spherical substrate", *Physical Review Fluids*, **3**(8), 084005, 2018.

[154] D. Kang, A. Nadim, and M. Chugnova, "Dynamics and equilibria of thin viscous coating films on a rotating sphere", *Journal of Fluid Mechanics*, **791**, 495–518, 2016.

[155] M. Jalaal, C. Seyfert, and J. H. Snoeijer, "Capillary ripples in thin viscous films", *Journal of Fluid Mechanics*, **880**, 430–440, 2019.

[156] S. D. R. Wilson and A. F. Jones, "The entry of a falling film into a pool and the air-entrainment problem", *Journal of Fluid Mechanics*, **128**, 219–230, 1983.

[157] L. Duchemin, J. R. Lister, and U. Lange, "Static shapes of levitated viscous drops", *Journal of Fluid Mechanics*, **533**, 161–170, 2005.

[158] E. S. Benilov, S. J. Chapman, J. B. McLeod, J. R. Ockendon, and V. S. Zubkov, "On liquid films on an inclined plate", *Journal of Fluid Mechanics*, **663**, 53–69, 2010.

[159] E. S. Benilov and M. S. Benilov, "A thin drop sliding down an inclined plane", *Journal of Fluid Mechanics*, **773**, 75–102, 2015.

[160] I. J. Hewitt, N. J. Balmforth, and J. R. De Bruyn, "Elastic-plated gravity currents", *European Journal of Applied Mathematics*, **26**(1), 1–31, 2015.

[161] R. Brandão and O. Schnitzer, "Leidenfrost levitation of a spherical particle above a liquid bath: evolution of the vapour-film morphology with particle size", *European Journal of Applied Mathematics*, **33**(6), 1117–1169, 2022.

[162] D. A. Saville, "Electrohydrodynamics: the Taylor–Melcher leaky dielectric model", *Annual Review of Fluid Mechanics*, **29**, 27–64, 1997.

[163] D. T. Papageorgiou, "Film flows in the presence of electric fields", *Annual Review of Fluid Mechanics*, **51**, 155–187, 2019.

[164] A. O. El Moctar, N. Aubry, and J. Batton, "Electro-hydrodynamic microfluidic mixer", *Lab on a Chip*, **3**(4), 273–280, 2003.

[165] H. Lin, B. D. Storey, C.-H. Chen, and J. G. Santiago, "Instability of electrokinetic microchannel flows with conductivity gradients", *Physics of Fluids*, **16**(6), 1922–1935, 2004.

[166] I. Glasgow, J. Batton, and N. Aubry, "Electroosmotic mixing in microchannels", *Lab on a Chip*, **4**(6), 558–562, 2004.

[167] R. Cimpeanu and D. T. Papegeorgiou, "Electrostatically induced mixing in confined stratified multi-fluid systems", *International Journal of Multiphase Flow*, **75**, 194–204, 2015.

[168] M. M. Hohman, M. Shin, G. Rutledge, and M. P. Brenner, "Electrospinning and electrically forced jets. I. Stability theory", *Physics of Fluids*, **13**(8), 2201–2220, 2001.

[169] D. H. Reneker and A. L. Yarin, "Electrospinning jets and polymer nanofibers", *Polymer*, **49**(10), 2387–2425, 2008.

[170] J. Xue, T. Wu, Y. Dai, and Y. Xia, "Electrospinning and electrospun nanofibers: methods, materials, and applications", *Chemical Reviews*, **119**(8), 5298–5415, 2019.

[171] S. Son, S. Lee, and J. Choi, "Fine metal line patterning on hydrophilic non-conductive substrates based on electrohydrodynamic printing and laser sintering", *Journal of Electrostatics*, **72**(1), 70–75, 2014.

[172] A. Daly, L. Riley, T. Segura, and J. Burdick, "Hydrogel microparticles for biomedical applications", *Nature Reviews Materials*, **5**(1), 20–43, 2019.

[173] L. Jiang, Y. Wang, X. Wang, F. Ning, S. Wen, Y. Zhou, S. Chen, A. Betts, S. Jerrams, and F.-L. Zhou, "Electrohydrodynamic printing of a dielectric elastomer actuator and its application in tunable lenses", *Composites Part A*, **147**, 106461, 2021.

[174] M. Kim and G. H. Kim, "Electrohydrodynamic direct printing of PCL/collagen fibrous scaffolds with a core/shell structure for tissue engineering applications", *Chemical Engineering Journal*, **279**(2), 317–326, 2015.

[175] I. Liashenko, J. Rosell-Llompart, and A. Cabot, "Ultrafast 3D printing with submicrometer features using electrostatic jet deflection", *Nature Communications*, **11**(1), 753, 2020.

[176] H. Niu, X. Wang, and T. Lin, "Needleless electrospinning: influences of fibre generator geometry", *The Journal of the Textile Institute*, **103**(7), 787–794, 2012.

[177] R. Rouhollahi, R. Gharraei, and S. Baheri Islami, "Intensification of wavy behavior of fully-developed falling film using electric field implied by a novel wire-plate electrode arrangement", *Experimental Thermal and Fluid Science*, **98**, 497–515, 2018.

[178] M. N. Pantzali, A. A. Mouza, and S. V. Paras, "Counter-current gas–liquid flow and incipient flooding in inclined small diameter tubes", *Chemical Engineering Science*, **63**(15), 3966–3978, 2008.

[179] D. Tseluiko and S. Kalliadasis, "Nonlinear waves in counter-current gas–liquid film flow", *Journal of Fluid Mechanics*, **673**, 19–59, 2011.

[180] C.-Y. Zhao, D. Qi, W.-T. Ji, P.-H. Jin, and W.-Q. Tao, "A comprehensive review on computational studies of falling film hydrodynamics and heat transfer on the horizontal tube and tube bundle", *Applied Thermal Engineering*, **202**, 117869, 2022.

[181] D. Jige, H. Miyata, and N. Inoue, "Falling film evaporation of R1234ze(E) and R245fa on a horizontal smooth tube", *Experimental Thermal and Fluid Science*, **105**, 58–66, 2019.

[182] M. S. Lopes, R. M. Filho, M. R. W. Maciel, and L. C. Medina, "Extension of the TBP curve of petroleum using the correlation DESTMOL", *Procedia Engineering*, **42**, 726–732, 2012.

[183] R. Kouhikamali, N. R. Abadi, and M. Hassani, "Numerical investigation of falling film evaporation of multi-effect desalination plant", *Applied Thermal Engineering*, **70**(1), 477–485, 2014.

[184] J. Darabi, M. M. Ohadi, and S. V. Dessiatoun, "Falling film and spray evaporation enhancement using an applied electric field", *Journal of Heat Transfer*, **122**(4), 741–748, 2000.

[185] J. Darabi, M. M. Ohadi, and S. V. Dessiatoun, "Augmentation of thin falling-film evaporation on horizontal tubes using an applied electric field", *Journal of Heat Transfer*, **122**(2), 391–398, 2000.

[186] J. W. Judy, "Microelectromechanical systems (MEMS): fabrication, design and applications", *Smart Material Structures*, **10**(6), 1115–1134, 2001.

[187] F. Bu, W. Zhou, Y. Xu, Y. Du, C. Guan, and W. Huang, "Recent developments of advanced micro-supercapacitors: design, fabrication and applications", *npj Flexible Electronics*, **4**, 31, 2020.

[188] I. P. Parkin and R. G Palgrave, "Self-cleaning coatings", *Journal of Materials Chemistry*, **15**(17), 1689–1695, 2005.

[189] R. Søndergaard, M. Hösel, D. Angmo, T. T. Larsen-Olsen, and F. C. Krebs, "Roll-to-roll fabrication of polymer solar cells", *Materials Today*, **15**(1–2), 36–49, 2012.

[190] N. Wu and W. B. Russel, "Micro- and nano-patterns created via electrohydrodynamic instabilities", *Nano Today*, **4**(2), 180–192, 2009.

[191] V. Shankar and A. Sharma, "Instability of the interface between thin fluid films subjected to electric fields", *Journal of Colloid and Interface Science*, **274**(1), 294–308, 2004.

[192] R. Mukherjee and A. Sharma, "Instability, self organization and pattern formation in thin soft films", *Soft Matter*, **11**(45), 8717–8740, 2015.

[193] S. Y. Chou and L. Zhuang, "Lithographically induced self-assembly of periodic polymer micropillar arrays", *Journal of Vacuum Science and Technology B*, **17**(6), 3197–3202, 1999.

[194] E. Schäffer, T. Thurn-Albrecht, T. P. Russel, and U. Steiner, "Electrically induced structure formation and pattern transfer", *Nature*, **403**(6772), 874–877, 2000.

[195] Q. Wang and D. T. Papageorgiou, "Using electric fields to induce patterning in leaky dielectric fluids in a rod-annular geometry", *Journal of Applied Mathematics*, **83**(1), 24–52, 2018.

[196] X. Li, J. Shao, Y.-H. Ding, H. Tian, and H. Liu, "Improving the height of replication in EHD patterning by optimizing the electrical properties of the template", *Journal of Micromechanics and Microengineering*, **21**(11), 115004, 2011.

[197] G. I. Taylor, "Studies in electrohydrodynamics I. The circulation produced in a drop by an electric field", *Proceedings of the Royal Society of London A*, **291**(1425), 159–166, 1966.

[198] J. R. Melcher and G. I. Taylor, "Electrohydrodynamics: a review of the role of interfacial stresses", *Annual Review of Fluid Mechanics*, **1**, 111–146, 1969.

[199] R. Feynman, R. B. Leighton, and M. Sands, *"The Feynman Lectures on Physics"*, vol. 2, Addison–Wesley Publishing Company, 1964.

[200] E. Tiesinga, P. J. Mohr, D. B. Newell, and B. N. Taylor, "CODATA recommended values of the fundamental physical constants: 2018", *Reviews of Modern Physics*, **93**(2), 025010, 2021.

[201] S. A. Roberts and S. Kumar, "AC electrohydrodynamic instabilities in thin liquid films", *Journal of Fluid Mechanics*, **631**, 255–279, 2009.

[202] P. Gambhire and R. Thaokar, "Electrohydrodynamic instabilities at interfaces subjected to alternating electric field", *Physics of Fluids*, **22**(6), 064103, 2010.

[203] R. V. Craster and O. K. Matar, "Electrically induced pattern formation in thin leaky dielectric films", *Physics of Fluids*, **17**(3), 032104, 2005.

[204] O. Ozen, D. T. Papageorgiou, and P. G. Petropoulos, "Nonlinear stability of a charged electrified viscous liquid sheet under the action of a horizontal electric field", *Physics of Fluids*, **18**(4), 042102, 2006.

[205] D. Tseluiko and D. T. Papageorgiou, "Wave evolution on electrified falling films", *Journal of Fluid Mechanics*, **556**, 361–386, 2006.

[206] R. Verma, A. Sharma, K. Kargupta, and J. Bhaumik, "Electric field induced instability and pattern formation in thin liquid films", *Langmuir*, **21**(8), 3710–3721, 2005.

[207] N. Wu, L. F. Pease III, and W. B. Russel, "Electric-field-induced patterns in thin polymer films: weakly nonlinear and fully nonlinear evolution", *Langmuir*, **21**(26), 12290–12302, 2005.

[208] R. Cimpeanu, D. T. Papageorgiou, and P. G. Petropoulos, "On the control and suppression of the Rayleigh–Taylor instability using electric fields", *Physics of Fluids*, **26**(2), 022105, 2014.

[209] L. F. Pease III and W. B. Russel, "Linear stability analysis of thin leaky dielectric films subjected to electric fields", *Journal of Non-Newtonian Fluid Mechanics*, **102**(2), 233–250, 2002.

[210] F. Li, O. Ozen, N. Aubry, and D. T. Papageorgiou, "Linear stability of a two-fluid interface for electrohydrodynamic mixing in a channel", *Journal of Fluid Mechanics*, **583**, 347–377, 2007.

[211] A. K. Uguz, O. Ozen, and N. Aubry, "Electric field effect on a two-fluid interface instability in channel flow for fast electric times", *Physics of Fluids*, **20**(3), 031702, 2008.

[212] L. Wu and S. Y. Chou, "Dynamic modeling and scaling of nanostructure formation in the lithographically induced self-assembly and self-construction", *Applied Physics Letters*, **82**(19), 3200–3202, 2003.

[213] D. Tseluiko and D. T. Papageorgiou, "Dynamics of an electrostatically modified Kuramoto–Sivashinsky–Korteweg–de Vries equation arising in falling film flows", *Physical Review E*, **82**(1), 016322, 2010.

[214] M. S. Keith, "Mathematical modelling of electrohydrodynamic flows", PhD thesis, University of Strathclyde, Glasgow, 2021.

[215] D. S. Pillai and R. Narayanan, "Nonlinear dynamics of electrostatic Faraday instability in thin films", *Journal of Fluid Mechanics*, **855**, R4, 2018.

[216] D. S. Pillai and R. Narayanan, "Electrostatic forcing of thin leaky dielectric films under periodic and steady fields", *Journal of Fluid Mechanics*, **890**, A20, 2020.

[217] R. J. Tomlin, R. Cimpeanu, and D. T. Papageorgiou, "Instability and dripping of electrified liquid films flowing down inverted substrates", *Physical Review Fluids*, **5**(1), 013703, 2020.

[218] A. W. Wray, O. K. Matar, and D. T. Papageorgiou, "Non-linear waves in electrified viscous film flow down a vertical cylinder", *IMA Journal of Applied Mathematics*, **77**(3), 430–440, 2012.

[219] A. W. Wray, D. T. Papageorgiou, and O. K. Matar, "Electrified coating flows on vertical fibres: enhancement or suppression of interfacial dynamics", *Journal of Fluid Mechanics*, **735**, 427–456, 2013.

[220] A. W. Wray, D. T. Papageorgiou, and O. K. Matar, "Electrostatically controlled large-amplitude, non-axisymmetric waves in thin film flows down a cylinder", *Journal of Fluid Mechanics*, **736**, R2, 2013.

[221] Q. Wang, S. Mählmann, and D. T. Papageorgiou, "Dynamics of liquid jets and threads under the action of radial electric fields: microthread formation and touchdown singularities", *Physics of Fluids*, **21**(3), 032109, 2009.

[222] Q. Wang and D. T. Papageorgiou, "Dynamics of a viscous thread surrounded by another viscous fluid in a cylindrical tube under the action of a radial electric field: breakup and touchdown singularities", *Journal of Fluid Mechanics*, **683**, 27–56, 2011.

[223] S. Sharma, B. Gupta, M. Pandey, A. K. Sharma, and R. N. Mishra, "Recent advancements in optimization methods for wind turbine airfoil design: a review", *Materials Today: Proceedings*, **47**(19), 6556–6563, 2021.

[224] P Zhao, J. Chen, Y. Song, X. Tao, T. Xu, and T. Mei, "Design of a control system for an autonomous vehicle based on adaptive-PID", *International Journal of Advanced Robotic Systems*, **9**(2), 44, 2012.

[225] S. Xu, H. Peng, and Y. Tang, "Preview path tracking control with delay compensation for autonomous vehicles", *IEEE Transactions on Intelligent Transportation Systems*, **22**(5), 2979–2989, 2021.

[226] B. Lian, H. Bang, and J. Hurtado, "Adaptive backstepping control based autopilot design for reentry vehicle", *European Conference on Life, AIAA Guidance, Navigation, and Control Conference and Exhibit*, 2004, 1210–1223.

[227] Y. Chen and Z. Lv, "A fractional optimal control model for a simple cash balance problem", *Communications in Nonlinear Science and Numerical Simulation*, **120**, 107194, 2023.

[228] M. D. Gunzburger, *"Perspectives in Flow Control and Optimization"*, Society for Industrial and Applied Mathematics, 2002.

[229] M. Sellier, "Inverse problems in free surface flows: a review", *Acta Mechanica*, **227**(3), 913–935, 2016.

[230] K. Pfeiffer, U. Schulz, A. Tünnermann, and A. Szeghalmi, "Antireflection coatings for strongly curved glass lenses by atomic layer deposition", *Coatings*, **7**(8), 118, 2017.

[231] Y. J. Du, M. Damron, G. Tang, H. Zheng, C.-J. Chu, and J. H. Osborne, "Inorganic/organic hybrid coatings for aircraft aluminum alloy substrates", *Progress in Organic Coatings*, **41**(4), 226–232, 2001.

[232] L. Geyao, D. Yang, C. Wanglin, and W. Chengyong, "Development and application of physical vapor deposited coatings for medical devices: a review", *Procedia CIRP*, **89**(2), 250–262, 2020.

[233] G. Karapetsas and V Bontozoglou, "The role of surfactants on the mechanism of the long wave instability in liquid film flows", *Journal of Fluid Mechanics*, **741**, 139–155, 2014.

[234] X.Y. Huang, "Feedback control of vortex shedding from a circular cylinder", *Experiments in Fluids*, **20**(3), 218–224, 1996.

[235] L. Soenksen, T. Kassis, M. Noh, L. Griffith, and D. Trumper, "Closed-loop feedback control for microfluidic systems through automated capacitive fluid height sensing", *Lab on a Chip*, **18**(6), 902–914, 2018.

[236] F. Ren, H.-B. Hu, and H. Tang, "Active flow control using machine learning: a brief review", *Journal of Hydrodynamics*, **32**(2), 247–253, 2020.

[237] J. Porter, P. S. Sanchez, V. Shevtsova, and V. Yasnou, "A review of fluid instabilities and control strategies with applications in microgravity", *Mathematical Modelling of Natural Phenomena*, **16**(207) 2021.

[238] A. E. Samoilova and A. Nepomnyashchy, "Nonlinear feedback control of Marangoni wave patterns in a thin film heated from below", *Physica D*, **412**, 132627, 2020.

[239] A. Glezer and M. Amitay, "Synthetic jets", *Annual Review of Fluid Mechanics*, **34**, 503–529, 2002.

[240] A. Armaou and P. D. Christofides, "Feedback control of the Kuramoto–Sivashinsky equation", *Physica D*, **137**(1–2), 49–61, 2000.

[241] A. Armaou and P. D. Christofides, "Wave suppression by nonlinear finite-dimensional control", *Chemical Engineering Science*, **55**(14), 2627–2640, 2000.

[242] P. D. Christofides and A. Armaou, "Global stabilization of the Kuramoto–Sivashinsky equation via distributed output feedback control", *Systems and Control Letters*, **39**(4), 283–294, 2000.

[243] E. Boujo and M. Sellier, "Pancake making and surface coating: optimal control of a gravity-driven liquid film", *Physical Review Fluids*, **4**(6), 064802, 2019.

[244] A. W. Wray, R. Cimpeanu, and S. N. Gomes, "Electrostatic control of the Navier–Stokes equations for thin films", *Physical Review Fluids*, **7**(12), L122001, 2022.

[245] E. Polak and G. Ribière, "Note sur la convergence de méthodes de directions conjuguées", *Revue française d'informatique et de recherche opérationnelle, Série rouge*, **3**(R1), 35–43 (in French), 1969.

[246] X. Wang, "Method of steepest descent and its applications", *IEEE Microwave and Wireless Components Letters*, **12**, 1–3, 2008.

[247] J. Kiefer, "Sequential minimax search for a maximum", *Proceedings of the American Mathematical Society*, **4**(3), 502–506, 1953.

[248] R. Fletcher and C. M. Reeves, "Function minimization by conjugate gradients", *The Computer Journal*, **7**(2), 149–154, 1964.

[249] N. Andrei, "Hybrid conjugate gradient algorithm for unconstrained optimization", *Journal of Optimization Theory and Applications*, **141**(2), 249–264, 2009.

[250] M. Hestenes and E. Stiefel, "Methods of Conjugate Gradients for Solving Linear Systems", *Journal of Research of the National Bureau of Standards*, **49**(6), 409–436, 1952.

[251] Y. H. Dai and Y. Yuan, "A nonlinear conjugate gradient method with a strong global convergence property", *SIAM Journal on Optimization*, **10**(1), 177–182, 1999.

[252] G. Yuan, Z. Wei, and Y. Yang, "The global convergence of the Polak–Ribière–Polyak conjugate gradient algorithm under inexact line search for nonconvex functions", *Journal of Computational and Applied Mathematics*, **362**, 262–275, 2019.

[253] J. A. Koupaei, S. M. M. Hosseini, and F. M. M. Ghaini, "A new optimization algorithm based on chaotic maps and golden section search method", *Engineering Applications of Artificial Intelligence*, **50**, 201–214, 2016.

[254] R. Shao, R. Wei, and L. Chang, "A multi-stage MPPT algorithm for PV systems based on golden section search method", *2014 IEEE Applied Power Electronics Conference and Exposition*, 2014, 676–683.

[255] R. O. Grigoriev, "Control of evaporatively driven instabilities of thin liquid films", *Physics of Fluids*, **14**(6), 1895–1909, 2002.

[256] M. Sellier and S. Panda, "Beating capillarity in thin film flows", *International Journal for Numerical Methods in Fluids*, **63**(4), 431–448, 2010.

[257] R. J. Tomlin, S. N. Gomes, G. A. Pavliotis, and D. T. Papageorgiou, "Optimal control of thin liquid films and transverse mode effects", *SIAM Journal on Applied Dynamical Systems*, **18**(1), 117–149, 2019.

[258] Y. Cao, M. Hussaini, and T. Zang, "Efficient Monte Carlo method for optimal control problems with uncertainty", *Computational Optimization and Applications*, **26**(3), 219–230, 2003.

[259] R. A. McKinlay, A. W. Wray, and S. K. Wilson, "Late-time draining of a thin liquid film on the outer surface of a circular cylinder", *Physical Review Fluids*, **8**(8), 084001, 2023.

[260] B. Kim, R. Kwak, H. J. Kwon, V. S. Pham, M. Kim, B. Al-Anzi, G. Lim, and J. Han, "Purification of high salinity brine by multi-stage ion concentration polarization desalination", *Scientific Reports*, **6**, 31850, 2016.

[261] L. R. B. Rebello, T. Siepman, and S. Drexle, "Correlations between TDS and electrical conductivity for high-salinity formation brines characteristic of South Atlantic pre-salt basins", *Water South Africa*, **46**(4), 602–609, 2020.

[262] J. Castillo-Rogez, B. Weiss, C. Beddingfield, J. Biersteker, R. Cartwright, A. Goode, M. M. Daswani, and M. Neveu, "Compositions and interior structures of the large moons of Uranus and implications for future spacecraft observations", *Journal of Geophysical Research: Planets*, **128**(1), e2022JE007432, 2023.

[263] X Zhang, Y. Yang, H. H. Ngo, W. Guo, H. Wen, X. Wang, J. Zhang, and T. Long, "A critical review on challenges and trend of ultrapure water production process", *Science of The Total Environment*, **785**, 147254, 2021.

[264] G. H. Aylward and T. J. V. Findlay, *"S.I. Chemical Data"*, 3rd ed., Wiley, 1994.

[265] Wolfram Research, Inc., *Mathematica, Version 13.1*, Champaign, IL, 2022, URL: `https://www.wolfram.com/mathematica`.

[266] C. Lamstaes and J. Eggers, "Arrested bubble rise in a narrow tube", *Journal of Statistical Physics*, **167**(3–4), 656–682, 2017.

[267] M. A. J. van Limbeek, B. Sobac, A. Rednikov, P. Colinet, and J. H. Snoeijer, "Asymptotic theory for a Leidenfrost drop on a liquid pool", *Journal of Fluid Mechanics*, **863**, 1157–1189, 2019.

[268] I. F. Edun and G. O. Akinlabi, "Application of the shooting method for the solution of second order boundary value problems", *Journal of Physics: Conference Series*, **1734**(1), 012020, 2021.

[269] D. Meade, S. Bala, and R. White, "The shooting technique for the solution of two-point boundary value problems", *Maple Tech*, **3**, 1–8, 1995.

[270] H. González, F. M. J. McCluskey, A. Castellanos, and A. Barrero, "Stabilization of dielectric liquid bridges by electric fields in the absence of gravity", *Journal of Fluid Mechanics*, **206**, 545–561, 1989.

[271] D. Xiao, *"Gas Discharge and Gas Insulation, Energy and Environment Research in China"*, 1st ed., Shanghai Jiao Tong University Press, Shanghai and Springer–Verlag Berlin Heidelberg, 2016.

[272] C. S. Yih, "Instability of a rotating liquid film with a free surface", *Proceedings of the Royal Society of London A*, **258**(1292), 63–89, 1977.

[273] C. Bender and S. Orszag, *"Advanced Mathematical Methods for Scientists and Engineers: Asymptotic Methods and Perturbation Theory"*, vol. 1, 1999, chap. Multiple-Scale Analysis, 544–569.

[274] P. G. de Gennes, "Wetting: statics and dynamics", *Reviews of Modern Physics*, **57**(3), 827–863, 1985.

[275] M. D. Morariu, N. E. Voicu, E. Schäffer, Z. Lin, T. P. Russel, and U. Steiner, "Hierarchical structure formation and pattern replication induced by an electric field", *Nature Materials*, **2**(1), 48–52, 2003.

[276] N. Arun, A. Sharma, P. S. G. Pattader, I. Banerjee, H. M. Dixit, and K. S. Narayan, "Electric-field-induced patterns in soft viscoelastic films: from long waves of viscous liquids to short waves of elastic solids", *Physical Review Letters*, **102**(25), 254502, 2009.

[277] T. R. Bewley, P. Moin, and R. Temam, "DNS-based predictive control of turbulence: an optimal benchmark for feedback algorithms", *Journal of Fluid Mechanics*, **447**, 179–225, 2001.

[278] C. Ruyer–Quil, B. Scheid, S. Kalliadasis, M. Velarde, and R. Zeytounian, "Thermocapillary long waves in a liquid film flow. Part 1. Low-dimensional formulation", *Journal of Fluid Mechanics*, **538**, 1–24, 2005.

[279] O. E. Jensen and J. B. Grotberg, "The spreading of heat or soluble surfactant along a thin liquid film", *Physics of Fluids*, **5**(1), 58–68, 1993.

[280] K. L. Maki and S. Kumar, "Fast evaporation of spreading droplets of colloidal suspensions", *Langmuir*, **27**(18), 11347–11363, 2011.

[281] G. Guennebaud and B. Jacob, *Eigen v3*, http://eigen.tuxfamily.org, 2010.